



HAL
open science

Getting inside the Galaxy history through stellar spectroscopy

Linda Lombardo

► **To cite this version:**

Linda Lombardo. Getting inside the Galaxy history through stellar spectroscopy. Astrophysics [astro-ph]. Université Paris sciences et lettres, 2022. English. NNT : 2022UPSLO011 . tel-04205118

HAL Id: tel-04205118

<https://theses.hal.science/tel-04205118>

Submitted on 12 Sep 2023

HAL is a multi-disciplinary open access archive for the deposit and dissemination of scientific research documents, whether they are published or not. The documents may come from teaching and research institutions in France or abroad, or from public or private research centers.

L'archive ouverte pluridisciplinaire **HAL**, est destinée au dépôt et à la diffusion de documents scientifiques de niveau recherche, publiés ou non, émanant des établissements d'enseignement et de recherche français ou étrangers, des laboratoires publics ou privés.



THÈSE DE DOCTORAT

DE L'UNIVERSITÉ PSL

Préparée à Observatoire de Paris,
GEPI, CNRS

Getting inside the Galaxy's history through stellar spectroscopy

Soutenue par

Linda Lombardo

Le 24 Novembre 2022

École doctorale n°127

**Astronomie et Astrophysique
d'Île-de-France**

Spécialité

Astronomie et Astrophysique

Composition du jury :

Yveline Lebreton LESIA, Observatoire de Paris	<i>Président</i>
Sophie Van Eck Université libre de Bruxelles	<i>Rapporteur</i>
Marcella Marconi Osservatorio astronomico di Capodimonte	<i>Rapporteur</i>
Céline Reylé Institut UTINAM, CNRS	<i>Examineur</i>
Norbert Christlieb University of Heidelberg	<i>Examineur</i>
Piercarlo Bonifacio GEPI, Observatoire de Paris, CNRS	<i>Directeur de thèse</i>
Patrick François GEPI, Observatoire de Paris	<i>Co-directeur de thèse</i>
Alessio Mucciarelli University of Bologna	<i>Invité</i>

Jump off the cliff and learn how to make wings on the way down.

—Ray Bradbury, one-day symposium on 'Future Style'
University of California, Irvine, October 1986

Résumé

Ce travail de thèse présente plusieurs études qui utilisent la spectroscopie à haute résolution pour déterminer les propriétés chimiques des différentes populations stellaires de la Voie Lactée. Le document est structuré comme suit :

- Le premier chapitre de la thèse, divisée en 3 sections, est une introduction générale à la structure de la Voie lactée et à ses populations stellaires, suivie d'une partie décrivant les différentes méthodes utilisées pour mesurer les abondances chimiques des étoiles. La première section décrit les différents scénarios concernant la structure et la formation de la Voie Lactée, en présentant en particulier les découvertes les plus récentes. La deuxième section introduit les concepts physiques de base nécessaires et les objectifs des études présentes dans ce travail de thèse. La troisième section décrit les méthodes utilisées dans l'analyse des données spectroscopiques.
- Le deuxième chapitre présente les travaux effectués dans la cadre du projet MINCE. La première étude concerne l'analyse de la composition chimique d'un échantillon d'étoiles géantes jeunes qui ont été découvertes par hasard au cours des premières missions d'observations du projet MINCE. J'ai déterminé les paramètres stellaires, analysé les spectres, mesuré les vitesses de rotation de ces étoiles et comparé les résultats aux modèles théoriques, en reportant tous ces résultats dans un article. La deuxième étude présente les résultats obtenus par l'analyse du premier échantillon d'étoiles propres au projet MINCE. J'ai contribué à l'analyse d'une partie des spectres stellaires de ce tout premier jeu de spectres MINCE.
- Le troisième chapitre porte sur les résultats d'une analyse faite dans le contexte du projet CERES. La première partie de ce travail présente une détermination détaillée de la composition chimique de l'étoile RAVE J110842.1-715300, dont le but est de savoir si cette étoile provient de l'amas globulaire Omega Centauri. Ma contribution porte sur la détermination des paramètres stellaires de cette étoile. La deuxième étude menée dans le contexte de ce projet CERES est constituée de l'analyse d'un échantillon d'étoiles. J'ai déterminé les paramètres stellaires, calculé les modèles d'atmosphère et les abondances chimiques, et écrit l'article.
- Le quatrième chapitre porte sur un travail fait dans le contexte du projet "High-speed stars" s'intéressant aux étoiles à grande vitesse transversales héliocentriques (≥ 500 km/s). La première étude porte sur le suivi spectroscopique à haute résolution de deux étoiles jeunes et pauvres en métaux de l'échantillon de Caffau et al. (2020), afin de déterminer si ces étoiles sont des "blue stragglers". J'ai obtenu et analysé les spectres UVES de ces deux étoiles. Les résultats ne sont pas encore

publiés. La deuxième étude concerne une analyse détaillée de deux étoiles à grande vitesse observées avec le spectrographe HDS au télescope Subaru. Pour cette étude, j'ai déterminé l'abondance du Carbone.

- Le cinquième chapitre présente les résultats obtenus à partir de l'analyse d'un échantillon d'étoiles sélectionnées au moyen de la photométrie de PRISTINE. La première étude porte sur la détermination de la composition chimique d'un échantillon d'étoiles qui ont pu être enrichies par les éjectae de l'explosion de supernovae à instabilité de paires. Mon travail a consisté à sélectionner les candidats les plus intéressants, puis d'effectuer une mission d'observation avec le spectrographe SOPHIE à l'Observatoire de la Haute Provence (OHP). La deuxième étude présente les résultats préliminaires de la détermination de la composition chimique d'un échantillon d'étoiles Pristine sélectionnées comme extrêmement pauvres en métaux. Mon travail a porté sur la détermination des paramètres stellaires et le calcul des abondances chimiques. Un article est en préparation.
- Le sixième chapitre présente les conclusions de ce travail de thèse et apporte quelques réflexions sur les projets à venir.

Abstract

This thesis project presents several studies that are focused on the investigation of the chemical properties of different stellar populations in the Milky Way by means of high-resolution spectroscopy. The thesis is structured as follows:

- The first chapter is an introduction to the thesis project, and is divided into three sections. The first section describes the structure and formation scenarios of the Milky Way, in particular by referring to the most recent discoveries. The second section introduces the basic concepts and objectives of the studies presented in this thesis work. The third section describes the methods used to analyse the spectroscopic data.
- The second chapter presents the studies carried out in the context of the MINCE project. The first study is devoted to the chemical analysis of a sample of young giant stars that was serendipitously discovered during the first MINCE observations. My contribution in this work was to derive the stellar parameters, analyse the spectroscopic data, measure the rotational velocities, compare the results with theoretical models and write the paper. The second study presents the results obtained from the analysis of the first sample of MINCE stars. In this work, I contributed to the analysis of some of the stars in the sample.
- The third chapter presents the results obtained in the context of the CERES project. The first study presents a detailed chemical analysis of the star RAVE J110842.1-715300, with the aim of understanding whether or not it originated in the Omega Centauri globular cluster. My contribution in this study was to derive the stellar parameters of the star. The second study presents the results obtained for the CERES star sample. My contribution was to derive the parameters, compute model atmospheres, measure the chemical abundances, and write the paper.
- The fourth chapter presents the results obtained in the context of the High-speed stars project. The first study reports the results obtained from the high-resolution follow-up of two young and metal-poor stars in the sample of Caffau et al. (2020), to check whether they are blue stragglers or not. My contribution in this study was to obtain the high-resolution observations with UVES and to analyse the data. These results have not been published yet. The second study presents a detailed analysis of two high-speed stars observed with Subaru. In this study I was involved in the C abundance determination.
- The fifth chapter presents the results obtained from the chemical analysis of samples of stars selected using the Pristine photometry. The first study presents the chem-

ical analysis of a sample of metal-poor stars that may have been enriched by the explosion of pair instability supernovae. My contribution was to select promising candidates and observe them with the SOPHIE spectrograph at Observatoire de la Haute Provence (OHP) in visitor mode. The second study presents the preliminary results obtained from the chemical analysis of a sample of Pristine extremely metal-poor candidates. My contribution in this study was to derive the stellar parameters and the chemical abundances. The paper is in preparation.

- The sixth chapter concludes the thesis and gathers final reflections and future projects.

Contents

1	Introduction	1
1.1	The Milky Way: a modern view	2
1.1.1	Main characteristics	2
1.1.2	Formation scenarios	4
1.2	Galactic Archaeology	8
1.2.1	Understanding the chemical evolution of the Galaxy	8
1.2.2	Searching for the most metal-poor stars in the Galaxy	11
1.3	From spectra to chemical abundances	13
1.3.1	Modelling the stellar photosphere	13
1.3.2	Measuring chemical abundances	15
2	MINCE survey	19
2.1	Young giants of intermediate mass	20
2.1.1	Target selection	21
2.1.2	Possible binary stars	23
2.1.3	Main results	23
2.1.4	Ba enhancement	26
2.2	MINCE I	29
3	CERES survey	31
3.1	Purveyors of fine halos III	31
3.2	CERES I	32
3.2.1	Stellar parameters	33
3.2.2	Line broadening	34
3.2.3	Main results	35
4	High-speed stars	41
4.1	A young metal-poor population in the Galactic halo?	42
4.1.1	Observations	44
4.1.2	Li abundance	45
4.1.3	Discussion and conclusions	48
4.2	Detailed investigation of two high-speed Galactic stars	50
5	PRISTINE survey	55
5.1	Pristine XIX	55
5.2	Pristine XXI	57
5.2.1	Target selection & observations	57

5.2.2	Radial velocities	58
5.2.3	Chemical abundances	58
5.2.4	Variable stars	59
5.2.5	Discussion and conclusions	63
6	Conclusion and future perspectives	65
A	Appendix of Pristine XXI	69

List of Figures

1.1	The Milky Way and its various components	3
1.2	Colour-magnitude diagram from Gaia DR2	6
1.3	Different substructures in the distribution of stars within 3 kpc of the Sun	7
1.4	Periodic table colour-coded by the origin of the elements in the solar system.	9
2.1	Abundance ratios in metal-poor stars versus Galactic chemical evolution models	19
2.2	Gaia colour-magnitude diagram for young intermediate-mass giants	21
2.3	Strömgren colour-magnitude diagram for young intermediate-mass giants.	22
2.4	Histogram of metallicities from Casagrande calibration	22
2.5	[C/Fe], [N/Fe], [O/Fe], and [(C + N + O)/Fe] abundances versus [Fe/H]	25
2.6	Log T_{eff} versus log g diagrams	26
2.7	[Y/Fe] and [Ba/Fe] abundance ratios versus [Fe/H]	27
2.8	MINCE spectra	29
3.1	Iterative procedure for deriving stellar parameters	33
3.2	v_{broad} versus FWHM relation	35
3.3	Stellar parameters and comparison with the literature	36
3.4	[CrI/FeI] and [CrII/FeII] versus [Fe/H] for stars in our sample	37
3.5	[CrI/FeI] and [CrII/FeII] versus [Fe/H] for stars in the studies presented in this thesis	37
3.6	[Zn/Fe] versus [Fe/H]	38
3.7	Kinetic energy versus main-sequence mass and [Zn/Fe] versus [Ni/Fe]	39
3.8	Normalised spectra of stars CES1237+1922 and CES1322–1355	40
4.1	Gaia colour-magnitude diagram for high speed stars	42
4.2	Spite plateau	43
4.3	Spectra of Blue Straggler stars in the region of the Li 6707 doublet.	44
4.4	Gaia colour-magnitude diagram for Li-depleted stars	45
4.5	Li abundance evolution as a function of time for Blue Stragglers	46
4.6	Spectra of GHS69 in the region of the Li 6707 doublet.	47
4.7	Spectra of GHS70 in the region of the Li 6707 doublet.	47
4.8	Spectra of GHS70 and BD+20 3603 in the region of the Li 6707 doublet.	48
4.9	V mag versus T_{eff} for stars in NGC 2243	49
4.10	Mass of Li dip cool-side versus open cluster’s metallicity	50
4.11	[Fe/H] distribution for high-speed stars	51
4.12	Action diamond diagram	52

5.1	Pristine Ca II H&K filter	56
5.2	Pristine colour-colour diagram for our selected targets.	57
5.3	The region of Mg I b triplet in star Pristine_159.5695+57.1688.	59
5.4	[Mg/Fe] and [Ca/Fe] versus [Fe/H] for our sample of stars	60
5.5	[Sc/Fe] and [Ba/Fe] versus [Fe/H] for our sample of stars	61
5.6	Ca II H&K lines of Pristine_148.3782+53.0957	62
5.7	H α emission in one of the two spectra of Pristine_326.5701+19.2445	62

List of Tables

2.1	Comparison between Gaia DR2, Gaia DR3 and measured radial velocities .	24
A.1	Log of the observations	70
A.2	Radial velocities for SB2 binaries	71
A.3	Stars observed with ESPaDoNS in period 20B	72
A.4	Derived stellar parameters for chemically analysed stars.	72
A.5	Derived chemical abundances for analysed stars.	73

Chapter 1

Introduction

Galactic archaeology is the field of astrophysics devoted to the study of the formation and evolution of the Milky Way and galaxies that can be resolved in stars, through the properties of their stellar populations. In recent years, Galactic archaeology has made a huge step forward thanks to the advent of the Gaia mission ([Gaia Collaboration et al. 2016, 2018b, 2021, 2022](#)) and the great availability of stellar spectra from large spectroscopic surveys, such as SDSS/SEGUE ([Yanny et al. 2009a](#)), SDSS/APOGEE ([Majewski et al. 2017](#)), GALAH ([De Silva et al. 2015](#)), RAVE ([Boeche et al. 2011](#)), LAMOST ([Deng et al. 2012](#)), which have revolutionised our understanding of the structure of our Galaxy. The combination of the chemical information from high-resolution spectroscopy with photometry, distances, and kinematics provided by Gaia is an excellent tool not only for investigating the formation history of our Galaxy, but also for increasing our understanding of the physical mechanisms and production sites of elements as well as the chemical evolution of stellar populations in the Milky Way and in nearby galaxies.

This thesis project presents several studies that are focused on the investigation of the chemical properties of different stellar populations in the Milky Way by means of high-resolution spectroscopy. The thesis is structured as follows:

- The first chapter is an introduction to the thesis project, and is divided into three sections. The first section describes the structure and formation scenarios of the Milky Way, in particular by referring to the most recent discoveries. The second section introduces the basic concepts and objectives of the studies presented in this thesis work. The third section describes the methods used to analyse the spectroscopic data.
- The second chapter presents the studies carried out in the context of the MINCE project. The first study is devoted to the chemical analysis of a sample of young giant stars that was serendipitously discovered during the first MINCE observations. My contribution in this work was to derive the stellar parameters, analyse the spectroscopic data, measure the rotational velocities, compare the results with theoretical models and write the paper. The second study presents the results obtained from the analysis of the first sample of MINCE stars. In this work, I contributed to the analysis of some of the stars in the sample.
- The third chapter presents the results obtained in the context of the CERES project. The first study presents a detailed chemical analysis of the star RAVE J110842.1-

715300, with the aim of understanding whether or not it originated in the Omega Centauri globular cluster. My contribution in this study was to derive the stellar parameters of the star. The second study presents the results obtained for the CERES star sample. My contribution was to derive the parameters, compute model atmospheres, measure the chemical abundances, and write the paper.

- The fourth chapter presents the results obtained in the context of the High-speed stars project. The first study reports the results obtained from the high-resolution follow-up of two young and metal-poor stars in the sample of Caffau et al. (2020b), to check whether they are blue stragglers or not. My contribution in this study was to obtain the high-resolution observations with UVES and to analyse the data. These results have not been published yet. The second study presents a detailed analysis of two high-speed stars observed with Subaru. In this study I was involved in the C abundance determination.
- The fifth chapter presents the results obtained from the chemical analysis of samples of stars selected using the Pristine photometry. The first study presents the chemical analysis of a sample of metal-poor stars that may have been enriched by the explosion of pair instability supernovae. My contribution was to select promising candidates and observe them with the SOPHIE spectrograph in visitor mode. The second study presents the preliminary results obtained from the chemical analysis of a sample of Pristine extremely metal-poor candidates. My contribution in this study was to derive the stellar parameters and the chemical abundances. The paper is in preparation.
- The sixth chapter concludes the thesis and gathers final reflections and future projects.

1.1 The Milky Way: a modern view

1.1.1 Main characteristics

The comparison with the global properties of other observable galaxies shows the Milky Way is a typical barred spiral galaxy (Bland-Hawthorn & Gerhard 2016), with a total mass of $\sim 7 \times 10^{11} M_{\odot}$ (Eilers et al. 2019) and a luminosity close to L_* , where L_* is the characteristic galaxy luminosity of the Schechter luminosity function¹ (Schechter 1976). The Milky Way has several visible components, as shown in Fig. 1.1, which differ not only in their spatial distribution, but also in their kinematics, ages and chemical distributions.

Bar/Bulge

The innermost component is the bar/bulge, which is characterised by a triaxial structure in rotation (boxy/peanut shape). The bulk of its stars is predominantly old (≥ 10 Gyr) and spans a metallicity range of $-1.5 < [\text{Fe}/\text{H}] < +0.5$, where only the more metal rich stars ($[\text{Fe}/\text{H}] > -0.5$) contribute to the boxy/peanut structure (Barbuy et al. 2018).

¹The Schechter luminosity function is $\varphi(L)dL = \varphi^*(L/L^*)^\alpha \exp(-L/L^*)d(L/L^*)$, where φ^* is a number per unit volume and L^* is the "characteristic luminosity".

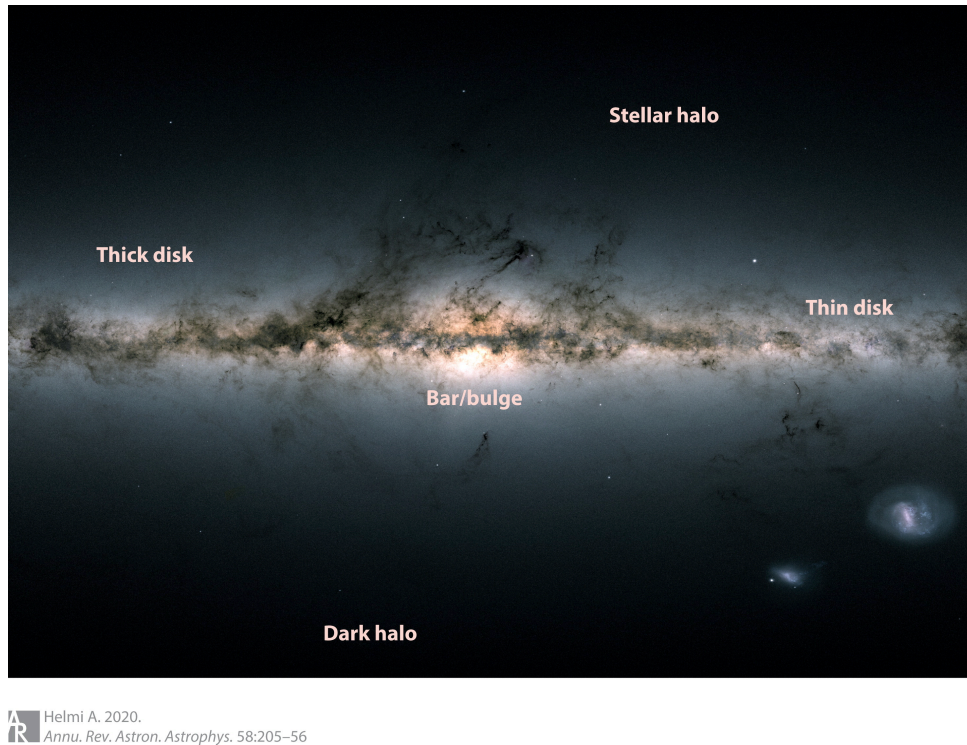


Figure 1.1: The Milky Way and its various components. This image was obtained using data from the second data release of the Gaia mission (Gaia Collaboration et al. 2018b). Figure from Helmi (2020).

Thin and thick disc

The characteristic component of our Galaxy, which also defines it as a spiral galaxy, is the disc, which is itself divided into two components, the thin and the thick disc. Gilmore & Reid (1983) distinguished these two components by demonstrating that, to fit the stellar distribution perpendicular to the Galactic disc, two exponential profiles with different scale heights² were required, one with a scale height of ~ 300 pc (thin disc) and the other with a scale height of ~ 1.5 kpc (thick disc). The thin disc is the most massive stellar component and the present star formation site of our Galaxy, most of its stars are on circular orbits, with ages $\sim 2-7$ Gyr and metallicities $[\text{Fe}/\text{H}] \gtrsim -0.7$ dex. The thick disc is the thicker, more diffuse and hotter component of the Galactic disc. Its stars are kinematically hotter, with lower rotational speeds and higher velocity dispersion, older ($\sim 10-12$ Gyr), and more metal-poor ($[\text{Fe}/\text{H}] \lesssim -0.4$) than thin disc stars (see e.g. Bensby et al. 2014). The two components are also characterised by different chemical compositions, particularly in the $[\alpha/\text{Fe}]$ abundance ratios, with the thick disc stars being $[\alpha/\text{Fe}]$ enhanced, and the thin disc ones having $[\alpha/\text{Fe}] \approx 0$, as showed by several spectroscopic studies of the Solar neighborhood stars (Fuhrmann 1998; Bensby et al. 2003; Fuhrmann 2011; Adibekyan et al. 2013; Bensby et al. 2014).

²Given the stellar distribution on z -axis described by the exponential law $n(z) \propto \exp\left(-\frac{|z|}{h}\right)$, h is the scale height, that specifies the thickness of the component.

Stellar halo

The most extended component of the Galaxy is the stellar halo, which has a very steep and centrally concentrated density profile (see e.g. [Deason et al. 2011](#)). The halo contains old (~ 12 Gyr) and metal-poor stars, with a mean metallicity of $\langle [\text{Fe}/\text{H}] \rangle = -1.5$ ([Deason et al. 2019](#)), both as field stars, characterised by random motions, and in globular clusters. It also contains the debris of disrupted galaxies and globular clusters accreted by the Milky Way. This debris are detectable as stellar streams (see e.g. [Ibata et al. 2021](#), and references therein).

Other components

The Milky Way has also a system of globular clusters, which is not an homogeneous population, in either chemical or dynamical sense. Globular clusters are self-gravitating systems of stars that are characterised by being compact, with a half-light radius typically from 3 to 5 pc, bright, with a mean absolute visual magnitude ~ -7 , and old, ages ~ 10 Gyr (see e.g. [Gratton et al. 2019](#), and references therein). They are present in the halo, in the thick disc, and in the bar/bulge, but not in the thin disc. They may have been formed in-situ or have been accreted (see e.g. [Searle & Zinn 1978](#); [Gaia Collaboration et al. 2018c](#); [Myeong et al. 2018](#)).

The Galaxy also contains a gaseous component in the form of cold gas, predominantly in the disc, and warm ionised gas in the halo ([Richter 2017](#)) and circumgalactic medium ([Zheng et al. 2019](#)). In addition to the visible component, the Milky Way, similarly to other galaxies, has a dark matter halo, in which most of the mass of the system lies, and hosts a supermassive black hole at its centre, Sagittarius A*, which was finally observed by the Event Horizon telescope in 2017 ([Event Horizon Telescope Collaboration et al. 2022](#)), after its discovery as a bright radio source near the Galactic centre in 1974 ([Balick & Brown 1974](#); [Ekers et al. 1975](#); [Lo et al. 1975](#)).

1.1.2 Formation scenarios

According to the Λ -cold dark matter (Λ CDM) model (see e.g. the review by [Frenk & White 2012](#)), during the processes of collapse and formation of the dark matter halo, baryonic matter is attracted into the dark halo, and falls into its potential well. If the physical conditions (temperature of the gas, dark halo mass etc.) are able to hold the gas within the dark halo, then the gas can cool and form stars. During collapse and cooling, the gas may retain some of its angular momentum, thus giving rise to a rotationally supported disc ([Mo et al. 1998](#)), in which the stars will start to form. In such scenario, dark matter halos are embedded in a network of filaments, and massive halos form through hierarchical merging. Once they are formed, proto-galaxies can accrete further mass (dark and baryonic) through mergers, which were very frequent in the past due to the high density of the early Universe, and through stream of cold gas along the filaments, that can reach the central region of the dark halo and feed the disc growth ([Dekel et al. 2009](#)).

The canonical formation scenario of the Milky Way, or Eggen, Lynden-Bell & Sandage (ELS) scenario ([Eggen et al. 1962](#)), assumes that the Galaxy formed with a rapid ($\sim 10^8$ years) radial collapse of the proto-galactic cloud, followed by an equally rapid formation of a rotating disc. This scenario predicts a smooth distribution of stars and the mod-

elling of the Galaxy into distinct components: the bar/bulge, the thin disc, the thick disc, and the halo. The ELS scenario was initially challenged in the seminal work of [Searle & Zinn \(1978\)](#), who suggested that the Galactic Halo was formed by the merger of small “fragments”, each with its own chemical history. A major blow to ELS came from the discovery of complex substructures in the Galactic stellar distribution, such as the Sagittarius dwarf ([Ibata et al. 1994, 1995](#)) and associated stellar stream ([Ibata & Lewis 1998; Johnston et al. 1999](#)), and culminating with the discovery of the Gaia-Sausage-Enceladus (GSE) accretion ([Belokurov et al. 2018; Deason et al. 2018; Haywood et al. 2018; Helmi et al. 2018](#)).

How the different Galactic components formed is still matter of debate, since several formation scenarios seem to be able to explain some of their properties. Certainly, a merger event has the ability to profoundly change the structure of the interacting galaxies, and it may also be able to partially explain the various components that we observe in the Milky Way. Numerical simulations show that in disc galaxies, a merger could lead to the formation of the bulge ([Barnes 1992](#)) and the thickening of the disc ([Quinn et al. 1993](#)), depending on the mass ratio between the galaxies. The bar might form as a result of disc instabilities triggered by the merger ([Gerin et al. 1990](#)). This might be the case of the Milky Way, although it is not clear whether the stars in the bar/bulge comes from the thin disc ([Martinez-Valpuesta & Gerhard 2013](#)), or from the thick disc (see e.g. [Di Matteo et al. 2015; Fragkoudi et al. 2018](#), and references therein). The merger might also have led to the formation of the stellar halo from the migration of the stars of the primordial disc and those of the destroyed satellite ([Zolotov et al. 2009; Purcell et al. 2010](#)).

The studies presented in this thesis project are focused on the chemistry of stars in the halo and in the disc, so the following paragraphs report the most recent discoveries solely for these two components. Regarding the bulge/bar, I recommend the reviews by [Barbu et al. \(2018\)](#) and [Zoccali \(2019\)](#).

Inner halo or heated thick disc?

Our understanding of the Galaxy’s inner halo has profoundly changed since the Gaia DR2 release ([Gaia Collaboration et al. 2018a](#)), and, in particular, since the discovery that most of the halo stars in the solar neighbourhood (within 2.5 kpc from the Sun) belong to the debris of a single progenitor satellite, the GSE, that was accreted by the Milky Way around 10 Gyr ago ([Belokurov et al. 2018; Deason et al. 2018; Haywood et al. 2018; Helmi et al. 2018](#)). The remaining stars in the vicinity of the Sun belong instead to the thick disc, which were probably dynamically heated during the merger event ([Gaia Collaboration et al. 2018a; Haywood et al. 2018; Koppelman et al. 2018; Helmi et al. 2018; Di Matteo et al. 2019](#)). This separation between GSE and thick disc stars is clearly visible from the Gaia colour-magnitude diagram for stars selected with halo-like kinematics (with tangential velocities above 200 km s^{-1} (Fig. 1.2 , [Gaia Collaboration et al. 2018a](#)), where the stars in the metal-poor sequence likely belong to GSE.

The GSE candidates can be disentangled from thick disc stars due to their kinematics, as they show slightly retrograde orbits, while thick disc stars are in prograde orbits (see e.g. [Koppelman et al. 2018; Helmi et al. 2018; Di Matteo et al. 2019](#)). They also appear to have lower $[\alpha/\text{Fe}]$ abundance ratios compared to thick disc stars, which suggests an accreted origin ([Helmi et al. 2018; Haywood et al. 2018](#)). The presence of a population with retrograde orbits and low $[\alpha/\text{Fe}]$ was reported by [Nissen & Schuster \(2010, 2011\)](#),

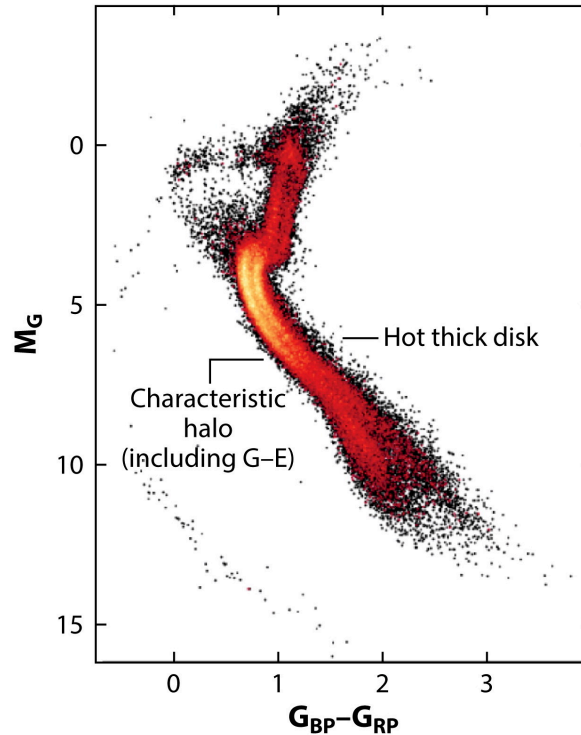


Figure 1.2: Colour-magnitude diagram from [Gaia Collaboration et al. \(2018a\)](#) that reveals two distinct sequences in a sample of stars kinematically selected to belong to the halo (with tangential velocities above 200 km s^{-1}). Figure adapted from [Helmi \(2020\)](#).

who also suggested an accreted origin.

These evidences show us that thinking of the stellar halo and the thick disc as separate entities is incorrect, at least as far as the inner part of the halo is concerned. Furthermore, the fact that, in the vicinity of the Sun, stars kinematically associated with the halo belong partly to the GSE and partly to the heated thick disc, could lead to think that there is no halo component formed in situ, as suggested by [Di Matteo et al. \(2019\)](#). This scenario is supported by the continuity of the kinematical and chemical properties of the stars over the entire metallicity range, as shown in [Di Matteo et al. \(2020\)](#).

From primordial disc to thick and thin disc

The formation history of the thick disc is still debated, mostly because it seems to depend heavily on the type of observations that are used to derive its properties, as discussed by [Kawata & Chiappini \(2016\)](#). Among the various formation scenarios, the one that is consistent with the Gaia DR2 observations assumes that the Galactic primordial disc formed part of its stars before merging with Gaia-Sausage-Enceladus, then the merger triggered the star formation that formed most of the thick disc stars, and dynamically heated the stars of the primordial disc into halo orbits ([Gallart et al. 2019](#)). After the merger event, about 8-6 Gyr ago, the gas cooled and formed the thin disc, which has continued to form stars to the present day ([Gallart et al. 2019](#)). This scenario is supported by both simulations ([Brook et al. 2004](#)) and chemical abundances of the stars in the disc ([Haywood et al. 2015, 2016](#)). In this context, some of the stars that formed in the proto-

Milky Way, so before the merger event, should be found in the thick disc, and should be characterised by extremely low metallicities. [Sestito et al. \(2019\)](#), in their sample of ultra-metal-poor stars with $[\text{Fe}/\text{H}] < -4$, found that a fraction of these stars are characterised by thick-disc kinematics. A similar result was found by [Di Matteo et al. \(2020\)](#) from the kinematics of the ESO Large Program "First stars", a sample of very metal-poor field giants and turnoff stars, with $-4.2 < [\text{Fe}/\text{H}] < -2$. These evidences further supports this formation scenario.

Substructures in the halo and thick disc: are they real debris of disrupted galaxies?

In the past decades, particularly after the discovery of the Sagittarius dwarf galaxy ([Ibata et al. 1994, 1995](#)), many efforts have been made to search for kinematic substructures in the stellar halo, but also in the thick disc, that could reveal the accretion history of the Milky Way. The search for stellar overdensities and streams also received a huge boost after Gaia DR2, thanks to the availability of precise measurements of the distances and proper motions of stars. Among the structures discovered, there is the substructure that is associated with the debris of a dwarf galaxy called "Sequoia" ([Myeong et al. 2019](#); [Koppelman et al. 2019](#)). Sequoia stars are characterised by retrograde motions, with less eccentric orbits and lower metallicities than the GSE, as shown in Fig. 1.3. [Koppelman et al. \(2019\)](#) reported that the lower $\sqrt{v_R^2 + v_Z^2}$ region of the diagram in Fig. 1.3, which is occupied by candidate stars of Sequoia, is likely part of a different structure, named "Thamnos".

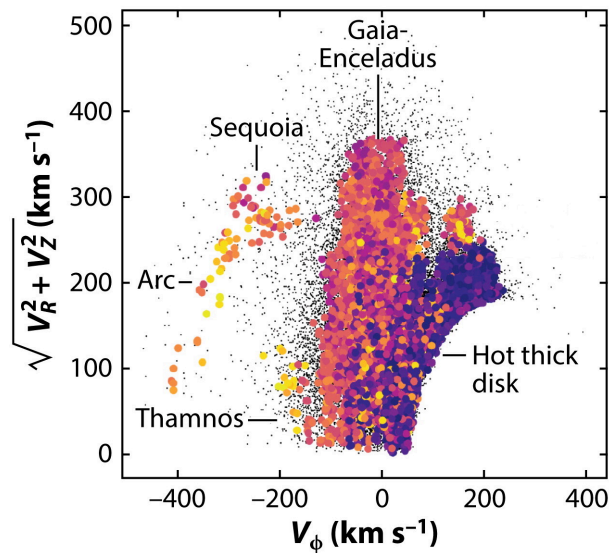


Figure 1.3: Distribution of stars within 3 kpc of the Sun kinematically selected to belong to the halo in [Koppelman et al. \(2019\)](#) and identified in different substructures. The colour code represent the metallicity of the stars. Figure adapted from [Helmi \(2020\)](#).

It is interesting to note that Sequoia candidates lie in the region occupied by the "arc" structure, which is assigned to GSE according to numerical simulations. This is due to the fact that, if GSE had a metallicity gradient, part of the metal-poor stars in the outskirts

of GSE would be pushed on more retrograde orbits, similar to that of Sequoia stars. It is therefore possible that the stars in retrograde orbits that we observe do not actually belong to Sequoia, but they could be the accelerated GSE stars, or the arc structure could contain a mixture of GSE and Sequoia stars.

These evidences highlight the difficulty of determining the origin of the Galactic substructures, and the impossibility of achieving that based solely on the stars kinematics, as discussed extensively in [Jean-Baptiste et al. \(2017\)](#). In conclusion, to reconstruct the Milky Way accretion history, we need a large amount of accurate spectroscopic data, which must be complemented by an equally accurate analysis of the kinematical properties.

1.2 Galactic Archaeology

Although the different properties of the Galactic components might suggest that these formed independently from one another, the Milky Way is actually a complex and dynamic system, whose structure is the result of interactions with other galaxies. In order to understand how our Galaxy and its components formed, we must study the properties of the stellar populations that constitute it, as they contain the memory of the environment in which they formed. The field of astrophysics that deals with that is called Galactic Archaeology. The following sections provide an introduction to the Galactic archaeology studies that are presented in this thesis work.

1.2.1 Understanding the chemical evolution of the Galaxy

As shown in the previous section, the most effective way to study the formation and evolution of the Galaxy is to combine the kinematics with the detailed chemical composition of the stars. Kinematics allow us to understand where stars were formed, since the memory of their origin is imprinted in their proper motions. In the case of an axisymmetric galaxy, a trajectory, or orbit, can be characterised by the integrals of motions, such as the total energy E , or the actions³ J_Z , J_R , L_Z .

During a merger event, the accreted galaxy is disrupted by tidal forces, but its stars maintain the trajectories they had in the galaxy in which they formed. In small galaxies, the orbits of stars are similar and, if these are conserved over time, the tidally stripped stars will maintain similar orbits, thus forming a stellar stream ([Helmi et al. 1999](#)). For more massive objects, the tidal forces act in the same way, but the stars have a larger variety of orbits, given the higher complexity of the galaxy structure, so the stripped stars will occupy a larger region in the kinematic space, eventually overlapping with the populations formed in situ. Furthermore, a merger event with a mass ration of 1:10, like the GSE, can modify the motions of in situ (or accreted) stars and create groups in the kinematic space, as discussed in [Jean-Baptiste et al. \(2017\)](#).

³The action for the i^{th} coordinate of a dynamical system is defined as $J_i = \oint p_i dq_j$ (see e.g. [Goldstein 1950](#)). In our case the coordinates q_i are the cylindrical coordinates (R, z, ϕ) and as momenta we take the velocities, i.e. the derivatives with respect to time of the coordinates. The actions are then denoted as (J_r, J_z, J_ϕ) . J_ϕ is the angular momentum in the direction of z and can be alternatively denoted as L_z . Note that in these definitions the mass of the star is absent in the definition of p_i . One should therefore talk about “specific angular momentum”, “specific energy”, etc. In the literature the “specific” is generally omitted, and in the text we shall follow this convention.

Therefore, it is not possible to distinguish between an accreted or in situ origin by only assigning stars to kinematically associated groups, but we need to complement the information we get from kinematics with the one from chemical abundances. As stars born together have similar abundance patterns, if a population has been accreted, it would show an abundance pattern that is different from that of the populations in the host galaxy, making it possible to identify accreted substructures following a merger event (Freeman & Bland-Hawthorn 2002).

Stars at different metallicities show a wide variety of chemical abundance patterns because their constituent elements were synthesized in different environments and on different timescales (McWilliam 1997). Since different elements have different nucleosynthetic channels, formation sites and timescales, chemical abundances reveal to us the chemical evolution of galaxies.

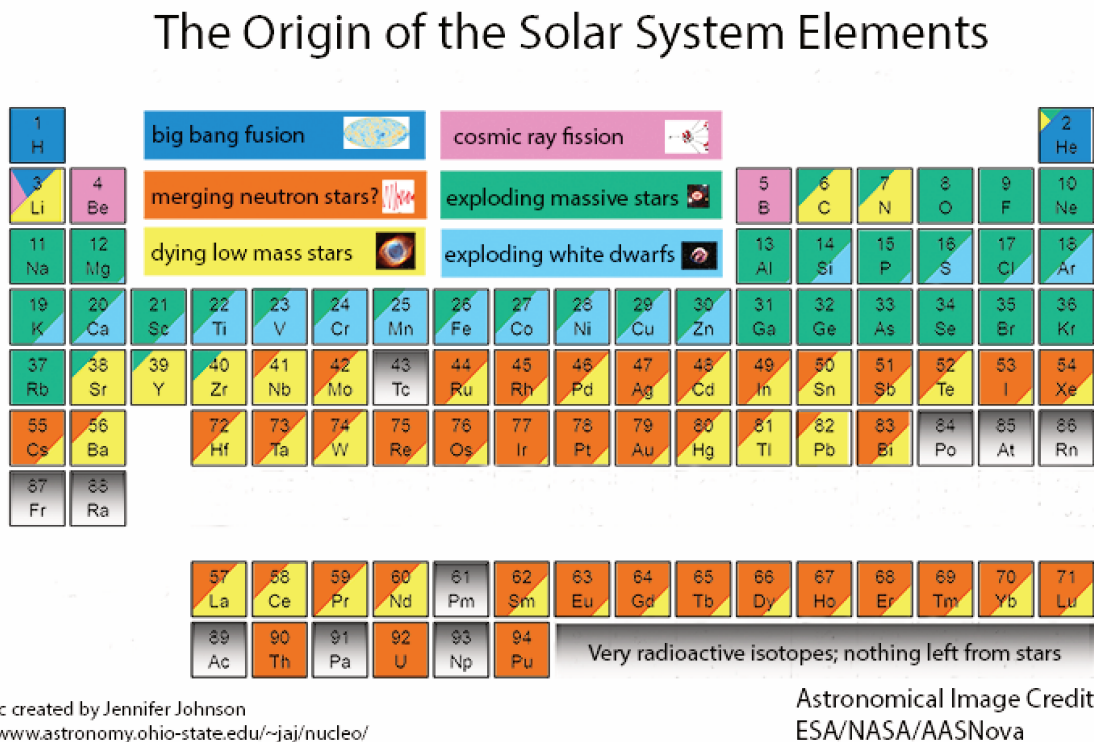


Figure 1.4: Periodic table colour-coded by the origin of the elements in the solar system. Figure created by Jennifer Johnson. <https://www.astronomy.ohio-state.edu/johnson.3064/nucleo/>

Figure 1.4 shows the periodic table with the main production mechanisms and formation sites of elements in the solar system. Elements such as O, Ne, Mg, Si, S, Ca, and Ti are formed through the capture of α particles (He nuclei with two protons and two neutrons), hence α -elements. These elements are synthesised in massive stars and are released into the interstellar medium predominantly through core-collapse (type II) supernova explosions (see e.g. Kobayashi et al. 2020, and references therein). Also odd light elements, such as Na and Al, are synthesised in massive stars and released through

core-collapse supernova.

The heaviest elements that are synthesised through thermonuclear reactions are the iron-peak elements, namely Sc, V, Cr, Mn, Fe, Co, Ni, Cu and Zn. They are mainly produced by explosive nucleosynthesis in type Ia supernovae, which are the result of a thermonuclear explosion of a white dwarf in a binary system, with a non-negligible contribution from type II supernovae and hypernovae. The nucleosynthesis of these elements is still rather uncertain, as some elements may have multiple formation channels, with the further complication that the stellar yields can depend on the metallicity of the progenitor star or on the characteristics of the explosion (see e.g. the review by [Nomoto et al. 2013](#)).

Elements beyond the iron-peak ($Z > 30$) are referred to as neutron-capture elements, since they are produced through neutron captures on a seed nucleus, usually an iron-peak element, followed by β decays ([Burbidge et al. 1957](#)). Neutron captures can be distinguished in three distinct processes, depending on the neutron flux. At neutron densities below $\sim 10^8 \text{ cm}^{-3}$, such as in the envelopes of asymptotic giant branch stars, the timescale between two consecutive neutron captures is less than that of β -decay (see e.g. [Busso et al. 1999a](#), and references therein). This process is called slow neutron capture, or *s*-process. When the neutron flux is so high that the seed nucleus can capture several neutrons before decaying, at densities above 10^{24} cm^{-3} , the process is called rapid neutron captures, or *r*-process (see e.g. [Kratz et al. 2007](#), and references therein). In the intermediate neutron density range, between 10^{14} cm^{-3} and 10^{16} cm^{-3} , we refer to the intermediate neutron capture process, or *i*-process ([Cowan & Rose 1977](#)).

The site of the *s*-process is mainly identified with the region of AGB stars that lies between the He-burning shell and the H-burning shell. An injection of protons in the H-burning region can produce ^{13}C that results in a production of an excess of neutrons through $^{13}\text{C}(\alpha, n)^{16}\text{O}$ reaction, at higher temperatures the $^{22}\text{Ne}(\alpha, n)^{25}\text{Mg}$ is another effective neutron source (see e.g. [Busso et al. 1999b](#); [Käppeler et al. 2011](#)). At low metallicity also rapidly rotating massive stars can be a source of *s*-process elements. Primary production of ^{22}Ne provides a suitable neutron source and the rotational mixing provides a mechanism to extract the products of nucleosynthesis and disperse it in the interstellar medium through the stellar wind (see the review by [Maeder & Meynet 2012](#), and references therein).

As extensively discussed in the recent review by [Cowan et al. \(2021\)](#), neutron densities high enough to allow the *r*-process can be reached in different environments, for example in neutrino winds from core-collapse supernovae, in electron-capture supernovae, in magnetorotational supernovae, and in the mergers between two neutron stars or between a neutron star and a black hole. The recent identification of strontium in the merger of two neutron stars by [Watson et al. \(2019\)](#) demonstrates that the *r*-process does occur in neutron-star mergers. However, it is still unclear whether other formation sites exist, if there are different nucleosynthetic channels, and under which physical conditions the various neutron capture elements can be formed, particularly at low metallicities (see e.g. reviews by [Snedden et al. 2008](#); [Cowan et al. 2021](#)). The surveys presented in Chapt. 2 and 3 attempt to answer these questions through the chemical analysis of samples of metal-poor giant stars.

The site of the *i*-process is more elusive, rapidly accreting white dwarfs have been proposed by [Denissenkov et al. \(2017\)](#). Another possibility is the proton ingestion in a convectively unstable He-burning region (see e.g. [Cristallo et al. 2009](#)). [Caffau et al.](#)

(2019) claimed that this phenomenon can explain the peculiar abundance pattern of n -capture elements in the star SDSS J0222-0313. Whatever the site(s) of the i -process its contribution to the Galactic chemical evolution is minor with respect to the r and s processes.

1.2.2 Searching for the most metal-poor stars in the Galaxy

If the Universe was initially homogeneous, then, according to Standard Big Bang Nucleosynthesis (see e.g. [Wagoner et al. 1967](#); [Coc & Vangioni 2017](#)), the Universe, a few minutes after the Big Bang, was composed only by the Hydrogen, Helium, Lithium. If the Universe had instead some inhomogeneity, tiny amounts of Boron and Beryllium could also have been produced ([Boyd & Kajino 1989](#); [Malaney & Fowler 1989](#); [Kajino & Boyd 1990](#)). The hypothesis of inhomogeneities at the time of Big Bang, is currently ruled out because one should observe, at low metallicity, a constant Be abundance (Be-plateau), that is not observed, and a Be/B ratio that is higher than what predicted by spallation reactions, that is also not observed, see [Molaro et al. \(1997\)](#) for a discussion on this and [Spite et al. \(2019\)](#) on the non-detection of a Be-plateau.

In any case the abundances of trace elements are very low, and the bulk of the Universe is made of H and He. To form stars one needs to collapse a gas cloud under the effect of gravity, up to the stage when the central temperature is high enough to start the nuclear H-burning. If the mass is very large, this can happen whatever the chemical composition of the gas. However, if one aims at forming a low-mass star, of one solar mass or smaller, the temperature due to the compression may become sufficient to stop the contraction and the star will not form. In order to allow the gas to continue its collapse, it is necessary to cool the centre of the cloud during the collapse. In a gas of solar composition this is easily achieved through collisional excitation and radiative de-excitation of low-lying levels of metallic atoms. However in a primordial gas there are no metals, H and He do not have low enough energy levels that can be collisionally excited during the collapse of the cloud. The H_2 molecule ([Palla et al. 1983](#)) and also the HD and LiH molecules ([Galli & Palla 1998](#)) have low lying rotational levels that can help cooling the collapsing cloud. According to most theoretical simulations the cooling of these molecules, in absence of metals, was not sufficient to form low-mass stars and [Bromm & Loeb \(2003\)](#) found that, at low metallicity, the metallic line cooling is dominated by the lines of singly ionized carbon and neutral oxygen. They thus derived a “critical” abundance of C and O below which the formation of low-mass stars is not possible. The discovery of the extremely metal-poor star SDSS J102915+172927 ($Z \leq 6.9 \times 10^{-7}$, [Caffau et al. 2011](#)), with C abundance below the critical threshold, challenged this theory. [Schneider et al. \(2012\)](#) showed that dust cooling can allow low-mass star formation even for a gas cloud as metal-poor as SDSS J102915+172927. [Greif et al. \(2011\)](#) computed star formation hydrodynamical simulations of the formation of primordial stars, and found that the collapsing clouds did fragment leading to the formation of protostars of masses between 0.1 and 10 M_\odot . From an observational point of view, what is relevant for the formation of low-mass stars is that their lifetimes can be longer than the age of the Universe. If a low-mass star was formed from a cloud of primordial gas, it may be directly observed by us. On the contrary, higher mass stars have evolved and are not observable any more. We have so far not observed any star with a primordial composition, the most metal-poor object (in terms of total metal

content Z) is SDSS J102915+172927. The search of metal-poor and extremely metal-poor stars is significant because it can allow us to determine if there is a critical metallicity, below which no low-mass stars can be found, and if so what is this metallicity, or if low mass stars can be formed even out of a primordial gas. If there is a critical metallicity, the metallicity distribution of extremely metal-poor stars should show a sharp drop at the critical metallicity. But to probe the existence and the metallicity of this sharp drop we need to find large numbers of extremely metal-poor stars.

After the first generation of massive stars begin to explode as Supernovae, they pollute with metals the interstellar medium. In this way the second generation of stars can form low-mass stars using metal line cooling. Second generation stars are an essential source for understanding the nature of the first generation of massive stars. The mass distribution of the first generation of stars is imprinted in the chemical composition of their descendants, the second generation of stars. They are also fundamental to study the chemical evolution of the Galaxy.

Until recently it was thought that metal-poor stars could only be found the Galactic Halo or in the thick disc (see e.g. [Sestito et al. 2019](#)). However recently it became clear that some may also found the thin disc on circular orbits ([Meléndez et al. 2016](#); [Schlaufman et al. 2018](#)). This implies that a thin disc was formed very early in the history of the galaxy. Whichever the Galactic environment, stars of very low metallicity are very rare, and, unless they are serendipitously discovered, we require specific techniques to find them.

High proper-motion surveys

The first, and the oldest, technique to find extremely metal-poor stars is through their kinematics, by selecting stars that have high proper motions relative to the Galactic disc. The first star with $[\text{Fe}/\text{H}] < -3$, G64-12, was discovered by [Carney & Peterson \(1981\)](#) from its high proper motion. This technique was used, for instance, for the surveys of [Ryan & Norris \(1991\)](#) and [Carney et al. \(1996\)](#). The studies presented in Chap. 4 are based on the high proper-motion survey of [Caffau et al. \(2020b\)](#).

Photometric surveys

The second technique relies on photometric systems, and, in particular, the use of filters that are sensitive to the metallicity of the stars, followed by a spectroscopic follow-up to check their metallicity. An example of a photometric survey that is very effective in identifying extremely metal-poor candidates is the Pristine survey ([Starkenburg et al. 2017](#)). The Pristine survey at Canada France Hawaii Telescope (CFHT) is a photometric survey that uses the wide-field imager MegaCam with a narrow band filter centred on the metallicity-sensitive Ca H&K lines. In combination with a broad-band photometric survey, such as the Sloan Digital Sky Survey (SDSS) or Gaia, Pristine can infer photometric metallicities down to $[\text{Fe}/\text{H}] < -3$, and, up to now, ~ 100 new extremely metal-poor stars with such low metallicities have been found thanks to it ([Aguado et al. 2019](#)). The studies in Chap. 5 present the chemical analysis of two samples of Pristine metal-poor candidates. Although the Pristine survey has proven to be extremely effective in finding extremely metal-poor stars, when choosing metal-poor candidates by photometry, we must exclude all the possible contaminants, such as variable stars and binaries, as discussed in Sect. 5.2.

Spectroscopic surveys

The third technique is based on the direct acquisition of stellar spectra through spectroscopic surveys, which allow us to obtain the parameters, ages and abundances of thousands of stars. In the '70s and '80s of the 20th century several objective prism surveys were used to search for metal-poor stars (Bond 1970; Bidelman & MacConnell 1973), however the first objective prism survey to discover extremely metal-poor stars was the HK survey (Beers et al. 1985). But it was only thanks to the Hamburg-ESO objective prism survey (Christlieb et al. 2008) that the first star with $[\text{Fe}/\text{H}] < -5$ was discovered (Christlieb et al. 2002). In the more recent years, wide field low resolution spectroscopic surveys based on fibre-fed spectrographs like SDSS/SEGUE/BOSS (York et al. 2000; Yanny et al. 2009b; Dawson et al. 2013) and LAMOST (Deng et al. 2012) provided spectra for millions of stars, and these data bases can be effectively exploited to search for metal-poor stars (see e.g. Caffau et al. 2013; Li et al. 2015; Aguado et al. 2016; Li et al. 2022). More recent higher resolution surveys like RAVE (Steinmetz et al. 2006; Boeche et al. 2011), APOGEE (Majewski et al. 2017) and GALAH (De Silva et al. 2015; Buder et al. 2021) were less successful in finding metal-poor stars, that was not in fact their main objective. In particular APOGEE, that is an infra-red survey, is not at all suitable for the detection or study of metal-poor stars that have most of the line in the UV-blue region. We can expect a major step forward by the third release of the Gaia mission (Gaia Collaboration et al. 2022) that covers the whole sky and provides low resolution prism spectra (De Angeli et al. 2022; Montegriffo et al. 2022) and medium resolution ($R \sim 11\,500$) spectra (Sartoretti et al. 2022). The catalogue provides astrophysical parameters from both the prism spectra (Andrae et al. 2022) and the medium resolution spectra (Recio-Blanco et al. 2022). In the near future we expect major advances in this field by the wide field surveys WEAVE (Jin et al. 2022) and 4MOST (Christlieb et al. 2019). MOONS (Cirasuolo et al. 2020; Gonzalez et al. 2020) shall also provide a contribution, essentially relying on the I band spectra that cover the CaII infra-red triplet.

1.3 From spectra to chemical abundances

The studies presented in this thesis project rely on high-resolution spectra to investigate the chemical composition of the stars. This chapter describes the methods used for the analysis of these stellar spectra. Section 1.3.1 presents an overview of model atmospheres and synthetic spectra. Section 1.3.2 describes the methods used to derive chemical abundances from spectral lines.

1.3.1 Modelling the stellar photosphere: model atmospheres and synthetic spectra

To derive the chemical abundances of a star, we need to compare the observed spectrum with a synthetic one, containing information on the physics and chemistry of the star we are analysing. In order to be computed, synthetic spectra require model atmospheres, which are mathematical models that describe the physical conditions of the stellar photosphere. In this thesis work I used and computed one-dimensional (1D) models that assume a plane-parallel geometry.

In the calculation of 1D plane-parallel models, we make several assumptions and approximations in order to simplify the problem both physically and computationally. We therefore assume that:

1. the atmosphere is thin with respect to the stellar radius, so we can describe it through plane layers;
2. the atmosphere is homogeneous except in the vertical direction, and structures such as granulation, spots or magnetic fields are ignored;
3. the atmosphere is in hydrostatic equilibrium, so the pressure balances the gravitational attraction;
4. the atmosphere is in a steady state, so the gas state and the radiation transport are constant with time;
5. the atmosphere is in radiative equilibrium, that is the energy absorbed is exactly balanced by that emitted in the atmosphere, which implies that the flux of energy is constant with depth in the atmosphere;
6. the atomic abundances are specified and constant throughout the atmosphere.

We also assume that each layer is in thermodynamic equilibrium, which means that the state of the gas depends only on the local values of the radiation fields. This implies that for each layer the occupation numbers and the ionization stages can be described by the Boltzmann and Saha equations respectively. Since the thermodynamic equilibrium is applied to volumes of the model atmosphere that are small with respect to the total volume of the atmosphere, we refer to this approximation as *local* thermodynamic equilibrium (LTE). Given these assumptions, each layer can be treated separately, and it can be described by thermodynamic quantities such as temperature, pressure, number density and opacity.

The procedure for computing a 1D LTE model atmosphere in radiative equilibrium is an iterative process to find the thermodynamic parameters that describe each layer of the model atmosphere. It starts with an initial guess of the temperature structure, and calculates the pressure, number densities, and opacity at each layer. Using these derived quantities, the radiation field can be determined at each point, and the condition of the radiative equilibrium must be satisfied (the total flux must be constant). If this does not happen, the temperature distribution is modified according to a temperature correction method, and the procedure is iterated until the model converges to a solution that satisfies the radiative equilibrium within a fixed error range.

Once the model atmosphere computation has converged, the computation of the synthetic spectrum is straightforward. The core of the computation of a synthetic spectrum consists of the calculation of line opacities, continuum opacities and source functions. As soon as the source function is known, the surface flux or the surface intensity can be obtained by integration. For the studies presented in this thesis work in which I have computed model atmospheres, I used ATLAS 9 and ATLAS 12 codes (Kurucz 1970, 1993a; Sbordone et al. 2004; Kurucz 2005). For the ATLAS 9 models I used the opacity distribution functions (ODF) by Castelli & Kurucz (2003). For the computation of synthetic spectra, I used the code SYNTHE (Kurucz 1993b; Sbordone et al. 2004; Kurucz 2005).

1.3.2 Measuring chemical abundances

The chemical abundance of a certain element in a star can be derived through the equivalent widths (EWs) of the spectral lines or by spectrum synthesis. The equivalent width is defined as $\int r(\lambda)d\lambda$, where r is the residual intensity also called normalized flux. The integral is formally extended from minus infinity to plus infinity in the idealized case in which there is only one line in the spectrum. In practice, it is extended over an interval $[\lambda_1, \lambda_2]$ that contains the whole line, that is to say, the wings of the line reach the continuum. Again this concept of “isolated line” is an idealisation, that is never met in reality, but in some cases real spectra come close to this idealisation.

Equivalent widths method

The EWs method consists in measuring the EW of the observed line and comparing it with the theoretical one computed from the curve of growth of the line. The curve of growth is a theoretical relation between the EW of the line and the abundance of the element that produces the line. In the study presented in Sect. 2.1 (Lombardo et al. 2021), I used the EW method to derive the abundances of O, Mg, Al, Ca, and Fe. Oxygen abundance was derived from the EW of the [O I] line at 6300 Å. For this line, the EW was measured with the `iraf`⁴ task `splot`. The EWs of Mg, Al, Ca, Fe I, and Fe II lines were measured with the FITLINE code (Lemasle et al. 2007). FITLINE is a semi-interactive FORTRAN code developed by P. François that uses genetic algorithms (Charbonneau 1995) to measure EWs of lines in high-resolution spectra. The program performs a fit on the line using a Gaussian defined by four parameters: the central wavelength, the width of the line, the depth of the line, and the continuum value. For each line, the program generates an initial set of Gaussians, giving random values to the four parameters, and it estimates the fit quality by calculating the χ^2 . Then, a new set of Gaussians is computed from the 20 best fits, after adding random modifications to the initial set of parameters values. The new set of Gaussians replaces the old set, and the program estimates again its accuracy using a χ^2 evaluation. The process is thus iterated until the convergence to the best Gaussian fit is achieved.

The choice of this method comes from the fact that all the stars in this sample have a high rotational velocity, so their line profiles are predominantly rotational. Rotation affects the line profile by making it non-Gaussian, but it does not change the EW of the line. In fact, for the most rotating stars, FITLINE was modified to take both Gaussian and rotational profiles into account. To derive chemical abundances from the measured EWs I used the code GALA (Mucciarelli et al. 2013) with ATLAS 9 1D plane-parallel model atmospheres in LTE as input models. GALA is a FORTRAN wrapper that uses a modified version of the WIDTH9 code developed by R. L. Kurucz (Sbordone et al. 2004; Kurucz 2005) for deriving the chemical abundance of single, unblended line using the EW method.

Spectrosynthesis

The spectrosynthesis method consists in comparing the observed line profile with the profile of the same line of a synthetic spectrum. For each line, a set of synthetic spectra is

⁴<https://iraf-community.github.io/>

calculated from the same model atmosphere for different values of the elemental abundance, and the chemical abundance is derived by performing a χ^2 minimisation fit on the observed line profile. In the studies presented in this thesis, this type of approach was used to derive the abundances of the heavy elements, and S in the MINCE I paper (see Sect. 2.1, [Cescutti et al. 2022](#)).

In the studies presented in this thesis project, the chemical abundances for the majority of elements were derived using the code MyGIsFOS ([Sbordone et al. 2014](#)). MyGIsFOS is an automatic pipeline that derives chemical abundances by comparing selected spectral features with a grid of synthetic spectra precomputed at varying T_{eff} , $\log g$, v_{turb} , $[\text{Fe}/\text{H}]$, and $[\alpha/\text{Fe}]$. For each feature analysed, MyGIsFOS finds the best fit spectrum by interpolating in this grid. The grids of synthetic spectra employed in the studies were computed with SYNTH3 using ATLAS 12 1D plane-parallel model atmospheres in LTE.

An important property of MyGIsFOS is that it calculates abundances for lines of all elements assuming that they all scale equally with metallicity (with the exception of α enhancement). Thus, MyGIsFOS assumes that varying $[\text{Fe}/\text{H}]$ at fixed $[\text{X}/\text{Fe}]$ is equivalent to varying $[\text{X}/\text{Fe}]$ at fixed $[\text{Fe}/\text{H}]$. However, some stars can have extreme $[\text{X}/\text{Fe}]$ abundance ratios, and, in these cases, MyGIsFOS may not be the ideal tool for deriving abundances. I refer to [Sbordone et al. \(2014\)](#) for a detailed discussion on specifications and limitations of MyGIsFOS.

MyGIsFOS has been conceived to analyse spectra dominated by the instrumental profile, so it is a convenient tool when a large amount of roughly homogeneous spectroscopic data needs to be analysed quickly, for instance in the context of large spectroscopic surveys, such as the Gaia-ESO Public Spectroscopic Survey ([Gilmore et al. 2012](#); [Smiljanic et al. 2014](#)), or to extend pre-existing literature datasets. On the other hand, when analysing spectra obtained with different instruments, MyGIsFOS begins to show some limitations. The analysis of spectra obtained with different instruments implies that the wavelength range of each spectrum is different. Since the grids can only be calculated at limited wavelength intervals, if the spectrum or a portion of it is not covered by the grid, it cannot be analysed. This means that, if the same grid is used to analyse spectra obtained from different instruments, part of the chemical information provided by the spectrum is lost. Therefore we must compute different grids for spectra from different instruments, which requires a large amount of time.

Another limitation of MyGIsFOS is related to the broadening of the synthetic spectra grid. The grid of synthetic spectra must be broadened to take into account all broadening sources (rotation, macroturbulence, instrumental profile...; see Sect. 3.2.2). However, if the spectra have a very high resolution, instead of the instrumental broadening, the line broadening is dominated by the macroturbulence of the star. This implies that each star must be analysed individually, using a grid with a broadening value equivalent to its macroturbulence, slowing down the procedure considerably. A similar situation occurs when the stars rotate. In this case, a grid of synthetic spectra must be calculated for each star by adding a rotational broadening equivalent to the star rotation. As old giants do not rotate, in [Lombardo et al. \(2022\)](#), to obtain a better estimate of the chemical abundances, we developed a procedure to derive the best v_{broad} value for a sample of giants stars observed at high resolution. The procedure is described in detail in Sect. 3.2.2.

I mainly used MyGIsFOS to derive the abundances of elements from Na to Zn, and for Y and Zr. For heavy elements (Sr and elements heavier than Zr), the abundances were

derived by matching the observed spectrum around the line of interest with a synthetic one computed with the spectrum synthesis code `TurboSpectrum` (Alvarez & Plez 1998). The reason of this choice is that the partition functions for these elements in `TurboSpectrum` are more up-dated than the ones in `SYNTHE`.

EW or spectroscopy?

In the light of what has been discussed in the previous paragraphs, one naturally wonders which method is preferable to use. The answer is that it depends on the situation.

The EW method is useful in the case of isolated and non-saturated lines. This method is slow by nature, as the EW measurement is performed on each line, which must be checked individually. Tools for measuring EWs have been developed to speed up this process, and the measurement is performed using a Gaussian fit, as in the case of `FITLINE`. This suggests that, in the case of lines with a non-Gaussian profile, these codes must be adjusted to take the rotational profile into account, as was done for deriving the abundances in Lombardo et al. (2021).

Spectroscopy, instead, is effective in all those cases in which abundances need to be calculated from blended lines, or from lines affected by fine or hyperfine splitting, or with an isotopic structure. In fact, atomic data are directly included in the synthetic spectrum when this is computed, so the theoretical line profile already contains this information.

In conclusion, in the case of isolated, non-saturated lines without hyperfine structures, the two methods are equivalent and can be used without preference. In the case of rotating stars, for example, the EW method is preferable, since rotation does not change the EW of the line. Spectrum synthesis requires the rotational velocity to be known independently. One can fit a profile using both rotational velocity and abundance, but the two fitting parameters are strongly correlated, implying a larger uncertainty in both parameters. On the other hand, spectroscopy is preferable, for example, to derive the abundances of heavy elements, since their lines often have hyperfine or isotopic structures, or in the case of molecular bands, such as CH and CN, in which the abundance can only be derived through fit.

Chapter 2

MINCE survey

The abundance of neutron-capture elements in metal-poor stars are needed to understand the physics of the neutron-capture processes (slow, intermediate, and rapid) as well as the chemical evolution of the Galaxy. The abundances of these elements in stars with metallicities in the range $-2.5 \leq [\text{Fe}/\text{H}] \leq -1.5$ are particularly important because they allow us to distinguish between different formation scenarios for neutron-capture elements. The main differences among chemical evolution models for neutron-capture elements are in fact found in this intermediate metallicity (see Fig. 2.1). Surprisingly, there are far less measurements of neutron-capture elements abundances in this intermediate metallicity interval than at lower metallicities.

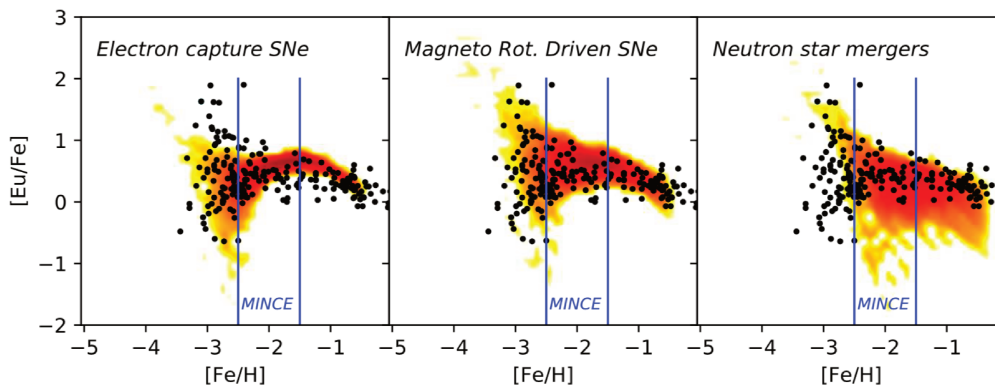


Figure 2.1: Observed abundance ratios in metal-poor stars compared to Galactic chemical evolution models for different r -process events (from left to right): 20% electron capture SNe, 10% magneto rotational driven SNe, 3% neutron star mergers (compared to SNe II). Figure adapted from [Cescutti & Chiappini \(2014\)](#), [Cescutti et al. \(2015\)](#).

The project Measuring at Intermediate metallicity Neutron-Capture Elements (MINCE) is a large international collaboration that aims at gathering chemical abundances for neutron-capture elements of several hundred (> 500) giant stars in the intermediate metallicity. The targets for the MINCE project are bright giants with Gaia G magnitude ≤ 11 mag, in order to be observed with small and medium-sized telescopes. The collaboration has already obtained high resolution and high signal-to-noise ratio stellar spectra for about 400 stars with different facilities: Neo-Narval at TBL, SOPHIE at OHP, ESPaDOnS ([Donati et al. 2006](#)) at CFHT, the High Accuracy Radial velocity Planet Searcher for the

Northern hemisphere (HARPS-N; [Cosentino et al. 2012](#)) at Telescopio Nazionale Galileo (TNG), the Fiber-fed Echelle Spectrograph (FIES; [Telting et al. 2014](#)) at Nordic Optical Telescope (NOT), the Vilnius University Echelle Spectrograph (VUES; [Jurgenson et al. 2016](#)) at Moletai Astronomical Observatory, the Fiber-fed Extended Range Optical Spectrograph (FEROS; [Stahl et al. 1999](#)) at MPG/ESO 2.2-metre telescope at ESO's La Silla Observatory, and the Magellan Inamori Kyocera Echelle (MIKE; [Bernstein et al. 2003](#)) at the Magellan Telescopes at Las Campanas Observatory. We also added to the project giant stars observed as "filler program" (a low priority program in which MINCE stars are observed in case of poor weather conditions) with the Ultraviolet and Visual Echelle Spectrograph (UVES; [Dekker et al. 2000](#)) at ESO Very Large Telescope (VLT) at Cerro Paranal.

In this chapter two studies based on MINCE data are presented. The study in Sect. 2.1 presents the results obtained for a sample of giant stars with solar metallicity and rotational velocities above 10 km s^{-1} that we serendipitously discover during the first observational runs of MINCE. The study in Sect. 2.2 presents the first sample of MINCE stars and the chemical abundance analysis of elements up to Zn.

2.1 Young giants of intermediate mass. Evidence of rotation and mixing (Lombardo et al. 2021)

For the first observational runs of MINCE, we mostly employed the Strömgren photometry from the [Paunzen \(2015\)](#) catalogue and the metallicity calibration for giants of [Casagrande et al. \(2014\)](#) to select metal-poor stars in the metallicity range $-2.5 \leq [\text{Fe}/\text{H}] \leq -1.5$. We observed our targets with three different high resolution spectrographs: SOPHIE at OHP, ESPaDOnS at CFHT, and HARPS-N at TNG. However, when we inspected the spectra, we found that all stars have about solar metallicity and several are rotating rapidly.

The stars have kinematics compatible with the thin-disc population, masses between 2.5 and $6 M_{\odot}$, and ages between 0.1 and 0.55 Gyr (see Fig. 2.2). This sample of stars was not suitable for the purpose of the project, since the metallicity of the stars is around solar. However, the data were still analysed as they represent a stellar population which is poorly studied, given the short time spent by stars in this evolutionary stage. The high stellar masses suggest that these stars were of A- to B-type when they were on the main sequence, therefore this sample allows us to directly compare the properties of evolved A- to B-type stars with their main sequence counterparts. In particular, it is an opportunity for testing the predictions of stellar evolutionary models in terms of the evolution of chemical abundances and rotational velocities.

In this study we derived the chemical abundances of 16 elements (C, N, O, Mg, Al, Ca, Fe, Sr, Y, Ba, La, Ce, Pr, Nd, Sm, and Eu) for a sample of 26 young solar metallicity giant stars. In Sect. 2.1.1 we discuss the possible reasons for the failure of our target selection. In Sect. 2.1.2 we discuss the possible presence of binary stars in our sample. In Sect. 2.1.3 and Sect. 2.1.4 we present the main results of the study.

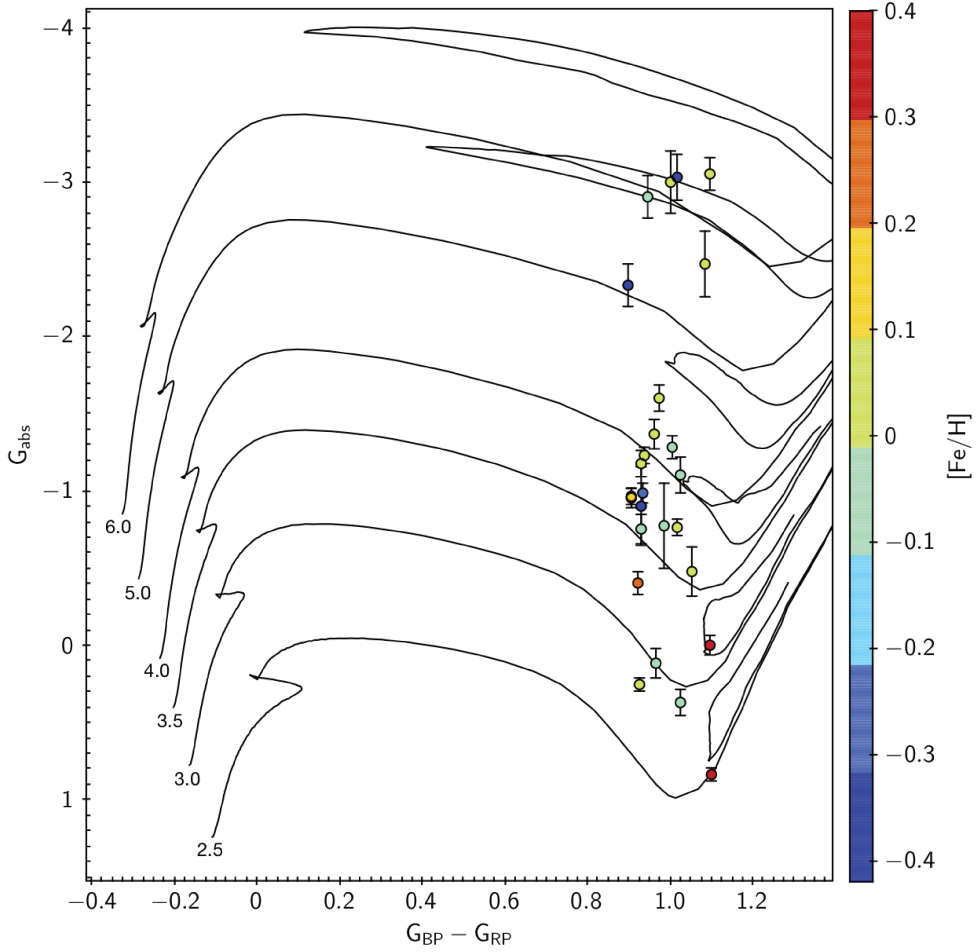


Figure 2.2: Colour-magnitude diagram of Gaia EDR3 absolute magnitude G and dereddened colour $G_{BP} - G_{RP}$ comparing the observed stars with Ekström et al. (2012) evolutionary tracks without rotation at metallicity $Z = 0.014$ for stellar masses between $2.5 M_{\odot}$ and $6.0 M_{\odot}$. Error bars represent the uncertainty on G_{abs} , corresponding to 3σ error on parallax. The colour index indicates our derived $[Fe/H]$ of the stars. Figure from Lombardo et al. (2021).

2.1.1 Target selection

Our method for the target selection was not able to correctly estimate the metallicity of the stars and we would like to understand the causes of this error. Figure 2.3 shows the Strömgren colour-magnitude diagram for our targets compared to Parsec solar metallicity isochrones of ages between 0.1 and 1 Gyr, and a Parsec isochrone with $[Fe/H] = -2.0$ and age 12 Gyr (Bressan et al. 2012). We clearly note that in the region in which our targets lie, the young solar metallicity isochrones overlap with the red giant branch of the old metal-poor isochrone. For this reason, we interpret the failure of our selection method as a consequence of the age-metallicity degeneracy in the colour-magnitude diagram. Our targets have Strömgren indices within the validity range of Casagrande et al. (2014) calibration. If we use the Casagrande et al. (2014) calibration to estimate the metallicity for our stars, we obtain the metallicity distribution shown in Fig. 2.4. The metallicity values are underestimated for all targets, making the stars appear more metal-poor than

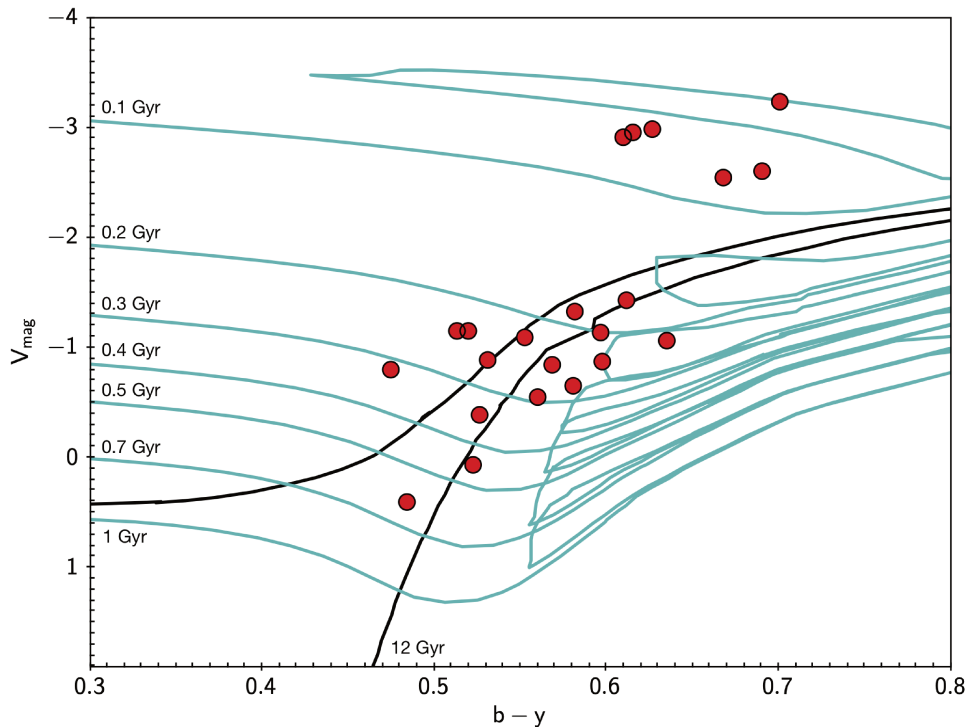


Figure 2.3: Strömrgren colour-magnitude diagram for the sample stars (red dots). The targets are compared to Parsec isochrones with solar metallicity and ages between 0.1 and 1 Gyr (cyan lines) and with $[\text{Fe}/\text{H}] = -2$ dex and age 12 Gyr (black line).

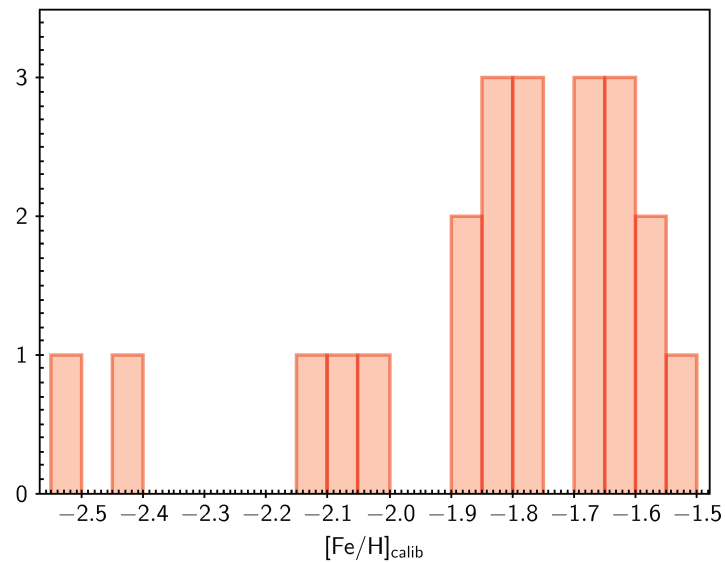


Figure 2.4: Histogram of $[\text{Fe}/\text{H}]$ estimated with Casagrande calibration for the sample stars.

they really are. In our opinion the problem lies in the fact that the [Casagrande et al. \(2014\)](#) calibration was defined using only old stars as calibrators and therefore it provides wrong metallicity estimates when applied to young stars.

2.1.2 Possible binary stars

Two stars in our sample (HD 195375 and HD 278) are listed in the Washington Double Star Catalog (Mason et al. 2001). We looked at the Gaia astrometric parameters of these stars and their companions, and we found that only the star HD 195375 and its companion have consistent parallaxes, meaning that they are in a physical binary system. On the contrary, HD 278 and its companion have different parallaxes, which suggests that these stars are not in a binary system. Some stars in our sample show radial velocity variability when compared to the values provided by Gaia Data Release 2 (DR2) (Gaia Collaboration et al. 2016, 2018b). Radial velocity variability can be due to the presence of a companion in a binary system, so we looked for other hints of binarity in our stars. Six stars have a Gaia radial velocity error above 1 km s^{-1} , which is the maximum error due to photon noise for stars of similar magnitude (Sartoretti et al. 2018). Ten stars in our sample have been identified as probable binary stars by Kervella et al. (2019) from proper motion variations by comparing HIPPARCOS (ESA 1997) and Gaia DR2 proper motions. Since the stars HD 192045 and HD 213036 show all the above mentioned properties, in Lombardo et al. (2021) we suggested that they are with high probability binary stars.

Our study was carried out before the advent of the Gaia DR3. Thanks to the new Gaia data release, we can check if the radial velocities of the stars in our sample have varied over time, and if some of these stars have been identified as members of binary systems. In Table 2.1 our measured radial velocities are compared to the values provided by Gaia DR2 and DR3. We note that 15 stars have Gaia DR3 radial velocities that differ more than 1σ respect to Gaia DR2, while only for the star HD 19267 they differ more than 3σ . Six stars in the sample have a "non single star" flag in the Gaia DR3 catalogue: HD 192045 is labelled as an eclipsing binary with a period of 298.40 days; HD 19267, HD 189879, and HD 63856 are labelled as spectroscopic binaries; HD 219925, and HD 55077 are labelled as astrometric binaries. Our hypothesis of binarity for the star HD 192045 seems therefore to be confirmed by the Gaia DR3.

2.1.3 Main results

The chemical analysis revealed that all but one star have low [C/Fe] and high [N/Fe] abundance ratios with constant [(C+N+O)/Fe] (see Fig. 2.5), implying that the stars have undergone mixing and the products of the H-burning through the CNO cycle are visible on the stellar surfaces. The stars do not show any other chemical peculiarities, except for the Ba abundance. In fact, the majority of the stars in the sample show a Ba abundance higher than solar, but solar s-process elemental abundances (see Sect. 2.1.4).

I measured the rotational velocities ($v \sin i$) of these stars and compared the results with theoretical models with rotation. To derive the $v \sin i$, I selected for each star a set of isolated FeI lines, and measured the iron abundance from their EW. For each line, I computed three synthetic spectra with the same FeI abundance, corresponding to that derived from the EW of the line itself, and different rotational velocities. Then, I derived the $v \sin i$ by performing a χ^2 minimisation fit on the observed line profile using the synthetic spectra. It is important to note that this approach does not permit to distinguish the rotational contribution from the other sources of broadening, such as macroturbulence. For rapidly rotating stars, the line profile is dominated by rotation, so the other sources of line broadening can be considered negligible. In contrast, for slowly rotating stars,

Star	v_{rad} km s ⁻¹	$v_{\text{rad}}(\text{GaiaDR2})$ km s ⁻¹	$v_{\text{rad}}(\text{GaiaDR3})$ km s ⁻¹
HD 192045	-4.834 ± 0.077	-43.846 ± 2.253	-43.838 ± 2.401
HD 191066	-9.349 ± 0.001	-5.911 ± 3.451	-6.161 ± 2.994
HD 205732	-3.971 ± 0.001	-3.150 ± 0.147	-3.484 ± 0.125
HD 213036	-40.89 ± 0.128	-4.369 ± 1.662	-10.764 ± 1.854
HD 217089	-7.684 ± 0.001	-7.441 ± 0.150	-7.735 ± 0.124
HD 9637	-2.361 ± 0.002	-1.879 ± 0.169	-2.106 ± 0.147
HD 21269	-12.602 ± 0.002	-15.676 ± 0.262	-15.415 ± 0.250
HD 19267	2.697 ± 0.001	3.387 ± 0.153	2.763 ± 0.127
HD 13882	-29.038 ± 0.001	-28.545 ± 0.170	-29.012 ± 0.131
HD 189879	-29.532 ± 0.001	-10.391 ± 4.430	-8.562 ± 3.021
HD 195375	-10.276 ± 0.001	-9.352 ± 0.154	-9.714 ± 0.130
HD 221232	-30.649 ± 0.001	-29.894 ± 0.158	-30.283 ± 0.124
HD 219925	-22.916 ± 0.001	-14.596 ± 2.837	-24.033 ± 2.658
HD 278	-60.526 ± 0.003	-26.143 ± 7.736	-26.103 ± 5.861
HD 11519	-11.260 ± 0.001	-10.625 ± 0.177	-11.054 ± 0.131
TYC 2813-1979-1	-17.170 ± 0.002	-16.201 ± 0.338	-16.786 ± 0.214
BD+42 3220	-19.298 ± 0.053	-18.523 ± 0.219	-18.958 ± 0.158
BD+44 3114	-15.216 ± 0.055	-17.302 ± 0.170	-17.492 ± 0.196
TYC 3136-878-1	1.034 ± 0.053	0.922 ± 0.985	1.016 ± 0.262
HD 40509	-1.656 ± 0.005	-1.223 ± 0.310	-1.258 ± 0.140
HD 41710	-7.917 ± 0.002	-6.812 ± 0.269	-7.231 ± 0.135
HD 40655	7.332 ± 0.001		8.435 ± 0.148
HD 45879	7.047 ± 0.001	5.902 ± 0.224	5.889 ± 0.166
HD 55077	-25.499 ± 0.003	-25.729 ± 0.514	-26.018 ± 0.411
HD 61107	10.476 ± 0.001	12.126 ± 0.738	8.952 ± 0.897
HD 63856	19.755 ± 0.001	22.402 ± 0.206	22.066 ± 0.169

Table 2.1: Comparison between Gaia DR2, Gaia DR3 and measured radial velocities for the sample stars.

the effects of rotation and macroturbulence on the line broadening are comparable, thus $v \sin i$ must be interpreted as an upper limit. For the stars in our sample, we found a good agreement between the observed and predicted $v \sin i$. The $v \sin i$ we obtained for stars with $3.5 M_{\odot}$ and $4 M_{\odot}$ and $-0.1 < [\text{Fe}/\text{H}] < 0.1$ ($5 < v \sin i < 22 \text{ km s}^{-1}$) are compatible with the rotational velocity values predicted by the [Georgy et al. \(2013\)](#) models with $0.3 < \omega < 0.6$ at solar metallicity for stars in the corresponding region of the $\log T_{\text{eff}}$ versus $\log g$ diagram (Fig. 2.6). ω is defined as $\omega = \Omega_{in}/\Omega_{crit}$, where Ω_{in} is the initial angular velocity and Ω_{crit} is the critical angular velocity. Ω_{crit} is the angular velocity at which the centrifugal acceleration is equal to the sum of the gravitational and radiative acceleration on the stellar surface. We also found that the $[\text{N}/\text{C}]$ abundance ratios of the stars are compatible with the values predicted by rotational models for clump stars (the clump, or blue loop, is the region of the color-magnitude diagram where stars are located when they undergo central He-burning).

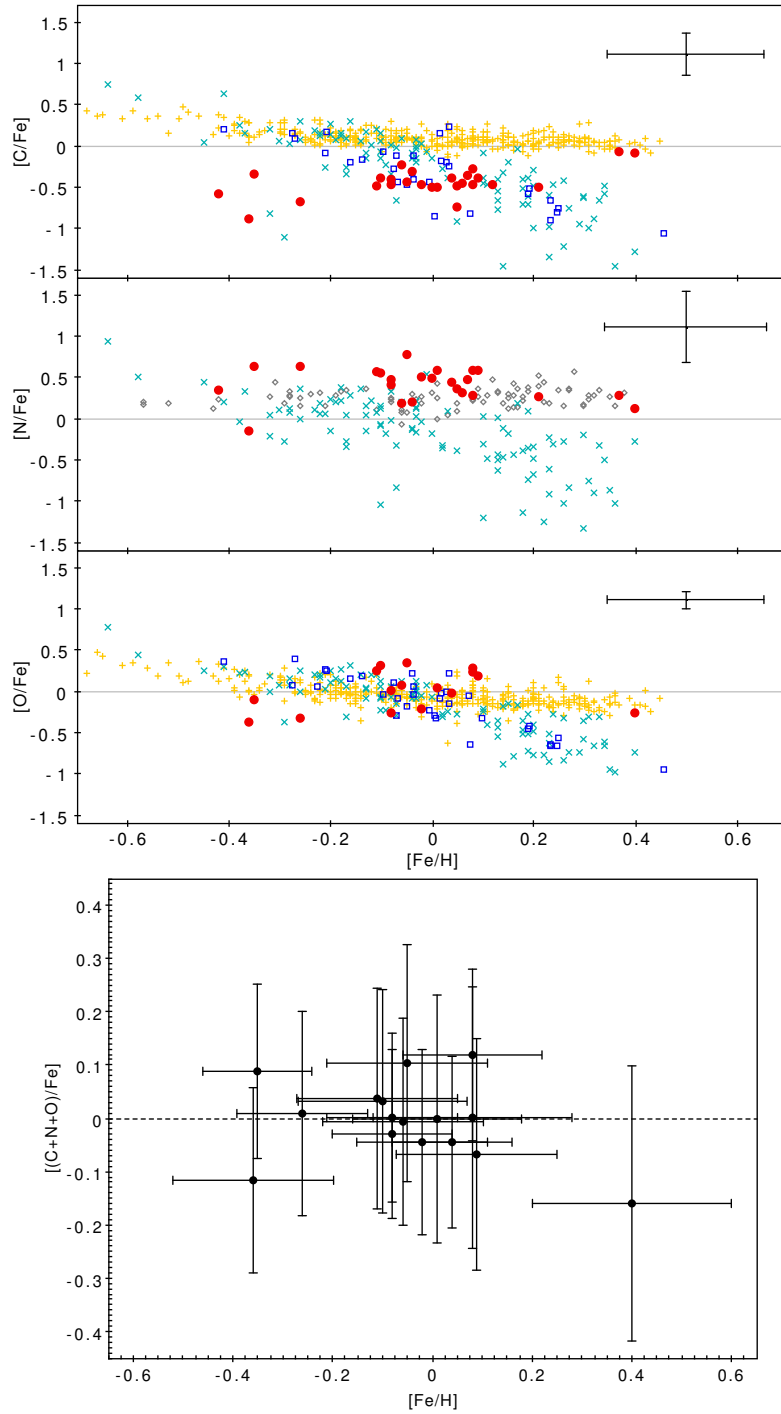


Figure 2.5: *Upper panel:* $[C/Fe]$, $[N/Fe]$ and $[O/Fe]$ abundances as a function of $[Fe/H]$ for our sample stars (red dots). Comparison with targets from Takeda et al. (2018) (cyan crosses), Royer et al. (2014) (blue squares), Delgado Mena et al. (2010) (yellow crosses) and Ecuillon et al. (2004) (grey diamonds). *Lower panel:* $[(C+N+O)/Fe]$ abundance ratios as a function of $[Fe/H]$. Figure from Lombardo et al. (2021).

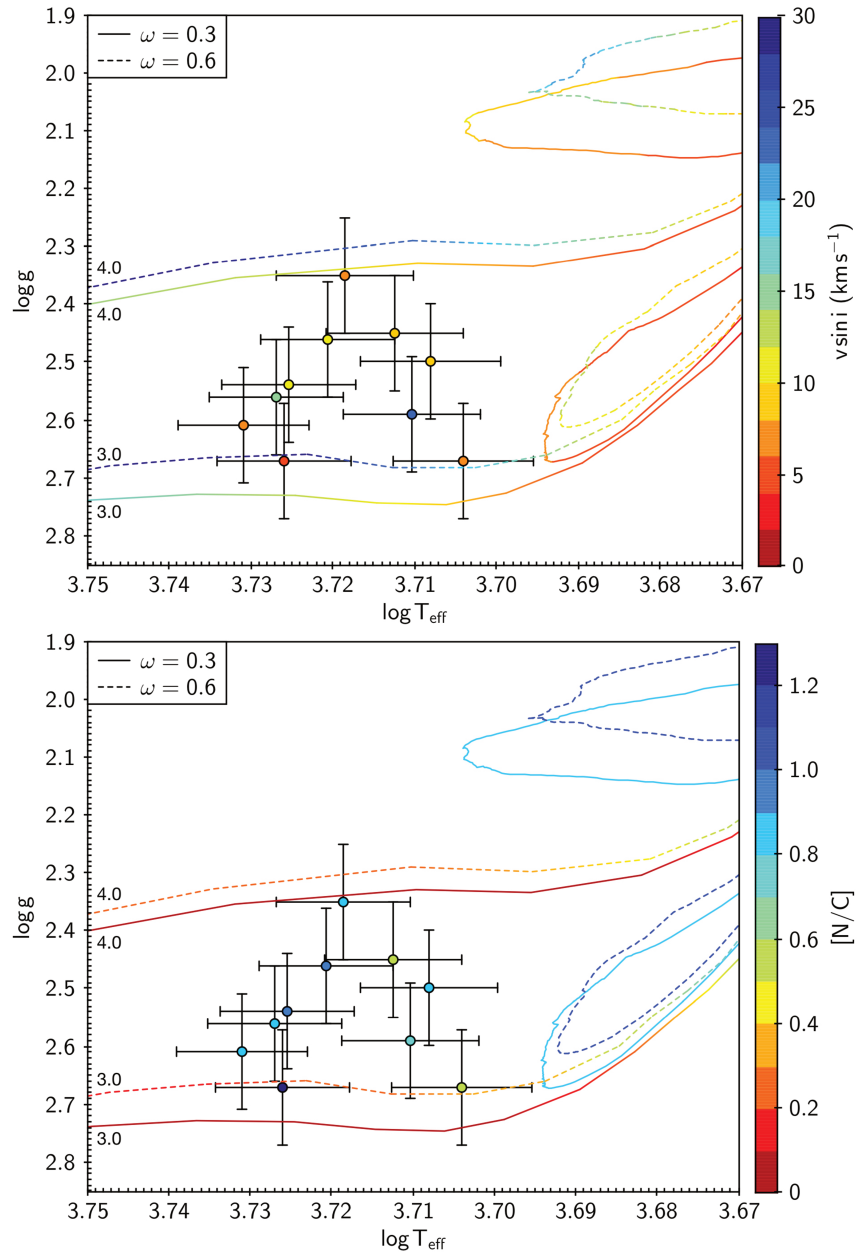


Figure 2.6: $\log T_{\text{eff}}$ versus $\log g$ diagram for the [Georgy et al. \(2013\)](#) evolutionary tracks with $Z = 0.014$, $M = 3 M_{\odot}$, $4 M_{\odot}$, and $\omega = 0.3$ (solid lines) and 0.6 (dashed lines). Stars in the sample with $-0.1 < [\text{Fe}/\text{H}] < 0.1$ and $M = 3.5 M_{\odot}$, $4 M_{\odot}$ are shown with error bars. Upper panel: colour index indicates the equatorial velocity for evolutionary tracks and the observed $v \sin i$ for sample stars. Lower panel: colour index indicates the $[\text{N}/\text{C}]$ abundance ratio. Figure from [Lombardo et al. \(2021\)](#).

2.1.4 Ba enhancement

The most intriguing result we found in our study is the fact that almost all the stars in our sample show neutron-capture element abundances around solar but an enrichment in Ba (see Fig. 2.7). This evidence cannot be easily explained from the point of view of stellar nucleosynthesis. In solar-type material, neutron-capture elements are produced

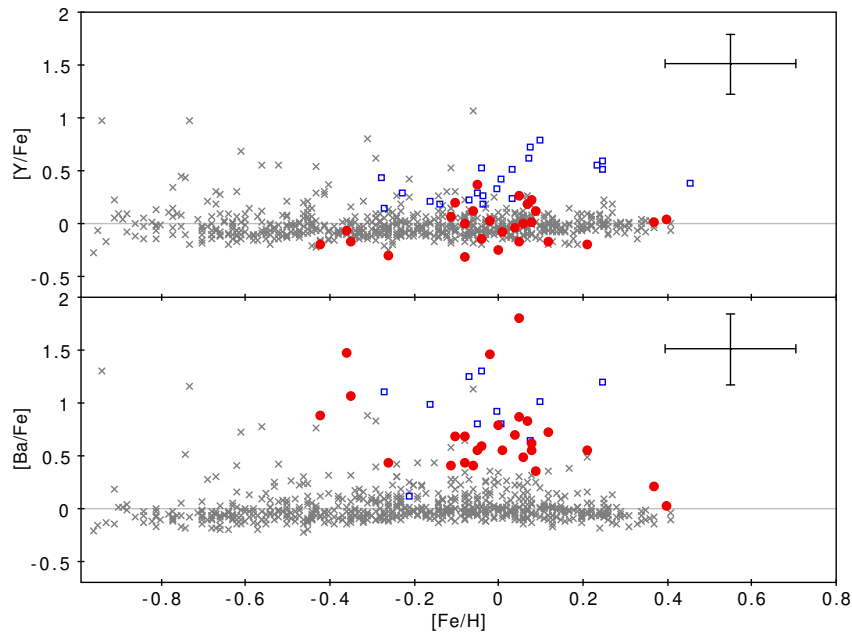


Figure 2.7: $[Y/Fe]$ and $[Ba/Fe]$ abundances as a function of $[Fe/H]$ for our sample stars (red dots). Comparison with targets from [Bensby et al. \(2014\)](#) (grey crosses) and [Royer et al. \(2014\)](#) (blue squares). Figure from [Lombardo et al. \(2021\)](#).

through s-process in asymptotic giant branch (AGB) stars and, during the third dredge up, the enriched material is brought to the surface of the star ([Burbidge et al. 1957](#); [Iben & Renzini 1983](#); [Busso et al. 2001](#)). As described in Sect. 7.3 of [Lombardo et al. \(2021\)](#), the stars in our sample are not yet on the AGB, but are instead in the sub-giant or clump phase. The abundance of Ba observed on their surface cannot therefore be due to the third dredge up. Among the possible explanations, we rule out the possibility that an atmospheric phenomenon during the main sequence phase could be at the basis of this peculiarity, since this would have been cancelled by mixing during the evolution of the star towards the giant branch.

Mild Ba stars?

We investigated whether these stars could be Ba stars, which are peculiar stars characterised by an over-abundance of barium and, in general, s-process elements. The chemical peculiarity of Ba stars is the result of a mass transfer in a binary system with an AGB star, which polluted the surface of the current giant star when it was on the main sequence phase ([McClure et al. 1980](#)). As we have shown in [Lombardo et al. \(2021\)](#), only three stars in the sample have a chemistry compatible with that of mild Ba stars, which show a weaker s-element enrichment than classical Ba stars and are not enriched in carbon ([Snedden et al. 1981](#)). The other stars in the sample, on the other hand, have an abundance of s-process elements similar to normal giant stars, so it is unlikely that they are Ba stars.

Magnetic field?

Since these stars show an anomaly only for Ba abundance, we questioned whether there is any physical phenomenon that is able to influence Ba more than the other n-capture elements. One possibility is the magnetic field of the star. The magnetic field can in fact split the levels of a given atomic transition into its different components by the Zeeman effect, leading to a broadening of the line profile. The enrichment in Ba would therefore be fictitious, due only to an anomalous increase in the equivalent width of the line caused by the magnetic field of the star (Babcock 1949). As we do not have any measurement of the magnetic field of the stars in the sample, to test this hypothesis we measured the Ba abundance in the magnetic giant star EK Eridani (EK Eri). EK Eri is a giant of solar metallicity with atmospheric parameters similar to that of our sample stars ($T_{\text{eff}} \sim 5000$ K and $\log g \sim 3.3$ dex) but characterised by a magnetic field of 98.6 G (Aurière et al. 2015). We derived the atmospheric parameters from Gaia EDR3 photometry and parallax (Gaia Collaboration et al. 2016, 2021), similarly to the stars in our sample, and we found $T_{\text{eff}} = 4955$ K and $\log g = 3.35$ dex, in agreement with the results derived by Strassmeier et al. (1999) ($T_{\text{eff}} = 5125$ K and $\log g = 3.25$ dex). We then measured the Ba abundance from the Ba II line at 585.4 nm by spectroscopy and found $[\text{Ba}/\text{Fe}] \sim -1.0$. EK Eri turns out to be under-abundant in Ba, contrary to what we found for our stars. The magnetic field therefore does not seem to be responsible for the Ba enrichment we observe in our sample stars.

Microturbulent velocity?

Another possible explanation for this anomaly may be related to our choice of stellar parameters, in particular for the microturbulence value. The microturbulence, or microturbulent velocity, is an additional broadening that is added in quadrature to the Doppler broadening in the 1D model atmosphere. It is essentially a corrective parameter, that is used in 1D models to compensate for the incomplete description of the motions of gas in stellar photospheres, especially convection. Ba abundance derived from Ba II lines is strongly sensitive to the microturbulence of the stellar model. We observed that for the star HD 55077, increasing the microturbulence by 0.6 km s^{-1} decreases the Ba abundance by 0.6 dex. This would imply that all the microturbulence values we have derived are underestimated, and that these stars should have a microturbulence of $\sim 3 \text{ km s}^{-1}$. However, such high microturbulence values would affect not only the abundance of Ba but also other elements. The problem of Ba enrichment in these young giants therefore remains unexplained. One possible way to understand whether this problem is related to an incorrect microturbulent velocity could be to derive Ba abundance using 3D models instead of 1D models. In 3D models microturbulence is not necessary, as these models take into account the photospheric motions by modelling the effects of stellar granulation (the top of the convective zone). Gallagher et al. (2020) compared the Ba abundance derived from 1D and 3D models in both LTE and NLTE in the Sun, and found that the 3D-NLTE abundances are similar to the 1D-LTE ones, while the 3D-LTE and 1D-NLTE abundances appear to be larger and lower, respectively, than those derived in 1D-LTE. They suggested that the similarity between 3D-NLTE and 1D-LTE is due to the opposing effects that the realistic modelling of line formation (NLTE) or convection (3D) have on Ba abundance. The inclusion of NLTE in the computation produces deeper Ba lines, thus,

for a given observed Ba line, the derived barium abundance in NLTE is lower compared to that in LTE. On the contrary, 3D geometry weakens the Ba lines, hence a larger barium abundance is required to match the Ba line profile compared to 1D. In 3D-NLTE both physical processes are taken into account, but, since they affect the barium abundance in opposite ways, their effects are cancelled out, and the derived abundance is similar to that in 1D-LTE, in which these effects are ignored. Since this study has only been done for the Sun so far, it would be interesting to investigate what would be the effect of using 3D models for deriving Ba abundance in giant stars, and to see if these models could explain this anomalous overabundance.

2.2 MINCE I. Presentation of the project and of the first year sample (Cescutti et al. 2022)

The first paper of the MINCE series presents the chemical analysis of the first sample of MINCE giant stars. The targets were selected using *StarHorse* code (Anders et al. 2019), which provides Bayesian stellar parameters, distances, and extinctions for hundreds of millions of stars by combining Gaia DR2 parallaxes and photometry with the photometric catalogues of Pan-STARRS1, 2MASS, and AllWISE. To select halo stars with $[\text{Fe}/\text{H}] \leq -1$ a constraint on the kinematics has been applied ($v_{\text{tot}} > 200 \text{ km s}^{-1}$). Two stars in the sample were instead selected from the Apache Point Observatory Galactic Evolution Experiment (APOGEE) survey (Eisenstein et al. 2011). An example of the quality of data used in this study is shown in Fig. 2.8.

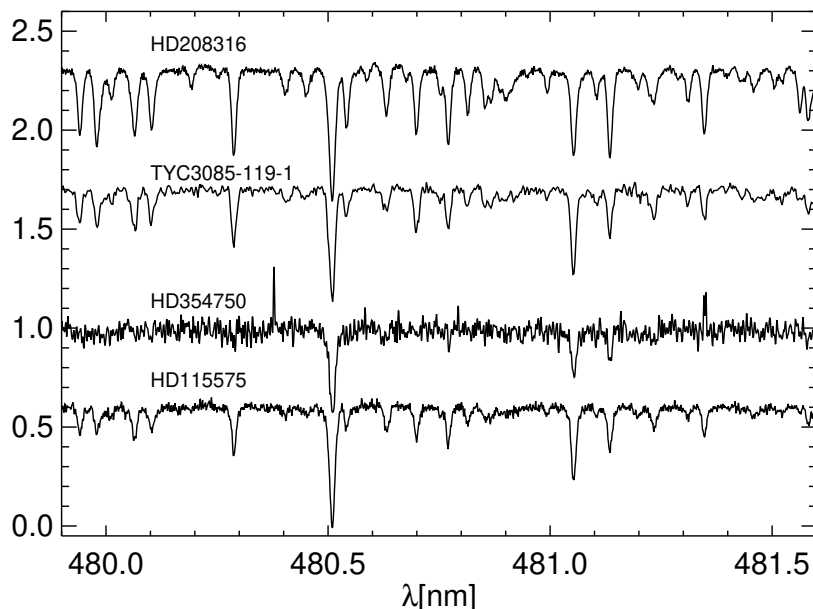


Figure 2.8: An example of the spectra acquired during the MINCE survey. The spectral region around the Zn I line at 4810 Å. The normalised spectra have been shifted vertically for display purposes. Figure from Cescutti et al. (2022).

The stellar parameters were derived using Gaia EDR3 photometry and parallaxes as

described in Sect. 3.2.1. We investigated the kinematics of all stars in the sample using Gaia astrometric parameters and the measured radial velocities. We find that 12 stars have a kinematic compatible with the Gaia-Sausage-Enceladus (GSE) and three stars with Sequoia. Eight stars appear to have thin disc kinematics, one star likely belongs to the thick disc, and the remaining stars, which cannot be associated to the mentioned structures, may be associated with the halo. We derived the abundances of elements up to the iron peak (C, O, Na, Mg, Al, Si, S, Ca, Sc, Ti, V, Cr, Mn, Fe, Co, Ni, Cu, Zn) for 33 stars. The chemical abundances were derived using MyGIsFOS (Sbordone et al. 2014). We could also derive the S abundance from the SI multiplet at 920 nm. In the cases where the SI multiplet was not contaminated by telluric lines, we measured the S abundance using the spectrum synthesis code SALVADOR (Mucciarelli in prep.). To derive chemical abundances, SALVADOR performs a χ^2 minimisation fit of the observed line profiles using a grid of synthetic spectra. The grid of synthetic spectra is computed by SALVADOR using the code SYNTHE (Kurucz 2005) and ATLAS 9 model atmospheres based on ODFs by Castelli & Kurucz (2003). When the SI multiplet was partially blended with telluric lines, the S abundance was derived from equivalent width using the `splot iraf`¹ task with the "deblending" option.

We compared the derived abundance ratios with the prediction of chemical evolution models, in particular for the Milky Way disc (Spitoni et al. 2021) and the GSE accretion event (Belokurov et al. 2018; Haywood et al. 2018; Helmi et al. 2018). The chemical evolution model by Spitoni et al. (2021) is a revised version of the classical two-infall chemical evolution model (Chiappini et al. 1997) that has been developed for reproducing the Galactic disc components as traced by the APOGEE 16th Data Release (APOGEE DR16, Ahumada et al. 2020) abundance ratios. This model assumes that the Galactic disc was formed by two separate and consecutive episodes of gas accretion, with a delay between the two gas infall of ~ 4 Gyr, that gave rise to the thick and the thin disc components. The chemical evolution model for the GSE, described in detail in Cescutti et al. (2020), is similar to that of dwarf spheroidal galaxies (Lanfranchi et al. 2008).

For α -elements we cannot find any specific difference between halo stars and GSE or Sequoia, neither between GSE and Sequoia, as the stars appear to share the same plateau. We find a similar situation for iron-peak elements, since we cannot observe any specific trend or offset between halo stars and GSE. For the three Sequoia stars we find that the [V/Fe], [Cr/Fe], [Mn/Fe] and [Co/Fe] abundance ratios appear to increase with increasing metallicity, while [Ni/Fe] and [Zn/Fe] decrease towards higher metallicities.

Thanks to the improved target selection and the use of multiple middle-sized facilities, it was possible to collect a large amount of high-quality data in a short time. The stellar parameters derived in this study will be used to derive the abundances of neutron-capture elements in the next paper of the series.

¹<https://iraf-community.github.io/>

Chapter 3

CERES survey

The Chemical Evolution of R-process Elements in Stars (CERES) project has the aim to obtain a complete chemical inventory of a sample of halo stars with metallicities below -1.5 in order to understand the physical conditions and formation scenarios of neutron capture elements. To achieve this, we rely on a sample of high quality spectra, i.e. high resolution and high signal-to-noise ratio, obtained with UVES at the ESO/VLT. The data-set consists of spectra obtained under ESO programme 0104.D-0059 and reduced spectra from the ESO Science Archive Facility. The targets were selected by looking for metal-poor stars ($[\text{Fe}/\text{H}] < -1.5$) with less than five heavy elements ($Z > 30$) known from the literature.

In this chapter we present two studies that are based on CERES data. The study in Sect. 3.1 presents the detailed chemical abundance analysis for the star RAVE J110842.1-715300, which was previously kinematically associated with the ω Centauri (ω Cen) globular cluster, in order to investigate its nature as an ω Cen star. The study in Sect. 3.2 presents the chemical abundance analysis of elements from Na to Zr for the whole CERES sample.

3.1 Purveyors of fine halos III. Chemical abundance analysis of a potential ω Cen associate (Koch-Hansen, Hansen, Lombardo et al. 2021)

In the context of the CERES project, we observed the giant star RAVE J110842.1-715300. Combining radial velocities, distances, and $[\text{Fe}/\text{H}]$ abundances from the Fourth Data Release of the Radial Velocity Experiment survey (RAVE DR4; [Kordopatis et al. 2013](#)) with proper motions from the US Naval Observatory CCD Astrograph Catalog (UCAC4; [Zacharias et al. 2013](#)), [Fernández-Trincado et al. \(2015\)](#) kinematically associated the halo star RAVE J110842.1-715300 with the ω Cen globular cluster. The authors suggest that the star had a close encounter at high relative velocity and interacted with ω Cen between 45 and 290 Myr ago. In their opinion, it seems unlikely that the star directly escaped from the globular cluster, since the relative velocity of the encounter is quite high ($v_{rel} = 275 \text{ km s}^{-1}$). Since the RAVE spectra allowed to derive only Fe, Al and Ni for this star, in [Koch-Hansen et al. \(2021\)](#) we performed a detailed chemical abundance analysis in order to confirm or reject the possibility of a previous association with ω Cen, and, in the case,

to classify it as a first or second generation star.

We derived the chemical abundances of 33 species of 31 elements (C, H, O, Na, Mg, Si, Ca, Sc, Ti, V, Cr, Mn, Fe, Co, Ni, Cu, Zn, Sr, Y, Zr, Ba, La, Ce, Pr, Nd, Sm, Eu, Gd, Dy, Hf, and Pb) using *ATLAS 9* model atmosphere grids (Castelli & Kurucz 2003) and the spectrum synthesis code *MOOG* (Snedden et al. 2012). The metallicity of the star, $[\text{Fe II}/\text{H}] = -2.10 \pm 0.02(\text{stat.}) \pm 0.07(\text{sys.})$, is compatible with the metal-poor tail of ω Cen metallicity distribution, and its chemical composition for elements with $Z \geq 12$ is compatible with that of ω Cen stars. However, the abundance distribution of ω Cen largely overlaps with that of metal-poor field stars in the halo at metallicities around -2 , so it is not possible to confirm the globular cluster origin of RAVE J110842.1-715300 from its heavy elements abundances. On the other hand, the abundances of lighter elements seem to suggest a possible association of this star with ω Cen. Globular clusters are characterised by the presence of multiple stellar populations, and exhibit star-to-star variations in the abundances of some elements, like He, C, N, O, Na, and Al (Carretta et al. 2009; Milone et al. 2017; Bastian & Lardo 2018; Gratton et al. 2019). Due to proton-capture reactions in the CNO cycle in the first generation of stars, the second generation of stars in the globular cluster, which formed in the gas polluted by the first generation, is enriched in He, N, Na, and Al, while it is depleted in C, O, and Mg (Kayser et al. 2008; Carretta et al. 2009; Bastian & Lardo 2018). This gives rise to the characteristic anticorrelations (Na-O, Mg-Al) and bimodalities (e.g., in CN) observed in globular clusters (Cohen 1978; Carretta et al. 2009; Bastian & Lardo 2018). The chemical analysis revealed that the star is CN-strong, but it appears to be a C-normal star, while second generation globular cluster stars are CH-weak. The star has $[\text{Na}/\text{Fe}] = 0.55$, which makes it similar to Na-strong second generation globular cluster stars, while the value $[\text{O}/\text{Fe}] = 0.65$ is compatible with that of metal-poor, α -enhanced halo stars. Although the star appears CH-normal and enhanced in O, we conclude that, due to its enhancement in CN and Na, this star may be a second generation ω Cen star that escaped from the cluster.

3.2 CERES I. Stellar parameters and chemical abundances from Na to Zr (Lombardo et al. 2022)

In this study we derived the stellar parameters and chemical abundances of selected elements from Na to Zr for a sample of 52 giant stars with $-3.6 \leq [\text{Fe}/\text{H}] \leq -1.8$. The stellar parameters for the stars in our sample were determined using Gaia EDR3 photometry and parallaxes (Gaia Collaboration et al. 2016, 2021). We developed an iterative procedure to derive the effective temperature and the surface gravity for each star, as described in detail in Sect. 3.2.1. Since in high resolution spectra ($R \geq 60000$) the line widths are dominated by the macroturbulence of the stars, we developed a procedure to estimate the line broadening for each observed spectrum in order to obtain a more accurate measurement of the chemical abundances. The employed procedure is described in detail in Sect. 3.2.2. Thanks to the high quality of our spectra, the chemical abundances for 26 species of 18 elements (Na, Mg, Al, Si, Ca, Sc, Ti, V, Cr, Mn, Fe, Co, Ni, Zn, Sr, Y and Zr) were derived using *MyGIsFOS*. We could also measure the abundances of Si II, Sc I, Mn II, and Zr I. The lines of these transitions in the stellar spectrum are usually difficult to measure,

since they are very weak, and require high resolution and high signal-to-noise spectra to be detected. The main results of this study are described in Sect. 3.2.3.

3.2.1 Stellar parameters

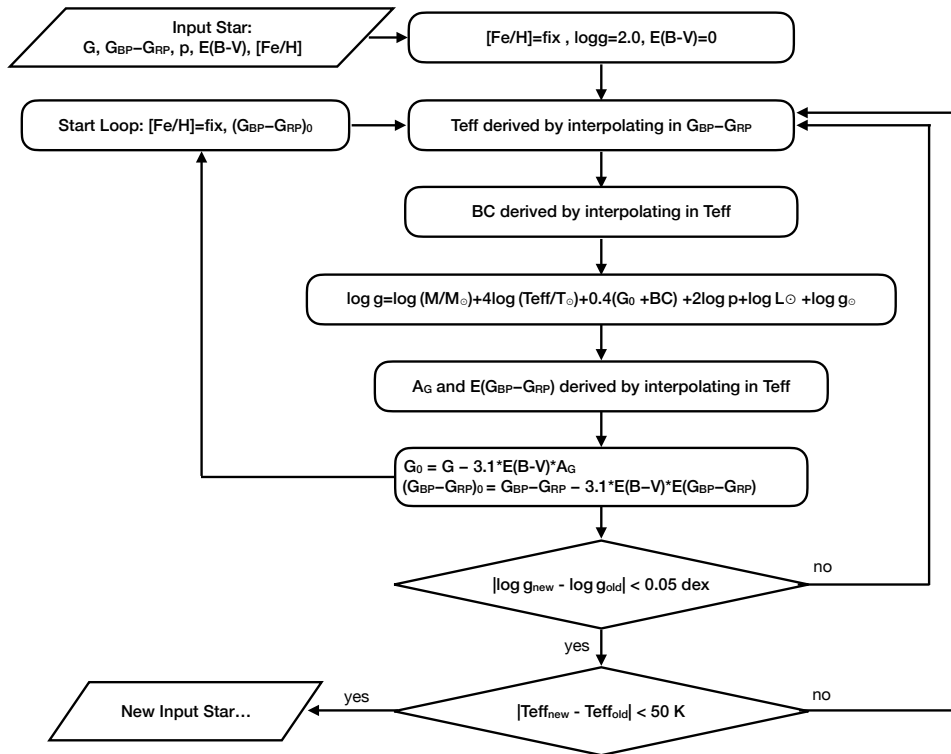


Figure 3.1: Diagram of the iterative procedure employed to derive the stellar parameters.

The effective temperatures (T_{eff}) and surface gravities ($\log g$) for our sample of stars have been derived using the iterative procedure shown in Fig. 3.1. The procedure is based on a grid, defined in the parameters' space, which contains theoretical values of $G_{BP}-G_{RP}$, bolometric correction (BC_G), and extinction coefficients A_G , $E(G_{BP}-G_{RP})$, for each set of T_{eff} , $\log g$, and $[\text{Fe}/\text{H}]$. The grid is defined in the range of parameters $3500 \leq T_{\text{eff}} \leq 6000$, $0 \leq \log g \leq 4$, and $-4 \leq [\text{Fe}/\text{H}] \leq +0.5$. The α -elements are enhanced by $+0.4$ dex for all models with $[\text{Fe}/\text{H}] \leq -1$, and they are solar-scaled for higher metallicity models. Synthetic colours and extinction coefficients are calculated using grids of ATLAS 9 1D plane-parallel model atmosphere by Castelli & Kurucz (2003). The reddening $E(G_{BP}-G_{RP})$ is computed using the reddening law of Fitzpatrick et al. (2019).

The procedure illustrated in the diagram can be described as follows. To derive the stellar parameters the procedure needs the Gaia photometry (G , $G_{BP}-G_{RP}$) and parallax, the reddening $E(B-V)$, and the metallicity of the star. At the beginning of the first run, $[\text{Fe}/\text{H}]$ is fixed at the input value, $\log g$ is fixed at 2.0 dex, and the reddening is

assumed to be zero. Since the sample stars are giants, a $0.8 M_{\odot}$ mass is assumed. The procedure derives the T_{eff} and $\log g$ in different steps. Firstly, T_{eff} is derived using the input $G_{BP} - G_{RP}$ by interpolating this value in the grid. Secondly, BC_G is found by interpolating the newly found T_{eff} in the grid. Finally, the new $\log g$ is determined using T_{eff} and BC_G found in the previous steps from the Stefan-Boltzmann equation (see equation in Fig. 3.1). At this point, the procedure derives the extinction coefficients A_G and $E(G_{BP} - G_{RP})$ by interpolating the new T_{eff} in the grid, and uses these values to obtain G_0 and $(G_{BP} - G_{RP})_0$. The procedure is then repeated with the new value of $(G_{BP} - G_{RP})_0$ and a new set of T_{eff} and $\log g$ is derived, until the difference in $\log g$ between consecutive runs is smaller than 0.05 dex and the difference in T_{eff} is less than 50 K. The metallicity of the star is fixed at the input value (which can be a guess value) during all the procedure, so the parameters need to be derived with a more accurate value of metallicity. The iron abundance is derived using MyGIsFOS with the new set of stellar parameters, and the procedure is repeated with the newly found $[\text{Fe}/\text{H}]$ as input. If the difference between the new and the old T_{eff} is more than 50 K, we derive again the Fe abundance and the procedure is repeated until the parameters converge. The convergence is usually reached after two iterations.

3.2.2 Line broadening

The observed line width in a stellar spectrum is due to several effects: the instrumental resolution, the thermal broadening, and the stellar rotation. Old giant stars usually have low rotational velocities, $v_{\text{rot}} \sim$ a few km s^{-1} , because of the angular momentum loss during the main sequence phase and the increase of the stellar radius when evolving towards the red giant branch. The contribution of the rotational broadening is therefore negligible in their spectral lines. For spectra of giant stars with a resolution $R \geq 60000$, the contribution to line broadening due to the instrument becomes negligible, and the line width is dominated by the thermal broadening. Since the thermal broadening is already included in the model atmosphere and in the synthetic spectrum, for spectra of this resolution we would expect the broadening of the observed lines to be equal to that of the synthetic lines. This is not the case, and instead we find that the observed lines have a larger broadening than the theoretical ones, and that this broadening is different for each star. This leads us to assume that there is an additional broadening effect that depends on the star, and this effect is the macroturbulence.

To perform the chemical analysis, MyGIsFOS uses a grid of synthetic spectra with a given broadening value (v_{broad}). This parameter takes into account the instrumental and the macroturbulence broadening, allowing us to obtain an accurate measurement of the chemical abundances. For this purpose, we developed a procedure to estimate the line broadening for each observed spectrum. We selected a list of isolated, non-saturated lines in the observed spectra and measured their full width half maximum (FWHM). We calculated a set of synthetic spectra with stellar parameters similar to those of the stars in the sample and different v_{broad} . The line broadening due to macroturbulence in the synthetic spectra has been reproduced by adding a Gaussian broadening. We then measured the FWHM of the same lines in the set of synthetic spectra, and for each v_{broad} we determined the mean FWHM over the set of synthetic lines. This allowed us to derive a relation between v_{broad} and the mean measured FWHM (see Fig. 3.2). Finally,

we derived the v_{broad} value to broaden the input grid of synthetic spectra for MyGIsFOS by interpolating in this relation.

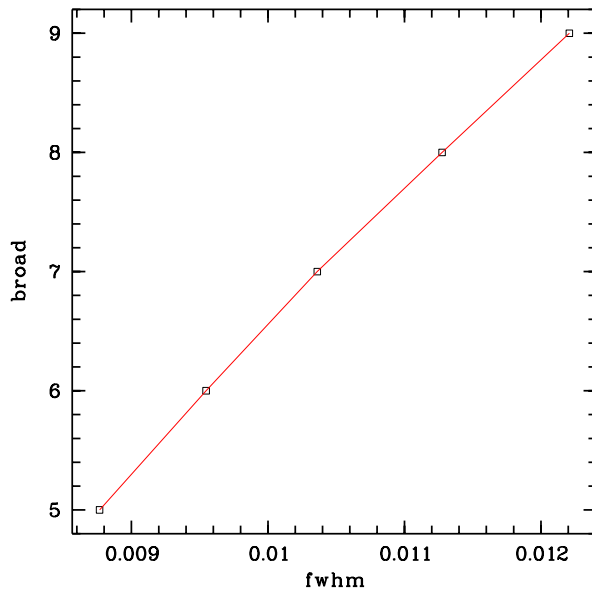


Figure 3.2: Relation between v_{broad} and the mean measured FWHM for a set of synthetic lines.

3.2.3 Main results

Comparison with the literature

The stellar parameters we obtained are, in general, in good agreement with the ones in the literature, as shown in Fig. 3.3. Each symbol in the figure represent a different method employed to derive the stellar parameters: open circles represent T_{eff} and $\log g$ derived from photometry (as done in this study), open squares represent T_{eff} and $\log g$ derived from spectroscopy, and open triangles represent $\log g$ derived from theoretical isochrones. In the spectroscopic method, T_{eff} is obtained by imposing the excitation equilibrium of Fe I lines, that is by requiring that the Fe abundance is independent from the excitation potential of the line, while $\log g$ is obtained by imposing the ionisation equilibrium, thus by requiring that the Fe abundance derived from Fe I must be equal to the one derived from Fe II lines. Our derived T_{eff} are on average hotter than the ones in the literature by ~ 70 K, which is compatible with our uncertainty of ± 100 K. We note that, for six out of seven stars, [Roederer et al. \(2014\)](#) derived a $T_{\text{eff}} \sim 300$ K lower than our derived value. Surface gravities in the literature appear to be on average ~ 0.3 dex lower than our derived values. According to [Mucciarelli & Bonifacio \(2020\)](#), for stars with metallicity around -2.5 , spectroscopic T_{eff} and $\log g$ are on average ~ 350 K and ~ 1.0 dex lower than the respective photometric ones. This is in line with the difference between our derived values and the literature ones, which suggests that the observed discrepancy is only due to the different approaches for the parameters determination.

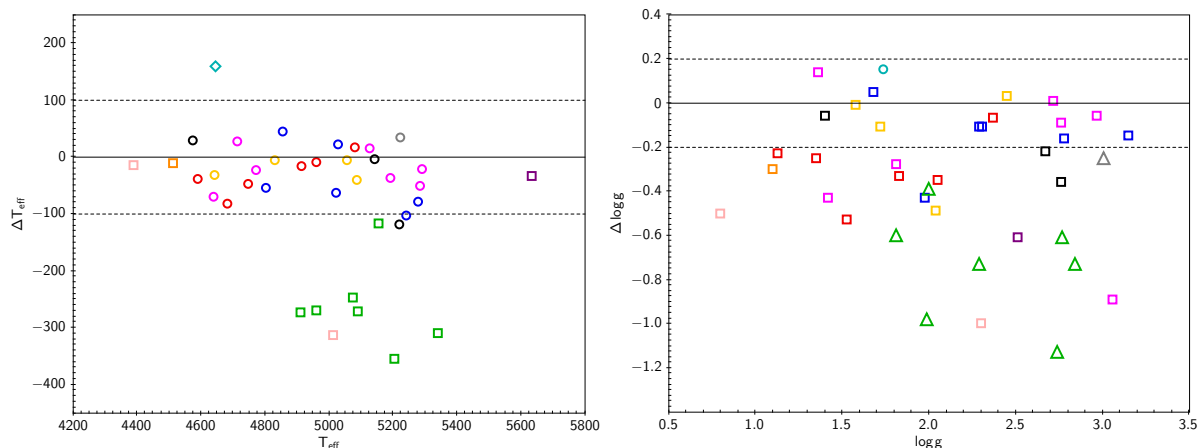


Figure 3.3: Comparison between T_{eff} (left panel) and $\log g$ (right panel) derived in this work and in the literature. ΔT_{eff} and $\Delta \log g$ represent the difference between the literature and the values derived in this study. Comparison data are from Barklem et al. (2005) (black), Cayrel et al. (2004) (red), Hansen et al. (2020) (cyan), Ishigaki et al. (2012) (yellow), Johnson (2002) (pink), Lai et al. (2008) (grey), Luck & Bond (1985) (1985) (orange), Mashonkina et al. (2017) (blue), Pereira et al. (2013) (purple), Roederer et al. (2014) (green), and Siqueira Mello et al. (2014) (magenta). Figure adapted from Lombardo et al. (2022).

Cr abundances

In general, our derived chemical abundances are in good agreement with the ones in the literature for halo stars, particularly when comparing our results with those obtained by Cayrel et al. (2004) and Ishigaki et al. (2012, 2013). We note, however, that the Cr abundances for our sample of stars show some discrepancies with the literature values, as shown in Fig. 3.4. The first difference consists of an offset between the derived abundance ratios and those in the literature. We found that our derived $[\text{Cr I}/\text{Fe I}]$ abundance ratios are ~ 0.15 dex higher than literature values, and $[\text{Cr II}/\text{Fe II}]$ abundance ratios are ~ 0.2 dex lower than Ishigaki et al. (2013) values. The second difference concerns the trend of $[\text{Cr}/\text{Fe}]$ abundance ratios as a function of the metallicity of the stars. In both Cayrel et al. (2004) and Ishigaki et al. (2013) samples, a decreasing trend is observed with metallicity, that is $[\text{Cr I}/\text{Fe I}]$ abundance ratios decrease with decreasing $[\text{Fe}/\text{H}]$. This trend is not as evident in our sample, but instead it appears to increase again at the lowest observed metallicities ($[\text{Fe}/\text{H}] < -3.2$). Another important difference that we observe is that, in our sample, both $[\text{Cr I}/\text{Fe I}]$ and $[\text{Cr II}/\text{Fe II}]$ are ~ 0 , which is theoretically expected since Cr and Fe are both formed under the same physical conditions. We attribute these discrepancies to the different line selections, since previous investigations, as in Cayrel et al. (2004), relied mostly on Cr I resonance lines, which are strongly affected by NLTE effects. Apparently, the Cr I lines we chose for the analysis seem to be less affected by NLTE, which explains why we do not observe the trend with metallicity, but, instead, we observe the ionisation balance between Cr I and Cr II. Figure 3.5 shows the results we obtained for $[\text{Cr I}/\text{Fe I}]$ and $[\text{Cr II}/\text{Fe II}]$ in the different studies presented in this thesis work. In all studies, Cr I and Cr II were derived using MyGIsFOS adopting the same Cr

line list. We note that the results agree quite well, and no clear trend between $[\text{Cr I}/\text{Fe I}]$ and the metallicity of the stars is observed.

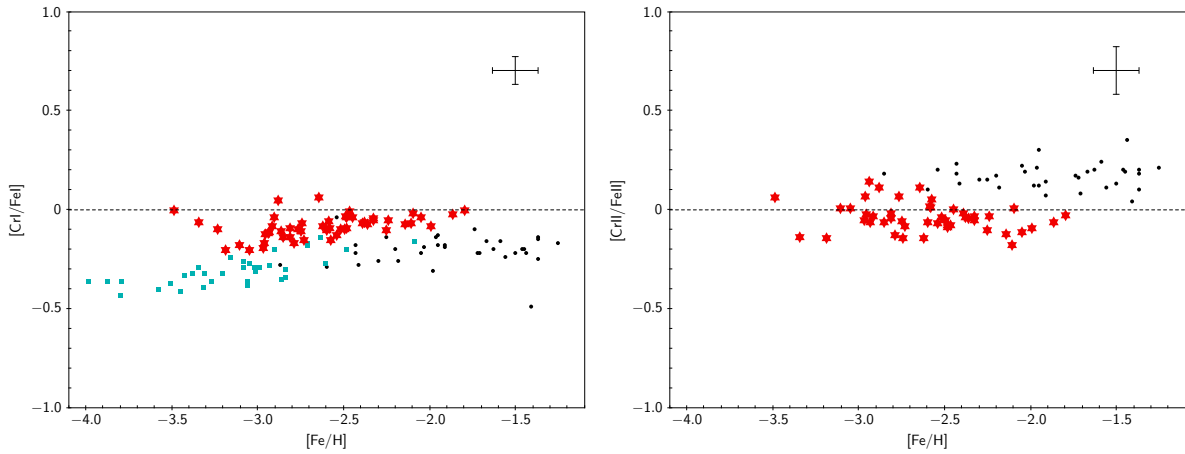


Figure 3.4: $[\text{Cr I}/\text{Fe I}]$ and $[\text{Cr II}/\text{Fe II}]$ as a function of $[\text{Fe}/\text{H}]$ for stars in our sample (red star symbols). Cyan squares and black dots are stars from [Cayrel et al. \(2004\)](#) and [Ishigaki et al. \(2013\)](#), respectively. A representative error is plotted in the upper-right corner of each panel. Figure adapted from [Lombardo et al. \(2022\)](#).

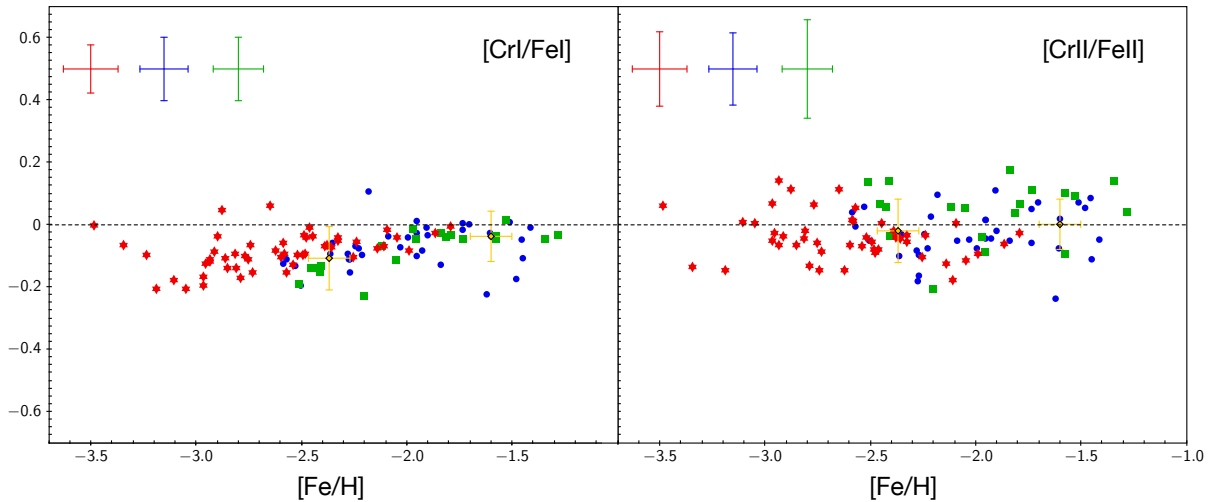


Figure 3.5: $[\text{Cr I}/\text{Fe I}]$ and $[\text{Cr II}/\text{Fe II}]$ as a function of $[\text{Fe}/\text{H}]$ for stars in the studies presented in this thesis: red star symbols are stars in CERES sample, blue circles are MINCE stars from [Cescutti et al. \(2022\)](#), green squares are stars from Pristine XIX ([Caffau et al. 2023](#)), yellow diamonds are stars from [Matas Pinto et al. \(2022\)](#). A representative error for the different samples is plotted in the upper-left corner of each panel.

Zn-rich stars

The analysis revealed the presence of two stars with a Zn abundance ($[\text{Zn}/\text{Fe}] \sim 0.7$) higher than that of the other stars in the sample with similar metallicity: CES1543+0201, also

known as CS 30312-100, and CES2254-4209, also known as HE2252-4225 (see Fig. 3.6). Most intriguingly, the two stars appear to have different enrichment histories, since CES1543+0201 is r-poor ($[\text{Eu}/\text{Fe}]=-0.2$, Roederer et al. 2014) and CES2254-4209 is r-rich ($[\text{r}/\text{Fe}]=+0.8$, Mashonkina et al. 2014). This makes it unlikely that the Zn is produced by the r -process in both stars.

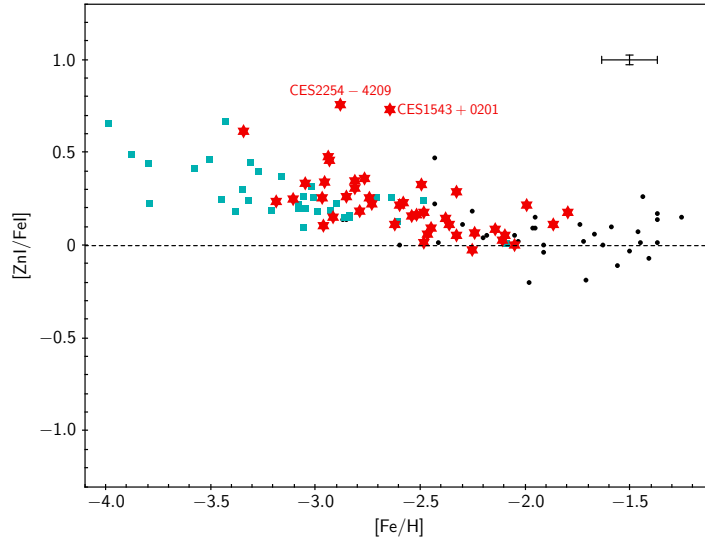


Figure 3.6: $[\text{Zn}/\text{Fe}]$ as a function of $[\text{Fe}/\text{H}]$ for stars in our sample (red star symbols). Cyan squares and black dots represent the same quantities for stars in Cayrel et al. (2004) and in Ishigaki et al. (2013) respectively. A representative error is plotted in the upper right corner of each panel. Figure from Lombardo et al. (2022).

$[\text{Zn}/\text{Fe}]$ versus $[\text{Ni}/\text{Fe}]$

Following the study of Skúladóttir et al. (2017) about Zn abundance in red giant branch stars of the Sculptor dwarf galaxy, we found a correlation between Zn and Ni abundances in our sample. In particular, we note that the stars appear to follow two different branches in the $[\text{Zn}/\text{Fe}]$ vs $[\text{Ni}/\text{Fe}]$ plane, as shown in Fig. 3.7. We think that this two branches could be due to different explosion energies of the supernovae (SNe) for a given mass of the progenitor star (Fig. 3.7, left panel; see e.g. Nomoto et al. 2013, and references therein). Hypernovae are a type of core collapse SNe with explosion energies in excess of than 10^{52} erg. Hypernova explosion can produce larger amount of iron-peak elements, particularly Zn, than classical SNe through α -rich freeze-out (see e.g. Galama et al. 1998; Iwamoto et al. 1998; Nomoto et al. 2001; Umeda & Nomoto 2002). Therefore, it is possible that the stars along the high Zn branch formed in a gas cloud enriched by hypernovae, while the stars with normal Zn formed from gas enriched by classic SNe.

Stars with peculiar abundance patterns

Six stars in the sample present peculiar light neutron-capture element abundance patterns:

- CES1237+1922 (aka BS 16085-0050) is deficient in Sr, Y and Zr compared to stars

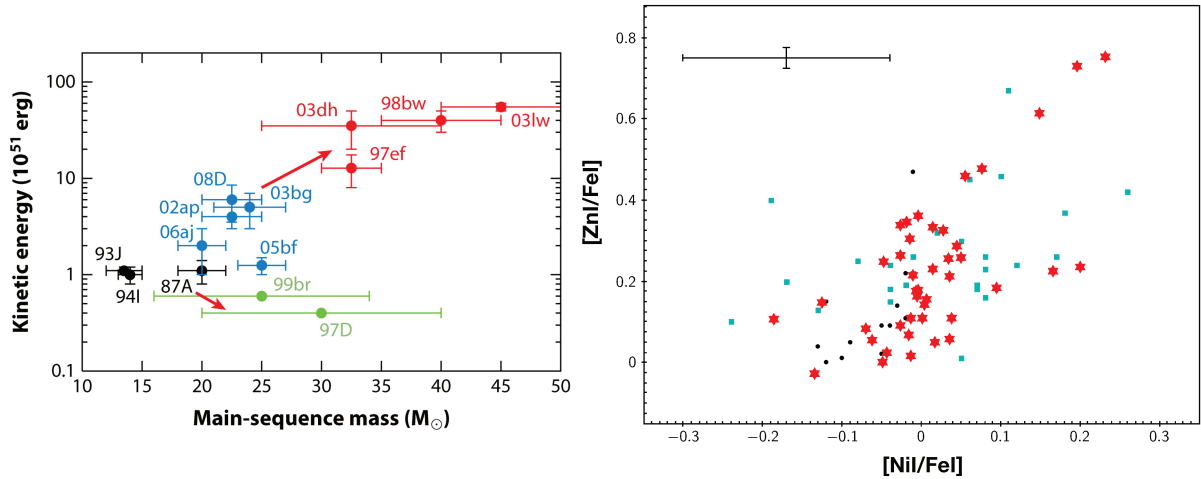


Figure 3.7: *Left panel:* Explosion energy as a function of the main sequence mass of the progenitor stars for several supernovae/hypernovae. Figure from Nomoto et al. (2013). *Right panel:* [Zn/Fe] as a function of [Ni/Fe] for stars in our sample (red star symbols). Cyan squares and black dots represent the same quantities for stars of similar metallicity in Cayrel et al. (2004) and in Ishigaki et al. (2013) respectively. A representative error is plotted in the upper left corner. Figure from Lombardo et al. (2022).

of similar metallicity (see Fig. 3.8), with $[\text{Sr II}/\text{Fe II}] = -1.66$, $[\text{Y II}/\text{Fe II}] = -1.21$, and $[\text{Zr II}/\text{Fe II}] = -1.04$.

- CES0109-0443 (aka CS 22183-031) is underabundant in Sr with respect to Y and Zr, with $[\text{Y II}/\text{Sr II}] = +0.34$ and $[\text{Zr II}/\text{Sr II}] = +0.59$.
- CES2250-4057 (aka CD-41 15048, aka HE 2247-4113) is overabundant in Sr with respect to Y and Zr, with $[\text{Y II}/\text{Sr II}] = -0.80$ and $[\text{Zr II}/\text{Sr II}] = -0.46$.
- CES1322-1355 (aka HE 1320-1339), is overabundant in Sr with respect to Y and Zr, with $[\text{Y II}/\text{Sr II}] = -0.55$ and $[\text{Zr II}/\text{Sr II}] = -0.33$.
- CES0547-1739 (aka TYC 5922-517-1) is overabundant in Zr with respect to Sr and Y, with $[\text{Zr II}/\text{Sr II}] = +0.68$ and $[\text{Zr II}/\text{Y II}] = +0.70$.
- CES0424-1501 (aka BD-15 779) is overabundant in Zr with respect to Sr and Y, with $[\text{Zr II}/\text{Sr II}] = +0.54$ and $[\text{Zr II}/\text{Y II}] = +0.62$.

The homogeneity of the analysis allowed us to highlight many chemical peculiarities in our sample stars. Stellar parameters derived in this study will be used to determine other heavy neutron-capture element abundances in future papers of this project. When a complete chemical inventory for these stars will be available, this will allow us to draw more conclusions on the formation scenarios and the possible formation channels of these elements.

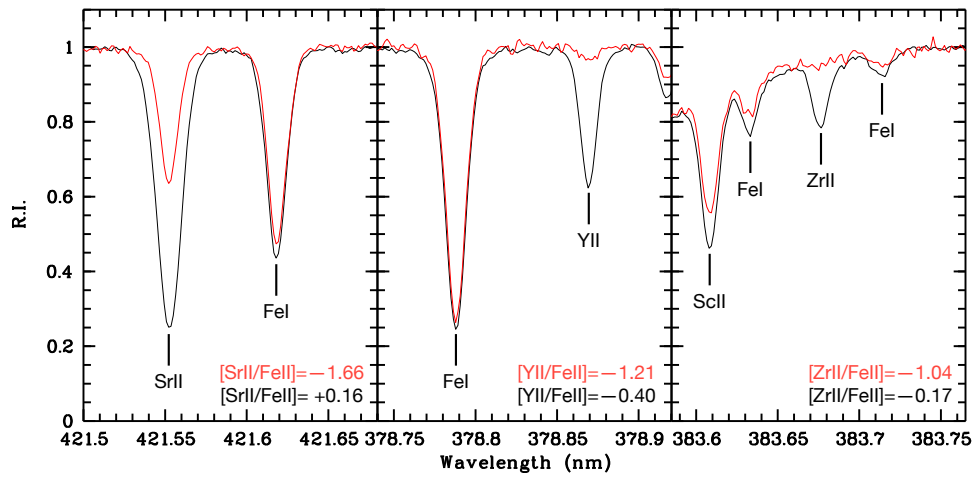


Figure 3.8: Normalised spectra of stars CES1237+1922 (red) and CES1322-1355 (black) around Sr II line at 421.5 nm (left panel), Y II line at 378.8 nm (central panel), and Zr II line at 383.6 nm (right panel). The stars have similar stellar parameters ($T_{\text{eff}}=4960$, $\log g=1.8$, $v_{\text{turb}}=1.9$, $[\text{Fe}/\text{H}]=-3$). Figure from [Lombardo et al. \(2022\)](#).

Chapter 4

High-speed stars

In [Caffau et al. \(2020b\)](#), a sample of 72 giant stars with transverse velocity larger than 500 km s^{-1} and in the G magnitude range 14-14.5 was selected using Gaia DR2 parallaxes and proper motions. The stars were observed with the FOcal Reducer/low dispersion Spectrograph 2 (FOR2; [Appenzeller et al. 1998](#)) at ESO VLT, with a signal-to-noise ratio (SNR) of the order of 90 at 520 nm, allowing to derive chemical abundances for some elements (C, Mg, Ca, Fe, Ti, Sr, and Ba). The aim of this study was to improve our understanding of the early stages of the Galactic star formation history as well as the build-up of the Milky Way.

The study of the kinematics of these stars revealed that all stars have very eccentric halo orbits. In particular, five stars in the sample are unbound to the Galaxy, while the others belong to the Galactic halo. From the chemical investigation it resulted that these stars are chemically homogeneous, with metallicities in the range $-2.61 < [\text{Fe}/\text{H}] < -0.95$ and a peak at ~ -1.5 , and their chemistry is compatible with that of Galactic metal-poor stars. The authors also found that the sub-giant stars in the sample ($\log g > 3$) appear to be younger than expected for metal-poor stars, with ages equal to or less than 8 Gyr. These stars may be evolved Blue Stragglers, or a metal-poor intermediate-age population. Among the possible explanations for the origin of this sample of high-velocity stars, one could be that these stars may have originated in globular clusters, and were then accelerated by gravitational interaction with an intermediate-mass black hole at the centre of the clusters (see e.g. [Fragione & Gualandris 2019](#), and references therein). This scenario is supported by the metallicity distribution and the $[\alpha/\text{Fe}]$ ratios of the sample stars, which is compatible with that of Galactic globular clusters.

This chapter collects two studies that are based on high-speed stars. In the context of the [Caffau et al. \(2020b\)](#) study, Li abundances for two sub-giant stars in the [Caffau et al. \(2020b\)](#) sample were derived using UVES high resolution spectra in order to prove if they are Blue Stragglers or not. The preliminary results are presented in Sect. 4.1. In Sect. 4.2, the results obtained from the chemical analysis of two high-speed stars observed at high resolution with the High Dispersion Spectrograph (HDS) at the Subaru 8.2 m telescope ([Noguchi et al. 2002](#)) are presented.

4.1 A young metal-poor population in the Galactic halo?

An intriguing finding in Caffau et al. (2020b) is that the sub-giant stars ($\log g > 3$) in the sample appear younger than expected. As shown in Fig. 4.1, the sub-giant stars lie in a region of the Gaia colour-magnitude diagram compatible with Parsec isochrones (Bressan et al. 2012) of ages between 2 and 8 Gyr, much less than the expected ages for metal-poor stars in the Galactic halo (10-12 Gyr) (see e.g. Jofré & Weiss 2011; Haywood et al. 2016).

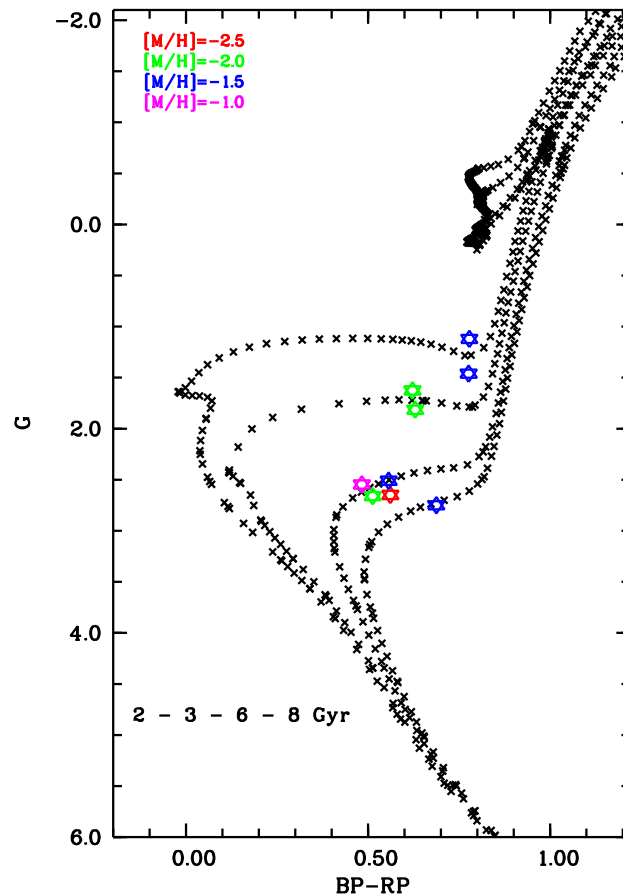


Figure 4.1: Gaia DR2 colour-magnitude diagram of G magnitude and $G_{BP} - G_{RP}$ colour, comparing the observed stars with Parsec isochrones (Bressan et al. 2012) of metallicity $[\text{Fe}/\text{H}] = -1.5$ for four ages (2, 3, 6 and 8 Gyr). The colour-code for the stars define the metallicity of the isochrone used to derive the stellar parameters. Figure adapted from Caffau et al. (2020b).

Different formation scenarios could explain this evidence:

- the stars could represent a young metal-poor population formed in situ, that has so-far never been revealed in the Galaxy.
- the stars could be genuine intermediate-age stars with an extragalactic origin, that were later accreted by the Milky Way (Preston et al. 1994; Unavane et al. 1996);

- the stars could be old field Blue Straggler stars that are evolving to the red giant branch (Preston & Sneden 2000);

All the above-mentioned scenarios are highly interesting. Confirming the existence of a metal-poor young population formed in the Galactic halo would provide a new perspective on the evolution of our Galaxy. The presence of young metal-poor stars formed in situ can only be explained by the existence of a star-forming region in the Galactic halo, composed of metal-poor gas, that formed stars 4-5 Gyr ago. So far, such a scenario has never been revealed in the Galaxy. On the other hand, field Blue Straggler stars are rare objects and their study is necessary to understand the formation paths of Blue Stragglers.

A possible way to understand if these stars are Blue Stragglers or not is to measure their Li abundance. Metal-poor, warm, main-sequence and sub-giant stars with low metallicity ($[\text{Fe}/\text{H}] < -1.5$) have the characteristic of sharing the same Li abundance, the so-called Spite plateau at $A(\text{Li}) \sim 2.2$ (Spite & Spite 1982; Sbordone et al. 2010). As shown in Fig. 4.2, for stars with $T_{\text{eff}} > 5900$ K and metallicity $-2.8 < [\text{Fe}/\text{H}] < -2.0$ the Li abundance is independent of the effective temperature and the metallicity, and remains constant at the value of the Spite plateau.

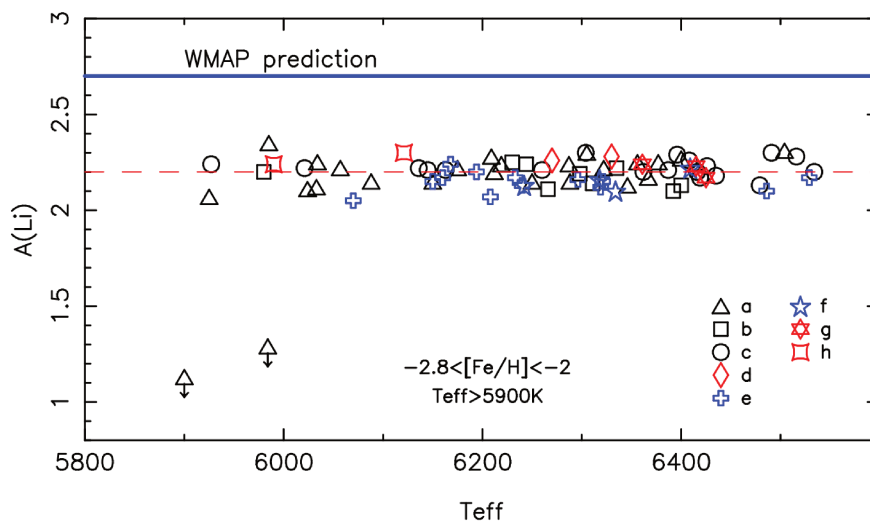


Figure 4.2: Lithium abundance versus T_{eff} for stars with effective temperatures above 5900K and in the metallicity range $-2.8 < [\text{Fe}/\text{H}] < -2.0$. The different symbols correspond to: a) Charbonnel & Primas (2005), b) Asplund et al. (2006), c) Meléndez et al. (2010), d) Aoki et al. (2009), e) Hosford et al. (2009), f) Bonifacio et al. (2007), g) Sbordone et al. (2010), h) Schaeuble & King (2012). The two stars with upper limits are G 122-69 ($T_{\text{eff}} \sim 5900$ K) and G 139-08 ($T_{\text{eff}} \sim 6000$ K). Figure from Spite et al. (2012).

On the other hand, Blue Straggler stars do not lie on the Spite plateau, as they show no detectable Li (Hobbs & Mathieu 1991; Pritchett & Glaspey 1991; Glaspey et al. 1994; Ryan et al. 2001). In Fig. 4.3 the region of Li doublet at 6707 Å for the Blue Stragglers BD+51° 1817, G 202-65, Wolf 550, the Li-depleted star CD-31° 19466, and the Li-normal star CD-31° 305 ($A(\text{Li})=2.24$) in Ryan et al. (2001) are shown. Like the sub-giants in Caffau et al. (2020b), the Blue Stragglers in Fig. 4.3 appear younger than expected for stars of similar metallicity, as shown in Fig. 4.4 (Bonifacio et al. 2019b). The stars

BD+51° 1817, G 202-65, Wolf 550 are all bluer than the isochrones corresponding to the spectroscopic metallicity derived by [Ryan et al. \(2001\)](#), assuming an age of 11.8 Gyr as representative for thick disc stars. The situation is different for the star CD−31° 19466. As discussed in [Bonifacio et al. \(2019b\)](#), for CD−31° 19466, none of Parsec isochrones of metallicity -1.89 is compatible with the position of this star in the colour-magnitude diagram, but its position is compatible with isochrones of metallicity -1.10 .

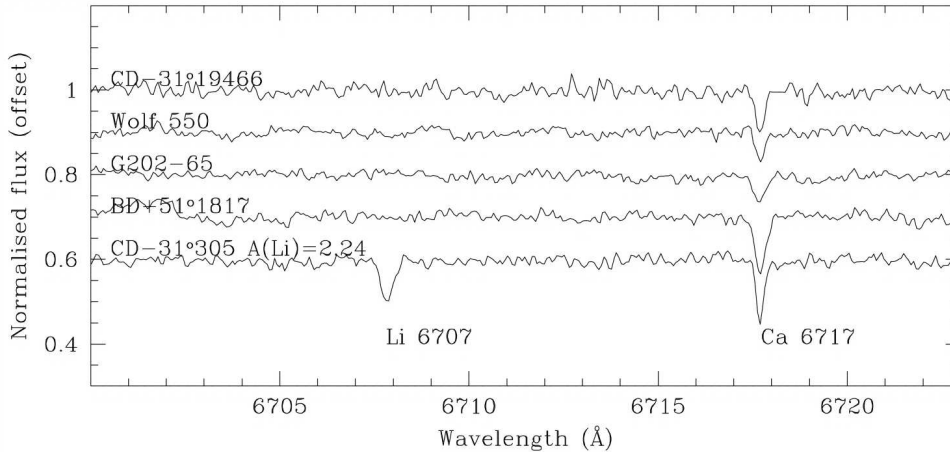


Figure 4.3: Spectra of four Li-depleted stars in the region of the Li 6707 doublet. A fifth stars with Li abundance close to the Spite plateau is shown for comparison. Figure from [Ryan et al. \(2001\)](#).

Li depletion in Blue Stragglers is also predicted by theoretical models. [Glebbeek et al. \(2010\)](#) showed that the Li abundance on the surface of Blue Stragglers is lower than the Spite plateau, and also depends on the Blue Straggler’s formation channel. As shown in Fig. 4.5, if the Blue Straggler is formed through direct physical collision between individual stars, it should be Li depleted, with $A(\text{Li}) \sim 1$ (blue dotted line), while if it is formed through mass transfer due to Roche lobe overflow in a binary system, then its Li abundance should not be measurable (solid red line).

The aim of this study is therefore to understand the nature of this sample of stars from their Li abundance. If some/all the sub-giant stars in the [Caffau et al. \(2020b\)](#) sample are real intermediate-age stars, then their Li abundance should lie on the Spite plateau; on the contrary, if the stars are Blue Stragglers, their Li abundance should be below the Spite plateau.

4.1.1 Observations

With the FORS2 spectra it is not possible to distinguish between a Blue Straggler and a normal star, because the Li doublet is not within the observed wavelength range. For this reason, we requested a high resolution follow-up of these stars with UVES in the ESO period 108, in order to measure the Li doublet at 6707 Å. We obtained 9 hours of observation, but only 2 were executed. The stars GHS69 and GHS70 were observed between December 2021 and March 2022 in service mode under the ESO program 0108.D-0372(A) (PI:Lombardo) using the standard setting DIC1 390+580 (3260–4540 Å in the blue arm and 4760–6840 Å in the red arm). With a slit of 1” and a 1×1 binning this setting

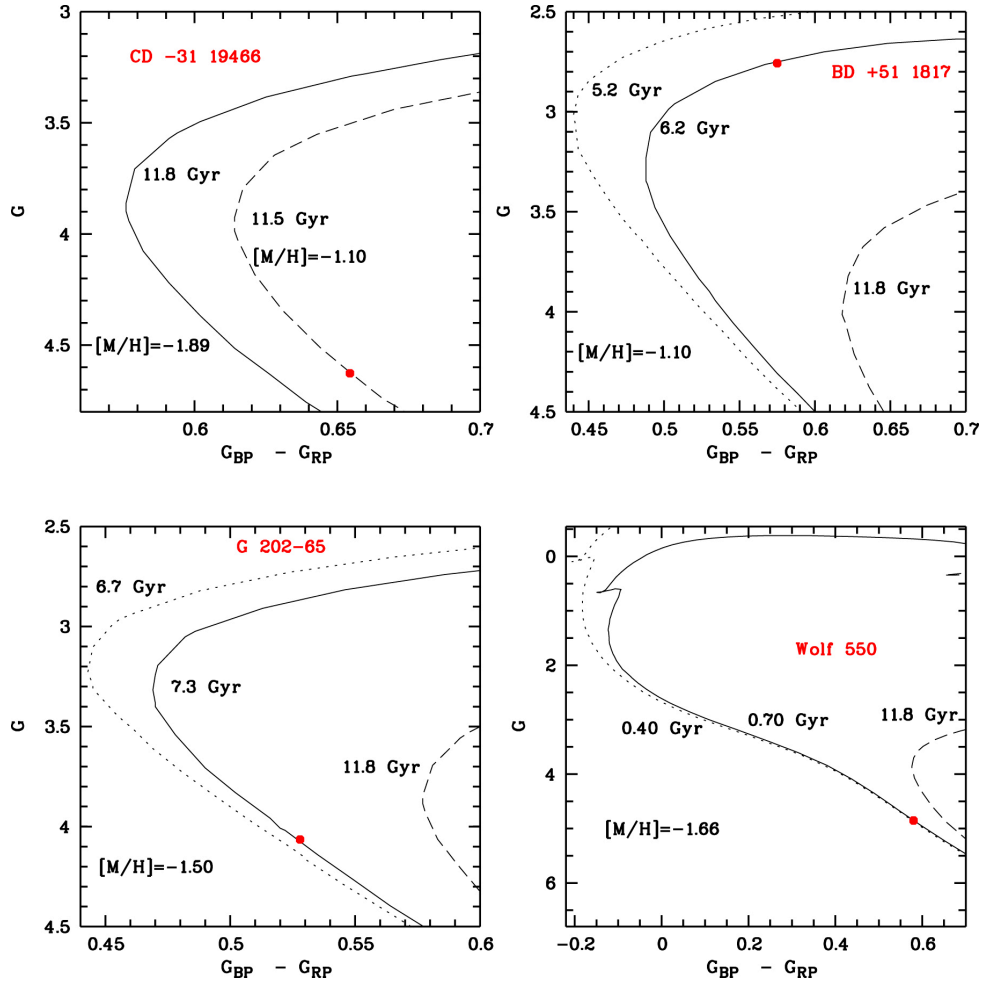


Figure 4.4: Gaia colour-magnitude diagram for the four Li-depleted stars in Fig. 4.3. In each panel Parsec isochrones are shown. Figure from [Bonifacio et al. \(2019b\)](#).

provides a resolving power of ~ 40000 . With one hour observing blocks (corresponding to 3000s integration) we expected to obtain $60 \leq \text{SNR} \leq 80$ at 6710 \AA and $30 \leq \text{SNR} \leq 40$ at 4000 \AA . The stars were observed with seeing < 1 and airmass ~ 2 . The star GHS70 was observed two times, as the mean seeing of the first observation was above the requested one (seeing ≤ 1.2). With these constraints, we achieved a mean SNR lower than expected around the Li doublet, with SNR ~ 42 for GHS69, and SNR ~ 55 for GHS70 (by summing the two exposures).

4.1.2 Li abundance

With the stellar parameters in [Caffau et al. \(2020b\)](#) and the new spectra obtained with UVES, I derived again the metallicities for the stars GHS69 and GHS70 using MyGIsFOS ([Sbordone et al. 2014](#)). I obtained $[\text{Fe}/\text{H}] = -2.40 \pm 0.19$ for GHS69 and $[\text{Fe}/\text{H}] = -1.91 \pm 0.12$ for GHS70. The new metallicities are slightly lower than the one found in [Caffau et al. \(2020b\)](#) ($[\text{Fe}/\text{H}] = -1.94$ for GHS69, and $[\text{Fe}/\text{H}] = -1.59$ for GHS70). In our opinion, this difference in metallicity is due to the different resolution of the spectra that were analysed in the two studies, as in [Caffau et al. \(2020b\)](#) only the FORS2 low resolution spectra

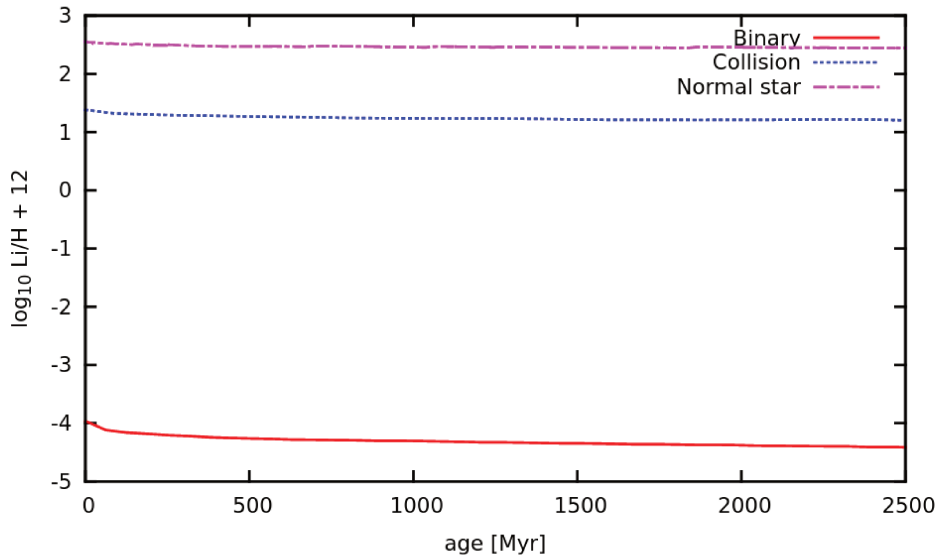


Figure 4.5: Li abundance evolution as a function of time for Blue Straggler stars formed through collision (dashed blue line) and from mass transfer (solid red line). The Li abundance of a normal star with the same mass is included for reference (dash-dotted magenta line). Figure from [Glebbeeck et al. \(2010\)](#).

were available. The SNR ratios obtained allowed us to derive only upper limits for the Li abundance for the two stars. To obtain upper limits on Li abundance, I estimated the minimum measurable EW at 3σ detection for the Li doublet using the Cayrel formula¹ ([Cayrel 1988](#)). I then computed the curve of growth for the Li doublet by measuring the EW of the Li doublet in synthetic spectra for different values of $A(\text{Li})$. The synthetic spectra were computed with the spectral-synthesis code SYNTHE (see [Kurucz 2005](#); [Sbordone et al. 2004](#)), starting from ATLAS 9 1D plane-parallel model atmosphere computed using an ODF by [Castelli & Kurucz \(2003\)](#), and atomic data including the hyperfine structure of the Li doublet from Kurucz’s database².

GHS69

For the star GHS69, for a model atmosphere with $T_{\text{eff}}=6700$, $\log g=3.9$, $v_{\text{turb}}=1 \text{ km s}^{-1}$, and $[\text{Fe}/\text{H}]=-2.5$, a $\text{SNR} \sim 42$ would imply a minimum measurable EW for the Li doublet of $8 \text{ m}\text{\AA}$, which corresponds to a Li abundance of 2.0 dex. The spectrum of GHS69 (black) is compared to three synthetic spectra with $A(\text{Li})=1.0, 1.5, 2.0$ dex in Fig. 4.6. In blue, the GHS69 spectrum degraded with a broadening of 3 km s^{-1} is plotted for a better comparison.

GHS70

For the star GHS70, for a model atmosphere with $T_{\text{eff}}=6500$, $\log g=3.8$, $v_{\text{turb}}=1 \text{ km s}^{-1}$, and $[\text{Fe}/\text{H}]=-2.0$, a $\text{SNR} \sim 55$ would imply a minimum measurable EW for the Li doublet

¹Cayrel’s formula estimates the root mean square error on the EW of a line ($\langle \delta W^2 \rangle^{1/2}$), and it is written in the form $\langle \delta W^2 \rangle^{1/2} \simeq (\text{FWHM} * \delta x) / \text{SNR}$, where δx is the pixel size of the spectrum.

²<http://kurucz.harvard.edu/atoms/0300/>

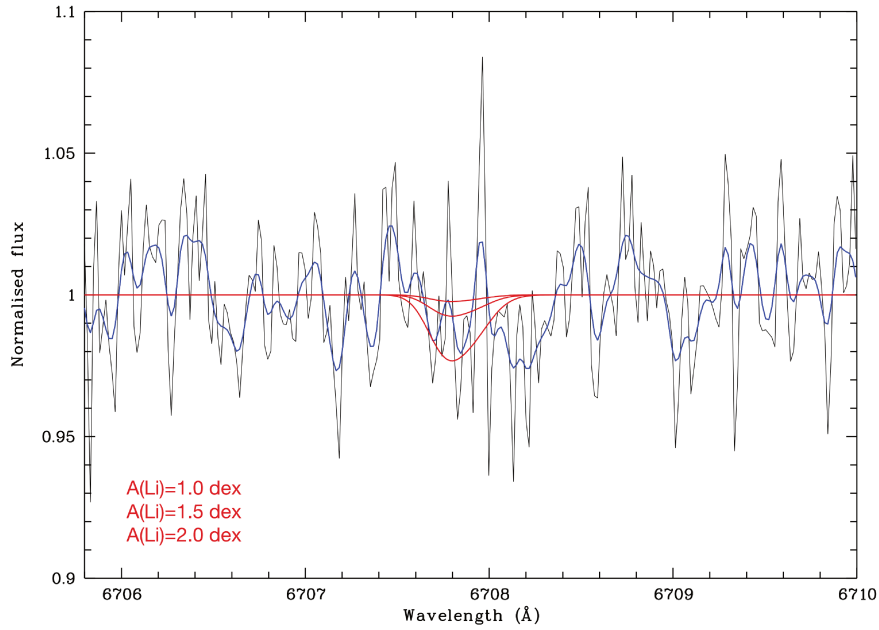


Figure 4.6: Spectra of GHS69 in the region of the Li 6707 Å doublet. Red lines represent synthetic spectra with Li abundances of $A(\text{Li})=1.0$, 1.5, 2.0 dex. Blue line represents GHS69 spectrum with a broadening of 3 km s^{-1} .

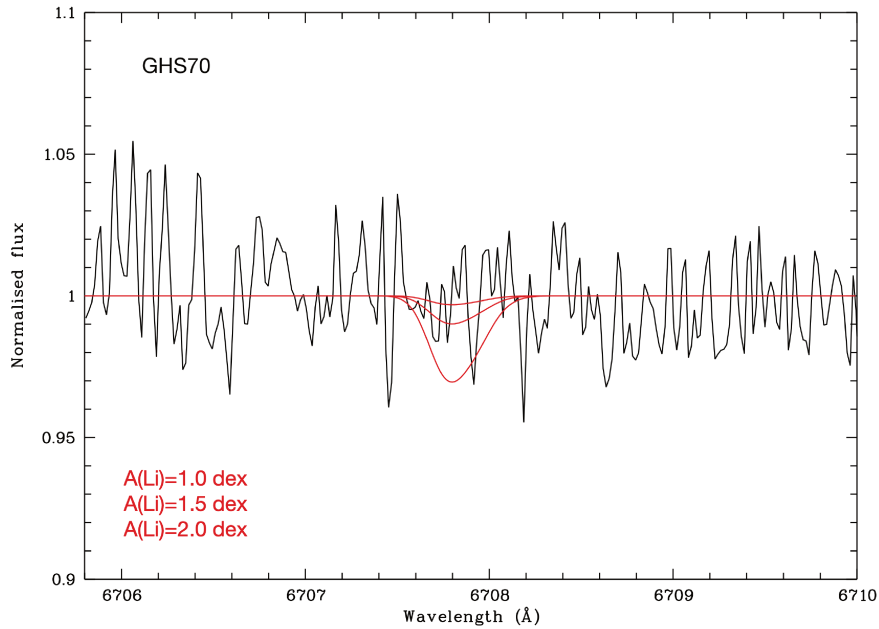


Figure 4.7: Spectra of GHS70 in the region of the Li 6707 Å doublet. Red lines represent synthetic spectra with Li abundances of $A(\text{Li})=1.0$, 1.5, 2.0 dex.

of 6 mÅ , which corresponds to a Li abundance of 1.8 dex. The spectrum of GHS70 (black) is compared to three synthetic spectra with $A(\text{Li})=1.0$, 1.5, 2.0 dex in Fig. 4.7.

4.1.3 Discussion and conclusions

Although the upper limits I derived for Li are relatively close to the Spite plateau, they still give us some clues about the nature of these stars. The first hint can be found by considering the upper limits values found for the two stars. Li abundance is lower than the Spite plateau for both stars ($A(\text{Li}) < 2.0$ dex for GHS69 and $A(\text{Li}) < 1.8$ dex for GHS70), which makes them similar to Blue Stragglers. The second clue comes from comparing the spectra with observations of comparable quality. Figure 4.8 shows the regions around the Li 6707 doublet for the stars GHS70 and the Li-normal star BD+20 3603. The spectrum of BD+20 3603 shown in figure was obtained in April 2000 in visitor mode under the ESO program 65.L-0507(A) using the standard setting DIC1 346+580 (3030–3880 Å in the blue arm and 4730–6840 Å in the red arm). The spectrum has a resolution of $R=42310$ and $\text{SNR}=260$. According to [Bonifacio & Molaro \(1997\)](#), BD+20 3603 has stellar parameter similar to that of GHS70 ($T_{\text{eff}}=6441\text{K}$, $\log g=4.30$ dex, $[\text{Fe}/\text{H}]=-2.05$) and $A(\text{Li})=2.40$ dex. At $\text{SNR}=55$, the Li doublet is clearly measurable in BD+20 3603, while it is not in GHS70. This suggests that, if the Li abundance of GHS70 was on the Spite plateau, the Li doublet should be detectable at this SNR. Again, this makes GHS70 more similar to Blue Stragglers than to Li-normal stars.

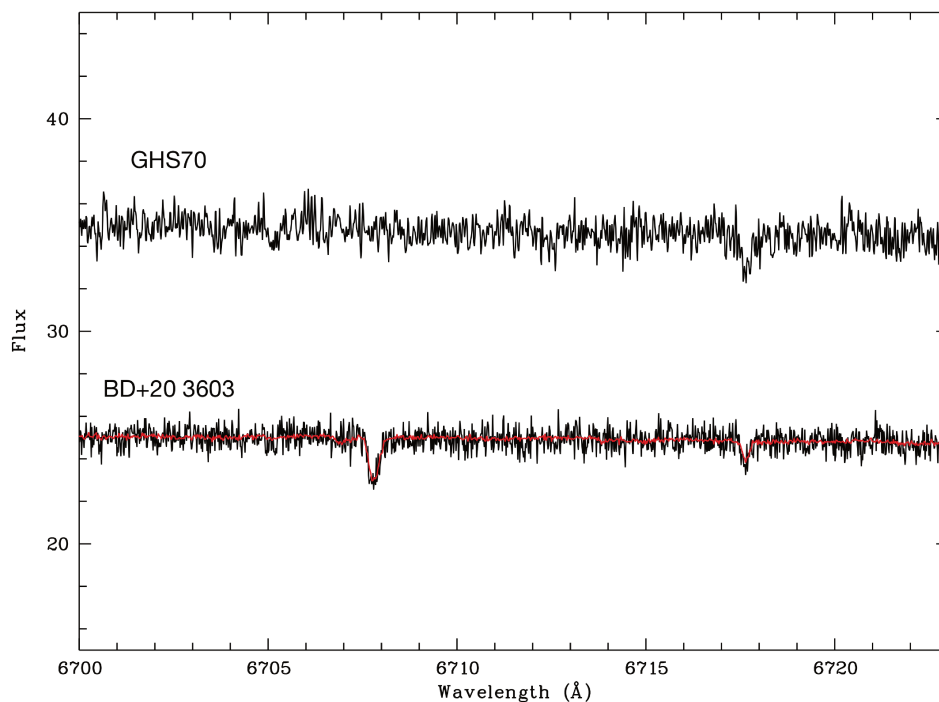


Figure 4.8: Spectra of GHS70 and BD+20 3603 in the region of the Li 6707 Å doublet. The spectrum in red for BD+20 3603 is a UVES spectrum of the star with $\text{SNR}=260$. The spectrum in black for BD+20 3603 is the spectrum in red degraded to $\text{SNR}=55$.

These evidences seem to suggest that the stars are more likely blue stragglers rather than intermediate-age stars. However, [Boesgaard & Tripicco \(1986\)](#) found that dwarf stars in the Hyades open cluster with T_{eff} similar to GHS69 and GHS70 ($6400 \leq T_{\text{eff}} \leq 6800$ K) are depleted in Li, the so-called Li dip. The Li dip is also detected in other open clusters

older than 200 Myr, like NGC 752 (Hobbs & Pilachowski 1986; Pilachowski & Hobbs 1988), Praesepe (Boesgaard & Budge 1988; Soderblom et al. 1993), M67 (Balachandran 1995), and M34 (Jones et al. 1997), while it is not detected in young clusters (see e.g. Boesgaard & Budge 1988) and among field stars (Lambert & Reddy 2004). Several interpretations for the Li dip have been proposed, such as diffusion (Michaud 1986; Proffitt et al. 1990), rotationally induced mixing (Pinsonneault et al. 1992; Böhm-Vitense 2004; Talon & Charbonnel 2003), and mass loss (Schramm et al. 1990). It could therefore be possible that these two stars may actually be intermediate-age stars that are depleted in Li because of the Li dip.

François et al. (2013) studied the Li dip in the old metal-poor open cluster NGC 2243. This cluster is one of the most metal-poor open clusters in the Galaxy, with $[\text{Fe}/\text{H}] \sim -0.5$ and an age of ~ 4 Gyr (Kaluzny et al. 2006). The authors found that, in NGC 2243, the stars without a Li detection are located in the warmest part of the Zero Age Main Sequence (ZAMS) (Fig. 4.9), and that the Li dip is shifted to higher temperatures with respect to the other open clusters, with $6700 \leq T_{\text{eff}} \leq 6900$ K. Comparing different open clusters, Balachandran (1995) found that the mass at which the Li dip occurs depends on the stellar metallicity, while the ZAMS temperature does not. François et al. (2013) confirmed this evidence, and found a correlation between the mass of the Li dip’s cool-side and the metallicity of the open cluster (Fig. 4.10). They estimated the mass of the red side of the Li dip, corresponding to a T_{eff} of 6700 K and $[\text{Fe}/\text{H}] = -0.5$, to be $1.03 M_{\odot}$.

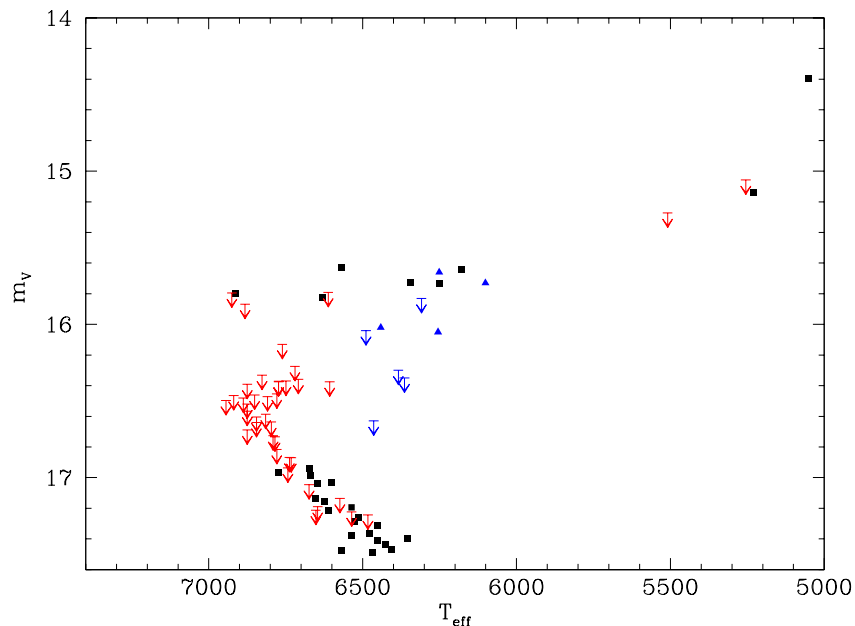


Figure 4.9: V magnitude as a function of stellar effective temperature. Black squares are measurements for targets in François et al. (2013). Arrows represent upper limits of Li abundance measurements. Blue symbols are results from Hill & Pasquini (2000). Figure from François et al. (2013).

According to Parsec isochrones with $[\text{Fe}/\text{H}] = -2$ and an age of 8 Gyr, GHS69 and GHS70 should have a mass $\sim 0.9 M_{\odot}$. Assuming that the two stars are in the mass range covered by the Li dip at $[\text{Fe}/\text{H}] = -2$, the relation in Fig. 4.10 should have a trend such

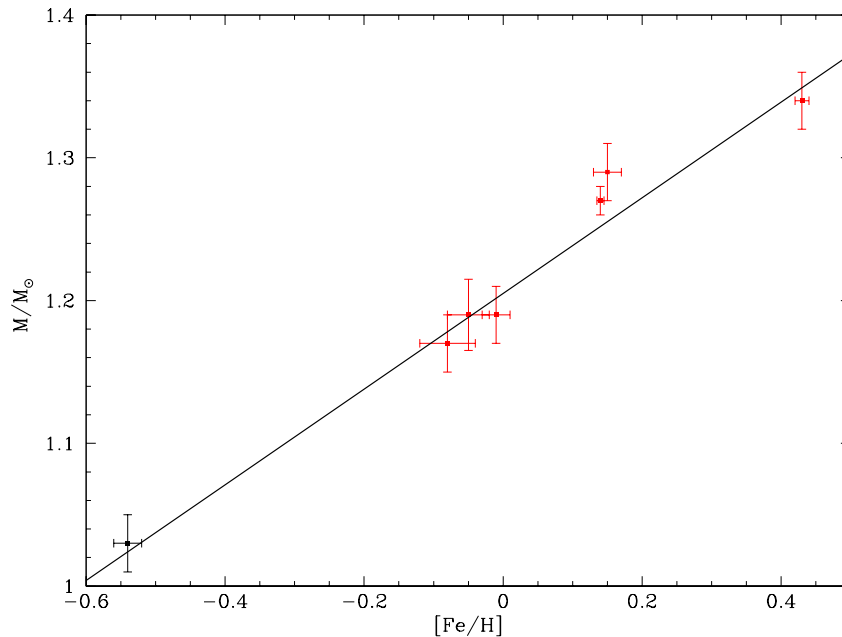


Figure 4.10: Correlation between the mass of Li dip cool-side and the cluster metallicity. Black symbol represents the result obtained for NGC 2243 in [François et al. \(2013\)](#). Red symbols are data from the literature. The black line represents a linear regression fit to the data. The slope value is 0.33 and the correlation coefficient is 0.98. Figure from [François et al. \(2013\)](#).

that the mass of the red edge of the Li dip is slightly less than $0.9 M_{\odot}$. Since the trend of this relation is not known for metallicities below -0.5 , and the mass range covered by the Li dip appears to be rather narrow, it seems unlikely that GHS69 and GHS70 are in the Li dip. Furthermore, the Li dip has never been observed in metal-poor halo stars so far. In conclusion, it appears more likely that GHS69 and GHS70 are Blue Stragglers rather than intermediate-age metal-poor star, even if we cannot completely exclude the second hypothesis.

4.2 Detailed investigation of two high-speed evolved Galactic stars (Matas Pinto et al. 2022)

According to the results obtained in [Caffau et al. \(2020b\)](#), the high-speed stars appear to have a very homogeneous chemistry, compatible with that of halo stars. However, low resolution spectra allow us to derive abundances only for a few elements, so the determination of the chemical pattern is very limited. It is only through high-resolution observations that we can understand whether the high-speed stars harbour any peculiarities in their abundance patterns.

For this reason, we selected a sample of bright high-speed stars to be observed as backup targets in case of bad weather conditions for our observing run at Subaru telescope. The stars were selected from the Gaia DR2 catalogue with $G < 11$ and total

speed with respect to the Sun $> 500 \text{ km s}^{-1}$. In this study we performed the detailed chemical analysis and determination of the kinematic and orbital properties of two giant stars, TYC 622–742–1 and TYC 1193–1918–1. These stars belong to the Subaru backup sample and were observed on September 13th 2019 with the HDS at Subaru. The stellar parameters were derived using photometry and parallaxes of the Gaia EDR3 catalogue (Gaia Collaboration et al. 2016, 2021) as described in Sect. 3.2.1. The detailed chemical abundances for 32 species of 28 elements (C, N, O, Na, Mg, Al, Si, Ca, Sc, Ti I, Ti II, V, Cr I, Cr II, Mn, Fe I, Fe II, Co, Ni, Cu, Zn, Sr, Y, Zr I, Zr II, Ba, La, Ce, Pr, Nd, Sm, and Eu) were derived using the code MyGIsFOS (Sbordone et al. 2014) up to Zn and using TurboSpectrum (Alvarez & Plez 1998) for the heavy elements.

The chemical analysis revealed that the two stars share a similar chemical pattern:

- both stars are metal-poor, with $[\text{Fe}/\text{H}] = -2.37 \pm 0.10$ and $[\text{Fe}/\text{H}] = -1.60 \pm 0.10$ for TYC 622–742–1 and TYC 1193–1918–1 respectively;
- both stars are α -enhanced, as expected for metal-poor stars;
- both stars are poor in C and rich in N, as expected for evolved stars, with the stars TYC 1193–1918–1 having a low $^{12}\text{C}/^{13}\text{C}$ isotopic ratio ($^{12}\text{C}/^{13}\text{C} = 4.9_{-1.9}^{+6.5}$);
- their chemistry is compatible with that of the other Galactic halo stars of similar metallicity.

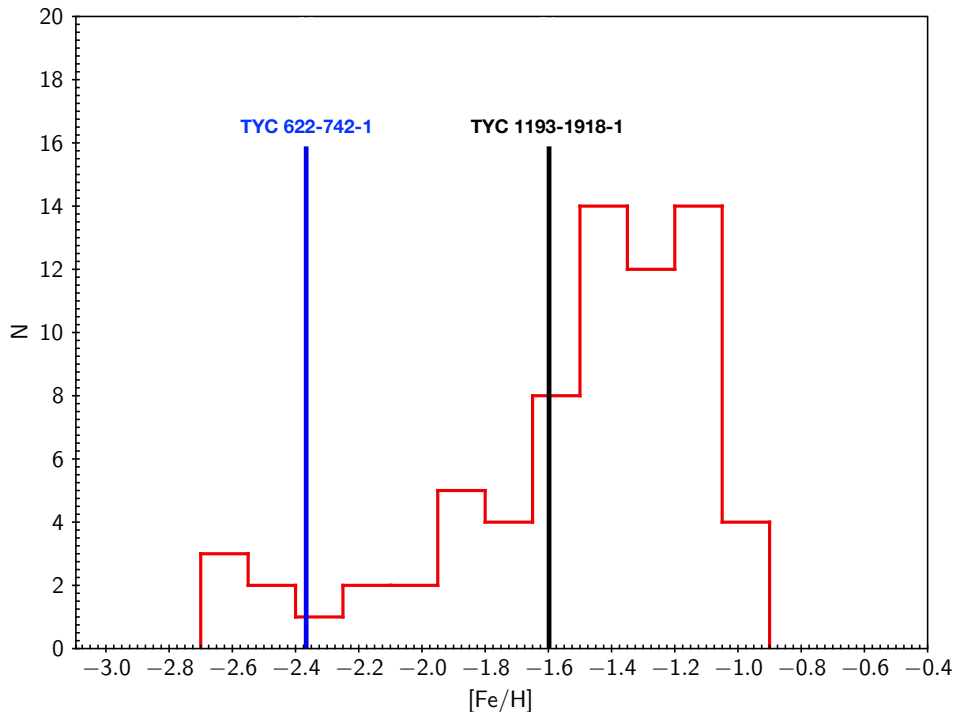


Figure 4.11: Metallicity distribution for stars in Caffau et al. (2020b) (solid red). The vertical lines represent the metallicity of stars TYC 622–742–1 (blue) and TYC 1193–1918–1 (black).

Furthermore, the stars are in the same metallicity range as the Caffau et al. (2020b) sample, as shown in Fig. 4.11. These results confirm what has been found in Caffau et al. (2020b), namely that high-speed stars appear to be in a narrow metallicity range, with no extreme metal-poor stars.

The study of the kinematics showed that the two stars have retrograde orbits with high ellipticity. Figure 4.12 shows the so-called action diamond diagram, that is the difference between the vertical and radial actions ($J_Z - J_R$) versus the azimuthal action ($J_\phi = L_Z$), normalised to the total action $J_{tot} = |J_Z| + |J_R| + |J_\phi|$. Feuillet et al. (2021) used this diagram to select stars that are likely members of GSE (magenta dots in figure) and Sequoia (cyan dots in figure) accretion events. In the action diamond diagram, Galactic disc stars are located in the middle-right corner of the figure, GSE candidates are highly eccentric (large $\sqrt{J_R}$) and with a small angular momentum (small $J_\phi = L_Z$), and Sequoia candidates are highly retrograde (large and negative $J_\phi = L_Z$) and have orbits less eccentric than those of GSE candidates.

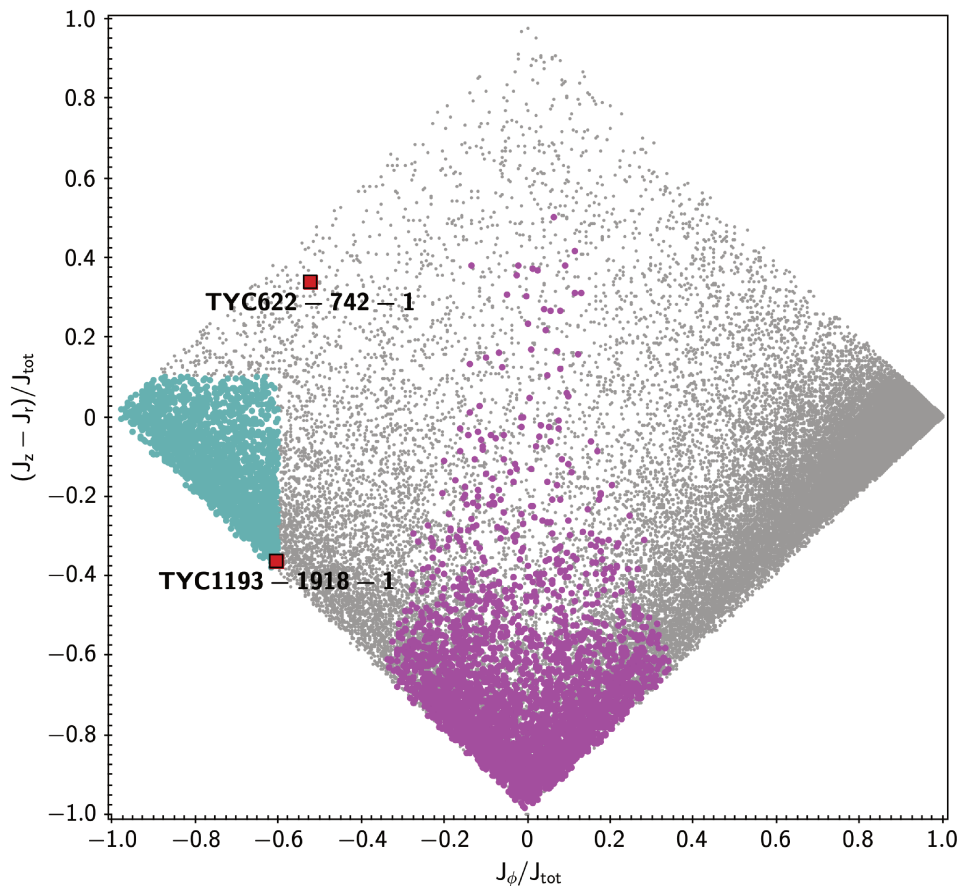


Figure 4.12: Action diamond diagram. Red squares are the two stars in our study. Gray points are the "good parallaxes sample" of Bonifacio et al. (2021) and is presented for reference. Magenta points are stars selected from the background population as likely GSE members ($-500 \leq L_Z \leq 500$ kpc km s $^{-1}$ and $30 \leq \sqrt{J_R} \leq 55$ (kpc km s $^{-1}$) $^{1/2}$), and cyan points are likely Sequoia members ($-1.0 < (J_Z - J_R)/J_{tot} < -0.6$ and $-1.0 < J_\phi/J_{tot} < 0.1$) according to Feuillet et al. (2021).

We note that the kinematics of TYC 1193-1918-1 is compatible with the one of Sequoia

candidates. Recently, from the chemical analysis of a sample of high-resolution spectra of nine GSE and Sequoia candidates kinematically selected from Gaia DR2, [Aguado et al. \(2021\)](#) found that both GSE and Sequoia potential stars show an enhancement in Eu abundance, with a mean $[\text{Eu}/\text{Fe}] = +0.65$ and a low scatter. This, combined with $[\text{Ba}/\text{Fe}] \sim 0$, suggests a production of n-capture elements in both GSE and Sequoia mainly through r-processes. They also found an offset in $[\text{Ba}/\text{Fe}]$ between GSE and Sequoia, with Sequoia candidates being ~ 0.2 dex richer in Ba with respect to GSE ones. If we compare the Ba and Eu abundances we derived for TYC 1193–1918–1 ($[\text{Ba}/\text{Fe}] = -0.08 \pm 0.04$, $[\text{Eu}/\text{Fe}] = 0.47 \pm 0.14$), we see that they are compatible within errors with the mean values derived by [Aguado et al. \(2021\)](#) for Sequoia candidates ($\langle [\text{Ba}/\text{Fe}] \rangle = -0.01$ $\sigma = 0.07$, $\langle [\text{Eu}/\text{Fe}] \rangle = 0.70$ $\sigma = 0.07$, where σ is the standard deviation). This evidence seems to suggest that the star may belong to Sequoia. However, it is worth keeping in mind that, although [Aguado et al. \(2021\)](#) found this signature in the Eu abundance, no clear patterns were found in the abundances of other elements. In conclusion, even if the Eu abundance in TYC 1193–1918–1 supports the hypothesis that the star belongs to Sequoia, the abundance of other elements make it basically indistinguishable from other halo stars.

Chapter 5

PRISTINE survey

This chapter presents the chemical analysis of two samples of stars selected using Pristine photometry. The Pristine survey (Starkenburg et al. 2017) is a photometric narrow-band survey at Canada–France–Hawaii Telescope (CFHT) that combines the wide-field imager MegaCam with a narrow-band filter centered on the metallicity-sensitive Ca II H&K lines at 3968.5 and 3933.7 Å. Figure 5.1 shows the region covered by the Pristine filter (black dashed line) and the comparison between synthetic spectra with different stellar parameters and metallicities. It is evident from the figure how, given the same stellar parameters, the depth of the Ca II H&K lines decreases as the metallicity decreases. Combining the Pristine photometry with broad-band surveys (SDSS and Gaia), we can infer photometric metallicities with an accuracy of ~ 0.2 dex from $[\text{Fe}/\text{H}] = -0.5$ down to $[\text{Fe}/\text{H}] < -3.0$. This technique has shown to be highly effective, as proved by the excellent results obtained by the Pristine collaboration (see e.g. Starkenburg et al. 2018; Bonifacio et al. 2019a; Aguado et al. 2019; Venn et al. 2020; Caffau et al. 2020a; Kielty et al. 2021; Lardo et al. 2021; Lucchesi et al. 2022).

The study in Sect. 5.1 presents the chemical analysis of a sample of Pristine giant metal-poor candidates with estimated $[\text{Fe}/\text{H}] \sim -1.5$. The aim of this study is to understand the Galactic chemical evolution of Cu and Zn and to search for potential descendants of Pair Instability Supernovae (PISN; see Heger & Woosley 2002).

In Sect. 5.2, the preliminary results obtained from the study of a sample of Pristine very metal-poor candidates with estimated $[\text{Fe}/\text{H}] \sim -3$ observed with the Echelle SpectroPolarimetric Device for the Observation of Stars (ESPaDOnS; Donati et al. 2006) at CFHT are presented.

5.1 Pristine XIX: hunting for PISN descendants (Caffau, Lombardo et al. 2022)

In this study we derived the detailed chemical abundances of 22 species of 18 elements (Na, Mg, Al, Si, Ca, Sc, Ti, V, Cr, Mn, Fe, Co, Ni, Cu, Zn, Y, Zr, Ba) and the kinematic properties for a sample of 36 giant stars. The targets were selected in the range of magnitudes $9.5 < G < 11$ by combining the Pristine photometry with the Gaia EDR3 photometry and parallaxes (Gaia Collaboration et al. 2021) using the procedure described in Bonifacio et al. (2019a). The stars were observed with the Spectrographe pour l’Observation

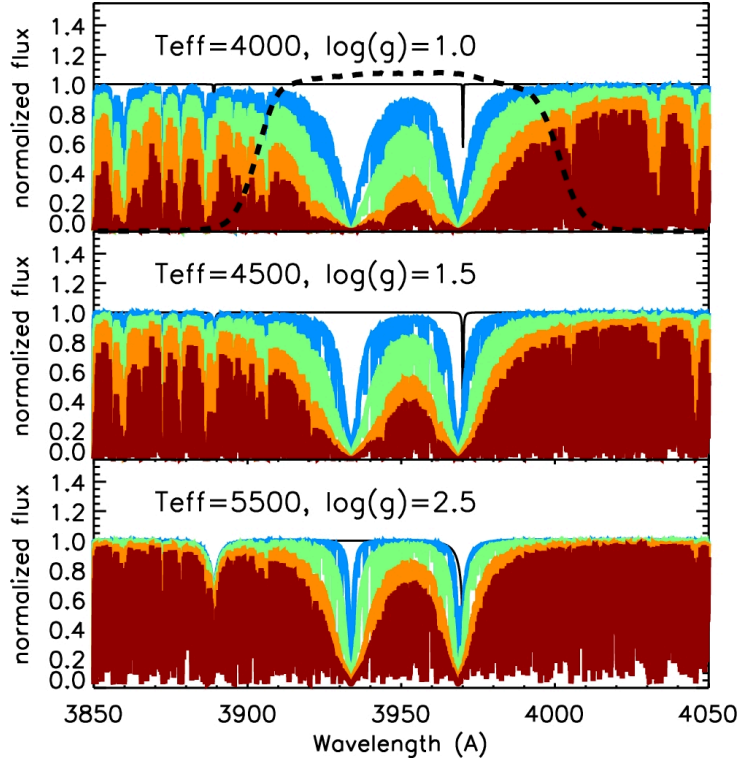


Figure 5.1: Region of the spectrum covered by the Pristine filter around the Ca II H&K lines (black dashed line). Comparison between synthetic spectra with different stellar parameters and metallicities: $[\text{Fe}/\text{H}]=0.0$ (red), $[\text{Fe}/\text{H}]=-1.0$ (orange), $[\text{Fe}/\text{H}]=-3.0$ (blue) and no metals (black). Figure from [Starkenburg et al. \(2017\)](#).

des Phénomènes des Intérieurs stellaires et des Exoplanètes (SOPHIE; [Bouchy & Sophie Team 2006](#)) on the 1.93 m telescope at Observatoire de Haute-Provence (OHP) and Neo-Narval on the 2 m telescope Bernard Lyot (TBL) at Observatoire Midi Pyrénées (OMP). The Pristine photometry, combined with Gaia photometry and parallaxes, proved to be extremely effective in selecting stars of metallicity around -2.0 , with a 77% rate of success for the SOPHIE sample and 100% rate of success for the Neo-Narval sample. The stellar parameters were determined using Gaia DR3 photometry and parallaxes using the procedure described in Sect. 3.2.1. The chemical abundances were derived using MyGIsFOS (see [Sbordone et al. 2014](#)). We also computed Non-local Thermodynamic Equilibrium (NLTE) abundance corrections for several elements (Na, Mg, Al, Si, Ca, Ti, Fe, Zn, and Zr). The chemical analysis revealed that three stars in the sample (TYC 1118-595-1, TYC 2207-992-1 and TYC 1194-507-1) have a chemical pattern compatible with the one predicted by theoretical models of PISN chemical enrichment computed by [Salvadori et al. \(2019\)](#). These stars could therefore be possible PISN descendants. The kinematics of the stars revealed that 17% of the sample stars belong to the disc, with 8% of the stars being on thin disc orbits. From 11% to 14% of sample stars belong to the Gaia-Sausage-Enceladus structure. The remaining 70% of sample stars could belong to the halo or have an extragalactic origin.

5.2 Pristine XXI: exploring the metal-poor boundary with ESPaDoNS

(Lombardo et al. submitted)

In this study we analysed a sample of high resolution spectra of stars that have a photometric metallicity estimate below -3.5 from the Pristine photometry. The Pristine survey will provide extremely metal-poor candidates for the WEAVE spectroscopic survey (Jin et al. 2022), so the purpose of this study is to understand what kind of stars populate this parameter space, together with extremely metal-poor stars.

5.2.1 Target selection & observations

The targets were selected from the Pristine catalogue in order to have estimated metallicity below -3.5 from both $g-i$ and $g-r$ colours. In Fig. 5.2 we show the location of our targets on the de-reddened colour-colour diagram $(CaHK - g)_0 - 1.5(g - i)_0$ versus $(g - i)_0$, in which the stars are colour-coded with the metallicity estimate obtained from the Pristine CaHK photometry and $g - i$. The lines in the figure represent theoretical colours for two different values of surface gravity and metallicity. We note that, in this diagram, all stars appear to be more metal-poor than -4.0 .

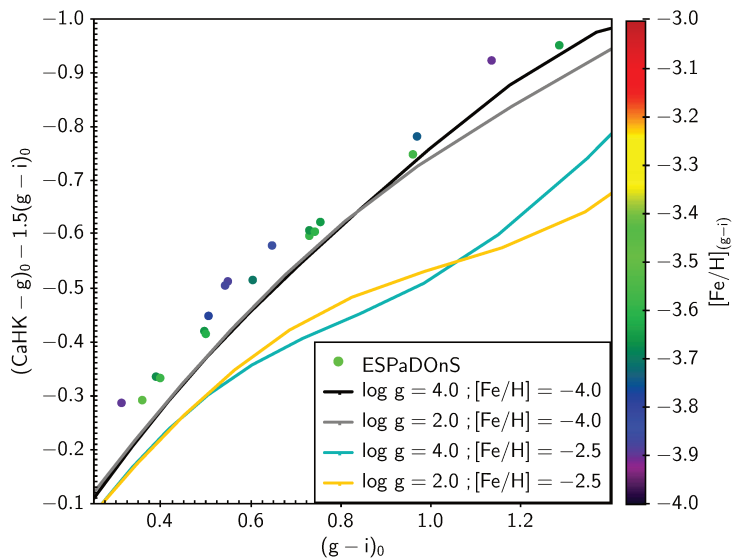


Figure 5.2: Pristine colour-colour diagram for our selected targets. The solid lines are theoretical curves for two values of metallicity and surface gravity. The points are coloured according to their photometric metallicity estimate. Figure from Lombardo et al. (submitted).

The targets were observed with ESPaDoNS (Donati et al. 2006) in the Queued Service Observation mode of CFHT between November 29th 2020 and December 8th 2020. A complete log of the observations is provided in Table A.1 in appendix. All stars were observed twice, one exposure after the other, with exposure times between ~ 1300 s and

2400 s. The spectra have been reduced by CFHT with the Upena¹ pipeline using routines of the Libre-ESPRIT software (Donati et al. 1997). Upena corrects the spectra for the heliocentric radial velocity. The “Star+Sky” mode was used to observe the stars, which covers the spectral range 370 nm to 1051 nm with a resolving power of 65 000. We performed the order merging using an ESO-MIDAS² script developed by us for this purpose, and then co-added the pairs of spectra.

5.2.2 Radial velocities

Before analysing the stars, we visually inspected the spectra, and some of these led us to suspect that we were looking at binary systems. We then checked for spectroscopic binaries through cross-correlation, and found that 8 out of 19 stars are double spectrum spectroscopic binaries (SB2). For these stars, we measured the radial velocities of each component from both exposures using our own cross-correlation code and a synthetic template. The radial velocities for SB2 stars are listed in Table A.2. The component are labelled as "A" and "B", where "A" is the component with the highest peak in the cross-correlation function. For the stars that did not show a secondary component, we measured the radial velocities with our own template matching code. The radial velocities for these stars are listed in Table A.1.

The uncertainties (σ in the tables) are the formal errors derived from the χ^2 in case of the template matching and from the Tonry & Davis (1979) formalism for cross-correlation. We note that, for some stars, the difference in radial velocity between the two consecutive exposures is larger than the combined statistical and systematic errors. In that cases, we think that these variations are real, as for in the case of the two RR Lyrae stars observed, that show clear radial velocity variations.

5.2.3 Chemical abundances

The chemical analysis was performed on 7 out of 19 stars in the sample using MyGIsFOS code (Sbordone et al. 2014). For the SB2 binaries we did not provide the stellar parameters nor perform chemical analysis because we need information on the luminosities of the two stars to disentangle the spectra. This information may come from the orbital solution, combined with theoretical isochrones. We also did not analyse four more stars we estimate to be of metallicity -0.5 or higher, mainly because they were rotating rapidly and/or the signal-to-noise ratio (SNR) was too low to allow a proper analysis. The targets are listed in Table A.3, together with the labels "A", if the star has been analysed, and "N" if not.

The stellar parameters were derived using Gaia DR3 photometry and parallaxes, adopting the procedure described in Sect. 3.2.1, with a grid of ATLAS9 model atmosphere defined in the range of parameters: $3500 \leq T_{\text{eff}} \leq 6750$ K, $0.5 \leq \log g \leq 5.0$ dex, and $-4 \leq [M/H] \leq 0.5$. Given the low SNR of the spectra, the chemical inventory is very limited. No element was derived for all seven stars, at most for six out of seven. The derived stellar parameters and metallicities are listed in Table A.4. A portion of the spectra of the star Pristine_159.5695+57.1688 around the Mg Ib triplet is shown in Fig. 5.3. This

¹<http://www.cfht.hawaii.edu/Instruments/Upena/>

²<https://www.eso.org/sci/software/esomidias/>

is one of the spectra with the highest SNR, and the star is one of the two most metal-poor in the sample.

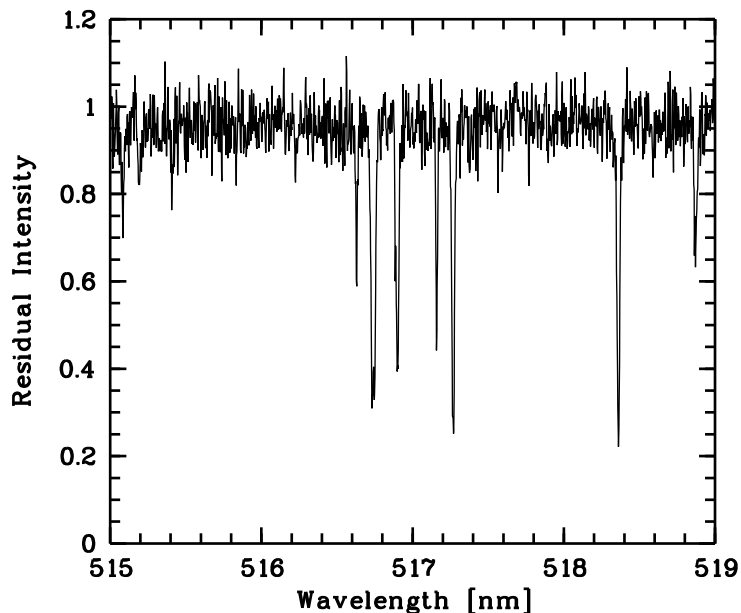


Figure 5.3: The region of Mg I b triplet in star Pristine_159.5695+57.1688.

The analysed stars are present in several catalogues, but no chemical analysis is available in the literature. In this study, the chemical abundances of these star are provided for the first time. The results we obtained for Fe abundances are listed in Table A.4. We could measure Mg, Ca, Sc, and Ti abundances in five out of seven stars, and Ba abundances in six out of seven stars. The derived chemical abundances are listed in Table A.5.

[Mg/Fe], [Ca/Fe], [Sc/Fe], and [Ba/Fe] abundance ratios as a function of [Fe/H] are shown in Fig. 5.4 and 5.5, and compared to the results obtained in the literature. In general, the abundance ratios appear in agreement with the literature values within errors. The star Pristine_327.5170+19.8622 has [Ca/Fe]= +0.6, and [Ti II/Fe II]=+0.6, both values higher than the reference sample. However, it has [Mg/Fe]=+0.3, and, taking into account the errors, this appears to be consistent with an average $[\alpha/\text{Fe}] \sim 0.4$. The only star with a remarkable [Sc/Fe] abundance ratio is Pristine_355.2747+26.4757, the most metal-rich star of the sample, with [ScII/FeII]=+0.7. Since the measure is based on seven Sc II lines with a line-to-line scatter of 0.1 dex, we consider the measure precise. The star Pristine_327.5170+19.8622 appears to display a higher [Ba/Fe] than stars of similar metallicity, with [Ba/Fe]=+0.7. For this star we have also derived [Y/Fe]=+0.2. It would be interesting to measure abundances of other n -capture elements in this star. As discussed below, this star is a binary of RS Canum Venaticorum (RS CVn) type.

5.2.4 Variable stars

From the investigation of this sample of stars, we found that most of them were already known in the literature for their variability. Table A.3 lists the variability flags that we found in the literature for each star. According to the General Catalogue of Variable Stars (GCVS, Samus' et al. 2017), the stars in our sample belong to two different groups ac-

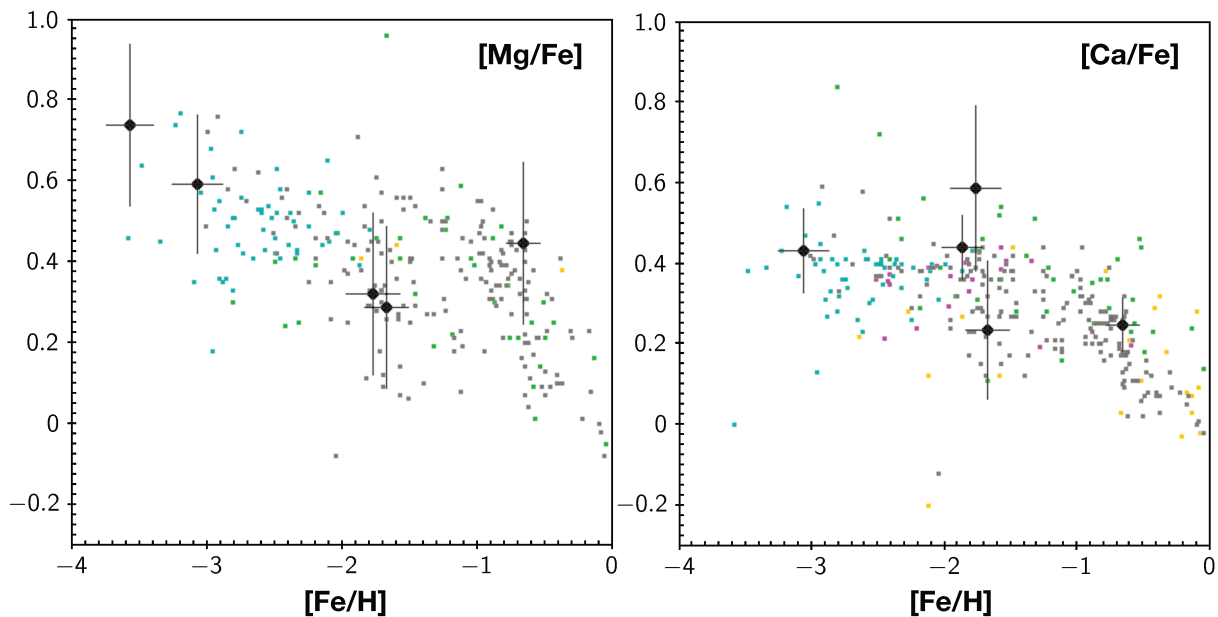


Figure 5.4: $[Mg/Fe]$ and $[Ca/Fe]$ as a function of $[Fe/H]$ for our sample of stars. Magenta dots are the stars from the Pristine XIX paper (Caffau et al. 2023), green dots are from the Pristine V paper (Bonifacio et al. 2019a), orange dots are from the Pristine II paper (Caffau et al. 2017), cyan dots are from Lombardo et al. (2022) and grey dots are from Fulbright (2000).

according to their photometric variability: eclipsing binary systems, and pulsating variables, like RR Lyrae.

Eclipsing binary systems

Eclipsing binaries are binary systems in which the orbital planes are inclined at a small angle to the line of sight, so that the components periodically eclipse each other. This implies that the brightness of the system change with a period coincident with that of the components orbital motion. In our case, they are characterised by short periods and high rotational velocities, likely due to synchronisation of rotational and orbital periods. Thirteen stars in our sample have been identified in the literature as eclipsing binaries. Of these, six are classified as W Ursae Majoris type (EW), three as Algol (Beta Persei) type (EA), two as RS CVn type, one as both EW and RS CVn, and one simply as an eclipsing binary (see Table A.3; for more details on individual stars see Section 5 in Lombardo et al. submitted).

- EW are binary systems with ellipsoidal components almost in contact, a period shorter than 1 day and light variation amplitudes < 0.8 mag in V. The components are generally of F-G types.
- EA are binaries with spherically or slightly ellipsoidal components. They may have very different periods, between 0.2 to more than 10^4 days. Light amplitudes are also different and may reach several magnitudes.

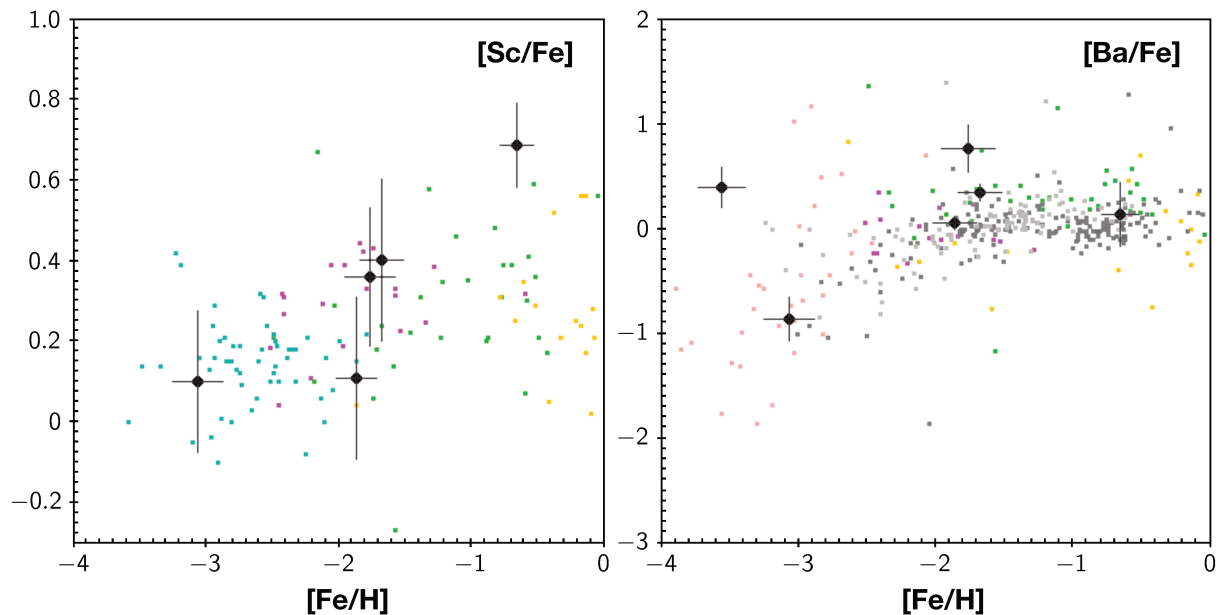


Figure 5.5: $[\text{Sc}/\text{Fe}]$ and $[\text{Ba}/\text{Fe}]$ as a function of $[\text{Fe}/\text{H}]$ for our sample of stars. Magenta dots are the stars from the Pristine XIX paper (Caffau et al. 2023), green dots are from the Pristine V paper (Bonifacio et al. 2019a), orange dots are from the Pristine II paper (Caffau et al. 2017), cyan dots are from Lombardo et al. (2022), pink dots are from François et al. (2007), grey dots are from Fulbright (2000) and light grey dots are from Ishigaki et al. (2013).

- RS CVn are close binaries where the hottest (primary) component is a subgiant or giant star of F-K type, and the coolest (secondary) component is a dwarf or subgiant of G-M type (see e.g. Martínez et al. 2022, and references therein). They are fast rotators tidally synchronized, and are characterised by the presence in their spectra of strong Ca II H&K and H α emission lines of variable intensity, indicating increased chromospheric activity of the solar type. Such systems may also be characterised by the presence of radio and X-ray emission.

Figures 5.6 and 5.7 show the Ca II H&K and H α emission lines we detected in the star Pristine_148.3782+53.0957 and Pristine_326.5701+19.2445 respectively. Both stars are classified as RS CVn. The star Pristine_327.5170+19.8622 has been classified as both EW and RS CVn. In this star we do not detect any Ca II H&K or H α emission lines, nor other sign of activity. We also checked for X-ray emission in the Second ROSAT all-sky survey (2RXS) source catalogue (Boller et al. 2016), but we could not find any X-ray source within 2 arcminutes from this star. We therefore believe that this star is probably not an RS CVn, but rather an EW. Furthermore, other known RS CVn are at most moderately metal-poor (see e.g. Randich et al. 1994) and this star, to our knowledge, would be the most metal-poor known RS CVn ($[\text{Fe}/\text{H}] = -1.76 \pm 0.20$).

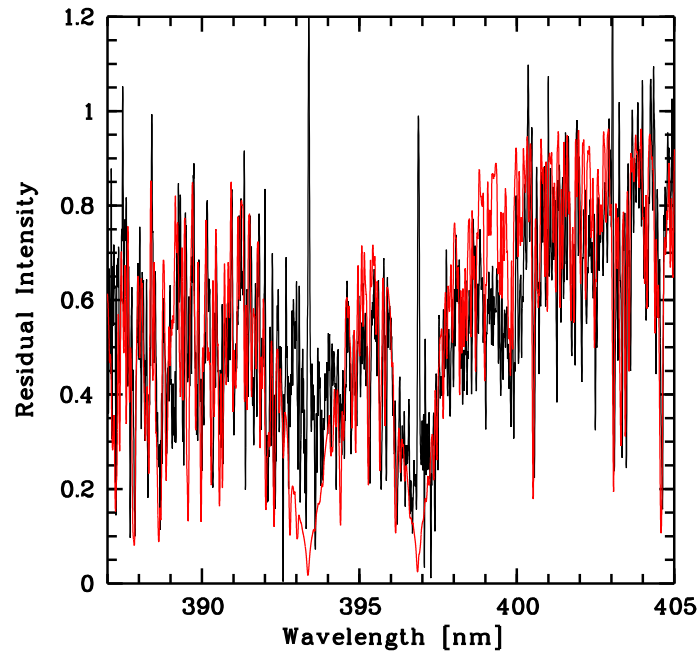


Figure 5.6: The Ca II H&K lines of Pristine_148.3782+53.0957, showing a strong emission. For display purposes the spectrum, sum of the two observed spectra, has been smoothed with a Gaussian with FWHM of 15 km s^{-1} . To guide the eye, the red line is a synthetic spectrum with $T_{\text{eff}}/\log g/[M/H]$ 4527/3.16/-1.5 and a rotational velocity of 26.5 km s^{-1} . Figure from Lombardo et al. submitted.

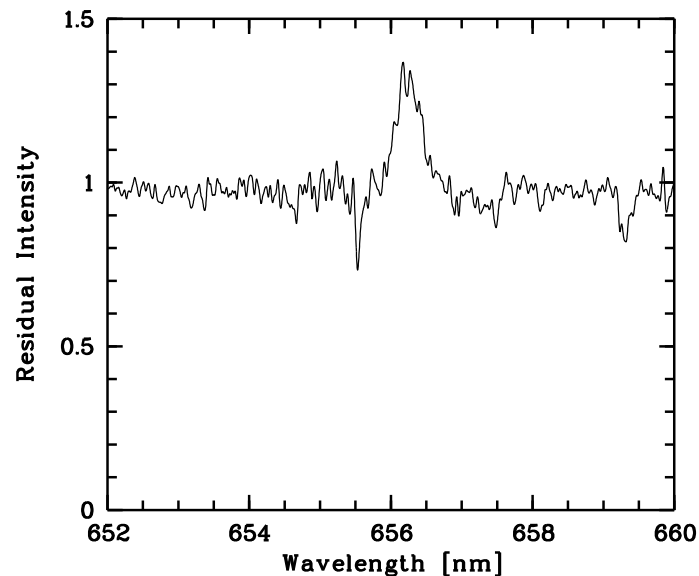


Figure 5.7: The $H\alpha$ emission in one of the two spectra of Pristine_326.5701+19.2445. For display purposes the spectrum has been smoothed with a Gaussian of 15 km s^{-1} FWHM. Figure from Lombardo et al. submitted.

Pulsating variables (RR Lyrae)

RR Lyrae variables are radially-pulsating giant A-F stars with light amplitudes from 0.2 to 2 mag in V. They may have variable light-curve shapes as well as variable periods.

They are sometimes called short-period Cepheids or cluster-type variables. The star Pristine_335.8412+9.0219 has been classified as a fundamental-mode RR Lyrae variable with asymmetric light curve (steep ascending branches, RRab) in several studies (Drake et al. 2014; Sesar et al. 2017; Heinze et al. 2018; Chen et al. 2020) and also in the Gaia DR2 and DR3 RR Lyrae catalogues (Clementini et al. 2019, 2022). RRab variables are characterised by periods from 0.3 to 1.2 days, and amplitudes from 0.5 to 2 mag in V. All studies converge on a period of ~ 0.67 days. The star Pristine_333.2117+20.1267 has been classified as a variable with period ~ 0.35 days in many studies (see e.g. Watson et al. 2006; Drake et al. 2014; Sesar et al. 2017; Chen et al. 2018; Heinze et al. 2018; Clementini et al. 2022). Watson et al. (2006) and Chen et al. (2018) classify it as an eclipsing binary of EW-type, while Sesar et al. (2017) classify it as an RR-Lyrae variable. The lines in the spectrum are very wide, implying a high rotational velocity. This can be compatible with a EW-type eclipsing variable, but not with an RR Lyrae. For this reason, we believe that the star is likely an EW-type eclipsing variable rather than an RR Lyrae.

5.2.5 Discussion and conclusions

We derived chemical abundances for 7 out of 19 stars belonging to a sample of extremely metal-poor candidates ($[\text{Fe}/\text{H}] < -3.5$) selected with the Pristine photometry. We found that only two stars in the sample have $[\text{Fe}/\text{H}] < -3$, and only one can be considered extremely metal-poor (Pristine_328.6116+20.3914, $[\text{Fe}/\text{H}] = -3.56 \pm 0.17$). The other stars appear metal-poor basically because their Ca II lines appear weak, and therefore their Ca II H&K photometry is also “weak”. We now attempt to understand the reasons for this.

For the stars not analysed the main reason is the photometric variability, combined with the fact that a large fraction of these “weak” Ca II H&K stars are SB2 binaries (8 out of 19). In fact, fast rotators and active stars also have “weak” Ca II H&K lines. For the analysed stars, two are photometric variables, Pristine_327.5170+19.8622 and Pristine_335.8411+09.0218, and so it is not surprising that, although metal-poor, they are not as metal-poor as expected from the Pristine photometry. We consider Pristine_008.1724+21.8215, and Pristine_009.1439+15.7850 metal-poor, although they are not as metal-poor as expected, while Pristine_355.2747+26.4757 is significantly more metal-rich than expected. For these stars the reason why the metallicity estimate based on Pristine and SDSS photometry failed is not clear.

The results of this investigation are interesting in the prospect of extensively using Pristine photometry in large spectroscopic surveys, like WEAVE (Jin et al. 2022), to select metal-poor stars. What we learnt from analysing this sample is that, in order to obtain a sample with a reliable photometric metallicity estimate, variables stars should always be removed, possibly by cross-matching with catalogues that contain variability information.

Chapter 6

Conclusion and future perspectives

The aim of this thesis project was to investigate the chemical properties of stellar populations in the Galaxy, using high-resolution spectroscopy. High-resolution and high signal-to-noise spectra are an invaluable tool for understanding the evolution of stars and galaxies. Thanks to them, we can obtain detailed chemical abundance patterns for individual stars, which allow us to compare observations with predictions of theoretical models.

In [Lombardo et al. 2021](#) (Sect. 2.1), the chemical abundances analysis of a sample of young giant stars with high rotational velocities revealed that such stars have metallicities around solar, and show low $[C/Fe]$, high $[N/Fe]$ and almost constant $[(C+N+O)/Fe]$ abundance ratios, implying that the stars have undergone mixing. We compared our results with the predictions of stellar evolution models with rotation, and we found that the rotational velocities of the stars are compatible with that predicted by models at solar metallicity, and the $[N/C]$ abundances ratios are compatible with the values predicted for clump stars.

In the first paper of the CERES series (Sect. 3.2, [Lombardo et al. 2022](#)), the high quality of the spectra combined with the homogeneity of the analysis, allowed us to highlight peculiar chemical abundance patterns in a sample of metal-poor halo stars. We found that, in this sample, two stars have Zn abundances much higher than other stars with similar metallicity, and several stars show peculiar light neutron-capture element abundance patterns. In subsequent papers of the series, in which I will be involved, the abundances of heavy elements will be derived. When a complete chemical inventory will be available for these stars, we will then be able to draw more conclusions about the formation sites and possible nucleosynthetic channels for these elements by comparing the abundance patterns with models of stellar yields.

Another fundamental tool is the Gaia catalogue, which allows us to know the distances, proper motions, and radial velocities of a very large sample of stars. Combining the kinematics information from Gaia with the chemical one derived from spectra, we are able to investigate the structure of our Galaxy, and put strong constraints on its evolutionary history. Some examples of the results that can be obtained with this method are given in [Koch-Hansen et al. 2021](#) (Sect. 3.1), in [Caffau et al. 2020b](#) (see Chapt.4), and in [Matas Pinto et al. 2022](#) (Sect. 4.2).

In [Koch-Hansen et al. \(2021\)](#), the chemical analysis of the star RAVE J110842.1-715300, which was kinematically associated to the ω Centauri globular cluster, revealed that the stars is CN-strong and enhanced in Na, making its chemistry compatible with

that of second generation ω Cen stars. This suggests that the star may be a second generation ω Cen star that escaped from the cluster.

Caffau et al. (2020b) selected a sample of 72 stars with Gaia DR2 transverse velocities above 500 km s^{-1} , and observed this sample of stars with FORS2. From the analysis of this sample, they found that the stars have very eccentric halo orbits, with metallicities in a quite narrow range, compatible with that of Galactic metal-poor halo stars, without extremely metal-poor stars. In addition, the subgiant stars in the sample appear to be younger than expected at this metallicity (ages below 8 Gyr), which are now proved to be Blue Stragglers (see Sect. 4.1). The results obtained for the Blue Stragglers will be probably published in the next future.

Following the results of Caffau et al. (2020b), in Matas Pinto et al. (2022) we performed a detailed chemical analysis of two high-speed stars in order to find any peculiarities in their abundance patterns. Also in this case, the two stars appear to have a similar abundance pattern, compatible with that of other halo stars, and metallicity in the range of the Caffau et al. (2020b) sample. Both stars also show retrograde orbits with high ellipticity, and one of them is kinematically compatible with Sequoia candidates. The Eu abundance of this star is also compatible with that of Sequoia candidates analysed in Aguado et al. (2021). However, we cannot draw any strong conclusions about its origin, since the abundances of other elements make it indistinguishable from other halo stars.

Gaia also allows us to select samples of bright stars with the desired properties, which could then be observed with small-to-medium size telescopes, as done in the MINCE project (Chapt. 2). In this project we selected metal-poor stars with $-2.5 < [\text{Fe}/\text{H}] < -1.0$ using the StarHorse code, which combines Gaia DR2 data with that of other photometric catalogues, like Pan-STARRS1, 2MASS, and AllWISE, to provide stellar parameters, distances and extinctions. In the first paper of the series (Sect. 2.1, Cescutti et al. 2022), we investigated the kinematics of this sample of stars, and we found that 12 out of 33 stars have kinematics compatible with GSE, 3 with Sequoia, 8 with the thin disc, one maybe with the thick disc, and the rest with the halo. We derived chemical abundances for elements up to Zn, and compared them with chemical evolution models for the Milky Way and the GSE. We could not observe any specific trend or offset in the chemical abundances between halo and GSE stars, neither between GSE and Sequoia stars. In the following paper of the series, in which I am involved, we will derive the abundances of heavy elements in order to complete the chemical patterns.

Narrow-band photometry, like the Ca II H&K photometry, combined with broadband photometry, is also an essential tool for understanding the chemical evolution of the Galaxy, since it allows us to select metal-poor stars. This technique proved to be effective in identifying extremely metal-poor stars, as shown by the excellent results obtained by the Pristine collaboration (see e.g. Starkenburg et al. 2018; Bonifacio et al. 2019a; Aguado et al. 2019; Venn et al. 2020; Caffau et al. 2020a; Kielty et al. 2021; Lardo et al. 2021; Lucchesi et al. 2022), provided that photometric variables can be robustly eliminated (see Sect. 5.2, Lombardo et al. submitted). As discussed in Sect. 5.2, the parameter space in the Pristine photometry occupied by extremely metal-poor stars ($[\text{Fe}/\text{H}] < -3.5$) is contaminated by photometric variable stars, in particular by short period eclipsing binaries and RR Lyrae, for which the Ca II H&K lines appear weak. In the study presented in the Sect. 5.1 (Caffau et al. 2023), we combined Pristine and Gaia photometries to select stars with metallicity ~ -1.5 , in order to study the Galactic chemical evolution

of Cu and Zn and to search for possible pair instability supernovae (PISN) descendants. This approach for the target selection has proven to be very effective in selecting stars with metallicity ~ -2 , with a 77% rate of success for the SOPHIE sample and 100% rate of success for the Neo-Narval sample. The chemical analysis revealed that three stars in the sample have abundance patterns compatible with the one predicted by PISN chemical enrichment models, and thus they could be possible PISN descendants. Given the efficiency of this technique in finding metal-poor stars, one of the possible projects I would like to work on in the near future is to combine Pristine and Gaia photometries to select hot metal-poor stars in order to check whether or not they are Blue Stragglers.

Recently, I have joined the 4MOST survey of dwarf galaxies and their stellar streams (4DWARFS, PI: Skúladóttir), which is one of the 4MOST Galactic consortium surveys that will provide high-quality spectra for millions of stars, and map different regions of the Milky Way and Magellanic clouds in unprecedented detail. 4DWARFS will target the main bodies of three large dwarf spheroidal galaxies, Sagittarius, Fornax, and Sculptor, as well as the Sagittarius stream, thus complementing the information from other surveys and increasing our understanding of Galactic evolution.

Appendix A

Appendix of Pristine XXI

This appendix contains tables from Sect. 5.2 (Pristine XXI, Lombardo et al. submitted). A list of acronyms used for variable stars in Table A.3 is given below.

- **EA**: Algol (Beta Persei)-type eclipsing binary
- **EW**: W Ursae Majoris-type eclipsing binary
- **RS CVn**: RS Canum Venaticorum-type system
- **SB2**: double spectroscopic binary system
- **RR Lyr**: RR Lyrae-type variable

Star	date YYY MM DD	UT hms	HJD days	Texp s	V_R km s ⁻¹	$\sigma(V_R)$ km s ⁻¹
Pristine_326.5701+19.2445	2020 11 29	04:40:55	2459182.69458	2400.0	-77.553	0.091
Pristine_326.5701+19.2445	2020 11 29	05:21:31	2459182.72277	2400.0	-77.434	0.088
Pristine_355.2749+26.4759	2020 11 29	06:09:54	2459182.75884	2400.0	-14.271	0.026
Pristine_355.2749+26.4759	2020 11 29	06:50:30	2459182.78705	2400.0	-14.343	0.024
Pristine_024.5944+25.4689	2020 11 29	09:04:03	2459182.88178	2400.0		
Pristine_024.5944+25.4689	2020 11 29	09:44:39	2459182.90997	2400.0		
Pristine_029.3591+21.3783	2020 12 03	07:14:54	2459186.80599	2400.0		
Pristine_029.3591+21.3783	2020 12 03	07:55:31	2459186.83420	2400.0		
Pristine_034.7189+25.9539	2020 12 04	10:41:09	2459187.94933	1770.3		
Pristine_034.7189+25.9539	2020 12 04	11:11:29	2459187.97040	1798.5		
Pristine_148.3782+53.0957	2020 12 04	13:11:14	2459188.05071	2222.0	23.606	0.049
Pristine_148.3782+53.0957	2020 12 04	13:48:55	2459188.07689	2227.7	23.503	0.050
Pristine_159.5695+57.1688	2020 12 04	14:47:41	2459188.11710	2393.0	-135.220	0.054
Pristine_159.5695+57.1688	2020 12 04	15:27:53	2459188.14502	2359.8	-135.259	0.056
Pristine_109.8329+41.3782	2020 12 05	11:06:51	2459188.96665	2400.0	18.360	0.015
Pristine_109.8329+41.3782	2020 12 05	11:47:28	2459188.99485	2400.0	18.566	0.015
Pristine_163.9735+13.4823	2020 12 05	14:46:24	2459189.11558	1371.3	22.880	4.170
Pristine_163.9735+13.4823	2020 12 05	15:09:48	2459189.13183	1363.7	30.900	6.610
Pristine_327.5170+19.8622	2020 12 06	04:35:28	2459189.69016	2400.0	-122.611	0.030
Pristine_327.5170+19.8622	2020 12 06	05:16:04	2459189.71836	2400.0	-121.771	0.030
Pristine_328.6116+20.3914	2020 12 06	05:58:37	2459189.74801	2400.0	-282.961	0.092
Pristine_328.6116+20.3914	2020 12 06	06:39:14	2459189.77621	2400.0	-284.115	0.131
Pristine_002.0937+22.6545	2020 12 06	07:22:25	2459189.80903	2400.0		
Pristine_002.0937+22.6545	2020 12 06	08:03:01	2459189.83721	2400.0		
Pristine_008.1724+21.8215	2020 12 06	08:45:21	2459189.86709	2400.0	-120.437	0.126
Pristine_008.1724+21.8215	2020 12 06	09:25:57	2459189.89529	2400.0	-120.986	0.158
Pristine_331.5576+27.2164	2020 12 07	04:31:50	2459190.68800	1944.8		
Pristine_331.5576+27.2164	2020 12 07	05:06:44	2459190.71224	2171.9		
Pristine_333.2010+09.6132	2020 12 07	05:48:03	2459190.74079	2400.0		
Pristine_333.2010+09.6132	2020 12 07	06:28:38	2459190.76898	2400.0		
Pristine_348.1325+11.2206	2020 12 07	07:15:53	2459190.80314	1572.5		
Pristine_348.1325+11.2206	2020 12 07	07:42:51	2459190.82187	1591.9		
Pristine_333.2117+20.1267	2020 12 08	04:27:58	2459191.68523	1544.0		
Pristine_333.2117+20.1267	2020 12 08	04:54:47	2459191.70385	1599.8		
Pristine_335.8411+09.0218	2020 12 08	05:20:47	2459191.72198	1307.7	62.307	0.059
Pristine_335.8411+09.0218	2020 12 08	05:43:09	2459191.73751	1304.2	63.898	0.056
Pristine_009.1439+15.7850	2020 12 08	06:07:40	2459191.75749	1252.4	-63.249	0.238
Pristine_009.1439+15.7850	2020 12 08	06:29:07	2459191.77239	1252.2	-64.053	0.193

Table A.1: Log of the observations. σ represents the uncertainty on the radial velocity. Radial velocities for SB2 stars are given in Table A.2

ID	HJD days	$V_R(A)$ km s ⁻¹	$\sigma[V_R(A)]$ km s ⁻¹	$V_R(B)$ km s ⁻¹	$\sigma[V_R(B)]$ km s ⁻¹
Pristine_002.0937+22.6545	2459189.80903	-61.27	0.83	11.31	0.87
Pristine_002.0937+22.6545	2459189.83721	-54.68	2.33		
Pristine_024.5944+25.4689	2459182.88178	-138.30	6.00	166.60	5.60
Pristine_024.5944+25.4689	2459182.90997	-138.30	5.60	145.10	5.40
Pristine_029.3591+21.3783	2459186.80599	71.70	6.80	-212.70	3.20
Pristine_029.3591+21.3783	2459186.83420	83.80	6.80	-243.70	3.60
Pristine_034.7189+25.9539	2459187.94933	-12.00	2.90	269.10	1.60
Pristine_034.7189+25.9539	2459187.97040	-20.50	4.40	282.30	2.30
Pristine_331.5576+27.2164	2459190.68800	66.09	5.90	-253.58	3.60
Pristine_331.5576+27.2164	2459190.71224	65.88	6.60	-194.60	4.60
Pristine_333.2010+09.6132	2459190.74079	-25.63	0.28	71.83	0.40
Pristine_333.2010+09.6132	2459190.76898	-31.07	0.33	77.05	0.94
Pristine_333.2117+20.1267	2459191.68523	43.50	6.10	-256.85	3.30
Pristine_333.2117+20.1267	2459191.70385	67.58	7.10	-262.50	3.50
Pristine_348.1325+11.2206	2459190.80314	-13.68	0.25	12.43	0.23
Pristine_348.1325+11.2206	2459190.82187	-15.08	0.23	13.41	0.23

Table A.2: Radial velocities for SB2 binaries. σ represents the uncertainty on the radial velocity.

Star	RA(CaHK) deg	DEC(CaHK) deg	G mag	$G_{BP} - G_{RP}$ mag	A/N	Comment
Pristine_002.0937+22.6545	2.09372497	+22.65452766	14.590	1.024	N	EA (SB2)
Pristine_008.1724+21.8215	8.1724329	+21.82150269	15.252	0.700	A	
Pristine_009.1439+15.7850	9.1439209	+15.78506374	15.371	0.692	A	
Pristine_024.5944+25.4689	24.59447861	+25.46895218	14.471	1.253	N	EW (SB2)
Pristine_029.3591+21.3783	29.35915756	+21.3783741	14.474	0.910	N	EW (SB2)
Pristine_034.7189+25.9539	34.71894073	+25.95391083	13.881	0.848	N	EW (SB2)
Pristine_109.8329+41.3782	109.83296967	+41.37827682	14.844	0.940	N	EA
Pristine_148.3782+53.0957	148.37820435	+53.09577179	13.562	1.207	N	RS CVn
Pristine_159.5695+57.1688	159.56959534	+57.16887665	14.334	1.129	A	
Pristine_163.9735+13.4823	163.973526	+13.48232746	14.668	0.772	N	EW
Pristine_326.5701+19.2445	326.57019043	+19.24455833	14.509	1.500	N	RS CVn
Pristine_327.5170+19.8622	327.51705933	+19.8622036	15.014	0.913	A	EW, RS CVn(?)
Pristine_328.6116+20.3914	328.61169434	+20.39147758	14.953	1.009	A	
Pristine_331.5576+27.2164	331.55767822	+27.21646309	14.628	0.988	N	EW (SB2)
Pristine_333.2010+09.6132	333.2010498	+9.61327744	14.545	1.041	N	EA (SB2)
Pristine_333.2117+20.1267	333.21176147	+20.126791	14.294	0.849	N	EW (SB2), RR-Lyr(?)
Pristine_335.8411+09.0218	335.84118652	+9.02187824	15.223	0.727	A	RR-Lyr
Pristine_348.1325+11.2206	348.13250732	+11.22061634	13.813	0.816	N	E (SB2)
Pristine_355.2747+26.4757	355.27474976	+26.47573662	13.645	0.942	A	

Table A.3: Stars observed with ESPaDoNS in period 20B. The label "A" refers to analysed stars, while label "N" refers to not-analysed stars.

ID	T_{eff} K	$\log g$ dex	v_{turb} km s ⁻¹	[Fe/H] dex	Nlines	[Fe/H] _{gi} dex	[Fe/H] _{gr} dex	S/N @550 nm
Pristine_008.1724+21.8215	6051	2.39	2.07	-1.87 ± 0.16	20	-3.52	-3.56	12
Pristine_009.1439+15.7850	6278	4.29	1.29	$-2.58^a \pm 0.30$	1	-3.90	-3.81	10
Pristine_159.5695+57.1688	4798	1.42	2.06	-3.07 ± 0.19	43	-3.74	-3.52	28
Pristine_327.5170+19.8622	5817	2.53	1.91	-1.76 ± 0.20	46	-3.67	-3.51	18
Pristine_328.6116+20.3914	5245	2.87	1.62	-3.56 ± 0.17	5	-3.85	-3.63	13
Pristine_335.8411+09.0218	6091	2.88	1.88	-1.68 ± 0.17	28	-3.58	-3.55	12
Pristine_355.2747+26.4757	5586	4.10	0.98	-0.66 ± 0.13	147	-3.88	-3.72	30

^a This iron abundance is based on one Fe II line.

Table A.4: Derived stellar parameters for chemically analysed stars.

Star	Nlines_Na	A(Na)	σ (Na)	Nlines_Mg	A(Mg)	σ (Mg)	Nlines_Al	A(Al)	σ (Al)
Pr_08.1724+21.8215	0			0			0		
Pr_09.1439+15.7851	0			0			0		
Pr_159.5696+57.1689	1	3.218	0.2	2	5.067	0.17	0		
Pr_327.5170+19.8622	0			1	6.097	0.2	0		
Pr_328.6118+20.3915	0			1	4.714	0.2	0		
Pr_335.8412+9.0219	0			1	6.152	0.2	0		
Pr_355.2749+26.4759	3	5.786	0.034	1	7.327	0.2	1	6.032	0.2
Star	Nlines_SiI	A(SiI)	σ (SiI)	Nlines_SiII	A(SiII)	σ (SiII)	Nlines_Ca	A(Ca)	σ (Ca)
Pr_08.1724+21.8215	0			0			5	4.905	0.079
Pr_09.1439+15.7851	0			0			0		
Pr_159.5696+57.1689	0			0			5	3.695	0.106
Pr_327.5170+19.8622	0			0			9	5.155	0.205
Pr_328.6118+20.3915	0			0			0		
Pr_335.8412+9.0219	0			0			5	4.89	0.173
Pr_355.2749+26.4759	8	7.139	0.03	1	7.515	0.2	8	5.919	0.067
Star	Nlines_ScII	A(ScII)	σ (ScII)	Nlines_TiI	A(TiI)	σ (TiI)	Nlines_TiII	A(TiII)	σ (TiII)
Pr_08.1724+21.8215	1	1.342	0.2	0			1	3.401	0.2
Pr_09.1439+15.7851	0			0			0		
Pr_159.5696+57.1689	3	0.136	0.175	2	1.942	0.192	5	2.106	0.067
Pr_327.5170+19.8622	5	1.698	0.173	0			5	3.73	0.176
Pr_328.6118+20.3915	0			0			0		
Pr_335.8412+9.0219	1	1.828	0.2	1	3.839	0.2	2	3.706	0.228
Pr_355.2749+26.4759	7	3.127	0.104	16	4.512	0.072	17	4.79	0.174
Star	Nlines_V	A(V)	σ (V)	Nlines_CrI	A(CrI)	σ (CrI)	Nlines_CrII	A(CrII)	σ (CrII)
Pr_08.1724+21.8215	0			0			0		
Pr_09.1439+15.7851	0			0			0		
Pr_159.5696+57.1689	0			0			0		
Pr_327.5170+19.8622	0			1	3.694	0.2	0		
Pr_328.6118+20.3915	0			0			0		
Pr_335.8412+9.0219	0			0			0		
Pr_355.2749+26.4759	4	3.363	0.07	8	4.953	0.11	5	5.37	0.197
Star	Nlines_Mn	A(Mn)	σ (Mn)	Nlines_Co	A(Co)	σ (Co)	Nlines_Cu	A(Cu)	σ (Cu)
Pr_08.1724+21.8215	0			0			0		
Pr_09.1439+15.7851	0			0			0		
Pr_159.5696+57.1689	0			0			0		
Pr_327.5170+19.8622	0			0			0		
Pr_328.6118+20.3915	0			0			0		
Pr_335.8412+9.0219	0			0			0		
Pr_355.2749+26.4759	10	4.585	0.147	2	4.452	0.245	2	3.511	0.108
Star	Nlines_Zn	A(Zn)	σ (Zn)	Nlines_YII	A(YII)	σ (YII)	Nlines_BaII	A(BaII)	σ (BaII)
Pr_08.1724+21.8215	0			0			2	0.362	0.065
Pr_09.1439+15.7851	0			0			0		
Pr_159.5696+57.1689	0			0			2	-1.76	0.208
Pr_327.5170+19.8622	0			2	0.651	0.023	1	1.174	0.22
Pr_328.6118+20.3915	0			0			1	-0.995	0.2
Pr_335.8412+9.0219	0			0			2	0.848	0.082
Pr_355.2749+26.4759	2	4.296	0.154	1	1.352	0.2	2	1.643	0.307

Table A.5: Derived chemical abundances for analysed stars.

Bibliography

- 1997, ESA Special Publication, Vol. 1200, The HIPPARCOS and TYCHO catalogues. Astrometric and photometric star catalogues derived from the ESA HIPPARCOS Space Astrometry Mission
- Adibekyan, V. Z., Figueira, P., Santos, N. C., et al. 2013, *Astron. Astrophys.*, 554, A44
- Aguado, D. S., Allende Prieto, C., González Hernández, J. I., et al. 2016, *Astron. Astrophys.*, 593, A10
- Aguado, D. S., Belokurov, V., Myeong, G. C., et al. 2021, *Astrophys. J. Lett.*, 908, L8
- Aguado, D. S., Youakim, K., González Hernández, J. I., et al. 2019, *Mon. Not. R. Astron. Soc.*, 490, 2241
- Ahumada, R., Prieto, C. A., Almeida, A., et al. 2020, *Astrophys. J. Suppl.*, 249, 3
- Alvarez, R. & Plez, B. 1998, *Astron. Astrophys.*, 330, 1109
- Anders, F., Khalatyan, A., Chiappini, C., et al. 2019, *Astron. Astrophys.*, 628, A94
- Andrae, R., Fouesneau, M., Sordo, R., et al. 2022, arXiv e-prints, arXiv:2206.06138
- Aoki, W., Barklem, P. S., Beers, T. C., et al. 2009, *Astrophys. J.*, 698, 1803
- Appenzeller, I., Fricke, K., Fürtig, W., et al. 1998, *The Messenger*, 94, 1
- Asplund, M., Lambert, D. L., Nissen, P. E., Primas, F., & Smith, V. V. 2006, *Astrophys. J.*, 644, 229
- Aurière, M., Konstantinova-Antova, R., Charbonnel, C., et al. 2015, *Astron. Astrophys.*, 574, A90
- Babcock, H. W. 1949, *Astrophys. J.*, 110, 126
- Balachandran, S. 1995, *Astrophys. J.*, 446, 203
- Balick, B. & Brown, R. L. 1974, *Astrophys. J.*, 194, 265
- Barbuy, B., Chiappini, C., & Gerhard, O. 2018, *Annu. Rev. Astron. Astrophys.*, 56, 223
- Barklem, P. S., Christlieb, N., Beers, T. C., et al. 2005, *Astron. Astrophys.*, 439, 129
- Barnes, J. E. 1992, *Astrophys. J.*, 393, 484

- Bastian, N. & Lardo, C. 2018, *Annu. Rev. Astron. Astrophys.*, 56, 83
- Beers, T. C., Preston, G. W., & Shectman, S. A. 1985, *Astron. J.*, 90, 2089
- Belokurov, V., Erkal, D., Evans, N. W., Koposov, S. E., & Deason, A. J. 2018, *Mon. Not. R. Astron. Soc.*, 478, 611
- Bensby, T., Feltzing, S., & Lundström, I. 2003, *Astron. Astrophys.*, 410, 527
- Bensby, T., Feltzing, S., & Oey, M. S. 2014, *Astron. Astrophys.*, 562, A71
- Bernstein, R., Shectman, S. A., Gunnels, S. M., Mochnacki, S., & Athey, A. E. 2003, in *Society of Photo-Optical Instrumentation Engineers (SPIE) Conference Series*, Vol. 4841, *Instrument Design and Performance for Optical/Infrared Ground-based Telescopes*, ed. M. Iye & A. F. M. Moorwood, 1694–1704
- Bidelman, W. P. & MacConnell, D. J. 1973, *Astron. J.*, 78, 687
- Bland-Hawthorn, J. & Gerhard, O. 2016, *Annu. Rev. Astron. Astrophys.*, 54, 529
- Boeche, C., Siebert, A., Williams, M., et al. 2011, *Astron. J.*, 142, 193
- Boesgaard, A. M. & Budge, K. G. 1988, *Astrophys. J.*, 332, 410
- Boesgaard, A. M. & Tripicco, M. J. 1986, *Astrophys. J. Lett.*, 302, L49
- Böhm-Vitense, E. 2004, *Astron. J.*, 128, 2435
- Boller, T., Freyberg, M. J., Trümper, J., et al. 2016, *Astron. Astrophys.*, 588, A103
- Bond, H. E. 1970, *Astrophys. J. Suppl.*, 22, 117
- Bonifacio, P., Caffau, E., Sestito, F., et al. 2019a, *Mon. Not. R. Astron. Soc.*, 487, 3797
- Bonifacio, P., Caffau, E., Spite, M., & Spite, F. 2019b, *Research Notes of the American Astronomical Society*, 3, 64
- Bonifacio, P. & Molaro, P. 1997, *Mon. Not. R. Astron. Soc.*, 285, 847
- Bonifacio, P., Molaro, P., Sivarani, T., et al. 2007, *Astron. Astrophys.*, 462, 851
- Bonifacio, P., Monaco, L., Salvadori, S., et al. 2021, *Astron. Astrophys.*, 651, A79
- Bouchy, F. & Sophie Team. 2006, in *Tenth Anniversary of 51 Peg-b: Status of and prospects for hot Jupiter studies*, ed. L. Arnold, F. Bouchy, & C. Moutou, 319–325
- Boyd, R. N. & Kajino, T. 1989, *Astrophys. J. Lett.*, 336, L55
- Bressan, A., Marigo, P., Girardi, L., et al. 2012, *Mon. Not. R. Astron. Soc.*, 427, 127
- Bromm, V. & Loeb, A. 2003, *Nature*, 425, 812
- Brook, C. B., Kawata, D., Gibson, B. K., & Freeman, K. C. 2004, *Astrophys. J.*, 612, 894

- Buder, S., Sharma, S., Kos, J., et al. 2021, *Mon. Not. R. Astron. Soc.*, 506, 150
- Burbidge, E. M., Burbidge, G. R., Fowler, W. A., & Hoyle, F. 1957, *Reviews of Modern Physics*, 29, 547
- Busso, M., Gallino, R., Lambert, D. L., Travaglio, C., & Smith, V. V. 2001, *Astrophys. J.*, 557, 802
- Busso, M., Gallino, R., & Wasserburg, G. J. 1999a, *Annu. Rev. Astron. Astrophys.*, 37, 239
- Busso, M., Gallino, R., & Wasserburg, G. J. 1999b, *Annu. Rev. Astron. Astrophys.*, 37, 239
- Caffau, E., Bonifacio, P., François, P., et al. 2011, *Nature*, 477, 67
- Caffau, E., Bonifacio, P., Sbordone, L., et al. 2013, *Astron. Astrophys.*, 560, A71
- Caffau, E., Bonifacio, P., Sbordone, L., et al. 2020a, *Mon. Not. R. Astron. Soc.*, 493, 4677
- Caffau, E., Bonifacio, P., Starkenburg, E., et al. 2017, *Astronomische Nachrichten*, 338, 686
- Caffau, E., Lombardo, L., Mashonkina, L., et al. 2023, *Mon. Not. R. Astron. Soc.*, 518, 3796
- Caffau, E., Monaco, L., Bonifacio, P., et al. 2019, *Astron. Astrophys.*, 628, A46
- Caffau, E., Monaco, L., Bonifacio, P., et al. 2020b, *Astron. Astrophys.*, 638, A122
- Carney, B. W., Laird, J. B., Latham, D. W., & Aguilar, L. A. 1996, *Astron. J.*, 112, 668
- Carney, B. W. & Peterson, R. C. 1981, *Astrophys. J.*, 245, 238
- Carretta, E., Bragaglia, A., Gratton, R., & Lucatello, S. 2009, *Astron. Astrophys.*, 505, 139
- Casagrande, L., Silva Aguirre, V., Stello, D., et al. 2014, *Astrophys. J.*, 787, 110
- Castelli, F. & Kurucz, R. L. 2003, in *IAU Symposium*, Vol. 210, *Modelling of Stellar Atmospheres*, ed. N. Piskunov, W. W. Weiss, & D. F. Gray, A20
- Cayrel, R. 1988, in *The Impact of Very High S/N Spectroscopy on Stellar Physics*, ed. G. Cayrel de Strobel & M. Spite, Vol. 132, 345
- Cayrel, R., Depagne, E., Spite, M., et al. 2004, *Astron. Astrophys.*, 416, 1117
- Cescutti, G., Bonifacio, P., Caffau, E., et al. 2022, *Astron. Astrophys.*, 668, A168
- Cescutti, G. & Chiappini, C. 2014, *Astron. Astrophys.*, 565, A51
- Cescutti, G., Molaro, P., & Fu, X. 2020, *Mem. S. A. It.*, 91, 153

- Cescutti, G., Romano, D., Matteucci, F., Chiappini, C., & Hirschi, R. 2015, *Astron. Astrophys.*, 577, A139
- Charbonneau, P. 1995, *Astrophys. J. Suppl.*, 101, 309
- Charbonnel, C. & Primas, F. 2005, *Astron. Astrophys.*, 442, 961
- Chen, X., Deng, L., de Grijs, R., Wang, S., & Feng, Y. 2018, *Astrophys. J.*, 859, 140
- Chen, X., Wang, S., Deng, L., et al. 2020, *Astrophys. J. Suppl.*, 249, 18
- Chiappini, C., Matteucci, F., & Gratton, R. 1997, *Astrophys. J.*, 477, 765
- Christlieb, N., Battistini, C., Bonifacio, P., et al. 2019, *The Messenger*, 175, 26
- Christlieb, N., Bessell, M. S., Beers, T. C., et al. 2002, *Nature*, 419, 904
- Christlieb, N., Schörck, T., Frebel, A., et al. 2008, *Astron. Astrophys.*, 484, 721
- Cirasuolo, M., Fairley, A., Rees, P., et al. 2020, *The Messenger*, 180, 10
- Clementini, G., Ripepi, V., Garofalo, A., et al. 2022, arXiv e-prints, arXiv:2206.06278
- Clementini, G., Ripepi, V., Molinaro, R., et al. 2019, *Astron. Astrophys.*, 622, A60
- Coc, A. & Vangioni, E. 2017, *International Journal of Modern Physics E*, 26, 1741002
- Cohen, J. G. 1978, *Astrophys. J.*, 223, 487
- Cosentino, R., Lovis, C., Pepe, F., et al. 2012, in *Society of Photo-Optical Instrumentation Engineers (SPIE) Conference Series*, Vol. 8446, *Ground-based and Airborne Instrumentation for Astronomy IV*, ed. I. S. McLean, S. K. Ramsay, & H. Takami, 84461V
- Cowan, J. J. & Rose, W. K. 1977, *Astrophys. J.*, 212, 149
- Cowan, J. J., Sneden, C., Lawler, J. E., et al. 2021, *Reviews of Modern Physics*, 93, 015002
- Cristallo, S., Piersanti, L., Straniero, O., et al. 2009, *PASA*, 26, 139
- Dawson, K. S., Schlegel, D. J., Ahn, C. P., et al. 2013, *Astron. J.*, 145, 10
- De Angeli, F., Weiler, M., Montegriffo, P., et al. 2022, arXiv e-prints, arXiv:2206.06143
- De Silva, G. M., Freeman, K. C., Bland-Hawthorn, J., et al. 2015, *Mon. Not. R. Astron. Soc.*, 449, 2604
- Deason, A. J., Belokurov, V., & Evans, N. W. 2011, *Mon. Not. R. Astron. Soc.*, 416, 2903
- Deason, A. J., Belokurov, V., Koposov, S. E., & Lancaster, L. 2018, *Astrophys. J. Lett.*, 862, L1
- Deason, A. J., Belokurov, V., & Sanders, J. L. 2019, *Mon. Not. R. Astron. Soc.*, 490, 3426

- Dekel, A., Birnboim, Y., Engel, G., et al. 2009, *Nature*, 457, 451
- Dekker, H., D’Odorico, S., Kaufer, A., Delabre, B., & Kotzlowski, H. 2000, in *Society of Photo-Optical Instrumentation Engineers (SPIE) Conference Series*, Vol. 4008, *Optical and IR Telescope Instrumentation and Detectors*, ed. M. Iye & A. F. Moorwood, 534–545
- Delgado Mena, E., Israelian, G., González Hernández, J. I., et al. 2010, *Astrophys. J.*, 725, 2349
- Deng, L.-C., Newberg, H. J., Liu, C., et al. 2012, *Research in Astronomy and Astrophysics*, 12, 735
- Denissenkov, P. A., Herwig, F., Battino, U., et al. 2017, *Astrophys. J. Lett.*, 834, L10
- Di Matteo, P., Gómez, A., Haywood, M., et al. 2015, *Astron. Astrophys.*, 577, A1
- Di Matteo, P., Haywood, M., Lehnert, M. D., et al. 2019, *Astron. Astrophys.*, 632, A4
- Di Matteo, P., Spite, M., Haywood, M., et al. 2020, *Astron. Astrophys.*, 636, A115
- Donati, J. F., Catala, C., Landstreet, J. D., & Petit, P. 2006, in *Astronomical Society of the Pacific Conference Series*, Vol. 358, *Solar Polarization 4*, ed. R. Casini & B. W. Lites, 362
- Donati, J. F., Semel, M., Carter, B. D., Rees, D. E., & Collier Cameron, A. 1997, *Mon. Not. R. Astron. Soc.*, 291, 658
- Drake, A. J., Graham, M. J., Djorgovski, S. G., et al. 2014, *Astrophys. J. Suppl.*, 213, 9
- Ecuivillon, A., Israelian, G., Santos, N. C., et al. 2004, *Astron. Astrophys.*, 418, 703
- Eggen, O. J., Lynden-Bell, D., & Sandage, A. R. 1962, *Astrophys. J.*, 136, 748
- Eilers, A.-C., Hogg, D. W., Rix, H.-W., & Ness, M. K. 2019, *Astrophys. J.*, 871, 120
- Eisenstein, D. J., Weinberg, D. H., Agol, E., et al. 2011, *Astron. J.*, 142, 72
- Ekers, R. D., Goss, W. M., Schwarz, U. J., Downes, D., & Rogstad, D. H. 1975, *Astron. Astrophys.*, 43, 159
- Ekström, S., Georgy, C., Eggenberger, P., et al. 2012, *Astron. Astrophys.*, 537, A146
- Event Horizon Telescope Collaboration, Akiyama, K., Alberdi, A., et al. 2022, *Astrophys. J. Lett.*, 930, L12
- Fernández-Trincado, J. G., Robin, A. C., Vieira, K., et al. 2015, *Astron. Astrophys.*, 583, A76
- Feillet, D. K., Sahlholdt, C. L., Feltzing, S., & Casagrande, L. 2021, *Mon. Not. R. Astron. Soc.*, 508, 1489

- Fitzpatrick, E. L., Massa, D., Gordon, K. D., Bohlin, R., & Clayton, G. C. 2019, *Astrophys. J.*, 886, 108
- Fragione, G. & Gualandris, A. 2019, *Mon. Not. R. Astron. Soc.*, 489, 4543
- Fragkoudi, F., Di Matteo, P., Haywood, M., et al. 2018, *Astron. Astrophys.*, 616, A180
- François, P., Depagne, E., Hill, V., et al. 2007, *Astron. Astrophys.*, 476, 935
- François, P., Pasquini, L., Biazzo, K., Bonifacio, P., & Palsa, R. 2013, *Astron. Astrophys.*, 552, A136
- Freeman, K. & Bland-Hawthorn, J. 2002, *Annu. Rev. Astron. Astrophys.*, 40, 487
- Frenk, C. S. & White, S. D. M. 2012, *Annalen der Physik*, 524, 507
- Fuhrmann, K. 1998, *Astron. Astrophys.*, 338, 161
- Fuhrmann, K. 2011, *Mon. Not. R. Astron. Soc.*, 414, 2893
- Fulbright, J. P. 2000, *Astron. J.*, 120, 1841
- Gaia Collaboration, Babusiaux, C., van Leeuwen, F., et al. 2018a, *Astron. Astrophys.*, 616, A10
- Gaia Collaboration, Brown, A. G. A., Vallenari, A., et al. 2018b, *Astron. Astrophys.*, 616, A1
- Gaia Collaboration, Brown, A. G. A., Vallenari, A., et al. 2021, *Astron. Astrophys.*, 649, A1
- Gaia Collaboration, Helmi, A., van Leeuwen, F., et al. 2018c, *Astron. Astrophys.*, 616, A12
- Gaia Collaboration, Prusti, T., de Bruijne, J. H. J., et al. 2016, *Astron. Astrophys.*, 595, A1
- Gaia Collaboration, Vallenari, A., Brown, A. G. A., et al. 2022, arXiv e-prints, arXiv:2208.00211
- Galama, T. J., Vreeswijk, P. M., van Paradijs, J., et al. 1998, *Nature*, 395, 670
- Gallagher, A. J., Bergemann, M., Collet, R., et al. 2020, *Astron. Astrophys.*, 634, A55
- Gallart, C., Bernard, E. J., Brook, C. B., et al. 2019, *Nature Astronomy*, 3, 932
- Galli, D. & Palla, F. 1998, *Astron. Astrophys.*, 335, 403
- Georgy, C., Ekström, S., Granada, A., et al. 2013, *Astron. Astrophys.*, 553, A24
- Gerin, M., Combes, F., & Athanassoula, E. 1990, *Astron. Astrophys.*, 230, 37
- Gilmore, G., Randich, S., Asplund, M., et al. 2012, *The Messenger*, 147, 25

- Gilmore, G. & Reid, N. 1983, *Mon. Not. R. Astron. Soc.*, 202, 1025
- Glaspey, J. W., Pritchett, C. J., & Stetson, P. B. 1994, *Astron. J.*, 108, 271
- Glebbeek, E., Sills, A., Hu, H., & Stancliffe, R. J. 2010, in *American Institute of Physics Conference Series*, Vol. 1314, *International Conference on Binaries: in celebration of Ron Webbink's 65th Birthday*, ed. V. Kalogera & M. van der Sluys, 113–119
- Goldstein, H. 1950, *Classical mechanics*
- Gonzalez, O. A., Mucciarelli, A., Origlia, L., et al. 2020, *The Messenger*, 180, 18
- Gratton, R., Bragaglia, A., Carretta, E., et al. 2019, *Astron. Astrophys. Rev.*, 27, 8
- Greif, T. H., Springel, V., White, S. D. M., et al. 2011, *Astrophys. J.*, 737, 75
- Hansen, C. J., Koch, A., Mashonkina, L., et al. 2020, *Astron. Astrophys.*, 643, A49
- Haywood, M., Di Matteo, P., Lehnert, M. D., et al. 2018, *Astrophys. J.*, 863, 113
- Haywood, M., Di Matteo, P., Snaith, O., & Lehnert, M. D. 2015, *Astron. Astrophys.*, 579, A5
- Haywood, M., Lehnert, M. D., Di Matteo, P., et al. 2016, *Astron. Astrophys.*, 589, A66
- Heger, A. & Woosley, S. E. 2002, *Astrophys. J.*, 567, 532
- Heinze, A. N., Tonry, J. L., Denneau, L., et al. 2018, *Astron. J.*, 156, 241
- Helmi, A. 2020, *Annu. Rev. Astron. Astrophys.*, 58, 205
- Helmi, A., Babusiaux, C., Koppelman, H. H., et al. 2018, *Nature*, 563, 85
- Helmi, A., White, S. D. M., de Zeeuw, P. T., & Zhao, H. 1999, *Nature*, 402, 53
- Hill, V. & Pasquini, L. 2000, in *The Light Elements and their Evolution*, ed. L. da Silva, R. de Medeiros, & M. Spite, Vol. 198, 293
- Hobbs, L. M. & Mathieu, R. D. 1991, *Publ. Astron. Soc. Pac.*, 103, 431
- Hobbs, L. M. & Pilachowski, C. 1986, *Astrophys. J. Lett.*, 309, L17
- Hosford, A., Ryan, S. G., García Pérez, A. E., Norris, J. E., & Olive, K. A. 2009, *Astron. Astrophys.*, 493, 601
- Ibata, R., Malhan, K., Martin, N., et al. 2021, *Astrophys. J.*, 914, 123
- Ibata, R. A., Gilmore, G., & Irwin, M. J. 1994, *Nature*, 370, 194
- Ibata, R. A., Gilmore, G., & Irwin, M. J. 1995, *Mon. Not. R. Astron. Soc.*, 277, 781
- Ibata, R. A. & Lewis, G. F. 1998, *Astrophys. J.*, 500, 575
- Iben, I., J. & Renzini, A. 1983, *Annu. Rev. Astron. Astrophys.*, 21, 271

- Ishigaki, M. N., Aoki, W., & Chiba, M. 2013, *Astrophys. J.*, 771, 67
- Ishigaki, M. N., Chiba, M., & Aoki, W. 2012, *Astrophys. J.*, 753, 64
- Iwamoto, K., Mazzali, P. A., Nomoto, K., et al. 1998, *Nature*, 395, 672
- Jean-Baptiste, I., Di Matteo, P., Haywood, M., et al. 2017, *Astron. Astrophys.*, 604, A106
- Jin, S., Trager, S. C., Dalton, G. B., et al. 2022, arXiv e-prints, arXiv:2212.03981
- Jofré, P. & Weiss, A. 2011, *Astron. Astrophys.*, 533, A59
- Johnson, J. A. 2002, *Astrophys. J. Suppl.*, 139, 219
- Johnston, K. V., Zhao, H., Spergel, D. N., & Hernquist, L. 1999, *Astrophys. J. Lett.*, 512, L109
- Jones, B. F., Fischer, D., Shetrone, M., & Soderblom, D. R. 1997, *Astron. J.*, 114, 352
- Jurgenson, C., Fischer, D., McCracken, T., et al. 2016, *Journal of Astronomical Instrumentation*, 5, 1650003
- Kajino, T. & Boyd, R. N. 1990, *Astrophys. J.*, 359, 267
- Kaluzny, J., Pych, W., Rucinski, S. M., & Thompson, I. B. 2006, *Acta. Astron.*, 56, 237
- Käppeler, F., Gallino, R., Bisterzo, S., & Aoki, W. 2011, *Reviews of Modern Physics*, 83, 157
- Kawata, D. & Chiappini, C. 2016, *Astronomische Nachrichten*, 337, 976
- Kayser, A., Hilker, M., Grebel, E. K., & Willemsen, P. G. 2008, *Astron. Astrophys.*, 486, 437
- Kervella, P., Arenou, F., Mignard, F., & Thévenin, F. 2019, *Astron. Astrophys.*, 623, A72
- Kielty, C. L., Venn, K. A., Sestito, F., et al. 2021, *Mon. Not. R. Astron. Soc.*, 506, 1438
- Kobayashi, C., Karakas, A. I., & Lugaro, M. 2020, *Astrophys. J.*, 900, 179
- Koch-Hansen, A. J., Hansen, C. J., Lombardo, L., et al. 2021, *Astron. Astrophys.*, 645, A64
- Koppelman, H., Helmi, A., & Veljanoski, J. 2018, *Astrophys. J. Lett.*, 860, L11
- Koppelman, H. H., Helmi, A., Massari, D., Price-Whelan, A. M., & Starkenburg, T. K. 2019, *Astron. Astrophys.*, 631, L9
- Kordopatis, G., Gilmore, G., Steinmetz, M., et al. 2013, *Astron. J.*, 146, 134
- Kratz, K.-L., Farouqi, K., Pfeiffer, B., et al. 2007, *Astrophys. J.*, 662, 39
- Kurucz, R. 1993a, ATLAS9 Stellar Atmosphere Programs and 2 km/s grid. Kurucz CD-ROM No. 13. Cambridge, 13

- Kurucz, R. 1993b, SYNTHE Spectrum Synthesis Programs and Line Data. Kurucz CD-ROM No. 18. Cambridge, 18
- Kurucz, R. L. 1970, SAO Special Report, 309
- Kurucz, R. L. 2005, *Memorie della Societa Astronomica Italiana Supplementi*, 8, 14
- Lai, D. K., Bolte, M., Johnson, J. A., et al. 2008, *Astrophys. J.*, 681, 1524
- Lambert, D. L. & Reddy, B. E. 2004, *Mon. Not. R. Astron. Soc.*, 349, 757
- Lanfranchi, G. A., Matteucci, F., & Cescutti, G. 2008, *Astron. Astrophys.*, 481, 635
- Lardo, C., Mashonkina, L., Jablonka, P., et al. 2021, *Mon. Not. R. Astron. Soc.*, 508, 3068
- Lemasle, B., François, P., Bono, G., et al. 2007, *Astron. Astrophys.*, 467, 283
- Li, H., Aoki, W., Matsuno, T., et al. 2022, *Astrophys. J.*, 931, 147
- Li, H., Aoki, W., Zhao, G., et al. 2015, *Publ. Astron. Soc. Japan*, 67, 84
- Lo, K. Y., Schilizzi, R. T., Cohen, M. H., & Ross, H. N. 1975, *Astrophys. J. Lett.*, 202, L63
- Lombardo, L., Bonifacio, P., François, P., et al. 2022, *Astron. Astrophys.*, 665, A10
- Lombardo, L., François, P., Bonifacio, P., et al. 2021, *Astron. Astrophys.*, 656, A155
- Lucchesi, R., Lardo, C., Jablonka, P., et al. 2022, *Mon. Not. R. Astron. Soc.*, 511, 1004
- Luck, R. E. & Bond, H. E. 1985, *Astrophys. J.*, 292, 559
- Maeder, A. & Meynet, G. 2012, *Reviews of Modern Physics*, 84, 25
- Majewski, S. R., Schiavon, R. P., Frinchaboy, P. M., et al. 2017, *Astron. J.*, 154, 94
- Malaney, R. A. & Fowler, W. A. 1989, *Astrophys. J. Lett.*, 345, L5
- Martínez, C. I., Mauas, P. J. D., & Buccino, A. P. 2022, *Mon. Not. R. Astron. Soc.*, 512, 4835
- Martinez-Valpuesta, I. & Gerhard, O. 2013, *Astrophys. J. Lett.*, 766, L3
- Mashonkina, L., Christlieb, N., & Eriksson, K. 2014, *Astron. Astrophys.*, 569, A43
- Mashonkina, L., Jablonka, P., Sitnova, T., Pakhomov, Y., & North, P. 2017, *Astron. Astrophys.*, 608, A89
- Mason, B. D., Wycoff, G. L., Hartkopf, W. I., Douglass, G. G., & Worley, C. E. 2001, *Astron. J.*, 122, 3466
- Matas Pinto, A. d. M., Caffau, E., François, P., et al. 2022, *Astronomische Nachrichten*, 343, e10032

- McClure, R. D., Fletcher, J. M., & Nemec, J. M. 1980, *Astrophys. J. Lett.*, 238, L35
- McWilliam, A. 1997, *Annu. Rev. Astron. Astrophys.*, 35, 503
- Meléndez, J., Casagrande, L., Ramírez, I., Asplund, M., & Schuster, W. J. 2010, *Astron. Astrophys.*, 515, L3
- Meléndez, J., Placco, V. M., Tucci-Maia, M., et al. 2016, *Astron. Astrophys.*, 585, L5
- Michaud, G. 1986, *Astrophys. J.*, 302, 650
- Milone, A. P., Piotto, G., Renzini, A., et al. 2017, *Mon. Not. R. Astron. Soc.*, 464, 3636
- Mo, H. J., Mao, S., & White, S. D. M. 1998, *Mon. Not. R. Astron. Soc.*, 295, 319
- Molaro, P., Bonifacio, P., Castelli, F., & Pasquini, L. 1997, *Astron. Astrophys.*, 319, 593
- Montegriffo, P., De Angeli, F., Andrae, R., et al. 2022, arXiv e-prints, arXiv:2206.06205
- Mucciarelli, A. & Bonifacio, P. 2020, *Astron. Astrophys.*, 640, A87
- Mucciarelli, A., Pancino, E., Lovisi, L., Ferraro, F. R., & Lapenna, E. 2013, *Astrophys. J.*, 766, 78
- Myeong, G. C., Evans, N. W., Belokurov, V., Sanders, J. L., & Koposov, S. E. 2018, *Astrophys. J. Lett.*, 863, L28
- Myeong, G. C., Vasiliev, E., Iorio, G., Evans, N. W., & Belokurov, V. 2019, *Mon. Not. R. Astron. Soc.*, 488, 1235
- Nissen, P. E. & Schuster, W. J. 2010, *Astron. Astrophys.*, 511, L10
- Nissen, P. E. & Schuster, W. J. 2011, *Astron. Astrophys.*, 530, A15
- Noguchi, K., Aoki, W., Kawanomoto, S., et al. 2002, *Publ. Astron. Soc. Japan*, 54, 855
- Nomoto, K., Kobayashi, C., & Tominaga, N. 2013, *Annu. Rev. Astron. Astrophys.*, 51, 457
- Nomoto, K., Maeda, K., Umeda, H., & Nakamura, T. 2001, in *Astrophysics and Space Science Library*, Vol. 264, *The Influence of Binaries on Stellar Population Studies*, ed. D. Vanbeveren, 507
- Palla, F., Salpeter, E. E., & Stahler, S. W. 1983, *Astrophys. J.*, 271, 632
- Paunzen, E. 2015, *Astron. Astrophys.*, 580, A23
- Pereira, C. B., Jilinski, E. G., Drake, N. A., Ortega, V. G., & Roig, F. 2013, *Astron. Astrophys.*, 559, A12
- Pilachowski, C. A. & Hobbs, L. M. 1988, *Publ. Astron. Soc. Pac.*, 100, 336
- Pinsonneault, M. H., Deliyannis, C. P., & Demarque, P. 1992, *Astrophys. J. Suppl.*, 78, 179

- Preston, G. W., Beers, T. C., & Shectman, S. A. 1994, *Astron. J.*, 108, 538
- Preston, G. W. & Sneden, C. 2000, *Astron. J.*, 120, 1014
- Pritchett, C. J. & Glaspey, J. W. 1991, *Astrophys. J.*, 373, 105
- Proffitt, C. R., Michaud, G., & Richer, J. 1990, in *Astronomical Society of the Pacific Conference Series, Vol. 9, Cool Stars, Stellar Systems, and the Sun*, ed. G. Wallerstein, 351
- Purcell, C. W., Bullock, J. S., & Kazantzidis, S. 2010, *Mon. Not. R. Astron. Soc.*, 404, 1711
- Quinn, P. J., Hernquist, L., & Fullagar, D. P. 1993, *Astrophys. J.*, 403, 74
- Randich, S., Giampapa, M. S., & Pallavicini, R. 1994, *Astron. Astrophys.*, 283, 893
- Recio-Blanco, A., de Laverny, P., Palicio, P. A., et al. 2022, arXiv e-prints, arXiv:2206.05541
- Richter, P. 2017, in *Astrophysics and Space Science Library, Vol. 430, Gas Accretion onto Galaxies*, ed. A. Fox & R. Davé, 15
- Roederer, I. U., Preston, G. W., Thompson, I. B., et al. 2014, *Astron. J.*, 147, 136
- Royer, F., Gebran, M., Monier, R., et al. 2014, *Astron. Astrophys.*, 562, A84
- Ryan, S. G., Beers, T. C., Kajino, T., & Rosolankova, K. 2001, *Astrophys. J.*, 547, 231
- Ryan, S. G. & Norris, J. E. 1991, *Astron. J.*, 101, 1835
- Salvadori, S., Bonifacio, P., Caffau, E., et al. 2019, *Mon. Not. R. Astron. Soc.*, 487, 4261
- Samus', N. N., Kazarovets, E. V., Durlevich, O. V., Kireeva, N. N., & Pastukhova, E. N. 2017, *Astronomy Reports*, 61, 80
- Sartoretti, P., Katz, D., Cropper, M., et al. 2018, *Astron. Astrophys.*, 616, A6
- Sartoretti, P., Marchal, O., Babusiaux, C., et al. 2022, arXiv e-prints, arXiv:2206.05725
- Sbordone, L., Bonifacio, P., Caffau, E., et al. 2010, *Astron. Astrophys.*, 522, A26
- Sbordone, L., Bonifacio, P., Castelli, F., & Kurucz, R. L. 2004, *Memorie della Societa Astronomica Italiana Supplementi*, 5, 93
- Sbordone, L., Caffau, E., Bonifacio, P., & Duffau, S. 2014, *Astron. Astrophys.*, 564, A109
- Schaeuble, M. & King, J. R. 2012, *Publ. Astron. Soc. Pac.*, 124, 164
- Schechter, P. 1976, *Astrophys. J.*, 203, 297
- Schlaufman, K. C., Thompson, I. B., & Casey, A. R. 2018, *Astrophys. J.*, 867, 98
- Schneider, R., Omukai, K., Limongi, M., et al. 2012, *Mon. Not. R. Astron. Soc.*, 423, L60

- Schramm, D. N., Steigman, G., & Dearborn, D. S. P. 1990, *Astrophys. J. Lett.*, 359, L55
- Searle, L. & Zinn, R. 1978, *Astrophys. J.*, 225, 357
- Sesar, B., Hernitschek, N., Mitrović, S., et al. 2017, *Astron. J.*, 153, 204
- Sestito, F., Longeard, N., Martin, N. F., et al. 2019, *Mon. Not. R. Astron. Soc.*, 484, 2166
- Siqueira Mello, C., Hill, V., Barbuy, B., et al. 2014, *Astron. Astrophys.*, 565, A93
- Skúladóttir, Á., Tolstoy, E., Salvadori, S., Hill, V., & Pettini, M. 2017, *Astron. Astrophys.*, 606, A71
- Smiljanic, R., Korn, A. J., Bergemann, M., et al. 2014, *Astron. Astrophys.*, 570, A122
- Snedden, C., Bean, J., Ivans, I., Lucatello, S., & Sobek, J. 2012, MOOG: LTE line analysis and spectrum synthesis, *Astrophysics Source Code Library*, record ascl:1202.009
- Snedden, C., Cowan, J. J., & Gallino, R. 2008, *Annu. Rev. Astron. Astrophys.*, 46, 241
- Snedden, C., Lambert, D. L., & Pilachowski, C. A. 1981, *Astrophys. J.*, 247, 1052
- Soderblom, D. R., Fedele, S. B., Jones, B. F., Stauffer, J. R., & Prosser, C. F. 1993, *Astron. J.*, 106, 1080
- Spite, M., Bonifacio, P., Spite, F., et al. 2019, *Astron. Astrophys.*, 624, A44
- Spite, M. & Spite, F. 1982, *Nature*, 297, 483
- Spite, M., Spite, F., & Bonifacio, P. 2012, *Memorie della Societa Astronomica Italiana Supplementi*, 22, 9
- Spitoni, E., Verma, K., Silva Aguirre, V., et al. 2021, *Astron. Astrophys.*, 647, A73
- Stahl, O., Kaufer, A., & Tubbesing, S. 1999, in *Astronomical Society of the Pacific Conference Series*, Vol. 188, *Optical and Infrared Spectroscopy of Circumstellar Matter*, ed. E. Guenther, B. Stecklum, & S. Klose, 331
- Starkenburger, E., Aguado, D. S., Bonifacio, P., et al. 2018, *Mon. Not. R. Astron. Soc.*, 481, 3838
- Starkenburger, E., Martin, N., Youakim, K., et al. 2017, *Mon. Not. R. Astron. Soc.*, 471, 2587
- Steinmetz, M., Zwitter, T., Siebert, A., et al. 2006, *Astron. J.*, 132, 1645
- Strassmeier, K. G., Stępień, K., Henry, G. W., & Hall, D. S. 1999, *Astron. Astrophys.*, 343, 175
- Takeda, Y., Kawanomoto, S., Ohishi, N., et al. 2018, *Publ. Astron. Soc. Japan*, 70, 91
- Talon, S. & Charbonnel, C. 2003, *Astron. Astrophys.*, 405, 1025
- Telting, J. H., Avila, G., Buchhave, L., et al. 2014, *Astronomische Nachrichten*, 335, 41

- Tonry, J. & Davis, M. 1979, *Astron. J.*, 84, 1511
- Umeda, H. & Nomoto, K. 2002, *Astrophys. J.*, 565, 385
- Unavane, M., Wyse, R. F. G., & Gilmore, G. 1996, *Mon. Not. R. Astron. Soc.*, 278, 727
- Venn, K. A., KIELTY, C. L., Sestito, F., et al. 2020, *Mon. Not. R. Astron. Soc.*, 492, 3241
- Wagoner, R. V., Fowler, W. A., & Hoyle, F. 1967, *Astrophys. J.*, 148, 3
- Watson, C. L., Henden, A. A., & Price, A. 2006, *Society for Astronomical Sciences Annual Symposium*, 25, 47
- Watson, D., Hansen, C. J., Selsing, J., et al. 2019, *Nature*, 574, 497
- Yanny, B., Rockosi, C., Newberg, H. J., et al. 2009a, *Astron. J.*, 137, 4377
- Yanny, B., Rockosi, C., Newberg, H. J., et al. 2009b, *Astron. J.*, 137, 4377
- York, D. G., Adelman, J., Anderson, John E., J., et al. 2000, *Astron. J.*, 120, 1579
- Zacharias, N., Finch, C. T., Girard, T. M., et al. 2013, *Astron. J.*, 145, 44
- Zheng, Y., Peek, J. E. G., Putman, M. E., & Werk, J. K. 2019, *Astrophys. J.*, 871, 35
- Zoccali, M. 2019, *Boletín de la Asociación Argentina de Astronomía La Plata Argentina*, 61, 137
- Zolotov, A., Willman, B., Brooks, A. M., et al. 2009, *Astrophys. J.*, 702, 1058

Young giants of intermediate mass

Evidence of rotation and mixing[★]

Linda Lombardo¹, Patrick François¹, Piercarlo Bonifacio¹, Elisabetta Caffau¹, Aroa del Mar Matas Pinto¹, Corinne Charbonnel^{2,3}, Georges Meynet², Lorenzo Monaco⁴, Gabriele Cescutti^{5,6,7}, and Alessio Mucciarelli^{8,9}

¹ GEPI, Observatoire de Paris, Université PSL, CNRS, 5 place Jules Janssen, 92195 Meudon, France
e-mail: Linda.Lombardo@observatoiredeparis.psl.eu

² Department of Astronomy, University of Geneva, Chemin Pegasi 51, 1290 Versoix, Switzerland

³ IRAP, CNRS UMR 5277 and Université de Toulouse, 14 Avenue Edouard Belin, 31400 Toulouse, France

⁴ Departamento de Ciencias Físicas, Universidad Andres Bello, Fernandez Concha 700, Las Condes, Santiago, Chile

⁵ INAF, Osservatorio Astronomico di Trieste, Via Tiepolo 11, 34143 Trieste, Italy

⁶ IFPU, Istitute for the Fundamental Physics of the Universe, Via Beirut, 2, 34151 Grignano, Trieste, Italy

⁷ INFN, Sezione di Trieste, Via A. Valerio 2, 34127 Trieste, Italy

⁸ Dipartimento di Fisica e Astronomia, Università degli Studi di Bologna, Via Gobetti 93/2, 40129 Bologna, Italy

⁹ INAF – Osservatorio di Astrofisica e Scienza dello Spazio di Bologna, Via Gobetti 93/3, 40129 Bologna, Italy

Received 28 May 2021 / Accepted 24 September 2021

ABSTRACT

Context. In the search of a sample of metal-poor bright giants using Strömgren photometry, we serendipitously found a sample of 26 young (ages younger than 1 Gyr) metal-rich giants, some of which have high rotational velocities.

Aims. We determined the chemical composition and rotational velocities of these stars in order to compare them with predictions from stellar evolution models. These stars were of spectral type A to B when on the main sequence, and we therefore wished to compare their abundance pattern to that of main-sequence A and B stars.

Methods. Stellar masses were derived by comparison of the position of the stars in the colour-magnitude diagram with theoretical evolutionary tracks. These masses, together with *Gaia* photometry and parallaxes, were used to derive the stellar parameters. We used spectrum synthesis and model atmospheres to determine chemical abundances for 16 elements (C, N, O, Mg, Al, Ca, Fe, Sr, Y, Ba, La, Ce, Pr, Nd, Sm, and Eu) and rotational velocities.

Results. The age-metallicity degeneracy can affect photometric metallicity calibrations. We identify 15 stars as likely binary stars. All stars are in prograde motion around the Galactic centre and belong to the thin-disc population. All but one of the sample stars present low [C/Fe] and high [N/Fe] ratios together with constant [(C+N+O)/Fe], suggesting that they have undergone CNO processing and first dredge-up. The observed rotational velocities are in line with theoretical predictions of the evolution of rotating stars.

Key words. stars: abundances – stars: evolution – stars: atmospheres

1. Introduction

The project Measuring at Intermediate metallicity Neutron Capture Elements (MINCE) (Cescutti et al., in prep.) has the goal of obtaining chemical abundances for stars in the intermediate metallicity range ($-2.5 \leq [\text{Fe}/\text{H}] \leq -1$). The aim is a detailed inventory of the neutron-capture elements.

The target selection of the first few observational runs in the northern hemisphere heavily relied on Strömgren photometry. As detailed in Sect. 2, this selection was unsuccessful in finding metal-poor giants. Its sample even proved to consist of young stars with masses in the range 2.5–6 solar masses in a narrow metallicity range of about solar metallicity.

The most frequently studied G-K stars in this mass range are particular cases of peculiar stars, such as Ba stars (Bidelman & Keenan 1951; Sneden et al. 1981; Antipova et al. 2003; Liang et al. 2003; Allen & Barbuy 2006; Smiljanic et al. 2007; Pereira et al. 2011; de Castro et al. 2016) and Cepheids (Lemasle et al. 2007, 2008, 2013; Genovali et al. 2014, 2015).

[★] Based on observations obtained at Observatoire de Haute Provence, Canada-France-Hawaii Telescope and Telescopio Nazionale *Galileo*.

As these stars were of A to B type when they were on the main sequence, the serendipitous discovery of this sample of giant stars allowed us to study this evolutionary stage directly. This stage is not very well characterised by observations so far because the time spent by stars in this phase is short. In addition, it allows a direct comparison with the properties of A- to B-type stars. For this reason, it is a unique opportunity for testing the predictions of stellar evolutionary models in terms of the evolution of chemical abundances and rotational velocities.

We expect a large number of such stars to be observed in the course of wide-field surveys such as WEAVE (Dalton et al. 2020) and 4MOST (de Jong et al. 2019). The findings of our investigation can be used to select these stars from the wide surveys.

2. Target selection

For the stars presented in this paper, we used the Strömgren photometry from the Paunzen (2015) catalogue and the metallicity calibration for giants of Casagrande et al. (2014) to select candidate intermediate-metallicity stars. To our surprise, all the stars

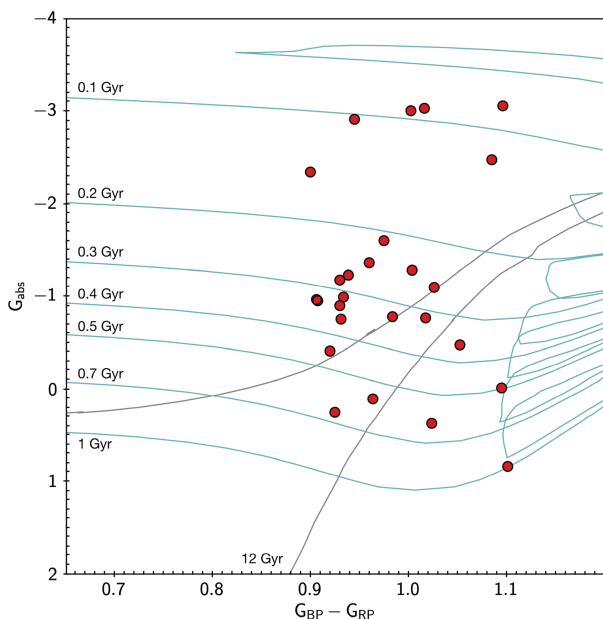


Fig. 1. Colour-magnitude diagram of *Gaia* EDR3 absolute magnitude G and dereddened colour $G_{BP} - G_{RP}$ comparing the observed stars with Parsec isochrones with solar metallicity and ages between 0.1 and 1 Gyr (cyan), and with $[Fe/H] = -2.0$ dex and age 12 Gyr (grey).

appeared to be at about solar metallicity when we inspected the spectra, and several rotate rapidly (are therefore young and massive).

The question was whether a mistake was made in the star selection. We examined the synthetic photometry of Parsec solar metallicity isochrones of ages in the range 0.1–1 Gyr (Bressan et al. 2012). As shown in Fig. 1, in the region of the *Gaia* Early Data Release 3 (EDR3) (Gaia Collaboration 2016, 2021) colour-magnitude diagram in which our targets lie, the young solar metallicity isochrones clearly overlap the locus occupied by the red giant branch (RGB) of old metal-poor isochrones. This is what is meant by age-metallicity degeneracy. Furthermore, the Strömberg indices of many of the points along the young solar metallicity isochrones are within the validity range of the Casagrande et al. (2014) calibration. If they were used as input to the Casagrande et al. (2014) calibration, the majority of these photometric values would provide a metal-poor metallicity estimate. This is another manifestation of the age-metallicity degeneracy. The Casagrande et al. (2014) calibration in our opinion performs poorly on such metal-rich young stars because these stars were absent from the calibrators used by Casagrande et al. (2014) to define the calibration. However, even if these calibrators had been used, it is not clear if the degeneracy could have been lifted without introducing some age-sensitive quantity in the calibration.

3. Observations

The spectra used in this paper have been obtained with three different telescopes and spectrographs. The log of the observations and the observed radial velocities are provided in Table 1.

3.1. SOPHIE at OHP

SOPHIE (Bouchy & Sophie Team 2006) is a fibre-fed high-resolution spectrograph operated at the Observatoire de Haute

Provence (OHP) 1.93 m telescope. The spectra were obtained in visitor mode during three nights from September 13th to 16th 2019, the observer was one of the co-authors (A.d.M. Matas Pinto). The SOPHIE high-resolution mode, which provides a resolving power $R \sim 75\,000$, was used for all the observations. The spectral range we covered is 387.2 nm to 694.3 nm. The wavelength calibration relied on a Th-Ar lamp and on a Fabry-Pérot etalon. The data were reduced automatically on the fly by the SOPHIE pipeline. Radial velocities (v_{rad}) were provided with the K5 template from the SOPHIE pipeline. For HD 192045 and HD 213036, the SOPHIE pipeline failed because the input radial velocity, taken from the *Gaia* second data release (hereafter *Gaia* DR2, Gaia Collaboration 2016, 2018; Arenou et al. 2018; Sartoretti et al. 2018), was too different from the observed radial velocity of the star. The v_{rad} were derived by us by measuring the cross-correlation function over the interval $500 \text{ nm} \leq \lambda \leq 650 \text{ nm}$. A synthetic template with appropriate stellar parameters was used.

3.2. ESPaDOnS at CFHT

ESPaDOnS (Donati et al. 2006) is a fibre-fed spectropolarimeter operated at the 3.6 m Canada-France-Hawaii telescope (CFHT) on the summit of Mauna Kea. The observation was obtained in the Queued Service Observation mode of the CFHT in November 2019. The spectroscopic mode “Star+Sky” was used, providing a resolving power of $R \sim 65\,000$. It covers the spectral range 370 nm–1051 nm. The data were delivered to us reduced with the Upena pipeline¹, which uses the routines of the Libre-ESPRIT software (Donati et al. 1997). The output spectrum is provided in an order-by-order format. We merged the orders using an ESO-MIDAS² script written by ourselves. Radial velocities were derived measuring the cross-correlation function over the interval $420 \text{ nm} \leq \lambda \leq 680 \text{ nm}$.

3.3. HARPS-N at TNG

HARPS-N (Cosentino et al. 2012) is a fibre-fed high-resolution spectrograph operated at the 3.5 m Telescopio Nazionale Galileo (TNG) at the Canary Island La Palma. It is essentially a copy of HARPS (Mayor et al. 2003), operated by ESO on its 3.6 m telescope at La Silla. The observations were obtained in service mode in December 2019. We used the high-resolution mode, which provides a resolving power $R \sim 115\,000$. The wavelength range covered is 383 nm to 690 nm. The data were reduced on the fly by the HARPS pipeline. Radial velocities were provided with the G2 template from the HARPS-N pipeline.

4. Analysis

4.1. Stellar parameters

To derive stellar parameters, we used *Gaia* EDR3 photometry (G and $G_{BP} - G_{RP}$) and parallaxes. We defined a grid in the parameter space using the ATLAS 9 model atmosphere grids by Mucciarelli et al. (in prep.). The range of atmospheric parameters covered by the grid is shown in Table 2.

We computed theoretical values of $G_{BP} - G_{RP}$, bolometric correction (BC_G), and extinction coefficients A_G , $E(G_{BP} - G_{RP})$ using the reddening law of Fitzpatrick et al. (2019) for the whole grid. Effective temperatures (T_{eff}) and surface gravities ($\log g$) were derived iteratively with the following procedure:

¹ <http://www.cfht.hawaii.edu/Instruments/Upena/>

² <https://www.eso.org/sci/software/esomidas/>

Table 1. Log of the observations.

Star	Date	MJD	Instrument	Exposure time [s]	v_{rad} [km s ⁻¹]	err v_{rad} [km s ⁻¹]	S/N at 680 nm
HD 191066	2019-09-13	58739.812	SOPHIE@OHP1.93m	344	-9.350	0.002	60
HD 192045	2019-09-13	58739.821	SOPHIE@OHP1.93m	3600	-4.834	0.077	200
HD 191066	2019-09-13	58739.867	SOPHIE@OHP1.93m	3600	-9.348	0.001	230
HD 205732	2019-09-13	58739.912	SOPHIE@OHP1.93m	3600	-3.971	0.001	200
HD 213036	2019-09-13	58739.956	SOPHIE@OHP1.93m	3600	-40.89	0.128	200
HD 217089	2019-09-14	58739.999	SOPHIE@OHP1.93m	3600	-7.684	0.001	175
HD 9637	2019-09-14	58740.043	SOPHIE@OHP1.93m	3600	-2.361	0.002	210
HD 21269	2019-09-14	58740.086	SOPHIE@OHP1.93m	1800	-12.602	0.002	260
HD 19267	2019-09-14	58740.11	SOPHIE@OHP1.93m	1800	2.697	0.001	170
HD 13882	2019-09-14	58740.132	SOPHIE@OHP1.93m	3600	-29.038	0.001	280
HD 189879	2019-09-14	58740.878	SOPHIE@OHP1.93m	3600	-29.532	0.001	200
HD 195375	2019-09-14	58740.921	SOPHIE@OHP1.93m	3600	-10.276	0.001	150
HD 221232	2019-09-15	58740.965	SOPHIE@OHP1.93m	3600	-30.649	0.001	170
HD 219925	2019-09-15	58741.008	SOPHIE@OHP1.93m	3600	-22.916	0.001	140
HD 278	2019-09-15	58741.053	SOPHIE@OHP1.93m	3600	-60.526	0.003	200
HD 11519	2019-09-15	58741.141	SOPHIE@OHP1.93m	3183	-11.260	0.001	120
TYC2813-1979-1	2019-09-16	58742.101	SOPHIE@OHP1.93m	3600	-17.163	0.002	60
TYC2813-1979-1	2019-09-16	58742.144	SOPHIE@OHP1.93m	3295	-17.177	0.002	40
BD+42 3220	2019-11-20	58807.176	ESPaDOnS@CFHT	2380	-19.298	0.053	180
BD+44 3114	2019-11-21	58808.176	ESPaDOnS@CFHT	2380	-15.216	0.055	260
TYC 3136-878-1	2019-11-21	58808.205	ESPaDOnS@CFHT	2380	1.034	0.053	280
HD 40509	2019-12-21	58838.888	HARPS-N@TNG	1800	-1.656	0.005	280
HD 41710	2019-12-21	58838.911	HARPS-N@TNG	900	-7.917	0.002	175
HD 40655	2019-12-21	58838.928	HARPS-N@TNG	2100	7.332	0.001	290
HD 45879	2019-12-21	58838.955	HARPS-N@TNG	1500	7.047	0.001	360
HD 55077	2019-12-21	58838.974	HARPS-N@TNG	1200	-25.499	0.003	400
HD 61107	2019-12-21	58838.991	HARPS-N@TNG	1200	10.476	0.001	410
HD 63856	2019-12-22	58839.007	HARPS-N@TNG	1800	19.755	0.001	200

Table 2. Range of atmospheric parameters of the ATLAS 9 model atmosphere grid.

Parameter	Start	End	Step
T_{eff}	3500 K	5625 K	125 K
$\log g$	0.00 dex	3.00 dex	0.50 dex
$[M/H]$	-5.00 dex	-2.50 dex	0.50 dex
$[M/H]$	-2.50 dex	0.50 dex	0.25 dex

1. The mass and the metallicity of the star were fixed at input values.
2. T_{eff} was derived by interpolating in $G_{\text{BP}} - G_{\text{RP}}$ at fixed metallicity, and the bolometric correction was derived by interpolation from the new T_{eff} .
3. $\log g$ was derived using T_{eff} and bolometric correction found in the previous step from the equation

$$\log g = \log(M/M_{\odot}) + 4 \log(T_{\text{eff}}/T_{\odot}) + 0.4 (G_0 + BC_G) + 2 \log p + \log L_{\odot} + \log g_{\odot} \quad (1)$$

where M is the stellar mass, G_0 is the dereddened apparent G magnitude, BC_G is the bolometric correction, and p is the parallax.

4. A_G and $E(G_{\text{BP}} - G_{\text{RP}})$ were derived by interpolating in the theoretical grid adopting the $E(B - V)$ from STILISM maps (Capitanio et al. 2017).
5. G and $G_{\text{BP}} - G_{\text{RP}}$ were dereddened using $E(G_{\text{BP}} - G_{\text{RP}})$.
6. The procedure was iterated until the difference between the new and the old T_{eff} was smaller than ± 50 K and the difference between the new and the old $\log g$ was smaller than 0.05 dex.

After we derived the stellar parameters, we used the measured equivalent widths (EWs) of the Fe I lines (see Sect. 4.2) and the GALA code (Mucciarelli et al. 2013) to derive the metallicity of the stars. With the new metallicity values, we again derived the stellar parameters and stopped the iteration when the difference between the new and the old T_{eff} was smaller than ± 50 K. To confirm the values of T_{eff} and $\log g$ obtained from the procedure, we derived effective temperatures and surface gravities using a new implementation of the Mucciarelli & Bellazzini (2020) InfraRed Flux Method (IRFM) colour- T_{eff} calibration for giants stars based on EDR3 data (Mucciarelli et al. 2021). The two effective temperatures agree well, in particular, T_{eff} from IRFM calibration is 70 K cooler on average than those estimated with the method described above.

As final parameters, we adopted T_{eff} and $\log g$ derived from the Mucciarelli et al. calibration because the IRFM method is less dependent on the adopted models with respect to the method described in the procedure. We fixed the uncertainty on T_{eff} at ± 100 K, according to the dispersion of the Mucciarelli et al. calibration. In Table 3 we present the stellar parameters. Microturbulent velocities (ξ) were estimated using the calibration derived by Dutra-Ferreira et al. (2016). The uncertainty on ξ is ± 0.1 km s⁻¹ according to the uncertainty of Dutra-Ferreira et al. calibration.

In Fig. 2 we compare *Gaia* EDR3 photometry of the observed stars to the Ekström et al. (2012) evolutionary tracks without rotation at solar metallicity for stellar masses between $2.5 M_{\odot}$ and $6.0 M_{\odot}$ provided by the SYCLIST code (Georgy et al. 2014), or interpolated between fully computed tracks. From Fig. 2 we deduce that these stars are very young, with ages between 0.1 Gyr (0.06 Gyr if we consider the evolutionary track for $6 M_{\odot}$) and 0.55 Gyr. The stellar masses we deduced from the evolutionary tracks are listed in Table 3. The uncertainty on stellar mass depends on the parallax error and on the stellar model adopted. If we adopt stellar models with

Table 3. Coordinates, atmospheric parameters, metallicities, and rotational velocities of the observed stars.

Star	RA J2000	Dec J2000	G [mag]	T_{eff} [K]	$\log g$ [cgs]	ξ [km s $^{-1}$]	Mass [M_{\odot}]	[FeI/H] [dex]	[FeII/H] [dex]	$v \sin i$ [km s $^{-1}$]	σ	d
HD 192045	20:12:18.44	+16:13:01.6	7.068	5239	2.91	1.31	3.0	-0.11 ± 0.16	-0.27 ± 0.18	5.42	0.49	0.55
HD 191066	20:07:28.92	+17:01:13.9	7.411	5346	3.01	1.32	3.0	0.08 ± 0.20	-0.18 ± 0.14	6.30	0.16	0.20
HD 205732	21:36:08.54	+41:55:57.1	7.560	5314	2.54	1.59	4.0	0.09 ± 0.16	-0.22 ± 0.18	10.35	0.72	0.75
HD 213036	22:27:33.13	+51:58:35.9	7.556	5163	1.94	1.91	6.0	0.07 ± 0.16	-0.19 ± 0.11	8.57	0.57	0.67
HD 217089	22:57:26.91	+46:49:21.6	7.825	5381	2.61	1.59	3.5	-0.08 ± 0.13	-0.05 ± 0.14	7.72	0.51	0.57
HD 9637	01:35:19.49	+44:55:34.6	8.476	5362	2.83	1.43	3.5	0.21 ± 0.10	0.29 ± 0.19	12.81	0.11	0.13
HD 21269	03:27:02.31	+34:25:46.2	6.386	4964	1.83	1.82	6.0	0.05 ± 0.26	0.14 ± 0.28	16.23	0.55	0.50
HD 19267	03:09:22.16	+64:17:58.8	6.550	5106	2.50	1.46	4.0	-0.08 ± 0.12	0.21 ± 0.35	8.10	0.26	0.30
HD 13882	02:16:49.26	+51:31:44.2	7.179	5157	2.45	1.53	4.0	-0.04 ± 0.14	0.24 ± 0.25	9.80	0.67	0.70
HD 189879	20:00:12.51	+47:55:57.7	8.017	4987	2.08	1.65	6.0	0.01 ± 0.17	-0.02 ± 0.36	7.22	0.66	0.70
HD 195375	20:29:08.30	+45:44:04.5	7.878	5304	2.56	1.56	3.5	-0.26 ± 0.13	0.10 ± 0.24	7.72	0.26	0.22
HD 221232	23:29:53.55	+50:46:38.9	8.183	5256	2.46	1.60	4.0	0.00 ± 0.12	0.25 ± 0.16	10.32	0.13	0.15
HD 219925	23:19:10.68	+49:13:59.9	8.539	5199	2.61	1.46	3.5	-0.10 ± 0.17	-0.35 ± 0.01	6.02	0.51	0.60
HD 278	00:07:37.41	+52:46:22.7	7.319	5133	2.59	1.42	3.5	0.06 ± 0.20	0.05 ± 0.20	22.17	0.57	0.60
HD 11519	01:54:39.55	+53:53:30.6	7.706	5230	2.35	1.65	4.0	0.04 ± 0.12	0.04 ± 0.08	6.87	0.46	0.50
TYC 2813-1979-1	01:23:49.59	+38:14:06.7	10.107	5058	2.67	1.32	3.5	0.08 ± 0.14	0.08 ± 0.05	6.37	0.45	0.55
BD+42 3220	19:00:47.36	+43:07:18.7	9.761	4982	3.02	1.09	2.5	0.40 ± 0.20	0.41 ± 0.07	4.00	0.14	0.10
BD+44 3114	19:22:04.14	+44:44:31.0	9.327	4990	2.77	1.22	3.0	0.37 ± 0.17	0.38 ± 0.10	5.98	0.26	0.30
TYC 3136-878-1	19:46:28.83	+39:15:59.4	10.602	5112	2.96	1.20	3.0	-0.06 ± 0.16	-0.07 ± 0.09	5.42	0.66	0.80
HD 40509	06:03:48.81	+64:05:20.1	7.731	5390	2.62	1.58	3.5	0.12 ± 0.18	0.32 ± 0.27	27.40	0.55	0.60
HD 41710	06:07:46.85	+22:42:27.6	7.104	5292	2.03	1.95	6.0	-0.02 ± 0.13	0.17 ± 0.14	10.05	0.85	0.84
HD 40655	06:00:55.34	+17:53:24.8	7.844	5379	2.21	1.88	5.0	-0.35 ± 0.11	-0.13 ± 0.13	9.52	1.08	1.20
HD 45879	06:30:57.65	+21:48:17.0	7.232	5112	1.90	1.90	6.0	-0.36 ± 0.16	0.07 ± 0.08	11.81	0.88	1.05
HD 55077	07:16:01.93	+64:46:51.6	7.077	5297	2.59	1.54	3.5	-0.42 ± 0.11	-0.25 ± 0.23	22.96	0.74	0.77
HD 61107	07:39:25.81	+40:40:16.8	7.137	5332	2.56	1.58	4.0	0.05 ± 0.15	0.17 ± 0.21	15.30	0.80	0.75
HD 63856	07:51:25.12	+11:09:56.5	7.888	5321	2.67	1.50	3.5	-0.05 ± 0.16	-0.32 ± 0.08	5.32	0.46	0.56

Notes. Uncertainties on $v \sin i$ are expressed in σ and in mid-range (d).

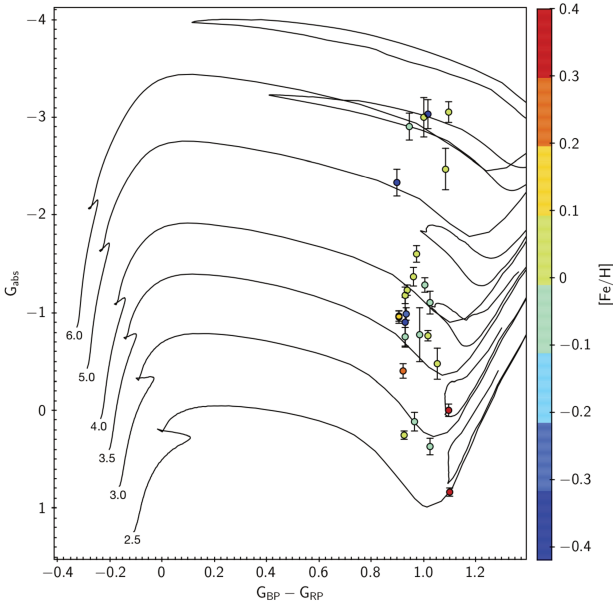


Fig. 2. Colour-magnitude diagram of *Gaia* EDR3 absolute magnitude G and dereddened colour $G_{\text{BP}} - G_{\text{RP}}$ comparing the observed stars with Ekström et al. (2012) evolutionary tracks without rotation at metallicity $Z = 0.014$ for stellar masses between $2.5 M_{\odot}$ and $6.0 M_{\odot}$. Error bars represent the uncertainty on G_{abs} , corresponding to 3σ error on parallax. The colour index indicates our derived [Fe/H] of the stars.

rotation, for example, the evolutionary tracks are more luminous than the respective tracks without rotation (see Fig. 10 in Georgy et al. 2013). For this reason, we estimate an uncertainty in mass from $0.5 M_{\odot}$ for the less massive stars to $1 M_{\odot}$ for those that lie in the region of the colour-magnitude diagram in which different evolutionary tracks overlap. We estimated an uncer-

tainty of ± 0.1 dex on $\log g$ by varying the stellar mass in Eq. (1) according to the mass error.

4.2. Iron abundances

Fe abundances were derived from the EW of the lines. The EWs were measured with the FITLINE code developed by P. François (Lemasle et al. 2007). FITLINE is a semi-interactive FORTRAN program that measures EWs of high-resolution spectra using genetic algorithms (Charbonneau 1995). Lines are fitted by a Gaussian defined by four parameters: the central wavelength, the width and depth of the line, and the continuum value. For each line, the algorithm runs as follows: (1) the program generates an initial set of Gaussians, giving random values to the four parameters of the Gaussian. (2) The fit quality is estimated by calculating the χ^2 . (3) A new “generation” of Gaussians is calculated from the 20 best fits after adding random modifications to the initial set of parameters. (4) The new set of parameters replaces the old set, and its accuracy is estimated again using a χ^2 evaluation. Finally, (5) the process is iterated until the convergence to the best Gaussian fit is achieved. For the most highly rotating stars (HD 21269, HD 278, HD 40509, HD 55077, and HD 61107) FITLINE was modified to take the Gaussian and rotational profile of the lines into account. To derive Fe abundances from EWs, we used the GALA code (Mucciarelli et al. 2013), which compares the measured EW for each line with the theoretical EW computed from the curve of growth of the line. The Fe I and Fe II abundances we derived for this sample of stars are listed in Table 3.

4.3. Rotational velocities

Rotational velocities ($v \sin i$) were measured by fitting the observed line profiles with the corresponding theoretical line profiles that were obtained from a synthetic spectrum computed

Table 4. Fe I lines used to derive the rotational velocity of stars.

	5778 Å	5809 Å	6096 Å	6151 Å	6380 Å	6627 Å	6726 Å	6752 Å	6806 Å	6810 Å	6820 Å	6862 Å
HD 192045			x	x	x				x			
HD 191066			x	x			x		x			
HD 205732				x					x	x	x	
HD 213036	x	x	x								x	
HD 217089				x	x			x	x			
HD 9637				x	x			x		x		
HD 21269				x				x	x			
HD 19267							x		x	x	x	
HD 13882					x			x		x	x	
HD 189879			x				x		x		x	
HD 195375				x	x			x	x			
HD 221232				x	x			x			x	
HD 219925			x	x			x		x			
HD 278				x	x			x	x			
HD 11519							x	x	x		x	
TYC 2813-1979-1			x				x	x			x	
BD+42 3220				x						x		
BD+44 3114						x	x			x		x
TYC 3136-878-1				x	x				x		x	
HD 40509				x	x			x	x			
HD 41710				x	x			x	x			
HD 40655				x	x			x	x			
HD 45879				x	x			x	x			
HD 55077				x	x			x	x			
HD 61107				x	x			x	x			
HD 63856		x	x	x					x			

Notes. The X represents the lines we used for each star.

with the spectral synthesis code SYNTHE (Kurucz 2005; Sbordone et al. 2004) based on ATLAS 9 1D plane-parallel model atmospheres (Kurucz 2005). In order to better compare $v \sin i$ between different stars, we selected a set of Fe I lines to be fitted. The list of Fe I lines we used to measure $v \sin i$ is shown in Table 4. For each line, we performed a χ^2 minimisation fit on the observed line profile using three synthetic spectra computed with different rotational velocities. The metallicity of the synthetic spectra was fixed at the value of iron abundance derived from the EW of the single line. We made the assumption that the line broadening of synthetic spectra was equal to the instrumental broadening. The values of $v \sin i$ we obtained are presented in Table 3. This approach does not allow us to distinguish between $v \sin i$ and other sources of line broadening, such as macroturbulence. The spectra of five stars with similar T_{eff} but different $v \sin i$ are shown in Fig. 3. For the faster-rotating stars, the line profile is dominated by the rotational profile, and we can assume that other broadening effects are negligible with respect to $v \sin i$. For the more slowly rotating stars, however, the contribution of macroturbulence in line broadening is comparable to the rotational contribution, so that the values of $v \sin i$ obtained for these stars must be interpreted as upper limits.

4.4. Chemical abundances of other elements

We were able to derive for the stars in the sample the elemental abundances of C, N, O, Mg, Al, and Ca and for the neutron capture elements Sr, Y, Ba, La, Ce, Pr, Nd, Sm, and Eu. For all elements we adopted the solar abundances determined by Caffau et al. (2011) and Lodders et al. (2009) (see Table 5). The chemical abundances we obtained are listed in Tables A.1–A.3. The values $A(X)$ are expressed in the

form $A(X) = \log(X/H) + 12$. The abundance ratios $[X/Fe]^3$ are expressed as $[X/Fe] = [X/H] - [Fe/H]$ for elements up to Ca and as $[X/Fe] = [X/H] - [FeII/H]$ for O and n -capture elements.

The carbon abundance was derived from the G -band by minimisation of the χ^2 when we compared the observed spectrum to a grid of synthetic spectra with different C abundances. The synthetic spectra were computed with SYNTHE (Kurucz 2005) using the ATLAS 9 model (Kurucz 2005) computed for each star (see Bonifacio & Caffau 2003, for details). The G -band is strong for all the stars, and we estimate an uncertainty in the range 0.2–0.5 dex in the C abundances, which is mainly related to the continuum placement. The nitrogen abundances were determined in a similar way using the violet CN band at 412.5 nm, assuming the C abundance derived from the G -band to be fixed. The error is mainly due to the uncertainty of placing the continuum and is in the range 0.3–0.6 dex. Oxygen was determined from the EW of the [OI] 630 nm line. This was measured with the iraf⁴ task `sp1ot` only when the line was not affected by blends with telluric lines or the blend was minor and could be taken into account using the `deblend` option of `sp1ot`. Mg, Al, and Ca abundances were derived using the procedure described in Sect. 4.2. The uncertainty showed in Table A.2 represents the line-to-line scatter if the abundance was derived from ≥ 2 lines, otherwise it represents the abundance error due to continuum placement. For the neutron-capture elements, the abundance was determined by matching the observed spectrum around each line of the list with a synthetic spectrum computed using the local thermodynamic equilibrium (LTE) spectral line analysis code `turbospectrum` (Alvarez & Plez 1998; Plez 2012), which treats

³ $[X/Fe] = \log_{10}(X/Fe) - \log_{10}(X/Fe)_{\odot}$.

⁴ <https://iraf-community.github.io/>

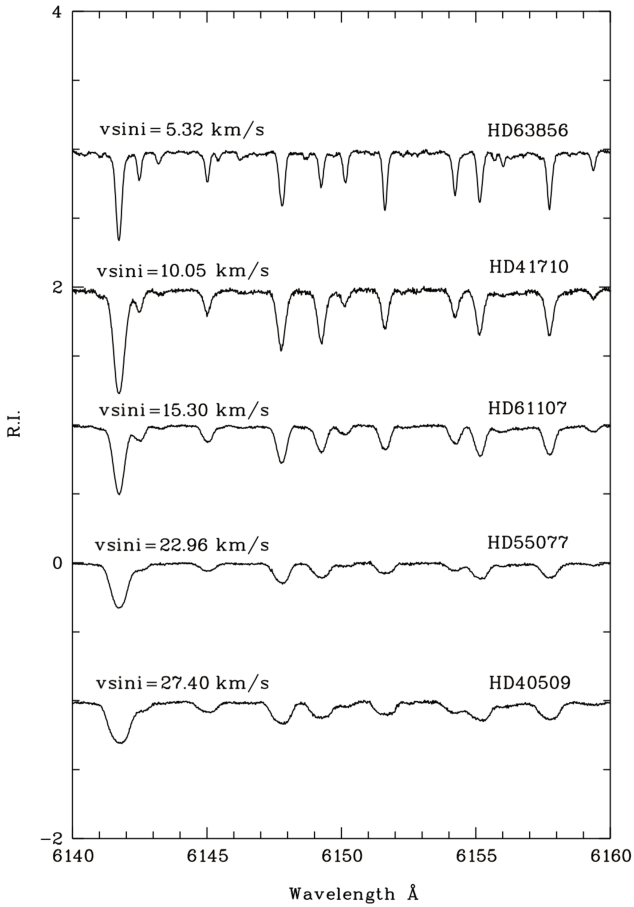


Fig. 3. Spectra of five stars with similar T_{eff} and different $v \sin i$. The spectra have been normalised and are shifted to facilitate visualisation.

scattering in detail. The computed errors in the elemental abundances ratios due to uncertainties in the stellar parameters are listed in Table A.4. The errors were estimated varying T_{eff} by ± 100 K, $\log g$ by ± 0.5 dex, and ξ by ± 0.5 dex in the model atmosphere of HD 13882. The results for other stars are similar. The main uncertainty comes from the error in the continuum placement when the synthetic line profiles are matched to the observed spectra. This error is of the order of 0.1 dex. When several lines are available, the typical line-to-line scatter for a given element is 0.1 dex.

5. Possible binary stars

Stars HD 195375 and HD 278 are listed in the Washington Double Star Catalog (Mason et al. 2001). We checked the *Gaia* EDR3 astrometric parameters of these two binary systems. We found that HD 278 and its companion have different parallaxes, so that these stars are probably in a visual double system but not in a physical one, as suggested by Muller (1984). In contrast, HD 195375 and its companion have consistent parallaxes, which implies that they are in a physical binary system. As binarity is a possible cause of radial velocity variability, we compared our measured radial velocities with those of *Gaia* DR2 (Gaia Collaboration 2018). The brightness of our stars implies that the error on the radial velocity due to photon noise is smaller than 1 km s^{-1} (Sartoretti et al. 2018). As shown in Table 6, six stars have a larger error, which means that they are very likely radial velocity variables. The *Gaia* radial velocity

Table 5. Solar abundance values adopted in this work.

Element	$A(X)$	References
C	8.50	Caffau et al. (2011)
N	7.86	Caffau et al. (2011)
O	8.76	Caffau et al. (2011)
Mg	7.54	Lodders et al. (2009)
Al	6.47	Lodders et al. (2009)
Ca	6.33	Lodders et al. (2009)
Fe	7.52	Caffau et al. (2011)
Sr	2.92	Lodders et al. (2009)
Y	2.21	Lodders et al. (2009)
Ba	2.17	Lodders et al. (2009)
La	1.14	Lodders et al. (2009)
Ce	1.61	Lodders et al. (2009)
Pr	0.76	Lodders et al. (2009)
Nd	1.45	Lodders et al. (2009)
Sm	1.00	Lodders et al. (2009)
Eu	0.52	Caffau et al. (2011)

Table 6. Comparison between *Gaia* DR2 and observed radial velocities for our stars.

Star	v_{radGDR2} [km s^{-1}]	v_{rad} [km s^{-1}]	Flag
HD 192045	-43.846 ± 2.253	-4.834 ± 0.077	• ◦ ★
HD 191066	-5.911 ± 3.451	-9.349 ± 0.001	• ★
HD 205732	-3.150 ± 0.147	-3.971 ± 0.001	◦
HD 213036	-4.369 ± 1.662	-40.890 ± 0.128	• ◦ ★
HD 217089	-7.441 ± 0.150	-7.684 ± 0.001	
HD 9637	-1.879 ± 0.169	-2.361 ± 0.002	
HD 21269	-15.676 ± 0.262	-12.602 ± 0.002	◦
HD 19267	3.387 ± 0.153	2.697 ± 0.001	★
HD 13882	-28.545 ± 0.170	-29.038 ± 0.001	
HD 189879	-10.391 ± 4.430	-29.532 ± 0.001	• ★
HD 195375 *	-9.352 ± 0.154	-10.276 ± 0.001	◦
HD 221232	-29.894 ± 0.158	-30.649 ± 0.001	
HD 219925	-14.596 ± 2.837	-22.916 ± 0.001	• ★
HD 278 *	-26.143 ± 7.736	-60.526 ± 0.003	•
HD 11519	-10.625 ± 0.177	-11.260 ± 0.001	
TYC 2813-1979-1	-16.201 ± 0.338	-17.170 ± 0.002	
BD+42 3220	-18.523 ± 0.219	-19.298 ± 0.053	
BD+44 3114	-17.302 ± 0.170	-15.216 ± 0.055	◦
TYC 3136-878-1	0.922 ± 0.985	1.034 ± 0.053	
HD 40509	-1.223 ± 0.310	-1.656 ± 0.005	
HD 41710	-6.812 ± 0.269	-7.917 ± 0.002	
HD 40655		7.332 ± 0.001	
HD 45879	5.902 ± 0.224	7.047 ± 0.001	◦ ★
HD 55077	-25.729 ± 0.514	-25.499 ± 0.003	★
HD 61107	12.126 ± 0.738	10.476 ± 0.001	★
HD 63856	22.402 ± 0.206	19.755 ± 0.001	◦ ★

Notes. Stars with an asterisk are in the Washington Double Star Catalog. Filled circles indicate stars with *Gaia* DR2 radial velocity errors $> 1 \text{ km s}^{-1}$. Open circles represent stars with *Gaia* DR2 radial velocities that differ by more than 5σ from our observed v_{rad} . The five-pointed star indicates stars that were identified as possible binary stars from proper motion anomalies by Kervella et al. (2019).

of eight stars differs by more than 5σ from our measured velocity. They are again very likely radial velocity variables. Ten stars have been identified as probable binary stars by Kervella et al. (2019) from the comparison between HIPPARCOS (ESA 1997) and *Gaia* DR2 proper motions. We note that stars HD 192045 and HD 213036 show all the properties mentioned above. This strongly suggests that they are binary stars. It is likely that the

end-of-mission *Gaia* data, which will combine astrometry, epoch photometry, and radial velocities, will allow us to determine the orbits of the confirmed binaries.

6. Kinematics and Galactic orbits

We characterised the stellar orbital parameters with the Galpot code⁵ (McMillan 2017; Dehnen & Binney 1998) using the stellar coordinates, radial velocities, *Gaia* DR2 distances, and proper motions. We derived the stellar coordinates and velocity components in the galactocentric cylindrical (R , z , φ , v_R , v_Z , v_φ) and Cartesian systems (X , Y , Z , v_X , v_Y , v_Z). We derived the minimum and maximum cylindrical (R_{\min} , R_{\max}) and spherical (r_{\min} , r_{\max}) radii, the eccentricity ($e = (r_{\max} - r_{\min}) / (r_{\max} + r_{\min})$), the maximum height above the Galactic plane (Z_{\max}), the total energy (E), and the z-component of the angular momentum (L_z). We found that all stars have typical disc kinematics. All stars have prograde motions, and the eccentricity ($e < 0.11$) for 25 out of 26 stars ($e \sim 0.2$ for HD 278) is very low. The maximum height above the Galactic plane is lower than 400 pc for 25 out of 26 stars ($Z_{\max} \sim 600$ pc for TYC 2813-1979-1).

7. Discussion

7.1. Photometric $\log g$ versus spectroscopic $\log g$

In order to verify the values of $\log g$ that we obtained from *Gaia* photometry and parallaxes, we derived surface gravities by imposing the ionisation equilibrium of the Fe I and Fe II lines. As shown in Table 7, photometric and spectroscopic $\log g$ are compatible within 0.1 dex for ten stars, while the difference between photometric and spectroscopic gravities is $-0.6 \leq \Delta \log g \leq 0.9$ dex for the remaining stars. We deduced the corresponding stellar masses from spectroscopic gravities by inverting Eq. (1). We obtained that the masses should be $0.7 \leq M/M_\odot \leq 18.9$; two stars have $M < 0.8 M_\odot$. These very low masses are incompatible with stellar evolutionary models (unless we assume that they are older than 14 Gyr). We therefore conclude that the spectroscopic gravities are not reliable for the majority of these stars. The reason for the observed discrepancy is not trivial because for solar metallicity stars, we expect spectroscopic and photometric approaches to be equivalent (see the discussion in Mucciarelli & Bonifacio 2020). As the difference in $\log g$ reflects the difference between Fe I and Fe II abundances, the discrepancy for the most highly rotating stars could be due to a bias in the line selection. Stellar rotation allowed us to detect only the strongest and consequently most saturated Fe II lines. However, the same discrepancy is found for some stars with low rotational velocity, therefore some other effect must be responsible for it. The observed scatter in $\Delta \log g$ for stars with $v \sin i < 10 \text{ km s}^{-1}$ seems to suggest that this effect is due to inadequacies of the adopted physics, in particular, the assumption of 1D geometry and LTE, as discussed for metal-poor giants in Mucciarelli & Bonifacio (2020). We confirmed that non-LTE (NLTE) effects under the assumption of 1D geometry are not sufficient to solve the $\log g$ discrepancy. We applied the NLTE corrections provided by Bergemann et al. (2012)⁶ to the Fe I lines of the star HD 191066, for which we obtained $[\text{FeI}/\text{FeII}] = 0.26$ dex using photometric $\log g$. We found that the mean correction value was 0.005 dex with a maximum value of 0.06 dex for the Fe I line at 5956.693 Å. This means that applying this NLTE correction to Fe I the imbalance would be even worse.

⁵ <https://github.com/PaulMcMillan-Astro/GalPot>

⁶ <http://nlte.mpia.de/>

Table 7. Comparison between photometric and spectroscopic $\log g$ and derived stellar masses.

Star	$\log g_{\text{phot}}$ [dex]	$\log g_{\text{spec}}$ [dex]	$\Delta \log g$ [dex]	Mass [M_\odot]	Mass _{spec} [M_\odot]
HD 192045	2.91	3.21	-0.30	3.0	6.1
HD 191066	3.01	3.51	-0.50	3.0	9.5
HD 205732	2.54	3.14	-0.60	4.0	16.1
HD 213036	1.94	2.44	-0.50	6.0	18.9
HD 217089	2.61	2.61	0.00	3.5	3.5
HD 9637	2.83	2.73	0.10	3.5	2.8
HD 21269	1.83	1.73	0.10	6.0	4.7
HD 19267	2.50	1.90	0.60	4.0	1.0
HD 13882	2.45	1.85	0.60	4.0	1.0
HD 189879	2.08	2.08	0.00	6.0	6.0
HD 195375	2.56	1.86	0.70	3.5	0.7
HD 221232	2.46	1.96	0.50	4.0	1.3
HD 219925	2.61	3.11	-0.50	3.5	11.1
HD 278	2.59	2.59	0.00	3.5	3.5
HD 11519	2.35	2.35	0.00	4.0	3.9
TYC 2813-1979-1	2.67	2.67	0.00	3.5	3.5
BD+42 3220	3.02	3.02	0.00	2.5	2.5
BD+44 3114	2.77	2.77	0.00	3.0	3.0
TYC 3136-878-1	2.96	2.96	0.00	3.0	3.0
HD 40509	2.62	2.22	0.40	3.5	1.4
HD 41710	2.03	1.63	0.40	6.0	2.4
HD 40655	2.21	1.71	0.50	5.0	1.6
HD 45879	1.90	1.00	0.90	6.0	0.7
HD 55077	2.59	2.29	0.30	3.5	1.7
HD 61107	2.56	2.36	0.20	4.0	2.5
HD 63856	2.67	3.17	-0.50	3.5	11.1

7.2. Chemical composition

7.2.1. C, N, O

In Fig. 4 we show our measured C, N and O abundance ratios. The $[\text{C}/\text{Fe}]$ ratios are lower than solar for all stars in our sample ($\langle [\text{C}/\text{Fe}] \rangle = -0.44$ dex and $\sigma = 0.17$), with the exception of two stars with $[\text{Fe}/\text{H}] \sim 0.4$ dex that show a $[\text{C}/\text{Fe}]$ of about zero. Our interpretation is that all the stars with sub-solar $[\text{C}/\text{Fe}]$ show material in the photosphere that has been mixed with material that has experienced nuclear hydrogen burning through the CNO cycle. This interpretation is supported by the super-solar $[\text{N}/\text{Fe}]$ ratios. The $[(\text{C}+\text{N}+\text{O})/\text{Fe}]$ ratio is shown in Fig. 5. This quantity is nearly constant and close to the solar value within the error bars. This indicates that the underabundances in C and the overabundances in N result from pure H-burning via the CNO cycle, and that no He-burning products have yet been transported to the stellar surface. The value of $[\text{C}/\text{Fe}]$ of a given star is probably independent of the original $[\text{C}/\text{Fe}]$ value that characterised the star on the main sequence, but depends only on the amount of mixing. This is supported by the fact that there is no clear trend of $[\text{C}/\text{Fe}]$ with metallicity. If our interpretation is correct, the two more metal-rich stars of our sample are mixed very little with respect to the others. Some mixing is only suggested by a slight enhancement of $[\text{N}/\text{Fe}]$ in both stars. These two stars belong to the stars with the highest gravity in the sample, which is in line with the notion of little or no mixing. We caution, however, that there are stars with similarly high $\log g$ that have a low $[\text{C}/\text{Fe}]$. There clearly is no one-to-one correspondence between surface gravity and mixing.

It is interesting to compare our results with those in the literature. We selected two samples of CNO abundances in A-type stars (Takeda et al. 2018 and Royer et al. 2014). The Takeda and Royer samples both consists of A-type main-sequence stars. Royer stars are also characterised by $v \sin i \leq 65 \text{ km s}^{-1}$. We also

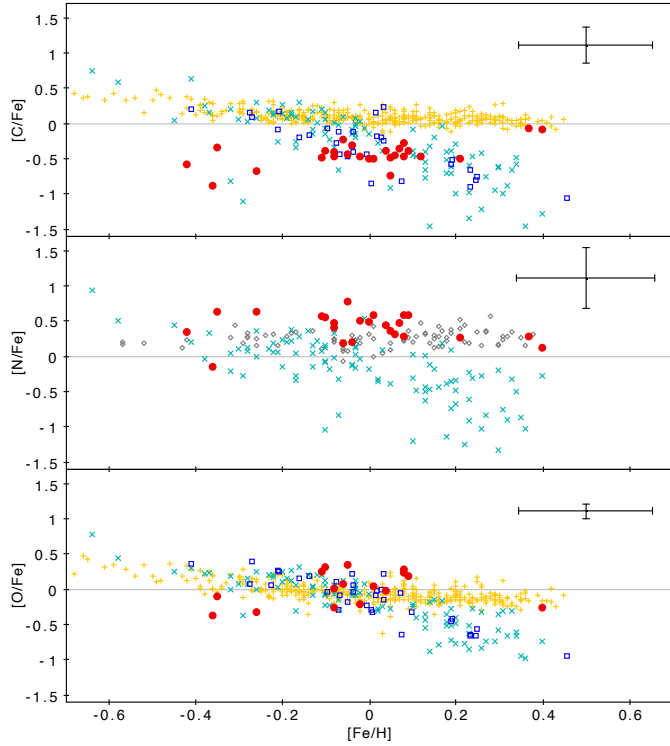


Fig. 4. [C/Fe], [N/Fe] and [O/Fe] abundances as a function of [Fe/H]. Comparison with targets from [Takeda et al. \(2018\)](#) (cyan crosses), [Royer et al. \(2014\)](#) (blue squares), [Delgado Mena et al. \(2010\)](#) (yellow crosses) and [Ecuivillon et al. \(2004\)](#) (grey diamonds).

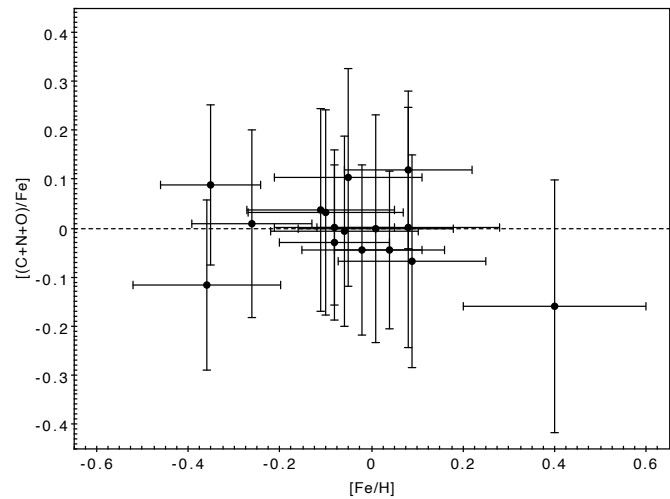


Fig. 5. [(C+N+O)/Fe] abundance ratios as a function of [Fe/H].

added samples of CNO samples in FGK dwarf stars with a metallicity comparable to that of our sample: [Delgado Mena et al. \(2010\)](#) provided C and O abundances for 370 FGK dwarfs stars, and [Ecuivillon et al. \(2004\)](#) provided N abundances for 91 solar-type stars. The top panel of Fig. 4 clearly shows that the majority of our stars have lower [C/Fe] than the FGK dwarfs (yellow crosses), with the exception of the two stars with the highest metallicity, which appear to be quite compatible. It is striking that the [C/Fe] abundance in A-type stars displays a decreasing trend with increasing metallicity for the samples of [Takeda et al. \(2018\)](#) (cyan crosses) and [Royer et al. \(2014\)](#) (blue squares). This trend is at odds with the flat trend shown by FGK

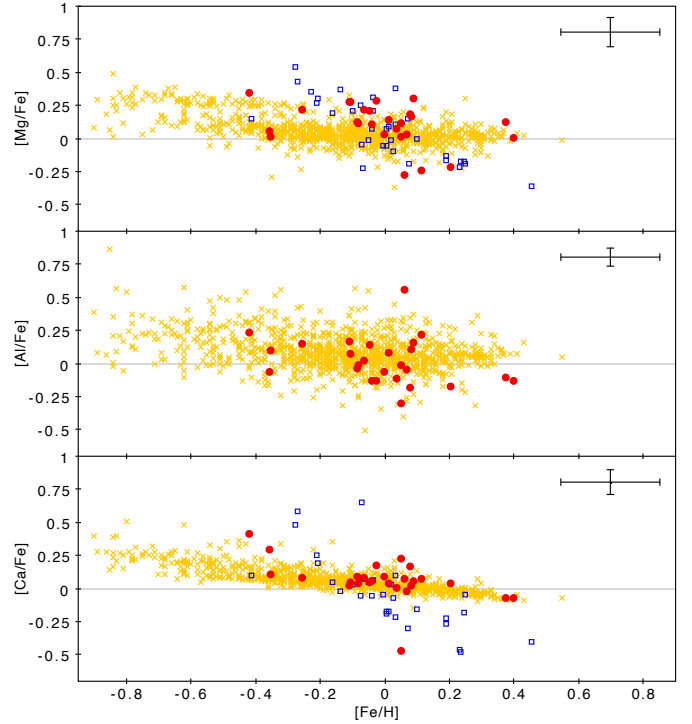


Fig. 6. [Mg/Fe], [Al/Fe], and [Ca/Fe] abundances as a function of [Fe/H]. Comparison with targets from [Adibekyan et al. \(2012\)](#) (yellow crosses) and [Royer et al. \(2014\)](#) (blue squares).

stars. This trend in A stars has been noted and discussed by [Takeda et al. \(2018\)](#), see also references therein). A stars show the phenomenon of chemical peculiarities (CP stars), which gives rise to many sub-classes of CP stars (see [Ghazaryan et al. 2018](#), and references therein). The most popular explanation of the chemical peculiarities for most classes of CP stars is diffusion (see e.g., [Richer et al. 2000](#), and references therein), possibly in the presence of rotational mixing ([Talon et al. 2006](#)). As pointed out by [Takeda et al. \(2018\)](#), this anti-correlation of [C/Fe] with [Fe/H] can be understood if the mechanism causing the chemical peculiarities acts in opposite directions for CNO and Fe. We do not detect any chemical peculiarities, except for the CNO pattern expected from mixing on the RGB and Ba (see Sect. 7.2.3). This strongly suggests that these peculiarities, even if they were present when the star was on the main sequence, are erased as the star evolves to the RGB by the onset of convective mixing as the star cools and its atmosphere is no longer in radiative equilibrium, as was the case while the star was on the main sequence.

7.2.2. Mg, Al, and Ca

Figure 6 shows Mg, Al, and Ca abundance ratios as a function of [Fe/H]. Our results are compared to the analysis by [Adibekyan et al. \(2012\)](#) (yellow crosses) and [Royer et al. \(2014\)](#) (blue squares). The Adibekyan sample consists of F, G, and K dwarf stars, which means that they have lower masses than our sample stars, but T_{eff} is similar. Our derived [Mg/Fe], [Al/Fe], and [Ca/Fe] abundance ratios appear to be in line with the results obtained by other authors. The dispersion in [Mg/Fe] ($\langle[\text{Mg/Fe}]\rangle = 0.10$ dex and $\sigma = 0.16$), [Al/Fe] ($\langle[\text{Al/Fe}]\rangle = 0.02$ dex and $\sigma = 0.17$) and [Ca/Fe] ($\langle[\text{Ca/Fe}]\rangle = 0.06$ dex and $\sigma = 0.15$) is larger than is expected from our estimated errors. In the case of [Mg/Fe], we

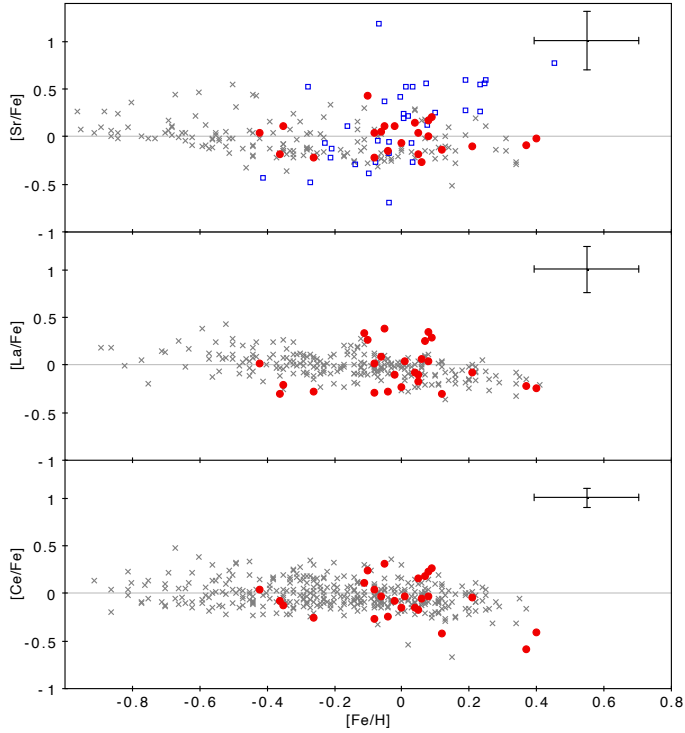


Fig. 7. [Sr/Fe], [La/Fe], and [Ce/Fe] abundances as a function of [Fe/H]. Comparison with targets from Battistini & Bensby (2016) (grey crosses) and Royer et al. (2014) (blue squares).

note that the Adibekyan et al. and Royer et al. stars also show a large dispersion despite the high quality of spectra. The observed scatter is therefore probably intrinsic. The [Mg/Fe] ratio of two stars in our sample appears to be compatible with the values of stars in the upper sequence in the Adibekyan et al. sample. They were labelled thick-disc stars by the authors. However, the kinematics of these two stars clearly shows that they are thin-disc stars. A purely chemical selection is not sufficient to distinguish between thin- and thick-disc stars, as has been pointed out by several authors (see e.g., Franchini et al. 2020; Romano et al. 2021). Specifically, Romano et al. (2021) reported that only 25% of the high- α stars in their sample can be classified kinematically as belonging to the thick-disc population. It is therefore not surprising that we find thin-disc high- α stars. Some unexpected results were found for stars HD 278 and HD 21269. Star HD 278 shows a higher Al abundance than the other stars in the sample ([Al/Fe] = 0.55 dex, $\sigma = 0.24$). Star HD 21269 instead shows a higher than solar Mg abundance ([Mg/Fe] = 0.11 dex, $\sigma = 0.36$) and lower than solar Al and Ca abundance ([Al/Fe] = -0.30 dex, $\sigma = 0.11$; [Ca/Fe] = -0.47, $\sigma = 0.26$). These stars rotate rapidly ($v \sin i \sim 22 \text{ km s}^{-1}$ for HD 278 and $v \sin i \sim 16 \text{ km s}^{-1}$ for HD 21269) and the uncertainty on the abundances is large. As discussed in Sect. 7.1, rotation can affect the estimate of the EW of the lines, which may lead to an incorrect abundance estimate. However, we note that some stars in the Adibekyan et al. sample show the same Al abundance. This implies that it is possible for a star to have such a low [Al/Fe] ratio.

7.2.3. Neutron-capture elements

In Figs. 7–9 we show the abundances of several neutron-capture elements. The Sr abundance ratio is compared to the analysis by Royer et al. (2014) (blue squares) and Battistini & Bensby

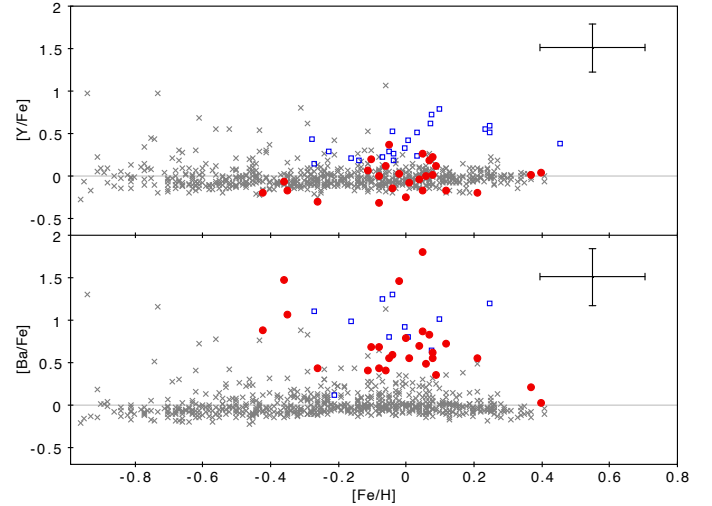


Fig. 8. [Y/Fe] and [Ba/Fe] abundances as a function of [Fe/H]. Comparison with targets from Bensby et al. (2014) (grey crosses) and Royer et al. (2014) (blue squares).

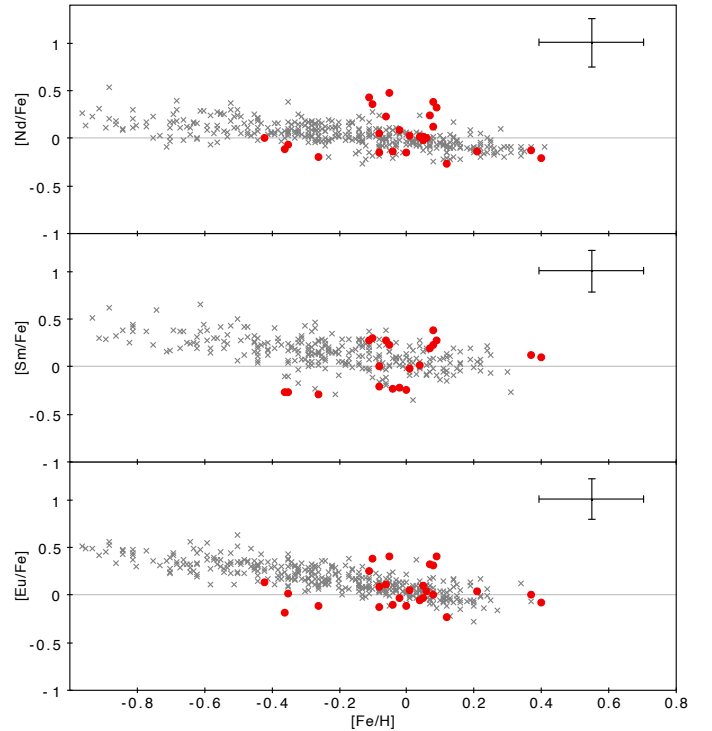


Fig. 9. [Nd/Fe], [Sm/Fe], and [Eu/Fe] abundances as a function of [Fe/H]. Comparison with targets from Battistini & Bensby (2016) (grey crosses).

(2016) (grey crosses), and the [Y/Fe] and [Ba/Fe] ratios are compared to the results of the analysis by Royer et al. (2014) (blue squares) and Bensby et al. (2014) (grey crosses). The La, Ce, Nd, Sm, and Eu abundances ratios are compared to the analysis by Battistini & Bensby (2016) (grey crosses). The Bensby et al. (2014) sample consists of F and G dwarf and subgiant stars, and Battistini & Bensby (2016) provided abundances of several n -capture elements for the same stars. We observe that in the case of n -capture elements, the abundances ratios we measured are also in line with the results found by other authors. A remarkable result is the Ba abundance, which is higher than solar for

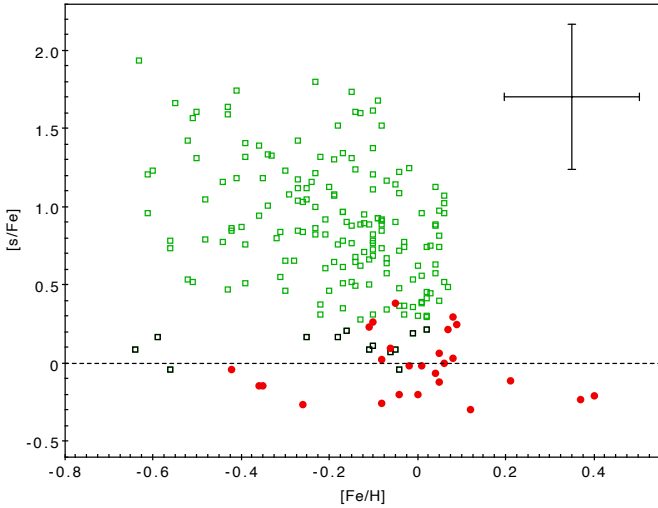


Fig. 10. Mean abundance ratio $[s/Fe]$ of s-process elements ($[Y/Fe]$, $[La/Fe]$, $[Ce/Fe]$, and $[Nd/Fe]$) as a function of $[Fe/H]$. Red circles represent the $[s/Fe]$ ratio for the stars analysed in this work. Green squares represent barium stars analysed in de Castro et al. (2016). Black squares represent the targets rejected as barium stars in de Castro et al. (2016).

the majority of stars in our sample. The same result has been found for main-sequence stars by Royer et al. (2014). The NLTE correction for Ba lines provided by Korotin et al. (2015) would decrease the Ba abundances by 0.1 dex, which is insufficient to match the observed values with other n -capture abundances. We exclude the possibility that an atmospheric phenomenon could explain the observed Ba abundance: if the Ba overabundance were due to atmospheric processes during the main-sequence phase, it would be erased by mixing when the star evolves to the red giant phase.

In Fig. 10 we compare our results to the s-process abundance ratios $[s/Fe]$, that is, the mean abundance ratio $[X/Fe]$ of s-process elements $[Y/Fe]$, $[La/Fe]$, $[Ce/Fe]$, and $[Nd/Fe]$ of barium stars derived by de Castro et al. (2016). We observe that three stars in our sample have $[s/Fe]$ above 0.25 dex, which is the lower limit for $[s/Fe]$ in Ba stars according to de Castro et al. (2016), and only one star (HD 63856) has $[s/Fe] = 0.38$ dex. These low values of the $[s/Fe]$ ratio are compatible with those of mild Ba stars, which have weaker s-process enhancements than classical barium stars, only few or no anomalous molecular band strengths (Eggen 1972; Morgan & Keenan 1973), and no carbon enrichment (Snedden et al. 1981). However, we stress that the Ba II abundance is strongly dependent on microturbulent velocity. We note that an increase in microturbulence of 0.6 km s^{-1} decreases the Ba abundance by 0.6 dex for star HD 55077. This effect was first observed by Hyland & Mould (1974), who showed that high microturbulent velocities might cause the Ba II resonance lines to become anomalously strong in stars with solar s-process elements. In our case, we have no observation that supports such a high microturbulence, which would also affect the abundances of other elements. There probably is no strong evidence implying that stars in our sample are mild Ba stars, but the high $[Ba/Fe]$ ratios are puzzling and unexplained.

In their study of dwarf stars in five open clusters and one star-forming region, Baratella et al. (2021) found an enhancement in Ba similar to what we have found in our stars. Remarkably, Ba is more enhanced for the younger clusters. The Ba enhancement is accompanied by mild Y enhancement of the order of 0.2 dex. A larger enhancement is again found for the younger clusters.

These two results are consistent with our findings. At face value, our derived $[Y/Fe]$ abundance ratios are ~ 0.2 dex, but we do not give much weight to the Y enhancement as it is consistent with $[Y/Fe] = 0$ within the errors. Baratella et al. (2021) examined several causes for this Ba anomaly, including the role of magnetic fields. They failed to propose any convincing explanation of their observations, however. We therefore conclude that the increase in Ba that we observe may be related to what has been observed in other young stars.

7.2.4. Chemical abundances and rotational velocities

We investigated the presence of trends between elemental abundances and rotational velocity in our sample. To limit evolutionary effects, we considered only stars with metallicity in the range $-0.1 < [Fe/H] < 0.1$. We found that for only four elements ($[O/H]$, $[Ca/H]$, $[Ba/H]$, and $[Eu/H]$) does non-parametric Kendall's τ test provides a correlation probability higher than 95% with $v \sin i$. However, parametric fitting did not confirm any trend between these quantities. We therefore conclude that the correlations are not significant.

7.3. Comparison with models

We compared our results with the predictions of two sets of stellar evolution models including the effects of rotation: the models of Georgy et al. (2013), which were computed with the Geneva stellar evolution code (GENEC), and the models of Lagarde et al. (2012), which were computed with the code STAREVOL (Mowlavi & Forestini 1994; Siess et al. 2000; Palacios et al. 2003, 2006; Decressin et al. 2009); see Lagarde et al. (2012) for a comparison between these two sets of models.

Because the observed rotational velocities depend on the inclination angle of the stars along the line of sight, a direct comparison between observed and predicted rotational velocities is not possible. However, the observed values of $v \sin i$ are lower limits for the actual surface rotation of stars. As shown in the upper panel of Fig. 11, the $v \sin i$ we obtained for stars with $3.5 M_{\odot}$ and $4 M_{\odot}$ in the metallicity range $-0.1 < [Fe/H] < 0.1$ ($5 < v \sin i < 22 \text{ km s}^{-1}$) are compatible with the rotational velocity values predicted by the Georgy et al. models with $0.3 < \omega < 0.6^7$ at solar metallicity for stars in the corresponding region of the $\log T_{\text{eff}}$ versus $\log g$ diagram.

As described in Sect. 7.2.1, we found that almost all stars in the sample show lower than solar C abundances and higher than solar N abundances. This indicates that the stars have undergone mixing and that the products of the H-burning CNO cycle are visible on the stellar surface. In the lower panel of Fig. 11, the observed $[N/C]$ abundance ratios of stars with $3.5 M_{\odot}$ and $4.0 M_{\odot}$ in the metallicity range $-0.1 < [Fe/H] < 0.1$ are compared with the values predicted by the Georgy et al. models for stars in the same region of the $\log T_{\text{eff}}$ versus $\log g$ diagram. The stars are warmer than the maximum extent of the clump, or blue loop, where stars are located when they undergo central He-burning. However, because this phase is much longer than the crossing of the Hertzsprung gap, we consider it to be highly probable that all the stars are on the clump. We also note that the $[N/C]$ abundance ratios for the majority of stars are consistent with the values predicted for clump stars in the Georgy et al. models. For all these quantities, a similar agreement is obtained with the models of Lagarde et al. (2012), as shown in Fig. 12.

⁷ $\omega = \Omega_{\text{in}}/\Omega_{\text{crit}}$.

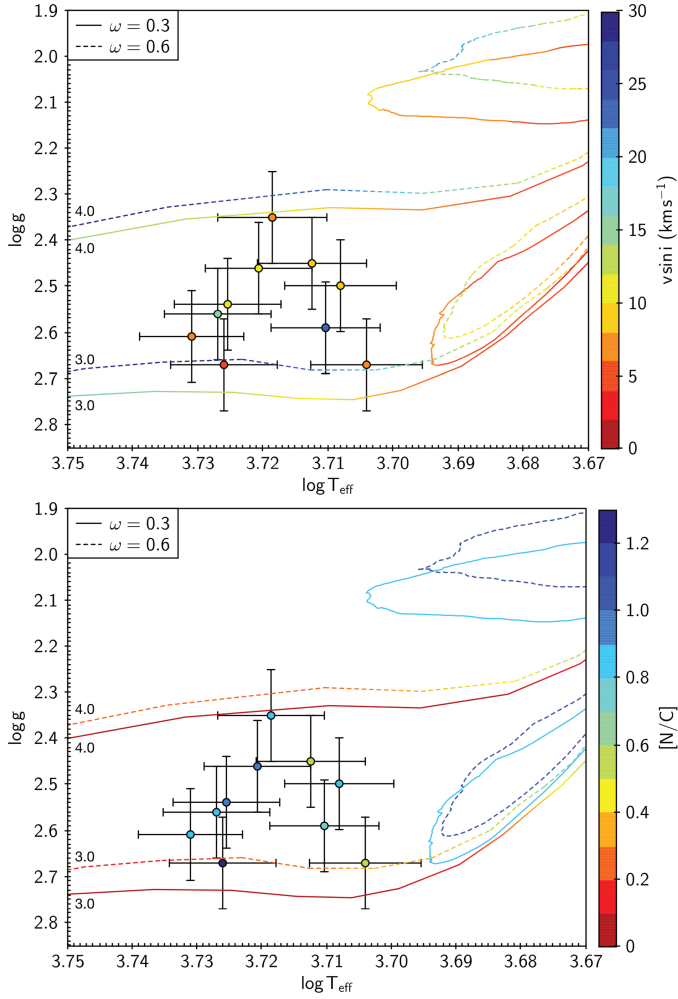


Fig. 11. Log T_{eff} vs. log g diagram for the [Georgy et al. \(2013\)](#) evolutionary tracks with $Z = 0.014$, $M = 3 M_{\odot}$, $4 M_{\odot}$, and $\omega = 0.3$ (solid lines) and 0.6 (dashed lines). Stars in the sample with $-0.1 < [\text{Fe}/\text{H}] < 0.1$ and $M = 3.5 M_{\odot}$, $4 M_{\odot}$ are shown with error bars. *Upper panel:* colour index indicates the equatorial velocity for evolutionary tracks and the observed $v \sin i$ for sample stars. *Lower panel:* colour index indicates the $[\text{N}/\text{C}]$ abundance ratio.

8. Conclusions

We observed a sample of 26 bright giant stars that had a photometric metallicity estimated to be in the range $-2.5 \leq [\text{Fe}/\text{H}] \leq -1$. The aim was a detailed inventory of the neutron-capture elements. The analysis of the sample showed that all stars were metal rich ($-0.4 \leq [\text{Fe}/\text{H}] \leq 0.4$), with ages between 0.1 Gyr and 0.55 Gyr. Ten stars rotate rapidly ($v \sin i > 10 \text{ km s}^{-1}$).

The main conclusions of our study are listed below.

- Photometric metallicity calibrations may show an age-metallicity degeneracy.
- Several stars show radial velocity variability, with an error on the *Gaia* DR2 radial velocity above 1 km s^{-1} and/or a *Gaia* DR2 radial velocity that differs by more than 5σ from our observed v_{rad} . Ten stars have also been identified as binary stars by [Kervella et al. \(2019\)](#) from proper motion anomalies. Stars HD 192045 and HD 213036 show radial velocity and proper motion variations. We therefore suggest that they are binary stars.
- The kinematic data indicate that all the stars are in prograde rotation around the Galactic centre on low-eccentricity orbits. This is typical of members of the thin-disc population.

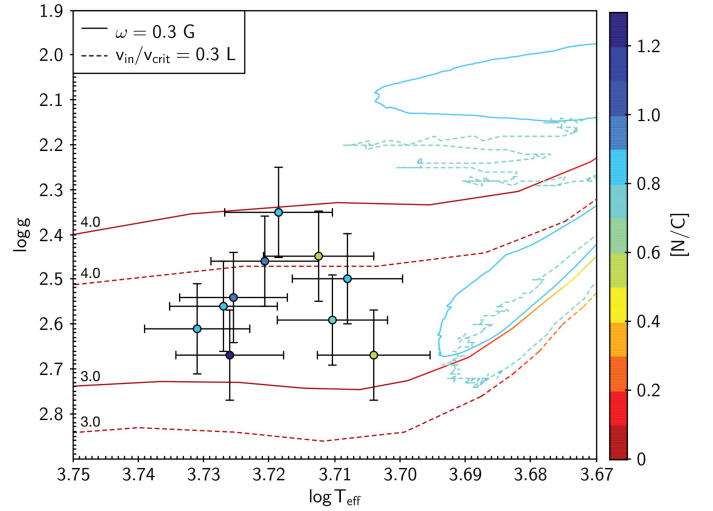


Fig. 12. Comparison between the [Georgy et al. \(2013\)](#) (solid lines) and [Lagarde et al. \(2012\)](#) (dashed lines) evolutionary tracks with rotation at $Z = 0.014$ for $M = 3 M_{\odot}$, $4 M_{\odot}$. Stars in the sample with $M = 3.5 M_{\odot}$, $4 M_{\odot}$ and $-0.1 < [\text{Fe}/\text{H}] < 0.1$ are shown with error bars. The colour index indicates the $[\text{N}/\text{C}]$ abundance ratios.

- Stellar masses between $2.5 M_{\odot}$ and $6.0 M_{\odot}$ suggest that the sample is composed of evolved stars that were of A and B type when they were on the main sequence. This hypothesis is supported by the chemistry of the stars, which is similar to that of A- and B-type stars in other studies.
- The A-type stars include chemically peculiar stars (see the catalogue of [Ghazaryan et al. 2018](#), and references therein). None of the stars observed by us shows any of the typical signs of CP stars, but they are similar to the normal A stars studied by [Royer et al. \(2014\)](#). This suggests that chemical peculiarities are an atmospheric phenomenon that is erased when the stars evolve to the red giant phase.
- The derived $v \sin i$ agree with the theoretical values that have been predicted for these stars by two sets of stellar evolution models computed by the Geneva group with two different codes that include rotation effects in a similar way. This implies that the residual rotational velocity is the result of the secular expansion of the stellar radius in post-main-sequence evolution.
- The $[\text{C}/\text{Fe}]$ ratio is lower than solar and $[\text{N}/\text{Fe}]$ is higher than solar in all the stars except one. This suggests that the stars have undergone mixing and that the material shows the effects of CNO processing. This is in line with the predictions from stellar evolution models.
- The stars show a Ba enhancement but a low $[\text{s}/\text{Fe}]$ ratio. This makes them similar to mild Ba stars. This might be due to a microturbulence that is higher than what we have assumed.
- We did not robustly detect any correlation between chemical abundances and rotational velocities. Again, this is in line with theoretical predictions.

Acknowledgements. We are grateful to the anonymous referee whose report helped us to improve our paper. P.B. is grateful to Luca Casagrande for an interesting exchange on photometric metallicity calibrations. We gratefully acknowledge support from the French National Research Agency (ANR) funded project “Pristine” (ANR-18-CE31-0017). This work was partially supported by the EU COST Action CA16117 (ChETEC). C. C. acknowledges support from the Swiss National Science Foundation (Project 200020-192039 PI CC). G. M. has received funding from the European Research Council (ERC) under the European Union’s Horizon 2020 research and innovation programme

(grant agreement No 833925, project STAREX). This work has made use of data from the European Space Agency (ESA) mission *Gaia* (<https://www.cosmos.esa.int/gaia>), processed by the *Gaia* Data Processing and Analysis Consortium (DPAC, <https://www.cosmos.esa.int/web/gaia/dpac/consortium>). Funding for the DPAC has been provided by national institutions, in particular the institutions participating in the *Gaia* Multilateral Agreement.

References

- Adibekyan, V. Z., Sousa, S. G., Santos, N. C., et al. 2012, *A&A*, 545, A32
- Allen, D. M., & Barbuy, B. 2006, *A&A*, 454, 895
- Alvarez, R., & Plez, B. 1998, *A&A*, 330, 1109
- Antipova, L. I., Boyarchuk, A. A., Pakhomov, Y. V., et al. 2003, *Astron. Rep.*, 47, 648
- Arenou, F., Luri, X., Babusiaux, C., et al. 2018, *A&A*, 616, A17
- Baratella, M., D’Orazi, V., Sheminova, V., et al. 2021, *A&A*, 653, A67
- Battistini, C., & Bensby, T. 2016, *A&A*, 586, A49
- Bensby, T., Feltzing, S., & Oey, M. S. 2014, *A&A*, 562, A71
- Bergemann, M., Lind, K., Collet, R., et al. 2012, *MNRAS*, 427, 27
- Bidelman, W. P., & Keenan, P. C. 1951, *ApJ*, 114, 473
- Bonifacio, P., & Caffau, E. 2003, *A&A*, 399, 1183
- Bouchy, F., & Sophie Team 2006, *Tenth Anniversary of 51 Peg-b: Status of and prospects for hot Jupiter studies*, 319
- Bressan, A., Marigo, P., Girardi, L., et al. 2012, *MNRAS*, 427, 127
- Caffau, E., Ludwig, H.-G., Steffen, M., et al. 2011, *Sol. Phys.*, 268, 255
- Capitain, L., Lallement, R., Vergely, J. L., et al. 2017, *A&A*, 606, A65
- Casagrande, L., Silva Aguirre, V., Stello, D., et al. 2014, *ApJ*, 787, 110
- Charbonneau, P. 1995, *ApJS*, 101, 309
- Cosentino, R., Lovis, C., Pepe, F., et al. 2012, *Proc. SPIE*, 8446, 84461V
- Dalton, G., Trager, S., Abrams, D. C., et al. 2020, *Proc. SPIE*, 11447, 1144714
- de Castro, D. B., Pereira, C. B., Roig, F., et al. 2016, *MNRAS*, 459, 4299
- Decressin, T., Mathis, S., Palacios, A., et al. 2009, *A&A*, 495, 271
- Dehnen, W., & Binney, J. 1998, *MNRAS*, 294, 429
- Delgado Mena, E., Israelian, G., González Hernández, J. I., et al. 2010, *ApJ*, 725, 2349
- de Jong, R. S., Agertz, O., Berbel, A. A., et al. 2019, *Messenger*, 175, 3
- Donati, J.-F., Semel, M., Carter, B. D., et al. 1997, *MNRAS*, 291, 658
- Donati, J.-F., Catala, C., Landstreet, J. D., et al. 2006, *Sol. Polarization* 4, 358, 362
- Dutra-Ferreira, L., Pasquini, L., Smiljanic, R., et al. 2016, *A&A*, 585, A75
- Ecuivillon, A., Israelian, G., Santos, N. C., et al. 2004, *A&A*, 418, 703
- Eggen, O. J. 1972, *MNRAS*, 159, 403
- Ekström, S., Georgy, C., Eggenberger, P., et al. 2012, *A&A*, 537, A146
- ESA 1997, *ESA SP*, 1200
- Fitzpatrick, E. L., Massa, D., Gordon, K. D., et al. 2019, *ApJ*, 886, 108
- Franchini, M., Morossi, C., Di Marcantonio, P., et al. 2020, *ApJ*, 888, 55
- Gaia Collaboration (Prusti, T., et al.) 2016, *A&A*, 595, A1
- Gaia Collaboration (Brown, A. G. A., et al.) 2018, *A&A*, 616, A1
- Gaia Collaboration (Brown, A. G. A., et al.) 2021, *A&A*, 649, A1
- Genovali, K., Lemasle, B., Bono, G., et al. 2014, *A&A*, 566, A37
- Genovali, K., Lemasle, B., da Silva, R., et al. 2015, *A&A*, 580, A17
- Georgy, C., Ekström, S., Granada, A., et al. 2013, *A&A*, 553, A24
- Georgy, C., Granada, A., Ekström, S., et al. 2014, *A&A*, 566, A21
- Ghazaryan, S., Alecian, G., & Hakobyan, A. A. 2018, *MNRAS*, 480, 2953
- Hyland, A. R., & Mould, J. R. 1974, *ApJ*, 187, 277
- Kervella, P., Arenou, F., Mignard, F., et al. 2019, *A&A*, 623, A72
- Korotin, S. A., Andrievsky, S. M., Hansen, C. J., et al. 2015, *A&A*, 581, A70
- Kurucz, R. L. 2005, *Mem. Soc. Astron. It. Suppl.*, 8, 14
- Lagarde, N., Decressin, T., Charbonnel, C., et al. 2012, *A&A*, 543, A108
- Lemasle, B., François, P., Bono, G., et al. 2007, *A&A*, 467, 283
- Lemasle, B., François, P., Piersimoni, A., et al. 2008, *A&A*, 490, 613
- Lemasle, B., François, P., Genovali, K., et al. 2013, *A&A*, 558, A31
- Liang, Y. C., Zhao, G., Chen, Y. Q., et al. 2003, *A&A*, 397, 257
- Lodders, K., Palme, H., & Gail, H.-P. 2009, *Landolt Börnstein*, 4B, 712
- Mason, B. D., Wycoff, G. L., Hartkopf, W. I., et al. 2001, *AJ*, 122, 3466
- Mayor, M., Pepe, F., Queloz, D., et al. 2003, *Messenger*, 114, 20
- McMillan, P. J. 2017, *MNRAS*, 465, 76
- Mowlavi, N., & Forestini, M. 1994, *A&A*, 282, 843
- Morgan, W. W., & Keenan, P. C. 1973, *ARA&A*, 11, 29
- Mucciarelli, A., & Bellazzini, M. 2020, *Res. Notes Am. Astron. Soc.*, 4, 52
- Mucciarelli, A., & Bonifacio, P. 2020, *A&A*, 640, A87
- Mucciarelli, A., Pancino, E., Lovisi, L., et al. 2013, *ApJ*, 766, 78
- Mucciarelli, A., Bellazzini, M., & Massari, D. 2021, *A&A*, 653, A90
- Muller, P. 1984, *A&AS*, 57, 467
- Palacios, A., Talon, S., Charbonnel, C., et al. 2003, *A&A*, 399, 603
- Palacios, A., Charbonnel, C., Talon, S., et al. 2006, *A&A*, 453, 261
- Paunzen, E. 2015, *A&A*, 580, A23
- Pereira, C. B., Sales Silva, J. V., Chavero, C., et al. 2011, *A&A*, 533, A51
- Plez, B. 2012, *Turbospectrum : Code for spectral synthesis* (Astrophysics Source Code Library), 1205, 4
- Richer, J., Michaud, G., & Turcotte, S. 2000, *ApJ*, 529, 338
- Romano, D., Magrini, L., Randich, S., et al. 2021, *A&A*, 653, A72
- Royer, F., Gebran, M., Monier, R., et al. 2014, *A&A*, 562, A84
- Sartoretti, P., Katz, D., Cropper, M., et al. 2018, *A&A*, 616, A6
- Sbordone, L., Bonifacio, P., Castelli, F., et al. 2004, *Mem. Soc. Astron. It. Suppl.*, 5, 93
- Siess, L., Dufour, E., & Forestini, M. 2000, *A&A*, 358, 593
- Smiljanic, R., Porto de Mello, G. F., & da Silva, L. 2007, *A&A*, 468, 679
- Snedden, C., Lambert, D. L., & Pilachowski, C. A. 1981, *ApJ*, 247, 1052
- Takeda, Y., Kawanomoto, S., Ohishi, N., et al. 2018, *PASJ*, 70, 91
- Talon, S., Richard, O., & Michaud, G. 2006, *ApJ*, 645, 634

Appendix A: Chemical abundances**Table A.1.** Elemental abundances of C, N, O with errors.

Star	A(C) dex	σ	[C/Fe] dex	A(N) dex	σ	[N/Fe] dex	A(O) dex	σ	[O/Fe] dex
HD 192045	7.90	0.30	-0.49	8.31	0.40	0.56	8.72	0.12	0.23
HD 191066	8.10	0.40	-0.48	8.51	0.40	0.57	8.85	0.12	0.27
HD 205732	8.20	0.30	-0.39	8.52	0.40	0.57	8.72	0.10	0.18
HD 213036	8.20	0.30	-0.37	8.40	0.50	0.47			
HD 217089	8.00	0.20	-0.42	8.25	0.25	0.47	8.72	0.10	0.01
HD 9637	8.20	0.20	-0.51	8.33	0.40	0.26			
HD 21269	7.80	0.20	-0.75						
HD 19267	7.95	0.20	-0.47	8.18	0.40	0.40	8.71	0.09	-0.26
HD 13882	8.15	0.20	-0.31	8.01	0.40	0.19			
HD 189879	8.00	0.50	-0.51	8.45	0.50	0.58	8.78	0.07	0.04
HD 195375	7.55	0.20	-0.69	8.22	0.40	0.62	8.53	0.11	-0.33
HD 221232	8.00	0.20	-0.50	8.34	0.40	0.48			
HD 219925	8.00	0.30	-0.40	8.31	0.40	0.55	8.72	0.10	0.30
HD 278	8.10	0.30	-0.46	8.23	0.60	0.31			
HD 11519	8.15	0.20	-0.39	8.33	0.40	0.43	8.78	0.08	-0.02
TYC 2813-1979-1	8.30	0.20	-0.28	8.22	0.40	0.28	9.06	0.08	0.22
BD+42 3220	8.80	0.30	-0.10	8.37	0.40	0.11	8.91	0.21	-0.26
BD+44 3114	8.80	0.30	-0.07	8.51	0.40	0.28			
TYC 3136-878-1	8.20	0.30	-0.24	7.98	0.40	0.18	8.76	0.12	0.07
HD 40509	8.15	0.30	-0.47						
HD 41710	8.00	0.20	-0.48	8.33	0.40	0.49	8.71	0.07	-0.22
HD 40655	7.80	0.20	-0.35	8.14	0.40	0.63	8.51	0.09	-0.12
HD 45879	7.25	0.20	-0.89	7.34	0.40	-0.16	8.45	0.07	-0.38
HD 55077	7.50	0.20	-0.58	7.77	0.60	0.33			
HD 61107	8.05	0.20	-0.50	8.26	0.60	0.35			
HD 63856	8.00	0.30	-0.45	8.58	0.40	0.77	8.78	0.10	0.34

Table A.2. Elemental abundances of Mg, Al, and Ca with errors.

Star	A(Mg) dex	σ	[Mg/Fe] dex	A(Al) dex	σ	[Al/Fe] dex	A(Ca) dex	σ	[Ca/Fe] dex
HD 192045	7.71	0.09	0.28	6.52	0.01	0.16	6.24	0.10	0.01
HD 191066	7.79	0.09	0.16	6.66	0.01	0.10	6.43	0.02	0.02
HD 205732	7.93	0.10	0.30	6.72	0.07	0.15	6.48	0.15	0.05
HD 213036	7.63	0.08	0.02	6.48	0.06	-0.05	6.37	0.10	-0.02
HD 217089	7.57	0.07	0.11	6.38	0.01	-0.01	6.29	0.06	0.04
HD 9637	7.52	0.07	-0.22	6.50	0.01	-0.17	6.57	0.09	0.04
HD 21269	7.70	0.36	0.11	6.22	0.11	-0.30	5.91	0.26	-0.47
HD 19267	7.57	0.08	0.12	6.35	0.06	-0.04	6.34	0.01	0.09
HD 13882	7.60	0.08	0.10	6.30	0.06	-0.13	6.34	0.04	0.05
HD 189879	7.69	0.09	0.14	6.56	0.07	0.08	6.38	0.15	0.03
HD 195375	7.50	0.07	0.21	6.36	0.06	0.15	6.15	0.16	0.08
HD 221232	7.56	0.07	0.02	6.41	0.06	-0.06	6.42	0.06	0.09
HD 219925	7.71	0.09	0.27	6.43	0.06	0.07	6.27	0.10	0.05
HD 278	7.32	0.22	-0.28	7.08	0.24	0.55	6.46	0.04	0.07
HD 11519	7.65	0.08	0.07	6.39	0.06	-0.12	6.37	0.08	0.00
TYC 2813-1979-1	7.80	0.10	0.18	6.37	0.06	-0.18	6.57	0.08	0.16
BD+42 3220	7.94	0.01	0.00	6.74	0.06	-0.13	6.66	0.14	-0.07
BD+44 3114	8.04	0.09	0.12	6.74	0.10	-0.11	6.63	0.10	-0.08
TYC 3136-878-1	7.70	0.01	0.22	6.43	0.09	0.02	6.34	0.05	0.08
HD 40509	7.41	0.24	-0.25	6.80	0.15	0.22	6.51	0.06	0.07
HD 41710	7.80	0.19	0.29	6.31	0.05	-0.13	6.48	0.16	0.17
HD 40655	7.20	0.14	0.01	6.21	0.05	0.10	6.09	0.13	0.11
HD 45879	7.23	0.16	0.05	6.05	0.03	-0.07	6.27	0.07	0.29
HD 55077	7.46	0.16	0.34	6.28	0.11	0.23	6.32	0.03	0.41
HD 61107	7.60	0.17	0.01	6.50	0.10	-0.02	6.60	0.08	0.22
HD 63856	7.70	0.01	0.20	6.56	0.07	0.14	6.33	0.06	0.05

Table A.3. Elemental abundances of the n-capture elements Sr, Y, Ba, La, Ce, Pr, Nd, Sm, and Eu.

















Star	[Sr/Fe] dex	[Y/Fe] dex	[Ba/Fe] dex	[La/Fe] dex	[Ce/Fe] dex	[Pr/Fe] dex	[Nd/Fe] dex	[Sm/Fe] dex	[Eu/Fe] dex	[s/Fe] dex
HD 192045		0.07	0.40	0.34	0.12	-0.37	0.43	0.27	0.25	0.23
HD 191066	0.16	0.22	0.61	0.34	0.22	-0.36	0.38	0.38	0.31	0.29
HD 205732	0.20	0.11	0.35	0.28	0.26		0.32	0.27	0.40	0.24
HD 213036		0.18	0.82	0.25	0.18	-0.38	0.24	0.19	0.32	0.21
HD 217089	0.03	-0.01	0.68	0.01	0.04	-0.68	0.05	0.00	0.08	0.02
HD 9637	-0.11	-0.20	0.54	-0.08	-0.05		-0.14		0.04	-0.12
HD 21269	0.04	0.25	1.79	-0.18	0.15		0.01		0.09	0.06
HD 19267	-0.22	-0.32	0.42	-0.30	-0.27	-1.23	-0.16	-0.21	-0.12	-0.26
HD 13882	-0.16	-0.15	0.59	-0.28	-0.25	-1.26	-0.14	-0.24	-0.11	-0.21
HD 189879		-0.09	0.55	0.03	-0.04	-0.77	0.02	-0.03	0.05	-0.02
HD 195375	-0.22	-0.31	0.43	-0.29	-0.26	-1.12	-0.20	-0.30	-0.12	-0.26
HD 221232	-0.07	-0.26	0.78	-0.24	-0.16		-0.15	-0.25	-0.12	-0.20
HD 219925	0.43	0.19	0.68	0.26	0.24	-0.18	0.35	0.30	0.38	0.26
HD 278	-0.27	-0.01	0.48	0.06	-0.06		0.00		0.03	0.00
HD 11519	0.14	-0.05	0.69	-0.08	-0.15	-0.94	0.01	0.01	-0.06	-0.07
TYC 2813-1979-1	0.00	0.01	0.55	0.03	-0.04	-0.87	0.12	0.22	0.01	0.03
BD+42 3220	-0.03	0.03	0.02	-0.25	-0.42	-1.58	-0.21	0.09	-0.08	-0.21
BD+44 3114	-0.10	0.01	0.20	-0.22	-0.59	-1.73	-0.13	0.12	0.00	-0.23
TYC 3136-878-1	0.05	0.11	0.40	0.08	-0.04	-0.73	0.22	0.27	0.10	0.09
HD 40509	-0.14	-0.18	0.71	-0.31	-0.43		-0.27		-0.24	-0.30
HD 41710	0.11	0.02	1.46	-0.11	-0.08	-1.01	0.08	-0.22	-0.04	-0.02
HD 40655	0.11	-0.18	1.06	-0.21	-0.13	-0.76	-0.07	-0.27	0.01	-0.15
HD 45879	-0.19	-0.08	1.46	-0.31	-0.08		-0.12	-0.27	-0.19	-0.15
HD 55077	0.03	-0.21	0.88	0.01	0.04		0.00		0.13	-0.04
HD 61107	-0.19	-0.18	0.86	-0.11	-0.18		-0.02		-0.04	-0.12
HD 63856	0.10	0.36	0.55	0.38	0.31	-0.14	0.47	0.21	0.40	0.38

Table A.4. Estimated errors in element abundance ratios [X/Fe] for neutron-capture elements for the star HD 13882.

[X/Fe]	$\Delta T_{\text{eff}} =$ 100 K	$\Delta \log g =$ 0.5 dex	$\Delta \xi =$ 0.5 km s ⁻¹
Sr	0.10	0.15	-0.25
Y	0.10	0.10	-0.25
La	0.10	0.20	-0.10
Ce	0.05	0.05	-0.07
Pr	0.05	0.15	-0.05
Nd	0.15	0.20	-0.05
Sm	0.05	0.20	-0.08
Ba	0.20	0.25	-0.10
Eu	0.05	0.20	-0.05

MINCE

I. Presentation of the project and of the first year sample^{★,★★}

G. Cescutti^{1,2,3}, P. Bonifacio⁴, E. Caffau⁴, L. Monaco⁵, M. Franchini², L. Lombardo⁴, A. M. Matas Pinto⁴,
F. Lucertini^{5,6}, P. François^{4,7}, E. Spitoni^{8,9}, R. Lallement⁴, L. Sbordone⁶, A. Mucciarelli^{10,11}, M. Spite⁴,
C. J. Hansen¹², P. Di Marcantonio², A. Kučinskas¹³, V. Dobrovolskas¹³, A. J. Korn¹⁴, M. Valentini¹⁵,
L. Magrini¹⁶, S. Cristallo^{17,18}, and F. Matteucci^{1,2,3}

(Affiliations can be found after the references)

Received 15 July 2022 / Accepted 17 October 2022

ABSTRACT

Context. In recent years, Galactic archaeology has become a particularly vibrant field of astronomy, with its main focus set on the oldest stars of our Galaxy. In most cases, these stars have been identified as the most metal-poor. However, the struggle to find these ancient fossils has produced an important bias in the observations – in particular, the intermediate metal-poor stars ($-2.5 < [\text{Fe}/\text{H}] < -1.5$) have been frequently overlooked. The missing information has consequences for the precise study of the chemical enrichment of our Galaxy, in particular for what concerns neutron capture elements and it will be only partially covered by future multi object spectroscopic surveys such as WEAVE and 4MOST.

Aims. Measuring at Intermediate Metallicity Neutron Capture Elements (MINCE) is gathering the first high-quality spectra (high signal-to-noise ratio, S/N, and high resolution) for several hundreds of bright and metal-poor stars, mainly located in our Galactic halo.

Methods. We compiled our selection mainly on the basis of *Gaia* data and determined the stellar atmospheres of our sample and the chemical abundances of each star.

Results. In this paper, we present the first sample of 59 spectra of 46 stars. We measured the radial velocities and computed the Galactic orbits for all stars. We found that 8 stars belong to the thin disc, 15 to disrupted satellites, and the remaining cannot be associated to the mentioned structures, and we call them halo stars. For 33 of these stars, we provide abundances for the elements up to zinc. We also show the chemical evolution results for eleven chemical elements, based on recent models.

Conclusions. Our observational strategy of using multiple telescopes and spectrographs to acquire high S/N and high-resolution spectra for intermediate-metallicity stars has proven to be very efficient, since the present sample was acquired over only about one year of observations. Finally, our target selection strategy, after an initial adjustment, proved satisfactory for our purposes.

Key words. Galaxy: evolution – Galaxy: formation – Galaxy: halo – stars: abundances – stars: atmospheres – nuclear reactions, nucleosynthesis, abundances

1. Introduction

The project titled Measuring at Intermediate metallicity Neutron-Capture Elements (MINCE) is aimed at gathering abundances for neutron-capture elements for several hundreds stars at intermediate metallicity using different facilities worldwide. The main idea is to study the nucleosynthetic signatures that can be found in old stars, in particular, among the specific class of chemical elements with $Z > 30$, that is, the neutron-capture elements. They are mainly formed through multiple neutron captures and not through the fusion reaction that create the vast majority of elements up to the iron peak. The neutron-capture process is split in the rapid process (r-process) or slow process (s-process) depending on whether the timescale for neutron capture is faster or slower than radioactive beta decay, according to the initial definition by Burbidge et al. (1957). These elements have complex nucleosynthesis and they are not yet deeply

investigated as, such as α -elements. Recent investigations expanded the number of stars with detailed chemistry at extremely low metallicity up to approximately a thousand objects (e.g. Roederer et al. 2014; Yong et al. 2014). After this incredible effort in searching and measuring the most extreme metal-poor stars (which is still ongoing), it is natural to think that adding valuable knowledge in this field can be difficult or extremely expensive, especially in terms of observing time. However, the search for the lowest possible metallicity almost completely ignored all the stars in the intermediate range of metallicity between the very metal-poor stars ($[\text{Fe}/\text{H}] < -2.5$) and thin or thick disc stars ($[\text{Fe}/\text{H}] > -1.5$). In this region, the number of stars with any measurements of the neutron-capture elements is small, only 25% (332 objects) according to the sample gathered by the JINA database (1213) and less than 10% (103) with Eu measurements. According to the metallicity distribution function of the Galactic halo (Bonifacio et al. 2021) there are more halo stars in this region, by a factor of 12, than at lower metallicity; therefore, an enormous number of halo stars are yet unexplored as far as the abundances of neutron-capture elements are concerned.

That apart, the more general target of a complete census of the Galactic halo stars, several scientific questions can be

* Full Tables B.1, C.1–C.3 are only available at the CDS via anonymous ftp to cdsarc.cds.unistra.fr (130.79.128.5) or via <https://cdsarc.cds.unistra.fr/viz-bin/cat/J/A+A/668/A168>

** Based on observations made with HARPS-N at TNG, FIES at NOT, Sophie at OHP and ESPaDOnS at CFHT.

addressed thanks to new abundance measurements of neutron capture elements. It will be possible to study how the spread in the *n*-capture elements shrinks. The spread is produced by stochastic process driven by the rarity of the *r*-process events (Argast et al. 2004; Cescutti et al. 2008), but the way this dispersion shrinks at higher metallicity constrains the rate of the *r*-process events in the Galactic halo (Cavallo et al. 2021). Hidden in this region, we could find also signatures of different types of *r*-process(es) that can have polluted the interstellar medium at different timescales. This could be the case if both neutron star mergers and magneto rotational driven SNe have contributed to the present amount of *r*-process material (Cescutti et al. 2015; Côté et al. 2018; Simonetti et al. 2019). Moreover, considering the possibility that a large fraction of the Galactic halo originally evolved in a massive satellite (Haywood et al. 2018; Vincenzo et al. 2019; Cescutti et al. 2020), we also expect that the production of *s*-process elements by AGB stars has left a signature in the chemical abundances at this intermediate metallicity.

In this initial paper, we present a first sample of 59 stellar spectra (46 unique stars). We present the atmospheric parameters measured for 41 of them, while 5 stars show an initial estimate of $T_{\text{eff}} < 4000$ K and this temperature is outside the parameter space where we believe our stellar atmosphere models are fully reliable, so we prefer to exclude them. We perform the detailed abundances determinations only of 33 stars, with 8 stars being too metal-rich for MINCE goals. The spectra of these stars were taken at four different facilities thanks to four accepted proposals and it clearly shows the joint efforts of the MINCE team. Two stars, BD+07 4625 and BD+25 4520, have spectra taken from two different facilities; we decided to carry out the determination of the stellar atmospheres and chemical abundances two times independently, to check the consistency of our method.

We also introduce how we have selected our MINCE stars and the issues that we have found in the search of an optimal selection of bright halo stars for our telescopes. Finally, we describe the approach we intend to assume for all the MINCE stars to determine the atmospheric parameters of the stars. For this first sample, the results of the chemical abundances cover the elements up to zinc. The actual measurement of the heavy neutron capture elements will be tackled in the next MINCE paper. We also investigated the kinematics of the stars in our sample making use of the *Gaia* astrometric parameters and the radial velocities (RV) we measured. All the results obtained and published by MINCE project will produce a catalogue of high-quality spectra with precise atmospheric parameters and chemical abundances constructed by combining observations from several facilities.

2. Survey description

The concept for the survey was initiated in February 2019, thanks to a discussion between two of the authors (GC and PB) of this manuscript. The idea was (and still is) to fill an existing statistical gap in the stellar abundance with regard to neutron capture elements (but not exclusively) in the region between $-2.5 < [\text{Fe}/\text{H}] < -1.5$.

The organisation of the survey is not standard: we decided to avoid intensive applications for hundreds of stars within a single facility (or up to a few). It is a diffuse plan that allows us to use several different facilities, thanks to the large collaboration. At present, we have obtained data from more than ten facilities and possibly more will be included. We try to exploit at best the time of national infrastructures too, infrastructures at the top level in terms of resolution and quality of the spectrographs, but not

with the widest collecting areas (although we did apply also for ESO-VLT time). For these reasons, our targets were selected to be bright (most of them have $G < 11$), with the aim attaining a high signal-to-noise ratio (S/N). The principal investigator (PI) of the single proposal within MINCE is not always the same person, but they typically vary from one facility to the other (and from one semester to the other). We also decided to select K giant stars because they are cooler than turn-off stars and the lines are stronger (see e.g. Cayrel et al. 2001). We could have also used K dwarfs, that have the same effective temperatures as K giants, however, there are two further advantages of using K giants over K dwarfs: (i) the lines of ionised species, that is, the vast majority of the lines of *n*-capture elements, are stronger in giants than dwarfs; (ii) the K dwarfs are intrinsically faint, thus the survey volume is much smaller than when using giants – this would make it much more difficult to find bright metal-poor K dwarfs than it is to find bright metal-poor K giants.

The original concept was to obtain around 1000 stars in 5 yr. We obtained around 400 stellar spectra (see Table 1) in the first 2 yr of submissions, which perfectly matched our timetable. However, we have decided to slow down our proposal submissions to dedicate more time for the analysis of our data and the delivery of our results. We note that we plan to start submitting a subsequent proposal six months from now and we will most likely postpone the end of the survey.

Surely, present surveys such as WEAVE (Balcels et al. 2010) and 4MOST (de Jong et al. 2012) will produce spectra for these stars (although some of the MINCE stars may be too bright) in this range of metallicity. Still, the wavelength range of the high resolution surveys for these instruments is limited and will not deliver all the elements that we intend to provide as part of the MINCE project. We feel that MINCE can be seen as complementary to this huge surveys, while certainly considering the completely different means involved.

3. Target selection

The stellar candidates were selected to be metal-poor ($[\text{M}/\text{H}] < -0.7$) and bright ($V < 10$) giants ($T_{\text{eff}} < 5000$ K) based on Starhorse (Anders et al. 2019). We named this method ‘mince1’. Starhorse combines the precise parallaxes and optical photometry delivered by *Gaia*’s second data release with the photometric catalogues of Pan-STARRS1, 2MASS, and AllWISE and derived Bayesian stellar parameters, distances, and extinctions for 137 million stars. After the first night at the Telescopio Nazionale *Galileo* (TNG, details of the facility are given in Sect. 4.1) covering eight candidates, we found that the selection provided cool giant stars (see Fig. 1), but not the requested metallicity range: the candidates were too metal-rich ($-0.6 < [\text{Fe}/\text{H}] < 0$) for the MINCE goals. For this reason, we decide to add a constrain on the kinematics of the stars ($v_{\text{tot}} > 200$ km s⁻¹) to select halo stars, exploiting the precise measurements of *Gaia*. This selection scheme improved the success rate to 100%: all the stars present $[\text{Fe}/\text{H}] < -1.4$. We named this method ‘mince2’. The eight stars mentioned above are not fully considered here, given their metallicities are above the threshold we set for MINCE, and we present only their atmospheric parameters; the analysis of their chemical abundances will be carried out in a forthcoming paper devoted to more metal rich stars compared to MINCE limits. The sample comprises relative bright objects and we set the observations to approximately reach $S/N \sim 100$ at 500 nm. We also include two stars that were actually selected from the Apache Point Observatory Galactic Evolution Experiment (APOGEE) survey

Table 1. Awarded time in September 2022 by the MINCE project.

Telescope	Instrument	Time	Targets	Status
A40-41 TNG	HARPS-N	21 h	31	Observed
A42 TNG	HARPS-N	1n	12	Observed
A43 TNG	HARPS-N	1n	16	Observed
CFHT 2019B+20A	ESPaDOnS	30 h	12	Observed
CFHT 2020B	ESPaDOnS	24.5 h	6	Observed
OHP 2019B+20A	Sophie	6n	42	Observed
TBL 2020A	NeoNArval	13 h	12	Observed (reduction problematic)
2019B 2.2m	FEROS	4n	65(72)	Observed (2n cancelled)
2020B 2.2m	FEROS	2n	65	Observed
Magellan	MIKE	2n	14 (20)	Observed (1 night cancelled)
VL ESO period 105-107	UVES	50 h	50	Observed
VL ESO period 106	UVES	50 h	50	Observed
period 61, NOT	FIES	3n	16	Observed
period 62, NOT	FIES	8h	8	Observed
ChETEC-INFRA 1, NOT	FIES	3n	0 (16)	Not taken due to eruption
ChETEC-INFRA 3, NOT	FIES	3n	5 (16)	Bad seeing, success rate 30%
ChETEC-INFRA 5, NOT	FIES	3n	16	To be taken in Oct-Dec 2022
Moletai 1.65 m	VUES	38n	24	Observed

Notes. The column “targets” list the number of target observed; between brackets the requested number, when the observation was not fully successful.

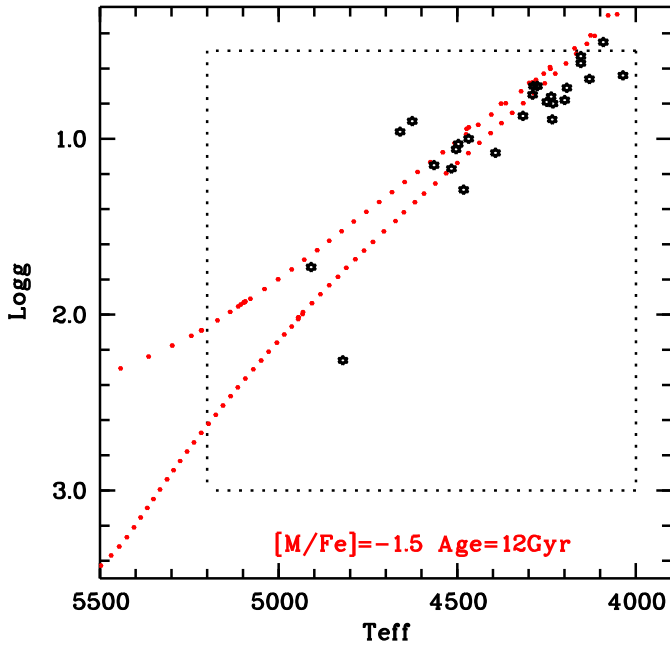


Fig. 1. T_{eff} , $\log g$ plot with the observed stars here analysed (black open stars) and a PARSEC (Bressan et al. 2012; Marigo et al. 2017) isochrone of 10 Gyr and metallicity -1.5 (red dots). The dotted lines delimit the grid used by MyGIsFOS in the chemical analysis.

(Eisenstein et al. 2011). With a higher resolution and different spectral coverage, MINCE can provide different elements and also a comparison with the results obtained by APOGEE in the infrared.

4. Observations and data reduction

As mentioned in the introduction, this sample comprises spectra taken from several facilities and obtained thanks to a total

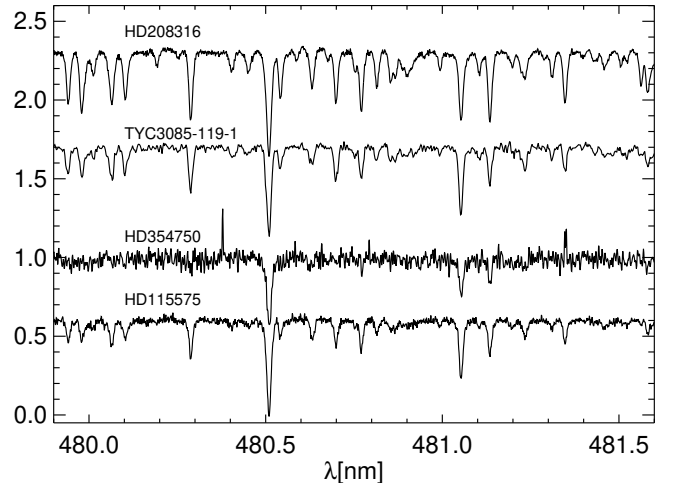


Fig. 2. Example of the spectra acquired to give an idea of the quality. The spectral region around the Zn I 481.0 nm line. The normalised spectra have been shifted vertically for display purposes.

of four proposals with three different PIs: Cescutti for HARPS-north at TNG, E. Spitoni for FIES at NOT and P. Bonifacio for Sophie at OHP, and ESPaDOnS at CFHT. Details on the observations are provided in Tables A.1 to A.4. An example of the spectra acquired is shown in Fig. 2, where two spectra have the desired S/N (~ 100 at 550 nm, the first two from the top); clearly, during an observational campaign not everything is perfect and indeed the other two spectra present a S/N lower, in particular, HD 354750 with a S/N ~ 50 .

4.1. TNG HARPS-N

The 3.58 m telescope TNG, is the Italian facility located at the Roque de Los Muchachos Observatory in the Canary island of La Palma. We used HARPS-N (Cosentino et al. 2012), which is

Table 2. Stellar parameters of the sample with extra information.

Star	T_{eff} (K)	$\log g$ (cgs)	ξ (km s^{-1})	(Fe/H)	Selection	Parallax (mas)	G (mag)	$G_{\text{BP}} - G_{\text{RP}}$ (mag)	teff50 (K)	logg50 (cgs)	vel_{tot} (km s^{-1})
TYC 4-369-1	4234	0.89	1.94	-1.84	mince2	0.216	10.78	1.49	4439	0.96	345.0
BD+04 18	4053	0.74	1.9	-1.48	mince2	0.293	9.19	1.6	4284	0.67	484.0
TYC 33-446-1	4289	0.75	2.07	-2.22	mince2	0.185	10.09	1.52	4323	0.69	280.0
TYC 2824-1963-1	4036	0.64	1.95	-1.6	mince2	0.185	10.06	1.69	4241	0.66	433.0
TYC 4331-136-1	4133	0.5	2.13	-2.53	mince2	0.513	9.53	2.11	4385	0.74	201.0
HD 87740	4746	1.89	1.62	-0.56	mince1	1.448	8.56	1.2	4838	1.96	45.0
BD+31 2143	4565	1.15	2.03	-2.37	mince2	0.595	8.87	1.3	4689	1.26	359.0
HD 91276	4610	1.73	1.63	-0.58	mince1	1.372	8.57	1.26	4802	1.83	60.0
BD+13 2383	4458	1.54	1.65	-0.56	mince1	1.319	8.54	1.35	4751	1.68	27.0
BD-07 3523	4193	0.71	2.02	-1.95	mince2	0.408	9.12	1.58	4410	0.83	249.0
HD 115575	4393	1.08	1.94	-1.99	mince2	0.694	9.02	1.45	4579	1.26	324.0
BD+48 2167	4468	1.0	2.04	-2.29	mince2	0.429	9.32	1.36	4498	1.09	255.0
BD+06 2880	4167	0.82	1.91	-1.45	mince2	0.616	9.18	1.53	4463	1.14	378.0
BD+32 2483	4516	1.17	1.99	-2.25	mince2	0.404	9.83	1.32	4473	1.3	259.0
HD 130971	4045	1.21	1.61	-0.64	mince1	1.247	8.6	1.68	4658	1.48	40.0
BD+24 2817	4722	1.89	1.56	0.02	mince1	1.61	8.54	1.3	4981	2.12	73.0
HD 238439	4154	0.53	2.1	-2.09	mince2	0.29	9.26	1.6	4533	0.96	415.0
HD 138934	4725	2.41	1.34	-0.19	mince1	2.296	8.01	1.26	4947	2.12	27.0
HD 139423	4287	0.7	2.05	-1.71	mince2	0.808	8.02	1.5	4369	0.92	431.0
HD 142614	4316	0.87	1.96	-1.46	mince2	0.668	8.73	1.45	4370	1.12	412.0
BD+11 2896	4254	1.07	1.83	-1.41	mince2	0.771	8.72	1.48	4243	1.21	286.0
BD+20 3298	4154	0.57	2.07	-1.95	mince2	0.476	8.77	1.64	4742	1.39	423.0
TYC 2588-1386-1	4130	0.66	1.99	-1.74	APOGEE	0.129	11.73	1.58	4319*	1.27*	289.0
TYC 3085-119-1	4820	2.26	1.56	-1.51	APOGEE	0.954	10.38	1.12	4745*	2.14*	122.0
BD+39 3309	4909	1.73	1.94	-2.58	mince2	0.704	9.6	1.1	4855	1.9	300.0
HD 165400	4942	1.68	1.79	-0.25	mince1	1.37	8.34	1.27	4825	1.78	23.0
TYC 1008-1200-1	4199	0.78	2.01	-2.23	mince2	0.226	10.19	1.74	4335	0.7	426.0
TYC 4221-640-1	4295	0.66	2.12	-2.27	mince2	0.188	10.59	1.55	4421	0.82	387.0
TYC 4584-784-1	4232	0.8	2.0	-2.04	mince2	0.192	10.62	1.59	4261	0.78	326.0
TYC 3944-698-1	4091	0.45	2.11	-2.18	mince2	0.225	9.9	1.81	4523	0.96	270.0
HD 354750	4626	0.9	2.17	-2.36	mince2	0.177	10.59	1.43	4426	0.94	235.0
BD-00 3963	4970	1.92	1.68	-0.13	mince1	1.68	8.54	1.3	4936	2.0	43.0
BD+07 4625 ^(a)	4757	1.64	1.86	-1.93	mince2	1.209	8.61	1.24	4877	1.79	570.0
BD+07 4625 ^(b)	4757	1.64	1.86	-1.95	mince2	1.209	8.61	1.24	4877	1.79	570.0
BD+25 4520 ^(b)	4276	0.7	2.08	-2.28	mince2	0.245	9.25	1.61	4386	0.72	445.0
BD+25 4520 ^(c)	4276	0.7	2.08	-2.27	mince2	0.245	9.25	1.61	4386	0.72	445.0
HD 208316	4249	0.79	1.98	-1.61	mince2	0.654	8.35	1.51	4390	0.9	315.0
TYC 4267-2023-1	4660	0.96	2.11	-1.74	mince2	0.62	9.5	1.84	4607	1.16	372.0
BD+21 4759	4503	1.06	2.05	-2.51	mince2	0.397	9.44	1.37	4565	1.15	266.0
BD+35 4847	4237	0.76	2.01	-1.92	mince2	0.644	8.46	1.61	4725	1.48	263.0
BD-00 4538	4482	1.29	1.88	-1.9	mince2	0.853	8.77	1.34	4607	1.41	320.0
TYC 4001-1161-1	4129	0.75	1.94	-1.62	mince2	0.42	10.09	1.87	4556	1.07	423.0
BD+03 4904	4497	1.03	2.06	-2.58	mince2	0.398	9.5	1.38	4528	1.1	307.0

Notes. ^(a)FIES spectrum. ^(b)SOPHIE spectrum. ^(c)HARPS-N spectrum. For the column labeled ‘selection’, see Sect. 3; columns labeled parallax, G , and $G_{\text{BP}} - G_{\text{RP}}$ are from *Gaia* (DR2), teff50, and log50 are from the Starhorse database (excluding *, which is taken from the APOGEE survey); vel_{tot} was computed from *Gaia* (DR2) data considering proper motions, parallax, and radial velocity.

a high-resolution (resolving power $R = 115\,000$), high-stability visible (383–693 nm) spectrograph. Long-term stability allows an accuracy better than $<1\text{ m s}^{-1}$ in the radial velocity measurements and it is excellent for the discovery and characterisation of exoplanets, but it is also well suited for stellar abundance spectroscopy. The spectra were taken in service mode in two nights in May and June 2020. For the reduction of the echelle spectra, we used the standard pipeline. The radial velocities are determined by the pipeline through cross-correlation with a mask that is appropriate for the spectral type of the star.

4.2. NOT FIES

The Nordic Optical Telescope (NOT) is a 2.56-m telescope also located at the Spanish Roque de los Muchachos Observatory, about 1 km away from the TNG. We used FIES (Telting et al. 2014), a cross-dispersed high-resolution echelle spectrograph with a maximum spectral resolution of $R = 67\,000$. The entire spectral range 370–830 nm is covered without gaps in a single, fixed setting. Most of the spectra were taken in service mode during June 2020 (see Table A.2 for specific dates). Also

in this case, we used the output of the standard pipeline, which are available upon request. Radial velocities are not provided by the pipeline. They have been determined by template matching (see e.g. Kozlov et al. 2011) over the range between 400 nm to 660 nm. The template was a synthetic spectrum computed with the parameters provided in Table 2. The error provided in Table A.2 is just based on the χ^2 of the fit and does not take into account systematic errors. The systematic errors due to the fact that the calibration arc was taken several hours before the observation can be of the order of a few 100 m^{-1} (J. Telting, priv. comm.). The mid-exposure time was taken from the descriptor DATE-AVG in the FITS header of each observation. From this time, the Barycentric Julian Date (BJD) and the barycentric correction were computed using the tools OSU Online Astronomy Utilities¹ that implement the methods and algorithms described in Wright & Eastman (2014).

4.3. OHP 1.93 Sophie

The OHP 1.93 m telescope is located in at the Observatoire de Haute-Provence, in southern France. The spectra were obtained with the Sophie spectrograph (Bouchy & Sophie Team 2006) in high-resolution mode, providing a resolving power $R = 75\,000$ and a spectral range from 387.2 nm to 694.3 nm. The spectra were obtained in visitor mode, over three nights from August 24 to 26, 2020, and the observer was P. Bonifacio. The wavelength calibration relied both on a Th–Ar lamp and on a Fabry–Pérot etalon. The data were reduced automatically on-the-fly by the Sophie pipeline. In a similar way as for HARPS-N, the pipeline determines radial velocities from cross-correlation with a suitable mask.

4.4. CFHT ESPaDOnS

The 3.6 m Canada–France–Hawaii telescope (CFHT) is located on the summit of Mauna Kea, on the island of Hawaii, USA. The spectra were obtained with the fibre-fed spectropolarimeter ESPaDOnS (Donati et al. 2006). The observation were obtained in the queued service observation mode of CFHT in 2020. The spectroscopic mode “Star+Sky” was used, providing a resolving power of $R = 65\,000$ and the spectral range 370–1051 nm. The data was delivered to us reduced with the Upena² pipeline that uses the routines of the Libre-ESPRIT software (Donati et al. 1997). The output spectrum is provided in an order-by-order format, we merged the orders using an ESO-MIDAS³ with a script written by ourselves. The pipeline applies the barycentric correction to the reduced spectrum and provides the Heliocentric Julian Date (HJD), we transformed this to BJD using a specific tool⁴ that implements the methods and algorithms described in Wright & Eastman (2014). The pipeline corrects the wavelength scale using the telluric absorption lines and this should compensate for the difference in temperature and pressure between the time when the calibration arc was taken and the time of the observation. As for the FIES spectra we measured the radial velocities by template matching over the range 400 nm to 660 nm. We underline that the error provided in Table A.4 is based on the χ^2 of the fit, thus taking into account only the noise in the spectrum and not any systematic error. In spite of the fact that ESPaDOnS is

protected by two thermal enclosures, its temperature and pressure are not actively controlled, just as those of HARPS-N or Sophie. According to the documentation the expected precision using the telluric correction is 20 ms^{-1} . For star TYC 3085-119-1 we have two spectra, but although the radial velocity was measured for both, the chemical analysis was performed only on the second spectrum that has $S/N \sim 100$ at 500 nm against ~ 60 for the first spectrum. The improvement in S/N by coadding the two spectra would be marginal.

4.5. Radial velocities

Our measured radial velocities are generally in very good agreement with the *Gaia* DR3 radial velocities (Katz et al. 2022). However there are twenty spectra, with sixteen stars for which the difference between our measurement and *Gaia* DR3 exceeds 3σ , where σ is computed by adding under quadrature the errors associated to each measurement. In some cases, this is certainly due to real radial velocity variations and this may be because the star is in a binary system. In none of our spectra we detect a secondary spectrum of a companion, so if any of the stars is binary indeed, the companion must be much less luminous, implying a small veiling of the spectrum. This gives us confidence on our approach of analysing all stars as single stars.

The most clear case is TYC 4584-784-1 for which our Sophie radial velocity differ by 7.18 km s^{-1} from that of *Gaia* DR3. Also the error on the *Gaia* radial velocity is large for a star of this brightness, 2.34 km s^{-1} . Other very clear cases are TYC 4331-136-1, BD-07 3523, BD+24 2817, HD 139423, HD 354750, and TYC565-1564-1. A borderline case is that of TYC2824-1963-1 two Sophie spectra provide radial velocities that differ by just over 3σ from that of *Gaia*, which, however, has a an error of only 0.28 km s^{-1} .

A controversial case is put forth by BD+07 4625. For this star, we observed two spectra: with FIES and with Sophie. The Sophie radial velocity is at 4σ of the *Gaia* one, while the two FIES radial velocities are at 4. and 1.5σ from the *Gaia* one, which has a small error of 0.13 km s^{-1} . The FIES spectra were taken 55.75 days before the Sophie ones. It is also useful to consider that the standard deviation of the FIES and Sophie radial velocities is of 0.48 km s^{-1} and the mean is perfectly consistent with *Gaia*. Another suspicious case is BD+25 4520. This star has been observed with HARPS-N and 77 days later with Sophie. While the radial velocity derived from the Sophie agrees with the *Gaia* radial velocity to better than 1σ , with regard to the HARPS-N spectrum it differs by almost 2σ . It is interesting to note that the *Gaia* radial velocity has changed by about 1 km s^{-1} from DR2 to DR3, and that the *Gaia* error, 0.42 km s^{-1} , is very similar to the standard deviation of the two HARPS-N and SOPHIE measurements, 0.35 km s^{-1} . We suspect this star to be a radial velocity variable of low amplitude, possibly on the order of 1 km s^{-1} .

5. Analysis

5.1. Stellar parameters

The sample presented here is the first of a series and we expect to have many spectra to be analysed in the future (as explained in Sect. 3). We then need a way to analyze these stars that is as automated and objective as possible.

The stellar parameters were derived from the photometry and the parallax, by using the *Gaia* data release early three (*Gaia* EDR3). We first dereddened the *Gaia* photometry by using

¹ <https://astrutils.astronomy.osu.edu/>

² <http://www.cfht.hawaii.edu/Instruments/Upena/>

³ <https://www.eso.org/sci/software/esomidas/>

⁴ <https://astrutils.astronomy.osu.edu/time/utc2bjd.html>

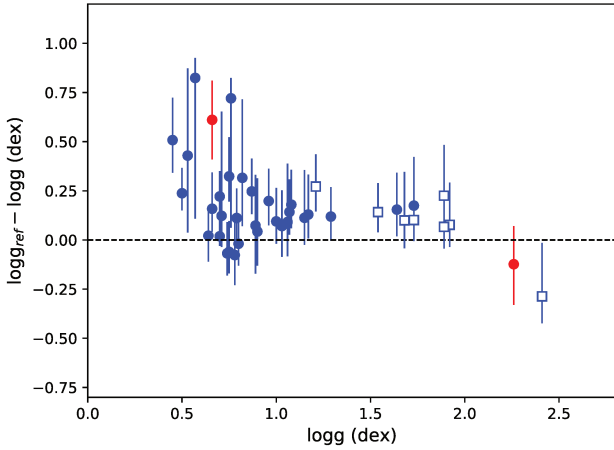


Fig. 3. Comparison of the $\log g$ obtained for our MINCE stars to the $\log g$ obtained by the reference databases. For most of the stars, the reference is [Anders et al. \(2019\)](#). They are shown in blue symbols: filled dots for stars selected with the mince2 selection, open squares for those selected with mince1. The error-bars considered are 84th and 16th percentile obtained from the Bayesian approach used in Starhorse. For two stars, shown in red, the reference database for the $\log g$ and its error is the APOGEE survey database.

the maps from [Schlafly & Finkbeiner \(2011\)](#) and by iterating the computation of the dereddening we took into account the stellar parameters. With the dereddened G magnitude, we derived the absolute G magnitude by applying the parallax, corrected for the zero point as suggested by [Lindegren et al. \(2021\)](#). The $G_{BP} - G_{RP}$ dereddened colour, the absolute G magnitude with a first guess metallicity have been compared to synthetic colours in order to derive the first guess stellar parameters.

This first guess of the stellar parameters are fed to MyGISFOS ([Sbordone et al. 2014](#)) to derive the metallicity. The metallicity derived by MyGISFOS was then used as input to derive new stellar parameters, from the photometry and parallax, as described above. MyGISFOS repeats this process until the changes in stellar parameters were less than 10 K in T_{eff} , and less than 0.05 dex in $\log g$. For the micro-turbulence, we used the calibration by [Mashonkina et al. \(2017\)](#) at any iteration and applied these values as the final choice. The stellar parameters and derived metallicity are reported in Table 2.

5.2. Comparison of the stellar parameters with Starhorse

The results obtained for the stellar parameters from our spectra can be compared to those obtained by Starhorse. This comparison can be important to evaluate the use of this database. In Fig. 3, we show the case of $\log g$ where a positive offset (0.16 dex) and a dispersion are visible, in particular, for $\log g < 1$, with a standard deviation of 0.20 dex. In Fig. 4, we present the case of T_{eff} . Again, there is a positive offset of 154 K, with a standard deviation of 176 K that is most prominent for $T_{\text{eff}} < 4300$ K. Overall, the Starhorse database concerning the metallicities is not good enough (as mentioned in Sect. 3), but it is certainly suitable for selecting giant stars. For this reason, in the future, we will also consider to use the values derived by Starhorse as first guess of the stellar parameters T_{eff} and $\log g$ applying suitable corrections inferred by the comparison with our results, omitting the procedure described above. In both figures, we present also the comparison to the measurements obtained by the APOGEE survey, although only for a sample of two stars. We cannot draw valid conclusions from only two objects, but clearly for the

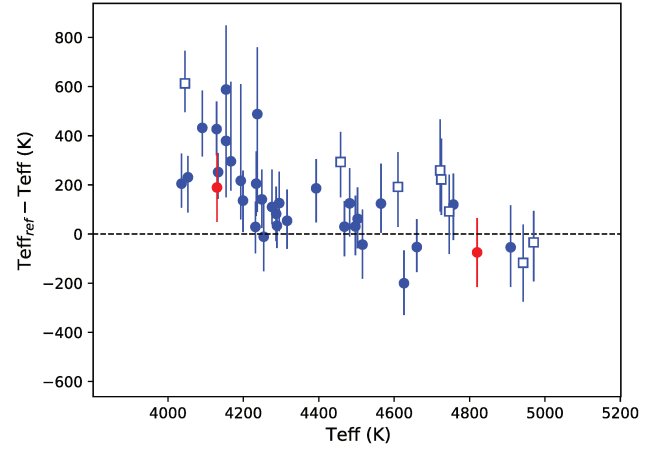


Fig. 4. Comparison of the T_{eff} obtained for our MINCE stars to the T_{eff} obtained by the reference databases. The details are the same as in Fig. 3.

cooler star the difference in $\log g$ is not negligible, although the T_{eff} shows only a moderate difference of ~ 200 K.

5.3. Kinematics

We investigated the kinematics of the stars in our sample making use of the *Gaia* EDR3 astrometric parameters and radial velocities (RV) we measured. In particular, for the RVs we adopted weighted means for stars having SOPHIE, HARPS-N, ESPADONS, and *Gaia* values. In the case of ESPADONS RVs, we adopted an error on the RV of 20 m s^{-1} . For stars having FIES and *Gaia* measures or with measures more than 3σ different from the *Gaia* values, we adopted the non-weighted means of the values available.

In order to evaluate kinematic quantities and the actions, we used the *galpy* code ([Bovy 2015](#)) together with the MWPotential14 potential and the solar motion of [Schönrich et al. \(2010\)](#). We adopted a solar distance from the Galactic Centre of 8 kpc and a circular velocity at the solar distance of 220 km s^{-1} ([Bovy et al. 2012](#)).

Following [Bonifacio et al. \(2021\)](#), we evaluated the corresponding errors using the *pyia* code. For each stars, we extracted 1000 instances of the input parameters (coordinates, proper motions, distance, and radial velocity) from a multivariate Gaussian, which takes into account the covariance matrix. Each instance is then fed to *galpy*. For each parameter calculated, we adopt as errors the standard deviations of the 1000 realisations. We notice that the quantities reported in Tables 3 and 4 are the value obtained from the input parameters taken at face value, only the reported errors are evaluated with the procedure described above.

In Fig. 5, we present our targets (black filled symbols) in four planes commonly used to characterise the stellar kinematic. For reference, we plot in gray in each panel the “good parallax” sample from [Bonifacio et al. \(2021\)](#). This is the sample of TO stars that have parallaxes of $\varpi > 3 \times \Delta\varpi$. It is useful as high-quality reference sample to see the Galactic dynamics in action space.

Considering Galactocentric cylindrical coordinates, in panel c) we present the component of the velocity in the plane of the Galaxy (V_T) versus a combination of the radial and vertical component of the velocity ($\sqrt{V_R^2 + V_Z^2}$), namely, a version of the Toomre diagram. In this plane, disc stars are visible as the roughly circular concentration of stars in the bottom-right

Table 3. Kinematic properties of the sample.

Star	V_R (km s ⁻¹)	V_T (km s ⁻¹)	V_Z (km s ⁻¹)	r_{ap} (kpc)	r_{peri} (kpc)	ecc.	Z_{max} (kpc)
TYC 4-369-1 ^(b)	194.02 ± 9.62	-5.07 ± 18.12	-86.58 ± 5.91	0.10 ± 0.26	16.10 ± 1.37	0.99 ± 0.03	5.88 ± 0.75
BD+04 18 ^(b)	190.95 ± 7.09	11.10 ± 9.07	-48.12 ± 3.20	0.20 ± 0.14	13.29 ± 0.53	0.97 ± 0.02	2.58 ± 0.20
TYC 33-446-1	-16.17 ± 1.51	45.68 ± 8.91	61.42 ± 1.57	1.42 ± 0.28	10.35 ± 0.13	0.76 ± 0.04	4.93 ± 0.20
TYC 2824-1963-1 ^(b)	185.87 ± 5.74	45.06 ± 11.94	-73.40 ± 3.13	1.08 ± 0.29	16.57 ± 0.65	0.88 ± 0.04	4.87 ± 0.60
TYC 4331-136-1	-4.74 ± 2.54	35.36 ± 4.54	83.62 ± 3.38	0.89 ± 0.11	9.81 ± 0.08	0.83 ± 0.02	4.53 ± 0.42
HD 87740 ^(c)	-62.00 ± 0.56	232.26 ± 0.21	-2.20 ± 0.12	7.20 ± 0.01	11.36 ± 0.02	0.22 ± 0.00	0.61 ± 0.01
BD+31 2143 ^(a)	-22.14 ± 0.69	-91.74 ± 6.53	28.40 ± 0.71	2.33 ± 0.22	8.90 ± 0.02	0.59 ± 0.03	1.74 ± 0.01
HD 91276 ^(c)	44.29 ± 0.63	238.94 ± 0.13	2.56 ± 0.37	7.79 ± 0.00	11.43 ± 0.05	0.19 ± 0.00	0.81 ± 0.01
BD+13 2383 ^(c)	1.91 ± 0.45	235.69 ± 0.07	-9.24 ± 0.15	8.19 ± 0.01	9.92 ± 0.02	0.10 ± 0.00	0.88 ± 0.02
BD-07 3523	98.45 ± 5.64	65.21 ± 4.10	46.18 ± 1.06	1.32 ± 0.10	8.64 ± 0.10	0.74 ± 0.02	2.22 ± 0.05
HD 115575 ^(a)	-41.75 ± 2.61	-100.62 ± 7.76	20.72 ± 4.20	2.20 ± 0.21	7.61 ± 0.03	0.55 ± 0.03	1.35 ± 0.03
BD+48 2167	-102.66 ± 2.48	32.19 ± 3.42	-11.10 ± 1.89	0.65 ± 0.07	9.42 ± 0.06	0.87 ± 0.01	2.18 ± 0.09
BD+06 2880	-349.70 ± 12.25	-13.19 ± 9.67	-165.05 ± 7.93	0.19 ± 0.12	49.77 ± 10.63	0.99 ± 0.00	21.83 ± 5.15
BD+32 2483	-84.34 ± 2.61	25.28 ± 5.70	61.27 ± 1.42	0.61 ± 0.14	8.36 ± 0.04	0.86 ± 0.03	4.74 ± 0.28
BD+41 2520	45.10 ± 0.65	63.42 ± 2.27	108.43 ± 1.17	1.68 ± 0.05	8.44 ± 0.02	0.67 ± 0.01	4.61 ± 0.11
HD 130971 ^(c)	-39.22 ± 0.22	197.81 ± 0.63	8.35 ± 0.30	5.71 ± 0.04	7.97 ± 0.02	0.16 ± 0.00	0.65 ± 0.01
BD+24 2817 ^(c)	54.91 ± 0.92	197.72 ± 0.60	-3.98 ± 1.57	5.73 ± 0.04	8.75 ± 0.01	0.21 ± 0.00	0.61 ± 0.01
HD 238439 ^(b)	191.91 ± 6.52	-50.25 ± 12.20	116.43 ± 6.96	1.10 ± 0.29	15.41 ± 1.16	0.87 ± 0.02	6.86 ± 0.76
HD 138934 ^(c)	-29.60 ± 0.27	232.14 ± 0.23	17.50 ± 0.13	7.49 ± 0.01	9.50 ± 0.01	0.12 ± 0.00	0.41 ± 0.00
HD 139423	-345.55 ± 6.84	-88.84 ± 10.14	76.66 ± 2.39	1.50 ± 0.15	36.97 ± 3.53	0.92 ± 0.00	17.66 ± 1.43
HD 142614 ^(b)	331.80 ± 2.36	-31.19 ± 4.77	-51.67 ± 4.14	0.47 ± 0.07	26.85 ± 0.47	0.97 ± 0.00	11.05 ± 0.12
HD 143348	54.52 ± 0.90	87.65 ± 3.21	38.02 ± 2.57	1.86 ± 0.08	8.02 ± 0.00	0.62 ± 0.01	1.19 ± 0.08
BD+11 2896	122.65 ± 0.52	0.32 ± 3.79	-87.24 ± 1.19	0.01 ± 0.04	8.62 ± 0.04	1.00 ± 0.01	4.32 ± 0.06
BD+20 3298 ^(b)	335.50 ± 5.25	-22.99 ± 5.07	98.30 ± 7.70	0.30 ± 0.07	30.87 ± 2.28	0.98 ± 0.00	7.04 ± 1.06
TYC 2588-1386-1	4.08 ± 12.41	-48.65 ± 3.54	-83.86 ± 6.18	1.96 ± 0.03	8.80 ± 0.39	0.64 ± 0.02	6.90 ± 0.07
TYC 3085-119-1	-22.21 ± 0.51	139.98 ± 0.09	-62.56 ± 0.12	3.71 ± 0.00	7.91 ± 0.00	0.36 ± 0.00	1.68 ± 0.01
BD+39 3309 ^(b)	207.09 ± 1.80	7.16 ± 0.90	-11.00 ± 1.30	0.11 ± 0.01	12.16 ± 0.10	0.98 ± 0.00	1.16 ± 0.01
HD 165400 ^(c)	-11.43 ± 0.11	217.20 ± 0.31	-4.44 ± 0.28	7.01 ± 0.03	7.64 ± 0.02	0.04 ± 0.00	0.21 ± 0.00
TYC 1008-1200-1 ^(b)	365.43 ± 3.42	-28.81 ± 4.85	-27.82 ± 3.16	0.33 ± 0.05	29.71 ± 0.60	0.98 ± 0.00	5.52 ± 0.19
TYC 2113-471-1	74.56 ± 2.29	-27.53 ± 1.28	-73.78 ± 1.30	0.48 ± 0.03	7.29 ± 0.05	0.88 ± 0.01	2.22 ± 0.06
TYC 4221-640-1 ^(b)	-195.33 ± 8.35	4.23 ± 4.92	81.33 ± 9.43	0.14 ± 0.54	15.33 ± 1.15	0.98 ± 0.05	13.93 ± 2.40
TYC 4584-784-1	-100.72 ± 2.88	-38.07 ± 3.71	-15.45 ± 4.24	0.86 ± 0.09	11.01 ± 0.14	0.85 ± 0.01	1.77 ± 0.08
TYC 3944-698-1	-83.95 ± 2.19	11.73 ± 1.87	-23.89 ± 1.16	0.22 ± 0.04	9.54 ± 0.10	0.95 ± 0.01	1.06 ± 0.01
HD 354750	240.06 ± 6.94	58.46 ± 6.18	41.90 ± 0.41	0.87 ± 0.10	12.61 ± 0.41	0.87 ± 0.02	2.51 ± 0.21
BD-00 3963 ^(c)	31.86 ± 0.17	205.68 ± 0.05	17.30 ± 0.06	6.25 ± 0.01	8.08 ± 0.00	0.13 ± 0.00	0.32 ± 0.00
BD+07 4625	-29.08 ± 3.55	-278.29 ± 1.54	248.46 ± 0.39	7.57 ± 0.02	40.41 ± 0.86	0.68 ± 0.01	24.78 ± 0.47
BD+25 4520	150.05 ± 6.23	178.22 ± 4.84	-223.04 ± 9.51	5.60 ± 0.06	23.87 ± 1.84	0.62 ± 0.03	16.57 ± 1.94
HD 208316	-58.60 ± 4.63	-58.91 ± 6.55	-12.86 ± 4.13	1.14 ± 0.15	7.77 ± 0.04	0.74 ± 0.03	1.10 ± 0.10
TYC 4267-2023-1 ^(a)	-25.68 ± 1.12	-132.41 ± 0.77	54.88 ± 1.39	3.56 ± 0.05	8.65 ± 0.01	0.42 ± 0.01	1.41 ± 0.05
TYC 565-1564-1 ^(b)	236.11 ± 10.06	-14.20 ± 12.56	-17.13 ± 8.83	0.24 ± 0.20	14.78 ± 1.21	0.97 ± 0.02	5.27 ± 0.58
BD+21 4759	-106.37 ± 3.16	33.01 ± 0.11	42.01 ± 1.76	0.63 ± 0.00	9.28 ± 0.08	0.87 ± 0.00	1.53 ± 0.02
BD+35 4847	109.43 ± 3.64	19.10 ± 3.14	-98.70 ± 4.69	0.38 ± 0.06	9.82 ± 0.17	0.92 ± 0.01	4.37 ± 0.44
TYC 2228-838-1 ^(b)	195.91 ± 10.10	2.14 ± 9.27	-3.21 ± 4.35	0.04 ± 0.10	13.19 ± 0.79	0.99 ± 0.01	2.37 ± 0.21
BD-00 4538	164.76 ± 3.70	-35.84 ± 4.11	65.71 ± 2.39	0.74 ± 0.09	11.05 ± 0.17	0.87 ± 0.01	4.48 ± 0.06
TYC 4001-1161-1 ^(b)	-305.15 ± 3.81	-10.34 ± 4.63	11.49 ± 1.67	0.17 ± 0.07	28.67 ± 1.09	0.99 ± 0.01	0.88 ± 0.04
BD+03 4904	-179.50 ± 7.26	52.61 ± 1.76	103.86 ± 3.35	1.15 ± 0.07	13.90 ± 0.46	0.85 ± 0.01	5.61 ± 0.18

Notes. ^(a)Sequoia candidate. ^(b)GSE candidate. ^(c)Thin disc. Cylindrical galactocentric velocity components (V_R , V_T , V_Z), pericentric (r_{peri}) and apocentric (r_{ap}) distances, orbit's eccentricities (ecc.) and maximum height over the Galactic plane (Z_{max}) obtained using the Galpy code as described in Sect. 5.3.

of the figure. Stars in prograde motions are found at $V_T > 0$. The panel b) shows the relation between two integrals of motion, namely the orbital energy per unit mass E versus the vertical component of the angular momentum, L_Z . In this plane, disc stars are found as a concentration in the middle right part of the figure. Stars in prograde motions are found at $L_Z > 0$.

The panel d) shows the so-called action diamond, namely, the difference between the vertical and radial actions ($J_Z - J_R$) versus the azimuthal action ($J_\phi = L_Z$), normalised to $J_{\text{tot}} = |J_\phi| + J_Z + J_R$. In this plane, disc stars are found in the middle-right corner of the figure. Finally, panel c) presents the square root of the radial action, $\sqrt{J_R}$, versus

Table 4. Dynamical properties of the sample.

Star	E ($\text{km}^2 \text{s}^{-2}$)	L_Z (kpc km s^{-1})	J_R (kpc km s^{-1})	J_Z (kpc km s^{-1})
TYC 4-369-1 ^(b)	-34227.63 ± 3291.84	-44.03 ± 158.21	1197.95 ± 78.51	119.72 ± 9.06
BD+04 18 ^(b)	-42513.31 ± 1635.62	92.87 ± 75.73	1016.43 ± 71.04	45.15 ± 2.83
TYC 33-446-1	-50421.65 ± 152.82	446.14 ± 82.86	490.18 ± 46.82	179.34 ± 5.00
TYC 2824-1963-1 ^(b)	-32798.81 ± 1356.66	464.84 ± 118.00	1047.38 ± 105.01	92.10 ± 11.10
TYC 4331-136-1	-53172.43 ± 407.65	341.14 ± 41.80	546.21 ± 17.06	175.52 ± 23.48
HD 87740 ^(c)	-35668.33 ± 20.63	1917.26 ± 0.98	67.49 ± 0.92	6.29 ± 0.15
BD+31 2143 ^(a)	-55728.06 ± 721.22	-802.73 ± 58.57	301.37 ± 25.08	45.69 ± 0.46
HD 91276 ^(c)	-34291.52 ± 94.96	1994.38 ± 2.18	49.31 ± 1.25	10.46 ± 0.24
BD+13 2383 ^(c)	-36851.45 ± 67.52	1924.87 ± 1.44	11.86 ± 0.22	14.82 ± 0.64
BD-07 3523	-59178.43 ± 310.18	477.42 ± 31.41	419.23 ± 22.81	65.91 ± 1.22
HD 115575 ^(a)	-62436.30 ± 569.91	-740.81 ± 55.13	235.95 ± 25.27	37.22 ± 1.08
BD+48 2167	-56753.65 ± 246.36	261.40 ± 27.62	598.58 ± 16.69	56.42 ± 2.97
BD+06 2880	5622.52 ± 5730.94	-92.51 ± 67.22	3584.74 ± 667.63	184.49 ± 8.93
BD+32 2483	-59630.68 ± 255.87	189.39 ± 43.00	443.13 ± 15.36	216.69 ± 17.41
BD+41 2520	-57201.08 ± 24.02	499.68 ± 17.95	309.05 ± 5.88	226.49 ± 7.52
HD 130971 ^(c)	-48991.09 ± 173.44	1469.11 ± 7.06	28.05 ± 0.68	11.49 ± 0.35
BD+24 2817 ^(c)	-46355.49 ± 67.06	1532.55 ± 4.89	47.22 ± 1.59	9.15 ± 0.24
HD 238439 ^(b)	-35278.11 ± 3032.28	-409.69 ± 100.28	920.41 ± 28.28	171.13 ± 14.78
HD 138934 ^(c)	-39560.78 ± 62.24	1828.31 ± 2.59	17.45 ± 0.11	4.24 ± 0.08
HD 139423	-3655.31 ± 3049.07	-632.91 ± 69.96	2369.28 ± 212.44	232.20 ± 6.38
HD 142614 ^(b)	-14886.95 ± 619.65	-213.86 ± 31.79	1910.64 ± 22.81	162.79 ± 7.20
HD 143348	-61607.48 ± 150.19	669.01 ± 25.39	308.18 ± 9.87	28.49 ± 2.82
BD+11 2896	-59067.51 ± 243.19	2.27 ± 27.22	599.82 ± 8.54	182.99 ± 3.29
BD+20 3298 ^(b)	-10201.18 ± 2540.13	-156.84 ± 33.80	2311.39 ± 141.13	62.76 ± 7.73
TYC 2588-1386-1	-54671.06 ± 1380.35	-339.89 ± 29.48	277.00 ± 34.50	410.02 ± 38.02
TYC 3085-119-1	-55313.29 ± 10.17	1085.79 ± 1.01	114.68 ± 0.30	53.54 ± 0.38
BD+39 3309 ^(b)	-46738.94 ± 340.89	54.40 ± 6.83	977.79 ± 11.03	15.09 ± 0.28
HD 165400 ^(c)	-46100.83 ± 135.27	1620.05 ± 4.77	2.04 ± 0.08	1.64 ± 0.07
TYC 1008-1200-1 ^(b)	-11569.16 ± 711.06	-173.10 ± 26.17	2235.15 ± 29.20	46.91 ± 0.92
TYC 2113-471-1	-67655.11 ± 154.57	-187.60 ± 8.12	452.52 ± 10.74	82.13 ± 3.89
TYC 4221-640-1 ^(b)	-34552.60 ± 3168.92	39.58 ± 47.04	905.59 ± 31.04	557.89 ± 175.20
TYC 4584-784-1	-50164.69 ± 653.59	-366.30 ± 36.51	696.68 ± 10.85	33.24 ± 1.78
TYC 3944-698-1	-57398.19 ± 497.16	102.71 ± 17.00	728.08 ± 0.83	18.32 ± 0.15
HD 354750	-44243.32 ± 1272.11	379.15 ± 41.22	813.65 ± 51.11	48.93 ± 4.02
BD-00 3963 ^(c)	-47007.38 ± 19.34	1565.26 ± 0.80	17.55 ± 0.11	3.27 ± 0.02
BD+07 4625	1544.83 ± 599.14	-2125.03 ± 10.56	1481.70 ± 53.38	698.28 ± 2.18
BD+25 4520	-15380.65 ± 2293.01	1376.01 ± 37.05	759.95 ± 112.46	672.75 ± 63.24
HD 208316	-65109.88 ± 682.23	-437.14 ± 47.53	399.44 ± 23.29	25.56 ± 3.68
TYC 4267-2023-1 ^(a)	-52771.29 ± 211.40	-1128.09 ± 8.00	161.60 ± 3.79	36.50 ± 2.29
TYC 565-1564-1 ^(b)	-37633.12 ± 3170.28	-104.55 ± 92.33	1071.44 ± 47.87	115.58 ± 6.37
BD+21 4759	-57871.41 ± 351.37	265.05 ± 0.98	608.16 ± 7.09	33.60 ± 1.12
BD+35 4847	-53688.33 ± 889.31	157.10 ± 25.69	644.01 ± 15.53	165.57 ± 22.46
TYC 2228-838-1 ^(b)	-42910.75 ± 2446.65	18.04 ± 78.59	1053.15 ± 62.93	40.17 ± 1.85
BD-00 4538	-48836.38 ± 650.68	-286.84 ± 32.93	670.27 ± 1.88	141.76 ± 5.30
TYC 4001-1161-1 ^(b)	-12998.56 ± 1348.15	-95.09 ± 42.13	2248.08 ± 101.24	2.58 ± 0.06
BD+03 4904	-39338.09 ± 1127.74	434.30 ± 13.76	809.03 ± 52.92	145.72 ± 15.00

Notes. ^(a)Sequoia candidate. ^(b)GSE candidate. ^(c)Thin disc. Stellar orbital energies (E), vertical component of the angular momentum (L_Z), and radial and vertical actions (J_R , J_Z).

the azimuthal action, J_ϕ . Disc stars are visible at the bottom right of the figure.

The panels c and d were used by [Feuillet et al. \(2021\)](#) to select candidates likely belonging to the *Gaia*-Sausage-Enceladus (GSE, [Belokurov et al. 2018](#); [Haywood et al. 2018](#); [Helmi et al. 2018](#)) and the Sequoia ([Barbá et al. 2019](#); [Villanova et al. 2019](#); [Myeong et al. 2019](#)) accretion events. The selection

box they used for GSE and Sequoia (red and green shaded areas in panels c and d) are indicated. Stars in the background populations following in these two selections box are reported in red (GSE candidates) and green (Sequoia candidates) in panels a and b.

GSE candidates are highly eccentric (large $\sqrt{J_R}$ values) and do not have a large angular momentum (small values of $J_\phi = L_Z$).

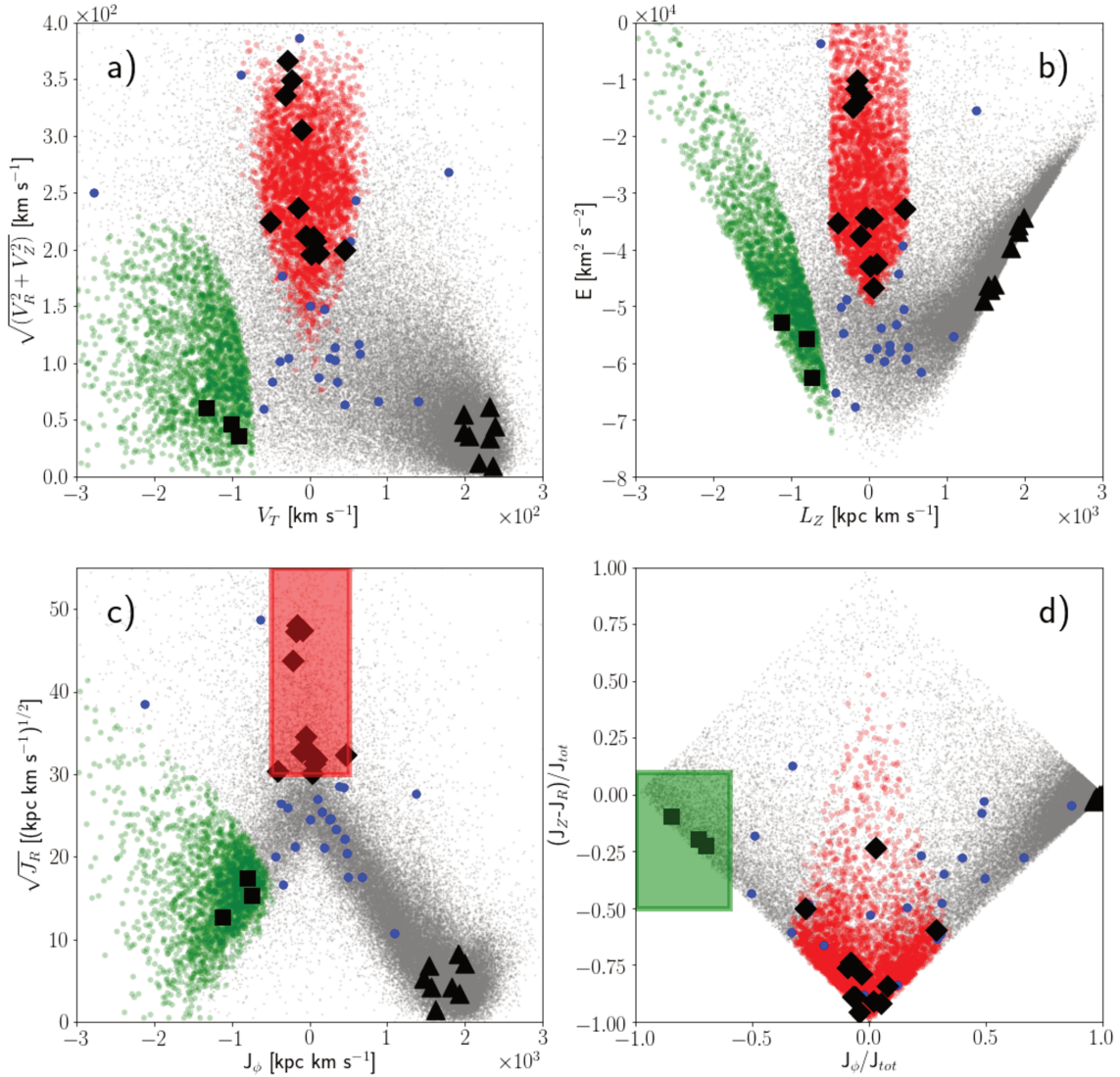


Fig. 5. Target stars kinematic properties are presented in various planes. Program stars are presented as big filled symbols. The background population (gray points) is the “good parallax sample” of Bonifacio et al. (2021) for reference. Red filled points in all planes are stars selected from the background population as likely GSE members according to the red shaded box of panel c. Green filled points are likely Sequoia members according to the green shaded box in panel d. Panel a: Toomre diagram ($\sqrt{V_R^2 + V_Z^2}$ versus V_T). Panel b: orbital energy E versus angular momentum, L_Z . Panel d (action diamond diagram): the difference in the vertical and radial actions ($J_Z - J_R$) versus the azimuthal action ($J_\phi = L_Z$). Quantities are normalised to the total action $J_{\text{tot}} = J_Z + J_R + |J_\phi|$. Panel c: $\sqrt{J_R}$ versus L_Z . Target stars likely belonging to GSE and Sequoia are marked as black-filled diamond and squares, respectively. Targets likely belonging to the thin disc are presented as black filled triangles. The remaining targets are presented as blue filled circles.

Sequoia candidates are highly retrograde (highly negative values of $J_\phi = L_Z$) and their orbits are not as eccentric as those of GSE candidates.

Among the stars in our sample, we identify 12 and 3 stars with kinematics compatible with the GSE (black-filled diamond) and Sequoia (black-filled squares) structures, respectively, according to the selections boxes of Fig. 5. We identify them in Tables 3 and 4. We also identified eight stars with thin disc kinematics (black filled triangles). These are the most metal-rich stars in the sample ($[\text{Fe}/\text{H}] > -0.7$ dex) and are confined to the disc ($Z < 0.8$ kpc and $Z_{\text{max}} < 0.9$ kpc). One star likely belongs to the thick disc (TYC 3085-119-1, filled blue circle at $V_T = +140$ km s $^{-1}$ in the top-left panel; $[\text{Fe}/\text{H}] = -1.5$, $e = 0.36$, $Z = 0.6$ kpc, $Z_{\text{max}} = 1.6$ kpc). The remaining stars (filled blue circles) may be associated with the halo and have in roughly equal number prograde and retrograde orbits. They are formally not

associated with GSE or Sequoia, although some of them lie quite close to GSE or Sequoia stars in the various planes.

Shall we use the classification scheme of Bensby et al. (2014), besides TYC 3085-119-1, we would also classify HD 143348 and HD 354750 as thick-disc stars, while the classification of the remaining stars as belonging to the thin disc or the halo would be confirmed. As expected, candidate GSE and Sequoia stars would be classified as halo stars. HD 143348 and HD 354750 are indeed confined to the disc ($Z_{\text{max}} = 1.19$ and 2.51 kpc, respectively). They have, however, highly eccentric orbits (ecc. = 0.62 and 0.87, respectively).

6. Abundances

With MyGIsFOS, we derived the abundances up to zinc. An example of the data provided is available in the

Table 5. Sensitivity of abundances on atmospheric parameters.

Element	ΔT_{eff} 100 K	$\Delta \log g$ 0.2 dex	$\Delta \xi$ 0.2 km s ⁻¹
O I	0.03	0.12	0.01
Na I	0.08	0.02	0.01
Mg I	0.08	0.03	0.03
Al I	0.06	0.01	0.00
Si I	0.03	0.02	0.01
S I	0.12	0.08	0.04
Ca I	0.10	0.02	0.04
Sc II	0.02	0.11	0.04
Ti I	0.16	0.02	0.03
Ti II	0.01	0.08	0.06
V I	0.18	0.01	0.00
Cr I	0.14	0.02	0.03
Cr II	0.04	0.08	0.01
Mn I	0.14	0.02	0.01
Fe I	0.12	0.01	0.05
Fe II	0.08	0.11	0.05
Co I	0.14	0.01	0.00
Ni I	0.10	0.01	0.02
Cu I	0.13	0.01	0.00
Zn I	0.04	0.06	0.03

Tables C.1–C.3⁵. As the uncertainty, we assumed the line-to-line scatter (σ). In the case that an abundance is based on a single line, we assumed the largest σ . Moreover, to these errors, one should add in quadrature the error generated from the assumed stellar atmospheres. Typical errors due to uncertainties in atmospheric parameters are reported in Table 5. Similar uncertainties were also obtained by [Matas Pinto et al. \(2022\)](#), seen in particular in their Table 8,) where two stars with parameters in the range of the MINCE targets were analyzed with the same methods.

When not specified, we adopted the abundance derived from Fe I lines as the metallicity. Since our surface gravities are derived from the parallaxes and not Fe ionisation equilibrium, in order to minimise the gravity dependence in abundance ratios, we adopted $[X/Fe] = [X/Fe I]$, where X is a neutral species and $[X/Fe] = [X/Fe II]$ for ionised species. The exception is oxygen: since all our oxygen abundances are derived from the forbidden lines, whose dependence on surface gravity is closer to that of an ionised species than to that of a neutral species we adopt $[O/Fe] = [O/Fe II]$ as done by [Cayrel et al. \(2004\)](#). The solar abundances we adopted are reported in Table 6 and these are the values we used to compute our stellar models as well as to derive $[X/H]$ and $[X/Fe]$ ratios.

A slightly different approach was adopted to derive the abundances of sulphur. Both the S I lines of Multiplet 1 at 920 nm and Multiplet 6 at 860 nm lie in the wavelengths ranges covered only by the spectra taken at CFHT with the spectrograph ESPaDOnS, but we considered only the lines at 920 nm because those at 860 nm are too weak to be measured. The strong S I lines of Multiplet 1 are located in a wavelength range contaminated by telluric absorptions. To assess the suitability of Mult. 1 lines for the estimation of sulphur abundances, we compared the observed spectrum of our stars with that of a B-type star. Sulphur lines contaminated by telluric ones were rejected, while we derived

⁵ Abundances and the linelist adopted for each star are available from CDS.

Table 6. Solar abundances used throughout this paper.

Element	A(X)	Reference
C	8.50	Caffau et al. (2011)
O	8.76	Caffau et al. (2011)
Na	6.30	Lodders et al. (2009)
Mg	7.54	Lodders et al. (2009)
Al	6.47	Lodders et al. (2009)
Si	7.52	Lodders et al. (2009)
S	7.16	Caffau et al. (2011)
Ca	6.33	Lodders et al. (2009)
Sc	3.10	Lodders et al. (2009)
Ti	4.90	Lodders et al. (2009)
V	4.00	Lodders et al. (2009)
Cr	5.64	Lodders et al. (2009)
Mn	5.37	Lodders et al. (2009)
Fe	7.52	Caffau et al. (2011)
Co	4.92	Lodders et al. (2009)
Ni	6.23	Lodders et al. (2009)
Cu	4.21	Lodders et al. (2009)
Zn	4.62	Lodders et al. (2009)

Table 7. Sulphur abundances.

ID	A(S) _{LTE}	A(S) _{NLTE}	[S/Fe] _{NLTE}
BD+39–3309	5.33	5.00	0.42
BD+31–2143	5.50	5.20	0.41
BD+32–2483	5.76	5.51	0.60
BD+20–3298	5.89	5.82	0.61
BD+48–2167	5.87	5.57	0.69
TYC 3085–119–1	6.05	5.79	0.14

Notes. From lines of Multiplet 1 in spectra obtained at CFHT with ESPaDOnS.

the sulphur abundances from not contaminated lines by spectro-synthesis. We used the code SALVADOR ([Mucciarelli, in prep.](#)) that computes a grid of synthetic spectra with the code SYNTH (Kurucz 1993b, 2005), using ATLAS9 α -enhanced model atmospheres ([Kurucz 1993a](#)) based on ODF by [Castelli & Kurucz \(2003\)](#). This code allows us to speed up the fitting procedure and it keeps the results consistent with the other elements because based on the same codes to compute theoretical synthesis and models atmospheres. SALVADOR (in the same way as MyGISFOS) finds the abundance from a line performing a χ^2 minimisation between observed and synthetic spectra. The difference in this case is that in the grid of synthetic spectra used by MyGISFOS, all the abundances scale with Fe, while SALVADOR computes the synthesis where just the S abundance changes.

In cases where the S lines were contaminated by telluric absorptions, we estimated the abundances from equivalent width (EW). In this way, by using the deblending option of IRAF, we could estimate in the feature contaminated by telluric lines the contribution in EW from the telluric line and the one from S.

The measured EW were converted in abundances using the code GALA. As explained by [Mucciarelli et al. \(2013\)](#), GALA computes the curve of growth of an element by using WIDTH code ([Kurucz 2005](#)) and computing an ATLAS model. In this way the S abundance derived from spectro-synthesis and EW are perfectly consistent. The results obtained are listed in Table 7.

We reported also the abundances corrected for deviations from local thermodynamic equilibrium (LTE). The non-LTE corrections were assumed following [Takeda et al. \(2005\)](#) and we found a mean correction of $\Delta \sim -0.25$. The $[S/Fe]$ values were obtained considering the solar value $[S/Fe]_{\odot}=7.16$ ([Caffau et al. 2014](#)).

7. Chemical evolution of the MINCE stars

The main scope of Galactic archaeology is to constrain the formation and evolution of the Milky Way from the observed chemical abundances. Hence, in Sects. 7.2-7.4, we compare the stellar abundance ratios from the MINCE project with the predictions of two chemical evolution models. In Sect. 7.1, we briefly recall the main characteristics of the reference chemical evolution we used in this study for: i) the Milky disc and ii) the GSE accretion event, respectively.

7.1. Reference chemical evolution models

7.1.1. Model for the disc components by [Spitoni et al. \(2021\)](#)

The inner halo ([Nissen & Schuster 2010](#)) and the oldest stars of the thick disc share the same chemical enrichment and it is likely that they were both formed during the same dissipative collapse process. This is why we decided to compare MINCE data with [Spitoni et al. \(2021\)](#), which provided a reliable model for the Milky disc components constrained by high-resolution spectroscopy data using a Bayesian framework. Moreover, we think that it is important also to show the low- α evolution (thin disc) of [Spitoni et al. \(2021\)](#) because the youngest stars predicted by the GSE model (with $[Fe/H] = -0.5$ dex, see Fig. 6) seem to share the same abundance ratio $[X/Fe]$ (where $X = O, Mg, Ca, Si, Ti, Sc, Co, Mn$) of the low-metallicity tail of the thin disc phase. [Spitoni et al. \(2021\)](#) presented a revised version of the classical two-infall chemical evolution model ([Chiappini et al. 1997](#)) in order to reproduce the Galactic disc components as traced by the APOGEE DR16 ([Ahumada et al. 2020](#)) abundance ratios. In this model, the Galactic disc is assumed to be formed by two independent, sequential episodes of gas accretion giving rise to the thick and thin disc components, respectively. As already pointed out by [Spitoni et al. \(2019b, 2020\)](#) and [Palla et al. \(2020\)](#) the signature of a delayed gas-rich merger (i.e. the delay between the two gas infall is ~ 4 Gyr) is imprinted in the APOGEE abundance ratios. We recall that in [Spitoni et al. \(2021\)](#) a Bayesian framework based on MCMC methods has been used to find the best chemical evolution model constrained by APOGEE DR16 $[Mg/Fe]$ and $[Fe/H]$ abundance ratios at different Galactocentric distances. In the solar neighbourhood, the dilution effect caused by the second infall produces a characteristic feature in the $[\alpha/Fe]$ and $[Fe/H]$ space. In fact, the late accretion of pristine gas has the effect of decreasing the metallicity of stars born immediately after the infall event, leading to an evolution at nearly constant $[\alpha/Fe]$ since both α and Fe are diluted by the same amount ([Spitoni et al. 2019b](#)). The [Scalo \(1986\)](#) initial stellar mass function (IMF), constant in time and space, was also adopted.

The model computed in the solar vicinity (8 kpc) assumes primordial infall for both infall episodes but different star formation efficiencies (SFEs): 2 Gyr^{-1} (thick disc) and 1 Gyr^{-1} (thin disc). We refer the reader to the middle column (model for the solar vicinity) of Table 2 in [Spitoni et al. \(2021\)](#) for the values of the best-fit model parameters as predicted by MCMC calculations: namely, gas infall timescales, present-day total surface mass density ratio and the delay between the two gas infall.

It is worth mentioning that the predicted present-day total surface mass density ratio between thin and thick disc sequences of $5.635^{+0.214}_{-0.162}$ is in very good agreement with the value derived by [Fuhrmann et al. \(2017\)](#) for the local mass density ratio (5.26).

In this paper, we compare observational data for α and iron-peak elements with model predictions in the solar neighbourhood adopting the same nucleosynthesis prescriptions as in [Spitoni et al. \(2021\)](#), i.e. applying the ones suggested by [François et al. \(2004\)](#). This set of yields has been widely used in the past ([Cescutti et al. 2007](#); [Mott et al. 2013](#); [Spitoni et al. 2015, 2019a,b](#)) and turned out to be able to reproduce the main chemical abundances of the solar neighbourhood. For most of the elements, the offsets of the model to the solar abundances is very small. However, we decided to apply a correction for each element to have the chemical evolution models passing exactly to $[X/Fe] = 0$ at $[Fe/H] = 0$. This correction is quoted for each element in the relative plot (Figs. 6–23). The elements Na, Al, V, Cr, and Cu were not considered in [François et al. \(2004\)](#) and we do not show model results for these elements here.

7.1.2. GSE

A large fraction of the halo stars in the solar vicinity are the result of an accretion event, associated to a disrupted satellite, dubbed GSE ([Belokurov et al. 2018](#); [Haywood et al. 2018](#); [Helmi et al. 2018](#)). As presented in the previous section, we study the kinematics of our sample and we can determine what the progenitors of our sample are, that is, if they used to belong to GSE or Sequoia. For this reason, we compared our data to a model built to describe the chemical enrichment evolution in GSE. In the following, we summarise the main characteristics of the model. The infall law is:

$$A(t) = M_{\text{Enc}} \text{Gauss}(\sigma_{\text{Enc}}, \tau_{\text{Enc}}), \quad (1)$$

where Gauss is a normalised Gaussian function, τ_{Enc} is time of the center of the peak and σ_{Enc} the standard deviation, and M_{Enc} is the total amount of the gas infall into *Gaia*-Enceladus. The star formation rate (SFR) is:

$$\psi(t) = \begin{cases} \nu_{\text{Enc}} \Sigma(t)^k & t \leq T_{\text{Enc}} \\ 0 & t > T_{\text{Enc}} \end{cases}, \quad (2)$$

where ν_{Enc} is the efficiency of the star formation, $\Sigma(r)$ is the surface mass density, and the exponent, k , is set equal to 1.5 ([Kennicutt 1989](#)), T_{Enc} is the time when *Gaia*-Enceladus stops forming star, due to the interaction with the Galaxy. A Galactic wind is considered as follows:

$$W(t) = \begin{cases} \nu_{\text{Enc}}^{\text{wind}} \psi(t) & t \geq T_{\text{Enc}}^{\text{wind}} \\ 0 & t < T_{\text{Enc}}^{\text{wind}} \end{cases}, \quad (3)$$

where $T_{\text{Enc}}^{\text{wind}}$ is when the galactic wind in *Gaia*-Enceladus starts due to interaction with the Galaxy and $\nu_{\text{Enc}}^{\text{wind}}$ is the wind efficiency. The seven parameters – ν_{Enc} , M_{Enc} , τ_{Enc} , σ_{Enc} , T_{Enc} , $T_{\text{Enc}}^{\text{wind}}$, and $\nu_{\text{Enc}}^{\text{wind}}$ – determine the equations of the chemical evolution model for *Gaia*-Enceladus and they are summarised in Table 8. The precise procedure is described in [Cescutti et al. \(2020\)](#).

To summarise the most important feature, its evolution is similar to a dwarf spheroidal galaxy ([Lanfranchi et al. 2008](#)), namely, it is less massive than our Galaxy by around a factor of 30 at the beginning. However, given its galactic winds and the less efficient star formation period ending 6 Gyr ago, its stellar content is only a hundredth of the Galactic stellar mass. The

Table 8. Parameters for the chemical evolution of *Gaia*-Enceladus.

Parameter	Best value after minimisation
ν_{Enc} (star formation efficiency)	1.3 Gyr^{-1}
M_{Enc} (surface mass density)	$2.0 M_{\odot}/pc^2$
τ_{Enc} (peak of the infall law)	550 Myr
σ_{Enc} (SD of the infall law)	1408 Myr
$\nu_{\text{Enc}}^{\text{wind}}$ (galactic wind efficiency)	5.0
$T_{\text{Enc}}^{\text{wind}}$ (start of the galactic wind)	2919 Myr
T_{Enc} (end of the star formation)	5767 Myr

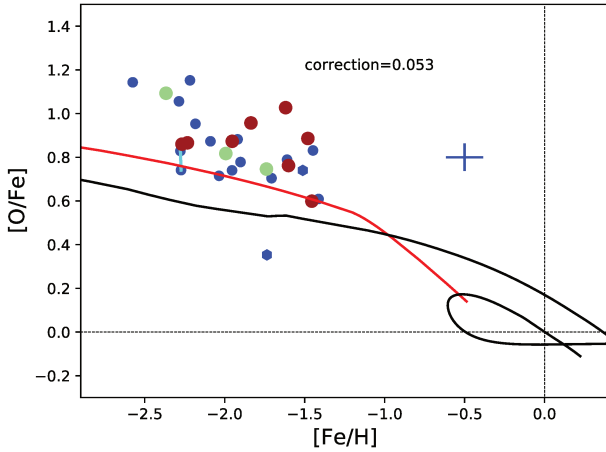


Fig. 6. $[O/Fe]$ versus $[Fe/H]$ abundances measured in the MINCE stars: blue solid dots stars selected with the mince2 selection, hexagons from APOGEE. Cyan lines connect the abundances measured for the same stars with spectra taken from two facilities. The colours of the dot refer to the substructures to which they belong: red for GSE, light green for Sequoia and blue for the remaining stars. The mean errors of the MINCE sample are reported as blue cross. The black lines refers to the chemical evolution model by Spitoni et al. (2021) for the discs of our Galaxy, whereas the red line is a model for GSE (Cescutti et al. 2020). Correction refers to the offset in $[O/Fe]$ applied to the models (see Sect. 7.1 for details).

nucleosynthesis adopted is basically the same of François et al. (2004), to be consistent with the model in Spitoni et al. (2021). The only difference is that the iron production assumed for SNe II is $0.07 M_{\odot}$ for the SNe II (Limongi & Chieffi 2018, see) in Cescutti et al. (2020), which is about a factor of 2 lower than the iron consider in François et al. (2004). For this reason, we decided to decrease accordingly the yields for iron peak elements from massive stars by a factor of 2; any other deviation is described for the specific element.

7.2. Results for α -elements

In Figs. 6–12, we show our results for the α -elements O, Mg, Si, Ca, Ti, and Ti II, respectively. In these plots, we include only those stars selected with a mince2 selection (and two stars chosen thanks to the APOGEE survey), providing stars belonging either to the halo or to the substructures GSE and Sequoia that we distinguish thanks to the colour coding.

Searching for specific differences between halo stars and Sequoia or GSE, but also between GSE and Sequoia, we cannot find within α -element abundances any clear signal, all the stars seem to share the same plateau with some dispersion. Surely, the star with the lowest $[\alpha/Fe]$ and a relative low $[Fe/H]$ (~ -2.25)

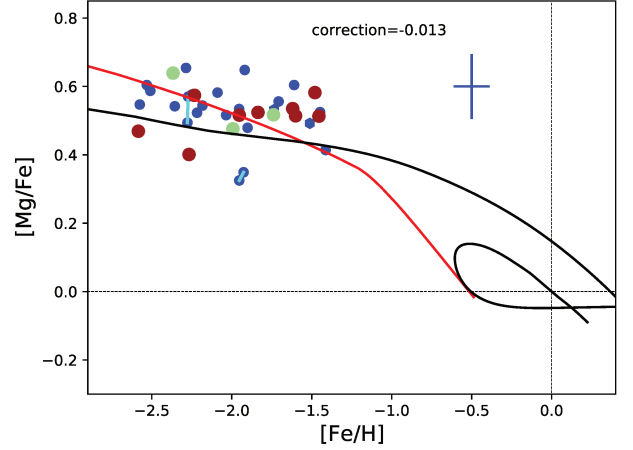


Fig. 7. $[Mg/Fe]$ versus $[Fe/H]$ abundances measured in the MINCE stars; the details are the same as Fig. 6.

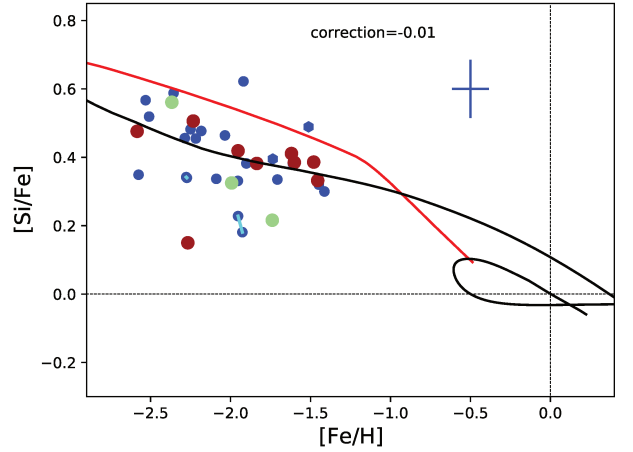


Fig. 8. $[Si/Fe]$ versus $[Fe/H]$ abundances measured in the MINCE stars; the details are the same as Fig. 6.

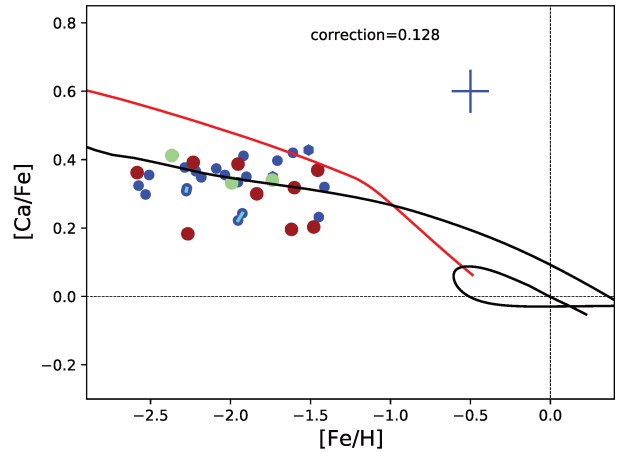


Fig. 9. $[Ca/Fe]$ versus $[Fe/H]$ abundances measured in the MINCE stars; the details are the same as Fig. 6.

belongs to GSE. The other feature that we can be acknowledged is that at $[Fe/H] \sim -1.5$, GSE stars show on average a lower $[\alpha/Fe]$.

Overall, this outcome is confirmed by the models results. In the models, the chemical differences expected between GSE and the disc of our Galaxy reside in the $[\alpha/Fe]$ versus $[Fe/H]$

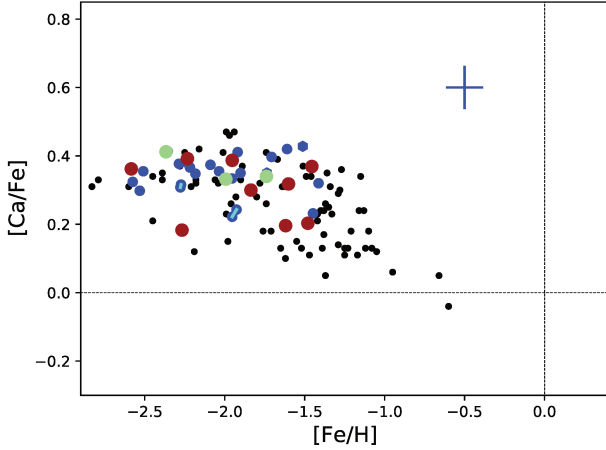


Fig. 10. $[\text{Ca}/\text{Fe}]$ versus $[\text{Fe}/\text{H}]$ abundances measured in the MINCE stars; the plot is the same as Fig. 9, but without the lines of models and with the results by Ishigaki et al. (2012) for halo stars (black dots).

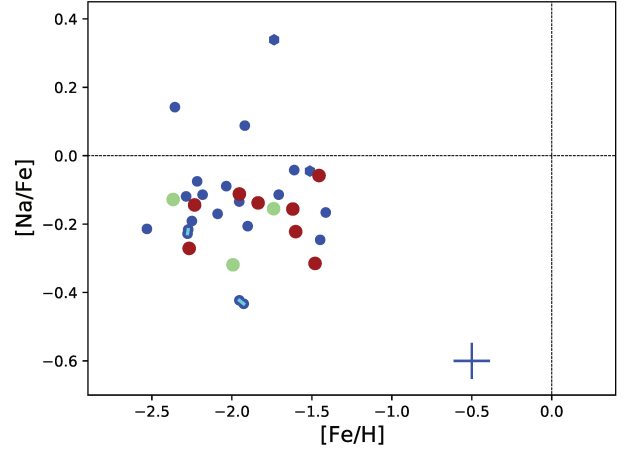


Fig. 13. $[\text{Na}/\text{Fe}]$ versus $[\text{Fe}/\text{H}]$ abundances measured in the MINCE stars; the details are the same as Fig. 6, but without the lines of models.

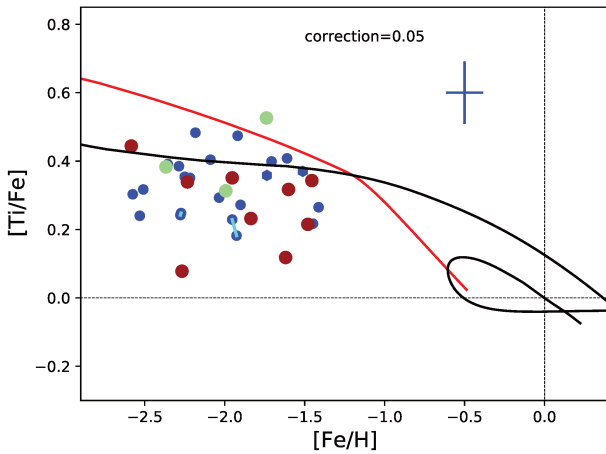


Fig. 11. $[\text{Ti}/\text{Fe}]$ versus $[\text{Fe}/\text{H}]$ abundances measured in the MINCE stars; the details are the same as Fig. 6.

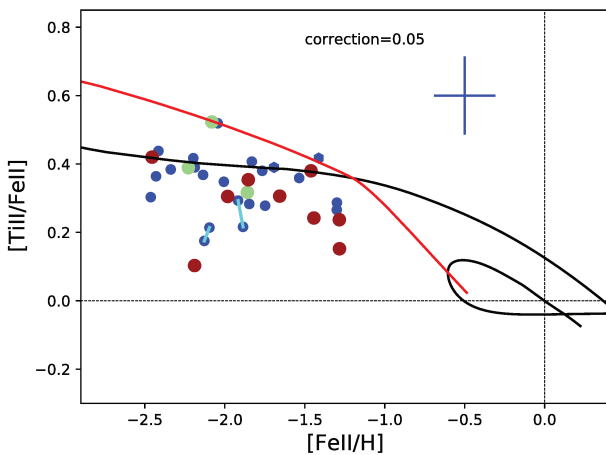


Fig. 12. $[\text{Ti II}/\text{Fe II}]$ versus $[\text{Fe II}/\text{H}]$ abundances measured in the MINCE stars; the details are the same as Fig. 6.

observed at $[\text{Fe}/\text{H}] > -1.5$, where the two models do show a clear difference. However, most of our stars have lower metallicity so they are not expected to be firmly distinguished chemically. Between the two models describing the chemical evolution of the discs of our Galaxy and the GSE, there is also an offset for what concern the plateau, with the one for GSE on average slightly

(0.1-0.2) above the trend of the discs model. This outcome is most likely connected to the choice of the iron yields. Probably, more interesting is that the models predict a slightly different steepness in the trend of α in the range $-2.5 < [\text{Fe}/\text{H}] < -1.5$, with GSE having a more negative behaviour. A hint towards this can be found in the fact that GSE stars show on average a lower $[\alpha/\text{Fe}]$ mentioned before, and surely more data may help confirming this feature.

In Fig. 10, we decided to present our results for $[\text{Ca}/\text{Fe}]$ compared to the results obtained by Ishigaki et al. (2012) for this element. The abundances taken from by Ishigaki et al. (2012) were re-normalised to our solar abundances to avoid spurious offsets. Overall, our results are in excellent agreement with the abundances obtained for halo stars by Ishigaki et al. (2012), although they can comprise also stars of GSE and Sequoia. The main visible difference is that this sample extends further at metallicity up to $[\text{Fe}/\text{H}] \sim -1$ (with two stars almost at $[\text{Fe}/\text{H}] \sim -0.5$).

7.3. Results for sodium and aluminium

In Fig. 13, we present the plot for sodium. It presents a dispersion in the data that can be at least partially due to NLTE effects; surely, it is an element where NLTE effects play an important role (see Sect. 8 and Table 9). An important feature is visible in the comparison between halo stars and GSE and Sequoia stars. In our sample, we have three stars enhanced in sodium and they all belong to the halo. Given the limited sample, strong conclusions cannot be obtained, but we will follow up this signature within our future MINCE stars. We show in Fig. 14 the ratio obtained for aluminium; the dispersion is not present for this element but again four stars show an enhancement of $[\text{Al}/\text{Fe}] > 0.4$ and again none of these stars belong to GSE or Sequoia.

7.4. Results for iron-peak elements

In Figs. 15–23, we present the results we obtained for the iron peak elements. Among them, copper presents the largest offset among the chemical abundance measurements of the two duplicate stars. The difference is anyway < 0.2 dex and for most of the other elements is well below 0.1 dex.

Not surprisingly, most of the iron peak elements have a chemical evolution similar to the one of iron, being produced in a similar manner by SNe II and SNe Ia and, therefore, presenting

Table 9. Approximate NLTE corrections for two MINCE stars.

H2020 MINCE	BD-10_3742 BD+07_4625	BD-12_106 BD+39_3309
Element	$\Delta NLTE$	$\Delta NLTE$
Cl	-0.06	-0.04
OI	-0.10	-0.10
NaI	-0.30	-0.21
MgI	0.03	0.08
SiI	-0.13	-0.12
SI	-	0.00
KI	-0.16	-0.14
CaI	0.09	0.04
ScII	-	-0.03
TiI	0.14	0.14
TiII	-0.03	-0.04
CrI	0.16	0.21
MnI	0.00	0.18
FeI	0.08	0.11
FeII	0.00	0.02
CoI	0.55	0.73

Notes. Based on [Hansen et al. \(2020, H2020\)](#).

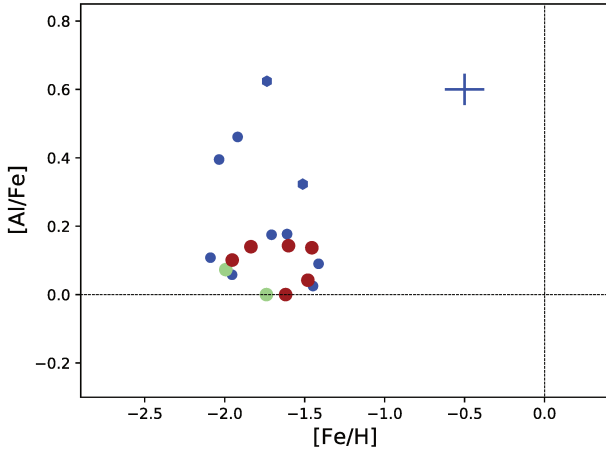


Fig. 14. [Al/Fe] versus [Fe/H] abundances measured in the MINCE stars; the details are the same as Fig. 6, but without the lines of models.

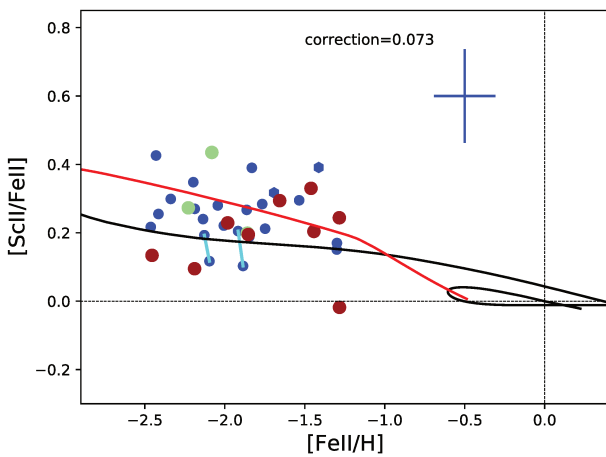


Fig. 15. [Sc II/Fe II] versus [Fe II/H] abundances measured in the MINCE stars; the details are the same as Fig. 6.

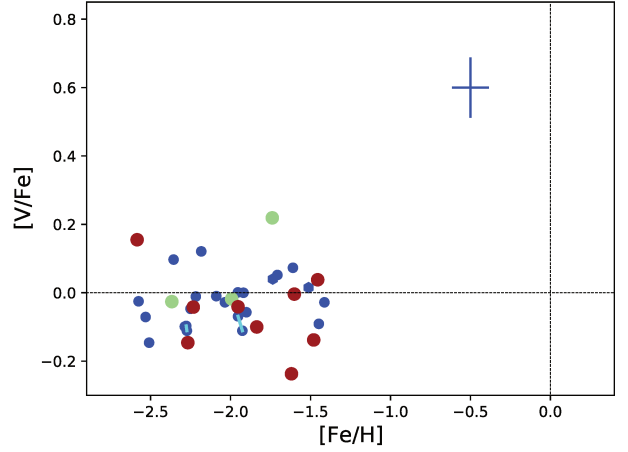


Fig. 16. [V/Fe] versus [Fe/H] abundances measured in the MINCE stars; the details are the same as Fig. 6, but without the lines of the models.

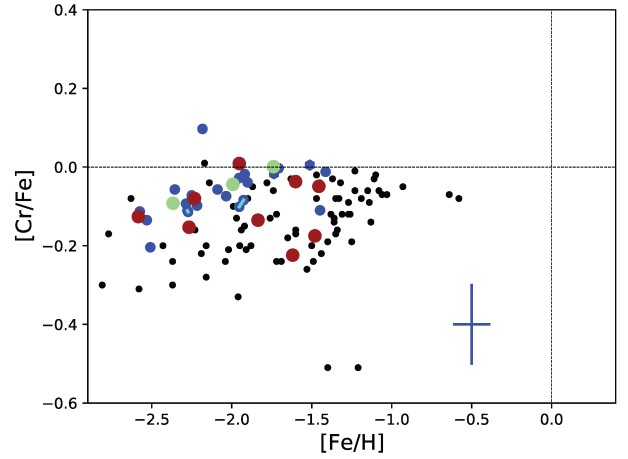


Fig. 17. [Cr/Fe] versus [Fe/H] abundances measured in the MINCE stars; the details are the same as Fig. 6, but without the lines of the models and with the results by [Ishigaki et al. \(2013\)](#) for halo stars (black dots).

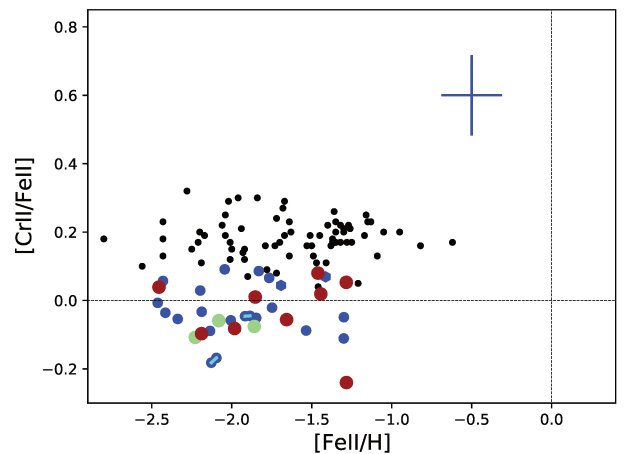


Fig. 18. [Cr II/Fe II] versus [Fe II/H] abundances measured in the MINCE stars; the details are the same as Fig. 17.

a solar ratio. The most intriguing exceptions are manganese and copper that in the stellar atmosphere of our sample have negative abundance ratios compared to iron (normalised to the Sun). Manganese is a remarkable element, because it has a single stable isotope and for this reason its production is quite sensitive

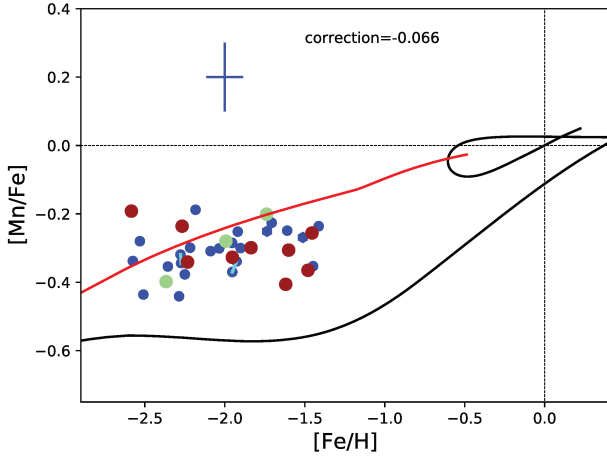


Fig. 19. [Mn/Fe] versus [Fe/H] abundances measured in the MINCE stars; the details are the same as Fig. 6.

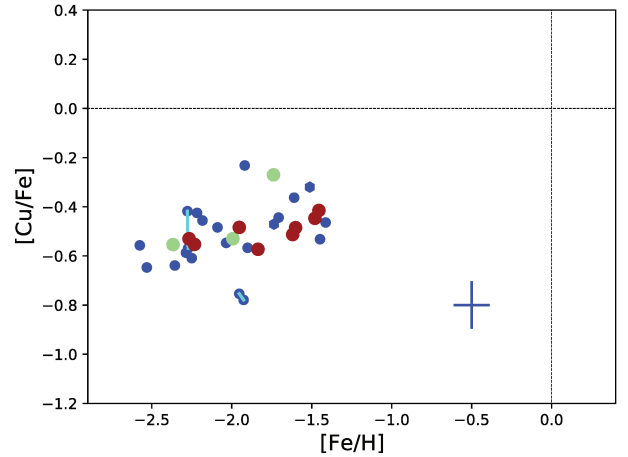


Fig. 22. [Cu/Fe] versus [Fe/H] abundances measured in the MINCE stars; the details are the same as Fig. 6, but without the lines of the models.

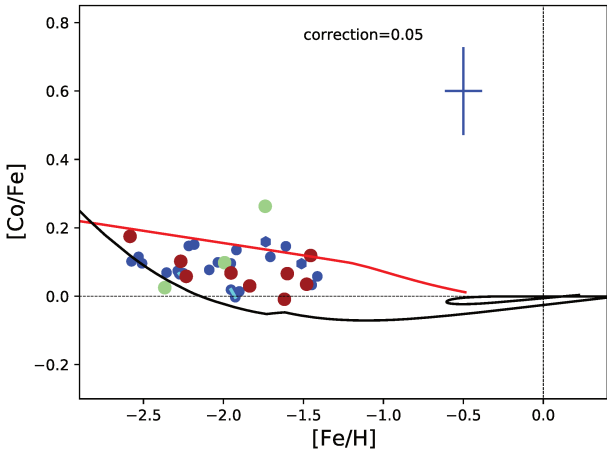


Fig. 20. [Co/Fe] versus [Fe/H] abundances measured in the MINCE stars; the details are the same as Fig. 6.

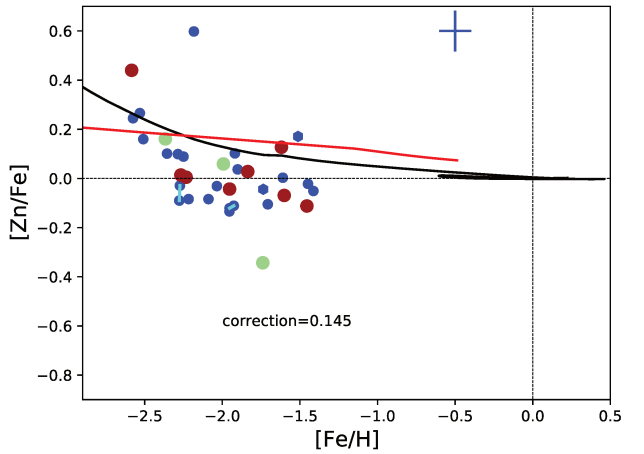


Fig. 23. [Zn/Fe] versus [Fe/H] abundances measured in the MINCE stars; the details are the same as Fig. 6.

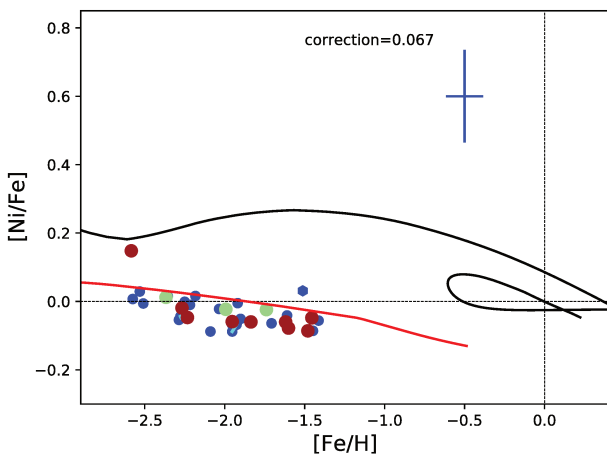


Fig. 21. [Ni/Fe] versus [Fe/H] abundances measured in the MINCE stars; the details are the same as Fig. 6.

to the explosion conditions. In fact, theoretical computations have found that different classes of supernovae Ia are expected to produce different amount of manganese (Kobayashi et al. 2015). Thanks to this characteristic, it was possible to exclude the exclusive enrichment of single degenerate SNe Ia from chemical evolution modelling. It was also possible to evaluate the fraction

of different SNe Ia contributing to the enrichment of manganese (Seitzzahl et al. 2013; Eitner et al. 2020), although the impact of NLTE in the determination and also the exact metallicity dependence of the yields of SNe II can impact the exact determination of this fraction. Moreover, the differential enrichment of manganese by the SNe Ia classes may also produce a spread in the enrichment, as shown in Cescutti & Kobayashi (2017).

On the other hand, copper is not expected to be significantly produced by SNe Ia, and the rise toward the solar metallicity is driven by a strong metal dependency in SNe II (Timmes et al. 1995). Contrary to copper and manganese, scandium presents a behaviour similar to the one of the α -elements, with a $[\text{Sc}/\text{Fe}] > 0$ for $[\text{Fe}/\text{H}] < -1$. This is controversial, in the sense that the results from François et al. (2004) seem to indicate a behaviour similar to standard iron peak elements, so approximately a constant $[\text{Sc}/\text{Fe}] \sim 0$. In this case, it is difficult also to rely to theoretical nucleosynthesis expectations, since the yields for scandium are usually too low by 1 dex (Romano et al. 2010; Kobayashi et al. 2011).

The chemical evolution deduced from the MINCE stars for the rest of our iron peak elements appears to be remarkably similar to iron. We also note that our estimates for Cr I and Cr II are in agreement, contrary to the discrepancy observed in the Ishigaki et al. (2013) data for this element between ionised

and neutral species; in fact, for this comparison data set it is present an average [Cr I/Fe I] ratio slightly below solar ratio, and slightly above for [Cr II/Fe II]. Also the different selection of Cr lines shall be accounted for the discrepancy as also remarked in Lombardo et al. (2022). This trend of [Cr/Fe] is also compatible to the results obtained applying NLTE corrections for chromium in Bergemann & Cescutti (2010).

Four stars appear to be enhanced in vanadium for [Fe/H] < -1.5 compared to rest of the sample. Moreover, the stars with high [V/Fe] at [Fe/H] ~ -2.5 also show a high [Ni/Fe] and [Zn/Fe] as well as a low [Sc II/Fe II]; notably, this star belong the GSE substructure.

We show the chemical evolution tracks also for iron peak elements, but we are afraid that the yields assumed (we recall that we use François et al. 2004) are not the final answer, as shown already for manganese (Cescutti et al. 2008; Seitzzahl et al. 2013; Cescutti & Kobayashi 2017) and possibly true for other elements. Clearly, the chemical evolution models can only be as good as their nucleosynthesis input and the iron peak nucleosynthesis is not so well understood at present (see e.g. Fig. 15 of Kobayashi et al. 2011). Still, the chemical evolution results for GSE seem to reproduce the observed ratios at least for manganese, cobalt, and nickel, indicating that the role and timescale of SNe Ia are well considered.

Again we do not see in the data any significant trend or offset between halo stars and GSE stars. On the other hand, the GSE star with the lowest iron content, BD+393309 shows peculiar abundance ratios of [V/Fe], [Ni/Fe] and [Zn/Fe] that appear to be all enhanced with respect to sample. The interpretation of this enhancement is not trivial; [Zn/Fe] – and to a lesser extent also [Ni/Fe] – is expected to be higher in the nucleosynthesis of hypernovae (Kobayashi et al. 2006), compared to standard SNe II. Hypernovae belong to a class of SNe II exploding with a kinetic energy ten (or more) times the typical energy for SNe II of 10^{51} erg and tend to eject a larger fraction of iron-peak elements. On the other hand, a hypernovae will be polluting with a lower ratios of $[\alpha/\text{Fe}]$ and this does not seem to be the case. Certainly, we plan to monitor the presence of these stars – enhanced in iron peak elements – in future MINCE data. Regarding Sequoia stars, the abundance ratios of V, Cr, Mn, and Co as compared to Fe are increasing toward higher metallicity, whereas the opposite happens to Zn and Ni. Clearly with three stars, we cannot consider these trends to be significant, but again we will keep track of this hint in future MINCE papers.

8. NLTE corrections

Depending on the exact choice of lines combined with the stellar parameters and the abundances itself, some elemental abundances suffer from the 1D, LTE assumptions, while others remain good chemical tracers. Several studies have targeted such improvements by computing either NLTE or 3D abundances (or both, see e.g. Amarsi et al. 2019; Bergemann et al. 2017, 2019; Caffau et al. 2008; Lind et al. 2012; Mashonkina 2020; Sitnova et al. 2016; Steffen et al. 2015).

The recent study by Hansen et al. (2020) presented corrected abundances for most of elements presented here, with the exception of Al. Owing to the overlap in stellar parameter space, we used their NLTE computations as an indication of where corrections for the LTE assumptions would affect the LTE abundances most. A full abundance correction will be presented in a forth coming paper. A few stars show a good agreement

(overlap) in stellar parameters and the corrections, which are sensitive to the stellar parameters, can therefore help us assess the level or at least direction the NLTE corrections would bring the corrected NLTE abundances in. From Hansen et al. (2020)–BD-10_3742 ($T/\log g/[\text{Fe}/\text{H}]/Vt$: $4678 \pm 120/1.38 \pm 0.04/ -1.96 \pm 0.07/1.9 \pm 0.1$) and BD-12_106 ($4889 \pm 50/2.03 \pm 0.05/ -2.11 \pm 0.04/1.5 \pm 0.2$) come close to two of the MINCE programme stars, namely BD+07_4625 ($4757/1.64/ -1.93/1.86$) and BD+39_3309 ($4909/1.73/ -2.58/1.94$). To estimate the order of magnitude of the corrections, we read off the NLTE corrections from their Table A.1, and we note that these are only approximate as the corrections also strongly depend on the use of lines and the actual size of the abundances as well. The NLTE corrections are presented as $\Delta\text{NLTE} = \text{NLTE} - \text{LTE}$.

From Table 9, it is clearly seen that the largest corrections for such stars are obtained for Na, (Si, K, Ti), Cr, Mn, and Co (especially the latter). In the case of Na, over recombination leads to strengthening of the lines and negative NLTE corrections. For K the corrections also exceed ± 0.1 dex, and here they are dictated by the source function, and caused by resonance line scattering, where similar to Na D lines an over population of the ground states shift the line formation outwards. This in turn deepens the K lines, so the effect is governed by the radiation field and rates. In this case, the values were interpolated using the grid from Reggiani et al. (2019). The corrections are positive for Si, where NLTE computations lead to weakened Ti I lines and, hence, result in positive corrections. Here the corrections are photoionisation dominated, which means that they are sensitive to overionisation driven by a non-local high-energy radiation field. This leads to weakening of low-excitation potential lines and in turn positive NLTE corrections (as LTE underestimates their abundances). However, the largest corrections are seen for the Fe-peak elements, especially Co. For this element, the NLTE corrections may completely change the picture of its chemical evolution and surely the nucleosynthesis adopted here, empirically deduced from LTE measurements, cannot be used, nor the original Woosley & Weaver (1995) yields will improve the situation. Moreover, also other available tables of nucleosynthesis (Kobayashi et al. 2011; Limongi & Chieffi 2018) will struggle to explain the evolution of cobalt. Detailed NLTE studies for Mn and Co are important to properly understand their chemical evolution (e.g. Eitner et al. 2020).

9. Conclusions

We describe the method adopted in the MINCE project to select our sample, determine the stellar atmosphere of our stellar targets, and measure at intermediate-low metallicity the chemical abundances of several α -elements and iron peak elements, Na and Al. The first selection criteria, based solely on Starhorse (Anders et al. 2019) was not ideal. It allowed us to properly select the characteristics of the stars in term of $\log g$ and T_{eff} . It also correctly determines metal-poor stars, but not as metal-poor as requested by our project ($[\text{Fe}/\text{H}] < -1$). For this reason, we also implemented a selection based on kinematics by requiring the $v_{\text{tot}} > 200 \text{ km s}^{-1}$, so halo stars. With this new constraint, the selection is successful in finding stars with metallicities below $[\text{Fe}/\text{H}] < -1$ and therefore within the MINCE metallicity range. Thanks to *Gaia* data, we were also able to distinguish among our sample those stars belonging to GSE (12) and Sequoia (3). We did not find specific trends and offsets compared to the sample of halo stars (defined as those not belonging neither to GSE

nor Sequoia). This is not completely unexpected given that the sample is still small; moreover, the chemical evolution results also did not predict the important feature in the metallicity range that we explore here – but it did indeed do so for slightly more metal-rich objects. The results of this first campaign show that the approach of using multiple middle-sized facilities allows to collect meaningful amounts of high-quality data in a short time. In the next paper of the series, we shall present the measurements of neutron capture elements in this sample of stars.

Acknowledgements. We gratefully acknowledge support from the French National Research Agency (ANR) funded project “Pristine” (ANR-18-CE31-0017). This work was partially supported by the European Union (ChETEC-INFRA, project no. 101008324). This work has made use of data from the European Space Agency (ESA) mission *Gaia* (<https://www.cosmos.esa.int/gaia>), processed by the *Gaia* Data Processing and Analysis Consortium (DPAC, <https://www.cosmos.esa.int/web/gaia/dpac/consortium>). Funding for the DPAC has been provided by national institutions, in particular the institutions participating in the *Gaia* Multilateral Agreement. This research has made use of the SIMBAD database, operated at CDS, Strasbourg, France. ES received funding from the European Union’s Horizon 2020 research and innovation program under SPACE-H2020 grant agreement number 101004214 (EXPLORE project). Funding for the Stellar Astrophysics Centre is provided by The Danish National Research Foundation (Grant agreement no.: DNRF106).

References

- Ahumada, R., Allende Prieto, C., Almeida, A., et al. 2020, *ApJS*, 249, 3
- Amarsi, A. M., Nissen, P. E., & Skúladóttir, Á. 2019, *A&A*, 630, A104
- Anders, F., Khalatyan, A., Chiappini, C., et al. 2019, *A&A*, 628, A94
- Argast, D., Samland, M., Thielemann, F.-K., & Qian, Y.-Z. 2004, *A&A*, 416, 997
- Balcells, M., Benn, C. R., Carter, D., et al. 2010, *SPIE Conf. Ser.*, 7735
- Barbá, R. H., Minniti, D., Geisler, D., et al. 2019, *ApJ*, 870, L24
- Belokurov, V., Erkal, D., Evans, N. W., Koposov, S. E., & Deason, A. J. 2018, *MNRAS*, 478, 611
- Bensby, T., Feltzing, S., & Oey, M. S. 2014, *A&A*, 562, A71
- Bergemann, M., & Cescutti, G. 2010, *A&A*, 522, A9
- Bergemann, M., Collet, R., Schönrich, R., et al. 2017, *ApJ*, 847, 16
- Bergemann, M., Gallagher, A. J., Eitner, P., et al. 2019, *A&A*, 631, A80
- Bonifacio, P., Monaco, L., Salvadori, S., et al. 2021, *A&A*, 651, A79
- Bouchy, F., & Sophie Team. 2006, in *Tenth Anniversary of 51 Peg-b: Status of and Prospects for Hot Jupiter Studies*, eds. L. Arnold, F. Bouchy, & C. Moutou, 319
- Bovy, J. 2015, *ApJS*, 216, 29
- Bovy, J., Allende Prieto, C., Beers, T. C., et al. 2012, *ApJ*, 759, 131
- Bressan, A., Marigo, P., Girardi, L., et al. 2012, *MNRAS*, 427, 127
- Burbidge, E. M., Burbidge, G. R., Fowler, W. A., & Hoyle, F. 1957, *Rev. Mod. Phys.*, 29, 547
- Caffau, E., Ludwig, H. G., Steffen, M., et al. 2008, *A&A*, 488, 1031
- Caffau, E., Bonifacio, P., François, P., et al. 2011, *Nature*, 477, 67
- Caffau, E., Monaco, L., Spite, M., et al. 2014, *A&A*, 568, A29
- Castelli, F. & Kurucz, R. L. 2003, in *Modelling of Stellar Atmospheres*, eds. N. Piskunov, W. W. Weiss, & D. F. Gray, 210, A20
- Cavallo, L., Cescutti, G., & Matteucci, F. 2021, *MNRAS*, 503, 1
- Cayrel, R., Hill, V., Beers, T. C., et al. 2001, *Nature*, 409, 691
- Cayrel, R., Depagne, E., Spite, M., et al. 2004, *A&A*, 416, 1117
- Cescutti, G., & Kobayashi, C. 2017, *A&A*, 607, A23
- Cescutti, G., Matteucci, F., François, P., & Chiappini, C. 2007, *A&A*, 462, 943
- Cescutti, G., Matteucci, F., Lanfranchi, G. A., & McWilliam, A. 2008, *A&A*, 491, 401
- Cescutti, G., Romano, D., Matteucci, F., Chiappini, C., & Hirschi, R. 2015, *A&A*, 577, A139
- Cescutti, G., Molaro, P., & Fu, X. 2020, *Mem. Soc. Astron. Italiana*, 91, 153
- Chiappini, C., Matteucci, F., & Gratton, R. 1997, *ApJ*, 477, 765
- Cosentino, R., Lovis, C., Pepe, F., et al. 2012, *SPIE Conf. Ser.*, 8446, 84461V
- Côté, B., Fryer, C. L., Belczynski, K., et al. 2018, *ApJ*, 855, 99
- de Jong, R. S., Bellido-Tirado, O., Chiappini, C., et al. 2012, *SPIE Conf. Ser.*, 8446
- Donati, J. F., Semel, M., Carter, B. D., Rees, D. E., & Collier Cameron, A. 1997, *MNRAS*, 291, 658
- Donati, J. F., Catala, C., Landstreet, J. D., & Petit, P. 2006, in *ASP Conf. Ser.*, 358, 362
- Eisenstein, D. J., Weinberg, D. H., Agol, E., et al. 2011, *AJ*, 142, 72
- Eitner, P., Bergemann, M., Hansen, C. J., et al. 2020, *A&A*, 635, A88
- Feuillet, D. K., Sahlholdt, C. L., Feltzing, S., & Casagrande, L. 2021, *MNRAS*, 508, 1489
- François, P., Matteucci, F., Cayrel, R., et al. 2004, *A&A*, 421, 613
- Fuhrmann, K., Chini, R., Kaderhandt, L., & Chen, Z. 2017, *MNRAS*, 464, 2610
- Hansen, C. J., Koch, A., Mashonkina, L., et al. 2020, *A&A*, 643, A49
- Haywood, M., Di Matteo, P., Lehner, M. D., et al. 2018, *ApJ*, 863, 113
- Helmi, A., Babusiaux, C., Koppelman, H. H., et al. 2018, *Nature*, 563, 85
- Ishigaki, M. N., Chiba, M., & Aoki, W. 2012, *ApJ*, 753, 64
- Ishigaki, M. N., Aoki, W., & Chiba, M. 2013, *ApJ*, 771, 67
- Katz, D., Sartoretti, P., Guerrier, A., et al. 2022, *A&A*, 668, A14
- Kennicutt, Robert C., J. 1989, *ApJ*, 344, 685
- Kobayashi, C., Umeda, H., Nomoto, K., Tominaga, N., & Ohkubo, T. 2006, *ApJ*, 653, 1145
- Kobayashi, C., Karakas, A. I., & Umeda, H. 2011, *MNRAS*, 414, 3231
- Kobayashi, C., Nomoto, K., & Hachisu, I. 2015, *ApJ*, 804, L24
- Koposov, S. E., Gilmore, G., Walker, M. G., et al. 2011, *ApJ*, 736, 146
- Kurucz, R. 1993a, *ATLAS9 Stellar Atmosphere Programs and 2 km/s Grid*. Kurucz CD-ROM No. 13. Cambridge, 13
- Kurucz, R. L. 1993b, SYNTHE spectrum synthesis programs and line data
- Kurucz, R. L. 2005, *Mem. Soc. Astron. Ital. Suppl.*, 8, 14
- Lanfranchi, G. A., Matteucci, F., & Cescutti, G. 2008, *A&A*, 481, 635
- Limongi, M., & Chieffi, A. 2018, *ApJS*, 237, 13
- Lind, K., Bergemann, M., & Asplund, M. 2012, *MNRAS*, 427, 50
- Lindgren, L., Bastian, U., Biermann, M., et al. 2021, *A&A*, 649, A4
- Lodders, K., Palme, H., & Gail, H. P. 2009, *Landolt-Börnstein*, 4B, 712
- Lombardo, L., Bonifacio, P., François, P., et al. 2022, *A&A*, 665, A10
- Marigo, P., Girardi, L., Bressan, A., et al. 2017, *ApJ*, 835, 77
- Mashonkina, L. 2020, *MNRAS*, 493, 6095
- Mashonkina, L., Jablonka, P., Sitnova, T., Pakhomov, Y., & North, P. 2017, *A&A*, 608, A89
- Matas Pinto, A. d. M., Caffau, E., François, P., et al. 2022, *Astron. Nachr.*, 343, e10032
- Mott, A., Spitoni, E., & Matteucci, F. 2013, *MNRAS*, 435, 2918
- Mucciarelli, A., Pancino, E., Lovisi, L., Ferraro, F. R., & Lapenna, E. 2013, GALA: Stellar atmospheric parameters and chemical abundances
- Myeong, G. C., Vasiliev, E., Iorio, G., Evans, N. W., & Belokurov, V. 2019, *MNRAS*, 488, 1235
- Nissen, P. E., & Schuster, W. J. 2010, *A&A*, 511, A10
- Palla, M., Matteucci, F., Spitoni, E., Vincenzo, F., & Grisoni, V. 2020, *MNRAS*, 498, 1710
- Reggiani, H., Amarsi, A. M., Lind, K., et al. 2019, *A&A*, 627, A177
- Roederer, I. U., Preston, G. W., Thompson, I. B., et al. 2014, *AJ*, 147, 136
- Romano, D., Karakas, A. I., Tosi, M., & Matteucci, F. 2010, *A&A*, 522, A32
- Sbordone, L., Caffau, E., Bonifacio, P., & Duffau, S. 2014, *A&A*, 564, A109
- Scalo, J. M. 1986, *Fund. Cosmic Phys.*, 11, 1
- Schlafly, E. F., & Finkbeiner, D. P. 2011, *ApJ*, 737, 103
- Schönrich, R., Binney, J., & Dehnen, W. 2010, *MNRAS*, 403, 1829
- Seitenzahl, I. R., Cescutti, G., Röpkke, F. K., Ruiter, A. J., & Pakmor, R. 2013, *A&A*, 559, L5
- Simonetti, P., Matteucci, F., Greggio, L., & Cescutti, G. 2019, *MNRAS*, 486, 2896
- Sitnova, T. M., Mashonkina, L. I., & Ryabchikova, T. A. 2016, *MNRAS*, 461, 1000
- Spitoni, E., Romano, D., Matteucci, F., & Ciotti, L. 2015, *ApJ*, 802, 129
- Spitoni, E., Cescutti, G., Minchev, I., et al. 2019a, *A&A*, 628, A38
- Spitoni, E., Silva Aguirre, V., Matteucci, F., Calura, F., & Grisoni, V. 2019b, *A&A*, 623, A60
- Spitoni, E., Verma, K., Silva Aguirre, V., & Calura, F. 2020, *A&A*, 635, A58
- Spitoni, E., Verma, K., Silva Aguirre, V., et al. 2021, *A&A*, 647, A73
- Steffen, M., Prakashvičius, D., Caffau, E., et al. 2015, *A&A*, 583, A57
- Takeda, Y., Hashimoto, O., Taguchi, H., et al. 2005, *PASJ*, 57, 751
- Telting, J. H., Avila, G., Buchhave, L., et al. 2014, *Astron. Nachr.*, 335, 41
- Timmes, F. X., Woosley, S. E., & Weaver, T. A. 1995, *ApJS*, 98, 617
- Villanova, S., Monaco, L., Geisler, D., et al. 2019, *ApJ*, 882, 174
- Vincenzo, F., Spitoni, E., Calura, F., et al. 2019, *MNRAS*, 487, L47
- Woosley, S. E., & Weaver, T. A. 1995, *ApJS*, 101, 181

Wright, J. T., & Eastman, J. D. 2014, [PASP](#), 126, 838

Yong, D., Alves Brito, A., Da Costa, G. S., et al. 2014, [MNRAS](#), 439, 2638

¹ Dipartimento di Fisica, Sezione di Astronomia, Università di Trieste, Via G. B. Tiepolo 11, 34143 Trieste, Italy
e-mail: gabriele.cescutti@inaf.it

² INAF – Osservatorio Astronomico di Trieste, Via Tiepolo 11, 34143 Trieste, Italy

³ INFN – Sezione di Trieste, Via A. Valerio 2, 34127 Trieste, Italy

⁴ GEPI – Observatoire de Paris, Université PSL, CNRS, 5 Place Jules Janssen, 92190 Meudon, France

⁵ Departamento de Ciencias Físicas, Facultad de Ciencias Exactas, Universidad Andres Bello, Av. Fernandez Concha 700, Las Condes, Santiago, Chile

⁶ ESO – European Southern Observatory, Alonso de Cordova 3107, Vitacura, Santiago, Chile

⁷ UPJV – Université de Picardie Jules Verne, Pôle Scientifique, 33 rue Saint-Leu, 80039, Amiens, France

⁸ Université Côte d’Azur, Observatoire de la Côte d’Azur, CNRS, Laboratoire Lagrange, Bd de l’Observatoire, CS 34229, 06304 Nice cedex 4, France

⁹ Stellar Astrophysics Centre, Department of Physics and Astronomy, Aarhus University, Ny Munkegade 120, 8000 Aarhus C, Denmark

¹⁰ Dipartimento di Fisica e Astronomia, Università degli Studi di Bologna, Via Gobetti 93/2, 40129 Bologna, Italy

¹¹ INAF – Osservatorio di Astrofisica e Scienza dello Spazio di Bologna, Via Gobetti 93/3, 40129 Bologna, Italy

¹² Goethe University Frankfurt, Institute for Applied Physics, Max-von-Laue-Str. 12, 60438, Frankfurt am Main, Germany; Institute for Nuclear Physics, Technical University Darmstadt, Schlossgartenstr. 2 (S2111), 64289 Darmstadt, Germany

¹³ Institute of Theoretical Physics and Astronomy, Vilnius University, Saulėtekio al. 3, Vilnius, 10257, Lithuania

¹⁴ Observational Astrophysics, Department of Physics and Astronomy, Uppsala University, Box 516, 751 20 Uppsala, Sweden

¹⁵ Leibniz-Institut für Astrophysik Potsdam (AIP), An der Sternwarte 16, 14482 Potsdam, Germany

¹⁶ INAF – Osservatorio Astrofisico di Arcetri, Largo E. Fermi 5, 5012, Firenze, Italy

¹⁷ INAF – Osservatorio Astronomico d’Abruzzo, Via Mentore Maggini snc, 64100 Teramo, Italy

¹⁸ INFN – Sezione di Perugia, Via A. Pascoli snc, 06123 Perugia, Italy

Appendix A: Log of the observations

Table A.1. Log of the observations and radial velocities for the stars observed with HARPS-N

Star	alpha2000 J2000	delta2000 J2000	BJD days	Date	t_{exp} s	RV km s ⁻¹	σ_{RV} km s ⁻¹
HD 87740	10:07:10.25	+03:41:23.3	2458980.40412383	2020-05-10	3000	-23.9993	0.0016
HD 91276	10:32:57.37	+35:22:56.6	2458980.44256365	2020-05-10	3000	+23.9350	0.0017
BD+13 2383	11:17:37.07	+12:24:10.0	2458980.48078609	2020-05-10	2400	-11.5311	0.0023
BD+41 2520	14:42:02.54	+41:14:11.6	2458980.60643665	2020-05-11	3600	+11.6820	0.0014
HD 130971	14:51:15.68	-08:59:01.8	2458980.56913504	2020-05-11	3600	+23.7756	0.0012
BD+24 2817	15:05:56.81	+24:05:51.7	2458980.65155434	2020-05-11	3000	-43.1845	0.0009
HD 138934	15:34:21.37	+23:12:36.6	2458980.68241001	2020-05-11	2100	+18.3412	0.0007
HD 143348	15:58:36.55	+34:11:33.4	2458980.70923832	2020-05-11	2400	-73.7397	0.0012
BD-073523	13:00:33.60	-07:59:38.2	2459010.45002716	2020-06-09	3600	+73.5710	0.0025
HD 115575	13:18:09.97	-13:58:45.8	2459010.40738054	2020-06-09	3600	+188.4806	0.0029
BD+062880	14:25:10.31	+06:07:14.9	2459010.49153284	2020-06-09	3000	+37.3641	0.0021
HD 238439	15:17:00.58	+54:35:38.6	2459010.53202863	2020-06-10	3600	-65.0949	0.0024
HD 139423	15:37:45.83	+11:36:11.6	2459010.56447555	2020-06-10	1200	+183.3917	0.0023
HD 142614	15:55:15.38	+08:13:27.8	2459010.58578868	2020-06-10	2100	-337.1939	0.0019
BD+254520	21:22:08.32	+25:45:15.8	2459010.61970877	2020-06-10	3600	+22.8268	0.0025
HD 208316	21:55:36.03	-04:13:27.4	2459010.65672317	2020-06-10	2100	-146.1986	0.0019

Table A.2. Log of the observations and radial velocities for the stars observed with FIES

STAR	α J2000	δ J2000	BJD days	Date	t_{exp} s	RV km s ⁻¹	σ_{RV} km s ⁻¹
BD+07 4625	21:07:13.10	+07:44:19.8	2459032.670574271	2020-07-02	2200	-494.883	0.004
	21:07:13.10	+07:44:19.8	2459032.696585007	2020-07-02	2200	-494.551	0.003
BD+35 4847	22:37:13.45	+36:08:21.6	2459033.675984722	2020-07-03	2800	-139.739	0.003
	22:37:13.45	+36:08:21.6	2459033.708940891	2020-07-03	2800	-139.742	0.003
BD+11 2896	16:01:04.87	+11:12:56.2	2459001.539097893	2020-06-01	3000	-218.821	0.002
	16:01:04.87	+11:12:56.2	2459001.574364527	2020-06-01	3000	-218.831	0.002
HD 165400	18:05:30.45	+09:49:30.4	2459000.690305141	2020-05-31	2800	-2.745	0.002
BD-00 3963	20:17:12.53	+00:21:22.7	2459036.622693848	2020-07-06	2200	-42.165	0.002
	20:17:12.53	+00:21:22.7	2459036.648704157	2020-07-06	2200	-42.159	0.002
BD-00 4538	23:38:18.78	+00:46:51.5	2459069.603750275	2020-08-08	2900	-190.753	0.003
	23:38:18.78	+00:46:51.5	2459069.637862387	2020-08-08	2900	-191.027	0.003

Table A.3. Log of the observations and radial velocities for the stars observed with Sophie

STAR	α J2000	δ J2000	BJD days	Date	t_{exp} s	RV km s ⁻¹	σ_{RV} km s ⁻¹
TYC 4-369-1	00:08:36.02	+02:58:01.7	2459087.56089588	2020-08-25	3600	+3.982	0.006
BD+04 18	00:12:49.90	+05:37:39.3	2459086.6077017	2020-08-25	3600	-29.987	0.002
TYC 33-446-1	01:54:22.17	+03:41:45.3	2459087.64126008	2020-08-26	3491	-99.892	0.004
TYC 2824-1963-1	01:58:38.93	+41:46:30.4	2459086.6437657	2020-08-25	2618	+52.907	0.003
	01:58:38.93	+41:46:30.4	2459087.5992952	2020-08-26	3105	+52.816	0.002
TYC 4331-136-1	03:57:14.19	+69:44:45.1	2459088.63728359	2020-08-27	3600	-110.967	0.005
TYC 1008-1200-1	18:06:31.58	+08:44:54.7	2459086.3381710	2020-08-24	3600	-393.813	0.007
	18:06:31.58	+08:44:54.7	2459087.3363853	2020-08-25	3600	-393.838	0.005
TYC 2113-471-1	18:56:41.55	+25:16:50.8	2459087.38188494	2020-08-25	3600	-252.760	0.004
	18:56:41.55	+25:16:50.8	2459088.32588031	2020-08-26	3600	-252.858	0.004
TYC 4221-640-1	19:09:19.27	+63:03:44.2	2459086.38173932	2020-08-24	3600		
	19:09:19.27	+63:03:44.2	2459088.36663955	2020-08-26	3600	-277.441	0.006
TYC 4584-784-1	19:22:56.40	+76:32:43.3	2459088.41633999	2020-08-26	3600	-295.607	0.004
TYC 3944-698-1	20:02:59.61	+58:01:07.1	2459086.4263490	2020-08-24	3600	-255.266	0.004
HD 354750	20:04:29.05	+13:35:31.0	2459088.46611671	2020-08-26	3600	-168.281	0.008
BD+25 4520	21:22:08.32	+25:45:15.8	2459087.42848911	2020-08-25	3600	+23.518	0.003
TYC 4267-2023-1	22:01:46.08	+62:27:40.6	2459086.4710943	2020-08-24	3600	-346.268	0.003
TYC 565-1564-1	22:10:38.77	+05:16:14.6	2459087.47351081	2020-08-25	3600	-175.181	0.003
BD+21 4759	22:28:46.35	+22:09:11.4	2459088.59697759	2020-08-27	3600	-202.045	0.006
TYC 2228-838-1	22:38:23.28	+27:34:24.7	2459088.5536172	2020-08-27	3600	-145.006	0.002
TYC 4001-1161-1	23:47:30.68	+53:47:16.5	2459086.5158160	2020-08-24	3600	-397.649	0.003
	23:47:30.68	+53:47:16.5	2459087.5143166	2020-08-25	3506	-397.617	0.003
BD+03 4904	23:55:28.37	+04:21:17.9	2459086.5634472	2020-08-25	3600	-208.370	0.006
BD+07 4625	21:07:13.10	+07:44:19.7	2459088.51050063	2020-08-27	3600	-495.699	0.002

Table A.4. Log of the observations and radial velocities for the stars observed with ESPaDOnS

STAR	α J2000	δ J2000	BJD days	Date	t_{exp} s	RV km s ⁻¹	σ_{RV} km s ⁻¹
BD+20 3298	16:36:33.15	+20:25:46.1	2459016.033335	2020-06-15	2380	-257.104	0.003
BD+31 2143	10:28:17.23	+30:26:29.2	2459180.153748	2020-11-26	2380	+64.157	0.004
BD+48 2167	13:59:19.74	+48:05:35.5	2459189.153872	2020-12-05	2380	-108.203	0.003
BD+39 3309	18:03:47.35	+39:32:31.3	2459016.091233	2020-06-15	2380	-249.092	0.005
BD+32 2483	14:31:38.96	+31:58:58.4	2459012.887960	2020-06-12	2380	+4.145	0.003
TYC 3085-119-1	17:16:36.98	+44:10:43.4	2458739.761057	2019-09-13	2380	-106.234	0.003
	17:16:36.98	+44:10:43.4	2458739.790407	2019-09-13	2380	-105.941	0.003
TYC 2588-1386-1	16:41:32.08	+36:24:42.6	2458739.725085	2019-09-13	2380	-249.674	0.003

Appendix B: Linelist

Table B.1. Example of the table available at the CDS with the list of the atomic data of the lines measured for each star of the MINCE sample

Element	Z	ion	Star	Wavelength nm	Loggf cm ⁻¹	Elow
O	8	0	BD+03 4904	636.3776	-10.19	161.311
Mg	12	0	BD+03 4904	457.1096	-5.623	0.0
Mg	12	0	BD+03 4904	470.2991	-0.44	35052.859
Mg	12	0	BD+03 4904	552.8405	-0.498	35052.859
Mg	12	0	BD+03 4904	571.1088	-1.724	35052.859
Si	14	0	BD+03 4904	568.4484	-1.553	39956.711
Ca	20	0	BD+03 4904	452.6928	-0.548	21849.562
Ca	20	0	BD+03 4904	457.8551	-0.697	20333.238
...

Appendix C: Chemical abundances

Table C.1. Example of the first part of table available at the CDS with the abundances of elements in their ionisation state from O I to Sc II in [X/H].

Star	Spect.	S/N@550nm	O I	σ	N	Na I	σ	N	Mg I	σ	N	Al I	σ	N	Si I	σ	N	Ca I	σ	N	Sc II	σ	N
BD-00 4538	FIES	> 100	-1.12	0.0	1	-2.11	0.05	3	-1.42	0.11	4	-99.0	0.0	0	-1.52	0.05	14	-1.55	0.06	25	-1.54	0.12	10

...

Notes. Sigma is based on the line to line dispersion and N is the number of lines for each ion.

Table C.2. Second part of the table available at the CDS with the abundances of elements from Ti I to Mn I in [X/H].

Star	Ti I	σ	N	Ti II	σ	N	VI	σ	N	Cr I	σ	N	Cr II	σ	N	Mn I	σ	N
BD-00 4538	-1.63	0.07	52	-1.47	0.12	28	-1.96	0.10	20	-1.93	0.09	23	-1.77	0.10	7	-2.20	0.07	14

...

Table C.3. Third part of the table available at the CDS with the abundances of elements from Fe I to Zn I in [X/H].

Star	Fe I	σ	N	Fe II	σ	N	Co I	σ	N	Ni I	σ	N	Cu I	σ	N	Zn I	σ	N
BD-00 4538	-1.90	0.09	276	-1.75	0.14	26	-1.89	0.09	19	-1.95	0.10	64	-2.47	0.15	4	-1.87	0.03	2

...

Purveyors of fine halos

III. Chemical abundance analysis of a potential ω Cen associate^{★,★★}

Andreas J. Koch-Hansen¹, Camilla Juul Hansen², Linda Lombardo³, Piercarlo Bonifacio³,
Michael Hanke¹, and Elisabetta Caffau³

¹ Zentrum für Astronomie der Universität Heidelberg, Astronomisches Rechen-Institut, Mönchhofstr. 12,
69120 Heidelberg, Germany
e-mail: andreas.koch@uni-heidelberg.de

² Max-Planck Institut für Astronomie, Königstuhl 17, 69117 Heidelberg, Germany

³ GEPI, Observatoire de Paris, Université PSL, CNRS, 5 place Jules Janssen, 92190 Meudon, France

Received 19 October 2020 / Accepted 5 November 2020

ABSTRACT

Globular clusters (GCs) are important donors to the build-up of the Milky Way (MW) stellar halo, having contributed at the ten percent level over the Galactic history. Stars that originated from the second generation of dissolved or dissolving clusters can be readily identified via distinct light-element signatures such as enhanced N and Na and simultaneously depleted C and O abundances. In this paper we present an extensive chemical abundance analysis of the halo star J110842, which was previously kinematically associated with the massive MW GC ω Centauri (ω Cen), and we discuss viable scenarios from escape to encounter. Based on a high-resolution, high signal-to-noise spectrum of this star using the UVES spectrograph, we were able to measure 33 species of 31 elements across all nucleosynthetic channels. The star's low metallicity of $[\text{Fe II}/\text{H}] = -2.10 \pm 0.02(\text{stat.}) \pm 0.07(\text{sys.})$ dex places it in the lower sixth percentile of ω Cen's metallicity distribution. We find that all of the heavier-element abundances, from α - and Fe-peak elements to neutron-capture elements are closely compatible with ω Cen's broad abundance distribution. However, given the major overlap of this object's abundances with the bulk of all of the MW components, this does not allow for a clear-cut distinction of the star's origin. In contrast, our measurements of an enhancement in CN and its position on the Na-strong locus of the Na-O anticorrelation render it conceivable that it originally formed as a second-generation GC star, lending support to a former association of this halo star with the massive GC ω Cen.

Key words. Galaxy: abundances – Galaxy: formation – globular clusters: general – globular clusters: individual: ω Centauri – Galaxy: halo – Galaxy: stellar content

1. Introduction

The stellar halo of the Milky Way (MW) galaxy conceivably formed through a variety of channels. Thus, in situ star formation within the host galaxy is contrasted by an ex situ formation, where the halo stars were born in satellite galaxies and accreted onto the host system only later on. The purported relative importance of either scenario varies in the literature and it is currently believed that our Galaxy experienced a mixture of both, where the ex situ component contributed to different degrees depending on galactocentric radius (Eggen et al. 1962; Searle & Zinn 1978; Dekel & Silk 1986; Bullock & Johnston 2005; Zolotov et al. 2009; Cooper et al. 2013; Pillepich et al. 2015; Naidu et al. 2020).

One important class of donors to the buildup of the MW halo is the globular clusters (GCs), and there is a wealth of evidence for their ongoing tidal disruption and for their accretion, ranging from observations of stellar streams (e.g., Odenkirchen et al. 2001; Lee et al. 2004) and extended envelopes of present-day

GCs (e.g., Jordi & Grebel 2010; Kuzma et al. 2018) to the chemodynamical identification of former GC stars in the MW halo field (Martell & Grebel 2010; Koch et al. 2019a; Fernández-Trincado et al. 2019; Tang et al. 2019; Hanke et al. 2020a)

The key signature to identify a bona fide cluster escapee lies in the chemical anomalies inherent in the multiple populations of the GSs (Carretta et al. 2009; Milone et al. 2017; Bastian & Lardo 2018; Gratton et al. 2019). As a result of high-temperature proton-capture reactions in the CNO cycle and its Ne-Na chain in a first generation of massive stars, the second generation that forms from the ejecta of these polluters is found to be rich in He, N, Na, and Al, while depleted in C, O, and Mg, which leads to the characteristic anticorrelations (Na-O, Mg-Al) and bimodalities (e.g., in CN) observed in any given GC (Cohen 1978; Carretta et al. 2009; Hanke et al. 2017; Bastian & Lardo 2018). The remainder of the chemical inventory of the second stellar generation remains largely unaltered by the involved nuclear reactions. These chemical patterns are indeed the best tracers of GC escapees, provided they were part of the second generation, as these characteristic abundances are predominantly found in GCs across the entire mass range, while absent in young open clusters, dwarf galaxies, and in situ halo field stars (Pilachowski et al. 1996; Geisler et al. 2007; Bragaglia et al. 2017; Bekki 2019).

* Full Table 2 is only available at the CDS via anonymous ftp to [cdsarc.u-strasbg.fr](ftp://cdsarc.u-strasbg.fr) (130.79.128.5) or via <http://cdsarc.u-strasbg.fr/viz-bin/cat/J/A+A/645/A64>

** Based on observations obtained at ESO Paranal Observatory, program 0104.D-0059.

Based on these chemical signatures, recent quantitative analyses have estimated that about 11% of the stellar MW halo originated from now defunct GCs (Martell & Grebel 2010; Martell et al. 2011; Koch et al. 2019a; Hanke et al. 2020a)¹, an order of magnitude that is bolstered by simulations (e.g., Reina-Campos et al. 2020). Typically, such studies employ low-resolution spectroscopy, which is suitable to determine CN-band strengths, but is not sufficient to perform detailed chemical abundance analyses that inform us about the chemical properties of the progenitor cluster (cf. Ramírez et al. 2012; Lind et al. 2015; Hendricks et al. 2016; Majewski et al. 2017; Fernández-Trincado et al. 2016, 2017). Taking the chemical identification of potentially former GC stars in the halo field one step further, Hanke et al. (2020a) added the kinematic dimensions afforded by the astrometry from the second data release (DR2) of the *Gaia* mission (Lindegren et al. 2018; Gaia Collaboration 2018). This allowed us not only to detect extra-tidal stars around known GCs, but also to trace back stars with common phase-space portions to potentially common progenitors (see also Savino & Posti 2019). In addition to disrupting GCs in the present-day MW halo, we also need to consider the accretion of (dwarf) galaxy satellites. On the one hand, this leads to the donation of their GC systems, thereby increasing the census of the GC population in the Galaxy (Cohen 2004; Forbes & Bridges 2010; Law & Majewski 2010; Carretta et al. 2017; Massari et al. 2019; Myeong et al. 2019; Kruijssen et al. 2019; Koch & Côté 2019; Forbes 2020). On the other hand, the most massive GCs in the MW system are often considered the former nuclei of disrupted dwarf galaxies, leading to broad abundance spreads and pronounced multiple populations that are unequalled in the lower-mass star clusters (Bassino & Muzzio 1995; Sarajedini & Layden 1995; Forbes et al. 2004; Hilker et al. 2004; Kayser et al. 2006; Johnson & Pilachowski 2010). Of these clusters the most massive GC in the MW system, ω Centauri (\equiv NGC 5139; hereafter ω Cen), has long been discussed as the core of a dwarf galaxy satellite (e.g., Lee et al. 1999; Bekki & Freeman 2003; Romano et al. 2007; Valcarce & Catelan 2011); its metallicities show a broad range from -2.5 to -0.8 dex and its chemical abundance inhomogeneities are many (Freeman & Rodgers 1975; Cohen 1981; Suntzeff & Kraft 1996; Hilker et al. 2004; McWilliam & Smecker-Hane 2005; Johnson & Pilachowski 2010; Villanova et al. 2014; Magurno et al. 2019; Johnson et al. 2020).

Based on a large spectroscopic sample from the RAdial Velocity Experiment (RAVE; Steinmetz et al. 2006; Kordopatis et al. 2013), Fernández-Trincado et al. (2015) kinematically associated 15 halo stars with ω Cen that were either subject to high-velocity ejections from it some 200 Myr ago or that had had close encounters with this particular GC at high relative velocities. In this work we present a high-resolution, high signal-to-noise (S/N) chemical abundance analysis of one of these candidates, the metal-poor ($[\text{Fe}/\text{H}] \sim -2$ dex) field star J110842.1–715260 (hereafter J110842)². As the relative velocity in the close encounter with ω Cen, at $v_{\text{rel}} = 275 \text{ km s}^{-1}$, is rather high, Fernández-Trincado et al. (2015) concluded that it is unlikely that this star (and other similar ones) directly escaped from the GC, rather that it encountered and interacted with the

GC between 45 and 290 Myr ago³. The full sample of the RAVE- ω Cen associates shows chemical abundances that are consistent with the stellar populations of this object; however, the RAVE spectra only allowed the determination of the α -elements Mg, Si, and Ti, and Al and Ni. For J110842 only Al and Ni could be determined. Therefore, a more complete sampling of the abundance space has yet to be conducted, in order to investigate whether the origin of this star is indeed similar to that of ω Cen stars and, if so, whether it classifies as a first- or second-generation star.

This paper is organized as follows. In Sect. 2 we describe the data, followed by details of the abundance analysis in Sect. 3. The resulting chemical abundances are presented in Sect. 4. We discuss the results in the context of ω Cen’s chemodynamical properties in Sect. 5.

2. Data

Star J110842 was observed on the night of March 03, 2020, with the Ultraviolet and Visual Echelle Spectrograph (UVES; Dekker et al. 2000) at the Very Large Telescope (Program 0104.D-0059; P.I. C.J. Hansen). We employed the 390/564 setting with dichroic 1, leading to a broad wavelength coverage of 3285–4518, 4623–5600, and 5672–6647 Å, and a high spectral resolving power of $R \sim 40\,000$. An exposure time of 2700 s yielded a S/N of ~ 50 , 120, and 150 per pixel at 4000, 5200, and 6200 Å. The data were reduced in the standard manner using the ESO UVES reduction workflow recipes (version 6.1.3) that perform bias correction, order tracing, flat fielding, and wavelength calibration using calibration data that were obtained on the same day as the observations.

We measured the star’s radial velocity from a cross-correlation against a template of similar stellar parameters using the Image Reduction and Analysis Facility (IRAF) *fxcor* task. This yielded a heliocentric velocity of $v_{\text{HC}} = 273.1 \pm 0.1 \text{ km s}^{-1}$, which agrees well with the values reported from the lower-resolution RAVE and *Gaia* spectra to within 0.4 km s^{-1} (see Table 1).

3. Chemical abundance analysis

We performed a standard abundance analysis that employed a mixture of equivalent width (EW) measurements, carried out via Gaussian fits with the IRAF *splot* task, and spectrum synthesis. Here we employed the same line list as in Koch & McWilliam (2014, see Table 2) with further additions in the syntheses from Biémont et al. (2000), Den Hartog et al. (2003, 2006), Lawler et al. (2007, 2008, 2009), Sneden et al. (2009), and Hansen et al. (2013).

Hyperfine splitting was included where appropriate. The main abundance analysis was carried out using the ATLAS grid of one-dimensional, 72-layer, plane-parallel, line-blanketed Kurucz models without convective overshoot and the α -enhanced opacity distribution functions AODFNEW (Castelli & Kurucz 2003). We further assumed that local thermodynamic equilibrium (LTE) holds for all species. All computations relied on the stellar abundance code MOOG (2014 version Sneden 1973) unless noted otherwise.

³ Depending on the adopted Galactic potential. The orbital analysis of Fernández-Trincado et al. (2015) also relied on proper motions from the UCAC4 (Zacharias et al. 2013), which, however, are in good agreement with the latest *Gaia* values.

¹ This value depends, among other factors, on the adopted fraction of first-generation stars that were lost from the GCs at early times. While Koch et al. (2019a) adopt a fraction of 56%, the recent analysis of Hanke et al. (2020a) assigns larger values of 50–80%, which would raise the inferred halo fraction to the 20% level.

² This star was observed as part of the CERES project (“Chemical Evolution of R-process Elements in Stars”) and thus has the alternate ID CES1108–7153 (Hansen et al., in prep.).

Table 1. Properties of the target star.

Parameter	Value	Reference
α (J2000.0)	11:08:42.12	1
δ (J2000.0)	-71:52:59.9	1
G	11.117	2
G_{BP}	11.117	2
G_{RP}	10.239	2
L	1224 L_{\odot}	2
ν_{HC}	$273.1 \pm 0.1 \text{ km s}^{-1}$	3
T_{eff}	$4421 \pm 50 \text{ K}$	3
$\log g$	0.61 ± 0.10	3
ξ	$2.19 \pm 0.10 \text{ km s}^{-1}$	3
[M/H]	-2.10	3
d (<i>Gaia</i>)	$4.6^{+0.7}_{-0.5} \text{ kpc}$	4
μ_{α}	-6.66 ± 0.05	1
μ_{δ}	0.50 ± 0.04	1

References. (1) [Lindegren et al. \(2018\)](#); (2) [Gaia Collaboration \(2018\)](#); (3) this work; (4) [Bailer-Jones et al. \(2018\)](#).

Table 2. Linelist.

λ [Å]	Species	EP [eV]	$\log gf$	EW [mÅ]
6300.31	O I	0.00	-9.819	42
6363.79	O I	0.02	-10.303	7
5682.63	Na I	2.10	-0.700	46
5688.20	Na I	2.10	-0.460	66
6154.23	Na I	2.10	-1.560	9
6160.75	Na I	2.10	-1.260	17
4702.99	Mg I	4.35	-0.440	141
5528.42	Mg I	4.35	-0.481	156
5711.09	Mg I	4.33	-1.728	62

Notes. The full table is available at the CDS.

3.1. Stellar parameters

To derive stellar parameters, we used photometry provided by *Gaia* DR2. We populated the parameter space using computed ATLAS9 model atmosphere grids by [Castelli & Kurucz \(2003\)](#). This contains theoretical values of $G_{\text{BP}}-G_{\text{RP}}$, A_G , $E(G_{\text{BP}}-G_{\text{RP}})$, and bolometric corrections for each set of effective temperatures (T_{eff}), surface gravities ($\log g$), and metallicities ([Fe/H]) in the range of $3500 \leq T_{\text{eff}} \leq 6000 \text{ K}$, $0 \leq \log g \leq 4$, and $-4 \leq [\text{Fe}/\text{H}] \leq +0.5$. The reddening $E(G_{\text{BP}}-G_{\text{RP}})$ was computed using the reddening law of [Fitzpatrick et al. \(2019\)](#). In order to determine the best suite of the stellar parameters T_{eff} and $\log g$ for our target star J110842, the following iterative procedure was used:

1. The initial metallicity was estimated via the literature value of -1.6 ([Kunder et al. 2017](#)) and T_{eff} was derived by interpolating in $G_{\text{BP}}-G_{\text{RP}}$;
2. The bolometric correction was derived by interpolation from the new T_{eff} ;
3. $\log g$ was derived using the above bolometric correction and T_{eff} ;
4. A_G and $E(G_{\text{BP}}-G_{\text{RP}})$ were derived by interpolating in T_{eff} ;
5. G and $G_{\text{BP}}-G_{\text{RP}}$ were de-reddened using the reddening maps by [Schlafly & Finkbeiner \(2011, \$A_V = 0.81\$ \)](#);

6. The procedure was iterated until the difference in temperature between successive runs was less than 50 K.

The microturbulence velocities (ξ) in each step were estimated using the calibration of [Mashonkina et al. \(2017\)](#). Here we note that the final value of 2.19 km s^{-1} provides an excellent balance in the plot of line-by-line abundances with equivalent widths of the Fe I lines.

The final photometric parameter set of $T_{\text{eff}} = 4421 \text{ K}$ and $\log g = 0.61 \text{ dex}$ yields an iron abundance from the neutral and ionized species of $[\text{Fe I}/\text{H}] = -1.84$ and $[\text{Fe II}/\text{H}] = -2.10 \text{ dex}$, respectively. Thus, there is a pronounced ionization imbalance seen in this star when employing the photometrically derived surface gravity. Moreover, no equilibrium of the Fe I abundance with excitation potential could be reached upon using the photometric temperature. This is a well-known problem for stars more metal poor than about -1.5 dex , as has been systematically evaluated by [Mucciarelli & Bonifacio \(2020\)](#). The suggested reasons for these discrepancies are the commonly used assumptions in the spectroscopic approach, to wit, LTE and/or the one-dimensional treatment of the atmospheres. Therefore, following the recommendation of [Mucciarelli & Bonifacio \(2020\)](#), we adopt in the following the stellar parameters derived photometrically above and we continue by choosing the Fe abundance from the ionized species as the metallicity scale of star J110842.

3.2. Abundance errors

The statistical errors on our abundance ratios were determined via the standard deviation and the number of measured lines per element used to derive its abundance. Furthermore, we performed a systematic error analysis by varying each stellar parameter about its respective uncertainty: $T_{\text{eff}} \pm 50 \text{ K}$, $\log g \pm 0.1 \text{ dex}$, $[\text{M}/\text{H}] \pm 0.1 \text{ dex}$, and $\xi \pm 0.1 \text{ km s}^{-1}$. We further ran the identical analyses as above using solar-scaled opacity distributions (ODFNEW) and take one-quarter of the ensuing deviation to mimic an ignorance of the α -enhancement in the star of 0.1 dex. The respective deviations of the abundance ratios from the bona fide results from the unaltered atmospheres are listed in Table 3; a conservative upper limit to the total systematic uncertainty in terms of the squared sum of all contributions is given in the last column, although strong correlations between the impacts from the various atmospheric parameters can be expected (see, e.g., [McWilliam et al. 1995](#); [Hanke et al. 2020b](#)).

4. Results

All abundance results and the errors as described above are listed in Table 4. These values adopt the solar abundance scale of [Asplund et al. \(2009\)](#). In the following figures we place our results into context with the MW halo, bulge, and disks, and ω Cen p. For ω Cen we used the data of [Johnson & Pilachowski \(2010\)](#) and [Simpson et al. \(2020\)](#), who chemodynamically extracted cluster candidates from the GALAH survey ([De Silva et al. 2015](#)). Here we also show the abundance ratios of those stars. Figures 1 and 4 show the abundance comparison, where we restrict ourselves to those elements in common between our study and that of ω Cen p. The remaining elements, though not explicitly shown, are discussed individually below.

4.1. Metallicity

At $[\text{Fe II}/\text{H}] = -2.10 \text{ dex}$, J110842 samples the metal-poor tail of ω Cen's metallicity distribution (Fig. 1, top). This distribution has long been known to show a large dispersion and covers a range of more than 1.7 dex ([Johnson & Pilachowski 2010](#)). As this object

Table 3. Systematic error analysis.

Species	T_{eff} ± 50 K	$\log g$ ± 0.1 dex	[M/H] ± 0.1 dex	ξ ± 0.1 km s $^{-1}$	ODF	Sys.
CH (<i>G</i> -band)	± 0.03	∓ 0.03	∓ 0.07	∓ 0.01	-0.08	0.08
O I	± 0.02	± 0.04	± 0.03	∓ 0.01	-0.08	0.07
Na I	± 0.05	∓ 0.02	∓ 0.01	∓ 0.01	0.04	0.06
Mg I	± 0.06	∓ 0.03	∓ 0.02	∓ 0.04	0.05	0.08
Si I	± 0.02	± 0.01	∓ 0.01	∓ 0.01	0.01	0.03
Ca I	± 0.07	∓ 0.02	∓ 0.02	∓ 0.04	0.05	0.09
Sc II	∓ 0.01	± 0.03	± 0.02	∓ 0.03	-0.06	0.06
Ti I	± 0.14	∓ 0.02	∓ 0.03	∓ 0.06	-0.03	0.16
Ti II	∓ 0.01	± 0.03	± 0.02	∓ 0.04	-0.05	0.06
V I	± 0.11	∓ 0.02	∓ 0.02	∓ 0.01	0.03	0.12
Cr I	± 0.12	∓ 0.02	∓ 0.03	∓ 0.05	0.02	0.14
Mn I	± 0.11	∓ 0.03	∓ 0.03	∓ 0.03	0.05	0.12
Fe I	± 0.08	∓ 0.02	∓ 0.02	∓ 0.05	0.04	0.10
Fe II	∓ 0.04	± 0.04	± 0.02	∓ 0.02	-0.06	0.07
Co I	± 0.09	∓ 0.02	∓ 0.02	∓ 0.04	0.05	0.11
Ni I	± 0.06	∓ 0.01	∓ 0.01	∓ 0.02	0.04	0.09
Cu I	± 0.08	∓ 0.01	∓ 0.01	∓ 0.02	0.04	0.09
Zn I	∓ 0.03	± 0.01	± 0.01	∓ 0.03	-0.01	0.05
Sr II	± 0.01	± 0.01	± 0.02	∓ 0.01	-0.05	0.03
Y II	∓ 0.01	± 0.03	± 0.02	∓ 0.04	-0.05	0.06
Zr II	∓ 0.01	± 0.03	± 0.02	∓ 0.01	-0.05	0.05
Ba II	± 0.03	± 0.04	± 0.02	∓ 0.08	-0.09	0.11
La II	± 0.02	± 0.02	± 0.01	∓ 0.04	-0.03	0.05
Ce II	± 0.01	± 0.03	± 0.02	∓ 0.01	-0.06	0.05
Pr II	± 0.02	± 0.03	± 0.02	∓ 0.01	-0.07	0.06
Nd II	± 0.01	± 0.02	± 0.01	∓ 0.03	-0.03	0.04
Sm II	± 0.02	± 0.03	± 0.02	∓ 0.01	-0.05	0.05
Eu II	± 0.02	± 0.02	± 0.02	∓ 0.07	-0.06	0.08
Gd II	± 0.01	± 0.02	± 0.01	∓ 0.01	-0.04	0.03
Dy II	± 0.02	± 0.02	± 0.01	∓ 0.02	-0.04	0.04
Hf II	± 0.05	± 0.05	± 0.05	∓ 0.03	-0.02	0.09
Pb II	± 0.10	∓ 0.02	∓ 0.07	∓ 0.01	0.10	0.13

Table 4. Abundance results.

Species	[X/Fe]	σ	N	Species	[X/Fe]	σ	N	Species	[X/Fe]	σ	N
CH (<i>G</i> -band)	-0.85	...	1 ^S	Mn I	-0.50	0.12	9 ^H	La II	0.40	0.09	6 ^H
O I	0.65	0.28	2 ^S	Fe I	-1.91	0.13	78	Ce II	0.13	0.07	3 ^S
Na I	0.51	0.05	4	Fe II	-2.01	0.05	8	Pr II	0.32	0.07	5 ^S
Mg I	0.54	0.14	3	Co I	0.15	0.15	5 ^H	Nd II	0.19	0.09	5 ^S
Si I	0.48	0.06	2	Ni I	-0.03	0.10	15	Sm II	0.24	0.07	3 ^S
Ca I	0.31	0.20	15	Cu I	-0.33	0.10	2	Eu II	0.00	...	1 ^S
Sc II	0.11	0.14	2 ^H	Zn I	0.13	0.08	2	Gd II	0.15	...	1 ^S
Ti I	0.29	0.12	11	Sr II	<0.30	...	1 ^S	Dy II	0.23	0.13	3 ^S
Ti II	0.38	0.15	10	Y II	0.10	0.08	5	Er II	-0.02	...	1 ^S
V I	0.13	0.03	6	Zr II	0.36	...	1	Hf II	-0.05	...	1 ^S
Cr I	-0.06	0.07	7	Ba II	0.23	0.01	3 ^H	Pb I	0.60	...	1 ^S

Notes. Abundance ratios for ionized species are given relative to Fe II. For iron itself, [Fe/H] is listed. The line-to-line scatter, σ , and number of measured lines, N , indicate the statistical error. “H” indicates that hyperfine structure was accounted for; “S” denotes abundances that were derived from spectrum synthesis.

is commonly considered the nucleus of a formerly more massive dwarf galaxy, such a large spread and the occurrence of very metal-poor stars down to -2.5 dex (Johnson et al. 2020) is not surprising as this is seen in many dwarf spheroidal galaxies in the Local Group (e.g., Koch 2009).

4.2. Light elements: C, N, O, Na

Fernández-Trincado et al. (2015) noted that ω Cen is special in that it covers a broad range in all of their analyzed abundance patterns to the point that it overlaps with all MW components.

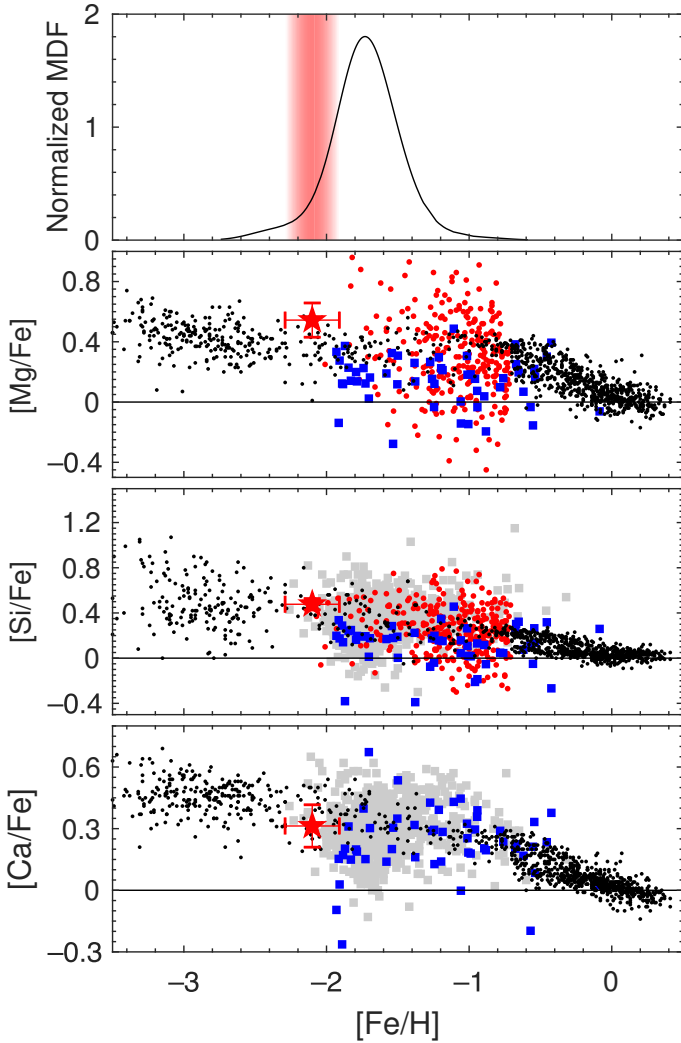


Fig. 1. Chemical abundances of J110842 (red star) in comparison with ω Cen (gray squares: Johnson & Pilachowski 2010; blue squares: Simpson et al. 2020) and the MW halo (Roederer et al. 2014) and disks (Bensby et al. 2014), shown as black dots. The 329 candidate ω Cen associates from Fernández-Trincado et al. (2015) are indicated as red points. The error bar accounts for statistical and systematic uncertainties. *Top panel:* error-weighted metallicity distribution from Johnson et al. (2020), on which is highlighted the 1σ error range of the metallicity determined in the present work.

They concluded that any similarity in these properties is “not very useful” to constrain the origin of the stars. However, their element abundances, drawn from the RAVE survey, were only limited to Fe, Al, and Ni⁴. Therefore, we highlight here some of the elements that provide a greater clue to any potential origin of J110842.

One of the characteristics of GCs is the presence of multiple stellar generations and the ensuing light-element variations as a result of p -capture reactions in an early generation of stars (Kayser et al. 2008; Carretta et al. 2009; Bastian & Lardo 2018). These variations include bimodalities in CN and associated anticorrelations with CH strength. We measured the strength of the commonly used CH and CN bands using the index definitions of Norris et al. (1981), which was then translated into a $\delta S(3839)$

⁴ Abundances for the other α -elements (Mg, Si, Ti) were reported for the remainder of the ω Cen candidates in Fernández-Trincado et al. (2015), but had not been derived for star J110842.

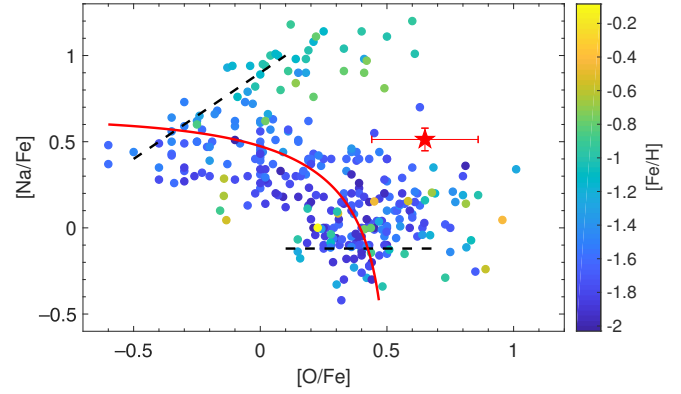


Fig. 2. Sodium-oxygen anticorrelation using data from Marino et al. (2011) and Simpson et al. (2020), color-coded by metallicity. Star J110842 is indicated by a red star. We also indicate the empirical separations into first, second, and extreme generations (dashed black) and the simplistic dilution model (red line) by Carretta et al. (2009).

index to remove dependencies on evolutionary status (Martell & Grebel 2010; Koch et al. 2019a). The main uncertainty in this quantity is the required absolute magnitude of the star, which relies on its distance that still shows large errors (see Table 1). At $\delta S(3839) = 0.253$, J110842 qualifies as a CN-strong star (see, e.g., Fig. 5 in Koch et al. 2019a). As such it would be tempting to characterize it as a second-generation star, bolstering its origin in a GC-like environment, which also requires it to be CH-weak. We measured an S(CH) index of 0.819, and combined with the lower [C/Fe] we conclude that this instead argues in favor of a C-normal star (e.g., Kirby et al. 2015; Koch et al. 2019b), with values that are appropriate for its luminosity of $1224 L_{\odot}$ (Gaia Collaboration 2018).

Similarly, genuine GCs are infamous for having a pronounced Na-O anticorrelation, which is also prominently seen in ω Cen (Norris & Da Costa 1995a; Gratton et al. 2011; Simpson et al. 2020) and particularly extended below -1.3 dex (Marino et al. 2011). In Fig. 2 we show our Na and O measurements for J110842 superimposed on the literature data from the above sources.

While the value of [O/Fe] for J110842 at 0.65 dex is compatible with that of a metal-poor, α -enhanced halo star, the [Na/Fe] value of 0.55 dex is rather high and makes this star fall into the regime of Na-strong second-generation GC stars. We note that all our abundances have been derived in an LTE framework. However, interpolating the grid of non-LTE (NLTE) corrections by Lind et al. (2011) yields a departure from the LTE abundance of ~ -0.06 dex, while the correction for oxygen is null for the parameters similar to our star (Sitnova et al. 2013). Thus, even if NLTE corrections are accounted for, we cannot exclude a second-generation origin for this star based on its Na abundance, and marginally supported by its O abundance and CN strength.

Finally, we note that GCs often show strong variations in Al that mildly correlate with Mg, owing to the hot branches of proton-burning. However, the spectral range of our UVES setting did not allow us to determine an Al abundance from the 6696 Å line. Conversely, the blue line at 3961 Å lies in the wing of the strong Ca H line, making a meaningful abundance determination difficult. Instead, we use the value of Fernández-Trincado et al. (2015) for further discussion. Considering the higher Mg and O abundances in our star, their adopted [Al/Fe] of 0.38 dex lies at the low branch of Al abundances, which is consistent with an association with a second stellar population in a GC (e.g., Carretta et al. 2013).

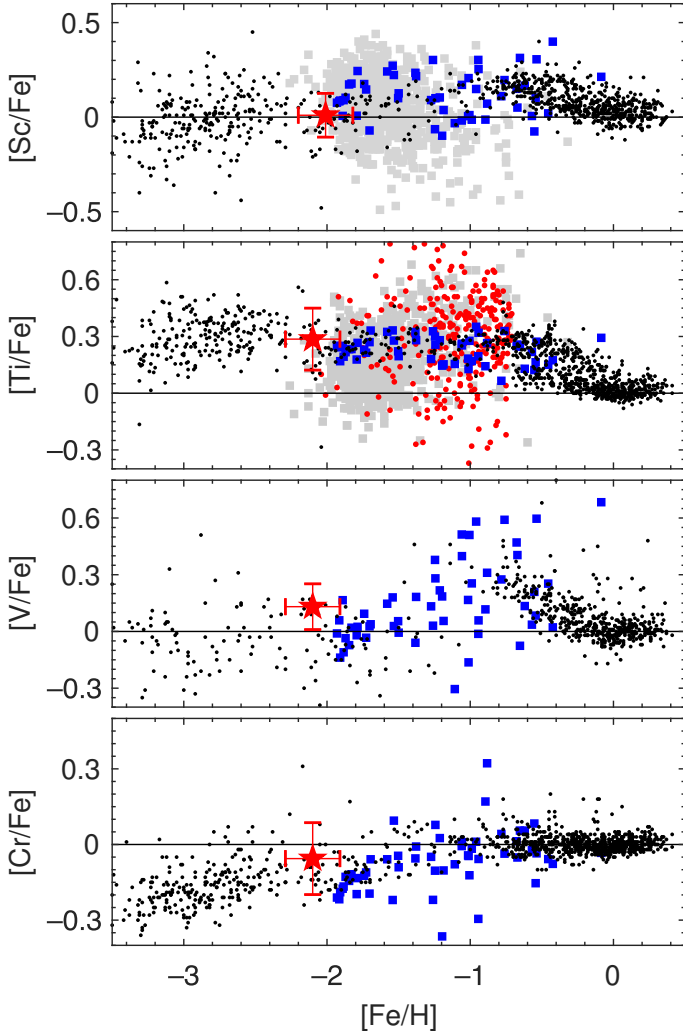


Fig. 3. Same as Fig. 1, but for the lighter Fe-peak elements. Disk values for Sc and V are from Battistini & Bensby (2015).

4.3. α -elements: Mg, Si, Ca, Ti

The α -elements in J110842 present few surprises. At an $[\alpha/\text{Fe}]$ value of 0.42 ± 0.03 dex it falls square on the α -plateau delineated by metal-poor halo stars and the bulk of ωCen 's broad abundance space (Figs. 1 and 3). This indicates enrichment via standard nucleosynthesis in supernovae of type II (SNe II) and does not allow us to further investigate the question of a peculiar origin of this star based on these chemical tracers.

4.4. Fe-peak elements: Sc, V, Cr, Mn, Co, Ni, Cu

As is true for the α -elements, the Fe-peak elements also follow the trends outlined by metal-poor halo and ωCen stars (see Figs. 3, 4, and also Cohen 1981; Norris & Da Costa 1995b; Smith et al. 1995; Pancino et al. 2011; Magurno et al. 2019 for ωCen) and that are mainly set by SN Ia nucleosynthesis (e.g., Kobayashi et al. 2006).

Copper (bottom panel of Fig. 4), in contrast, has been a matter of high interest in this GC, and Cunha et al. (2002) noted that Cu stays approximately constant and remains below the trend seen in halo stars over a broad metallicity range of ~ -2 to -0.8 dex. This was thought as being due to a lower-level contribution of SNe Ia to the chemical evolution in that metallicity range. Furthermore, by chemical similarity to the Sagittarius

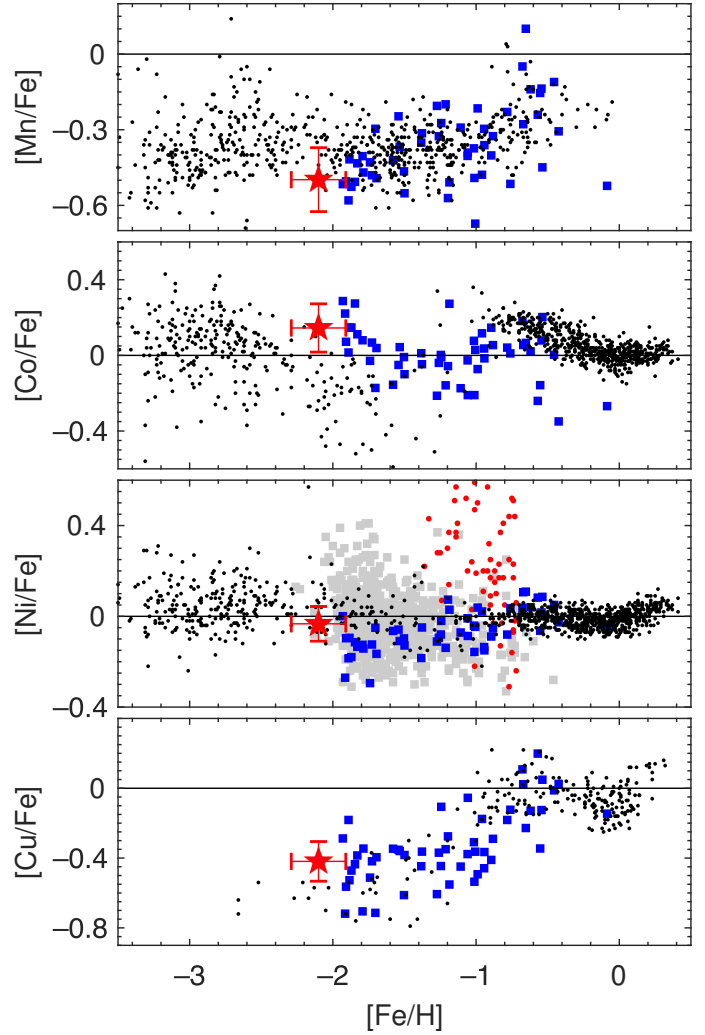


Fig. 4. Same as Fig. 1, but for the remaining Fe-peak elements. Abundances for Mn are from Sobeck et al. (2006), Co data are from Battistini & Bensby (2015), and Cu for the MW disks and halo are from Mishenina et al. (2002, 2011).

dwarf galaxy, McWilliam & Smecker-Hane (2005) lend support to the notion that ωCen is rather the nucleus of a former, more massive system. The target of this study, J110842, overlaps with the metal-poor halo and the metal-poor tail of the ωCen distribution. Our own values and the cited literature values were derived under the assumption of LTE. It appears that the Cu abundances are affected by NLTE effects (Andrievsky et al. 2018; Shi et al. 2018), although different model-atoms and NLTE codes provide different results, especially at low metallicity. This notion is reinforced by the observed deviation between Cu I and Cu II abundances observed by Roederer & Barklem (2018). Bonifacio et al. (2010) found strong granulation effects on the resonance lines (although not used here); however, the combined effect of granulation and NLTE effects still needs to be investigated. It would therefore be interesting to reinvestigate the Cu abundances in ωCen , and in J110842, using a more sophisticated modeling.

We can also use our measurements to address the broader context of Galactic chemical evolution. Here Hawkins et al. (2015) posited that the $[\text{Mg}/\text{Mn}]$ versus $[\text{Al}/\text{Fe}]$ plane is a powerful indicator for an origin in major, dwarf-galaxy-like accretion events versus in situ formed stars that are enhanced in the α -elements. In J110842 we measured a very high value for

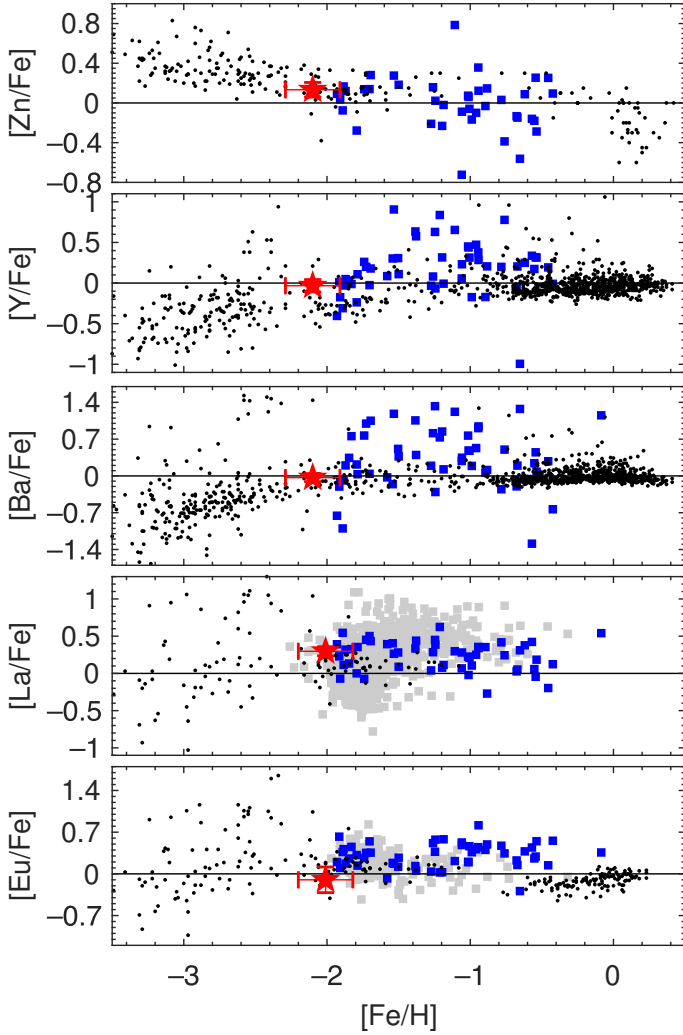


Fig. 5. Same as Fig. 1, but for the neutron-capture elements ($Z \geq 30$). The reference MW abundances are from [Barbuy et al. \(2015\)](#) for Zn, and from [Koch & Edvardsson \(2002\)](#) for Eu.

[Mg/Mn] of 1.04 ± 0.09 dex. If we had taken into account NLTE effects, this overabundance would be even larger ([Bergemann et al. 2019](#)). In order to qualify as an accreted object, the [Al/Fe] abundance in J110842 would need to be subsolar at its Mg and Mn abundances, according to the distinctive line in [Horta et al. \(2021\)](#). However, since [Fernández-Trincado et al. \(2015\)](#) reported on a higher [Al/Fe] of 0.38 dex, this instead argues for an in situ formation or that the birth environment has chemically evolved.

4.5. *n*-capture elements: Zn, Sr, Y, Zr, Ba, La, Ce, Pr, Nd, Sm, Eu, Gd, Dy, Er, Hf, Pb

Our abundance results for the selected heavy elements overlapping with the literature for ω Cen are shown in Fig. 5. In addition, the values for J110842 for these elements are in close agreement with metal-poor halo stars and the metal-poor end of the GC abundance distribution, indicating that the same nucleosynthetic processes were at play.

Among the neutron-capture elements we particularly note the *s*-process elements Y, Ba, and La (middle three panels of Fig. 5). Dating back to [Lloyd Evans \(1983\)](#), a bimodal behav-

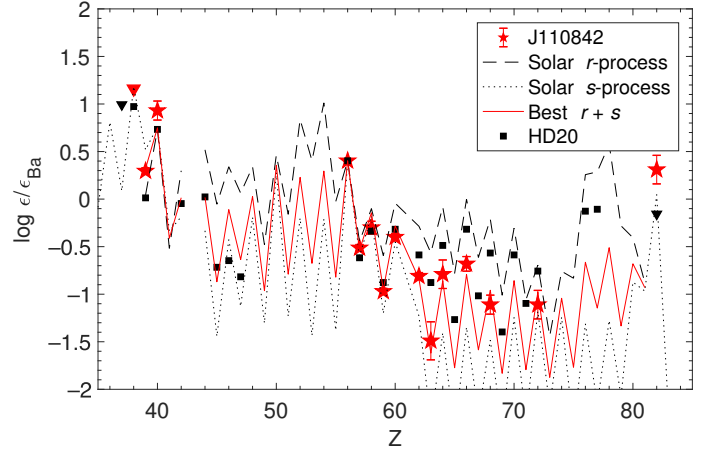


Fig. 6. Abundance distribution of the heavy elements, normalized to Ba. Also shown are the solar *s*- and *r*-process contributions ([Burris et al. 2000](#)) and the best-fit linear combination of the contributions. Finally, we overplot the *r*-process benchmark star HD 20 as black squares ([Hanke et al. 2020b](#)).

ior has now been established; for instance, from their high-resolution analysis of 113 RR Lyr stars in ω Cen [Magurno et al. \(2019\)](#) reported solar [Y/Fe] values for stars more metal poor than approximately -1.5 dex, while the more metal-rich component showed enhanced element abundances. This is also seen in terms of a significantly larger scatter above that metallicity cut in the data of [Simpson et al. \(2020\)](#), among others. Furthermore, the values for [La/Fe] found by [Johnson & Pilachowski \(2010\)](#) also show a clear bimodality. This has been interpreted in terms of markedly different stellar populations, where the more metal-rich component was (self-)enriched over a long timescale by low-mass asymptotic giant branch stars (e.g., [Norris & Da Costa 1995b](#); [Smith et al. 2000](#); [Cunha et al. 2002](#)), while the sudden increase in the abundance ratios with [Fe/H] is compatible with ω Cen being the remnant of a more massive dwarf galaxy ([Romano et al. 2007](#); [Magurno et al. 2019](#)). The solar value of [Y/Fe] in J110842 at its low metallicity and its solar [Ba/Fe] are fully compatible with the lower-metallicity component.

Figure 6 shows the overall abundance distribution of heavy ($Z > 30$) elements we were able to measure in J110842. Here we note that Sr in its spectrum shows very strong resonance lines (at 4077 and 4215 Å) that are likely saturated. Therefore, we were only able to place a limit of ~ 0.3 dex on the [Sr/Fe] value. As noted before, J110842 is mainly characterized by standard nucleosynthesis and the majority of elements lie between the (solar) *s*- and *r*-process distributions, as is expected if we consider, at this metallicity, that AGB stars have already started to contribute some *s*-process material to the Galactic chemical evolution (e.g., [Simmerer et al. 2004](#)). A χ^2 fit indicates that J110842 has received an admixture of *s*-process elements at the 60% level. Another assessment of the *r*- and *s*-process contributions can be made in comparison to the cleaner *r*-process tracer HD 20 (black symbols in Fig. 6), which at a metallicity that is lower than the Sun's displays a very clean *r*-process pattern. However, in this direct comparison J110842 also comes out as a *r*-*s* mixed star with not just one main polluter governing its formation. A further characterization of the donors to the chemical enrichment of this star, such as SNe or AGB stars, cannot be unambiguously made in stars like J110842, where the effects of mixing and dilution need to be properly dealt with ([Magg et al. 2020](#); [Hansen et al. 2020](#)).

5. Discussion

In our endeavor to find signs of a chemical association of the halo star J110842 with the massive GC ω Cen, as has been previously suggested from their relative dynamics, we performed an extensive chemical abundance study. We showed that the majority of the heavier elements ($Z \geq 12$) is fully compatible with those seen in ω Cen p. This is, however, not surprising given the large overlap of the GC abundance space with that of metal-poor halo field stars at this metallicity (-2.1 dex), and cannot unambiguously argue for a GC origin of J110842. Here it is more interesting to look at the light elements. The high Na abundance and its characterization as a CN-strong star indeed lend support to the hypothesis that it is a former second-generation GC star, while the enhancement in O and its CH-normal nature appear to mitigate this.

Fernández-Trincado et al. (2015) argued that it is unlikely that stars with high relative encounter speeds have been ejected from ω Cen, but just had chance encounters when their orbits coincided. The central escape velocity of the GC is on the order of $60\text{--}100\text{ km s}^{-1}$ (Gnedin et al. 2002; Gao et al. 2015), which compares to the computed encounter velocity with J110842 in excess of 200 km s^{-1} . On the other hand, extreme horizontal branch stars at high tangential motions of up to $90\text{--}310\text{ km s}^{-1}$ have been found in ω Cen, and they are most likely to escape the GC within the next Myr or so (Gao et al. 2015), in which case a former origin of our target star within the GC remains plausible. Here we note that Lind et al. (2015) associate a halo star with typical GC signatures such as enhanced Al and low Mg abundances with having escaped from ω Cen at high speed. Such high-speed ejections ($>100\text{ km s}^{-1}$) are suggested if interactions with binaries or black holes are evoked (Gvaramadze et al. 2009; Lützgendorf et al. 2012).

As to the origin of ω Cen itself, Myeong et al. (2019) have associated it with the recently discovered massive Sequoia accretion event, while Ibata et al. (2019) paired it with the Fimbulthul stream. The latter poses an intriguing parallel to our star as its abundance distribution is very similar to the most metal-poor stream candidate analyzed by Simpson et al. (2020). This emphasizes the power of chemical tagging in meaningfully investigating the manifold of eclectic GC-stream-halo-field interfaces.

Acknowledgements. The authors thank the anonymous referee for a swift and constructive report. AJKH gratefully acknowledges funding by the Deutsche Forschungsgemeinschaft (DFG, German Research Foundation) – Project-ID 138713538 – SFB 881 (“The Milky Way System”), subprojects A03, A05, A11. CJH acknowledges support from the Max Planck Society and from the ChETEC COST Action (CA16117), supported by COST (European Cooperation in Science and Technology). LL, PB and EC gratefully acknowledge support from the French National Research Agency (ANR) funded project “Pristine” (ANR-18-CE31-0017). This work has made use of data from the European Space Agency (ESA) mission *Gaia* (<https://www.cosmos.esa.int/gaia>), processed by the *Gaia* Data Processing and Analysis Consortium (DPAC, <https://www.cosmos.esa.int/web/gaia/dpac/consortium>). Funding for the DPAC has been provided by national institutions, in particular the institutions participating in the *Gaia* Multilateral Agreement. This research made use of atomic data from the INSPECT database, version 1.0 (www.inspect-stars.com).


References

- Andrievsky, S., Bonifacio, P., Caffau, E., et al. 2018, *MNRAS*, **473**, 3377
 Asplund, M., Grevesse, N., Sauval, A. J., & Scott, P. 2009, *ARA&A*, **47**, 481
 Bailer-Jones, C. A. L., Rybizki, J., Founesneau, M., Mantelet, G., & Andrae, R. 2018, *AJ*, **156**, 58
 Barbuy, B., Friaça, A. C. S., da Silveira, C. R., et al. 2015, *A&A*, **580**, A40
 Bassino, L. P., & Muzzio, J. C. 1995, *The Observatory*, **115**, 256
 Bastian, N., & Lardo, C. 2018, *ARA&A*, **56**, 83
 Battistini, C., & Bensby, T. 2015, *A&A*, **577**, A9
 Bekki, K. 2019, *MNRAS*, **490**, 4007
 Bekki, K., & Freeman, K. C. 2003, *MNRAS*, **346**, L11
 Bensby, T., Feltzing, S., & Oey, M. S. 2014, *A&A*, **562**, A71
 Bergemann, M., Gallagher, A. J., Eitner, P., et al. 2019, *A&A*, **631**, A80
 Biémont, E., Garnir, H. P., Palmeri, P., Li, Z. S., & Svanberg, S. 2000, *MNRAS*, **312**, 116
 Bonifacio, P., Caffau, E., & Ludwig, H. G. 2010, *A&A*, **524**, A96
 Bragaglia, A., Carretta, E., D’Orazi, V., et al. 2017, *A&A*, **607**, A44
 Bullock, J. S., & Johnston, K. V. 2005, *ApJ*, **635**, 931
 Burris, D. L., Pilachowski, C. A., Armandroff, T. E., et al. 2000, *ApJ*, **544**, 302
 Carretta, E., Bragaglia, A., Gratton, R., & Lucatello, S. 2009, *A&A*, **505**, 139
 Carretta, E., Gratton, R. G., Bragaglia, A., D’Orazi, V., & Lucatello, S. 2013, *A&A*, **550**, A34
 Carretta, E., Bragaglia, A., Lucatello, S., et al. 2017, *A&A*, **600**, A118
 Castelli, F., & Kurucz, R. L. 2003, in *Modelling of Stellar Atmospheres*, eds. N. Piskunov, W. W. Weiss, & D. F. Gray, *IAU Symp.*, **210**, A20
 Cohen, J. G. 1978, *ApJ*, **223**, 487
 Cohen, J. G. 1981, *ApJ*, **247**, 869
 Cohen, J. G. 2004, *AJ*, **127**, 1545
 Cooper, A. P., D’Souza, R., Kauffmann, G., et al. 2013, *MNRAS*, **434**, 3348
 Cunha, K., Smith, V. V., Suntzeff, N. B., et al. 2002, *AJ*, **124**, 379
 Dekel, A., & Silk, J. 1986, *ApJ*, **303**, 39
 Dekker, H., D’Odorico, S., Kaufer, A., Delabre, B., & Kotzlowski, H. 2000, in *Optical and IR Telescope Instrumentation and Detectors*, eds. M. Iye, & A. F. Moorwood, *SPIE Conf. Ser.*, **4008**, 534
 Den Hartog, E. A., Lawler, J. E., Sneden, C., & Cowan, J. J. 2003, *ApJS*, **148**, 543
 Den Hartog, E. A., Lawler, J. E., Sneden, C., & Cowan, J. J. 2006, *ApJS*, **167**, 292
 De Silva, G. M., Freeman, K. C., Bland-Hawthorn, J., et al. 2015, *MNRAS*, **449**, 2604
 Eggen, O. J., Lynden-Bell, D., & Sandage, A. R. 1962, *ApJ*, **136**, 748
 Fernández-Trincado, J. G., Robin, A. C., Vieira, K., et al. 2015, *A&A*, **583**, A76
 Fernández-Trincado, J. G., Robin, A. C., Moreno, E., et al. 2016, *ApJ*, **833**, 132
 Fernández-Trincado, J. G., Zamora, O., García-Hernández, D. A., et al. 2017, *ApJ*, **846**, L2
 Fernández-Trincado, J. G., Beers, T. C., Tang, B., et al. 2019, *MNRAS*, **488**, 2864
 Fitzpatrick, E. L., Massa, D., Gordon, K. D., Bohlin, R., & Clayton, G. C. 2019, *ApJ*, **886**, 108
 Forbes, D. A. 2020, *MNRAS*, **493**, 847
 Forbes, D. A., & Bridges, T. 2010, *MNRAS*, **404**, 1203
 Forbes, D. A., Strader, J., & Brodie, J. P. 2004, *AJ*, **127**, 3394
 Freeman, K. C., & Rodgers, A. W. 1975, *ApJ*, **201**, L71
 Gaia Collaboration (Brown, A. G. A., et al.) 2018, *A&A*, **616**, A1
 Gao, X.-H., Xu, S.-K., & Chen, L. 2015, *Res. Astron. Astrophys.*, **15**, 1639
 Geisler, D., Wallerstein, G., Smith, V. V., & Casetti-Dinescu, D. I. 2007, *PASP*, **119**, 939
 Gnedin, O. Y., Zhao, H., Pringle, J. E., et al. 2002, *ApJ*, **568**, L23
 Gratton, R. G., Johnson, C. I., Lucatello, S., D’Orazi, V., & Pilachowski, C. 2011, *A&A*, **534**, A72
 Gratton, R., Bragaglia, A., Carretta, E., et al. 2019, *A&ARv*, **27**, 8
 Gvaramadze, V. V., Gualandris, A., & Portegies Zwart, S. 2009, *MNRAS*, **396**, 570
 Hanke, M., Koch, A., Hansen, C. J., & McWilliam, A. 2017, *A&A*, **599**, A97
 Hanke, M., Koch, A., Prudil, Z., Grebel, E. K., & Bastian, U. 2020a, *A&A*, **637**, A98
 Hanke, M., Hansen, C. J., Ludwig, H.-G., et al. 2020b, *A&A*, **635**, A104
 Hansen, C. J., Bergemann, M., Cescutti, G., et al. 2013, *A&A*, **551**, A57
 Hansen, C. J., Koch, A., Mashonkina, L., et al. 2020, *A&A*, **643**, A49
 Hawkins, K., Kordopatis, G., Gilmore, G., et al. 2015, *MNRAS*, **447**, 2046
 Hendricks, B., Boeche, C., Johnson, C. I., et al. 2016, *A&A*, **585**, A86
 Hilker, M., Kayser, A., Richtler, T., & Willemsen, P. 2004, *A&A*, **422**, L9
 Horta, D., Schiavon, R. P., Mackereth, J. T., et al. 2021, *MNRAS*, **500**, 1385
 Ibata, R. A., Bellazzini, M., Malhan, K., Martin, N., & Bianchini, P. 2019, *Nat. Astron.*, **3**, 667
 Johnson, C. I., & Pilachowski, C. A. 2010, *ApJ*, **722**, 1373
 Johnson, C. I., Dupree, A. K., Mateo, M., et al. 2020, *AJ*, **159**, 254
 Jordi, K., & Grebel, E. K. 2010, *A&A*, **522**, A71
 Kayser, A., Hilker, M., Richtler, T., & Willemsen, P. G. 2006, *A&A*, **458**, 777
 Kayser, A., Hilker, M., Grebel, E. K., & Willemsen, P. G. 2008, *A&A*, **486**, 437
 Kirby, E. N., Guo, M., Zhang, A. J., et al. 2015, *ApJ*, **801**, 125
 Kobayashi, C., Umeda, H., Nomoto, K., Tominaga, N., & Ohkubo, T. 2006, *ApJ*, **653**, 1145
 Koch, A. 2009, *Astron. Nachr.*, **330**, 675
 Koch, A., & Côté, P. 2019, *A&A*, **632**, A55
 Koch, A., & Edvardsson, B. 2002, *A&A*, **381**, 500

- Koch, A., & McWilliam, A. 2014, *A&A*, **565**, A23
- Koch, A., Grebel, E. K., & Martell, S. L. 2019a, *A&A*, **625**, A75
- Koch, A., Xi, S., & Rich, R. 2019b, *A&A*, **627**, A70
- Kordopatis, G., Gilmore, G., Steinmetz, M., et al. 2013, *AJ*, **146**, 134
- Kruijssen, J. M. D., Pfeffer, J. L., Reina-Campos, M., Crain, R. A., & Bastian, N. 2019, *MNRAS*, **486**, 3180
- Kunder, A., Kordopatis, G., Steinmetz, M., et al. 2017, *AJ*, **153**, 75
- Kuzma, P. B., Da Costa, G. S., & Mackey, A. D. 2018, *MNRAS*, **473**, 2881
- Law, D. R., & Majewski, S. R. 2010, *ApJ*, **718**, 1128
- Lawler, J. E., den Hartog, E. A., Labby, Z. E., et al. 2007, *ApJS*, **169**, 120
- Lawler, J. E., Sneden, C., Cowan, J. J., et al. 2008, *ApJS*, **178**, 71
- Lawler, J. E., Sneden, C., Cowan, J. J., Ivans, I. I., & Den Hartog, E. A. 2009, *ApJS*, **182**, 51
- Lee, Y. W., Joo, J. M., Sohn, Y. J., et al. 1999, *Nature*, **402**, 55
- Lee, K. H., Lee, H. M., Fahlman, G. G., & Sung, H. 2004, *AJ*, **128**, 2838
- Lind, K., Asplund, M., Barklem, P. S., & Belyaev, A. K. 2011, *A&A*, **528**, A103
- Lind, K., Koposov, S. E., Battistini, C., et al. 2015, *A&A*, **575**, L12
- Lindgren, L., Hernández, J., Bombrun, A., et al. 2018, *A&A*, **616**, A2
- Lloyd Evans, T. 1983, *MNRAS*, **204**, 975
- Lützgendorf, N., Gualandris, A., Kissler-Patig, M., et al. 2012, *A&A*, **543**, A82
- Magg, M., Nordlander, T., Glover, S. C. O., et al. 2020, *MNRAS*, **498**, 3703
- Magurno, D., Sneden, C., Bono, G., et al. 2019, *ApJ*, **881**, 104
- Majewski, S. R., Schiavon, R. P., Frinchaboy, P. M., et al. 2017, *AJ*, **154**, 94
- Marino, A. F., Milone, A. P., Piotto, G., et al. 2011, *ApJ*, **731**, 64
- Martell, S. L., & Grebel, E. K. 2010, *A&A*, **519**, A14
- Martell, S. L., Smolinski, J. P., Beers, T. C., & Grebel, E. K. 2011, *A&A*, **534**, A136
- Mashonkina, L., Jablonka, P., Pakhomov, Y., Sitnova, T., & North, P. 2017, *A&A*, **604**, A129
- Massari, D., Koppelman, H. H., & Helmi, A. 2019, *A&A*, **630**, L4
- McWilliam, A., & Smecker-Hane, T. A. 2005, *ApJ*, **622**, L29
- McWilliam, A., Preston, G. W., Sneden, C., & Searle, L. 1995, *AJ*, **109**, 2757
- Milone, A. P., Piotto, G., Renzini, A., et al. 2017, *MNRAS*, **464**, 3636
- Mishenina, T. V., Kovtyukh, V. V., Soubiran, C., Travaglio, C., & Busso, M. 2002, *A&A*, **396**, 189
- Mishenina, T. V., Gorbaneva, T. I., Basak, N. Y., Soubiran, C., & Kovtyukh, V. V. 2011, *Astron. Rep.*, **55**, 689
- Mucciarelli, A., & Bonifacio, P. 2020, *A&A*, **640**, A87
- Myeong, G. C., Vasiliev, E., Iorio, G., Evans, N. W., & Belokurov, V. 2019, *MNRAS*, **488**, 1235
- Naidu, R. P., Conroy, C., Bonaca, A., et al. 2020, *ApJ*, **901**, 48
- Norris, J. E., & Da Costa, G. S. 1995a, *ApJ*, **441**, L81
- Norris, J. E., & Da Costa, G. S. 1995b, *ApJ*, **447**, 680
- Norris, J., Cottrell, P. L., Freeman, K. C., & Da Costa, G. S. 1981, *ApJ*, **244**, 205
- Odenkirchen, M., Grebel, E. K., Rockosi, C. M., et al. 2001, *ApJ*, **548**, L165
- Pancino, E., Mucciarelli, A., Sbordone, L., et al. 2011, *A&A*, **527**, A18
- Pilachowski, C. A., Sneden, C., & Kraft, R. P. 1996, *AJ*, **111**, 1689
- Pillepich, A., Madau, P., & Mayer, L. 2015, *ApJ*, **799**, 184
- Ramírez, I., Meléndez, J., & Chanamé, J. 2012, *ApJ*, **757**, 164
- Reina-Campos, M., Hughes, M. E., Kruijssen, J. M. D., et al. 2020, *MNRAS*, **493**, 3422
- Roederer, I. U., & Barklem, P. S. 2018, *ApJ*, **857**, 2
- Roederer, I. U., Preston, G. W., Thompson, I. B., et al. 2014, *AJ*, **147**, 136
- Romano, D., Matteucci, F., Tosi, M., et al. 2007, *MNRAS*, **376**, 405
- Sarajedini, A., & Layden, A. C. 1995, *AJ*, **109**, 1086
- Savino, A., & Posti, L. 2019, *A&A*, **624**, L9
- Schlafly, E. F., & Finkbeiner, D. P. 2011, *ApJ*, **737**, 103
- Searle, L., & Zinn, R. 1978, *ApJ*, **225**, 357
- Shi, J. R., Yan, H. L., Zhou, Z. M., & Zhao, G. 2018, *ApJ*, **862**, 71
- Simmerer, J., Sneden, C., Cowan, J. J., et al. 2004, *ApJ*, **617**, 1091
- Simpson, J. D., Martell, S. L., Da Costa, G., et al. 2020, *MNRAS*, **491**, 3374
- Sitnova, T. M., Mashonkina, L. I., & Ryabchikova, T. A. 2013, *Astron. Lett.*, **39**, 126
- Smith, V. V., Cunha, K., & Lambert, D. L. 1995, *AJ*, **110**, 2827
- Smith, V. V., Suntzeff, N. B., Cunha, K., et al. 2000, *AJ*, **119**, 1239
- Sneden, C. A. 1973, PhD Thesis, The University of Texas at Austin, USA
- Sneden, C., Lawler, J. E., Cowan, J. J., Ivans, I. I., & Den Hartog, E. A. 2009, *ApJS*, **182**, 80
- Sobeck, J. S., Ivans, I. I., Simmerer, J. A., et al. 2006, *AJ*, **131**, 2949
- Steinmetz, M., Zwitter, T., Siebert, A., et al. 2006, *AJ*, **132**, 1645
- Suntzeff, N. B., & Kraft, R. P. 1996, *AJ*, **111**, 1913
- Tang, B., Liu, C., Fernández-Trincado, J. G., et al. 2019, *ApJ*, **871**, 58
- Valcarce, A. A. R., & Catelan, M. 2011, *A&A*, **533**, A120
- Villanova, S., Geisler, D., Gratton, R. G., & Cassisi, S. 2014, *ApJ*, **791**, 107
- Zacharias, N., Finch, C. T., Girard, T. M., et al. 2013, *AJ*, **145**, 44
- Zolotov, A., Willman, B., Brooks, A. M., et al. 2009, *ApJ*, **702**, 1058

Chemical Evolution of *R*-process Elements in Stars (CERES)

I. Stellar parameters and chemical abundances from Na to Zr^{★,★★}

Linda Lombardo¹ , Piercarlo Bonifacio¹, Patrick François¹, Camilla J. Hansen², Elisabetta Caffau¹, Michael Hanke³, Ása Skúladóttir^{4,5}, Almudena Arcones^{6,7}, Marius Eichler⁶, Moritz Reichert^{6,8}, Athanasios Psaltis⁶, Andreas J. Koch Hansen³, and Luca Sbordone⁹

¹ GEPI, Observatoire de Paris, Université PSL, CNRS, 5 place Jules Janssen, 92195 Meudon, France
e-mail: Linda.Lombardo@observatoiredeparis.psl.eu

² Goethe University Frankfurt, Institute for Applied Physics, Max-von-Laue Str. 11, 60438 Frankfurt am Main, Germany

³ Zentrum für Astronomie der Universität Heidelberg, Astronomisches Rechen-Institut, Mönchhofstr. 12, 69120 Heidelberg, Germany

⁴ Dipartimento di Fisica e Astronomia, Università degli Studi di Firenze, Via G. Sansone 1, 50019 Sesto Fiorentino, Italy

⁵ INAF/Osservatorio Astrofisico di Arcetri, Largo E. Fermi 5, 50125 Firenze, Italy

⁶ Institut für Kernphysik, Technische Universität Darmstadt, Schlossgartenstr. 2, Darmstadt 64289, Germany

⁷ GSI Helmholtzzentrum für Schwerionenforschung GmbH, Planckstr. 1, Darmstadt 64291, Germany

⁸ Departament d'Astronomia i Astrofísica, Universitat de València, Edifici d'Investigació Jeroni Munyoz, C/ Dr. Moliner, 50, 46100 Burjassot, València, Spain

⁹ ESO – European Southern Observatory, Alonso de Cordova 3107, Vitacura, Santiago, Chile

Received 3 May 2022 / Accepted 30 May 2022

ABSTRACT

Aims. The Chemical Evolution of *R*-process Elements in Stars (CERES) project aims to provide a homogeneous analysis of a sample of metal-poor stars ($[\text{Fe}/\text{H}] < -1.5$). We present the stellar parameters and the chemical abundances of elements up to Zr for a sample of 52 giant stars.

Methods. We relied on a sample of high signal-to-noise UVES spectra. We determined stellar parameters from *Gaia* photometry and parallaxes. Chemical abundances were derived using spectrum synthesis and model atmospheres.

Results. We determined chemical abundances of 26 species of 18 elements: Na, Mg, Al, Si, Ca, Sc, Ti, V, Cr, Mn, Fe, Co, Ni, Cu, Zn, Sr, Y, and Zr. For several stars, we were able to measure both neutral and ionised species, including Si, Sc, Mn, and Zr. We have roughly doubled the number of measurements of Cu for stars at $[\text{Fe}/\text{H}] \leq -2.5$. The homogeneity of the sample made it possible to highlight the presence of two Zn-rich stars ($[\text{Zn}/\text{Fe}] \sim +0.7$), one *r*-rich and the other *r*-poor. We report the existence of two branches in the $[\text{Zn}/\text{Fe}]$ versus $[\text{Ni}/\text{Fe}]$ plane and suggest that the high $[\text{Zn}/\text{Fe}]$ branch is the result of hypernova nucleosynthesis. We discovered two stars with peculiar light neutron-capture abundance patterns: CES1237+1922 (also known as BS 16085-0050), which is ~ 1 dex underabundant in Sr, Y, and Zr with respect to the other stars in the sample, and CES2250-4057 (also known as HE 2247-4113), which shows a ~ 1 dex overabundance of Sr with respect to Y and Zr.

Conclusions. The high quality of our dataset allowed us to measure hardly detectable ions. This can provide guidance in the development of line formation computations that take deviations from local thermodynamic equilibrium and hydrodynamical effects into account.

Key words. Galaxy: abundances – Galaxy: evolution – stars: abundances – stars: Population II – stars: Population III abundances – nuclear reactions, nucleosynthesis

1. Introduction

The elements beyond the Fe-peak, that is, all elements with atomic number $Z > 30$, are commonly referred to as ‘heavy elements’ or ‘neutron-capture’ (n-capture) elements, as the most efficient way to form these elements is through neutron captures. A neutron capture tends to create a nucleus that is away from the

nuclear stability valley, and the system tries to fall back to the valley through β decay.

From a theoretical point of view, three neutron-capture processes can be distinguished, depending on the neutron flux. When the seed nucleus has time to β decay after each neutron capture, one refers to this as the slow neutron-capture process (*s* process), which occurs at neutron densities of less than about 10^8 cm^{-3} (e.g. Busso et al. 1999, and references therein). The rapid neutron-capture process (*r* process) occurs when the neutron flux is so high that a seed nucleus can capture several neutrons before decaying. The *r* process requires neutron densities in excess of 10^{24} cm^{-3} (e.g. Kratz et al. 2007, and references therein). In the intermediate neutron density regime ($10^{14} \text{ cm}^{-3} \leq N_n \leq 10^{16} \text{ cm}^{-3}$) one talks about the

* Chemical abundances (Table 3) are only available at the CDS via anonymous ftp to cdsarc.u-strasbg.fr (130.79.128.5) or via <http://cdsarc.u-strasbg.fr/viz-bin/cat/J/A+A/665/A10>

** Based on observations collected at the European Southern Observatory under ESO programme 0104.D-0059 and on data obtained from the ESO Science Archive Facility.

intermediate neutron-capture process (*i* process; Cowan & Rose 1977). Sometimes in the literature, Zn ($Z = 30$) is not considered part of this set of elements since it may also be formed through different nucleosynthetic channels, but neutron captures are definitely a possibility for synthesising Zn (Bisterzo et al. 2004). The same is true for Cu, but we consider Cu to be part of the iron-peak elements.

Observationally, it has been known for many years that, in metal-poor stars, the abundance ratios $[X/Fe]$, where X is an *n*-capture element, show a large scatter as a function of $[Fe/H]$ (McWilliam et al. 1995; Burris et al. 2000; François et al. 2007; Hansen et al. 2012), at variance with the lighter elements, for example Mg, which show a very tight relation with $[Fe/H]$ (McWilliam et al. 1995; Cayrel et al. 2004; Bonifacio et al. 2009). This has generally been interpreted as evidence that the production of *n*-capture elements occurs in different sites and under different physical conditions, in contrast to the lighter elements that are formed in either hydrostatic or explosive burning in Type II or Type Ia supernovae (SNe; see e.g. Arnett 1996).

Based on then-existing observations and theoretical considerations, Truran (1981) argued that in metal-poor stars the *n*-capture elements can only be formed through the *r* process, essentially because the only then-recognised source of *s*-process nucleosynthesis, asymptotic giant branch stars, would not have had enough time to enrich the interstellar medium before the metallicity rose above $[Fe/H] = -1.5$. This is sometimes referred to as the *r*-only paradigm. It is currently believed that fast rotating massive stars can produce *s*-process elements and deliver them through their winds, prior to the SN explosion (Prantzos et al. 1990; Pignatari et al. 2010; Choplin et al. 2018; Banerjee et al. 2018; Skúladóttir et al. 2020). Although the site of the *i* process has not yet been robustly identified, it is considered for the production of some isotopes (Hempel et al. 2016; Côté et al. 2018; Denissenkov et al. 2019; Koch et al. 2019; Skúladóttir et al. 2020; Choplin et al. 2021). More exotic phenomena, such as proton ingestion phenomena, are also believed to be responsible for the production of some *n*-capture elements (Hollowell et al. 1990; Fujimoto et al. 2000; Cristallo et al. 2009; Caffau et al. 2019). Even if Truran’s intuition is probably correct and the majority of *n*-capture elements at low metallicities are formed by the *r* process, other processes cannot be ignored and may, in fact, contribute to the large scatter observed in the abundance ratios of these elements and to the variety of abundance patterns. Furthermore, it is now accepted that the *r* process is not universal, but can occur in different astrophysical sites under different physical conditions, of which at least two are necessary to explain the observations (Qian & Wasserburg 2001, 2007; Hansen et al. 2014a; Spite et al. 2018; Skúladóttir & Salvadori 2020).

The Chemical Evolution of *R*-process Elements in Stars (CERES) project has the objective of characterising the abundances of as many *n*-capture elements as possible in a sample of giant stars of low metallicity ($[Fe/H] < -1.5$). The aim of CERES is to provide a high quality set of abundances that can be used to test different theoretical scenarios. To achieve this, we rely on a set of high resolution and high signal-to-noise ratio (S/N) spectra, and on the photometry and parallaxes provided by the *Gaia* satellite (Gaia Collaboration 2016) to analyse all the stars in a homogeneous way. In this first paper of the series, we provide the atmospheric parameters and abundances of 18 elements, Na, Mg, Al, Si, Ca, Sc, Ti, V, Cr, Mn, Fe, Co, Ni, Cu, Zn, Sr, Y, and Zr, the last three of which are *n*-capture elements. Abundances of other *n*-capture elements shall be provided in

subsequent papers of the series, based on the same atmospheric parameters.

The current paper is organised as follows: Sect. 2 describes the sample and observations, Sect. 3 the analysis, including stellar parameter and abundance determination, Sect. 4 details the results, and Sect. 5 provides a discussion. Finally, Sect. 6 presents our conclusions.

2. Sample selection and observational data

2.1. Sample selection

With the goal to derive as complete abundance patterns as possible – in particular with regard to the heavy elements – we targeted metal-poor stars ($[Fe/H] < -1.5$) with fewer than five measured heavy elements ($Z > 30$). The initial target sample was based on stars from Frebel et al. (2006), François et al. (2007), Hansen et al. (2012, 2020), the metal-poor tail of GALactic Archaeology with HERMES (GALAH; Buder et al. 2018), with further metal-poor candidates from Roederer et al. (2014a), Yong et al. (2013), Barklem et al. (2005). We avoided overlap with the R-Process Alliance survey (e.g. Hansen et al. 2018; Sakari et al. 2018) and the Hamburg/ESO *R*-process Enhanced Star (HERES) survey (Christlieb et al. 2004) as these stars typically have already been observed to target *n*-capture elements. The candidates were then checked against the literature, for example the Stellar Abundances for Galactic Archaeology (SAGA) database (Suda et al. 2008), to ensure that there were only a few available heavy element abundance measurements. Finally, we removed binaries and mainly avoid stars classified in the literature as carbon-enhanced metal-poor (CEMP) stars, as the strong CH and CN molecular bands affect the accuracy of heavy element abundance measurements.

As most of the heavy element absorption transitions fall in the blue part of the spectrum, a high S/N is needed in the blue wavelength range ($S/N = 50$ in more metal-rich stars, and $S/N = 120$ in the most metal-poor ones at 390 nm), resulting in considerable exposure times. To keep the observations feasible we thus limited the target sample to $V < 12.2$. Finally, from the stars where the Eu abundance is known, we included a mixture of high and low values to probe *r*-poor as well as *r*-rich stars. In case no Eu abundance is known, we keep the star in the sample for follow-up observations. Details about the final sample and observations can be found in Table A.1.

2.2. Observations

The target stars were observed with the Ultraviolet and Visual Echelle Spectrograph (UVES) of the Very Large Telescope (VLT) at the European Southern Observatory (ESO; Dekker et al. 2000) during two runs (November 2019 and March 2020) with differing exposures to reach a S/N of 50 to 120 per pixel at 390 nm for most stars (see Table A.1). For stars with $[Fe/H] < -2.7$, a S/N of 200 per pixel was requested. The observations were carried out using a 1'' slit, 1×1 binning, and a dichroic (Dic 1) where the blue and red arms were centred on 390 and 564 nm, respectively. This resulted in high-resolution ($R > 40\,000$) spectra that owing to the excellent observing conditions (low airmass, < 1.5 , and seeing, $< 1''0$), reached a median resolution of 49 800 in the blue arm and 47 500 in the red arm. In a few cases these requests were violated (airmass 1.6 and/or seeing as large as $1''5$) and the reduced spectra attained, nevertheless the required S/N . Further details related to the observations can be found in the observing log (Table A.1).

Our own observations were complemented with archival data of comparable quality. All the archival data used were acquired prior to 2019. In Table A.1, the wavelength ranges covered by different UVES arms are the following: $303 < \lambda < 388$ nm for BLUE346, $326 < \lambda < 454$ nm for BLUE390, $458 < \lambda < 668$ nm for RED564, and $476 < \lambda < 684$ nm for RED580.

3. Analysis

3.1. Chromospheric activity

As a preliminary step we inspected the Ca II H and K lines of all our targets to find signs of chromospheric activity. We found four stars that are clearly active and present emission in the core of the Ca II H and K lines: CES0547-1739¹, CES0747-0405, CES0900-6222, and CES1116-7250. Three more stars, show minor signs of activity, and should be further investigated: CES0919-6958, CES0413+0636, and CES0424-1501. Of the lines we used for abundance analysis only the Na I D resonance lines are sensitive to chromospheric effects, yet we do not notice any systematic effect on the abundances derived from these lines with respect to those derived from other lines. Thus, our analysis is likely immune to the effects of the chromosphere. It would be yet interesting to further investigate the chromospheres of these stars and their variations with time. Observations of the He I 1083 nm line, with a proper modelling of their chromosphere could provide He abundances for these stars (see e.g. Pasquini et al. 2011, and references therein).

3.2. Stellar parameters

The stellar parameters for our sample of stars were derived using *Gaia* Early Data Release 3 (EDR3) photometry (G , $G_{BP} - G_{RP}$) and parallaxes (*Gaia* Collaboration 2016, 2021). We defined a grid in the parameter space using ATLAS 9 model atmospheres by Castelli (2003). The sub-grid we used has effective temperatures (T_{eff}), surface gravities ($\log g$) and metallicity ($[M/H]$) in the range of $3500 \leq T_{\text{eff}} \leq 6000$, $0 \leq \log g \leq 4$, and $-4 \leq [M/H] \leq +0.5$. The α -elements are enhanced by +0.4 dex for all models with $[M/H] \leq -1$, and they are solar-scaled for higher metallicity models. The microturbulent velocity is 2 km s^{-1} for all models. Theoretical values of $G_{BP} - G_{RP}$, bolometric correction (BC_G), and extinction coefficients A_G , $E(G_{BP} - G_{RP})$, using the reddening law of Fitzpatrick et al. (2019), were computed for the entire grid. G and $G_{BP} - G_{RP}$ were de-reddened using the reddening maps by Schlafly & Finkbeiner (2011, $A_V = 0.81$). Effective temperatures and surface gravities were derived iteratively using the procedure described in Koch-Hansen et al. (2021). The errors on the effective temperature can be conservatively estimated by changing the $G_{BP} - G_{RP}$ by 0.02 mag. This is larger than the purely photometric errors, but we include also the uncertainty on the reddening. The new effective temperatures are offset by 88 K that we round to an error of ± 100 K. According to Bonifacio et al. (2018), the mean difference between the 3D corrected and 1D bolometric corrections computed from ATLAS 9 models is around 0.02 mag for stars with stellar parameters similar to those of our sample stars. We consider this value as the typical uncertainty on the bolometric correction. Surface gravities are offset by approximately 0.035 dex with a 100 K change in T_{eff} , while a 0.02 mag change in the bolometric correction implies a 0.01 dex change in $\log g$. Taking into account

¹ The name ID of the star is defined as the string CES followed by RA J2000 (hm, four digits), the sign of the declination, and Dec J2000 (dm, four digits).

the 1σ errors on parallaxes, the surface gravities are offset by about 0.02 dex. Microturbulent velocities (v_{turb}) were estimated using the calibration derived by Mashonkina et al. (2017a). The uncertainty on v_{turb} is 0.5 km s^{-1} , according to the maximum discrepancy between microturbulences derived from spectroscopy and from the formula in Mashonkina et al. (2017a). The derived stellar parameters are shown in Table 1, coordinates and other names for the targets can be found in Table A.1. $[\text{Fe}/\text{H}]$ indicates the iron abundance derived from Fe I. The mean uncertainty on $[\text{Fe}/\text{H}]$ is 0.13 dex, which corresponds to the mean line-to-line scatter.

3.3. Line broadening

In all the spectra analysed with a resolving power $R \gtrsim 60\,000$, the line width is often not dominated by the instrumental resolution but by the macroturbulence. In fact, the observed width is a convolution of instrumental resolution and macroturbulence and needs to be determined for each star and each instrumental resolution. To derive chemical abundances, we developed a procedure to estimate the line broadening in km s^{-1} (v_{broad}) for each observed spectrum. We first measured the full width half maximum (FWHM) for a set of isolated and non-saturated lines in the observed spectra. We then measured the FWHM for the same lines for a set of synthetic spectra, broadened assuming a Gaussian macroturbulence, for several values of v_{broad} . The stellar parameters of the synthetic spectra were chosen to be close to the parameters of the star analysed. For this purpose we used the parameters determined as described in Sect. 3.2 and first guess metallicities derived from our first run of the code My God It's Full Of Stars (MyGIsFOS; see Sect. 3.4; Sbordone et al. 2014), assuming a broadening of 7 km s^{-1} for all stars. The mean FWHM over the set of synthetic lines was determined for each input v_{broad} . This provided a relation between the input macroturbulence and the mean measured FWHM. Interpolation in this relation to the value of the FWHM measured in the observed spectrum provided the adopted v_{broad} . This value was used to broaden the synthetic grid input to MyGIsFOS (see Sect. 3.4). The values of v_{broad} we obtained for each spectrum are listed in Table A.1. The stellar parameters of the synthetic spectra used for the broadening estimate are listed in Table 2. The list of lines used to determine the broadening was different for the blue arm and the red arm of the UVES spectra, since the two arms often have different slit widths and therefore instrumental resolution. To perform this procedure we needed the lines to be on the linear part of the curve of growth. Since some lines that are non-saturated at low metallicities may become saturated at higher metallicities, for each setup we employed two line lists as a function of the stellar metallicity: one at $[\text{Fe}/\text{H}] < -2.5$ and another at $[\text{Fe}/\text{H}] \geq -2.5$. The typical uncertainty on v_{broad} is 0.3 km s^{-1} for stars with $v_{\text{broad}} \sim 7 \text{ km s}^{-1}$, and 2.0 km s^{-1} for stars with $v_{\text{broad}} \sim 10 \text{ km s}^{-1}$.

3.4. Chemical abundances

We derived chemical abundances of Na, Mg, Al, Si, Ca, Sc, Ti, V, Cr, Mn, Fe, Co, Ni, Cu, Zn, Y, and Zr, for our sample stars using the code MyGIsFOS (Sbordone et al. 2014). MyGIsFOS is an automatic pipeline that performs a χ^2 minimisation fit on the profile of the selected lines using a grid of synthetic spectra. The grid has been computed with the code SYNTHIE (see Kurucz 2005; Sbordone et al. 2004) based on 1D plane-parallel model atmospheres in local thermodynamic equilibrium (LTE), computed with the code ATLAS 12 (Kurucz 2005). Sr abundances

Table 1. Stellar parameters and *Gaia* de-reddened *G* magnitude for stars in our sample.

Star	G_0 (mag)	T_{eff} (K)	$\log g$ (dex)	v_{turb} (km s ⁻¹)	[Fe/H] (dex)
CES0031–1647	8.20	4960	1.83	1.91	-2.49
CES0045–0932	8.70	5023	2.29	1.76	-2.95
CES0048–1041	10.48	4856	1.68	1.93	-2.48
CES0055–3345	9.36	5056	2.45	1.66	-2.36
CES0059–4524	14.66	5129	2.72	1.56	-2.39
CES0102–6143	13.45	5083	2.37	1.75	-2.86
CES0107–6125	13.36	5286	2.97	1.54	-2.59
CES0109–0443	13.30	5206	2.74	1.69	-3.23
CES0215–2554	8.91	5077	2.00	1.91	-2.73
CES0221–2130	10.21	4908	1.84	1.84	-1.99
CES0242–0754	14.72	4713	1.36	2.03	-2.90
CES0301+0616	12.65	5224	3.01	1.51	-2.93
CES0338–2402	9.67	5244	2.78	1.62	-2.81
CES0413+0636	8.06	4512	1.10	2.01	-2.24
CES0419–3651	12.64	5092	2.29	1.78	-2.81
CES0422–3715	9.26	5104	2.46	1.68	-2.45
CES0424–1501	9.68	4646	1.74	1.74	-1.79
CES0430–1334	9.71	5636	3.07	1.63	-2.09
CES0444–1228	12.21	4575	1.40	1.92	-2.54
CES0518–3817	14.12	5291	3.06	1.49	-2.49
CES0527–2052	13.72	4772	1.81	1.84	-2.75
CES0547–1739	11.53	4345	0.90	2.01	-2.05
CES0747–0405	10.32	4111	0.54	2.08	-2.25
CES0900–6222	10.47	4329	0.94	1.98	-2.11
CES0908–6607	10.85	4489	0.90	2.12	-2.62
CES0919–6958	10.76	4430	0.70	2.17	-2.46
CES1116–7250	10.08	4106	0.48	2.14	-2.74
CES1221–0328	15.72	5145	2.76	1.6	-2.96
CES1222+1136	9.64	4832	1.72	1.93	-2.91
CES1226+0518	7.79	5341	2.84	1.60	-2.38
CES1228+1220	9.29	5089	2.04	1.87	-2.32
CES1237+1922	11.85	4960	1.86	1.95	-3.19
CES1245–2425	10.26	5023	2.35	1.72	-2.85
CES1322–1355	10.26	4960	1.81	1.96	-2.93
CES1402+0941	5.83	4682	1.35	2.01	-2.79
CES1405–1451	6.73	4642	1.58	1.81	-1.87
CES1413–7609	10.04	4782	1.72	1.87	-2.52
CES1427–2214	8.61	4913	1.99	1.85	-3.05
CES1436–2906	7.75	5280	3.15	1.42	-2.15
CES1543+0201	12.6	5157	2.77	1.57	-2.65
CES1552+0517	10.12	5013	2.30	1.72	-2.60
CES1732+2344	8.58	5370	2.82	1.65	-2.57
CES1804+0346	6.45	4390	0.80	2.12	-2.48
CES1942–6103	11.68	4748	1.53	2.01	-3.34
CES2019–6130	11.38	4590	1.13	2.09	-2.97
CES2103–6505	12.95	4916	2.05	1.85	-3.58
CES2231–3238	12.84	5222	2.67	1.67	-2.77
CES2232–4138	13.18	5194	2.76	1.59	-2.58
CES2250–4057	9.96	5634	2.51	1.88	-2.14
CES2254–4209	14.68	4805	1.98	1.79	-2.88
CES2330–5626	13.71	5028	2.31	1.75	-3.10
CES2334–2642	13.30	4640	1.42	2.02	-3.48

were derived by matching the observed spectrum around Sr lines with a synthetic one computed using the LTE spectral line analysis code Turbospectrum (Alvarez & Plez 1998; Plez 2012). The atomic data used in this study are provided by the *Gaia*-ESO

Table 2. Range of atmospheric parameters of the synthetic spectra used for the broadening estimates.

T_{eff} start (K)	T_{eff} end (K)	T_{eff} step (K)	$\log g$ (dex)	v_{turb} (km s ⁻¹)
4000	5200	200	1.5	2.0
5200	5600	200	3.0	2.0

Survey (GES) line list (Heiter et al. 2021, and references therein) complemented with atomic data from two lists from Castelli’s website² that cover the wavelength range not covered by the GES list from 300 to 420 nm. We were also able to detect the Si II line at 385.6 nm in 22 stars, the Sc I line at 391.1 nm in 19 stars, the Mn II line at 412.8 nm in 38 stars, and the Zr I line at 473.9 nm in seven stars.

The derived chemical abundances with uncertainties are provided in machine readable format at the Centre de Données astronomiques de Strasbourg (CDS). An example of the table provided at the CDS is shown in Table 3. Chemical abundances are expressed in the form $A(X)$ and $[X/H]$, where $A(X) = \log(X/H) + 12$, and $[X/H] = \log_{10}(X/H) - \log_{10}(X/H)_{\odot}$. The abundance ratios $[X/Fe]$ are expressed as $[X\text{ I}/Fe\text{ I}] = [X\text{ I}/H] - [Fe\text{ I}/H]$ for neutral species and as $[X\text{ II}/Fe\text{ II}] = [X\text{ II}/H] - [Fe\text{ II}/H]$ for singly ionised species. The uncertainties $s(X)$ represent the line-to-line scatter when the number of lines is ≥ 2 . When the abundance was derived from only one line, we adopted as $s(X)$ the mean line-to-line scatter over the stars with ≥ 2 lines of the same element X. For Si II, Sc I, Mn II, and Zr I abundances, we adopted as $s(X)$ the mean line-to-line scatter of the other ionisation state. We adopted the solar abundances provided by Caffau et al. (2011a,b) and Lodders et al. (2009; see Table 4).

4. Results

4.1. Comparison with literature

In Fig. 1 we compare our derived stellar parameters with those determined by other studies in the literature. Some stars were observed in the framework of the Large Program ‘First Stars’ (PI: R. Cayrel), and for these stars we use the results obtained in Cayrel et al. (2004) for the comparison, even if more recent values are available in literature.

In this study, we rely on *Gaia* EDR3 photometry and parallaxes to derive the stellar parameters (Sect. 3.2). However, in the traditional spectroscopic method, the effective temperature is obtained by requiring that there is no trend between the abundance and excitation potential of Fe I lines (i.e. excitation equilibrium). The surface gravity, instead, is obtained by requiring that Fe I and Fe II lines provide the same abundance (i.e. ionisation equilibrium). Another way of deriving surface gravity is to use theoretical isochrones, assuming the age, metallicity, and effective temperature of the star.

As shown in Fig. 1 (upper-left panel), T_{eff} values in the literature appear in line with our derived temperatures, with an average $\Delta T_{\text{eff}} = -72\text{ K}$ ($\sigma = 113\text{ K}$), where $\Delta T_{\text{eff}} = T_{\text{eff}}(\text{literature}) - T_{\text{eff}}(\text{this study})$ is compatible with our $\pm 100\text{ K}$ uncertainties on T_{eff} . One exception to this good agreement is Roederer et al. (2014a), where six out of seven stars have effective temperatures $\sim 300\text{ K}$ lower than our derived values.

² <https://wwwuser.oats.inaf.it/castelli/linelists.html>

Table 3. Derived chemical abundances with errors for our sample stars.

Star	Nlines	A(FeI) (dex)	s(FeI) (dex)	[FeI/H]	Nlines	A(FeII) (dex)	s(FeII) (dex)	[FeII/H]	...
CES0031–1647	304	5.03	0.12	−2.49	26	5.22	0.09	−2.31	...
CES0045–0932	176	4.57	0.14	−2.95	12	4.72	0.19	−2.80	...
CES0048–1041	314	5.04	0.13	−2.48	26	5.19	0.13	−2.33	...
CES0055–3345	340	5.16	0.11	−2.36	28	5.28	0.12	−2.24	...
CES0059–4524	146	5.13	0.09	−2.39	8	5.26	0.09	−2.26	...
...									

Notes. The complete table is available in machine readable format at the CDS.

Table 4. Solar abundance values adopted in this work.

Element	A(X)	References
Na	6.30	Lodders et al. (2009)
Mg	7.54	Lodders et al. (2009)
Al	6.47	Lodders et al. (2009)
Si	7.52	Lodders et al. (2009)
Ca	6.33	Lodders et al. (2009)
Sc	3.10	Lodders et al. (2009)
Ti	4.90	Lodders et al. (2009)
V	4.00	Lodders et al. (2009)
Cr	5.64	Lodders et al. (2009)
Mn	5.37	Lodders et al. (2009)
Fe	7.52	Caffau et al. (2011b)
Co	4.92	Lodders et al. (2009)
Ni	6.23	Lodders et al. (2009)
Cu	4.21	Lodders et al. (2009)
Zn	4.62	Lodders et al. (2009)
Sr	2.92	Lodders et al. (2009)
Y	2.21	Lodders et al. (2009)
Zr	2.62	Caffau et al. (2011a)

For the star CES1552+0517, Johnson (2002) also determined a $T_{\text{eff}} \sim 300$ K lower than our derived value. As discussed in Mucciarelli & Bonifacio (2020), for metal-poor stars with $[\text{Fe}/\text{H}] \sim -2.5$, the spectroscopic T_{eff} and $\log g$ appear to be lower than the photometric ones by ~ 350 K and ~ 1.0 dex, respectively. This is in agreement with the observed discrepancy.

Surface gravities in the literature appear lower than our derived values (see Fig. 1, upper-right panel), with average $\Delta \log g = -0.35$ ($\sigma = 0.32$). The largest discrepancy in $\log g$ is found for the Roederer et al. (2014a) values, which are systematically ~ -0.75 dex lower than our derived $\log g$. This result is not surprising, given their discrepancy with our T_{eff} . Since Roederer et al. (2014a) determined their $\log g$ using theoretical isochrones, we expect that along the red giant branch (RGB) the cooler the star, the lower is the surface gravity.

We also determined spectroscopic surface gravities for our sample stars and found that those are in agreement with literature values within 0.1 dex. The observed discrepancy between spectroscopic and photometric $\log g$ seems to arise from the different iron abundance obtained from Fe I and Fe II lines. At low metallicities, the neutral species are more affected by non-local thermodynamic equilibrium (NLTE) effects than ionised ones (e.g. Amarsi et al. 2016), which implies that the total abundance derived from each of the two species are different. Hence, when using ionisation equilibrium to derive $\log g$, these over-ionisation effects can lead to an underestimation of the

star’s surface gravity. A possible way to avoid this is to apply NLTE corrections before imposing ionisation equilibrium, as done in Mashonkina et al. (2017a), whose results are in good agreement with this work (blue squares in Fig. 1, upper-right panel).

In Fig. 1 (lower panels) we compare our derived chemical abundances for Fe I and Fe II with those in literature. Our results are in general agreement with the literature abundances, with average values $\Delta[\text{Fe I}/\text{H}] = +0.01$ ($\sigma = 0.15$ dex) and $\Delta[\text{Fe II}/\text{H}] = -0.08$ ($\sigma = 0.14$ dex). We note that the $[\text{Fe}/\text{H}]$ derived by Roederer et al. (2014a) are systematically lower than our values, which is a direct consequence of adopting lower T_{eff} and $\log g$.

4.2. Alpha elements: Mg, Si, Ca, and Ti

Figure 2 shows the derived Mg I, Si I, Si II, Ca I, Ti I, and Ti II over Fe abundance ratios as a function of $[\text{Fe}/\text{H}]$ for our sample of stars. Our results are compared to the values obtained by Cayrel et al. (2004) and Ishigaki et al. (2012) for giant stars in the same metallicity range. The abundance ratios of all elements are in good agreement with the results found in previous studies. All elements are enhanced respect to the Fe abundance (with sample averages and standard deviations of $[\text{Mg I}/\text{Fe I}] = +0.50 \pm 0.11$, $[\text{Si I}/\text{Fe I}] = +0.41 \pm 0.16$, $[\text{Si II}/\text{Fe II}] = +0.38 \pm 0.11$, $[\text{Ca I}/\text{Fe I}] = +0.37 \pm 0.07$, $[\text{Ti I}/\text{Fe I}] = +0.35 \pm 0.07$, $[\text{Ti II}/\text{Fe II}] = +0.35 \pm 0.10$), and the abundance ratios remain constant at different metallicities. The dispersion around the mean abundance ratio is equal or smaller than the mean uncertainty (σ) for Si, Ca and Ti ($\sigma_{\text{Si I}} = 0.16$ dex, $\sigma_{\text{Si II}} = 0.20$ dex, $\sigma_{\text{Ca I}} = 0.08$ dex, $\sigma_{\text{Ti I}} = 0.09$ dex, $\sigma_{\text{Ti II}} = 0.11$ dex) but slightly larger for Mg ($\sigma_{\text{Mg I}} = 0.07$ dex). The scatter appears to become larger at lower metallicities, as it was already observed by Cayrel et al. (2004) in their sample of stars, this is expected since at lower metallicities the lines become weaker. The error estimates are in line with what expected from the S/Ns.

We find a mean difference between $[\text{Si II}/\text{H}]$ and $[\text{Si I}/\text{H}]$ of 0.06 ± 0.14 dex, and a mean difference between $[\text{Ti II}/\text{H}]$ and $[\text{Ti I}/\text{H}]$ of 0.13 ± 0.06 dex. These differences are likely due to NLTE effects. Mashonkina et al. (2016a) found minimal departures from LTE for the lower levels of Si I lines typically used as abundance indicators in F-G-K stars. On the other hand, NLTE effects are particularly strong for Ti I lines (see Mashonkina et al. 2016b). According to Mashonkina et al. (2016b), for stars with stellar parameters similar to those of our targets, the NLTE corrections for Ti I are all positive, up to 0.4 dex, while the corrections for Ti II are positive and <0.1 dex. These values are compatible with the difference in Ti abundances observed in our stars.

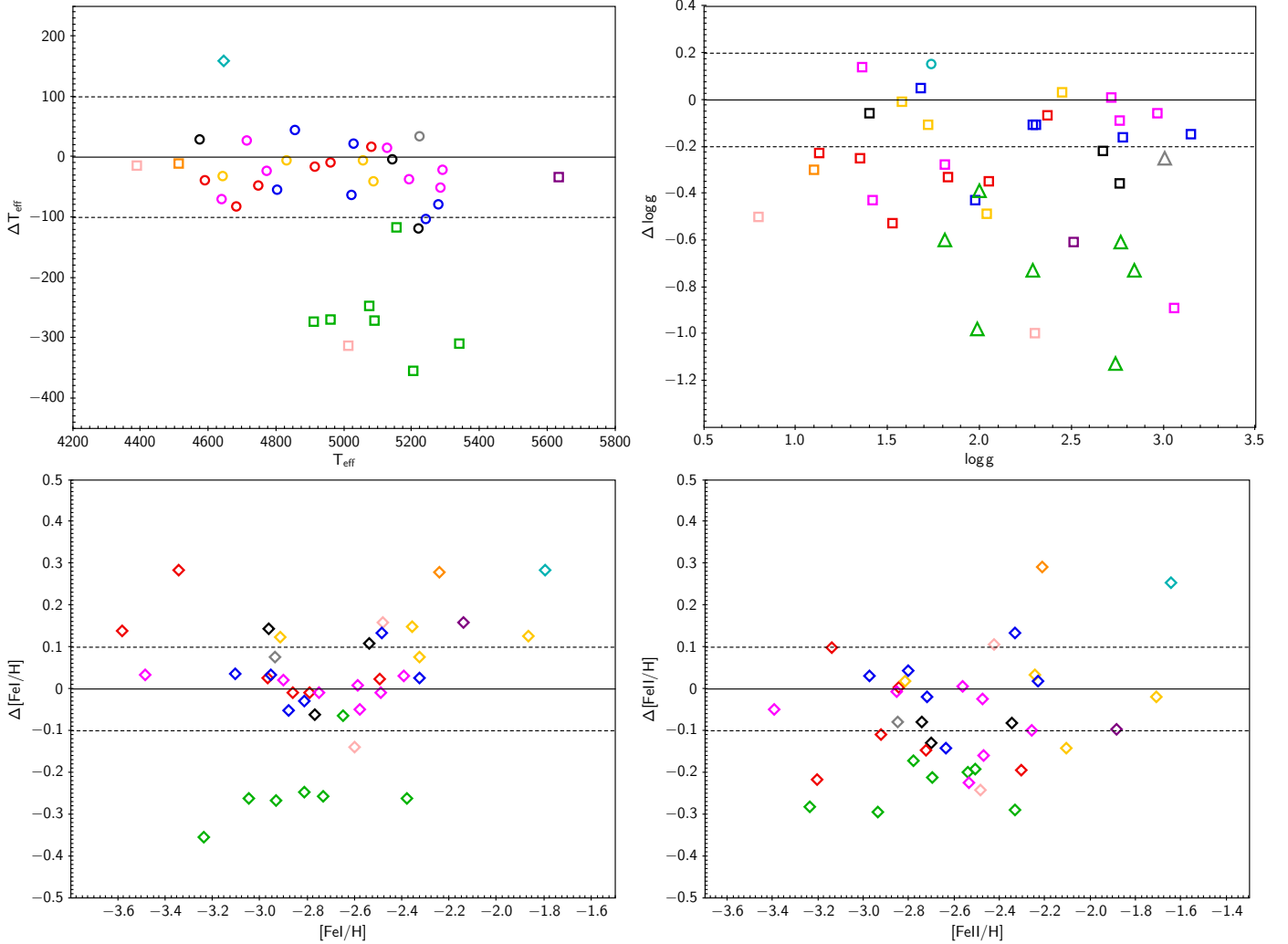


Fig. 1. Comparison between this work and the literature: T_{eff} (upper-left panel), $\log g$ (upper-right panel), Fe I (lower-left panel), and Fe II (lower-right panel). Open circles denote T_{eff} and $\log g$ derived from photometry, open squares denote the same derived from spectroscopy, and open triangles indicate $\log g$ derived from theoretical isochrones. Data are from Barklem et al. (2005) (black), Cayrel et al. (2004) (red), Hansen et al. (2020) (cyan), Ishigaki et al. (2012) (yellow), Johnson (2002) (pink), Lai et al. (2008) (grey), Luck & Bond (1985) (orange), Mashonkina et al. (2017b) (blue), Pereira et al. (2013) (purple), Roederer et al. (2014a) (green), and Siqueira Mello et al. (2014) (magenta).

4.3. Light odd-Z elements: Na and Al

Sodium abundances were derived from the Na I lines at 498.3 nm, 568.2 nm, 568.8 nm, and 616.0 nm and from the Na D resonance lines at 588.9 nm (D1) and 589.5 nm (D2). As Na I lines, especially the Na I D doublet, are known for being strongly sensitive to NLTE effects (e.g. Mashonkina et al. 1993; Baumüller et al. 1998), we applied the NLTE corrections provided by Lind et al. (2011)³ to each line to obtain a more accurate measurement of Na abundances. The NLTE corrections for Na I lines are all negative, with an average of -0.26 dex and down to -0.57 dex for the Na I D doublet.

Aluminium abundances were derived from the Al I resonance lines at 394.4 nm and 396.1 nm. Similarly to the Na D doublet, the Al resonance doublet is sensitive to NLTE effects, and when these lines are used in LTE approximation, the derived Al abundances are severely underestimated (Baumueller & Gehren 1997; Norris et al. 2001). To avoid this, we applied the NLTE corrections by Andrievsky et al. (2008). Nine stars in our sample have T_{eff} in the temperature range of the Andrievsky et al. (2008)

grid, so we provide NLTE Al abundances only for these stars. The NLTE corrections are all positive, with an average of $+0.63$ dex.

The derived abundance ratios of Na and Al over Fe as a function of $[\text{Fe}/\text{H}]$ are shown in Fig. 3. These are compared to the NLTE values obtained for the First Stars Large Program stars in Andrievsky et al. (2007, 2008, respectively). Again, our results appear in line with previous studies. The abundance ratios show a large scatter (0.17 dex for Na I, and 0.12 dex for Al I), and no clear trend with $[\text{Fe}/\text{H}]$.

4.4. Iron-peak elements

4.4.1. Sc and V

The derived abundance ratios of $[\text{Sc I}/\text{Fe I}]$, $[\text{Sc II}/\text{Fe II}]$, $[\text{V I}/\text{Fe I}]$, and $[\text{V II}/\text{Fe II}]$ as a function of $[\text{Fe}/\text{H}]$ are shown in Fig. 4, and compared to literature values for giant stars of similar metallicity. The mean abundance ratios and standard deviations are -0.09 ± 0.13 for $[\text{Sc I}/\text{Fe I}]$, -0.10 ± 0.10 for $[\text{V I}/\text{Fe I}]$, 0.15 ± 0.10 for $[\text{Sc II}/\text{Fe II}]$, and 0.05 ± 0.12 dex for $[\text{V II}/\text{Fe II}]$. The trend appears flat down to the lowest measured $[\text{Fe}/\text{H}]$ for

³ <http://www.inspect-stars.com>

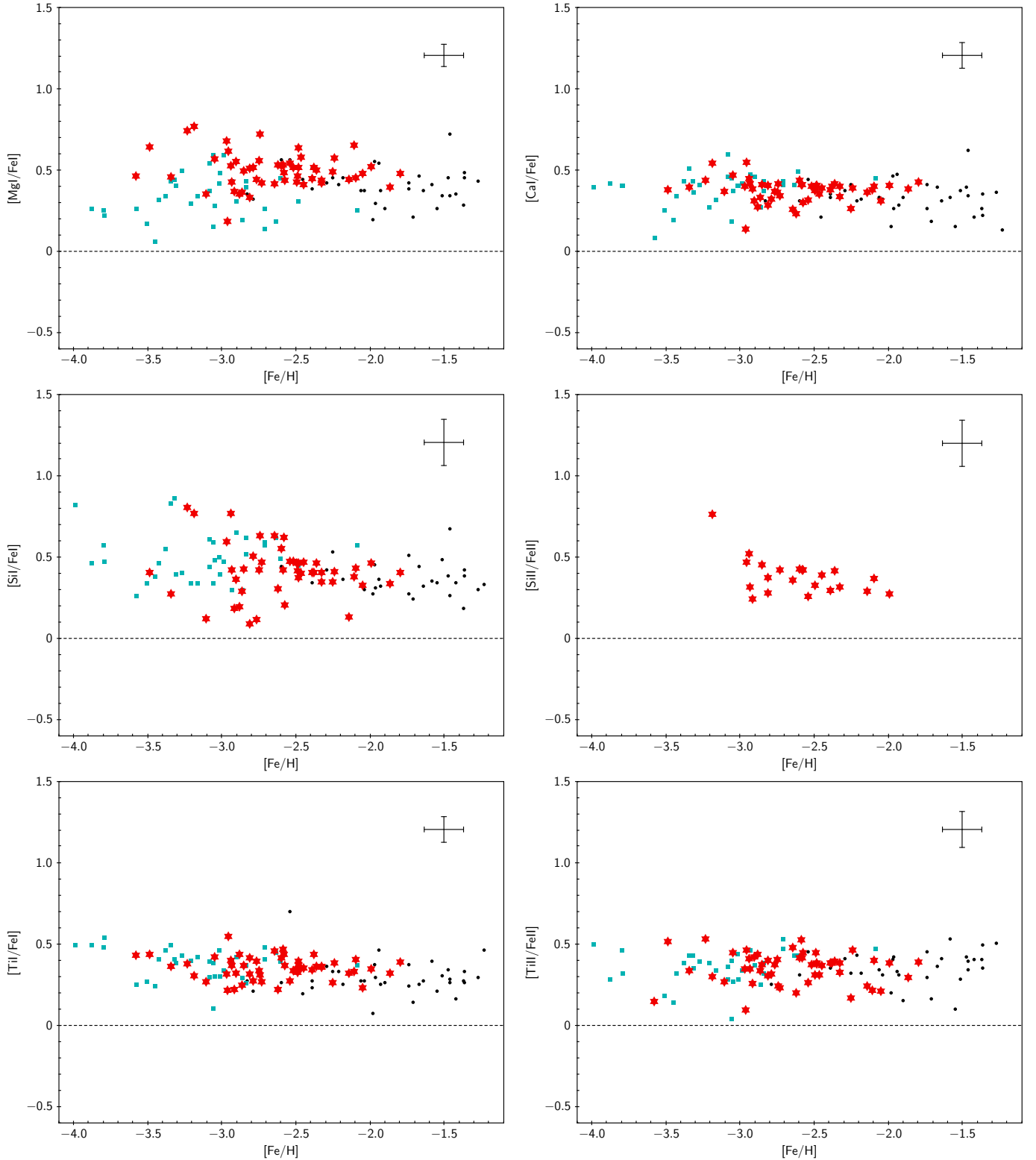


Fig. 2. Elemental abundance ratios of Mg I, Si I, Si II, Ca I, Ti I, and Ti II as a function of $[Fe/H]$ for stars in our sample (red star symbols). Cyan squares and black dots represent the same quantities for stars in Cayrel et al. (2004) and Ishigaki et al. (2012), respectively. A representative error is plotted in the upper-right corner of each panel.

both elements. This is in agreement with the results obtained by other authors.

We find a mean difference between $[Sc II/H]$ and $[Sc I/H]$ of 0.37 ± 0.16 dex, and a mean difference between $[V II/H]$ and $[V I/H]$ of 0.27 ± 0.11 dex. These large discrepancies seem to sug-

gest that NLTE effects on Sc and V are important. Zhang et al. (2008) and Zhao et al. (2016) provide NLTE corrections for Sc in cool dwarf stars, but we are not currently aware of any NLTE studies of scandium conducted on metal-poor giant stars. Similarly, we are not aware of any studies that have performed NLTE

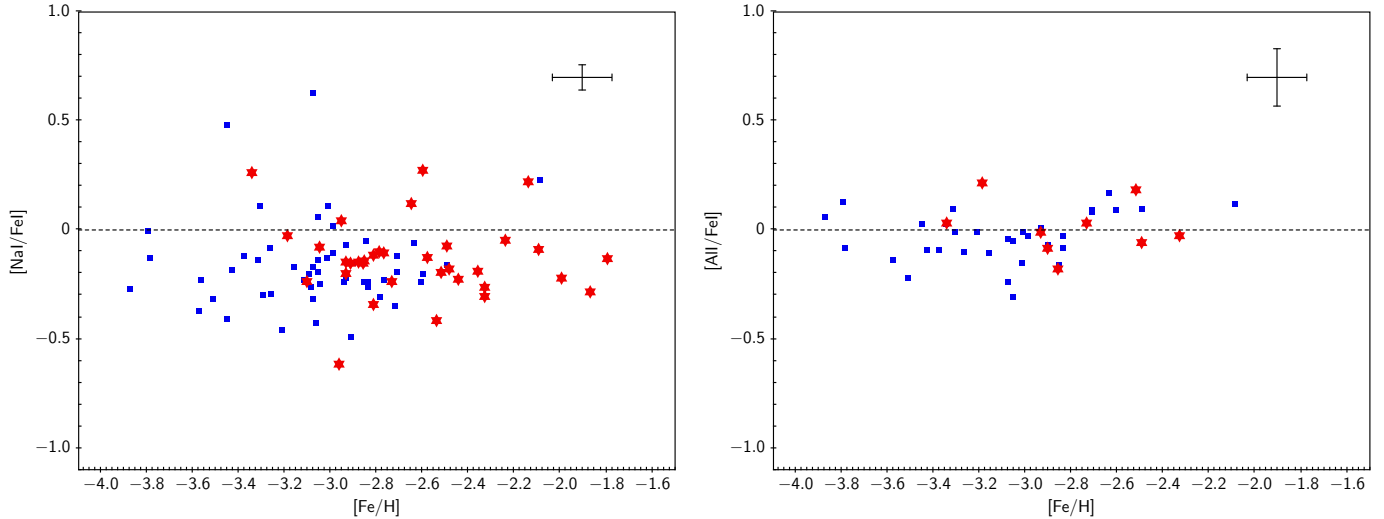


Fig. 3. NLTE abundance ratios of Na and Al as a function of $[\text{Fe}/\text{H}]$ for stars in our sample (red star symbols). Blue squares are stars from Andrievsky et al. (2007, 2008) for Na and Al, respectively. A representative error is plotted in the upper-right corner.

corrections for V. However, we note that Ou et al. (2020) found a difference between $[\text{V II}/\text{H}]$ and $[\text{V I}/\text{H}]$ of 0.25 ± 0.01 dex, which is in excellent agreement with that found in this study. Similar results have been obtained by Roederer et al. (2014a) and Hansen et al. (2020), who found higher V II than V I. We would like to stress that hyperfine splitting for Sc and V lines is not taken into account in the adopted GES line list. Roederer et al. (2014a) pointed out that the lack of hyperfine splitting for V II might lower V II abundances by <0.1 dex. We expect a similar behaviour for Sc II abundances. This may partially explain why we do not find an ionisation equilibrium for scandium and vanadium.

4.4.2. Cr and Mn

In Fig. 5 we compare the derived $[\text{Cr I}/\text{Fe I}]$, $[\text{Cr II}/\text{Fe II}]$, $[\text{Mn I}/\text{Fe I}]$, and $[\text{Mn II}/\text{Fe II}]$ abundance ratios to the values obtained in Cayrel et al. (2004) and in Ishigaki et al. (2013). The mean abundance ratios and standard deviations are $[\text{Cr I}/\text{Fe I}] = -0.09 \pm 0.06$, $[\text{Cr II}/\text{Fe II}] = -0.04 \pm 0.07$, $[\text{Mn I}/\text{Fe I}] = -0.33 \pm 0.10$, and $[\text{Mn II}/\text{Fe II}] = -0.26 \pm 0.17$. Contrary to Mn, for which the values found are in agreement with the literature, both $[\text{Cr I}/\text{Fe I}]$ and $[\text{Cr II}/\text{Fe II}]$ abundance ratios appear to differ from previous results.

For the stars that we have in common with the other studies, the derived $[\text{Cr I}/\text{Fe I}]$ ratios are 0.17 dex and 0.12 dex higher than the values in Cayrel et al. (2004) and Ishigaki et al. (2013), respectively. On the contrary, the derived $[\text{Cr II}/\text{Fe II}]$ ratios are 0.21 dex lower than the values in Ishigaki et al. (2013). Another difference compared to literature (see e.g. Cayrel et al. 2004; Bonifacio et al. 2009) is that the $[\text{Cr I}/\text{Fe I}]$ ratio does not decrease with metallicity in our sample, but instead seems to increase again at the lowest observed metallicities ($[\text{Fe}/\text{H}] < -3.2$).

The difference in the $[\text{Cr I}/\text{Fe I}]$ abundance ratios with Ishigaki et al. (2013) results seems to arise from the different Fe I abundances, as the mean $[\text{Cr I}/\text{H}]$ is almost the same in both studies ($\Delta[\text{Cr I}/\text{H}] \sim 0.01$). However, we note that the mean $[\text{Cr I}/\text{H}]$ abundance in our sample is 0.2 dex higher than in Cayrel et al. (2004). In this case, the difference in the abundance ratios is probably due to the different line selections. Cayrel et al. (2004) relied mainly on Cr I resonance lines to derive Cr abun-

dance. In Ishigaki et al. (2013) and in this study these lines were excluded from the line list, and the same set of Cr I lines were used. To test this hypothesis, we derived the Cr I abundance for the star CES1942-6103 (CS22891-209) employing the same lines used in Cayrel et al. (2004). We obtained $A(\text{Cr I}) = 2.02 \pm 0.14$ dex, which is in excellent agreement with the value found by Cayrel et al. (2004) ($A(\text{Cr I}) = 2.01 \pm 0.16$ dex). This confirms that the Cr I abundance depends on the lines chosen for the analysis and that the observed trend with metallicity is probably due to NLTE effects, which affect each line differently. We underline that for Cr I we used gf values taken from Sobek et al. (2007), which are more recent than those used in Cayrel et al. (2004).

Similarly to the Cr I, we observe a discrepancy of -0.18 dex between our mean $[\text{Cr II}/\text{H}]$ abundance and that of Ishigaki et al. (2013), as they adopted a different set of Cr II lines. For Cr II we used the gf values of Nilsson et al. (2006). The accuracy of the lifetimes used by these authors to derive the oscillator strengths has been questioned by Scott et al. (2015) in their solar abundance analysis. However, Sneden et al. (2016), in their analysis of the metal-poor dwarf HD 84937, showed that the use of the Nilsson et al. (2006) values considerably reduces the line-to-line scatter with respect to what was obtained using earlier gf values. For this reason, we decided to keep the gf values of Nilsson et al. (2006).

We find a mean difference between $[\text{Cr II}/\text{H}]$ and $[\text{Cr I}/\text{H}]$ of 0.18 ± 0.09 dex, and a mean difference between $[\text{Mn II}/\text{H}]$ and $[\text{Mn I}/\text{H}]$ of 0.20 ± 0.10 dex. According to Bergemann & Cescutti (2010) and Bergemann & Gehren (2008), these discrepancies are due to NLTE effects on neutral Cr and Mn. The NLTE corrections provided by Bergemann & Cescutti (2010) and Bergemann & Gehren (2008)⁴ for stars with similar parameters to those of our targets are between $+0.20$ and $+0.60$ dex for Cr I, and between $+0.40$ and $+0.60$ for Mn I. No corrections are available for the Cr II and Mn II lines we used, but we expect them to be positive and <0.1 dex, similar to the corrections calculated for metal-poor dwarf stars (Bergemann & Gehren 2008; Bergemann & Cescutti 2010; Bergemann et al. 2019). If we assume that the ionised species, which are the majority species in these stars, are formed close to LTE, the result of

⁴ <https://nlte.mpia.de>

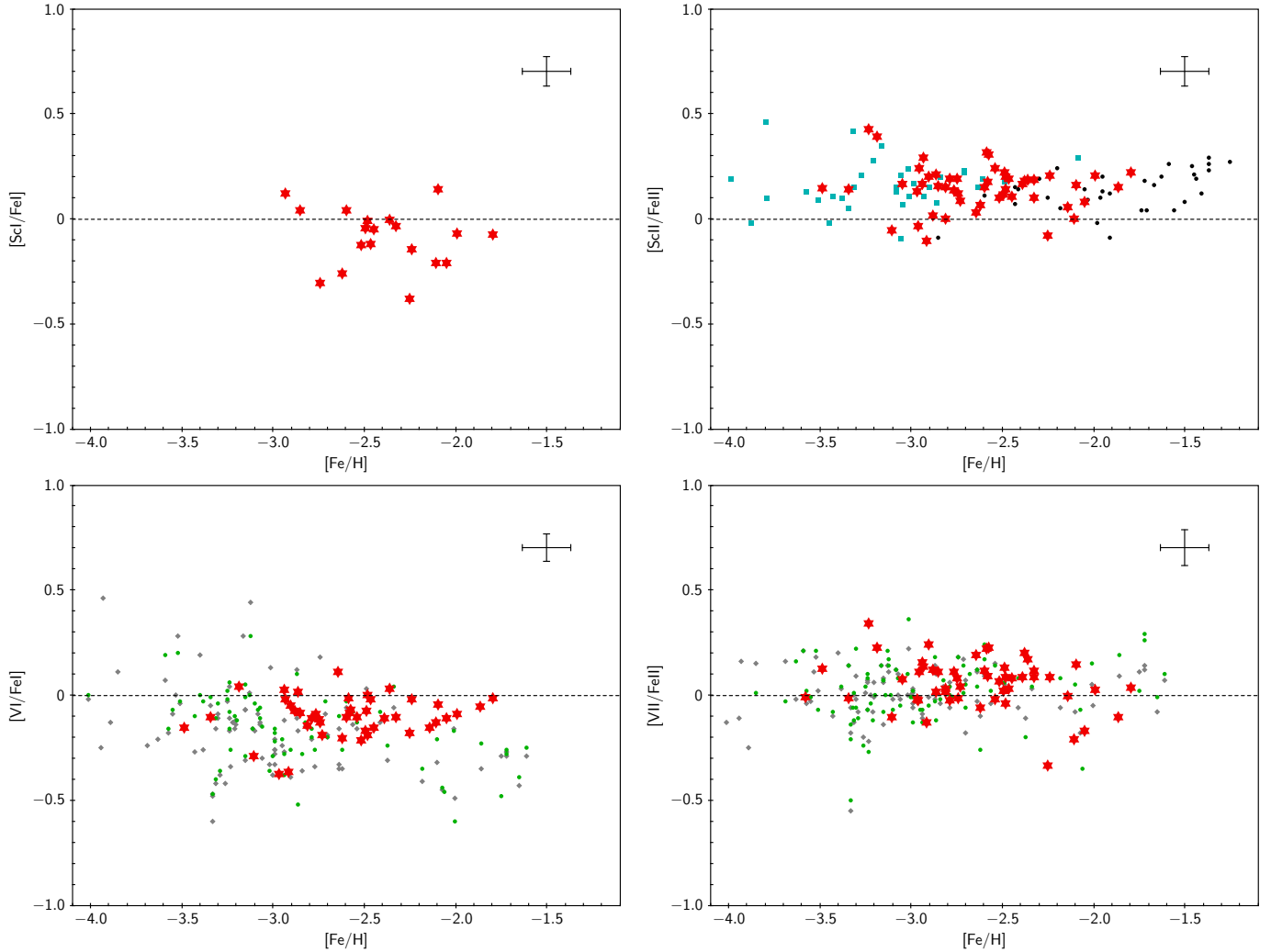


Fig. 4. Elemental abundance ratios of Sc and V as a function of $[\text{Fe}/\text{H}]$ for stars in our sample (red stars). Cyan squares and black dots represent Sc abundances for stars in the Large Program (Cayrel et al. 2004) and in Ishigaki et al. (2013), respectively. Green dots and grey diamonds represent V abundances for stars in Roederer et al. (2014a) and Ou et al. (2020), respectively. A representative error is plotted in the upper-right corner of each panel.

applying the above NLTE corrections to our Cr I and Mn I abundances would be to worsen the ionisation balance for both elements. A possible explanation is that hydrodynamical effects have not been taken into account.

For many lines of several elements the 1D NLTE corrections are positive while the 3D NLTE corrections are negative, and the full 3D NLTE correction is lower than the 1D NLTE. Bergemann et al. (2019) have computed 3D NLTE corrections for several Mn I lines and for one Mn II line. The 3D NLTE corrections for Mn I lines are positive and, surprisingly, larger than the 1D NLTE (see Fig. 17 of Bergemann et al. 2019), while the Mn II 348.8 nm line has the expected behaviour, with the 3D NLTE correction being smaller than the 1D NLTE correction. It thus seems that if the 3D NLTE corrections were applied, the ionisation balance for Mn would be worse than in LTE.

In the lower-right panel of Fig. 5, we compare our LTE Mn II abundances with the NLTE abundances of Eitner et al. (2020). In their study, they found a difference between Mn II and Mn I between 0.1 and 0.45 dex in the LTE approximation, which is in agreement with our results. In the NLTE approximation, this discrepancy becomes lower than 0.1 dex. This is further evidence

that the difference between the ionised and neutral species is due to NLTE effects that affect the Mn I lines.

4.4.3. Co, Ni, Cu, and Zn

Figure 6 shows the comparison between $[\text{Co}/\text{Fe I}]$, $[\text{Ni}/\text{Fe I}]$, $[\text{Cu}/\text{Fe I}]$, and $[\text{Zn}/\text{Fe I}]$ abundance ratios as a function of $[\text{Fe}/\text{H}]$ for our stars and the same quantities in literature. We observe a decreasing trend with metallicity for Co and Zn, and a flat trend with a mean value around zero for Ni. Our results appear in agreement with previous studies and confirm the trend with metallicity found by other authors (Cayrel et al. 2004; Takeda et al. 2005; Lai et al. 2008; Ishigaki et al. 2013, and references therein).

Previous studies have found that the $[\text{Cu}/\text{Fe}]$ abundance ratio decreases with decreasing metallicity in LTE (see e.g. Andrievsky et al. 2018; Roederer & Barklem 2018; Shi et al. 2018). However, the NLTE analysis of Andrievsky et al. (2018) found that the decrease is much smaller, with $[\text{Cu}/\text{Fe}] \gtrsim -0.3$, and for the extremely metal-poor giant CD-38 245 ($[\text{Fe}/\text{H}] = -4.19$) they found $[\text{Cu}/\text{Fe}] = -0.07$. Both our results and those of Ishigaki et al. (2013) are based on LTE and they seem to

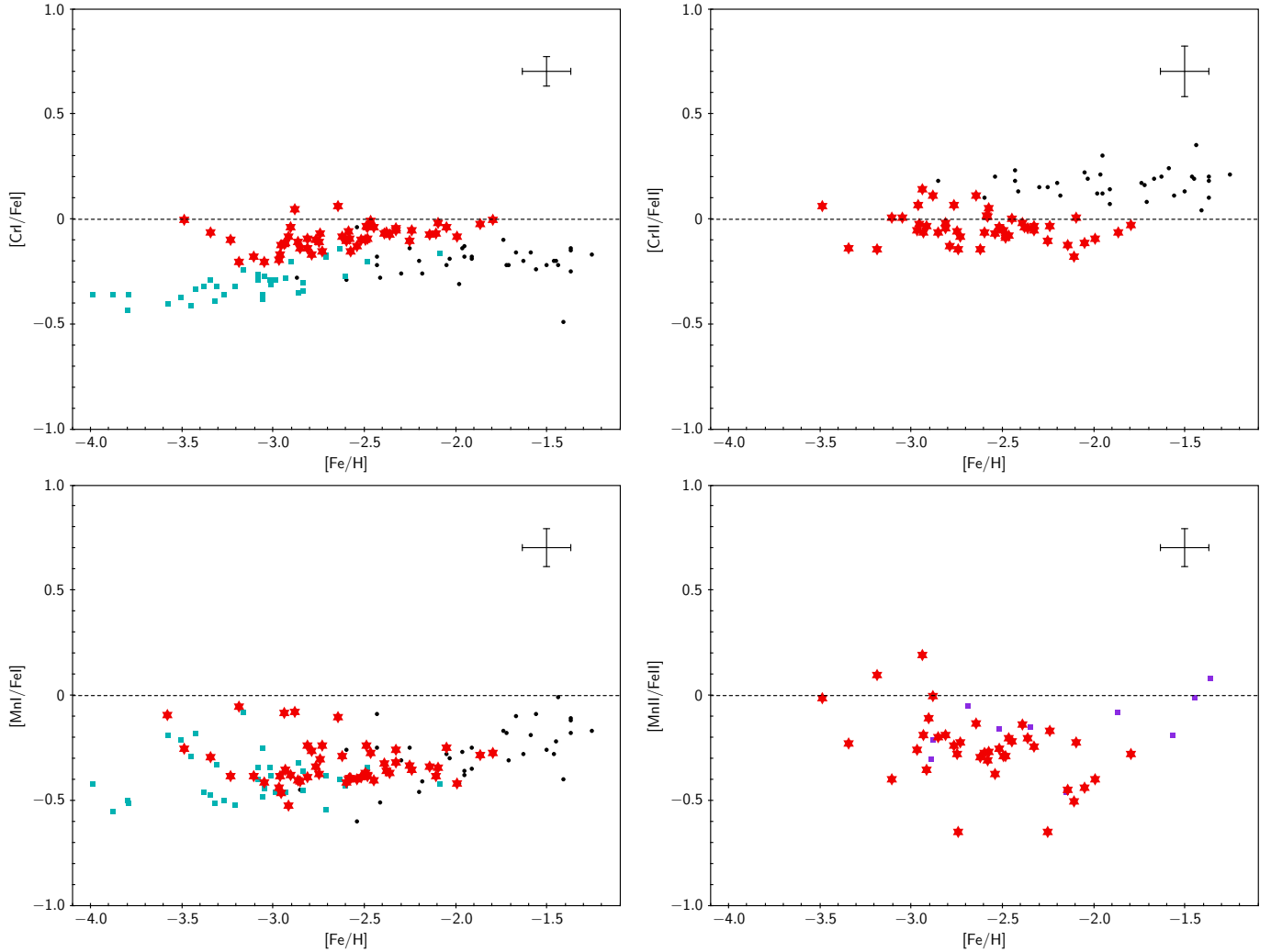


Fig. 5. Elemental abundance ratios of Cr and Mn as a function of $[\text{Fe}/\text{H}]$ for stars in our sample (red star symbols). Cyan squares and black dots are from Cayrel et al. (2004) and Ishigaki et al. (2013), respectively. Purple squares represent NLTE $[\text{Mn}/\text{Fe}]$ abundance ratios for stars in Eitner et al. (2020). A representative error is plotted in the upper-right corner of each panel.

suggest that the trend with metallicity flattens out at $[\text{Fe}/\text{H}] < -1.8$ for giant stars. We note that our derived $[\text{Cu I}/\text{Fe I}]$ ratios are ~ 0.25 dex higher than the values found by Ishigaki et al. (2013) for stars in the same range of metallicity. The origin of this discrepancy is not clear, since we do not have any Cu measurement in common with Ishigaki et al. (2013).

4.4.4. Zn-rich stars: CES1543+0201 and CES2254-4209

In Fig. 6, in the panel showing $[\text{Zn}/\text{Fe}]$, two stars stand out from the trend defined by the others and by the measurements in the literature, showing $[\text{Zn}/\text{Fe}] \sim +0.7$. CES2254-4209 (also known as HE2252-4225) was discovered in the context of the HERES survey by Mashonkina et al. (2014) as an r -enhanced star ($[r/\text{Fe}] = +0.80$). Mashonkina et al. (2014) found a lower enhancement for CES2254-4209 ($[\text{Zn}/\text{Fe}] = +0.43$), mostly due to the fact that both Fe and Zn abundances have been derived by applying NLTE corrections. The measured abundance of Th and the anomalously high Th/Eu ratio, corresponding to a radioactive age of 1.5 ± 1.5 Gyr, classify it as an actinide boost star, a class that still only contains a handful of stars and whose prototype is CS 31082-001 (Cayrel et al. 2001; Hill et al. 2002). Such an occurrence may suggest that the overabundance of Zn is in

fact due to its production through the r process. However, the other Zn-rich star, CES1543+0201 (also known as CS 30312-100), initially discovered by Aoki et al. (2002), has been classified as a CEMP star ($[\text{C}/\text{Fe}] = +0.98$) with no enhancement of n -capture elements (CEMP-no) by Aoki et al. (2007). This star has been analysed in detail in Roederer et al. (2014a), who found a similar enhancement as in our study ($[\text{Zn}/\text{Fe}] = +0.71$).

In Fig. 7 we show abundance patterns for stars CES1543+0201 (magenta) and CES2254-4209 (cyan). We tried to fit these patterns with different SN yields using STARFIT⁵ (Heger & Woosley 2010). For the lighter elements, the low mass SNe ($\sim 12 M_{\odot}$) derived by STARFIT provide reasonable fits to the observations, as quantified by χ^2 statistics, while they fail to reproduce the observed Zn abundance, and some models also fail at explaining the Sc abundances. This is expected since such models cannot account for the neutrino-driven ejecta, where the weak r process and/or the νp process may contribute to these and heavier elements.

From the abundance patterns in Fig. 7, we notice that the two Zn-rich stars also show a slight enhancement in Ni compared to the mean value observed for the sample stars of similar

⁵ <http://starfit.org/>

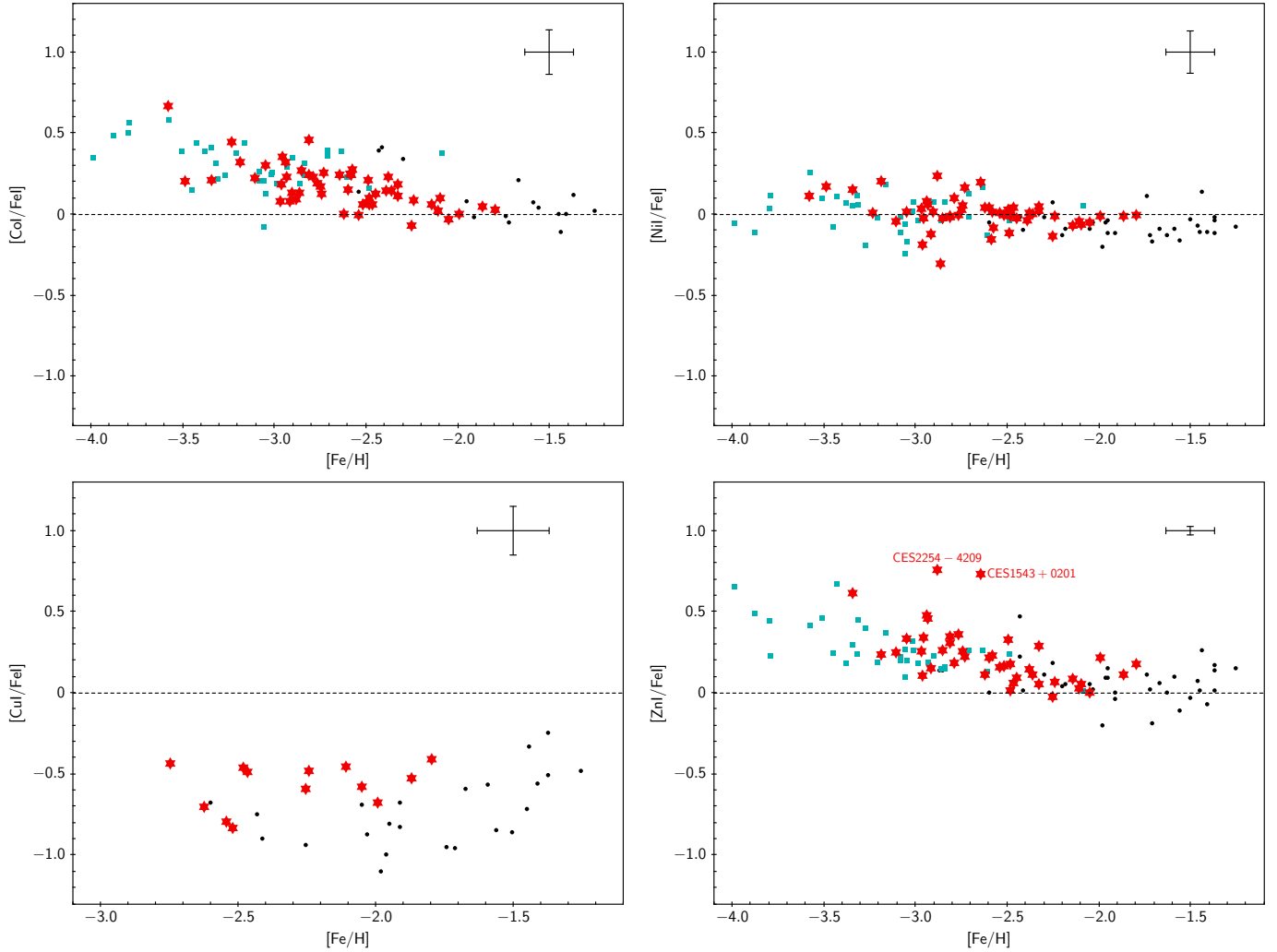


Fig. 6. Elemental abundance ratios of Co, Ni, Cu, and Zn as a function of $[Fe/H]$ for stars in our sample (red star symbols). Cyan squares and black dots represent the same quantities for stars in the Large Program (Cayrel et al. 2004) and in Ishigaki et al. (2013), respectively. A representative error is plotted in the upper-right corner of each panel.

metallicity. In their study of Zn abundances in RGB stars of the Sculptor dwarf galaxy, Skúladóttir et al. (2017) found a correlation between Zn and Ni abundances. We checked whether this correlation was also present in our sample by performing a non-parametric Kendall's τ test, and we found a correlation probability of 99.9%. Looking at Fig. 8, we note that the stars seem to follow two different branches in the plane for $[Ni/Fe] > 0.05$. For some stars $[Zn/Fe]$ increases with $[Ni/Fe]$, while for the others $[Zn/Fe]$ remains approximately constant as $[Ni/Fe]$ increases. In our opinion, this pattern could be due to a different explosion energy of the SN for a given mass of the progenitor star (see e.g. Nomoto et al. 2013, and references therein). Hypernovae (HNe), a type of core collapse SNe with extremely large explosion energies ($\geq 10^{52}$ erg), are able to produce a much larger amount of iron-peak elements, especially Zn, than classical SNe via α -rich freeze-out (e.g. Galama et al. 1998; Iwamoto et al. 1998; Nomoto et al. 2001; Umeda & Nomoto 2002). It is therefore possible that the Zn-rich stars in our sample formed in a gas cloud pre-enriched by HNe, while stars with approximately constant $[Zn/Fe]$ formed from gas enriched by SNe with lower explosion energies.

4.5. Light n -capture elements: Sr, Y, and Zr

The derived $[Sr II/Fe II]$, $[Y II/Fe II]$, and $[Zr II/Fe II]$ abundance ratios as a function of $[Fe/H]$ are shown in Fig. 9, and compared to literature values for giant stars of similar metallicity. Our results appear in general agreement with previous studies. For stars in Roederer et al. (2014a), we note that for $[Fe/H] < -3.0$ the dispersions around the mean value become larger and the abundance ratios of Sr and Y seem to decrease with metallicity. These trends have also been observed in other studies (see e.g. François et al. 2007). This is not the case for our targets, for which the trend remains approximately flat at these metallicities, with sample averages and standard deviations of $[Sr II/Fe II] = -0.08 \pm 0.32$, $[Y II/Fe II] = -0.24 \pm 0.25$, and $[Zr II/Fe II] = +0.16 \pm 0.26$. We stress the fact that, at metallicities below -3 , we only have measurements for about five stars in our sample, so it is possible that this difference in trend with the literature could be due to poor statistics.

For the seven stars for which we were able to measure Zr I, we find a mean difference between $[Zr II/H]$ and $[Zr I/H]$ of 0.57 ± 0.09 dex. We suspect that this difference is due to strong NLTE effects. According to Velichko et al. (2010), NLTE corrections for Zr II are $\sim +0.2$ dex for giant stars with $[Fe/H] \sim -3$.

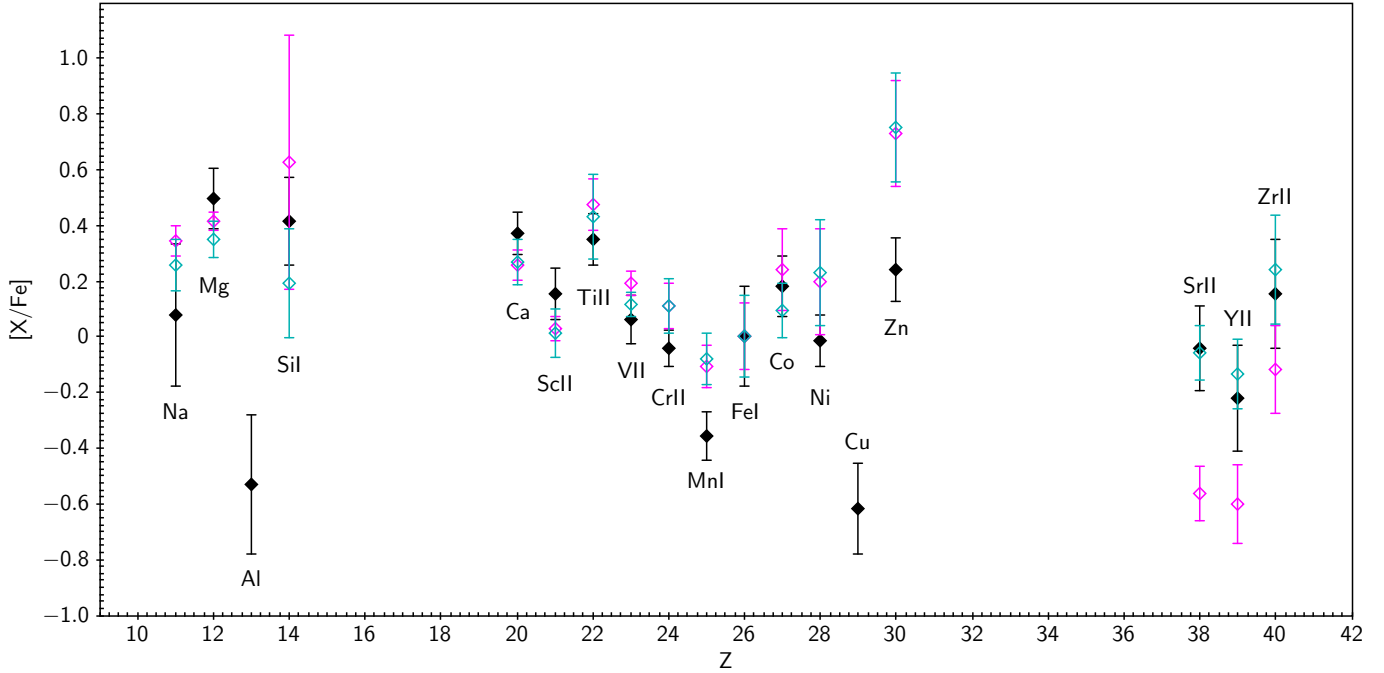


Fig. 7. Elemental abundance ratios versus atomic number, Z , for stars in the sample with $-3.1 < [\text{Fe}/\text{H}] < -2.4$. Coloured symbols indicate abundance patterns for stars CES1543+0201 (magenta) and CES2254-4209 (cyan) with errors. Black symbols indicate the average abundance ratios of Zn-normal stars. Black error bars represent the standard deviation around the mean abundance. Abundance ratios of neutral and ionised species are scaled to their Fe counterpart.

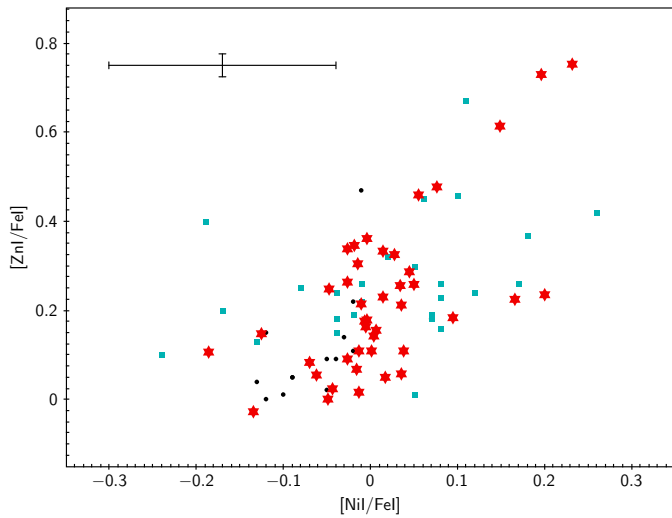


Fig. 8. $[\text{Zn}/\text{Fe}]$ versus $[\text{Ni}/\text{Fe}]$ abundance ratios for stars in our sample (red star symbols). Cyan squares and black dots represent the same quantities for stars of similar metallicity in the Large Program (Cayrel et al. 2004) and in Ishigaki et al. (2013), respectively. A representative error is plotted in the upper-left corner.

At solar metallicity, the NLTE corrections for Zr I are about +0.3 dex, while no correction is available for metal-poor stars.

5. Discussion

The abundances of Sr, Y, and Zr are critical to constrain the astrophysical conditions of their production site once nuclear physics uncertainties are reduced (Psaltis et al. 2022). The variations in the observationally derived abundances could be due to differences in the analysis as described above; therefore, it is impor-

tant to have homogeneously derived abundances for a large number of stars, as we presented here. In homogeneous analyses, the variations found in the observations can be linked to different astrophysical conditions and thus be used to constrain the site. A potential contribution to Sr, Y, and Zr are neutrino-driven ejecta in core-collapse SNe, where changes in the conditions (entropy, neutron richness, and expansion timescale) result in different patterns (see e.g. Hansen et al. 2014a). Since Sr, Y, and Zr are produced in SNe by a process that runs close to stability, the nuclear physics uncertainties are small or can be constrained by experiments in the near future. Therefore, homogeneous abundances of the lighter heavy elements are a strong diagnostic for the conditions in SN explosions.

In Fig. 10 we note that there are stars that show a $[\text{Y II}/\text{Sr II}]$ and $[\text{Zr II}/\text{Sr II}]$ ratio that is different, higher or lower, from the average of the other stars in the sample. In the following subsections we present these peculiar stars, and defer a deeper discussion on their abundance pattern in future articles, when a more complete inventory of the n-capture element abundances will be available.

5.1. CES1237+1922

The star CES1237+1922 (also known as BS 16085-0050) is deficient in Sr, Y and Zr compared to stars of similar metallicity (see Figs. 9 and 11), with $A(\text{Sr II}) = -1.78 \pm 0.04$ ($[\text{Sr II}/\text{Fe II}] = -1.66$), $A(\text{Y II}) = -2.03 \pm 0.05$ ($[\text{Y II}/\text{Fe II}] = -1.21$), and $A(\text{Zr II}) = -1.46 \pm 0.12$ ($[\text{Zr II}/\text{Fe II}] = -1.04$). The chemical composition of this star was first studied by Giridhar et al. (2001), who noted it for being rich in α -elements. This finding is confirmed by our analysis, as for this star we derived $A(\text{Mg I}) = +5.12 \pm 0.04$ ($[\text{Mg I}/\text{Fe I}] = +0.77$) and $A(\text{Ca I}) = +3.68 \pm 0.10$ ($[\text{Ca I}/\text{Fe I}] = +0.54$). Sr abundance derived by Giridhar et al. (2001) was low, and so was that in

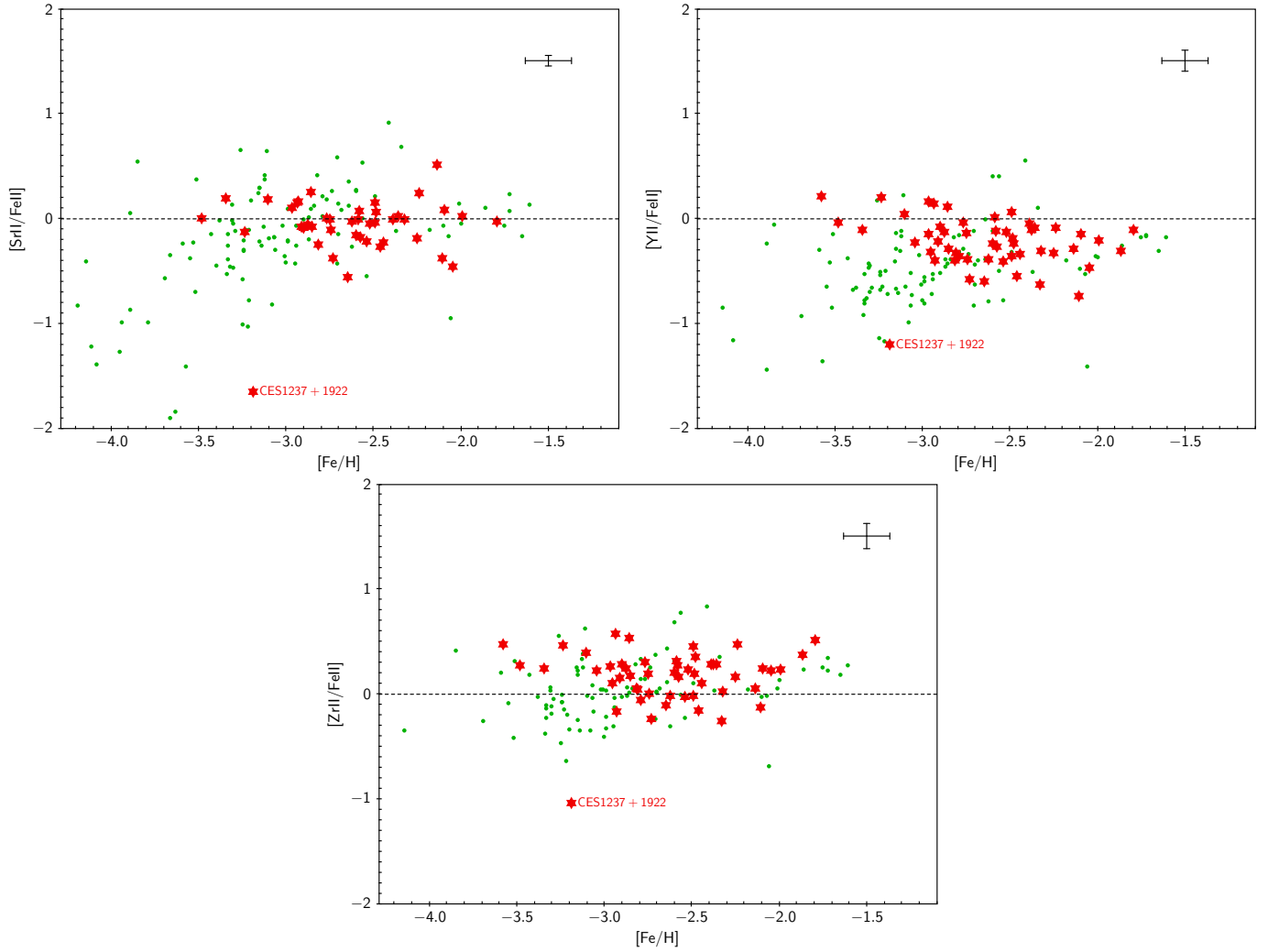


Fig. 9. Elemental abundance ratios of Sr, Y, and Zr as a function of $[Fe/H]$ for stars in our sample (red star symbols). Green dots represent Sr, Y, and Zr abundances derived in Roederer et al. (2014a). A representative error is plotted in the upper-right corner of each panel.

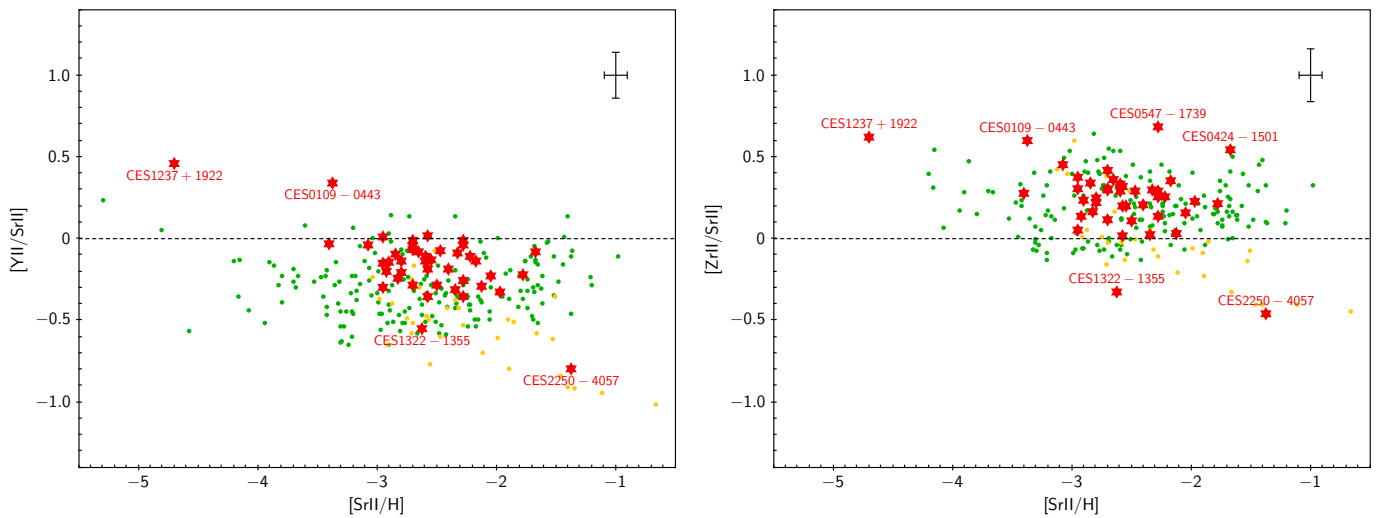


Fig. 10. $[Y II/Sr II]$ and $[Zr II/Sr II]$ as a function of $[Sr II/H]$ for stars in our sample (red star symbols). Green dots represent the same quantities derived for main sequence, RGB, and sub-giant stars in the Roederer et al. (2014a) sample. Yellow dots are the same quantities derived for horizontal branch stars in the Roederer et al. (2014a) sample. A representative error is plotted in the upper-right corner of each panel.

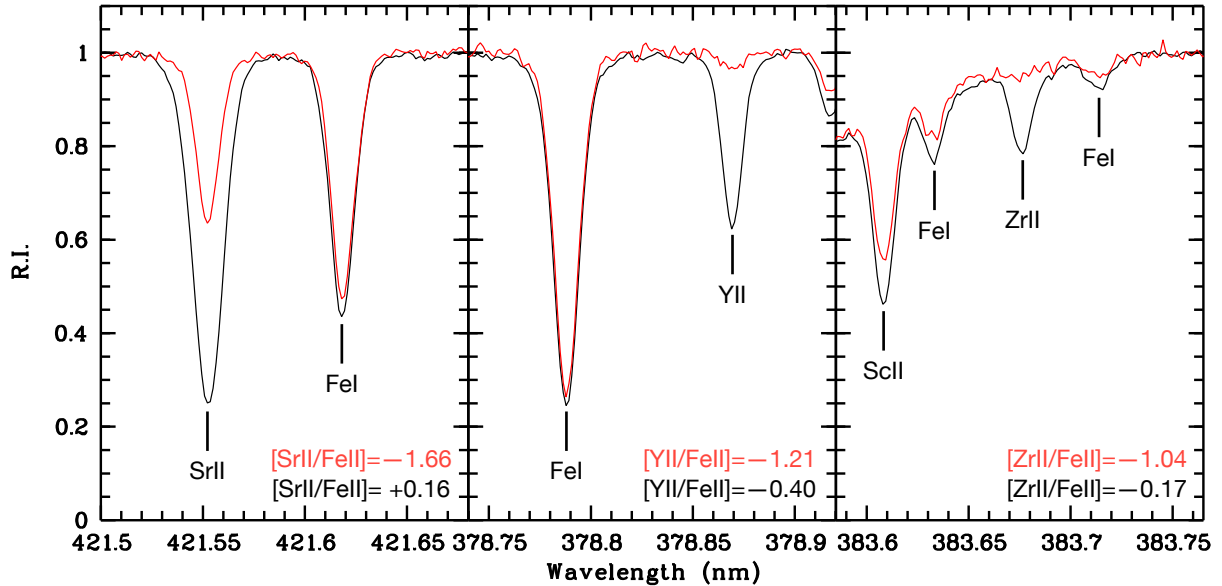


Fig. 11. Normalised spectra of stars CES1237+1922 (red) and CES1322-1355 (black) around the Sr II line at 421.5 nm (*left panel*), the Y II line at 378.8 nm (*central panel*), and the Zr II line at 383.6 nm (*right panel*). The stars have similar stellar parameters ($T_{\text{eff}} = 4960$, $\log g = 1.8$, $v_{\text{turb}} = 1.9$, $[\text{Fe}/\text{H}] = -3$).

Honda et al. (2004). This is essentially in line with our analysis, once the lower gravity adopted by Giridhar et al. (2001) is accounted for, with respect to ours and that of Honda et al. (2004). There are very few stars that have such low abundances of all three elements that populate the first peak of n-capture elements. We looked for stars with similar light n-capture elements abundances as CES1237+1922 in the SAGA database (Suda et al. 2008). We found that there are only seven stars with similar Sr and Y abundances, and only two of these have a measurement of Zr.

Figure 10 shows how CES1237+1922 stands out with respect to the rest of our sample (see also Figs. 1 and 3 of François et al. 2007). Qian & Wasserburg (2008) noted the difficulty in explaining the stars with low abundances of first peak elements. In a scenario in which all n-capture elements are formed via the *r* process, they invoked three distinct *r*-process sites to explain the observations. Faint SNe, with mixing and fall-back (Iwamoto et al. 2005), are appealing sites since they show an excess of hydrostatic burning products with respect to the explosive products, thus explaining the exceptional stars with very low $[\text{Sr}, \text{Y}, \text{Zr}/\text{Fe}]$.

Several studies have shown that the observed abundances of the first peak elements and that of second peak elements in low metallicity stars require the existence of at least two sites for n-capture nucleosynthesis (e.g. Hansen et al. 2012, 2014b,a; Spite et al. 2018). The Galactic chemical evolution models of Prantzos et al. (2018) seem incapable of producing low $[\text{Sr}/\text{Fe}]$, $[\text{Y}/\text{Fe}]$ and $[\text{Zr}/\text{Fe}]$ ratios as observed in CES1237+1922, even in the unrealistic hypothesis of switching off completely the *r*-process contribution.

Another possibility would be that the α -elements and Sr, Y, and Zr are produced in a neutrino-driven SN, while heavy n-capture elements (second peak and heavier) come from an *r*-process event where first peak elements are underproduced compared to heavier ones, like, for example, neutron star merger dynamical ejecta (Korobkin et al. 2012) and disk ejecta (Wu et al. 2016). The low abundance of Sr, Y, and Zr relative to the iron-group elements could point to proton-rich ejecta from

SN explosions. Under such conditions, the *vp* process can also produce Sr, Y, and Zr; however, their abundances are low relative to the iron-group nuclei (Hansen et al. 2014a; Fröhlich et al. 2006; Wanajo 2006; Pruet et al. 2006).

5.2. CES0109-0443

CES0109-0443 (also known as CS 22183-031) is underabundant in Sr with respect to Y and Zr, with $[\text{Y II}/\text{Sr II}] = +0.34$ and $[\text{Zr II}/\text{Sr II}] = +0.59$ (Fig. 10). This star was identified for the first time as an *r*-process-enhanced metal-poor star by Honda et al. (2004), with $[\text{Eu}/\text{Fe}] = +1.2$. It has also been analysed in detail by Roederer et al. (2014a), who confirmed the high enhancement in *r*-process material (Roederer et al. 2014a,b). For this star Roederer et al. (2014a) derived $A(\text{Sr}) = -0.84$ dex, $A(\text{Y}) = -1.61$ dex, and $A(\text{Zr}) = -0.7$ dex, which are significantly lower than those found in this study ($A(\text{Sr}) = -0.45 \pm 0.07$ dex, $A(\text{Y}) = -0.82 \pm 0.14$ dex, and $A(\text{Zr}) = -0.16 \pm 0.06$ dex). Since the lines used in our study and in Roederer et al. (2014a) are approximately the same but the parameters are different, we derived the abundances of these elements using the parameters obtained in Roederer et al. (2014a), and we found that our results are consistent with theirs. We conclude that the origin of the discrepancy is only due to the different choice of stellar parameters.

5.3. CES2250-4057 and CES1322-1355

The star CES2250-4057 (also known as CD-41 15048 also known as HE 2247-4113) is overabundant in Sr with respect to Y and Zr, with $[\text{Y II}/\text{Sr II}] = -0.80$ and $[\text{Zr II}/\text{Sr II}] = -0.46$ (Fig. 10). For this star we derived $A(\text{Sr II}) = +1.55 \pm 0.07$ ($[\text{Sr II}/\text{Fe II}] = +0.51$), $A(\text{Y II}) = +0.04 \pm 0.09$ ($[\text{Y II}/\text{Fe II}] = -0.29$), and $A(\text{Zr II}) = +0.79 \pm 0.06$ ($[\text{Zr II}/\text{Fe II}] = +0.05$). This pattern is striking in our sample, and more generally in the literature, with about a dozen stars showing a similar behaviour. This star is one of the Bidelman-MacConnell ‘weak-metal’ stars (Bidelman & MacConnell 1973; Norris et al. 1985). It is a red

horizontal branch star and has been studied by [Pereira et al. \(2013\)](#) as a potential star that is escaping the Galaxy. They do not measure Sr, but their Y and Zr abundances are compatible with ours, within errors, especially after the 0.6 dex lower gravity is accounted for. So this overabundance of Sr has not been noted before. In Fig. 10 we highlighted with yellow dots the horizontal branch stars in [Roederer et al. \(2014a\)](#). The star CES2250–4057 lies in the region occupied by other red horizontal branch stars.

There is another, slightly milder, case of this behaviour in our sample (Fig. 10), CES1322–1355 (also known as HE 1320–1339), for which we derived $A(\text{Sr II}) = +0.30 \pm 0.05$ ($[\text{Sr II}/\text{Fe II}] = +0.16$), $A(\text{Y II}) = -0.96 \pm 0.13$ ($[\text{Y II}/\text{Fe II}] = -0.40$), and $A(\text{Zr II}) = -0.33 \pm 0.07$ ($[\text{Zr II}/\text{Fe II}] = -0.17$). This star was initially studied within the HERES survey ([Barklem et al. 2005](#)), who found $[\text{Sr}/\text{Fe}] = +0.23 \pm 0.16$ and $[\text{Y}/\text{Fe}] = -0.13 \pm 0.15$. This star has been analysed also by [Sakari et al. \(2018\)](#) who provide $[\text{Sr}/\text{Fe}] = +0.50 \pm 0.14$. Our results are in line with previous studies once we take the different choice of stellar parameters into account. [Sakari et al. \(2018\)](#) classified this star as limited-*r*, a classification introduced by [Frebel \(2018\)](#) ($[\text{Eu}/\text{Fe}] < 0.3$, $[\text{Sr}/\text{Ba}] > 0.5$, and $[\text{Sr}/\text{Eu}] > 0.0$) with the aim of capturing the stars enriched under the condition of low neutron-to-seed ratios, a process more often referred to as ‘weak-*r*’ process. Yet since they do not have measurements of Y and Zr, [Sakari et al. \(2018\)](#) did not note the overabundance of Sr ($[\text{Y II}/\text{Sr II}] = -0.55$ and $[\text{Zr II}/\text{Sr II}] = -0.33$).

5.4. CES0547–1739 and CES0424–1501

Looking at the right panel in Fig. 10, we note that there are two stars (CES0547–1739 and CES0424–1501) with an overabundance of Zr with respect to Sr and Y, with $[\text{Zr II}/\text{Sr II}] = +0.68$ and $[\text{Zr II}/\text{Y II}] = +0.70$ for CES0547–1739, and $[\text{Zr II}/\text{Sr II}] = +0.54$ and $[\text{Zr II}/\text{Y II}] = +0.62$ for CES0424–1501. Star CES0547–1739 (also known as TYC 5922-517-1) has previously been observed by the GALAH survey, which provided stellar parameters and chemical abundances for some elements ([Martell et al. 2017](#); [Buder et al. 2018](#)). As no Sr and Zr abundance is present in the literature for this star, we provide them in this study for the first time. Star CES0424–1501 (also known as BD-15 779) has been studied in detail by [Hansen et al. \(2020\)](#), who found $[\text{Zr}/\text{Sr}] = +0.38$ and $[\text{Zr}/\text{Y}] = +0.68$. These results are compatible with ours taking into account the uncertainties and the difference in stellar parameters.

6. Conclusions

In this study we present a homogeneous set of stellar parameters and a chemical abundance analysis of elements from Na to Zr for a sample of 52 Galactic halo giant stars with $-3.58 \leq [\text{Fe}/\text{H}] \leq -1.79$. We compared our results to the ones in the literature and find a good agreement with previous studies. For stars that have a few chemical abundances in the literature, we completed the chemical inventory of light elements.

The main conclusions of this study are the following:

- For 22 stars we were able to measure the Si II abundances thanks to the high S/N and resolution of our dataset. Similar measures are not available in the literature for these stars. Quite interestingly, Si is very close to ionisation balance, with our parallax-based gravities, which suggests that either the NLTE effects are not large or they are similar for the neutral and singly ionised lines. This is in agreement with the results obtained by [Amarsi et al. \(2020\)](#), who find that NLTE effects on Si are small for stars in the GALAH survey,

although the metallicity of the stars in their sample is higher than ours.

- We were able to measure Sc I in 19 metal-poor giants, again a novelty with respect to previous studies. The ionisation imbalance is on average 0.37 dex. It would be interesting to study NLTE effects on Sc I to see if this is the cause of the ionisation imbalance.
- For Cr we have a very important result: for our choice of lines we find a flat trend of $[\text{Cr}/\text{Fe}] \approx 0$, both for the neutral and the singly ionised species, in our LTE treatment. This trend is theoretically expected since Cr and Fe are both formed under the same physical conditions. Previous investigations (e.g. [McWilliam et al. 1995](#); [Cayrel et al. 2004](#)) relied heavily on Cr I resonance lines, which are strongly affected by NLTE effects. This has been observationally confirmed by [Bonifacio et al. \(2009\)](#), who find that, for their sample of extremely metal-poor giants, the $[\text{Cr II}/\text{Fe}]$ is around zero, while $[\text{Cr I}/\text{Fe}]$ decreases with decreasing metallicity, suggesting NLTE effects on the Cr I lines. This is supported by the large scatter in Cr abundances, both from ionised and neutral species, from chemical studies of individual stars ([Snedden et al. 2016](#)).
- We were able to measure Mn II abundances for 38 stars; again, this measure is not generally available. Existing NLTE and 3D NLTE computations do not seem able to explain the ionisation imbalance and in fact seem to worsen it. Further theoretical investigation of the line formation of Mn I and Mn II stars is desirable.
- We have roughly doubled the number of measurements of Cu in the metallicity regime $[\text{Fe}/\text{H}] \leq -2.5$.
- We highlighted the existence of two Zn-rich stars in the sample. Both stars were previously known, and our measurements are consistent with the literature. The fact that one of the two stars (CES2254–4209) is rich in *r*-process elements (and is in fact an actinide boost star) while the other (CES1543+0201) is not essentially rules out the hypothesis that this enhancement is due to the production of Zn through neutron captures.
- We noted the existence of two branches in the $[\text{Zn}/\text{Fe}]$ versus $[\text{Ni}/\text{Fe}]$ plane and suggest that the high $[\text{Zn}/\text{Fe}]$ branch is due to a contribution of HNe to the chemical enrichment of the gas out of which the stars were formed. These two branches are also present in the [Cayrel et al. \(2004\)](#) sample, but they were not reported before. Our data help make the presence of the two branches more obvious.
- The measurement of Sr, Y, and Zr highlighted several stars with a peculiar pattern. CES1237+1922 is deficient in all three elements compared to the other stars in the sample. CES2250–4057 shows abundances of Y and Zr that are compatible with those of other stars with similar metallicity; however, $[\text{Sr}/\text{H}]$ is about 1 dex more abundant than $[\text{Y}/\text{H}]$ and $[\text{Zr}/\text{H}]$, making the production site of Sr – Zr far from clear.

The high quality of our spectra, both in terms of S/N and resolving power, allowed us to measure many weak lines that are in general not measured in stars in this metallicity range. In this way, we provided a unique sample of measures of Si II, Sc I, and Mn II. These observations can provide important guidelines in the development of line formation computations, more sophisticated than those presented here, that take deviations from LTE and hydrodynamical effects into account.

The homogeneity of our analysis was crucial in highlighting any chemical peculiarities in the stars of our sample. Stellar parameters derived in this study will be used to determine

the heavy n-capture element abundances in future papers of this project, and this will allow us to draw more conclusions about the chemistry of these peculiar stars.

Acknowledgements. We gratefully acknowledge A. Heger and C. Chan for allowing us to show the results obtained with STARFIT code. We gratefully acknowledge support from the French National Research Agency (ANR) funded project “Pristine” (ANR-18-CE31-0017). We acknowledge support from the Deutsche Forschungsgemeinschaft (DFG, German Research Foundation)-Project No. 279384907-SFB 1245, the European Research Council Grant No. 677912 EUROPIUM, and the State of Hesse within the Research Cluster ELEMENTS (Project ID 500/10.006). This project has received funding from the European Research Council (ERC) under the European Union’s Horizon 2020 research and innovation programme (grant agreement No. 804240). M.R. acknowledges the support by the Spanish Ministry of Science, Education and Universities (PGC2018-095984-B-I00) and the Valencian Community (PROM-ETEU/2019/071). A.J.K.H. gratefully acknowledges funding by the Deutsche Forschungsgemeinschaft (DFG, German Research Foundation) – Project-ID 138713538 – SFB 881 (“The Milky Way System”), subprojects A03, A05, A11. This work has made use of data from the European Space Agency (ESA) mission *Gaia* (<https://www.cosmos.esa.int/gaia>), processed by the *Gaia* Data Processing and Analysis Consortium (DPAC, <https://www.cosmos.esa.int/web/gaia/dpac/consortium>). Funding for the DPAC has been provided by national institutions, in particular the institutions participating in the *Gaia* Multilateral Agreement. This article is based upon work from the “ChETEC” COST Action (CA16117), supported by COST (European Cooperation in Science and Technology).

References

- Alvarez, R., & Plez, B. 1998, *A&A*, **330**, 1109
- Amarsi, A. M., Lind, K., Asplund, M., Barklem, P. S., & Collet, R. 2016, *MNRAS*, **463**, 1518
- Amarsi, A. M., Lind, K., Osorio, Y., et al. 2020, *A&A*, **642**, A62
- Andrievsky, S. M., Spite, M., Korotin, S. A., et al. 2007, *A&A*, **464**, 1081
- Andrievsky, S. M., Spite, M., Korotin, S. A., et al. 2008, *A&A*, **481**, 481
- Andrievsky, S., Bonifacio, P., Caffau, E., et al. 2018, *MNRAS*, **473**, 3377
- Aoki, W., Norris, J. E., Ryan, S. G., Beers, T. C., & Ando, H. 2002, *ApJ*, **567**, 1166
- Aoki, W., Beers, T. C., Christlieb, N., et al. 2007, *ApJ*, **655**, 492
- Arnett, D. 1996, *Supernovae and Nucleosynthesis: An Investigation of the History of Matter from the Big Bang to the Present* (Princeton: Princeton University Press)
- Banerjee, P., Qian, Y.-Z., & Heger, A. 2018, *MNRAS*, **480**, 4963
- Barklem, P. S., Christlieb, N., Beers, T. C., et al. 2005, *A&A*, **439**, 129
- Baumüller, D., & Gehren, T. 1997, *A&A*, **325**, 1088
- Baumüller, D., Butler, K., & Gehren, T. 1998, *A&A*, **338**, 637
- Bergemann, M., & Cescutti, G. 2010, *A&A*, **522**, A9
- Bergemann, M., Gallagher, A. J., Eitner, P., et al. 2019, *A&A*, **631**, A80
- Bergemann, M., & Gehren, T. 2008, *A&A*, **492**, 823
- Bidelman, W. P., & MacConnell, D. J. 1973, *AJ*, **78**, 687
- Bisterzo, S., Gallino, R., Pignatari, M., et al. 2004, *Mem. Soc. Astron. It.*, **75**, 741
- Bonifacio, P., Spite, M., Cayrel, R., et al. 2009, *A&A*, **501**, 519
- Bonifacio, P., Caffau, E., Ludwig, H. G., et al. 2018, *A&A*, **611**, A68
- Buder, S., Asplund, M., Duong, L., et al. 2018, *MNRAS*, **478**, 4513
- Burris, D. L., Pilachowski, C. A., Armandroff, T. E., et al. 2000, *ApJ*, **544**, 302
- Busso, M., Gallino, R., & Wasserburg, G. J. 1999, *ARA&A*, **37**, 239
- Caffau, E., Faraggiana, R., Ludwig, H. G., Bonifacio, P., & Steffen, M. 2011a, *Astron. Nachr.*, **332**, 128
- Caffau, E., Ludwig, H. G., Steffen, M., Freytag, B., & Bonifacio, P. 2011b, *Sol. Phys.*, **268**, 255
- Caffau, E., Monaco, L., Bonifacio, P., et al. 2019, *A&A*, **628**, A46
- Castelli, F. 2003, in *Modelling of Stellar Atmospheres*, eds. N. Piskunov, W. W. Weiss, & D. F. Gray, *IAU Symp.*, **210**, A20
- Cayrel, R., Hill, V., Beers, T. C., et al. 2001, *Nature*, **409**, 691
- Cayrel, R., Depagne, E., Spite, M., et al. 2004, *A&A*, **416**, 1117
- Choplin, A., Hirschi, R., Meynet, G., et al. 2018, *A&A*, **618**, A133
- Choplin, A., Siess, L., & Goriely, S. 2021, *A&A*, **648**, A119
- Christlieb, N., Beers, T. C., Barklem, P. S., et al. 2004, *A&A*, **428**, 1027
- Côté, B., Denissenkov, P., Herwig, F., et al. 2018, *ApJ*, **854**, 105
- Cowan, J. J., & Rose, W. K. 1977, *ApJ*, **212**, 149
- Cristallo, S., Piersanti, L., Straniero, O., et al. 2009, *PASA*, **26**, 139
- Dekker, H., D’Odorico, S., Kaufer, A., Delabre, B., & Kotzłowski, H. 2000, in *Optical and IR Telescope Instrumentation and Detectors*, eds. M. Iye, & A. F. Moorwood, *SPIE Conf. Ser.*, **4008**, 534
- Denissenkov, P. A., Herwig, F., Woodward, P., et al. 2019, *MNRAS*, **488**, 4258
- Eitner, P., Bergemann, M., Hansen, C. J., et al. 2020, *A&A*, **635**, A38
- Fitzpatrick, E. L., Massa, D., Gordon, K. D., Bohlin, R., & Clayton, G. C. 2019, *ApJ*, **886**, 108
- François, P., Depagne, E., Hill, V., et al. 2007, *A&A*, **476**, 935
- Frebel, A. 2018, *Ann. Rev. Nucl. Part. Sci.*, **68**, 237
- Frebel, A., Christlieb, N., Norris, J. E., et al. 2006, *ApJ*, **652**, 1585
- Fröhlich, C., Martínez-Pinedo, G., Liebendörfer, M., et al. 2006, *Phys. Rev. Lett.*, **96**, 142502
- Fujimoto, M. Y., Ikeda, Y., & Iben, I. J. 2000, *ApJ*, **529**, L25
- Gaia Collaboration (Prusti, T., et al.) 2016, *A&A*, **595**, A1
- Gaia Collaboration (Brown, A. G. A., et al.) 2021, *A&A*, **649**, A1
- Galama, T. J., Vreeswijk, P. M., van Paradijs, J., et al. 1998, *Nature*, **395**, 670
- Giridhar, S., Lambert, D. L., Gonzalez, G., & Pandey, G. 2001, *PASP*, **113**, 519
- Hampel, M., Stancliffe, R. J., Lugaro, M., & Meyer, B. S. 2016, *ApJ*, **831**, 171
- Hansen, C. J., Primas, F., Hartman, H., et al. 2012, *A&A*, **545**, A31
- Hansen, C. J., Montes, F., & Arcones, A. 2014a, *ApJ*, **797**, 123
- Hansen, C. J., Andersen, A. C., & Christlieb, N. 2014b, *A&A*, **568**, A47
- Hansen, T. T., Holmbeck, E. M., Beers, T. C., et al. 2018, *ApJ*, **858**, 92
- Hansen, C. J., Koch, A., Mashonkina, L., et al. 2020, *A&A*, **643**, A49
- Heger, A., & Woosley, S. E. 2010, *ApJ*, **724**, 341
- Heiter, U., Lind, K., Bergemann, M., et al. 2021, *A&A*, **645**, A106
- Hill, V., Plez, B., Cayrel, R., et al. 2002, *A&A*, **387**, 560
- Hollowell, D., Iben, I. J., & Fujimoto, M. Y. 1990, *ApJ*, **351**, 245
- Honda, S., Aoki, W., Kajino, T., et al. 2004, *ApJ*, **607**, 474
- Ishigaki, M. N., Chiba, M., & Aoki, W. 2012, *ApJ*, **753**, 64
- Ishigaki, M. N., Aoki, W., & Chiba, M. 2013, *ApJ*, **771**, 67
- Iwamoto, K., Mazzali, P. A., Nomoto, K., et al. 1998, *Nature*, **395**, 672
- Iwamoto, N., Umeda, H., Tominaga, N., Nomoto, K., & Maeda, K. 2005, *Science*, **309**, 451
- Johnson, J. A. 2002, *ApJS*, **139**, 219
- Koch, A., Reichert, M., Hansen, C. J., et al. 2019, *A&A*, **622**, A159
- Koch-Hansen, A. J., Hansen, C. J., Lombardo, L., et al. 2021, *A&A*, **645**, A64
- Korobkin, O., Rosswog, S., Arcones, A., & Winteler, C. 2012, *MNRAS*, **426**, 1940
- Kratz, K.-L., Farouqi, K., Pfeiffer, B., et al. 2007, *ApJ*, **662**, 39
- Kurucz, R. L. 2005, *Mem. Soc. Astron. It. Suppl.*, **8**, 14
- Lai, D. K., Bolte, M., Johnson, J. A., et al. 2008, *ApJ*, **681**, 1524
- Lind, K., Asplund, M., Barklem, P. S., & Belyaev, A. K. 2011, *A&A*, **528**, A103
- Lodders, K., Palme, H., & Gail, H. P. 2009, *Landolt BÖrstein*, **4B**, 712
- Luck, R. E., & Bond, H. E. 1985, *ApJ*, **292**, 559
- Martell, S. L., Sharma, S., Buder, S., et al. 2017, *MNRAS*, **465**, 3203
- Mashonkina, L. I., Sakhিবullin, N. A., & Shimanskii, V. V. 1993, *Astron. Rep.*, **37**, 192
- Mashonkina, L., Christlieb, N., & Eriksson, K. 2014, *A&A*, **569**, A43
- Mashonkina, L., Jablonka, P., Pakhomov, Y., Sitnova, T., & North, P. 2017a, *A&A*, **604**, A129
- Mashonkina, L., Jablonka, P., Sitnova, T., Pakhomov, Y., & North, P. 2017b, *A&A*, **608**, A89
- Mashonkina, L. I., Belyaev, A. K., & Shi, J. R. 2016a, *Astron. Lett.*, **42**, 366
- Mashonkina, L. I., Sitnova, T. N., & Pakhomov, Y. V. 2016b, *Astron. Lett.*, **42**, 606
- McWilliam, A., Preston, G. W., Sneden, C., & Searle, L. 1995, *AJ*, **109**, 2757
- Mucciarelli, A., & Bonifacio, P. 2020, *A&A*, **640**, A87
- Nilsson, H., Ljung, G., Lundberg, H., & Nielsen, K. E. 2006, *A&A*, **445**, 1165
- Nomoto, K., Maeda, K., Umeda, H., & Nakamura, T. 2001, in *The Influence of Binaries on Stellar Population Studies*, ed. D. Vanbeveren, *Astrophys. Space Sci. Libr.*, **264**, 507
- Nomoto, K., Kobayashi, C., & Tominaga, N. 2013, *ARA&A*, **51**, 457
- Norris, J., Bessell, M. S., & Pickles, A. J. 1985, *ApJS*, **58**, 463
- Norris, J. E., Ryan, S. G., & Beers, T. C. 2001, *ApJ*, **561**, 1034
- Ou, X., Roederer, I. U., Sneden, C., et al. 2020, *ApJ*, **900**, 106
- Pasquini, L., Mauas, P., Käufel, H. U., & Cacciari, C. 2011, *A&A*, **531**, A35
- Pereira, C. B., Jilinski, E. G., Drake, N. A., Ortega, V. G., & Roig, F. 2013, *A&A*, **559**, A12
- Pignatari, M., Gallino, R., Heil, M., et al. 2010, *ApJ*, **710**, 1557
- Plez, B. 2012, *Astrophysics Source Code Library* [record ascl:1205.004]
- Prantzos, N., Hashimoto, M., & Nomoto, K. 1990, *A&A*, **234**, 211
- Prantzos, N., Abia, C., Limongi, M., Chieffi, A., & Cristallo, S. 2018, *MNRAS*, **476**, 3432
- Pruet, J., Hoffman, R. D., Woosley, S. E., Janka, H. T., & Buras, R. 2006, *ApJ*, **644**, 1028
- Psaltis, A., Arcones, A., Montes, F., et al. 2022, *ApJ*, **935**, 27
- Qian, Y. Z., & Wasserburg, G. J. 2001, *ApJ*, **549**, 337
- Qian, Y. Z., & Wasserburg, G. J. 2007, *Phys. Rep.*, **442**, 237
- Qian, Y. Z., & Wasserburg, G. J. 2008, *ApJ*, **687**, 272
- Roederer, I. U., & Barklem, P. S. 2018, *ApJ*, **857**, 2
- Roederer, I. U., Preston, G. W., Thompson, I. B., et al. 2014a, *AJ*, **147**, 136

- Roederer, I. U., Cowan, J. J., Preston, G. W., et al. 2014b, [MNRAS](#), **445**, 2970
- Sakari, C. M., Placco, V. M., Farrell, E. M., et al. 2018, [ApJ](#), **868**, 110
- Sbordone, L., Bonifacio, P., Castelli, F., & Kurucz, R. L. 2004, [Mem. Soc. Astron. It. Suppl.](#), **5**, 93
- Sbordone, L., Caffau, E., Bonifacio, P., & Duffau, S. 2014, [A&A](#), **564**, A109
- Schlafly, E. F., & Finkbeiner, D. P. 2011, [ApJ](#), **737**, 103
- Scott, P., Asplund, M., Grevesse, N., Bergemann, M., & Sauval, A. J. 2015, [A&A](#), **573**, A26
- Shi, J. R., Yan, H. L., Zhou, Z. M., & Zhao, G. 2018, [ApJ](#), **862**, 71
- Siqueira Mello, C., Hill, V., Barbuy, B., et al. 2014, [A&A](#), **565**, A93
- Skúladóttir, Á., & Salvadori, S. 2020, [A&A](#), **634**, L2
- Skúladóttir, Á., Tolstoy, E., Salvadori, S., Hill, V., & Pettini, M. 2017, [A&A](#), **606**, A71
- Skúladóttir, Á., Hansen, C. J., Choplin, A., et al. 2020, [A&A](#), **634**, A84
- Snedden, C., Cowan, J. J., Kobayashi, C., et al. 2016, [ApJ](#), **817**, 53
- Sobeck, J. S., Lawler, J. E., & Sneden, C. 2007, [ApJ](#), **667**, 1267
- Spite, F., Spite, M., Barbuy, B., et al. 2018, [A&A](#), **611**, A30
- Suda, T., Katsuta, Y., Yamada, S., et al. 2008, [PASJ](#), **60**, 1159
- Takeda, Y., Hashimoto, O., Taguchi, H., et al. 2005, [PASJ](#), **57**, 751
- Truran, J. W. 1981, [A&A](#), **97**, 391
- Umeda, H., & Nomoto, K. 2002, [ApJ](#), **565**, 385
- Velichko, A. B., Mashonkina, L. I., & Nilsson, H. 2010, [Astron. Lett.](#), **36**, 664
- Wanajo, S. 2006, [ApJ](#), **647**, 1323
- Wu, M.-R., Fernández, R., Martínez-Pinedo, G., & Metzger, B. D. 2016, [MNRAS](#), **463**, 2323
- Yong, D., Norris, J. E., Bessell, M. S., et al. 2013, [ApJ](#), **762**, 26
- Zhang, H. W., Gehren, T., & Zhao, G. 2008, [A&A](#), **481**, 489
- Zhao, G., Mashonkina, L., Yan, H. L., et al. 2016, [ApJ](#), **833**, 225

Appendix A: Observation log

Table A.1. Observation log.

Name ID	CERES name	RA2000	DEC2000	UVES arm	R	v_{broad} km s ⁻¹	Date	MJD	exp. time s	S/N px ⁻¹	slit "
HD2796	CES0031-1647	00:31:16.91	-16:47:40.8	BLU390	71050	7.2	2005-11-18	53692.01	300	123	0.4
				RED580	107200	7.3	2005-11-18	53692.01	300	259	0.3
HD4306	CES0045-0932	00:45:27.16	-09:32:39.8	BLU346	40970	7.7	2001-10-09	52191.14	697	131	1.0
							2001-10-09	52191.12	660	126	1.0
							2001-10-09	52191.12	660	134	1.0
							2001-10-09	52191.13	697	129	1.0
							2001-10-09	52191.11	660	129	1.0
				RED580	56990	6.9	2001-10-09	52191.11	305	241	0.7
							2001-10-09	52191.12	305	233	0.7
							2001-10-09	52191.13	305	261	0.7
							2001-10-09	52191.11	305	244	0.7
							2001-10-09	52191.12	305	240	0.7
BD-11_145	CES0048-1041	00:48:24.31	-10:41:30.9	BLU390	40970	8.8	2019-11-19	58806.05	2200	128	1.0
				RED564	42310	8.0	2019-11-19	58806.05	2200	0	1.0
HD5426	CES0055-3345	00:55:41.05	-33:45:11.5	BLU390	40970	7.0	2019-11-20	58807.05	900	160	1.0
				RED564	42310	6.4	2019-11-20	58807.05	900	360	1.0
HE0057-4541	CES0059-4524	00:59:59.28	-45:24:53.4	BLU390	40970	6.7	2007-11-07	54411.04	3600	24	1.0
							2007-11-07	54411.14	3600	24	1.0
							2007-11-07	54411.10	3600	26	1.0
							2007-11-07	54411.18	3600	23	1.0
							2007-11-08	54412.23	3600	21	1.0
BPPSCS22953-003	CES0102-6143	01:02:15.87	-61:43:45.8	BLU390	49620	8.2	2002-08-03	52489.18	1800	18	0.8
							2002-08-03	52489.20	1800	20	0.8
				RED564	87410	6.8	2002-08-03	52489.18	1800	19	0.4
							2002-08-03	52489.20	1800	21	0.4
							2007-11-09	54413.22	4500	30	1.0
HE0105-6141	CES0107-6125	01:07:37.85	-61:25:17.7	BLU390	40970	6.6	2007-11-09	54413.22	4500	30	1.0
BPPSCS22183-031	CES0109-0443	01:09:05.09	-04:43:21.3	BLU390	40970	7.1	2017-09-26	58022.22	3005	62	1.0
HD13979	CES0215-2554	02:15:20.85	-25:54:54.9	BLU390	40970	8.4	2019-11-19	58806.18	600	147	1.0
				RED564	42310	8.6	2019-11-19	58806.18	600	330	1.0
BD-22_395	CES0221-2130	02:21:57.94	-21:30:43.0	BLU390	40970	8.7	2019-11-20	58807.07	2200	141	1.0
				RED564	42310	8.8	2019-11-20	58807.07	2200	357	1.0
HE0240-0807	CES0242-0754	02:42:57.73	-07:54:35.4	BLU390	40970	8.0	2007-11-07	54411.23	3600	19	1.0
							2007-11-08	54412.27	4500	16	1.0
							2007-11-10	54414.07	3600	17	1.0
							2007-11-10	54414.03	3600	12	1.0
							2007-11-10	54414.11	3600	18	1.0
							2007-11-10	54414.21	3600	19	1.0
							2007-11-10	54414.17	3600	19	1.0
							2007-11-10	54414.25	3600	15	1.0
BPPSCS31078-018	CES0301+0616	03:01:00.69	+06:16:31.8	BLU390	40970	6.7	2019-11-19	58806.08	4200	57	1.0
							2019-11-19	58806.13	4200	59	1.0
				BLU390	40970	6.7	2017-10-01	58027.19	3005	65	1.0
				RED564	42310	6.2	2019-11-19	58806.08	4200	141	1.0
							2019-11-19	58806.13	4200	142	1.0
HE0336-2412	CES0338-2402	03:38:41.49	-24:02:50.3	BLU346	40970	6.7	2001-12-13	52256.14	1175	122	1.0
							2001-12-13	52256.15	1175	122	1.0
							2001-12-13	52256.05	1475	121	1.0
							2001-12-13	52256.18	1175	111	1.0
							2001-12-13	52256.17	1175	119	1.0
							2001-12-13	52256.03	1475	124	1.0
				RED580	56990	6.3	2001-12-13	52256.15	560	180	0.7
							2001-12-13	52256.16	560	165	0.7
							2001-12-13	52256.14	560	165	0.7
							2001-12-13	52256.15	560	180	0.7
			2001-12-13	52256.19	560	163	0.7				

Table A.1. continued.

Name ID	CERES name	RA2000	DEC2000	UVES arm	R	v_{broad} km s^{-1}	Date	MJD	exp. time s	S/N px^{-1}	slit "
BD+06_648	CES0413+0636	04:13:13.11	+06:36:01.8	BLU390	40970	9.7	2001-12-13	52256.17	560	166	0.7
							2001-12-13	52256.17	560	175	0.7
							2001-12-13	52256.18	560	159	0.7
BPSCS22186-023	CES0419-3651	04:19:45.53	-36:51:36.0	BLU390	40970	7.5	2019-11-20	58807.21	600	70	1.0
							2019-11-20	58807.21	600	322	1.0
HD27928	CES0422-3715	04:22:55.14	-37:15:49.2	BLU390	40970	7.2	2006-10-18	54026.30	2400	60	1.0
							2019-11-19	58806.21	3600	64	1.0
							2019-11-19	58806.25	3600	52	1.0
							2019-11-19	58806.21	3600	144	1.0
							2019-11-19	58806.25	3600	122	1.0
							2006-10-18	54026.30	2400	137	1.0
BD-15_779	CES0424-1501	04:24:45.64	-15:01:50.7	BLU390	40970	8.0	2019-11-19	58806.20	900	148	1.0
							2020-03-02	58910.99	2700	157	1.0
HE0428-1340	CES0430-1334	04:30:51.42	-13:34:08.1	BLU390	40970	7.2	2020-03-02	58910.99	2700	506	1.0
							2019-11-20	58807.13	1800	159	1.0
HE0442-1234	CES0444-1228	04:44:51.71	-12:28:45.5	BLU390	58640	7.4	2019-11-20	58807.13	1800	344	1.0
							2003-02-05	52675.11	3600	37	0.6
							2003-02-05	52675.15	3197	28	0.6
							2003-02-05	52675.06	3600	35	0.6
							2003-02-06	52676.06	3600	44	0.6
							2003-02-06	52676.11	3600	39	0.6
							2003-02-08	52678.12	3600	31	0.6
							2003-02-05	52675.06	3600	129	0.6
							2003-02-05	52675.15	3205	114	0.6
							2003-02-05	52675.11	3600	136	0.6
							2003-02-06	52676.06	3600	149	0.6
							2003-02-06	52676.11	3600	139	0.6
HE0516-3820	CES0518-3817	05:18:12.92	-38:17:32.7	BLU390	40970	6.7	2003-02-08	52678.12	3600	124	0.6
							2007-11-09	54413.33	3600	29	1.0
HE0524-2055	CES0527-2052	05:27:04.44	-20:52:42.1	BLU390	40970	8.3	2007-11-07	54411.32	3600	38	1.0
							2007-11-07	54411.28	3600	39	1.0
							2007-11-08	54412.33	3300	25	1.0
							2007-11-10	54414.30	3600	30	1.0
							2019-11-20	58807.23	4080	49	1.0
TYC5922-517-1	CES0547-1739	05:47:20.81	-17:39:41.0	BLU390	40970	10.0	2019-11-20	58807.23	4080	49	1.0
							2019-11-20	58807.27	4080	43	1.0
TYC4840-159-1	CES0747-0405	07:47:15.82	-04:05:46.1	BLU390	40970	11.2	2019-11-20	58807.23	4080	224	1.0
							2019-11-20	58807.27	4080	204	1.0
							2020-03-03	58911.03	2500	38	1.0
							2020-03-03	58911.06	2500	36	1.0
							2020-03-04	58912.02	1800	28	1.0
							2020-03-04	58912.04	1800	31	1.0
TYC8931-1111-1	CES0900-6222	09:00:52.59	-62:22:52.8	BLU390	40970	8.9	2020-03-03	58911.03	2500	267	1.0
							2020-03-03	58911.05	2500	259	1.0
							2020-03-04	58912.02	1800	215	1.0
							2020-03-04	58912.04	1800	229	1.0
							2019-11-19	58806.30	4200	53	1.0
							2019-11-20	58807.33	2200	25	1.0
							2019-11-19	58806.30	4200	278	1.0
							2019-11-20	58807.33	2200	161	1.0
							2020-03-04	58912.19	3600	60	1.0
							2020-03-04	58912.19	3600	250	1.0
TYC9200-2292-1	CES0919-6958	09:19:16.29	-69:58:39.9	BLU390	40970	8.9	2020-03-04	58912.15	3600	50	1.0
							2020-03-04	58912.15	3600	242	1.0
UCAC2_1106907	CES1116-7250	11:16:54.01	-72:50:16.1	BLU390	40970	10.3	2020-03-04	58912.23	3600	24	1.0
							2020-03-04	58912.23	3600	213	1.0
HE1219-0312	CES1221-0328	12:21:34.14	-03:28:39.6	BLU346	58640	5.6	2020-03-04	58912.23	3600	213	1.0
							2004-02-20	53055.33	3600	6	0.6
							2004-02-20	53055.37	3600	5	0.6
							2004-02-20	53055.28	3600	6	0.6
							2004-04-16	53111.07	1198	1	0.6
							2004-05-11	53136.02	3600	6	0.6
							2004-05-11	53136.06	3600	6	0.6
							2004-05-24	53149.09	3600	4	0.6
							2004-05-23	53149.00	3600	4	0.6
							2004-05-24	53149.04	3600	4	0.6
							2005-01-19	53389.32	3600	6	0.6

Table A.1. continued.

Name ID	CERES name	RA2000	DEC2000	UVES arm	R	v_{broad} km s^{-1}	Date	MJD	exp. time s	S/N px^{-1}	slit "
							2005-04-08	53468.12	3600	6	0.6
							2005-04-08	53468.16	3600	6	0.6
							2005-04-08	53468.21	3600	6	0.6
							2005-04-10	53470.18	3600	7	0.6
							2005-04-10	53470.13	3600	6	0.6
							2005-04-10	53470.09	3600	6	0.6
							2005-04-11	53471.10	3600	6	0.6
							2005-04-11	53471.15	3600	5	0.6
				RED580	66320	6.4	2004-02-20	53055.28	3600	36	0.6
							2004-02-20	53055.33	3600	34	0.6
							2004-02-20	53055.37	3600	33	0.6
							2004-04-16	53111.07	1201	15	0.6
							2004-05-11	53136.02	3600	34	0.6
							2004-05-11	53136.06	3600	35	0.6
							2004-05-24	53149.09	3600	29	0.6
							2004-05-23	53149.00	3600	29	0.6
							2004-05-24	53149.04	3600	29	0.6
							2005-01-19	53389.32	3600	35	0.6
							2005-04-08	53468.16	3600	35	0.6
							2005-04-08	53468.12	3600	35	0.6
							2005-04-08	53468.21	3600	34	0.6
							2005-04-10	53470.13	3600	36	0.6
							2005-04-10	53470.09	3600	33	0.6
							2005-04-10	53470.18	3600	37	0.6
							2005-04-11	53471.10	3600	34	0.6
							2005-04-11	53471.15	3600	33	0.6
HD107752	CES1222+1136	12:22:52.72	+11:36:25.5	BLU390	40970	8.0	2020-03-03	58911.22	2400	163	1.0
							2020-03-03	58911.25	2400	163	1.0
				RED564	42310	8.1	2020-03-03	58911.22	2400	426	1.0
							2020-03-03	58911.25	2400	424	1.0
HD108317	CES1226+0518	12:26:36.83	+05:18:09.0	BLU346	40970	7.7	2002-02-04	52309.29	260	154	1.0
							2002-02-04	52309.29	260	127	1.0
							2002-02-04	52309.30	260	160	1.0
							2002-02-04	52309.31	260	155	1.0
							2002-02-04	52309.29	250	158	1.0
							2002-02-04	52309.30	260	132	1.0
							2002-02-04	52309.28	250	161	1.0
				RED580	56990	6.3	2002-02-04	52309.30	107	232	0.7
							2002-02-04	52309.30	107	170	0.7
							2002-02-04	52309.29	107	200	0.7
							2002-02-04	52309.30	107	182	0.7
							2002-02-04	52309.29	107	186	0.7
							2002-02-04	52309.30	107	202	0.7
							2002-02-04	52309.31	107	218	0.7
							2002-02-04	52309.30	107	168	0.7
							2002-02-04	52309.29	107	222	0.7
							2002-02-04	52309.31	107	205	0.7
HD108577	CES1228+1220	12:28:16.86	+12:20:41.1	BLU390	40970	8.8	2020-03-03	58911.20	1100	147	1.0
				RED564	42310	8.9	2020-03-03	58911.20	1100	359	1.0
BPSBS16085-0050	CES1237+1922	12:37:46.68	+19:22:49.6	BLU390	40970	7.9	2020-03-04	58912.28	3000	76	1.0
							2020-03-04	58912.32	3000	76	1.0
				RED564	42310	8.0	2020-03-04	58912.28	3000	182	1.0
							2020-03-04	58912.32	3000	189	1.0
HE1243-2408	CES1245-2425	12:45:53.85	-24:25:02.4	BLU390	40970	7.5	2020-03-03	58911.12	3250	133	1.0
							2020-03-03	58911.16	3250	138	1.0
				RED564	42310	7.6	2020-03-03	58911.12	3250	342	1.0
							2020-03-03	58911.16	3250	346	1.0
HE1320-1339	CES1322-1355	13:22:44.11	-13:55:31.4	BLU390	40970	8.3	2020-03-03	58911.28	2600	141	1.0
							2020-03-03	58911.31	2600	149	1.0
				RED564	42310	8.3	2020-03-03	58911.28	2600	340	1.0
							2020-03-03	58911.31	2600	358	1.0
HD122563	CES1402+0941	14:02:31.85	+09:41:09.9	BLU346	65030	7.0	2002-02-19	52324.39	86	84	0.5
							2002-02-19	52324.39	86	96	0.5

Table A.1. continued.

Name ID	CERES name	RA2000	DEC2000	UVES arm	R	v_{broad} km s^{-1}	Date	MJD	exp. time s	S/N px^{-1}	slit "
				RED564	51690	8.0	2000-04-12	51646.27	60	431	0.8
							2000-04-12	51646.27	60	413	0.8
							2000-04-12	51646.27	60	407	0.8
HD122956	CES1405-1451	14:05:13.02	-14:51:25.5	BLU346	40970	8.6	2003-06-07	52797.97	250	109	1.0
				RED564	42310	8.3	2000-04-12	51646.33	120	362	1.0
							2000-04-12	51646.34	120	376	1.0
TYC9427-1414-1	CES1413-7609	14:13:11.18	-76:09:50.4	BLU390	40970	8.1	2020-03-04	58912.36	2800	111	1.0
				RED564	42310	7.7	2020-03-04	58912.36	2800	341	1.0
HD126587	CES1427-2214	14:27:00.36	-22:14:39.0	BLU346	40970	7.6	2002-03-22	52355.33	836	178	1.0
							2002-03-22	52355.32	836	170	1.0
							2002-03-22	52355.34	836	170	1.0
							2002-03-22	52355.31	836	172	1.0
							2002-03-23	52356.32	827	161	1.0
							2002-03-23	52356.31	827	164	1.0
				RED580	56990	7.0	2002-03-22	52355.32	390	293	0.7
							2002-03-22	52355.31	390	303	0.7
							2002-03-22	52355.33	390	306	0.7
							2002-03-22	52355.34	390	301	0.7
							2002-03-22	52355.32	390	290	0.7
							2002-03-22	52355.34	390	288	0.7
							2002-03-22	52355.31	390	288	0.7
							2002-03-22	52355.33	390	307	0.7
HD128279	CES1436-2906	14:36:48.51	-29:06:46.6	BLU346	40970	5.9	2003-08-07	52858.99	800	252	1.0
				BLU346	40970	5.9	2002-02-04	52309.36	250	190	1.0
							2002-02-04	52309.36	250	184	1.0
							2002-02-04	52309.36	250	191	1.0
				RED564	42310	6.8	2000-04-12	51646.32	600	551	1.0
BPSCS30312-100	CES1543+0201	15:43:31.66	+02:01:17.3	BLU390	40970	6.9	2006-03-20	53814.39	900	27	1.0
							2006-03-20	53814.38	900	29	1.0
							2006-03-20	53814.40	900	28	1.0
				RED580	42310	6.5	2006-03-20	53814.4	900	76	1.0
							2006-03-20	53814.38	900	77	1.0
							2006-03-20	53814.39	900	74	1.0
BD+05_3098	CES1552+0517	15:52:17.26	+05:17:44.3	BLU390	40970	6.9	2020-03-03	58911.34	2200	148	1.0
				RED564	42310	7.1	2020-03-03	58911.34	2200	359	1.0
BD+23_3130	CES1732+2344	17:32:41.62	+23:44:11.6	BLU390	49620	6.3	2000-04-16	51650.35	600	151	0.8
							2000-04-16	51650.34	600	151	0.8
							2000-04-16	51650.33	600	155	0.8
HD165195	CES1804+0346	18:04:40.07	+03:46:44.7	BLU346	40970	9.3	2003-09-07	52889.02	625	108	1.0
				RED564	42310	8.5	2000-04-12	51646.36	120	352	1.0
							2000-04-12	51646.36	120	370	1.0
BPSCS22891-209	CES1942-6103	19:42:02.18	-61:03:44.5	BLU390	40970	7.7	2006-10-15	54023.97	1200	44	1.0
				RED580	42310	8.6	2006-10-15	54023.97	1200	133	1.0
BPSCS22873-166	CES2019-6130	20:19:22.04	-61:30:15.1	BLU390	40970	8.6	2006-10-17	54025.98	600	25	1.0
				RED580	42310	8.9	2006-10-17	54025.98	600	95	1.0
BPSCS22897-008	CES2103-6505	21:03:11.86	-65:05:08.9	BLU346	53750	7.3	2008-04-22	54578.36	5200	30	0.7
							2008-05-12	54598.36	5200	30	0.7
							2008-05-22	54608.26	5200	28	0.7
							2008-06-24	54641.36	5200	18	0.7
							2008-06-24	54641.30	5200	19	0.7
							2008-06-27	54644.17	5200	19	0.7

Table A.1. continued.

Name ID	CERES name	RA2000	DEC2000	UVES arm	R	v_{broad} km s^{-1}	Date	MJD	exp. time s	S/N px^{-1}	slit "
BPSCS29491-069	CES2231-3238	22:31:02.19	-32:38:36.5	BLU390	71050	4.5	2005-11-20	53694.08	3600	40	0.4
							2005-11-20	53694.12	3600	39	0.4
HE2229-4153	CES2232-4138	22:32:49.05	-41:38:25.2	BLU390	40970	7.1	2004-10-03	53281.00	3600	119	0.8
							2007-11-08	54412.05	2700	52	1.0
							2007-11-09	54413.01	2700	27	1.0
							2007-11-09	54413.99	2700	46	1.0
HE2247-4113	CES2250-4057	22:50:14.02	-40:57:42.8	BLU390	40970	10.9	2008-04-28	54584.36	1800	73	0.8
							2019-11-19	58806.01	1500	160	1.0
							2019-11-19	58806.03	1500	170	1.0
							2019-11-19	58806.01	1500	328	1.0
HE2252-4225	CES2254-4209	22:54:58.57	-42:09:19.4	BLU390	49620	7.1	2019-11-19	58806.03	1500	342	1.0
							2004-10-20	53298.15	3900	18	0.8
							2005-05-18	53508.39	3300	19	0.8
							2005-06-14	53535.29	3600	18	0.8
							2005-06-14	53535.34	3600	19	0.8
							2005-07-04	53555.37	3600	23	0.8
							2005-07-04	53555.33	3600	23	0.8
							2005-07-04	53555.29	3600	21	0.8
							2005-07-06	53557.32	3600	22	0.8
							2005-07-06	53557.37	3600	23	0.8
							2005-07-10	53561.26	3600	25	0.8
							2005-05-18	53508.39	3300	54	0.8
							2005-06-14	53535.29	3600	55	0.8
							2005-06-14	53535.34	3600	56	0.8
							2005-07-04	53555.33	3600	63	0.8
							2005-07-04	53555.37	3600	62	0.8
							2005-07-04	53555.29	3600	60	0.8
2005-07-06	53557.37	3600	63	0.8							
2005-07-06	53557.32	3600	61	0.8							
2005-07-10	53561.26	3600	67	0.8							
HE2327-5642	CES2330-5626	23:30:37.09	-56:26:14.4	BLU390	49620	7.0	2004-11-15	53324.07	3600	46	0.8
							2005-08-05	53587.17	3600	43	0.8
							2005-08-05	53587.26	3600	36	0.8
							2005-08-05	53587.21	3600	42	0.8
							2005-08-10	53592.29	3600	45	0.8
							2007-11-03	54407.02	3000	57	1.0
BPSCS30315-029	CES2334-2642	23:34:26.70	-26:42:14.0	BLU390	40970	7.6	2008-01-25	54490.03	3000	75	1.0
							2007-11-06	54410.99	3600	36	1.0
							2007-11-08	54412.09	3600	44	1.0
							2007-11-08	54412.13	3600	40	1.0

ORIGINAL ARTICLE

Detailed investigation of two high-speed evolved Galactic stars

Aroa del Mar Matas Pinto¹ | Elisabetta Caffau¹ | Patrick François^{2,3} |
 Monique Spite¹ | Piercarlo Bonifacio¹ | Shinya Wanajo^{4,5} | Wako Aoki⁶ |
 Lorenzo Monaco⁷ | Takuma Suda^{8,9} | François Spite¹ | Luca Sbordone¹⁰ |
 Linda Lombardo¹ | Alessio Mucciarelli^{11,12}

¹GEPI, Observatoire de Paris, Université PSL, CNRS, Meudon, France

²GEPI, Observatoire de Paris, Université PSL, CNRS, Paris, France

³UPJV, Université de Picardie Jules Verne, Amiens, France

⁴Max Planck Institute for Gravitational Physics (Albert Einstein Institute), Potsdam, Germany

⁵iTHEMS Research Group, RIKEN, Wako, Japan

⁶National Observatory of Japan, Mitaka, Japan

⁷Departamento de Ciencias Físicas, Universidad Andres Bello, Santiago, Chile

⁸Department of Liberal Arts, Tokyo University of Technology, Ota City, Japan

⁹Research Center for the Early Universe, The University of Tokyo, Bunkyo City, Japan

¹⁰ESO - European Southern Observatory, Santiago, Chile

¹¹Dipartimento di Fisica e Astronomia, Università degli Studi di Bologna, Bologna, Italy

¹²INAF - Osservatorio di Astrofisica e Scienza dello Spazio di Bologna, Bologna, Italy

Correspondence

Aroa del Mar Matas Pinto, GEPI, Observatoire de Paris, Université PSL, CNRS, 5 Place Jules Janssen, 92190 Meudon, France. Email: marmatpint@gmail.com

Funding information

French National Research Agency, Grant/Award Number: CE31-0017

Abstract

The study of metal poor stars provides clarification and knowledge about the primordial Universe. Specially, halo stars provide explanations of the nature of the first generations of stars and the nucleosynthesis in the metal-poor regime. We present a detailed chemical analysis and determination of the kinematic and orbital properties of two stars characterized by high speed with respect to the Sun. We analyzed two high-resolution Subaru spectra employing the MyGisFOS code, which allows to derive the detailed chemical abundances for 28 elements (C, N, O, Na, Mg, Al, Si, Ca, Sc, Ti, V, Cr, Mn, Fe, Co, Ni, Cu, Zn, Sr, Y, Zr, Ba, La, Ce, Pr, Nd, Sm, and Eu), and abundance from two ionization states in the case of four elements (Ti, Cr, Fe, and Zr). TYC 622–742–1 and TYC 1193–1918–1 are metal-poor stars ([Fe/H] of -2.37 and -1.60), they are similar in the chemical pattern with respect to Fe, they are α enhanced and show a slight excess in Eu abundance. Both giant stars are poor in C and rich in N, as expected for evolved stars, and this fact is supported by the low $^{12}\text{C}/^{13}\text{C}$ isotopic ratio in TYC 1193–1918–1. Nevertheless, the C abundance of TYC 622–742–1 is particularly low. TYC 622–742–1 and TYC 1193–1918–1 have a similar chemical composition to the other Galactic halo stars of comparable metallicity. According to their kinematics, both stars belong to the Galactic halo, but they are not a part of the Gaia-Sausage-Enceladus structure.

KEYWORDS

galaxy: abundances, galaxy: evolution, galaxy: formation, galaxy: halo, galaxy: kinematics and dynamics, stars: abundances

Based on observations made with HDS at Subaru.

1 | INTRODUCTION

The old, metal-poor stellar population provides us information about the Universe in its infancy. In fact, the majority of metal-poor stars have an age comparable to the age of the Universe (see e.g., Cayrel et al. 2001), so their chemical pattern reflects the chemical composition of the primordial Universe. These stars were born at a time when just one/few generations of massive stars had a chance to explode as supernovae and enrich the interstellar gas from where they formed. Metal-poor stars are rare, overall in the solar vicinity, meaning the part of the Galaxy accessible for high-resolution and high signal-to-noise spectroscopy.

In the recent years, two methods have mainly been used to select metal-poor candidates: (i) from low-resolution spectroscopy (see e.g., Christlieb et al. 2004); (ii) from narrow-band photometry (see e.g., Caffau et al. 2020b). Broad-band photometry (iii) also allowed to select metal-poor candidates, albeit with a lower success rate (Schlaufman & Casey 2014).

(i) Several low-resolution spectroscopic surveys collected large numbers of spectra from where metallicity and sometimes abundances for other elements could be derived. We here recall some very efficient surveys that allowed to find extremely metal-poor stars.

1. A list of weak-metal stars is provided by Bidelman & MacConnell (1973, see their table V) from their objective prism survey.
2. The Bond survey (Bond 1970) was based on objective prism observations at depth of $B \sim 10 - 10.5$ when the telescope used was at the University of Michigan, becoming $B \sim 11.5$ when the telescope was moved at Cerro Tololo in 1976. The result of this survey was presented in Bond (1980).
3. The HK Survey (Beers et al. 1985) observed with objective prism stars in a way to collect a kinematically unbiased sample of metal-poor stars. This survey allowed to discover the extremely metal-poor binary system CS 22876-032 (see Beers et al. 1985); the extremely metal-poor star CS 31082-001 with Th and U detectable (see Cayrel et al. 2001); to collect the stellar sample of metal-poor stars observed in the ESO large program “First Stars” (Cayrel et al. 2004) and usually used as the reference metal-poor sample.
4. The Hamburg-ESO survey (Christlieb et al. 2000; Christlieb et al. 2008), conceived to discover quasars, allowed to find out a large number of metal-poor stars (see e.g., Christlieb et al. 2002).
5. The Sloan Digital Sky Survey (SDSS York et al. 2000) in the latest 20 years provided low-resolution spectra for a large number of metal-poor candidates, whose

low metallicity has been confirmed at high-resolution investigation (see e.g. Aguado et al. 2018; Matsuno et al. 2017). In this context, the Turn-Off Primordial Stars project selected from the SDSS spectral database, the stars with turn off colors, and analyzed the spectra with an independent pipeline (see Caffau et al. 2013). Several extremely metal-poor stars have been discovered in this project (see Bonifacio et al. 2015; Bonifacio et al. 2018; Caffau et al. 2016).

6. The Large Sky Area Multi-Object fiber Spectroscopic Telescope (Cui et al. 2012) provided a large amount of stellar spectra that allowed to discover (see e.g., Li et al. 2015a; Li et al. 2018) and then also confirm with a high-resolution follow-up (see Li et al. 2015b), many metal-poor stars.
7. The Radial Velocity Experiment (Steinmetz et al. 2006) allowed to select a large sample of metal-poor stars (see e.g., Matijević et al. 2017).

(ii) The narrow-band photometry allows to observe a much larger number of stars with respect to the low-resolution spectroscopic surveys, but an efficient calibration is necessary in order to select interesting candidates.

1. The SkyMapper Telescope (Keller et al. 2007) observes also with an intermediate-band filter (about 40 nm Full Width Half Maximum [FWHM]) centered on the Ca II-H and -K lines. Several metal-poor candidates selected from the SkyMapper Survey (Wolf et al. 2018) have been confirmed from high-resolution spectroscopy to be extremely metal-poor stars (see e.g., Jacobson et al. 2015).
2. The Pristine survey (Starkenburg et al. 2017) is a photometric campaign observing with a narrow-band (about 20 nm FWHM) filter centered at the Ca II-H and -K lines. It is a very efficient project, allowing to select metal-poor candidates whose low-metallicity has been confirmed on high-resolution spectroscopy (see e.g., Starkenburg et al. 2018).
3. The S-plus survey (Mendes de Oliveira et al. 2019) uses several wide bands and narrow bands, among which J0395, centered on the Ca II-H and -K lines and has been successfully used to select metal-poor candidates (Placco et al. 2021; Monaco et al., in preparation; Whitten et al. 2021).
4. The J-plus survey uses a similar telescope and filter set as S-plus (Cenarro et al. 2019) and has also been able to select some metal-poor stars (Andrés Galarza et al. 2021).

(iii) Schlaufman & Casey (2014) used the photometric data from AAVSO Photometric All Sky Survey (Henden et al. 2009), Two Micron All-Sky Survey (2MASS),

TABLE 1 Observation log

Object	V mag	Observation date yyyy-mm-dd	Observation time UT	Exp. time s	S/N @ 480 nm
TYC 622-742-1	11.54	2019 September 13	13:04	600	200
TYC 1193-1918-1	10.70	2019 September 13	12:47	600	250

and Wide-field Infrared Survey Explorer (WISE) to select metal-poor candidates and confirmed by follow-up spectroscopy that 3.8% of the candidates had $[\text{Fe}/\text{H}] \lesssim -3$.

Metal-poor stars have long been known, before surveys provided us with large numbers of low-resolution spectra and narrow-band photometry were available. Seventy years ago, Chamberlain & Aller (1951) analyzed two stars (HD 19445 and HD 140283), nowadays denoted as the prototype of metal-poor stars. From the weak lines in their spectra, Chamberlain & Aller (1951) adopted a model of an F-type sub-dwarf to investigate them and claim a low abundance of Ca and Fe. Schwarzschild & Schwarzschild (1950) divided a sample of nine F stars in high- and low-velocity, and in their Figure 4 one can see that the high-velocity stars show generally smaller strength on the Fe I lines. Roman (1950) realized that stars of the same spectral type can have spectral lines of different strength. Dividing the stars in two groups, according to the strength of the spectral lines, she investigated the stellar velocity, concluding that the star with weak metallic lines have larger velocities and a larger dispersion in velocity. In Roman (1955), a catalog of high-speed stars is provided, and the two metal-poor prototype stars by Chamberlain & Aller (1951) are in. This suggests that selecting the high-velocity stars is a way to select metal-poor stars. In fact, stars that show a high velocity with respect to the Sun surely have an orbit widely different from the solar one so these stars cannot belong to the Galactic disk but, if bound, these are Halo stars. The stars indicated as “high proper-motion” or “high-velocity” star have kinematic noncompatible with the Galactic disk. This is not obviously translated in extreme kinematic with respect to the center of the Galaxy.

Thanks to the Gaia mission data (Gaia Collaboration et al. 2016), for a large number of stars it is presently possible to derive accurate kinematical and orbital parameters. Gaia catalogs also allow us to select stars with specific kinematics. In Caffau et al. (2020a), we selected a sample of high-speed stars to be observed at low-resolution. We derived chemical abundances for a few elements and deduced that the selected stars are mainly Halo stars, with a very homogeneous chemistry. From low-resolution spectroscopy, determination of the chemical pattern is very limited. We then decided to take the advantage of the

Subaru large telescope to secure high-quality spectra for two bright stars characterized by high speed with respect to the Sun.

We here investigate the detailed chemical pattern of these two stars to see if they show any peculiarity.

2 | TARGET SELECTION AND OBSERVATIONS

The two targets were part of a set of bright stars we selected as backup for our observing run at Subaru. The selection criterion was based on Gaia DR2 requiring $G < 11$ and total speed with respect to the Sun $> 500 \text{ km s}^{-1}$. The observations were carried out on September 13th 2019 with the High Dispersion Spectrograph installed on the Subaru telescope atop the Mauna Kea volcano in Hawaii (Noguchi et al. 2002). The bad weather conditions did not permit to perform the main program on faint targets. Instead, the two stars analyzed in this article were selected in the list of the backup program. The wavelength coverage goes from 408.4 to 689.2 nm. A binning 2×2 has been adopted leading to a resolving power of about 40,000. The log of the observations is given in Table 1. Standard data reduction procedures were carried out with the Image Reduction and Analysis Facility (IRAF) Echelle package.¹

To show the quality of the spectra, in Figure 1, the range of the 664 nm Eu II line is plotted.

3 | ANALYSIS

3.1 | Radial velocity and kinematics

The Gaia EDR3 data are listed in Table 2. The radial velocity is measured finding the maximum of the cross-correlation function (Tonry & Davis 1979). As the template, we employed a synthetic spectrum with the stellar parameters adopted for each star. Table 3 shows

¹IRAF is distributed by the National Optical Astronomy Observatories, which is operated by the Association of Universities for Research in Astronomy, Inc. under cooperative agreement with the National Science Foundation.

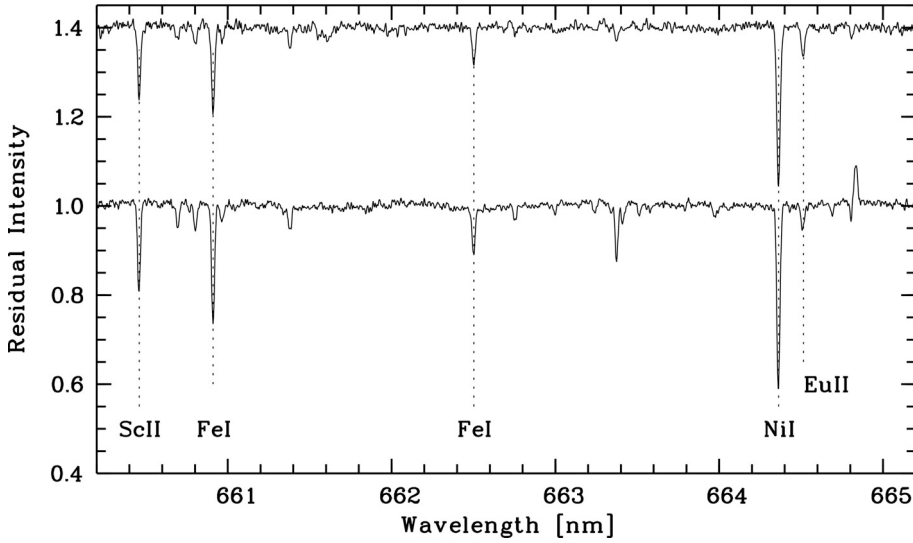


FIGURE 1 The two spectra are here shown in the range of the Eu II line

TABLE 2 Gaia eDR3 data

	TYC 622-742-1	TYC 1193-1918-1
RA	01:50:23.07	00:40:48.26
Dec	+08:14.31.7	+20:52:17.5
Parallax (p)	0.1693	0.5726
σ_p	0.0153	0.0156
p zero-point	-0.032	-0.035
pmRA	13.496	13.142
pmDec	-4.5610	-46.7576
Gmag	10.996	10.323
G_{BP}	11.765	10.859
G_{RP}	10.142	9.626
V_r [km/s]	-114.0	-364.3
σV_r [km/s]	0.4	0.3

TABLE 3 Radial velocities

Star	V_r	σV_r
TYC	km s ⁻¹	km s ⁻¹
TYC 622-742-1	-115.1	1.1
TYC 1193-1918-1	-365.2	0.9

the radial velocity of the two stars and their statistical uncertainties that reflects the S/N ratio of the spectrum. We report a radial velocity of -115.1 ± 1.1 km s⁻¹ for TYC 622-742-1 and -365.2 ± 0.9 km s⁻¹ for TYC 1193-1918-1 (see Table 3). The statistical error in the radial velocity determination is ~ 1.0 km s⁻¹. For the two stars Gaia DR2 provide a radial velocity of -114.0 ± 0.4 for TYC 622-742-1 and -364.3 ± 0.3 for TYC 1193-1918-1 (see Gaia Collaboration et al. 2018). The radial velocities we derive are compatible, within uncertainties, with the values provided by Gaia DR2.

We derived the zero-point for the parallax as described in Lindegren et al. (2021). The parallax corrected for the zero-point has been used to derive the stellar and orbital parameters.

The orbital parameters have been derived using the Galpy code² together with the MWPotential14 potential (Bovy 2015). We used the Gaia EDR3 coordinates, proper motions, and zero-point corrected parallax and the radial velocities we measured. We adopted the solar motions of Schönrich et al. (2010) and the solar distance from the galactic center of 8 kpc. In order to estimate the uncertainties on the derived quantities, we followed the same approach of Bonifacio et al. (2021). In particular, we used the pyia code³ (Price-Whelan 2018) to perform one thousand extractions of the six Galpy input parameters from a multivariate Gaussian, which takes into account both the errors on the parameters and their correlation coefficients in the construction of the covariance matrix. For each realization, an orbit integration is then performed using Galpy. We adopted as uncertainties, the standard deviations of the calculated orbital parameters (see Table 4).

3.2 | Stellar parameters

We derived the stellar parameters from the photometry and parallax of the Gaia EDR3 catalog (Gaia Collaboration et al. 2021, see Table 2). We dereddened the Gaia photometry (G and $G_{BP} - G_{RP}$) by using the maps by Schlafly &

² <http://github.com/jobovy/galpy>.

³ <https://github.com/adrn/pyia>.

TABLE 4 Target stars kinematical parameters

	TYC 622-742-1	TYC 1193-1918-1
V_R (km s ⁻¹)	-108 ± 11	-226 ± 3
V_T (km s ⁻¹)	-98 ± 25	-234 ± 6
V_Z (km s ⁻¹)	108 ± 1	-24 ± 7
R_{apo} (kpc)	13 ± 2	31 ± 2
R_{peri} (kpc)	7 ± 1	5.3 ± 0.1
e	0.32 ± 0.05	0.70 ± 0.01
Z_{max} (kpc)	11 ± 1	5 ± 1
E (km ² s ⁻²)	-31,831 ± 5,155	-8,178 ± 2,323
L_Z (kpc km s ⁻¹)	-1,047 ± 290	-2,026 ± 55
J_R (kpc km s ⁻¹)	136 ± 39	1,265 ± 117

Finkbeiner (2011). The parallax, after application of the zero-point, allowed us to derive the absolute G magnitude and then to derive the surface gravity by using the Stefan-Boltzmann equation.⁴ We adopted for both stars a mass of $0.8 M_{\odot}$ (see Bonifacio et al. 2019), a typical value for old stars now on the red giant branch (RGB). A change in the initial mass would affect the stellar parameters but well within the uncertainties: $\pm 0.1 M_{\odot}$ difference provides a change within about 10 K in effective temperature (T_{eff}) and 0.05 dex in the surface gravity ($\log g$). By comparing $(G_{\text{BP}} - G_{\text{RP}})_0$ to the theoretical color, we could derive the effective temperature. We assumed a metallicity $[\text{Fe}/\text{H}] = -1.0$ for the first guess parameters.

The process provides us with initial values for stellar parameters. These initial parameters have been assigned as input to the pipeline MyGIsFOS (Sbordone et al. 2014, see Section 3.3 for explanations) to derive the stellar metallicity. The metallicity provided by MyGIsFOS was used to derive new stellar parameters. The process was iterated up to when the variation in effective temperature and surface gravity were negligible (less than a few K for T_{eff} and below 0.01 dex for $\log g$). In this way, we derived the final T_{eff} and $\log g$ for the two stars that are the adopted stellar parameters, used for the chemical investigation and listed in Table 5.

The uncertainty in the G_{BP} and G_{RP} bands brings a very small variation in T_{eff} . But, as a sanity check, we derived the stellar parameters in other three ways.

⁴We use it in the form $\log g = \log(M) + 4 \log(T_{\text{eff}}/5,777) + 0.4 (G + \text{BCG}) + 2 \log \varpi + 0.11 + 4.4377$ where M is the mass of the star in units of solar masses, G is the Gaia magnitude of the star, BCG is the bolometric correction in the G band, ϖ is the parallax, 5,777 is the effective temperature of the Sun, 4.4377 is $\log g$ of the Sun, and 0.11 is a constant linked to the absolute bolometric magnitude of the Sun. See Nissen et al. (1997) for a derivation of this form of the formula.

- We used the calibration of Mucciarelli et al. (2021), based on the Infrared Flux Method temperatures of González Hernández & Bonifacio (2009), and derived T_{eff} about 10 and 100 K hotter for TYC 622-742-1 and TYC 1193-1918-1, respectively.
- We allow MyGIsFOS to derive the stellar parameters (all free) and obtained, for TYC 622-742-1: $T_{\text{eff}} = 4,187 \pm 30$ K, $\log g = 0.20 \pm 0.06$ (which is a value extrapolated in the grid), $\xi = 1.96 \pm 0.05$ km s⁻¹, and for TYC 1193-1918-1: $T_{\text{eff}} = 4,650 \pm 30$ K, $\log g = 1.59 \pm 0.05$, $\xi = 1.56 \pm 0.03$ km s⁻¹. So an extremely good agreement with the adopted parameters is obtained for both stars.
- The dereddened Gaia DR3 photometry is compared to Padova and Trieste Stellar Evolution Code (PARSEC) isochrones (Bressan et al. 2012; Marigo et al. 2017, see Figure 2) colored with the Gaia photometry in the color-magnitude diagram ($G_{\text{BP}} - G_{\text{RP}}, G_{\text{abs}}$), by using metallicity of -1.5 and -1.0 , respectively, for the two stars, and by adopting an age of 12 Gyr. The derived stellar parameters are 4,268 K and 0.71 for TYC 622-742-1 and 4,621 K and 1.75 for TYC 1193-1918-1. For both stars, the agreement with the adopted parameters is excellent.

The uncertainties in parallax are non-negligible for the two stars (see Table 2). We then checked what happens to $\log g$ when we add/subtract the uncertainty to the parallax and if we apply or do not apply the zero-point. We derived changes of about 0.08 dex in $\log g$.

In a conservative way, we adopt an uncertainty of 100 K for the effective temperature and 0.2 dex for the surface gravity.

For the micro-turbulence, we see two obvious calibrations that could be applied.

- Monaco et al. (2005) derived a calibration for Sgr stars. One of the two stars here investigated, TYC 1193-1918-1, has a metallicity comparable with the Sgr sample by Monaco et al. (2005), while the other is about 0.5 dex more metal-poor. For the two stars, by using this calibration, we derive a micro-turbulence of 2.04 and 1.71 km s⁻¹, respectively.
- With the calibration provided by Mashonkina et al. (2017), we derive a micro-turbulence of 2.07 and 1.74 km s⁻¹, respectively, for our stars.

The two calibrations provide micro-turbulence in close agreement, and also compatible with the values provided by MyGIsFOS. MyGIsFOS is able to derive the micro-turbulence by equalizing the Fe abundance derived from selected, cleaned Fe I lines of different strength. Since the spectra are of good quality and we have several suitable

TABLE 5 Parameters

Star	T_{eff} (K)	$\log g$ (cgs)	ξ (km s $^{-1}$)	[Fe/H]
TYC 622-742-1	$4,233 \pm 100$	0.71 ± 0.20	2.00 ± 0.20	-2.37 ± 0.10
TYC 1193-1918-1	$4,612 \pm 100$	1.67 ± 0.20	1.52 ± 0.20	-1.60 ± 0.10

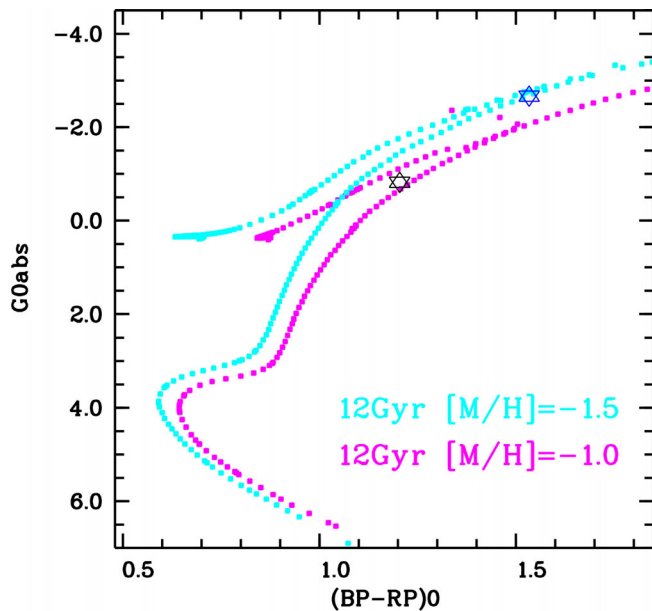


FIGURE 2 The two observed stars (blue TYC 622-742-1 and black TYC 1193-1918-1) in the color-magnitude diagram, compared to 12 Gyr PARSEC isochrones

Fe I lines, we decided to adopt these values for the micro-turbulence. In this way we derived a micro-turbulence of 2.00 ± 0.05 km s $^{-1}$ for TYC 622-742-1 and of 1.52 ± 0.03 km s $^{-1}$ for TYC 1193-1918-1, values reported in Table 5. In the case of TYC 622-742-1, the value is about 0.20 km s $^{-1}$ smaller than the value derived by using the calibration by Mashonkina et al. (2017) or by Monaco et al. (2005), while in the case of TYC 1193-1918-1 all the values are very close, within the uncertainty derived by MyGIsFOS. The uncertainties provided by MyGIsFOS are just statistic, while, comparing the adopted values with the ones derived from calibrations, we can assume an uncertainty of 0.2 km s $^{-1}$ for the micro-turbulence.

3.3 | Abundance determination

With the adopted stellar parameters, the observed spectra have been analyzed with MyGIsFOS to derive the metallicity and the detailed chemical abundances. As described by Sbordone et al. (2014), MyGIsFOS is a pipeline that interpolates in a pre-computed grid of synthetic spectra to find the best fit spectrum for each feature

analyzed. The grid of synthetic spectra, based on ATLAS 12 models (Kurucz 2005), was computed with SYNTHE (Kurucz 2005). The grid we used has: T_{eff} in the range 4,000–5,200 K with a 200 K step; $\log g$ from 0.5 to 3.0 with a 0.5 dex step; metallicity from -3.0 to -0.5 with 0.5 dex step; micro-turbulence of 1, 2 and 3 km s $^{-1}$; the enhancement in α -elements of -0.4 , 0.0 and $+0.4$. The atomic data for the lines are from the compilation of Heiter et al. (2021) (see in Appendix A: Table A1). All the elements up to Zn have been computed by MyGIsFOS. For the heavy elements, the abundances have been derived as well by best-fit but the synthesis is based on Turbospectrum (Alvarez & Plez 1998). The choice is related to the fact that the partition functions in Turbospectrum are more up-dated than the ones in SYNTHE. The use of SYNTHE to derive the abundances of the heavy elements would imply the use of older partition functions. On the one hand the SYNTHE grids are already available and we have invested considerable time to develop these grids (see e.g., Caffau et al. 2021). On the other hand, the use of Turbospectrum to compute complete grids of synthetic spectra would be much more time consuming than with SYNTHE.

The abundances we derived are provided in Table 6. As usual, for each element X, $A(X) = \log(N(X)/N(H)) + 12$, $[X/H] = A(X) - A(X)_{\odot}$, and $[X/Fe] = [X/H] - [Fe/H]$. The solar abundances, $A(X)_{\odot}$, here adopted are from Caffau et al. (2011) and Lodders et al. (2009) and are listed in Table 6. In all the figures, we show the LTE abundances, to be able to compare to the results from the literature.

We investigated in the literature for departure from local thermodynamical equilibrium and, when available, for each element, we discussed how the NLTE corrections summarized in Table 7 were derived. The NLTE corrections, sometimes derived from a subsample of lines, were applied to the LTE abundances derived from the complete sample of lines. We verified that the LTE abundance from the subsample of lines was very close to the abundance derived from the complete sample of selected lines.

3.4 | Iron abundance

Fe I is usually the reference in the abundance determination because there is a fairly large numbers of lines in the stellar spectra of late type stars. Thanks to the good quality of the spectra, for both stars we could investigate

TABLE 6 Abundance ratio of the elements

Element	Sun A(X)	TYC 622-742-1				TYC 1193-1918-1			
		A(X) _{LTE}	$\sigma(X)$	N(X)	A(X) _{NLTE}	A(X) _{LTE}	$\sigma(X)$	N(X)	
C	8.50	5.05	0.30	G-band		6.46	0.20	G-band	
N	7.86	6.90	0.50	CN		6.84	0.40	CN	
O I	8.76	7.25	0.13	2	7.25	7.75	0.14	1	7.75
Na I	6.30	3.83	0.01	2	3.83	4.52	0.10	5	4.52
Mg I	7.54	5.80	0.12	3	5.81	6.36	0.10	3	6.33
Al I	6.47					4.93	0.14	1	4.93
Si I	7.52	5.62	0.10	12	5.64	6.19	0.10	15	6.17
Ca I	6.33	4.35	0.10	21	4.49	5.17	0.08	28	5.22
Sc II	3.10	1.16	0.16	10		1.91	0.08	8	
Ti I	4.90	2.80	0.08	56		3.58	0.07	58	
Ti II	4.90	3.07	0.15	31	3.08	3.80	0.14	32	3.80
V I	4.00	1.56	0.11	15		2.34	0.08	18	
Cr I	5.64	3.16	0.10	17	3.46	4.00	0.08	17	4.21
Cr II	5.64	3.42	0.07	6		4.15	0.09	6	
Mn I	5.37	2.64	0.09	14	3.03	3.47	0.09	14	3.78
Fe I	7.52	5.15	0.10	254	5.25	5.92	0.10	298	5.98
Fe II	7.52	5.32	0.15	27	5.32	6.03	0.14	28	6.03
Co I	4.92	2.63	0.10	16	3.04	3.33	0.12	18	3.62
Ni I	6.23	3.85	0.12	52		4.60	0.13	58	
Cu I	4.21	1.29	0.08	3		2.08	0.12	4	
Zn I	4.62	2.20	0.16	1		3.08	0.03	2	
Sr II	2.92	0.70	0.16	1	0.80	1.25	0.14	1	1.25
Y II	2.21	-0.27	0.05	9		0.39	0.05	10	
Zr I	2.62	0.60	0.16	1		1.00	0.14	1	
Zr II	2.62	0.50	0.07	3		1.20	0.08	3	
Ba II	2.17	-0.08	0.02	3	-0.23	0.60	0.04	3	0.44
La II	1.14	-0.84	0.05	11		-0.34	0.04	14	
Ce II	1.61	-0.58	0.05	6		-0.03	0.07	7	
Pr II	0.76	-0.95	0.08	4		-0.62	0.06	3	
Nd II	1.45	-0.46	0.05	29		0.04	0.07	26	
Sm II	1.00	-0.78	0.04	9		-0.29	0.06	8	
Eu II	0.52	-1.00	0.16	1	-0.90	-0.50	0.14	1	-0.40

with MyGIsFOS a large number of Fe I lines and derive an average A(Fe) with a small line-to-line scatter of the order of 0.1 dex. The average Fe abundances we derived are reported in Table 6.

NLTE effects have been extensively studied in the literature (see e.g., Bergemann et al. 2012a; Bergemann et al. 2012b; Korn et al. 2003; Mashonkina et al. 2016), in a large range of stellar parameters and over the entire

spectrum from ultraviolet to infrared. It is at the lowest metallicities that NLTE corrections are usually the largest, while, for the same stellar parameters, these effects are usually small in the case of Fe II lines. Mashonkina et al. (2016) provided the NLTE corrections for a large sample of the Fe I lines.⁵ In this database, we searched for

⁵ <http://spectrum.inasan.ru/nLTE/>.

TABLE 7 NLTE corrections applied to the two stars in the sample

Element	TYC 622–742–1	TYC 1193–1918–1	References
	NLTE correction	NLTE correction	
O I	0.00	0.00	Sitnova et al. (2013)
Na I	0.00	0.00	Takeda et al. (2003)
Mg I	0.01	−0.03	Bergemann et al. (2017)
Al I		0.00	Nordlander & Lind (2017)
Si I	0.02	−0.02	Bergemann et al. (2013)
Ca I	0.14	0.05	Mashonkina et al. (2016)
Ti I	0.37	0.14	Mashonkina et al. (2016)
Ti II	0.01	0.00	Mashonkina et al. (2016)
Cr I	0.30	0.21	Bergemann et al. (2010)
Mn I	0.39	0.31	Bergemann & Gehren (2008)
Fe I	0.10	0.06	Mashonkina et al. (2016)
Fe II	0.00	0.00	Mashonkina et al. (2016)
Co I	0.41	0.32	Bergemann et al. (2010)
Cu I	0.50	0.50	Andrievsky et al. (2018)
Sr II	0.10		Andrievsky et al. (2011)
Ba II	−0.15	−0.16	Korotin et al. (2015)

the lines used in our analysis. We entered the parameters of each star (T_{eff} , $\log g$ and metallicity) and derived the NLTE correction for 94 and 102 lines for TYC 622–742–1 and TYC 1193–1918–1, respectively. The value for the NLTE correction of the Fe I we derive is +0.10 dex for TYC 622–742–1 and +0.06 dex for the star TYC 1193–1918–1 (see Table 7). From these lines, we derived an average LTE $A(\text{Fe})$ of 5.16 and 5.93, respectively, very close to the LTE Fe abundance derived from all the lines. We feel safe to apply these NLTE corrections to the $[\text{Fe}/\text{H}]$ LTE abundances, and we obtain $[\text{Fe}/\text{H}]$ of -2.27 and -1.54 for the two stars.

In the case of Fe II, by looking at the database https://nlte.mpia.de/gui-siuAC_secE.php (Bergemann et al. 2012a; Bergemann et al. 2012b), we see that the NLTE corrections provided are negligible in the case of our two stars. By applying the NLTE correction to our LTE analysis, $A(\text{Fe})$ derived for Fe I and Fe II lines are in agreement (-2.27 and -2.20 for TYC 622–742–1; -1.54 and -1.49 for TYC 1193–1918–1), so we find a good ionization equilibrium.

3.5 | Comparison samples

A goal of this investigation was to understand if these stars have peculiarities and the best way to do so is to compare the stars to literature investigations. We decided

to compare these two stars to: (a) the sample by Gratton et al. (2000) composed by field stars, 17 of which are evolved stars, in the metallicity range $-2 \leq [\text{Fe}/\text{H}] \leq -1$; (b) the metal-poor sample of giant stars analyzed by Cayrel et al. (2004), which consists of stars more metal-poor, but the extremely careful analysis is based on high-quality spectra and is a widely used reference sample; (c) the stars presented in Fulbright (2000) that are more extended in metallicity and this sample contains some high-speed stars; (d) two high-speed stars from Valentini et al. (2019); and (e) the FORS high-speed stars sample investigated by Caffau et al. (2020a).

3.6 | Light elements

3.6.1 | Lithium

The Li doublet at 670.7 nm is not detectable: as expected in evolved stars, both stars already destroyed Li in their photosphere (see e.g. Salaris & Weiss 2001).

3.6.2 | Carbon

The C abundance was derived from the G-band by line profile fitting, with χ^2 minimization (see Bonifacio &

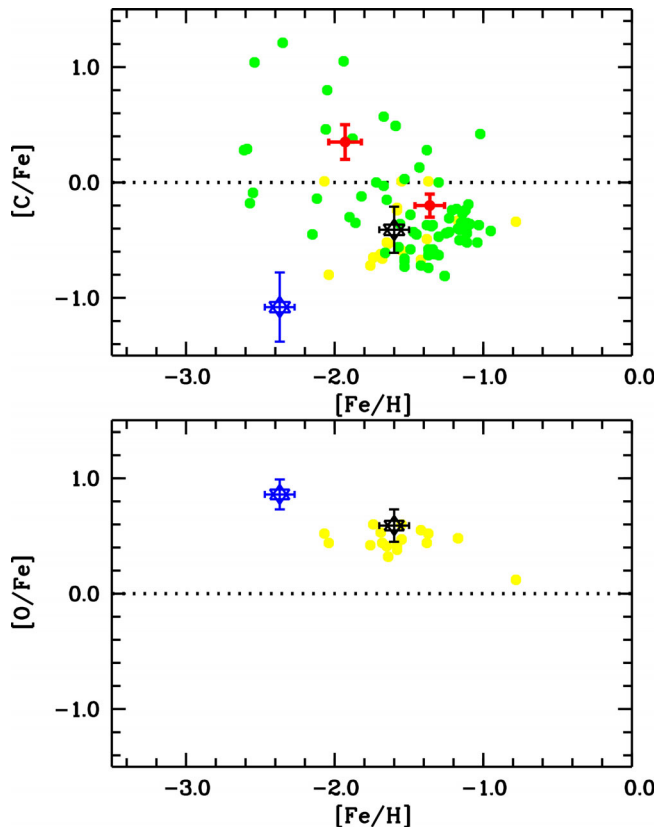


FIGURE 3 Abundance ratios of the $[C/Fe]$ (upper panel) and $[O/Fe]$ (lower panel) as a function of $[Fe/H]$. The blue and black stars refer to the present study, TYC 622–742–1 and TYC 1193–1918–1, respectively, compared to two high-speed stars from Valentini et al. (2019), high-speed stars from Caffau et al. (2020a, green dots), and the evolved stars from Gratton et al. (2000, yellow dots) sample

Caffau 2003). With the code SYNTHE (Kurucz 2005), we computed synthetic spectra based on ATLAS 12 models (Kurucz 2005) computed specifically for the two stars. The theoretical synthesis in the wavelength range of the band was computed by using the list of CH molecules provided by Masseron et al. (2014). The C abundances derived for the two stars are listed in Table 6.

In Figure 3, the $[C/Fe]$ ratios we derived are compared to literature results. Both stars have a low $[C/Fe]$ ratio ($[C/Fe]$ of -1.08 and -0.44 , respectively), and especially TYC 622–742–1, but, partially, this is expected in stars at these evolutionary stages. One can see from the figure that the low $A(C)$ is common in evolved stars. We are aware that this computation is sensitive to hydrodynamical effects, already investigated for unevolved stars by Gallagher et al. (2016). Although the stars here investigated are evolved, we do not have 3D models with such a low gravity, but negative 3D corrections could be expected.

We derived the isotopic ratio ($^{12}C/^{13}C = 4.91^{+6.5}_{-1.9}$) only for TYC 1193–1918–1 from the two CH lines at 423.14 nm.

The CH lines are too weak in TYC 622–742–1 to allow to derive the isotopic ratio.

3.6.3 | Nitrogen

Nitrogen abundances have been derived by fitting the weak CN band at around 418 nm. These weak lines lie in a crowded region, so the abundance determination is challenging. The procedure adopted was the same as for the C abundance determination, with the variance that in the spectral synthesis computation $A(C)$ was fixed at the values derived from the G-band. The N abundances we derived are reported in Table 6. $A(N)$ is very high for TYC 622–742–1 ($[N/Fe] = 1.42$), and this could be related to the low C abundance for the fact that C has been converted in N. The effect is less dramatic for TYC 1193–1918–1 ($[N/Fe] = +0.58$), but still visible by the enhancement in N. $A(N)$ determination is very uncertain overall for TYC 622–742–1 that is more metal-poor and we highlighted it in Table 6.

3.6.4 | Oxygen

Both forbidden $[OI]$ lines are in the range of the Subaru spectra and they are both strong enough on these evolved stars to be useful for abundance determination. Unfortunately, the line at 630 nm falls in a range polluted by telluric absorptions, so depending on the radial velocity of each star and on the observing time, this line is or is not clear from telluric contamination. We could then analyze this line only for TYC 622–742–1. The O abundances derived, based on both $[OI]$ lines for TYC 622–742–1 and only on the 636 nm line for TYC 1193–1918–1, are listed in Table 6. The forbidden oxygen lines form in conditions close to local thermodynamical equilibrium (see e.g., Sitnova et al. 2013). In Figure 3, the $[O/Fe]$ we derived for the two stars are compared to the analysis by Gratton et al. (2000).

3.7 | α elements

3.7.1 | Magnesium

To derive $A(Mg)$, the lines at 470.2, 552.8, and 571.0 nm have been retained by MyGIsFOS for both stars. For the star TYC 622–742–1, we obtained $[Mg/Fe] = 0.63 \pm 0.16$ dex and for the star TYC 1193–1918–1, we derived $[Mg/Fe] = 0.42 \pm 0.14$ dex. In Table 6, the Mg abundances are listed.

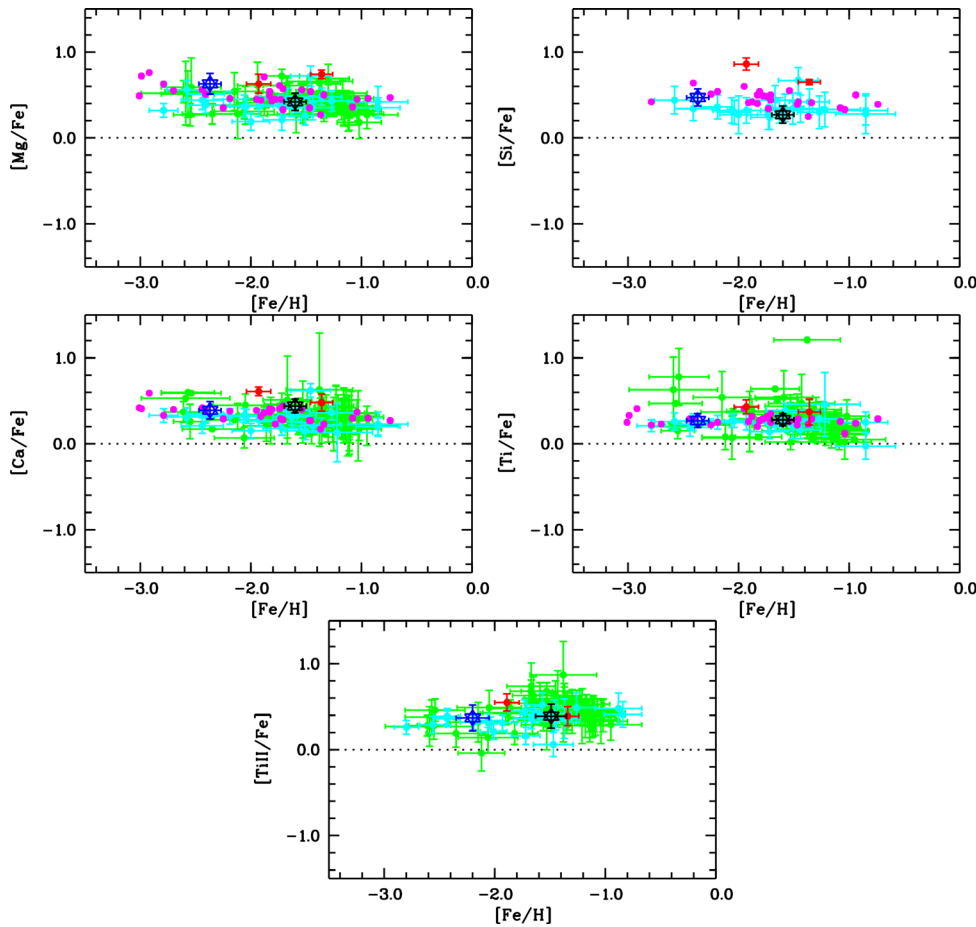


FIGURE 4 Abundance ratios of the α elements as a function of $[\text{Fe}/\text{H}]$. The blue and black star refer to the present study, TYC 622–742–1 and TYC 1193–1918–1, respectively, compared to two high-speed stars from Valentini et al. (2019, red dots), high-speed stars from Caffau et al. (2020a, green dots), and the evolved stars from Ishigaki et al. (2012, light blue dots) and from Fulbright (2000, pink dots) sample

In Alexeeva et al. (2018), a star with similar parameters (HD 122563) was investigated providing a negligible NLTE corrections for the two Mg I lines at 470.2 and 552.8 nm. We derived the NLTE corrections from Bergemann et al. (2017) by using the database.⁶ For the lines employed by the MyGIsFOS analysis, we obtained a correction of 0.01 dex for TYC 622–742–1 and of -0.03 dex for TYC 1193–1918–1 (see Table 7). By applying the NLTE corrections on Mg and Fe abundances, we derived $[\text{Mg}/\text{Fe}] = 0.54$ for TYC 622–742–1 and $[\text{Mg}/\text{Fe}] = 0.33$ for TYC 1193–1918–1. In Figure 4, the LTE $[\text{Mg}/\text{Fe}]$ versus $[\text{Fe}/\text{H}]$ are compared to literature data.

3.7.2 | Silicon

Several Si I features have been used (12 and 15 in the two stars, see Table 6) to derive the LTE Si abundance. Si I lines are sensitive to NLTE effects and the LTE silicon abundances are usually higher than the NLTE ones and these effects are more pronounced at low metallicity (see Bergemann et al. 2013). We derived the NLTE

correction provided by Bergemann et al. (2013). We looked for the line studied with MyGIsFOS and present in the database and we obtained small NLTE corrections: an NLTE correction of $+0.02$ dex for TYC 622–742–1 (see Table 7), from which we derive $[\text{Si}/\text{Fe}] = 0.39$ and an NLTE correction of -0.02 dex for TYC 1193–1918–1, which implies $[\text{Si}/\text{Fe}] = 0.19$. For both stars, the LTE Si abundance derived from the subsample of Si I lines for which an NLTE correction is available is just 0.02 dex higher.

3.7.3 | Calcium

Several Ca I lines are available in the wavelength of the Subaru spectra. For the two stars 22 and 28 lines, respectively, are used for the abundance determination and they provide a very low line-to-line scatter (see Table 6). According to Spite et al. (2012), in the case of $[\text{Ca}/\text{H}] \geq -2$ there is a negative NLTE correction: due to the NLTE effects, the line wings weaken while the line core strength compared to the LTE case. For the stellar parameters of the two stars here analyzed, the NLTE effects significantly affect the Ca I line profiles (see Mashonkina et al. 2016).

⁶ https://nlte.mpia.de/gui-siuAC_secE.php.

We derived the NLTE correction for a subsample of the Ca I lines (from which we derived an LTE $A[\text{Ca}]$ 0.03 and 0.02 dex higher than from the complete sample, respectively) here analyzed from Mashonkina et al. (2016) (using the same method described in Section 3.4): 0.14 dex for TYC 622–742–1 and 0.05 dex for TYC 1193–1918–1 (see Table 7). These NLTE corrections provide for the $[\text{Ca}/\text{Fe}]$ ratio the values 0.44 and 0.43, for the two stars, respectively.

In Figure 4, the LTE investigation of $[\text{Ca}/\text{Fe}]$ versus $[\text{Fe}/\text{H}]$ is shown. In the figure, one can see that few stars in the sample by Fulbright (2000) (pink dots) and in the sample by Caffau et al. (2020a) (green dots) have slightly lower $[\text{Ca}/\text{Fe}]$.

3.7.4 | Titanium

Ti abundance was derived from neutral and single ionized lines for both stars. The $[\text{Ti}/\text{Fe}]$ ratios when using Ti I lines are positive for both stars: 0.27 and 0.28, respectively. These values are consistent with the $[\text{Ti}/\text{Fe}]$ ratios derived when the abundances are from the Ti II and Fe II lines: 0.36 and 0.39, respectively. The difference between Ti abundance when derived from neutral and ionized lines is non-negligible (0.27 and 0.22 dex). These differences are also due to NLTE effects, which are strong in the case on Ti I lines (see Mashonkina et al. 2016). The NLTE effects for Ti I are more significant than for Fe I, which is directly reflected in the $[\text{Ti}/\text{Fe}]$ ratio becoming larger in NLTE. By looking at the results by Mashonkina et al. (2016), we expect for both stars an NLTE correction of the order of 0.2 or 0.3 dex (see Table 7).

We investigated the NLTE corrections derived by Mashonkina et al. (2016) for the Ti I lines we used and present in the database, with the same procedure described in Section 3.4. For the selected lines, we derive an NLTE correction for Ti I of +0.37 dex for TYC 622–742–1 and 0.14 dex for TYC 1193–1918–1. The lines with an NLTE correction available provide an LTE $A(\text{Ti})$ 0.01 and 0.03 dex higher than the abundance derived from the complete sample of Ti I lines, respectively, for the two stars. By applying this NLTE correction, we derived the $[\text{Ti}/\text{Fe}]$ ratios 0.54 and 0.36 for the two stars, respectively. By looking at Figure 1 by Mashonkina et al. (2016) we think that, due to the limited number among the Ti I lines, we used that are present in the investigation by Mashonkina et al. (2016), the NLTE correction for TYC 622–742–1 should be smaller, in the range 0.2–0.3 dex. In the case of Ti II, we derived small NLTE corrections: 0.01 dex for TYC 622–742–1 and 0.00 dex for TYC 1193–1918–1, which provides $[\text{Ti}/\text{Fe}]$ of 0.37 and 0.39 for the two stars (also in this case for $A(\text{Fe})$ we used is from Fe II lines). The Ti abundance

derived from the Ti II lines with NLTE correction is the same than when derived from the complete sample of lines.

3.7.5 | Summary α -elements

All the α -elements we could derive (Mg, Si, Ca and Ti) are enhanced in the two stars, as expected in metal-poor stars (see Spite et al. 2012). In Figure 4, our LTE results are compared to the literature data. The ratios of abundances of the α elements are in very good agreement with the two high-speed stars from Valentini et al. (2019, see red dots in Figure 4), the high-speed stars from Caffau et al. (2020a, green dots in Figure 4), the evolved stars from the sample by Ishigaki et al. (2012, light blue dots in Figure 4), the evolved stars from the sample by Ishigaki et al. (2012, light blue dots in Figure 4), and the evolved stars from Fulbright (2000, pink dots in Figure 4).

3.8 | Odd-Z elements

3.8.1 | Sodium

Several Na I lines (498.2, 568.2, 568.8, 588.9, 589.6, and 616.0 nm) have been investigated to derive $A(\text{Na})$ for the more metal-rich star TYC 1193–1918–1, and the line-to-line scatter we derived is small. The D1 and D2 lines provide abundances which are consistent with the values derived from the other weak lines; this fact could be explained by looking at Figure 2 by Takeda et al. (2003), an investigation on NLTE effects (on all the lines we investigated, except the line at 498.2 nm) where they deduce that NLTE effects are strong for saturated lines and become insignificant with decreasing or increasing the strength of the lines. For TYC 622–742–1, only the two weak lines at 568 nm are used to derive the Na abundance. In Figure 5, the abundances derived for the two stars are compared to literature analysis.

3.8.2 | Aluminum

Only for TYC 1193–1918–1, we could derive Al abundance, from the feature at 669.6 nm. Looking at the study by Nordlander & Lind (2017), we deduce that for the parameters of this star, the NLTE effects for aluminum are small. In Figure 5, the $[\text{Al}/\text{Fe}]$ ratio derived for TYC 1193–1918–1 is compared to the results by Fulbright (2000).

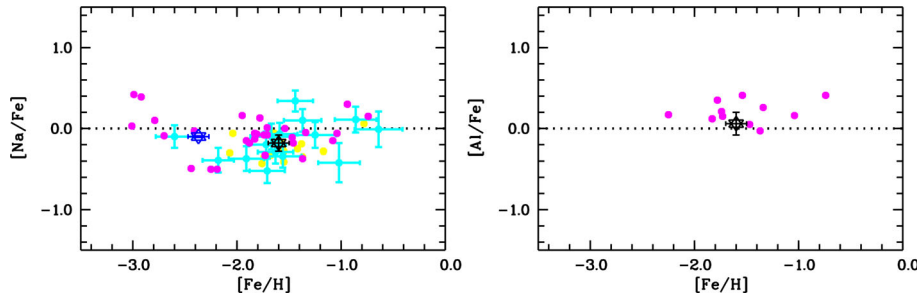


FIGURE 5 Abundance ratios of the odd-Z elements as a function of $[\text{Fe}/\text{H}]$. The blue and black star refer to the present study, TYC 622–742–1 and TYC 1193–1918–1, respectively, compared to the evolved stars from Gratton et al. (2000, yellow dots), from Ishigaki et al. (2013, light blue dots), and from Fulbright (2000, pink dots) sample

3.9 | Iron peak elements

3.9.1 | Scandium

We could derive $A(\text{Sc})$ from a sample of ionized lines that provide a small line-to-line scatter (see Table 6). The $[\text{Sc}/\text{Fe}]$ ratios, when using the Fe abundance from ionized lines, are of 0.25 and 0.30 dex for TYC 622–742–1 and TYC 1193–1918–1, respectively. In Figure 6, our results are compared to the ones by Ishigaki et al. (2012).

3.9.2 | Vanadium

For the abundance determination of V, a quite large sample of line has been used for both stars (see Table 7) that provide a small line-to-line scatter. The $[\text{V}/\text{Fe}]$ ratios derived for the two stars are close to zero (see Figure 6).

3.9.3 | Chromium

For the Cr abundance determination, we could rely on both neutral and single ionized lines. For both stars, the ionization balance is not good and the Cr abundances derived from neutral lines are smaller for both stars, by 0.28 and 0.15 dex, respectively. This discrepancy is related to NLTE effects (see Bergemann et al. 2010).

We determine the NLTE corrections for our stars using the database by Bergemann et al. (2010), looking at all the lines used by MyGIsFOS in the analysis. We derived an NLTE correction of 0.30 and 0.21 dex for the two stars (see Table 7). We then derived $[\text{Cr I}/\text{Fe}] = 0.09$ dex for TYC 622–742–1 and $[\text{Cr I}/\text{Fe}] = 0.11$ dex for TYC 1193–1918–1. These values have to be compared to the LTE $[\text{Cr}/\text{Fe}]$ ratio by taking into account the abundances derived from ionized lines, and we obtain: $[\text{Cr}/\text{Fe}]$ of -0.03 and 0.00 , for the two stars, in excellent agreement with the ratio from neutral lines once NLTE effects are taken into account. The LTE $[\text{Cr}/\text{Fe}]$ ratios we derived for both stars are shown in Figure 6.

3.9.4 | Manganese

Mn abundance was derived for the two stars from 14 features. Figure 6 shows how our two stars show slightly low Mn abundances, with $[\text{Mn}/\text{Fe}]$ ratios of the order of -0.3 dex, but fully compatible with the stars of other samples.

The LTE Mn abundances are systematically lower than NLTE abundances and the lower the metallicity, the larger the difference between NLTE and LTE. Bergemann & Gehren (2008) provided an NLTE corrections for Mn and we searched for the lines used in the MyGIsFOS analysis and derived an NLTE correction of 0.39 dex for TYC 622–742–1 and 0.31 dex for TYC 1193–1918–1 (see Table 7). If we take into account the NLTE corrections, we derive for the $[\text{Mn}/\text{Fe}]$ ratios -0.07 for TYC 622–742–1 and -0.05 dex for TYC 1193–1918–1.

3.9.5 | Cobalt

Co abundance is based on 16 and 18 Co I lines, respectively, for the two stars (see Table 6) that provide a low line-to-line scatter. The $[\text{Co}/\text{Fe}]$ ratio is close to zero (0.08 and 0.01, respectively, for the two stars, see Figure 6). Bergemann et al. (2010) provide the NLTE correction for Co I. We searched for the lines analyzed in MyGIsFOS and we obtain an NLTE correction of 0.41 dex for TYC 622–742–1, which provide $[\text{Co}/\text{Fe}] = 0.39$ dex, and $+0.32$ dex for TYC 1193–1918–1, providing $[\text{Co}/\text{Fe}] = 0.27$ (see Table 7).

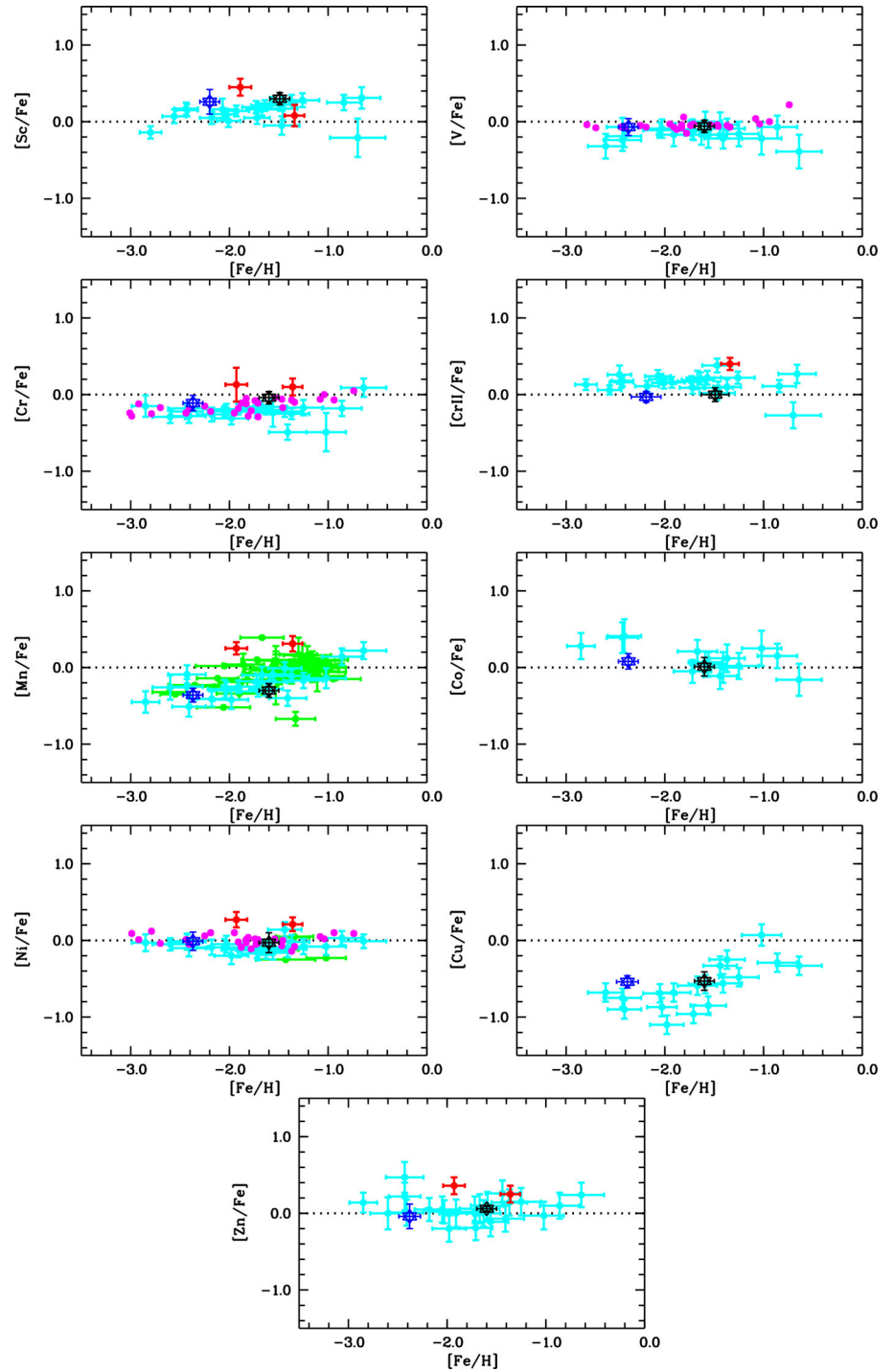
3.9.6 | Nickel

A large sample of Ni I lines (55) is used to derive $A(\text{Ni})$. For both stars, the line-to-line scatter is small (see Table 6) and the $[\text{Ni}/\text{Fe}]$ is close to zero. In Figure 6, $[\text{Ni}/\text{Fe}]$ ratios are compared to literature values. To our knowledge, no NLTE investigation exists on this element.

3.9.7 | Copper

Three Cu I lines are investigated at 510.5, 570.0, and 578.2 nm. For the star TYC 622–742–1, we also analyzed

FIGURE 6 Abundance ratios of iron peak elements as a function of $[\text{Fe}/\text{H}]$. The blue and black star refer to the present study, TYC 622–742–1, and TYC 1193–1918–1, respectively, compared to two high-speed stars from Valentini et al. (2019, red dots), high-speed stars Caffau et al. (2020a, green dots), high-speed stars from Ishigaki et al. (2013, light blue dots) and from Fulbright (2000, pink dots) sample



the line at 521.8 nm. The copper over iron ratio is very consistent in the two stars of the sample: $([\text{Cu}/\text{Fe}]) = -0.54 \pm 0.01$ dex. These values are in good agreement with the analysis by Ishigaki et al. (2013) (see Figure 6). The NLTE effects, investigated by Andrievsky et al. (2018), are large for the lines here analyzed. They get smaller as the metallicity increases. The NLTE effect would increase the Cu abundance and is of the order of ~ 0.5 dex (see Table 7) for the more metal-rich star here analyzed, and even larger for the other star (see Andrievsky et al. 2018). An NLTE

correction of the order of 0.5 dex would bring the $[\text{Cu}/\text{Fe}]$ ratio close to zero.

3.9.8 | Zinc

The Zn abundance was derived from the 481.1 nm line for TYC 622–742–1 and for the star TYC 1193–1918–1, we used the two Zn I lines at 481.1 and 472.2 nm lines. We derived $[\text{Zn}/\text{Fe}]$ ratios close to zero (-0.04 and 0.06 for the

two stars). In Figure 6, the $[Zn/Fe]$ ratios we derived are compared to the literature results.

3.10 | Neutron capture elements

For the heavy elements, we fitted the line profile of the lines. We computed the synthetic spectra with Turbospectrum (Alvarez & Plez 1998) by using ATLAS 12 models computed with the parameters derived for each star. Hyperfine splitting and solar mix isotopic ratios have been used for the computation of the abundances.

As one can see from Figure 6, the stars are coherent with the results from the literature in the heavy elements. Both stars show a low $[Y/Fe]$ ratio and an enhancement in Eu, as several stars in the sample by Ishigaki et al. (2013) and Fulbright (2000). TYC 622–742–1 shows a slight enhancement also in Zr, Pr, Nd, and Sm.

3.10.1 | Strontium

The Sr II line at 421.6 nm is employed to derive the Sr abundance. The $[Sr/Fe]$ ratios in the two stars are both slightly negative: -0.05 and -0.18 for TYC 622–742–1 and TYC 1193–1918–1, respectively. In Figure 7, the $[Sr/Fe]$ ratios we derived for the two stars are compared to the literature results. Andrievsky et al. (2011) analyzed the NLTE effects in a sample of very and extremely metal-poor stars. For the star TYC 622–742–1, the NLTE correction on the Sr line used should be of the order of 0.1 dex; the other star is too metal-rich to fit in this investigation.

3.10.2 | Yttrium

The Y abundance has been derived by analyzing 9 and 10 Y II lines for the two stars, respectively. We derive $[Y/Fe]$ very close for the two stars (-0.31 and -0.33 , respectively, when using $A(Fe)$ from ionized lines). In Figure 7, our results are compared to the literature values and we see a close coherence.

3.10.3 | Zirconium

For the determination of $A(Zr)$ both Zr I (473.9 nm) and Zr II (420.8, 461.3, and 511.2 nm) lines have been investigated. For both stars $A(Zr)$ derived from neutral and ionized lines are in agreement within the uncertainties (see Table 6). The star TYC 622–742–1 has a high value of $[Zr/Fe]$ when the ratio is derived from Zr I and Fe I lines, while this ratio is close to zero (0.05 dex) when the abundances

are from ionized lines, Zr II, and Fe II. For the star TYC 1193–1918–1, the values of $[Zr/Fe]$ are in good agreement when the abundances are derived from neutral Zr I and Fe I lines or ionized Zr II and Fe II lines. In Figure 7, $[Zr/Fe]$ from ionized lines is compared to the literature values.

3.10.4 | Barium

To derive $A(Ba)$ three Ba II lines have been selected for each star. For TYC 622–742–1, the selected lines (at 493.4, 585.3, and 649.6 nm) provided an LTE abundance of $A(Ba) = -0.08 \pm 0.02$ (see Table 6), with $[Ba/Fe] = -0.05$, when $A(Fe)$ is from Fe II lines. For TYC 1193–1918–1, in LTE, we derived $A(Ba) = 0.60 \pm 0.04$ (see Table 6, $[Ba/Fe] = -0.08$) by investigating three Ba II lines (at 585.3, 614.1, and 649.6 nm). Korotin et al. (2015) investigated the NLTE corrections for a sample of Ba II lines. For TYC 622–742–1 two lines are in the sample investigated by Korotin et al. (2015) (from which we derive an LTE abundance $A(Ba) = -0.07$) and for them we derived an NLTE correction of the order of -0.15 , which, applied to the LTE abundance derived from all lines we derive $A(Ba) = -0.22$ and $[Ba/Fe] = -0.20$ dex. For TYC 1193–1918–1, the three lines are in the set investigated by Korotin et al. (2015) and we derive an NLTE correction of about -0.16 , providing: $A(Ba) = 0.44$ and $[Ba/Fe] = -0.24$ dex. In Figure 7, $[Ba/Fe]$ is compared to results from the literature.

3.10.5 | Lanthanum

A considerable sample of La II lines (15 and 14, respectively) has been investigated to derive $A(La)$ of -0.84 ± 0.05 and -0.34 ± 0.04 for the two stars, respectively (see Table 6). By using the Fe abundance from the ionized lines, we derive $[La/Fe]$ ratios of 0.19 and 0.01, respectively (see Figure 7).

3.10.6 | Cerium

Seven Ce II features are used to derive $A(Ce)$ of -0.58 ± 0.05 and -0.03 ± 0.07 for the two stars (see Table 6), which provides $[Ce/Fe]$ of -0.02 and -0.15 , respectively, when using the Fe abundance derived from ionized lines.

3.10.7 | Praseodymium

The TYC 622–742–1 star presents a high value of Pr ($A(Pr) = -0.95 \pm 0.08$ and $[Pr/Fe] = 0.46$) derived from a sample

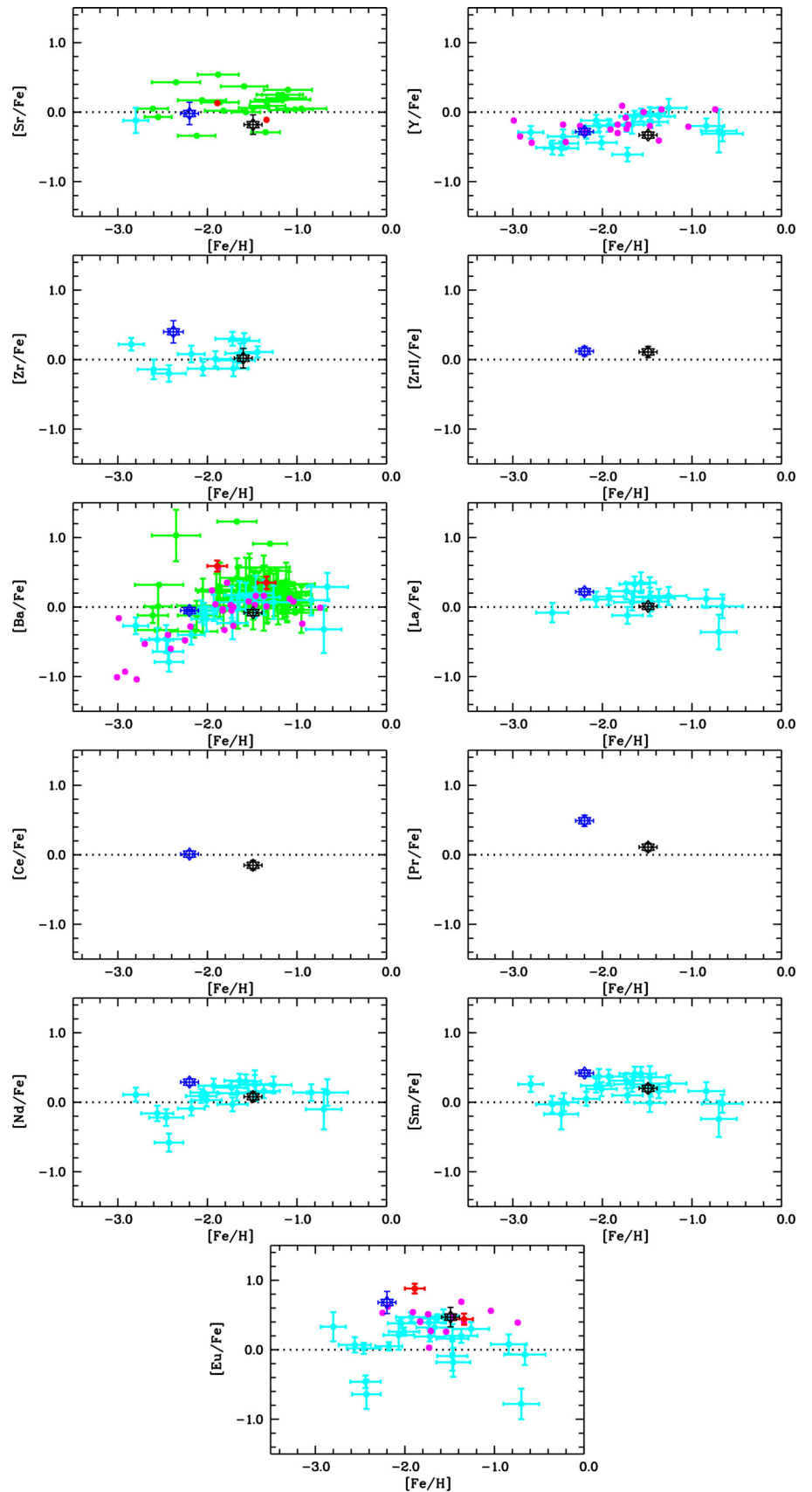


FIGURE 7 Same as Figure 6 for neutron capture elements

of four Pr II lines. For TYC 1193–1918–1, three lines analyzed provide $A(\text{Pr}) = -0.62 \pm 0.06$ and $[\text{Pr}/\text{Fe}] = 0.11$. For the $[\text{Pr}/\text{Fe}]$ ratios $A(\text{Fe})$ is from ionized lines. The Pr abundances are listed in Table 6 and shown in Figure 7.

3.10.8 | Neodymium

Nd is well represented in the Subaru spectra here analyzed: a sample of 29 and 26 lines have been analyzed for TYC 622–742–1 and TYC 1193–1918–1, respectively, providing $A(\text{Nd})$ of -0.46 ± 0.05 and 0.04 ± 0.07 for the two stars (see Table 6). We could then derive $[\text{Nd}/\text{Fe}]$ ratios of 0.26 and -0.08 dex (see Figure 7) for the two stars, with $A(\text{Fe})$ from Fe II lines.

3.10.9 | Samarium

To derive $A(\text{Sm})$ 11 and Sm II features have been analyzed, providing $A(\text{Sm})$ of -0.78 ± 0.04 and -0.29 ± 0.06 and $[\text{Sm}/\text{Fe}]$ of 0.39 and 0.20 dex, respectively. In Table 6, $A(\text{Sm})$ are reported.

3.10.10 | Europium

Just the Eu II line at 664.5 nm allowed us to derive $A(\text{Eu})$ of -1.0 and -0.5 (see Table 6), respectively. For both stars, we derive a positive $[\text{Eu}/\text{Fe}]$ ratio (0.65 and 0.47 for the two stars). Both stars, but particularly TYC 622–742–1, show a high value of Eu (see Figure 7).

3.11 | Uncertainties

When several lines are available in the abundance determination, we adopted the line-to-line scatter as uncertainty on the abundance determination, and the value is listed in Table 6. For the elements whose abundances are based on one single lines, we took the highest line-to-line scatter, which is 0.16 dex for TYC 622–742–1 and 0.14 dex for TYC 1193–1918–1.

Our uncertainties on the stellar parameters are: $\Delta T = 100$ K, $\Delta \log g = 0.10$ dex, and $\Delta \xi = 0.20$ km s⁻¹. A change in the stellar parameters brings a change in the abundance derived for the star. We then run MyGIsFOS by changing the stellar parameters with these uncertainties, to quantify the uncertainties in the abundances due to the uncertainties in the stellar parameters, and we derived the changes in the abundances listed in Table 8. The largest uncertainties in the abundance determination arise usually from the uncertainty in the temperature of the stars.

4 | DISCUSSION

4.1 | Parallax zero-point

To derive the stellar parameters, we applied the zero-point as described by Lindegren et al. (2021). In the case we have not applied the zero-point the star TYC 1193–1918–1 would have been barely affected, while for the star TYC 622–742–1 small changes, anyway within the uncertainties, would have affected the stellar parameters. We would have derived: (i) a T_{eff} hotter by about 30 K for TYC 622–742–1 and just few K for TYC 1193–1918–1; (ii) a $\log g$ smaller by more than 0.1 dex for TYC 622–742–1 and by 0.05 dex for TYC 1193–1918–1.

4.2 | Kinematics

The stellar orbits, integrated 10 Gyr backward, are presented in Figure 8 (blue and orange for TYC 622–742–1 and TYC 1193–1918–1, respectively). Both stars present retrograde, eccentric orbits ($e = 0.32$ and 0.70 , respectively, for TYC 622–742–1 and TYC 1193–1918–1). Their orbital and kinematical parameters are typical of halo stars. None of them seem to belong to the Gaia-Sausage-Enceladus (GSE) structure (Belokurov et al. 2018; Di Matteo et al. 2019; Haywood et al. 2018; Helmi et al. 2018). Figure 9 presents the position of the two stars (blue triangle and orange square for TYC 622–742–1 and TYC 1193–1918–1, respectively) in planes used to isolate GSE, employing Galactocentric cylindrical velocities (V_T , V_R , V_Z , top panels), the vertical component of the angular momentum (L_Z , bottom panels), the orbital energy (E , bottom-right panel), and the radial action (its square root $\sqrt{J_R}$, bottom-left panel). As a reference sample, stars of the “good parallax” sub-sample analyzed in Bonifacio et al. (2021) are also plotted in gray scale. The red-shaded area in the bottom-left panel corresponds to the criteria defined in Feuillet et al. (2020) to select GSE stars, namely -500 kpc km s⁻¹ $< L_Z < 500$ kpc km s⁻¹ and $30 < \sqrt{J_R} < 50$. Stars belonging to this area are then presented as red filled circles in the other panels. TYC 622–742–1 has V_T and L_Z relatively similar to GSE stars, but a significantly lower value of $\sqrt{J_R}$.

4.3 | Abundances

The stars mainly show a typical chemical pattern of metal-poor evolved stars, as also highlighted by the comparison with the literature samples.

The stars with retrograde motion studied by Matsuno et al. (2019) show decreasing trend of $[\alpha/\text{Fe}]$ with

TABLE 8 Sensitivity of abundances on atmospheric parameters

Element	TYC 622-742-1			TYC 1193-1918-1		
	$\Delta T_{\text{eff}} = \pm 100$ (K)	$\Delta \log g = \pm 0.2$	$\Delta \xi = \pm 0.2$ (km s^{-1})	$\Delta T_{\text{eff}} = \pm 100$ (K)	$\Delta \log g = \pm 0.2$	$\Delta \xi = \pm 0.2$ (km s^{-1})
O I	-0.03/ +0.02	-0.13/ +0.12	+0.00/ +0.00	-0.01/ +0.02	-0.11/ +0.13	+0.00/ +0.01
Na I	-0.10/ +0.04	+0.01/ -0.02	+0.00/ +0.00	-0.09/ +0.08	+0.02/ -0.04	+0.02/ -0.02
Mg I	-0.08/ +0.08	+0.02/ -0.03	+0.03/ -0.01	-0.09/ +0.09	+0.03/ -0.03	+0.06/ -0.05
Al I				-0.09/ +0.05	+0.00/ -0.01	+0.00/ +0.00
Si I	-0.02/ +0.05	-0.02/ +0.01	+0.00/ +0.00	+0.00/ +0.04	-0.02/ +0.03	+0.01/ +0.00
Ca I	-0.09/ +0.10	+0.02/ -0.02	+0.04/ -0.02	-0.11/ +0.10	+0.01/ -0.01	+0.06/ -0.06
Sc II	+0.02/ -0.02	-0.11/ +0.11	+0.04/ -0.02	+0.02/ -0.01	-0.12/ +0.12	+0.05/ -0.04
Ti I	-0.20/ +0.16	+0.02/ -0.01	+0.03/ -0.01	-0.15/ +0.15	+0.02/ -0.01	+0.05/ -0.03
Ti II	+0.02/ -0.01	-0.07/ +0.08	+0.06/ -0.04	-0.01/ +0.00	-0.10/ +0.10	+0.08/ -0.09
V I	-0.18/ +0.16	+0.01/ -0.02	+0.00/ +0.00	-0.19/ +0.16	+0.01/ -0.01	+0.00/ -0.01
Cr I	-0.16/ +0.14	+0.02/ -0.02	+0.03/ -0.03	-0.13/ +0.12	+0.01/ -0.01	+0.04/ -0.04
Cr II	+0.06/ -0.04	-0.07/ +0.09	+0.01/ +0.00	+0.02/ -0.01	-0.08/ +0.09	+0.03/ -0.02
Mn I	-0.14/ +0.14	+0.02/ -0.03	+0.01/ -0.01	-0.14/ +0.11	+0.01/ -0.01	+0.02/ -0.02
Fe I	-0.12/ +0.12	+0.02/ -0.01	+0.05/ -0.04	-0.11/ +0.11	+0.00/ +0.00	+0.06/ -0.06
Fe II	+0.10/ -0.06	-0.09/ +0.11	+0.05/ -0.02	+0.09/ -0.06	-0.12/ +0.12	+0.06/ -0.07
Co I	-0.13/ +0.15	+0.00/ -0.01	+0.00/ +0.00	-0.14/ +0.13	+0.00/ +0.01	+0.01/ +0.00
Ni I	-0.10/ +0.09	+0.00/ -0.01	+0.01/ -0.02	-0.09/ +0.09	-0.01/ +0.01	+0.03/ -0.03
Cu I	-0.12/ +0.13	+0.02/ -0.01	+0.00/ +0.00	-0.14/ +0.12	+0.00/ -0.01	+0.00/ -0.01
Zn I	+0.05/ -0.03	-0.06/ +0.05	+0.03/ -0.02	+0.04/ -0.01	-0.06/ +0.07	+0.08/ -0.06
Sr II	-0.10/ +0.09	+0.00/ -0.01	+0.15/ -0.12	-0.13/ +0.12	-0.01/ +0.03	+0.16/ -0.13
Y II	-0.05/ +0.05	-0.07/ +0.06	+0.04/ -0.03	-0.03/ +0.03	-0.09/ +0.09	+0.05/ -0.05
Zr I	-0.21/ +0.11	+0.00/ +0.00	+0.00/ +0.00	-0.13/ +0.12	-0.01/ +0.01	+0.00/ +0.00
Zr II	+0.02/ -0.01	-0.08/ +0.11	+0.04/ -0.02	+0.01/ +0.02	-0.11/ +0.13	+0.04/ -0.05
Ba II	-0.04/ +0.06	-0.09/ +0.10	+0.21/ -0.14	-0.05/ +0.05	-0.11/ +0.11	+0.28/ -0.23
La II	-0.04/ +0.04	-0.09/ +0.10	+0.01/ -0.01	-0.04/ +0.05	-0.08/ +0.10	+0.01/ -0.01
Ce II	-0.08/ +0.07	-0.07/ +0.07	+0.00/ +0.00	-0.07/ +0.05	-0.07/ +0.09	+0.03/ -0.01
Pr II	-0.04/ +0.05	-0.10/ +0.10	+0.00/ +0.00	-0.04/ +0.04	-0.09/ +0.12	+0.00/ +0.00
Nd II	-0.07/ +0.06	-0.07/ +0.09	+0.02/ +0.00	-0.04/ +0.04	-0.10/ +0.08	+0.00/ -0.01
Sm II	-0.06/ +0.05	-0.13/ +0.11	+0.03/ -0.02	-0.06/ +0.05	-0.10/ +0.10	+0.02/ -0.02
Eu II	+0.03/ -0.03	-0.12/ +0.16	+0.00/ +0.00	-0.02/ +0.00	-0.09/ +0.12	+0.01/ +0.00

increasing metallicity. The decrease appears at about $[\text{Fe}/\text{H}] > -2$. The two stars here analyzed differ in $[\text{Fe}/\text{H}]$, with TYC 622-742-1 having $[\text{Fe}/\text{H}] < -2$ and TYC 1193-1918-1 $[\text{Fe}/\text{H}] > -2$. From Figure 4 and Table 6, one can see that the most metal-rich star (TYC 1193-1918-1) has lower $[\text{Mg}/\text{Fe}]$ and $[\text{Si}/\text{Fe}]$ than the most metal-poor star (TYC 622-742-1) following exactly the trend suggested by Matsuno et al. (2019). This trend is also found for GSE stars, but it is more significant in retrograde stars.

TYC 1193-1918-1 is probably an RGB star (see Figure 2). TYC 622-742-1 could also be an RGB star, but the AGB solution is also reasonable from its photometry and parallax and we are more in favor of this latter possibility due to its low C and high N abundances. We recall the large uncertainty in the A(N) determination, but still the derived values are consistent with the literature results. The C abundance is low in both stars, while A(N) is high, but this can be expected in

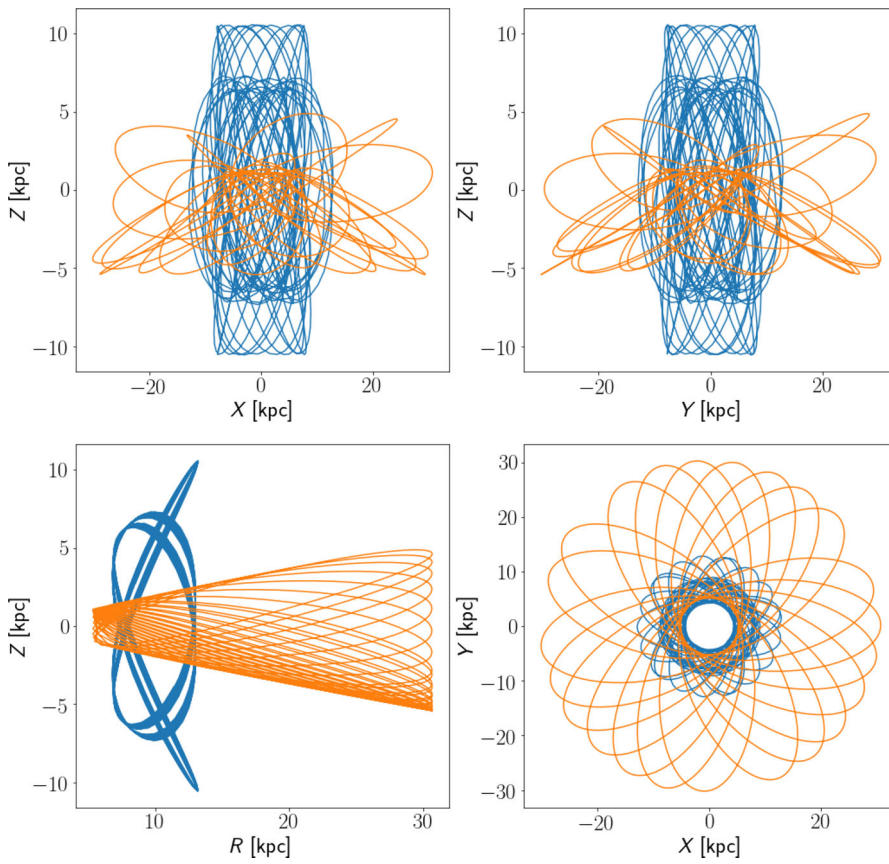


FIGURE 8 Orbits of the two stars (blue and orange for TYC 622–742–1 and TYC 1193–1918–1, respectively) in various planes in Galactocentric X , Y , Z Cartesian coordinates and in the Galactocentric distance R versus height over the galactic plane Z (lower left panel). Orbits were integrated 10 Gyr backward

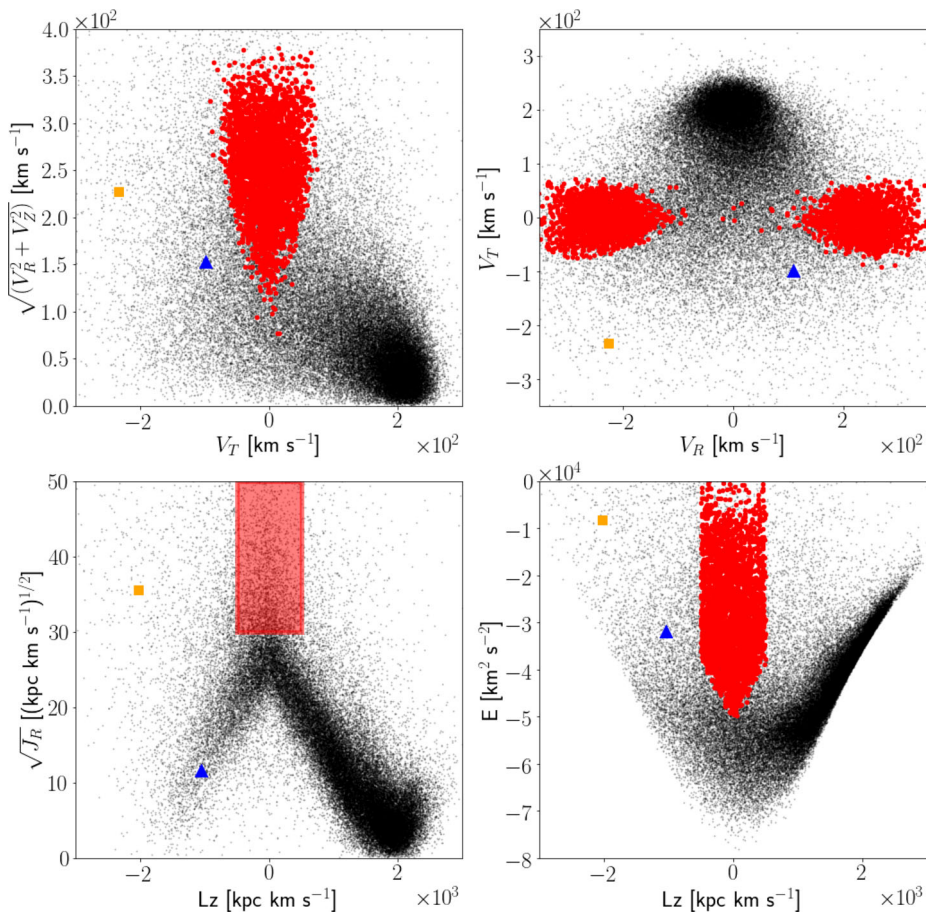


FIGURE 9 Top panels: position of the target stars (blue triangle and orange square for TYC 622–742–1 and TYC 1193–1918–1, respectively) according to their Galactocentric cylindrical velocities (V_T vs V_R and $\sqrt{V_R^2 + V_Z^2}$ vs V_T left and right panel, respectively). Bottom panels: position of the target stars in the orbital Energy (right) and $\sqrt{J_R}$ (left) versus L_Z planes. Stars from the good parallax sample of Bonifacio et al. (2021) are shown as black dots. The red-shaded area in the bottom-left panel outlines the region defined in Feuillet et al. (2020) to select GSE stars. Stars belonging to this area are presented as red filled circles in the other panels

evolved stars, when part of the carbon has been converted into nitrogen and due to some ill understood mechanism, occurring after the RGB bump often dubbed as extra mixing or nonstandard mixing (see e.g. Charbonnel et al. 2020, and references therein), it is brought to the stellar surface. Anyway, in TYC 622-742-1 the effect seems quite extreme (see Figure 3). The $[(C+N)/Fe]$, defined as $\log((C+N)/Fe) - \log((C+N)/Fe)_{\odot}$, is close to 0 for TYC 1193-1918-1, but it is +0.7 dex for TYC 622-742-1.

According to Placco et al. (2014), a star with the surface gravity of TYC 622-742-1, with a $\log g$ increased by 0.5 dex as they suggest, had the initial carbon of about 0.7 dex higher. So the star was C-poor also on the main sequence, with $[C/Fe]$ of about -0.4 dex. Looking at Figure 1 in Placco et al. (2014), the star TYC 622-742-1 was C-poor on the main sequence and also N-rich by about the same amount at the present evolutionary state. In Figure 10, the $[N/Fe]$ ratio is plotted as a function of the $[C/Fe]$ ratio. The star TYC 1193-1918-1 shows abundance ratios similar to many stars in the two comparison sample, while TYC 622-742-1 stands out, with an extremely low $[C/Fe]$ ratio joint to a high $[N/Fe]$.

The high $[N/Fe]$ and low $[C/Fe]$ ratios are surely an evolution effect. From Figure 11, one can see that the star TYC 1193-1918-1 is perfectly coherent with the comparison sample by Gratton et al. (2000, yellow dots), which is close in metallicity. Instead, the star TYC 622-742-1, compared to the sample by Spite et al. (2005, green dots) seems a bit on the edge (see Figure 11).

We queried the SAGA database (Suda et al. 2008) to select the metal-poor stars with low $[C/Fe]$ ($[C/Fe] < -0.8$). We removed the stars from Li et al. (2013), whose C abundance is derived from infrared CO lines. We end up with a sample of: nine stars from Hansen et al. (2018) who derived A(C) from the G-band (2MASS J02412152-1825376, J14164084-2422000, J15260106-0911388, J17094926-6239285, J19161821-5544454, J20093393-3410273, J21162185-0213420, J21262525-2144243, J21513595-0543398); two stars from Aoki & Honda (2008): HD 29574 observed also by Simmerer et al. (2004) who give a $[C/Fe]$ ratio 0.24 dex higher and BD+012916; the star HD 118055 from Gratton et al. (2000); the star HD 6268 from Meléndez & Barbuy (2002), observed also by McWilliam et al. (1995) providing $[C/Fe]$ 0.26 dex larger and by Honda et al. (2004) who derive $[C/Fe]$ 0.43 dex larger; the star WISE J211458.65-763146.8 by Placco et al. (2019). The stars from the literature and the two stars here investigated in Figure 12 are compared to the sample by Gratton et al. (2000) and Spite et al. (2005). Such low $[C/Fe]$ evolved stars are surely rare objects, but still at least a dozen are known, so it could simply be that the C

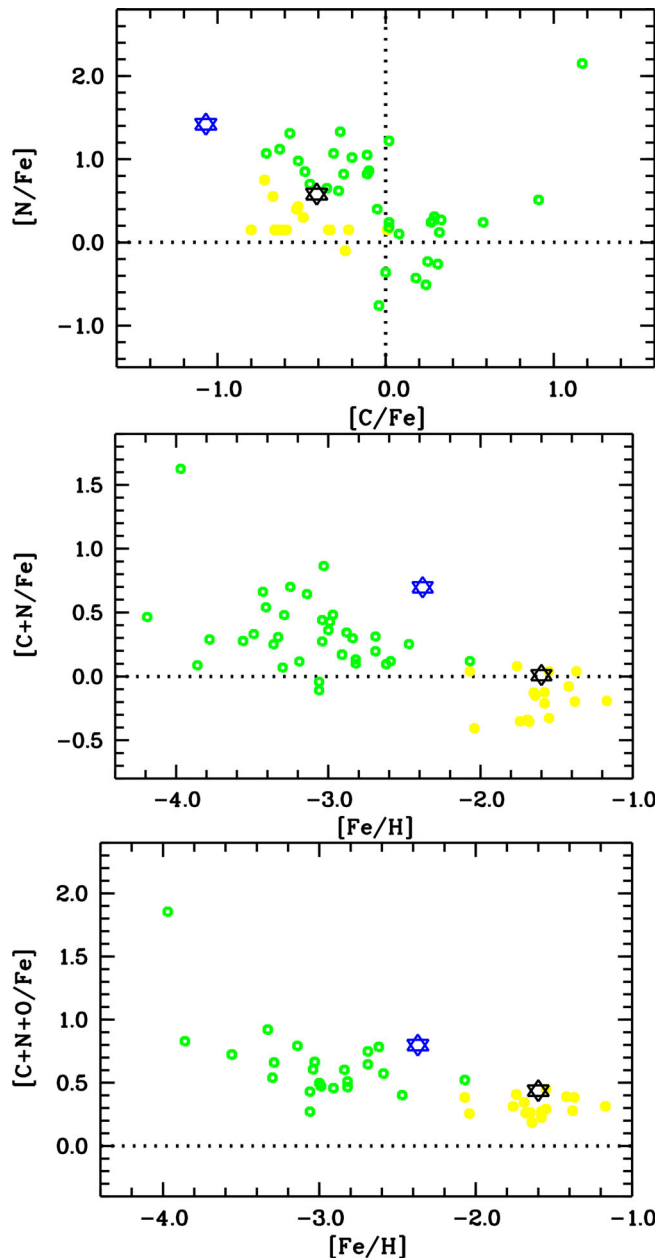


FIGURE 10 $[N/Fe]$ versus $[C/Fe]$, $[C+N/Fe]$ versus $[Fe/H]$ and $[C+N+O/Fe]$ versus $[Fe/H]$ of the two stars compared to the evolved stars from Gratton et al. (2000, yellow dots) sample and stars from Spite et al. (2005, green dots)

correction suggested by Placco et al. (2014) is too small in the case of luminous stars. But in the literature, we could find also unevolved metal-poor stars poor in carbon (see Aguado et al. 2016; Aoki et al. 2013; Placco et al. 2019). It is then possible that also TYC 622-742-1 was C-poor when it was on the main sequence. We remark here that the spectral lines in TYC 622-742-1 are rather broad, corresponding to a gaussian broadening of about 10 km s^{-1} . The quality of the data does not allow us to distinguish between rotational broadening and macroturbulence

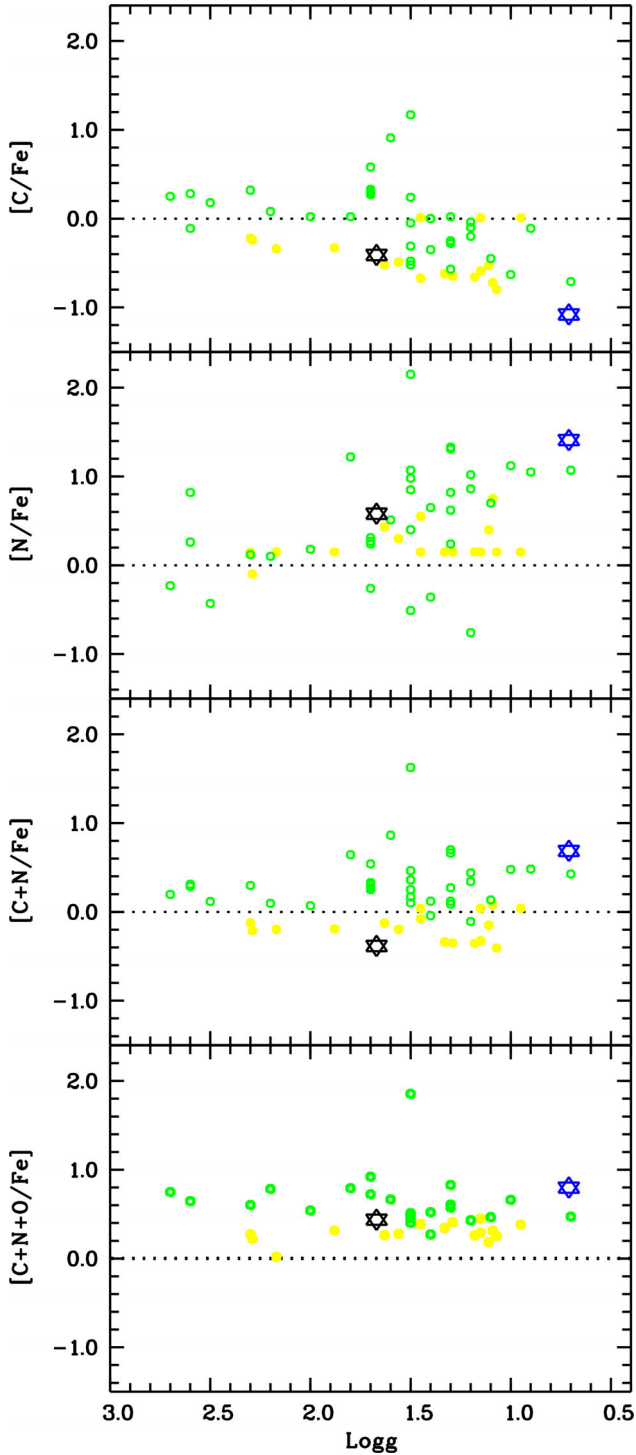


FIGURE 11 $[C/Fe]$, $[N/Fe]$, $[C+N/Fe]$, and $[C+N+O/Fe]$ versus $\log g$ of the two stars compared to the evolved stars from Gratton et al. (2000, yellow dots) sample and stars from Spite et al. (2005, green dots)

broadening. Either way it could be that the phenomenon responsible for broadening the lines is also responsible for a more efficient mixing that brings more nuclearily processed material, with low C and high N, into the atmosphere.

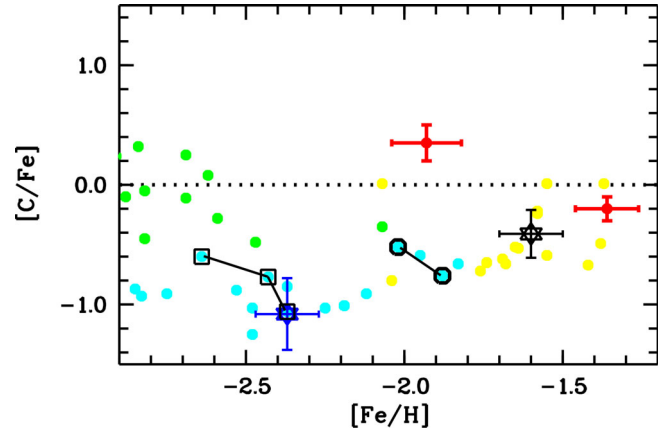


FIGURE 12 $[C/Fe]$ versus $[Fe/H]$ of the two stars compared to the evolved stars from the literature: Gratton et al. (2000, yellow dots), Spite et al. (2005, green dots), and from the database Suda et al. (2008, light blue dots). The star HD 6268 (light blue dots surrounded by black squares) has three independent analysis, one of which gave results very similar to TYC 622-742-1 and HD 29574 (light blue dots surrounded by black circles)

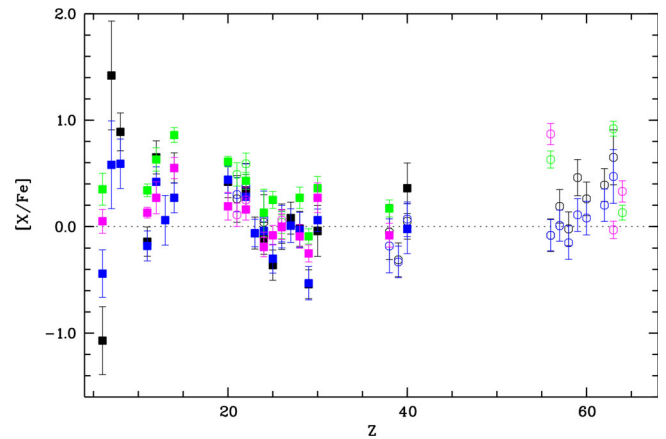


FIGURE 13 The chemical pattern of TYC 622-742-1 (black circles) and TYC 1193-1918-1 (blue circles) compared to the two high-speed stars in Valentini et al. (2019) (green and pink circles). Full symbols are used to show abundances derived from neutral lines and empty symbols from ionized lines

TYC 622-742-1 shows also an enhancement in O, Zr, Pr, Sm. Both stars are: (i) slightly enhanced in Sc; (ii) poor in Y; (iii) rich in Eu. As visible in Figure 13, the two stars show very similar $[X/Fe]$ ratios.

5 | CONCLUSIONS

We investigated high-quality spectra of two stars selected for their high speed and compared their chemical pattern to the literature analyses. We could derive abundances for 28 elements (C, N, O, Na, Mg, Al, Si, Ca, Sc, Ti, V, Cr, Mn,

Fe, Co, Ni, Cu, Zn, Sr, Y, Zr, Ba, La, Ce, Pr, Nd, Sm, Eu), and abundances from two ionization states in the case of four elements (Ti, Cr, Fe, and Zr). The two stars are similar in the chemical pattern with respect to Fe (see Figure 13). From a chemical point of view:

- the two stars are metal-poor;
- both are α -enhanced;
- both stars are poor in C and rich in N, as expected for evolved stars, and this fact is supported by the low $^{12}\text{C}/^{13}\text{C}$ isotopic ratio in TYC 1193–1918–1;
- the stars show a slight excess in Eu abundance.

From a kinematic point of view, these are Halo stars not belonging to the GSE structure. These two stars have retrograde orbits with high ellipticity. They display a chemical composition that is, by and large, indistinguishable from that of other halo stars of similar metallicity.

ACKNOWLEDGMENTS

We gratefully acknowledge support from the French National Research Agency (ANR) funded project “Pristine” (ANR-18-CE31-0017). This work has made use of data from the European Space Agency (ESA) mission *Gaia* (<https://www.cosmos.esa.int/gaia>), processed by the *Gaia* Data Processing and Analysis Consortium (DPAC, <https://www.cosmos.esa.int/web/gaia/dpac/consortium>). Funding for the DPAC has been provided by national institutions, in particular, the institutions participating in the *Gaia* Multilateral Agreement. This research has made use of the SIMBAD database, operated at CDS, Strasbourg, France.

CONFLICT OF INTEREST


The authors declare no potential conflict of interest.

AUTHOR CONTRIBUTIONS

A.M.M.P. analyzed the light elements, investigated the NLTE effects, prepared the tables and figures. E.C. supervised the analysis, wrote the paper. P.F. was the PI of the observing program, observed and reduced the spectra, analyzed the heavy elements. M.S. supervised the analysis. P.B. selected the targets, derived the stellar parameters, contributed writing the text. S.W. worked on the observing proposal and contributed on the preparation of the final text. W.A. worked on the observing proposal and contributed on the preparation of the final text. L.M. computed the kinematic properties and orbits. T.S. gave fundamental contributions on the C abundance and

contributed on the preparation of the final text. F.S. contributed on the discussion on the results and the preparation of the final text. L.S. provided updates in the pipeline used for the analysis and the model atmospheres used in the chemical investigation. L.L. was involved in the C abundance determination. A.M. provided the model atmospheres used in the determinations of the stellar parameters.

ORCID

Piercarlo Bonifacio  <https://orcid.org/0000-0002-1014-0635>

Takuma Suda  <https://orcid.org/0000-0002-4318-8715>

REFERENCES

- Aguado, D. S., Allende Prieto, C., González Hernández, J. I., et al. 2016, *A&A*, 593, A10. <https://doi.org/10.1051/0004-6361/201628371>.
- Aguado, D. S., Allende Prieto, C., González Hernández, J. I., et al. 2018, *ApJ*, 854, L34. <https://doi.org/10.3847/2041-8213/aaadb8>.
- Alexeeva, S., Ryabchikova, T., Mashonkina, L., & Hu, S. 2018, *ApJ*, 866, 153.
- Alvarez, R., & Plez, B. 1998, *A&A*, 330, 1109.
- Andrés Galarza, C., Daflon, S., Placco, V. M., et al. 2021, *A&A* in press, arXiv:2109.11600.
- Andrievsky, S., Bonifacio, P., Caffau, E., et al. 2018, *MNRAS*, 473, 3377.
- Andrievsky, S. M., Spite, F., Korotin, S. A., et al. 2011, *A&A*, 530, A105. <https://doi.org/10.1051/0004-6361/201116591>.
- Aoki, W., & Honda, S. 2008, *PASJ*, 60, L7. <https://doi.org/10.1093/pasj/60.3.L7>.
- Aoki, W., Suda, T., Boyd, R. N., Kajino, T., & Famiano, M. A. 2013, *ApJ*, 766, L13. <https://doi.org/10.1088/2041-8205/766/1/L13>.
- Beers, T. C., Preston, G. W., & Shectman, S. A. 1985, *AJ*, 90, 2089. <https://doi.org/10.1086/113917>.
- Belokurov, V., Erkal, D., Evans, N. W., Koposov, S. E., & Deason, A. J. 2018, *MNRAS*, 478, 611.
- Bergemann, M., Collet, R., Amarsi, A. M., Kovalev, M., Ruchti, G., & Magic, Z. 2017, *ApJ*, 847, 15.
- Bergemann, M., & Gehren, T. 2008, *A&A*, 492, 823.
- Bergemann, M., Kudritzki, R.-P., Plez, B., Davies, B., Lind, K., & Gazak, Z. 2012a, *ApJ*, 751, 156.
- Bergemann, M., Kudritzki, R.-P., Würl, M., Plez, B., Davies, B., & Gazak, Z. 2013, *ApJ*, 764, 115.
- Bergemann, M., Lind, K., Collet, R., Magic, Z., & Asplund, M. 2012b, *MNRAS*, 427, 27.
- Bergemann, M., Pickering, J. C., & Gehren, T. 2010, *MNRAS*, 401, 1334.
- Bidelman, W. P., & MacConnell, D. J. 1973, *AJ*, 78, 687. <https://doi.org/10.1086/111475>.
- Bond, H. E. 1970, *ApJS*, 22, 117. <https://doi.org/10.1086/190220>.
- Bond, H. E. 1980, *ApJS*, 44, 517. <https://doi.org/10.1086/190703>.
- Bonifacio, P., & Caffau, E. 2003, *A&A*, 399, 1183.
- Bonifacio, P., Caffau, E., Sestito, F., et al. 2019, *MNRAS*, 487, 3797. <https://doi.org/10.1093/mnras/stz1378>.
- Bonifacio, P., Caffau, E., Spite, M., et al. 2015, *A&A*, 579, A28. <https://doi.org/10.1051/0004-6361/201425266>.

- Bonifacio, P., Caffau, E., Spite, M., et al. 2018, *A&A*, 612, A65. <https://doi.org/10.1051/0004-6361/201732320>.
- Bonifacio, P., Monaco, L., Salvadori, S., et al. 2021, *A&A*, 651, A79. <https://doi.org/10.1051/0004-6361/202140816>.
- Bovy, J. 2015, *ApJS*, 216, 29.
- Bressan, A., Marigo, P., Girardi, L., Salasnich, B., Dal Cero, C., Rubele, S., & Nanni, A. 2012, *MNRAS*, 427, 127.
- Caffau, E., Bonifacio, P., Korotin, S. A., et al. 2021, *A&A*, 651, A20. <https://doi.org/10.1051/0004-6361/202140808>.
- Caffau, E., Bonifacio, P., Sbordone, L., et al. 2013, *A&A*, 560, A71.
- Caffau, E., Bonifacio, P., Sbordone, L., et al. 2020a, *MNRAS*, 493, 4677. <https://doi.org/10.1093/mnras/staa589>.
- Caffau, E., Bonifacio, P., Spite, M., et al. 2016, *A&A*, 595, L6. <https://doi.org/10.1051/0004-6361/201629776>.
- Caffau, E., Ludwig, H.-G., Steffen, M., Freytag, B., & Bonifacio, P. 2011, *Sol. Phys.*, 268, 255.
- Caffau, E., Monaco, L., Bonifacio, P., et al. 2020b, *A&A*, 638, A122.
- Cayrel, R., Depagne, E., Spite, M., et al. 2004, *A&A*, 416, 1117.
- Cayrel, R., Hill, V., Beers, T. C., et al. 2001, *Nature*, 409, 691.
- Cenarro, A. J., Moles, M., Cristóbal-Hornillos, D., et al. 2019, *A&A*, 622, A176. <https://doi.org/10.1051/0004-6361/201833036>.
- Chamberlain, J. W., & Aller, L. H. 1951, *ApJ*, 114, 52.
- Charbonnel, C., Lagarde, N., Jasniewicz, G., et al. 2020, *A&A*, 633, A34. <https://doi.org/10.1051/0004-6361/201936360>.
- Christlieb, N., Bessell, M. S., Beers, T. C., et al. 2002, *Nature*, 419, 904. <https://doi.org/10.1038/nature01142>.
- Christlieb, N., Reimers, D., & Wisotzki, L. 2004, *The Messenger*, 117, 40.
- Christlieb, N., Reimers, D., Wisotzki, L., Reetz, J., Gehren, T., & Beers, T. C. 2000, in: *The First Stars*, eds. A. Weiss, T. G. Abel, & V. Hill, Springer (Berlin), 49.
- Christlieb, N., Schörck, T., Frebel, A., Beers, T. C., Wisotzki, L., & Reimers, D. 2008, *A&A*, 484, 721. <https://doi.org/10.1051/0004-6361:20078748>.
- Cui, X.-Q., Zhao, Y.-H., Chu, Y.-Q., et al. 2012, *Res. Astron. Astrophys.*, 12, 1197. <https://doi.org/10.1088/1674-4527/12/9/003>.
- Di Matteo, P., Haywood, M., Lehnert, M. D., et al. 2019, *A&A*, 632, A4.
- Feillet, D. K., Feltzing, S., Sahlholdt, C. L., & Casagrande, L. 2020, *MNRAS*, 497, 109. <https://doi.org/10.1093/mnras/staa1888>.
- Fulbright, J. P. 2000, *AJ*, 120, 1841.
- Gaia Collaboration, Brown, A. G. A., Vallenari, A., et al. 2018, *A&A*, 616, A1.
- Gaia Collaboration, Brown, A. G. A., Vallenari, A., et al. 2021, *A&A*, 649, A1. <https://doi.org/10.1051/0004-6361/202039657>.
- Gaia Collaboration, Prusti, T., de Bruijne, J. H. J., et al. 2016, *A&A*, 595, A1.
- Gallagher, A. J., Caffau, E., Bonifacio, P., Ludwig, H. G., Steffen, M., & Spite, M. 2016, *A&A*, 593, A48.
- González Hernández, J. I., & Bonifacio, P. 2009, *A&A*, 497, 497. <https://doi.org/10.1051/0004-6361/200810904>.
- Gratton, R. G., Sneden, C., Carretta, E., et al. 2000, *A&A*, 354, 169.
- Hansen, T. T., Holmbeck, E. M., Beers, T. C., et al. 2018, *ApJ*, 858, 92. <https://doi.org/10.3847/1538-4357/aabacc>.
- Haywood, M., Di Matteo, P., Lehnert, M. D., et al. 2018, *ApJ*, 863, 113.
- Heiter, U., Lind, K., Bergemann, M., et al. 2021, *A&A*, 645, A106. <https://doi.org/10.1051/0004-6361/201936291>.
- Helmi, A., Babusiaux, C., Koppelman, H. H., Massari, D., Veljanoski, J., & Brown, A. G. A. 2018, *Nature*, 563, 85.
- Henden, A. A., Welch, D. L., Terrell, D., et al. 2009, American Astronomical Society Meeting Abstracts #214, Vol. 214, 407.02
- Honda, S., Aoki, W., Kajino, T., et al. 2004, *ApJ*, 607, 474. <https://doi.org/10.1086/383406>.
- Ishigaki, M. N., Aoki, W., & Chiba, M. 2013, *ApJ*, 771, 67.
- Ishigaki, M. N., Chiba, M., & Aoki, W. 2012, *ApJ*, 753, 64.
- Jacobson, H. R., Keller, S., Frebel, A., et al. 2015, *ApJ*, 807, 171. <https://doi.org/10.1088/0004-637X/807/2/171>.
- Keller, S. C., Schmidt, B. P., Bessell, M. S., et al. 2007, *PASA*, 24, 1. <https://doi.org/10.1071/AS07001>.
- Korn, A. J., Shi, J., & Gehren, T. 2003, *A&A*, 407, 691.
- Korotin, S. A., Andrievsky, S. M., Hansen, C. J., et al. 2015, *A&A*, 581, A70.
- Kurucz, R. L. 2005, *Memorie della Societa Astronomica Italiana Supplementi*, 8, 14.
- Li, H., Aoki, W., Zhao, G., Honda, S., Christlieb, N., & Suda, T. 2015a, *PASJ*, 67, 84. <https://doi.org/10.1093/pasj/psv053>.
- Li, H., Tan, K., & Zhao, G. 2018, *ApJS*, 238, 16. <https://doi.org/10.3847/1538-4365/aada4a>.
- Li, H. N., Ludwig, H.-G., Caffau, E., Christlieb, N., & Zhao, G. 2013, *ApJ*, 765, 51. <https://doi.org/10.1088/0004-637X/765/1/51>.
- Li, H.-N., Zhao, G., Christlieb, N., et al. 2015b, *ApJ*, 798, 110. <https://doi.org/10.1088/0004-637X/798/2/110>.
- Lindegren, L., Klioner, S. A., Hernández, J., et al. 2021, *A&A*, 649, A2. <https://doi.org/10.1051/0004-6361/202039709>.
- Lodders, K., Palme, H., & Gail, H.-P. 2009, *Landolt Börnstein*, 4B, 712. https://doi.org/10.1007/978-3-540-88055-4_34
- Marigo, P., Girardi, L., Bressan, A., et al. 2017, *ApJ*, 835, 77.
- Mashonkina, L., Jablonka, P., Pakhomov, Y., Sitnova, T., & North, P. 2017, *A&A*, 604, A129.
- Mashonkina, L. I., Sitnova, T. N., & Pakhomov, Y. V. 2016, *Astron. Lett.*, 42, 606.
- Masseron, T., Plez, B., Van Eck, S., et al. 2014, *A&A*, 571, A47.
- Matijević, G., Chiappini, C., Grebel, E. K., et al. 2017, *A&A*, 603, A19. <https://doi.org/10.1051/0004-6361/201730417>.
- Matsuno, T., Aoki, W., Beers, T. C., Lee, Y. S., & Honda, S. 2017, *AJ*, 154, 52. <https://doi.org/10.3847/1538-3881/aa7a08>.
- Matsuno, T., Aoki, W., & Suda, T. 2019, *ApJ*, 874, L35. <https://doi.org/10.3847/2041-8213/ab0ec0>.
- McWilliam, A., Preston, G. W., Sneden, C., & Searle, L. 1995, *AJ*, 109, 2757. <https://doi.org/10.1086/117486>.
- Meléndez, J., & Barbuy, B. 2002, *ApJ*, 575, 474. <https://doi.org/10.1086/341142>.
- Mendes de Oliveira, C., Ribeiro, T., Schoenell, W., et al. 2019, *MNRAS*, 489, 241. <https://doi.org/10.1093/mnras/stz1985>.
- Monaco, L., Bellazzini, M., Bonifacio, P., et al. 2005, *A&A*, 441, 141.
- Mucciarelli, A., Bellazzini, M., & Massari, D. 2021, *A&A*, in press, 653, A90. <https://doi.org/10.1051/0004-6361/202140979>.
- Nissen, P. E., Hoeg, E., & Schuster, W. J. 1997, *Hipparcos - Venice '97*, 402, 225.
- Noguchi, K., Aoki, W., Kawanomoto, S., et al. 2002, *PASJ*, 54, 855.
- Nordlander, T., & Lind, K. 2017, *A&A*, 607, A75.
- Placco, V. M., Frebel, A., Beers, T. C., & Stancliffe, R. J. 2014, *ApJ*, 797, 21. <https://doi.org/10.1088/0004-637X/797/1/21>.
- Placco, V. M., Roederer, I. U., Lee, Y. S., et al. 2021, *ApJ*, 912, L32. <https://doi.org/10.3847/2041-8213/abf93d>.
- Placco, V. M., Santucci, R. M., Beers, T. C., et al. 2019, *ApJ*, 870, 122. <https://doi.org/10.3847/1538-4357/aaf3b9>.
- Price-Whelan, A. 2018, A Python Package for Working with Data From the Gaia, Zenodo. <https://doi.org/10.5281/zenodo.1228136>.
- Roman, N. G. 1950, *ApJ*, 112, 554. <https://doi.org/10.1086/145367>.
- Roman, N. G. 1955, *ApJS*, 2, 195. <https://doi.org/10.1086/190021>.

- Salaris, M., & Weiss, A. 2001, *A&A*, 376, 955. <https://doi.org/10.1051/0004-6361:20010982>.
- Sbordone, L., Caffau, E., Bonifacio, P., & Duffau, S. 2014, *A&A*, 564, A109.
- Schlafly, E. F., & Finkbeiner, D. P. 2011, *ApJ*, 737, 103.
- Schlaufman, K. C., & Casey, A. R. 2014, *ApJ*, 797, 13. <https://doi.org/10.1088/0004-637X/797/1/13>.
- Schönrich, R., Binney, J., & Dehnen, W. 2010, *MNRAS*, 403, 1829.
- Schwarzschild, M., & Schwarzschild, B. 1950, *ApJ*, 112, 248. <https://doi.org/10.1086/145340>.
- Simmerer, J., Sneden, C., Cowan, J. J., Collier, J., Woolf, V. M., & Lawler, J. E. 2004, *ApJ*, 617, 1091. <https://doi.org/10.1086/424504>.
- Sitnova, T. M., Mashonkina, L. I., & Ryabchikova, T. A. 2013, *Astron. Lett.*, 39, 126.
- Spite, M., Andrievsky, S. M., Spite, F., et al. 2012, *A&A*, 541, A143.
- Spite, M., Cayrel, R., Plez, B., et al. 2005, *A&A*, 430, 655.
- Starkenburger, E., Aguado, D. S., Bonifacio, P., et al. 2018, *MNRAS*, 481, 3838. <https://doi.org/10.1093/mnras/sty2276>.
- Starkenburger, E., Martin, N., Youakim, K., et al. 2017, *MNRAS*, 471, 2587. <https://doi.org/10.1093/mnras/stx1068>.
- Steinmetz, M., Zwitter, T., Siebert, A., et al. 2006, *AJ*, 132, 1645. <https://doi.org/10.1086/506564>.
- Suda, T., Katsuta, Y., Yamada, S., et al. 2008, *PASJ*, 60, 1159. <https://doi.org/10.1093/pasj/60.5.1159>.
- Takeda, Y., Zhao, G., Takada-Hidai, M., Chen, Y. Q., Saito, Y. J., & Zhang, H. W. 2003, *Chin. J. Astron. Astrophys.*, 3, 316.
- Tonry, J., & Davis, M. 1979, *AJ*, 84, 1511. <https://doi.org/10.1086/112569>.
- Valentini, M., Chiappini, C., Bossini, D., et al. 2019, *A&A*, 627, A173.
- Whitten, D. D., Placco, V. M., Beers, T. C., et al. 2021, *ApJ*, 912, 147. <https://doi.org/10.3847/1538-4357/abee7e>.
- Wolf, C., Onken, C. A., Luvaul, L. C., et al. 2018, *PASA*, 35, e010. <https://doi.org/10.1017/pasa.2018.5>.
- York, D. G., Adelman, J., Anderson, J. E., et al. 2000, *AJ*, 120, 1579.

AUTHOR BIOGRAPHY

Aroa del Mar Matas Pinto is completing her doctoral dissertation at the Ecole Doctorale Astronomie et Astrophysique d'Ile de France, Paris.

SUPPORTING INFORMATION

Additional supporting information may be found online in the Supporting Information section at the end of this article.

How to cite this article: Matas Pinto, A. M., Caffau, E., François, P., et al. 2022, *Astron. Nachr.*, 343, e210032. <https://doi.org/10.1002/asna.20210032>

APPENDIX A. ATOMIC LINE DATA

The atomic line data used for the chemical analysis of the two high-velocity stars are provided in a table deposited to CDS; below in Table A1 the first row of this table are shown. In the table we list the atomic lines used for [OI], Na I, Mg I, Al I, Si I, Ca I, Sc II, Ti I, Ti II, V I, Cr I, Cr II, Mn I, Fe II, Co I, Ni I, Cu I, Zn I, Sr II, Y II, Zr I, Zr II, Ba II, La II, Ce II, Pr II, Nd II, Sm II, Eu II. The atomic data are from Heiter et al. (2021). Hyperfine splitting has been taken into account when deriving the abundances of the following elements V, Mn, Co, Cu, Ba, Pr, Nd, Eu, but is not listed below. The solar mix isotopic ratios provided in table 3 of Heiter et al. (2021) have been used for the computation of the abundances.

TABLE A1 Atomic line data sorted by chemical element, showing which spectral lines were used for the analysis of TYC 622-742-1 and TYC 1193-1918-1, respectively

Star	Element Z ion	Wavelength [nm]	log gf	Lower energy [cm⁻¹]
TYC 622-742-1	8 0	630.0304	-9.715	0.000
TYC 622-742-1	8 0	636.3776	-10.190	161.311
TYC 1193-1918-1	8 0	636.3776	-10.190	161.311
TYC 622-742-1	11 0	498.2814	-0.916	16,969.908
TYC 622-742-1	11 0	568.2633	-0.706	16,953.775
TYC 622-742-1	11 0	568.8205	-0.404	16,969.908
TYC 1193-1918-1	11 0	498.2814	-0.916	16,969.908
TYC 1193-1918-1	11 0	568.2633	-0.706	16,953.775
TYC 1193-1918-1	11 0	568.8205	-0.404	16,969.908
TYC 1193-1918-1	11 0	589.5924	-0.144	0.000
TYC 1193-1918-1	11 0	616.0747	-1.246	16,969.908
TYC 622-742-1	12 0	470.2991	-0.440	35,052.859
TYC 622-742-1	12 0	552.8405	-0.498	35,052.859
TYC 622-742-1	12 0	571.1088	-1.724	35,052.859
TYC 1193-1918-1	12 0	470.2991	-0.440	35,052.859
TYC 1193-1918-1	12 0	552.8405	-0.498	35,052.859

Note: These are only a few lines of the full table. The full table is made available both as Appendix S1 on the journal's web page (<https://link-to-online-material>) and at CDS (<https://cdsarc.cds.unistra.fr/viz-bin/cat/J/AN/Vol/Page/>).

The Pristine survey – XIX. Cu and Zn abundances in metal-poor giants

E. Caffau,^{1★} L. Lombardo,¹ L. Mashonkina², T. Sitnova,² P. Bonifacio³, A. M. Matas Pinto,¹ G. Kordopatis,³ F. Sestito⁴, D. Aguado,^{5,6} S. Salvadori^{5,6}, M. Spite,¹ P. François,^{1,7} L. Sbordone,⁸ A. Mucciarelli,^{9,10} N. Martin¹¹, E. Fernández-Alvar^{12,13} and J. I. González Hernández^{12,13}

¹GEPI, Observatoire de Paris, Université PSL, CNRS, Place Jules Janssen, F-92190 Meudon, France

²Institute of Astronomy, Russian Academy of Sciences, Pyatnitskaya st 48, 119017 Moscow, Russia

³Université Côte d'Azur, Observatoire de la Côte d'Azur, CNRS, Laboratoire Lagrange, Bd de l'Observatoire CS 34229 - F 06304 Nice Cedex 4, France

⁴Department of Physics and Astronomy, University of Victoria, Victoria, BC V8P 5C2, Canada

⁵Dipartimento di Fisica e Astronomia, Università degli Studi di Firenze, via G. Sansone 1, I-50019 Sesto Fiorentino, Italy

⁶INAF – Osservatorio Astrofisico di Arcetri, Largo E. Fermi 5, I-50125 Firenze, Italy

⁷GEPI, Observatoire de Paris, Université PSL, CNRS, 77 Av. Denfert-Rochereau, F-75014 Paris, France

⁸European Southern Observatory, Alonso de Cordova 3107, Vitacura, Santiago, Chile

⁹Dipartimento di Fisica e Astronomia 'Augusto Righi', Alma Mater Studiorum, Università di Bologna, Via Gobetti 93/2, I-40129 Bologna, Italy

¹⁰INAF – Osservatorio di Astrofisica e Scienza dello Spazio di Bologna, Via Gobetti 93/3, I-40129 Bologna, Italy

¹¹Observatoire astronomique de Strasbourg, Université de Strasbourg, CNRS, UMR 7550, F-67000, Strasbourg, France

¹²Instituto de Astrofísica de Canarias, E-38200 La Laguna, Tenerife, Spain

¹³Dept. Astrofísica, Universidad de La Laguna, E-38206 La Laguna, Tenerife, Spain

Accepted 2022 November 9. Received 2022 November 9; in original form 2022 August 29

ABSTRACT

Metal-poor stars formed from a gas enriched by the ejecta of the explosion of one/few generations of first massive stars. With the Pristine photometry combined with the *Gaia* data, we selected a sample of bright giants metal-poor candidates to be observed at high resolution. Of the 43 stars observed, 36 were confirmed to be metal-poor, supporting the high success-rate of Pristine in selecting metal-poor stars. We centred the investigation on Cu and Zn, which are elements usually neglected, also because they are the ‘killing elements’ for identifying the Pair Instability Supernovae (PISN) descendants, the explosion of very massive first stars. We derived detailed chemical abundances of 22 species of 18 elements for 36 giant stars. The study of the kinematics of the stars in the sample revealed the presence of metal-poor stars on disc-like orbits (17 per cent of the sample) and even on thin disc orbits (8 per cent of the sample). Four stars are members of the Gaia–Sausage–Enceladus, one star is also likely a member of it. Three stars in the sample (TYC 1118–595–1, TYC 2207–992–1, and TYC 1194–507–1) show a chemical pattern compatible with the one theoretically derived for the PISN descendants, i.e. stars formed out from a gaseous environment enriched by PISN (>50 per cent level) and subsequent generations of normal stars evolving as core-collapse SNe.

Key words: stars: abundances – stars: evolution – Galaxy: abundances – Galaxy: evolution.

1 INTRODUCTION

The formation of elements up to iron can take place in the stellar interior through exothermal nuclear reactions, while elements heavier than Fe need energy to be formed. The elements Cu and Zn (neighbours in the periodic table with 29 and 30 protons, respectively) belong to the iron peak and have to be formed via exothermal nuclear reactions. Both Cu and Zn are elusive in our understanding of their chemical evolution and their production sites.

Bisterzo et al. (2004) suggested several sites for the copper production: (i) explosive nucleosynthesis in Type II supernovae and (ii) in Type Ia supernovae, (iii) through the weak s-process (neutron-capture process followed by β decay) in massive stars, (iv) through the main s-process in asymptotic giant branch (AGB) stars, and (v) through the weak sr-process in the C-burning shell of massive

stars. In massive stars, the s-process is possible thanks to the $^{22}\text{Ne}(\alpha, n)^{25}\text{Mg}$ reaction, which provides neutrons. This is the main production channel of Cu, with a minor contribution from explosive nucleosynthesis (Bisterzo et al. 2005). According to Pignatari et al. (2010), the main production sites of Cu within the Milky Way are massive stars. This occurs through the weak s-process in the stellar core during the phase of He burning, and in the C-burning shell. On the other hand, copper and zinc are not expected to be efficiently produced by the s-process during the AGB phase. This view is supported by Kratz et al. (2008), who conclude that the main r-process is not an efficient way to produce Cu. Romano & Matteucci (2007) agree that the weak s-process is the main Cu contributor, but they state that, at extremely low metallicity, Cu is essentially produced by nucleosynthesis in massive stars explosions.

The efficiency in the Cu production via the weak s-process is dependent on the stellar metallicity, in particular, we observe that the [Cu/Fe] ratio decreases with decreasing metallicity (Bisterzo et al. 2005; Romano & Matteucci 2007). This strong dependence

* E-mail: elisabetta.caffau@obspm.fr

on metallicity of Cu production results from the use of 1D models and the assumption of local thermodynamic equilibrium (LTE) for investigating this element (see e.g. Mishenina et al. 2002; Bihain et al. 2004). Taking into account the departures from LTE (NLTE) in the investigation on Cu I lines, the decrease in [Cu/Fe] with decreasing metallicity is much reduced (see e.g. Yan, Shi & Zhao 2015; Shi et al. 2018) or cancelled (Andrievsky et al. 2018). Roederer & Barklem (2018) investigated neutral and single ionised Cu lines and highlighted a much smoother decrease of [Cu/Fe] with metallicity when using the abundances derived from Cu II lines, which form closer to LTE condition than neutral lines. The chemical evolution model by Romano & Matteucci (2007) is able to well reproduce the observations of Shi et al. (2018) by taking into account explosive nucleosynthesis.

The situation for Zn production is more complicated than for Cu, for an overview see e.g. Hirai et al. (2018). Several Zn isotopes are stable (^{64}Zn , ^{66}Zn , ^{67}Zn , ^{68}Zn , ^{70}Zn) and several astronomical sites and channels have been proposed to produce them. The Solar system per cent isotopic fractions of these five isotopes are: 49.17, 27.73, 4.04, 18.45, 0.61 (Lodders 2019). ^{64}Zn and ^{66}Zn can be produced in massive stars via α -rich freeze-out in ν winds (Pignatari et al. 2010). The heaviest Zn isotopes are produced in the weak s-process (Bisterzo et al. 2005). Other sources of Zn in the Galactic evolution are: hypernovae, electron-capture supernovae, and supernovae (Hirai et al. 2018). Romano et al. (2010) compared several models of chemical evolution of Zn to Galactic observed measurements, finding a reasonable agreement, but no model could really reproduce completely, in a quantitative way, the [Zn/Fe] versus [Fe/H] results.

Zn has been the object of several Galactic investigations in the past decades (see e.g. Duffau et al. 2017). So far the observations have not been able to confirm which are the favoured channels (if any) for the Cu and Zn production. The intermediate metallicity range from $-2.5 \leq [\text{Fe}/\text{H}] \leq -1.5$ is not usually the most investigated. In fact, several investigations on Zn at higher metallicity have been published (see e.g. Mishenina et al. 2016) and also large samples of stars have been analysed (see e.g. Delgado Mena et al. 2017) in a way to provide also a large statistic. The metallicity range $-3.0 < [\text{Fe}/\text{H}] < -1.5$ can count usually only on small samples (see e.g. Mishenina et al. 2002) and the same holds true for Cu, for which also at metal-rich regime the statistics are limited.

But there is something more. Cu and Zn are two of the key elements (another one being N) to select the stars formed from a gas predominantly enriched by zero-metallicity Pair Instability Supernovae (PISN; see Salvadori et al. 2019). Among the first generation (Pop III) stars, the massive ones with $140 M_{\odot} < M < 260 M_{\odot}$ are expected to conclude their lives as PISN, an energetic explosion that leaves no remnant (Woosley, Heger & Weaver 2002). In this way, all the stellar mass is released in the gas, with 50 per cent in the form of heavy elements. The frequency of PISN is unknown but it is expected to be very small (see e.g. de Bannassuti et al. 2017; Rossi, Salvadori & Skúladóttir 2021) and even their existence is still debated. A way to verify their existence and eventually determine their frequency is to search for their descendants. The descendent of PISN explosions are expected to be metal-poor stars, in a broad range ($-4 < [\text{Fe}/\text{H}] < -1$) with a peak at $[\text{Fe}/\text{H}] \sim -1.8$ (see Salvadori et al. 2019). As stated by Salvadori et al. (2019), from a chemical point of view the direct PISN descendent, meaning the stellar generations formed from a gas enriched by a PISN explosion, are characterized by some key elements underabundant with respect to Fe: N, F, Na, Sc, V, Cu, and Zn. However, when accounting for the chemical contribution of normal stars exploding as type II SNe, one obtains that only

the killing element ratios [N/Fe], [Cu/Fe], and [Zn/Fe] preserve a sub-solar value in PISN-dominated environment (>50 per cent of metals; Salvadori et al. 2019). Among these elements, the ones showing the most extreme paucity are N, F, Cu, and Zn. One has to take into account the fact that the PISN ejecta can be diluted in a gas enriched by Type II supernovae, so that the signature of low [Cu/Fe] and [Zn/Fe] ratios in the stellar atmosphere is also diminished. The ratios do not have a preferred value, in principle that can be as tiny as to be detectable. In our analysis, we put a cut at a contribution by PISN of 50 per cent.

One of the reasons why Cu and Zn are not often investigated is also the relatively small number of atomic lines in the stellar spectra. Few lines are available in the optical wavelength range to investigate these two elements. Four Cu I lines (510.5, 521.8, 570.0, and 578.2 nm) allow to derive the Cu abundance. These lines are not strong and they vanish in the metal-poor regime. Two Zn I lines at 472.2 and 481.0 nm are usually investigated to derive the Zn abundance. For extremely metal-poor ($[\text{Fe}/\text{H}] < -3.5$) stars, the Zn and Cu lines are very rarely detectable. Some Cu and Zn abundances are provided in the literature also in the extremely metal-poor regime ($[\text{Fe}/\text{H}] < -3.5$), in the case of Zn mainly for Zn-rich stars. On the contrary, in the metal-poor ($-2.0 < [\text{Fe}/\text{H}] < -1.0$) and very metal-poor ($-3.0 < [\text{Fe}/\text{H}] < -2.0$) regimes, the Zn and Cu lines are still well visible, but there is still a paucity of investigations.

We selected a sample of evolved stars expected to be around -2.0 in metallicity in order to investigate Cu and Zn, and we here present the results.

2 TARGET SELECTION AND OBSERVATIONS

2.1 Target selection

The stars have been selected from the Pristine photometry (see Starkenburg et al. 2017) combined with the *Gaia* EDR3 data (Gaia Collaboration 2021), as described in Bonifacio et al. (2019). Metal-poor stars from this catalogue shall be observed by WEAVE (Dalton et al. 2020) as discussed in Aguado et al. (2019). We selected metal-poor giant stars with $9.5 < G < 11$, as these stars are too bright to be observed by WEAVE.

We first selected stars bright enough to be observed with SOPHIE at the 1.93-m telescope at the Observatoire de Haute-Provence (OHP) and with a photometric metallicity around -2.0 , to be observable at the end of September 2021 from OHP. We were then limited in the stellar coordinates by selecting a sample of stars to be observed in a 4-d run. For this reason, we selected also stars expected to be slightly more metal-rich.

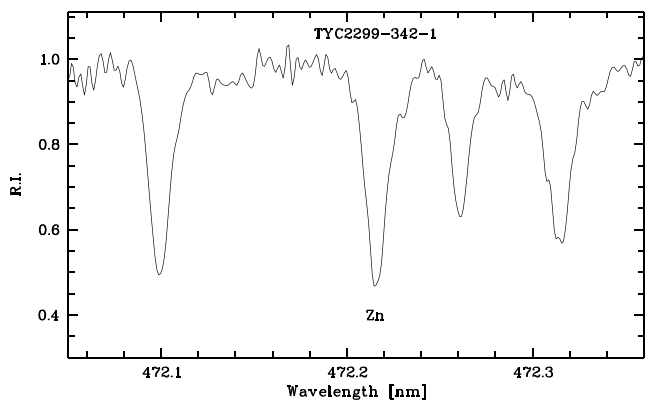
We then selected a sample of stars to be observed with Neo-Narval at the 2-m Télescope Bernard Lyot located at the Pic du Midi at 2878-m above sea level. The observations were carried out in service mode and the fact that we had no restriction on right ascension allowed us to select the best candidate, and for this reason no metal-rich star was detected in the sample.

2.2 Observations

27 stars were observed by L. Lombardo with SOPHIE at OHP (Bouchy & Sophie Team 2006) between 2021 September 20 and 23. We used the HR mode that provides a resolving power $R = 75\,000$ and covers the spectral range 387.2–694.4 nm. The log of their observations is listed in Table 1. In Fig. 1, an observed spectrum is shown. Of the 27 observed objects, we retained 20 stars. Of the other observed stars: one object (TYC 1770–1337–1) is a

Table 1. Radial velocities and details on the observations.

Star	RA [deg]	Dec. [deg]	V_{rad} [km s $^{-1}$]	Date	UT	Instrument	V_{rad} <i>Gaia</i> [km s $^{-1}$]
1745739764412146816 ^a	321.88919123759	11.24673772381	42.6283 ± 0.0025	2021-09-23	21:39:27.592	SOPHIE	43.19 ± 0.24
HU Peg	359.84236527518	13.78653405450	−177.0939 ± 0.0027	2021-09-23	00:48:20.326	SOPHIE	−177.35 ± 0.33
TYC 1118−595−1	320.67053605163	13.26123250708	−297.3112 ± 0.0027	2021-09-20	19:27:24.679	SOPHIE	−295.69 ± 0.44
TYC 1118−595−1	320.67053605163	13.26123250708	−297.3114 ± 0.0027	2021-09-20	20:30:08.420	SOPHIE	−295.69 ± 0.44
TYC 1118−595−1	320.67053605163	13.26123250708	−297.2833 ± 0.0024	2021-09-21	20:43:15.166	SOPHIE	−295.69 ± 0.44
TYC 1118−595−1	320.67053605163	13.26123250708	−297.2972 ± 0.0023	2021-09-21	21:48:13.585	SOPHIE	−295.69 ± 0.44
TYC 1123−1454−1	321.98461188234	11.11580205916	−161.0842 ± 0.0022	2021-09-22	20:41:05.090	SOPHIE	−159.36 ± 0.40
TYC 1125−548−1	325.93469148805	10.884461291	−96.4728 ± 0.0027	2021-09-23	22:41:52.341	SOPHIE	−96.30 ± 0.46
TYC 1159−895−1	343.41019128982	13.80142336401	−247.1121 ± 0.0020	2021-09-24	00:45:57.893	SOPHIE	−245.28 ± 0.23
TYC 1172−486−1	352.71221897294	10.22994243585	−164.6068 ± 0.0028	2021-09-22	23:46:31.901	SOPHIE	−164.07 ± 0.35
TYC 1194−507−1	11.36015858646	20.18865874663	−220.6973 ± 0.0015	2021-09-24	02:49:36.069	SOPHIE	−220.62 ± 0.14
TYC 1205−397−1	25.60006949474	16.20842014543	−215.1774 ± 0.0025	2021-09-21	02:46:03.552	SOPHIE	−211.65 ± 1.53
TYC 1688−640−1	330.87576156536	19.44485391121	−129.9363 ± 0.0024	2021-09-23	23:44:01.623	SOPHIE	−129.92 ± 0.44
TYC 1709−674−1	340.0191775293	21.36955712544	−119.0488 ± 0.0027	2021-09-21	22:50:45.205	SOPHIE	−116.05 ± 0.39
TYC 1709−674−1	340.0191775293	21.36955712544	−118.9278 ± 0.0027	2021-09-22	21:43:06.711	SOPHIE	−116.05 ± 0.39
TYC 1709−674−1	340.0191775293	21.36955712544	−118.9815 ± 0.0028	2021-09-22	22:44:35.726	SOPHIE	−116.05 ± 0.39
TYC 1742−324−1	12.17520695121	25.8632098167	−144.9814 ± 0.0014	2021-09-23	01:50:12.156	SOPHIE	−145.27 ± 0.32
TYC 1753−1167−1	18.76817037252	28.41816179373	−64.7050 ± 0.0020	2021-09-23	02:52:01.855	SOPHIE	−64.78 ± 0.25
TYC 1760−612−1	29.75439204397	26.64150070754	−40.7388 ± 0.0019	2021-09-21	03:48:40.271	SOPHIE	−53.94 ± 3.31
TYC 2086−422−1	260.1635473089	28.17628090437	−119.1516 ± 0.0019	2021-09-21	19:40:09.796	SOPHIE	−119.27 ± 0.37
TYC 2086−422−1	260.1635473089	28.17628090437	−119.0257 ± 0.0019	2021-09-23	20:36:55.738	SOPHIE	−119.27 ± 0.37
TYC 2207−992−1	330.64318457557	25.23600250867	−249.9804 ± 0.0021	2021-09-20	21:33:44.932	SOPHIE	−250.15 ± 0.18
TYC 2270−1021−1	8.06790877154	34.37544943326	−48.9931 ± 0.0017	2021-09-21	01:43:48.239	SOPHIE	−50.93 ± 0.25
TYC 2299−342−1	19.39556032887	35.10894563703	4.1301 ± 0.0013	2021-09-22	00:55:08.090	SOPHIE	−0.32 ± 1.19
TYC 2772−378−1	359.24602579191	32.26115537377	−245.3013 ± 0.0017	2021-09-21	23:53:12.644	SOPHIE	−244.94 ± 0.18
TYC 3084−1083−1	255.56155650328	43.47158629928	−218.6399 ± 0.0020	2021-09-22	19:37:54.825	SOPHIE	−218.33 ± 0.32
TYC 3084−1083−1	255.56155650328	43.47158629928	−218.5810 ± 0.0020	2021-09-23	19:35:14.983	SOPHIE	−218.33 ± 0.32
TYC 3060−408−1	238.06063090409	44.21095353327	−107.00 ± 0.08			Neo-Narval	−107.25 ± 0.18
TYC 2457−2294−1	112.5736440527	32.94891041111	−212.73 ± 0.08			Neo-Narval	−213.10 ± 0.25
TYC 3006−1127−1	153.06268163918	44.16492084722	126.83 ± 0.09			Neo-Narval	126.28 ± 0.24
TYC 286−299−1	180.77301654219	6.38273783758	188.19 ± 0.14			Neo-Narval	188.38 ± 0.19
TYC 1406−971−1	143.23536461939	18.38596473122	153.74 ± 0.12			Neo-Narval	153.08 ± 0.20
TYC 284−358−1	182.67671784716	3.05459391526	60.18 ± 0.07			Neo-Narval	60.01 ± 0.30
TYC 4182−1043−1	235.15863333571	61.95951610665	−99.22 ± 0.08			Neo-Narval	−99.43 ± 0.14
TYC 3458−980−1	189.59408656055	49.61650555607	−91.87 ± 0.13			Neo-Narval	−91.51 ± 0.22
TYC 3458−611−1	187.89255539781	48.82974228654	−17.67 ± 0.08			Neo-Narval	−17.57 ± 0.15
TYC 891−750−1	200.01448759931	7.70738827868	88.74 ± 0.08			Neo-Narval	89.05 ± 0.31
TYC 312−1416−1	207.62957843038	3.95407002247	4.34 ± 0.07			Neo-Narval	4.28 ± 0.24
TYC 914−128−1	221.91296639868	12.39335297616	−73.81 ± 0.08			Neo-Narval	−74.21 ± 0.36
TYC 333−942−1	223.86857608899	6.74545326013	−64.92 ± 0.36			Neo-Narval	−64.57 ± 0.68
TYC 877−422−1	186.53618052056	10.25013586841	339.61 ± 0.13			Neo-Narval	336.97 ± 0.71
TYC 905−551−1	212.3784102112	12.06841728236	−223.33 ± 0.12			Neo-Narval	−223.29 ± 0.28
1180300688463921792 ^a	223.83323169277	10.66753837455	74.31 ± 0.38			Neo-Narval	73.75 ± 0.43

^a*Gaia* DR3**Figure 1.** The spectrum of TYC 2299−342−1 in the range of a Zn I line. The S/N per pixel in this range is 47.

double lined binary system and the other six stars are too metal-rich ($[\text{Fe}/\text{H}] > -0.5$) for the goal of this investigation.

The radial velocities provided in Table 1 were derived by the SOPHIE pipeline using a cross-correlation with a K0 mask. We have four stars with more than one SOPHIE spectrum, and the rms of the observations is of the order of a few 10 m s $^{-1}$. This is larger than the errors of the individual spectra, as provided by the pipeline. It could plausibly be due to radial velocity jitter and pulsations (see e.g. Carney et al. 2003).

There are six stars (TYC 1159−895−1, TYC 1709−674−1, TYC 1760−612−1, TYC 2270−1021−1, TYC 2299−342−1, TYC 877−422−1) that are likely radial velocity variables, since the *Gaia* radial velocity differs by over 2.5σ from our measured radial velocities. The radial velocity we derived for TYC 1205−397−1 was in perfect agreement with the one derived by *Gaia* DR2 ($V_{\text{rad}} = -215.12 \pm 0.76$ km s $^{-1}$) but with the new determination

by *Gaia* DR3 a difference of -3.5 km s^{-1} appeared, which is still consistent at 2.5σ due to a larger uncertainty in the *Gaia* DR3 catalogue (see Table 1). These stars showing a difference in radial velocity between *Gaia* DR3 and SOPHIE, could be spectroscopic binaries, but we cannot detect any secondary spectrum, hence they should be SB1. We assume the veiling from a possible unseen companion to be negligible for our abundance analysis.

16 stars have been observed with Neo-Narval at the T el escope Bernard-Lyot (TBL). We used Neo-Narval with a fibre that provides a resolving power $R = 65\,000$ and covers the spectral range 370–1000 nm. The observations were acquired in service mode from 2021 September to 2022 March. For the Neo-Narval spectra, to derive the radial velocities, we shifted the spectra according to the value provided by *Gaia* DR3. The spectrum was then analysed with MYGISFOS (see Section 4), and we used the shift determined for each line kept for the chemical analysis to correct the *Gaia* DR3 radial velocity. We do not provide a date for these measures, since the chemical analysis and the determination of radial velocity were done on the co-added spectra. Individual spectra were corrected for the barycentric velocity before co-addition. Compared to the *Gaia* DR3 radial velocities, they differ within 2.5σ ; also TYC 877–422–1, whose difference in radial velocity of more than 2 km s^{-1} , is anyway within the uncertainties.

Neo-Narval is a refurbishment of Narval, very recently made available to the community, so the spectra still show the need for further work on the data reduction software. To check the quality of the spectra, we investigated the chemical pattern of a standard radial-velocity star, HD 185144, to assure the quality of the observations. We selected 70 high S/N spectra observed by SOPHIE and 70 observed by Neo-Narval. We compared the abundances derived from MYGISFOS by keeping the same stellar parameters ($T_{\text{eff}} = 5338 \text{ K}$, $\log g = 4.57$, and $\xi = 0.94 \text{ km s}^{-1}$) for all the spectra. We removed three spectra from the Neo-Narval sample because the iron abundance derived was lower (by more than 0.05 dex and in one case by 0.78 dex) than $A(\text{Fe})$ derived from the average of the others and from the SOPHIE spectra. The elements for which we derived agreement (within 0.05 dex) from the two spectrographs are: Fe I, Na I, Al I, Si I, Ca I, Sc II, V I, Mn I, Ni I, Cu I, Zn I, Y II. We would like to stress that also the S/N in the Neo-Narval spectra is generally much lower than in the SOPHIE spectra, providing a lower set of ‘good’ lines to investigate.

3 KINEMATICS

The orbital parameters were computed following the same recipe as in Kordopatis et al. (2022, see section 3.1), i.e. adopting the St ackel fudge method (Binney 2012; Sanders & Binney 2016) with the McMillan (2017) axisymmetric potential for the Galaxy and the GALPY (Bovy 2015) code. The Sun’s position is assumed to be $(R, Z) = (8.249, 0.0208) \text{ kpc}$ (Bennett & Bovy 2019; Gravity Collaboration 2020), and its peculiar velocities $(V_R, V_\phi, V_Z) = (-9.5, 250.7, 8.56) \text{ km s}^{-1}$ (Gravity Collaboration 2020; Reid & Brunthaler 2020).

In Fig. 2, the angular momentum versus the square root of the radial action is shown for both the SOPHIE and Neo-Narval samples. As Galactic comparison we show the sample of SDSS Turn-Off stars from Bonifacio et al. (2021). To fix the ideas we have coloured in pink the region where the Gaia–Sausage–Enceladus (GSE) stars are expected to be found, according to Feuillet et al. (2020) ($-500 \text{ kpc km s}^{-1} < L_z < 500 \text{ kpc km s}^{-1}$ and $30 (\text{kpc km s}^{-1})^{1/2} < \sqrt{J_r} < 50 (\text{kpc km s}^{-1})^{1/2}$), in green what we

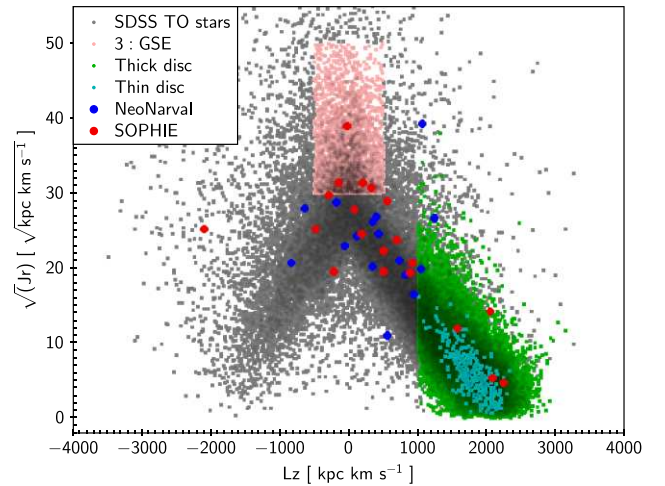


Figure 2. The SOPHIE (red dots) and the Neo-Narval (blue dots) stars compared to SDSS TO stars from Bonifacio et al. (2021) in the angular momentum–radial action plane. See text for details.

associate with the Galactic disc (thick + thin) ($L_z < 1000 \text{ kpc km s}^{-1}$ and $z_{\text{max}} < 3.0 \text{ kpc}$) and in light blue the thin disc ($L_z < 1000 \text{ kpc km s}^{-1}$ and $z_{\text{max}} < 0.3 \text{ kpc}$). From the orbital parameters, there are some interesting objects. 27 stars have a pericentre below 3.5 kpc from the Galactic centre, and are on high eccentricity orbits ($e > 0.5$). There is a clear anticorrelation between pericentre and eccentricity, which is obviously an observational bias. Six stars belong to the Galactic disc, three of which to the thin disc. Two of the thin disc stars are metal-poor: TYC 2270–1021–1 ($[\text{Fe}/\text{H}] = -1.28$) and *Gaia* DR3 1745739764412146816 ($[\text{Fe}/\text{H}] = -2.05$); one is slightly metal-poor TYC 22299–342–1 ($[\text{Fe}/\text{H}] = -0.59$). All three stars have low eccentricities, the largest being that of *Gaia* DR3 1745739764412146816 ($e = 0.33$). Four of the stars are likely members of the GSE structure (Belokurov et al. 2018; Haywood et al. 2018; Helmi et al. 2018). They span the metallicity range -1.3 to -2.4 , thus in the range where most of the GSE stars are expected to fall according to the GSE metallicity distribution function (MDF) of Bonifacio et al. (2021). However, according to the GSE MDFs of Feuillet et al. (2020) and Naidu et al. (2020) such stars should be rare. All the GSE stars are α enhanced, which is expected at these metallicities, while at higher metallicities the GSE should be characterized by lower α -to-iron ratios. Thus, at these metallicities it is impossible to distinguish between GSE stars born in the accreted galaxy and those that were born in the Milky Way disc and then scattered to these low angular-momentum, high radial action orbits, by the collision. Our sample is selected purely on a chemical basis and, based on our rough orbital selections, we have 11 per cent of GSE stars and 17 per cent of disc stars (8 per cent thin disc). The small size of the sample prevents us from drawing strong conclusions from these numbers.

4 ANALYSIS

In Fig. 3, the photometric metallicity, $[\text{M}/\text{H}]$, used to select the stars, is compared to the iron abundance, $[\text{Fe}/\text{H}]$, derived by analysing the spectra with MYGISFOS (Sbordone et al. 2014), keeping the same stellar parameters derived by the calibration and a micro-turbulence of 2 km s^{-1} .

We find a difference of $[\text{Fe}/\text{H}] - [\text{M}/\text{H}] = 0.22 \pm 0.31$. The agreement is very good for the 20 stars observed with SOPHIE

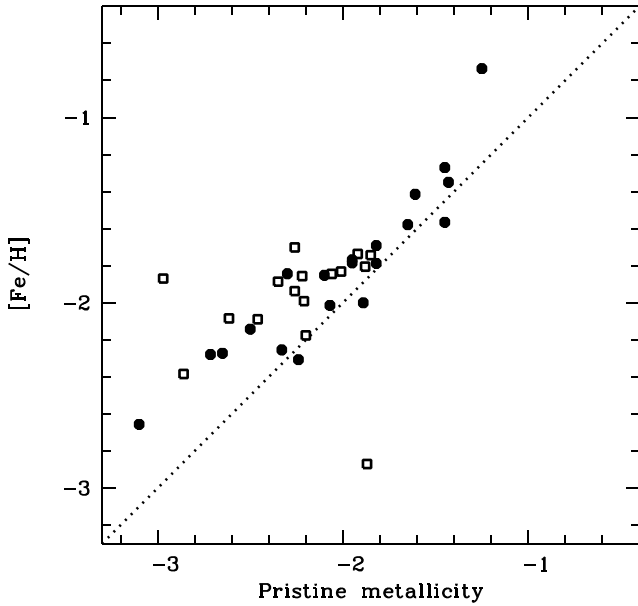


Figure 3. Comparison of the metallicity derived from the calibration and $[\text{Fe}/\text{H}]$ derived by using T_{eff} and $\log g$ from the calibration. Black filled circles are the SOPHIE observations and black open squares the Neo-Narval ones.

and chemically analysed, with a maximum difference of 0.51 dex in the case of TYC 2299–342–1. In the Neo-Narval sample we have no mistake in the metal-poor selection, with a success rate of 100 percent, but for two stars the metallicity derived from the photometry differs by about 1 dex with $[\text{Fe}/\text{H}]$ derived from the spectra: *Gaia* DR3 1180300688463921792 has a $[\text{Fe}/\text{H}]$ that is 1 dex lower than expected from the photometry and this could be also related to the low S/N of the spectrum; on the contrary, TYC 877–422–1 was expected to be close to -3.0 in metallicity but it is slightly more metal-rich than -2.0 in $[\text{Fe}/\text{H}]$.

We are extremely satisfied on the success in the selection on metal-poor stars and on the general good agreement in the two metallicities. However, in the selection of the SOPHIE stars, we picked also wrong targets. In the SOPHIE sample, six stars happen to be too metal-rich for our investigation, so we consider 77 per cent the success rate on our selection. In this computation, we removed the binary star observed several nights with SOPHIE.

4.1 Stellar parameters

The adopted stellar parameters are then derived by comparing the *Gaia* DR3 data (parallax, G magnitude, $\text{BP} - \text{RP}$ colour) to theoretical values, as described in Lombardo et al. (2021). The parallax was corrected for the zero-point (Lindgren et al. 2021).

The reddening was adopted from the Schlegel, Finkbeiner & Davis (1998) maps corrected as in Bonifacio, Monai & Beers (2000). The micro-turbulence was derived from the Mashonkina et al. (2017a) calibration. We use MYGISFOS to derive the detailed abundances for all stars except for TYC 2270–1021–1 for which we adopt a T_{eff} of 4000 K instead of 3872 K as derived from the procedure, because we had no grid available for MYGISFOS at this low temperature. The star HU Peg extrapolates in the grid for $\log g$ by less than 0.1 dex. The stars TYC 877–422–1 and *Gaia* DR3 1180300688463921792 also extrapolate in $\log g$ by 0.15 dex. In Fig. 4, the adopted stellar parameters are compared to PARSEC isochrones (Bressan et al.

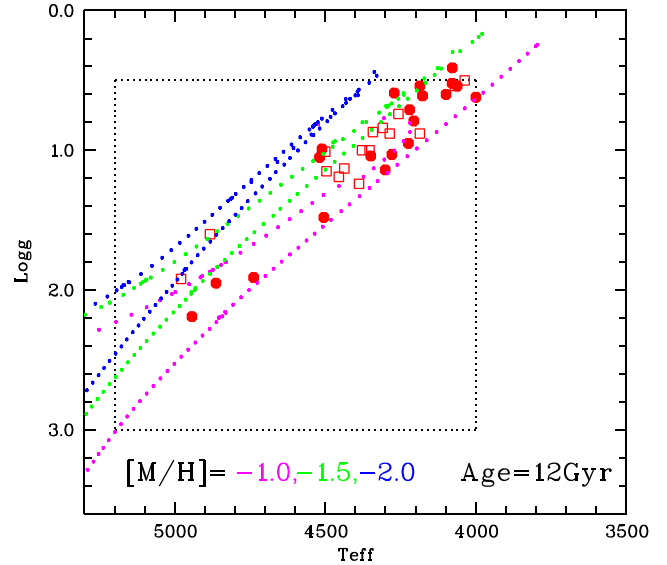


Figure 4. $\log g$ versus T_{eff} for the stars (red filled circles SOPHIE and red open squares Neo-Narval) compared to PARSEC isochrones (Bressan et al. 2012; Marigo et al. 2017). The black dotted lines denote the limits of the grid interpolated by MYGISFOS.

2012; Marigo et al. 2017). The adopted stellar parameters are reported in Table 2.

The comparison of the stellar parameters as derived from the calibration of Pristine photometry and those derived only from *Gaia* parallaxes and photometry, plus spectra, are shown in Fig. 5. One can see from the figure that the surface gravity is practically the same, while for the effective temperature the average difference is -65 ± 62 K for the SOPHIE sample and -52 ± 38 K for the Neo-Narval, being usually cooler the adopted T_{eff} , with the largest difference being -141 K. Mucciarelli, Bellazzini & Massari (2021) derive a colour–temperature relation combining the InfraRed Flux Method (IRFM) from González Hernández & Bonifacio (2009) with the photometry from *Gaia* EDR3. When we compare the adopted effective temperatures to the values derived by using the calibration by Mucciarelli et al. (2021), we find an average difference of $T_{\text{adopted}} - T_{\text{Mucciarelli}} = -51 \pm 52$ K and of $\log g_{\text{adopted}} - \log g_{\text{Mucciarelli}} = 0.02 \pm 0.02$ for the SOPHIE sample and -46 ± 48 and -0.01 ± 0.02 for the Neo-Narval stars. We assumed as uncertainty for the effective temperature 100 K.

We compared the adopted T_{eff} also to the effective temperatures derived from the González Hernández & Bonifacio (2009) calibration. Being a bright sample of stars, we retrieved the 2MASS and V Johnson photometry in the AAVSO Photometric All-Sky Survey APASS (Henden et al. 2012) and the JHKs magnitudes in the infrared bands from the Two Micron All-Sky Survey (2MASS; Skrutskie et al. 2006). The colours were de-reddened using the maps from Schlegel et al. (1998). For a few stars, with uncertainties higher than 0.1 mag, the SDSS (York et al. 2000) g and r magnitudes, of the SDSS Photometric Catalogue, Release 12 (Alam et al. 2015), have been converted into Johnson V. Removing the stars TYC 2270–1021–1 and *Gaia* DR3 1180300688463921792, with a V APASS photometry inconsistent with *Gaia* DR3, we derived a good agreement with the adopted T_{eff} : $T_{\text{adopted}} - T_{\text{IRFM}} = -9 \pm 83$ K.

For the surface gravity, the largest effect is the uncertainty on the parallax. When adding/subtracting the uncertainty on the parallax when deriving $\log g$ we derive a difference of 0.05. We assumed 0.1 dex as uncertainty in $\log g$.

Table 2. The adopted stellar parameters.

Star	T_{eff} [K]	$\log g$ [gcs]	ξ km s $^{-1}$	[Fe/H] dex	S/N @480 nm
1745739764412146816	4349	1.04	1.94	-2.05	23
HU Peg	4078	0.41	2.12	-2.21	26
TYC 1118-595-1	4186	0.54	2.11	-2.12	40
TYC 1123-1454-1	4177	0.61	2.09	-2.43	34
TYC 1125-548-1	4519	1.05	2.05	-2.41	25
TYC 1159-895-1	4206	0.79	1.98	-1.97	38
TYC 1172-486-1	4863	1.95	1.81	-2.52	33
TYC 1194-507-1	4224	0.95	1.87	-1.34	36
TYC 1205-397-1	4279	1.03	1.94	-2.41	26
TYC 1688-640-1	4738	1.91	1.71	-1.73	27
TYC 1709-674-1	4271	0.59	2.15	-2.46	43
TYC 1742-324-1	4099	0.60	2.01	-1.84	53
TYC 1753-1167-1	4301	1.14	1.84	-1.58	32
TYC 1760-612-1	4511	0.99	2.00	-1.53	37
TYC 2086-422-1	4062	0.54	2.04	-1.96	33
TYC 2207-992-1	4220	0.71	2.02	-1.79	30
TYC 2270-1021-1	4000	0.62	2.00	-1.28	30
TYC 2299-342-1	4943	2.19	1.58	-0.59	52
TYC 2772-378-1	4505	1.48	1.78	-1.58	44
TYC 3084-1083-1	4079	0.52	2.04	-1.82	42
TYC 3060-408-1	4266	0.70	2.05	-1.92	9
TYC 2457-2294-1	4374	0.90	2.04	-2.22	13
TYC 3006-1127-1	4365	0.75	2.03	-2.17	9
TYC 286-299-1	4888	1.52	1.98	-2.04	10
TYC 1406-971-1	4982	1.87	1.86	-2.00	11
TYC 284-358-1	4305	0.80	2.03	-1.98	12
TYC 4182-1043-1	4384	0.97	1.97	-1.88	7
TYC 3458-980-1	4447	1.06	1.97	-1.92	6
TYC 3458-611-1	4462	1.14	1.93	-1.85	11
TYC 891-750-1	4400	1.16	1.90	-1.86	10
TYC 312-1416-1	4335	0.70	2.05	-1.79	13
TYC 914-128-1	4208	0.77	1.98	-1.76	8
TYC 333-942-1	4517	0.88	2.18	-2.59	3
TYC 877-422-1	4076	0.35	2.12	-1.96	6
TYC 905-551-1	4483	1.05	1.99	-1.76	6
1180300688463921792	4076	0.35	2.12	-3.03	3

For micro-turbulence, the values derived from the equivalent width – abundance balance show an average difference with the adopted one of about 0.2 km s $^{-1}$. We assumed this value of 0.2 km s $^{-1}$ as the uncertainty in the micro-turbulence.

The LAMOST spectra of 13 stars in the sample are investigated by Zhang, Liu & Deng (2020) by using a machine learning method. The average difference in metallicity we find is of -0.27 , with the largest of -1.36 dex for *Gaia* DR3 1180300688463921792. Removing this star, the difference in metallicity becomes -0.18 dex. This small but systematic difference is surely related to the hotter (by -154 K on average) T_{eff} adopted by Zhang et al. (2020).

The same uncertainties we applied for similar quality data by Matas Pinto et al. (2022). The uncertainties in the stellar parameters imply uncertainties in the derived abundances. These uncertainties are largely discussed by Matas Pinto et al. (2022). In Table 3, we report an average uncertainty in the abundances related to the uncertainties in the stellar parameters.

4.2 Chemical investigation

The abundances have been derived with MyGIsFOS (see Sbordone et al. 2014). The adopted solar values are from Caffau et al. (2011) and Lodders, Palme & Gail (2009) and are listed in Table 4. The

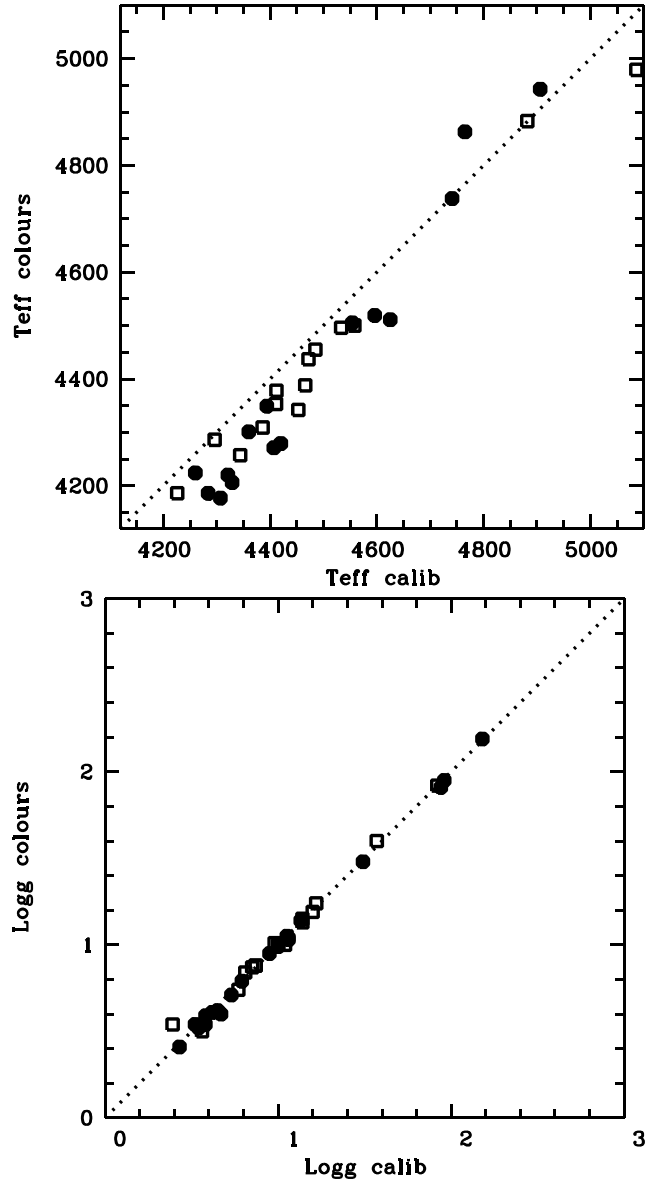


Figure 5. Comparison of the effective temperature and surface gravity when derived from the *Gaia* EDR3 data combined with Pristine narrow band photometry (horizontal axis) compared to *Gaia* DR3 and spectroscopic metallicities (vertical axis). Black filled circles represent the SOPHIE observations and open squares the Neo-Narval.

abundances are provided in two online tables (one for the SOPHIE sample and one for the Neo-Narval sample) with the line-to-line scatter as uncertainties as discussed in the appendix (see Section A). In Appendix B, an explanation on the lines used for the chemical investigation is provided for a table deposited to the Centre de Données astronomiques de Strasbourg (CDS).

For several elements (Na, Mg, Al, Si, Ca, Ti, Fe, Zn, and Zr), we computed a line-by-line investigation on the departure from NLTE. The NLTE calculations were performed using the methods treated by Alexeeva, Pakhomov & Mashonkina (2014, Na I), Mashonkina (2013, Mg I), Mashonkina, Belyaev & Shi (2016a, Al I), Mashonkina (2020, Si I), Mashonkina, Sitnova & Belyaev (2017b, Ca I), Sitnova, Mashonkina & Ryabchikova (2016, Ti II), Mashonkina et al. (2011, Fe I-Fe II), Sitnova et al. (2022, Zn I), and Velichko, Mashonkina &

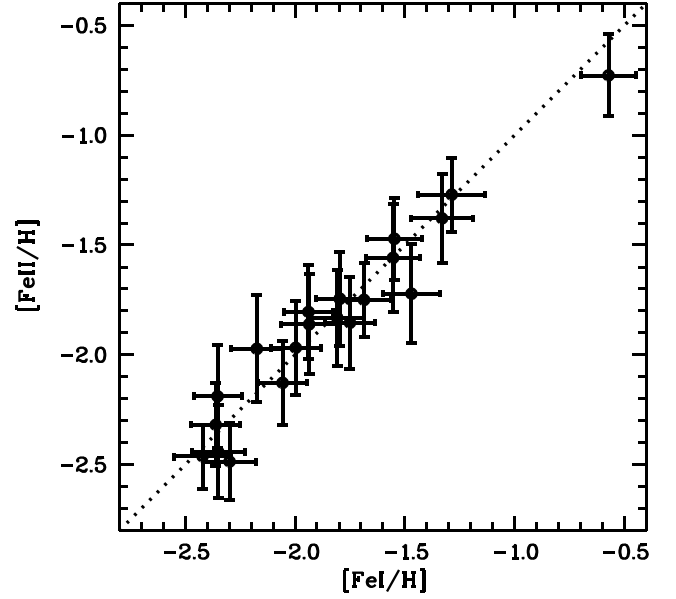
Table 3. Sensitivity of abundances on atmospheric parameters.

Element	ΔT_{eff} 100 K	$\Delta \log g$ 0.2 dex	$\Delta \xi$ 0.2 km s ⁻¹
Na I	0.08	0.02	0.01
Mg I	0.08	0.03	0.03
Al I	0.06	0.01	0.00
Si I	0.03	0.02	0.01
Ca I	0.10	0.02	0.04
Sc I	0.17	0.01	0.00
Sc II	0.02	0.11	0.04
Ti I	0.16	0.02	0.03
Ti II	0.01	0.08	0.06
V I	0.18	0.01	0.00
Cr I	0.14	0.02	0.03
Cr II	0.04	0.08	0.01
Mn I	0.14	0.02	0.01
Fe I	0.12	0.01	0.05
Fe II	0.08	0.11	0.05
Co I	0.14	0.01	0.00
Ni I	0.10	0.01	0.02
Cu I	0.13	0.01	0.00
Zn I	0.04	0.06	0.03
Zr I	0.15	0.01	0.00
Zr II	0.02	0.10	0.04
Ba II	0.05	0.10	0.20

Table 4. The adopted solar abundances and the sensitivity of abundances on atmospheric parameters.

Element	$A(X)_{\odot}$	Δ
Na I	6.30	0.08
Mg I	7.54	0.10
Al I	6.47	0.07
Si I	7.52	0.04
Ca I	6.33	0.11
Sc II	3.10	0.13
Ti I	4.90	0.17
Ti II	4.90	0.11
V I	4.00	0.18
Cr I	5.64	0.15
Cr II	5.64	0.09
Mn I	5.37	0.14
Fe I	7.52	0.13
Fe II	7.52	0.13
Co I	4.92	0.14
Ni I	6.23	0.10
Cu I	4.21	0.13
Zn I	4.62	0.09
Y II	2.21	0.10
Zr I	2.62	0.13
Zr II	2.62	0.11
Ba II	2.17	0.23

Nilsson (2010, Zr II). We applied the code DETAIL (Giddings 1981; Butler 1984) with a modified opacity package (as described by Mashonkina et al. 2011). The NLTE abundance corrections, $\Delta_{\text{NLTE}} = \varepsilon_{\text{NLTE}} - \varepsilon_{\text{LTE}}$, for individual spectral lines were computed with the code LINEC (Sakhbullin 1983) that uses the LTE and NLTE level populations from DETAIL.

**Figure 6.** [Fe/H] versus [FeII/H]. In the case of Fe I, NLTE corrections are included. The error bars are the line-to-line scatter.

4.2.1 Iron

For the SOPHIE sample, several Fe I features (from 148 to 235) have been investigated to derive the iron abundance from neutral lines and for the stars in the sample we derived $-2.51 < [\text{Fe}/\text{H}] < -0.58$. The line-to-line scatter is generally small ($\sigma = 0.12 \pm 0.01$ dex) with 0.15 dex as the highest value in the case of TYC 2270–1021–1. For a subsample of Fe I lines, we computed the NLTE correction to be applied to the LTE abundance. To verify that the NLTE correction is not strongly influenced by our choice of lines, we derived the LTE iron abundance only from the Fe I lines selected to compute the NLTE correction and compared it to the Fe abundance derived from the complete sample of Fe I lines. We derived an extremely good agreement in the LTE iron abundance, with a difference on average close to zero and, in any case, within 0.03 dex.

We investigated from 15 to 25 features to derive the Fe abundance from Fe II lines and we derived $-2.49 < [\text{Fe}/\text{H}] < -0.73$. The line-to-line scatter (from 0.15 to 0.24 dex) in the sample was $\sigma = 0.20 \pm 0.03$, larger than that for neutral Fe lines. The NLTE corrections for Fe II are negligible, being the largest of only -0.01 dex for the lines at 492.392 and 501.843 nm. We can then safely use the LTE investigation for the Fe abundance derived from Fe II lines.

The iron abundance derived from neutral and ionized lines are generally in good agreement, and anyway always within the uncertainties. In Fig. 6, we show the iron abundance derived from Fe II lines compared to the one from Fe I lines, taking into account the NLTE corrections in the latter case.

The spectra observed with Neo-Narval have lower S/N ratios than the SOPHIE sample, with an average value of 28 at 600 nm and a minimum of 9, to be compared to an average of 53 and a minimum of 38 for the SOPHIE sample. This translates in a smaller number of Fe I lines used (from 70 to 136 except for the two spectra of lowest S/N). The Neo-Narval sample spans in metallicity: $-2.59 < [\text{Fe}/\text{H}] < -1.75$. One star stands out from the range with $[\text{Fe}/\text{H}] = -3.03$, but the quality of the spectrum is poor, with S/N = 9 at 600 nm. Also the spectrum of TYC 333–942–1 has a similar S/N ratio, and only 16 Fe I lines are kept in the investigation. No Fe II line was retained in the analysis of the Neo-Narval spectra.

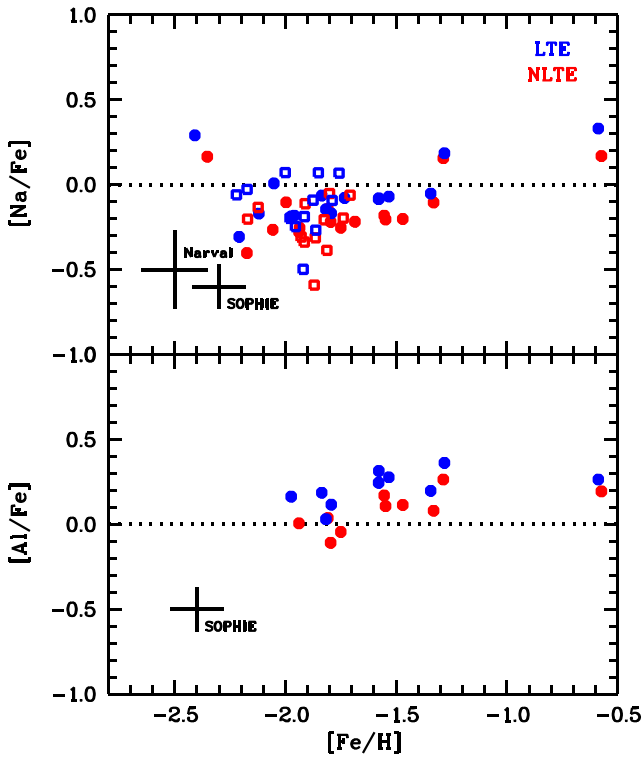


Figure 7. $[\text{Na}/\text{Fe}]$ and $[\text{Al}/\text{Fe}]$ versus $[\text{Fe}/\text{H}]$, LTE in blue and NLTE in red. For Na, filled circles are the SOPHIE stars and open squares the Neo-Narval ones. Error bars are average values based on the line-to-line scatter.

4.2.2 Sodium

Sodium has been derived in 16 SOPHIE and in 12 Neo-Narval stars, by using up to four of the lines at: 498.281, 568.263, 568.820, and 616.074 nm. We investigated the NLTE effects for individual lines, finding the NLTE corrections for the stars in the range from -0.15 to -0.03 dex. The results are shown in Fig. 7.

4.2.3 Aluminium

For 10 stars in the SOPHIE sample, we could derive the Al abundance by using from one to three Al I lines (555.706, 669.602, and 669.618 nm), deriving for the sample $\langle [\text{Al}/\text{Fe}] \rangle = 0.22 \pm 0.10$. The NLTE corrections are non-negligible, in the range from -0.12 to -0.06 . In Fig. 7, the results are shown.

4.2.4 Magnesium

Only for 18 stars in the SOPHIE sample, we could derive Mg abundance with $\langle [\text{Mg}/\text{Fe}] \rangle = 0.53 \pm 0.10$. From one to four lines have been used for the abundance determination (457.109, 470.299, 552.840, and 571.108 nm), but for the majority of cases (12 stars on 18) the Mg abundance is based on one single line, the one at 571.1 nm.

We investigated the NLTE effects on the Mg I lines and obtained that for all but one star for which the Mg abundance is based on more than one line, the line-to-line scatter on $[\text{Mg}/\text{H}]$ is drastically reduced when the NLTE correction is applied (the only exception being TYC 1172–486–1). NLTE corrections for the forbidden line at 457.109 nm are positive, for the other three lines they are negative, with only the exception for the line at 470.299 nm for the star

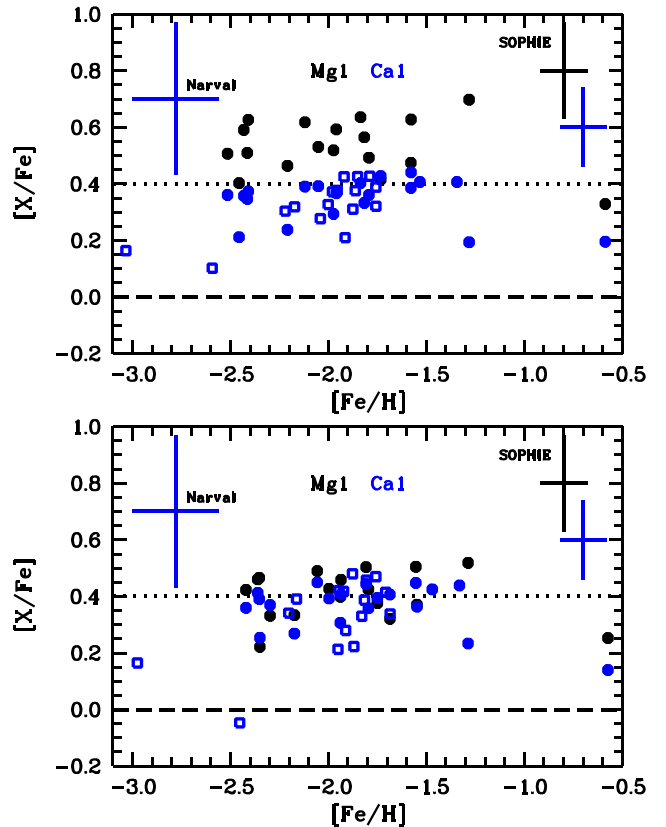


Figure 8. $[\text{Mg}/\text{Fe}]$ (black symbols) and $[\text{Ca}/\text{Fe}]$ (blue symbols) versus $[\text{Fe}/\text{H}]$. In the upper panel, the LTE results are presented and in the lower panel the NLTE corrections are applied. Filled circles are the SOPHIE stars, open squares the Neo-Narval ones. No Mg abundance has been derived in the Neo-Narval sample. Error bars are average values based on the line-to-line scatter.

TYC 1172–486–1. The NLTE correction ranges from -0.18 to $+0.01$.

In Fig. 8 $[\text{Mg}/\text{Fe}]$ versus $[\text{Fe}/\text{H}]$ is shown (together with the $[\text{Ca}/\text{Fe}]$ ratios), the LTE investigation and after the application of the NLTE corrections. From the figure, it is well visible that after applying the NLTE correction the $[\text{Mg}/\text{Fe}]$ star-to-star scatter decreases and it is also clear that while in LTE $[\text{Mg}/\text{Fe}]$ are systematically larger than $[\text{Ca}/\text{Fe}]$, in NLTE the two α elements behave, as expected, very consistently.

We provide no Mg abundance for the Neo-Narval sample (see Section 2.2).

4.2.5 Silicon

A sample of Si I lines (from one to 15) allowed us to derive Si abundance for 18 stars in the SOPHIE sample. For the sample, we obtained: $\langle [\text{Si}/\text{Fe}] \rangle = 0.43 \pm 0.14$, with, as expected, the lowest value for the most metal-rich star (TYC 2299–342–1: $[\text{Si}/\text{Fe}] = 0.18$). The highest $[\text{Si}/\text{Fe}]$ value (HU Peg: $[\text{Si}/\text{Fe}] = 0.78$) is based on just one Si I line, and the other two stars with a relatively high $[\text{Si}/\text{Fe}]$ (TYC 1123–1454–1: $[\text{Si}/\text{Fe}] = 0.62 \pm 0.18$ on three lines; TYC 1205–397–1: $[\text{Si}/\text{Fe}] = 0.67 \pm 0.21$ on six lines) have the highest line-to-line scatter in the sample.

In the Neo-Narval sample, we could derive Si abundance for 12 stars by analysing from one to 11 lines. The $\langle [\text{Si}/\text{Fe}] \rangle = 0.48 \pm 0.14$ is consistent with the SOPHIE sample. Two stars show a high $[\text{Si}/\text{Fe}]$

ratio: TYC 2457–2294–1 with $[\text{Si}/\text{Fe}] = 0.79$ based on five lines and TYC 286–299–1 with $[\text{Si}/\text{Fe}] = 0.79$ based on one line.

4.2.6 Calcium

For all the stars in the SOPHIE sample we could derive the Ca abundance, by using from 13 to 25 lines. We derived a mean LTE abundance of: $\langle \text{Ca}/\text{Fe} \rangle = 0.34 \pm 0.08$ with a small line-to-line scatter (from 0.05 to 0.12 dex). Having a substantial sample of lines for the Ca investigation, we decided to exclude the Ca I lines: at 452.692 nm, because its upper level is not included in the model atom, and at 657.277 nm, because for this forbidden line the NLTE computations are not completely reliable. Without these two lines, we could base our investigation on a sample of 11 to 23 lines and derive an $A(\text{Ca})$ that is extremely close to what obtained without excluding these lines. The average line-to-line scatter improves, from 0.070 to 0.067 dex. The NLTE corrections range from -0.04 to $+0.15$.

For all the stars in the Neo-Narval sample, we could derive the Ca abundance by investigating from 4 to 18 lines and deriving $\langle \text{Ca}/\text{Fe} \rangle = 0.32 \pm 0.09$, very consistent with the SOPHIE sample. With $[\text{Ca}/\text{Fe}] < 0.2$, two stars (TYC 333–942–1 and *Gaia* DR3 1180300688463921792) are slightly poor in Ca, but the abundance determination is based on only four lines.

In Fig. 8, the $[\text{Ca}/\text{Fe}]$ ratios (in LTE and NLTE) versus $[\text{Fe}/\text{H}]$ are shown together with the $[\text{Mg}/\text{Fe}]$ ratios.

4.2.7 Titanium

For all the stars in the SOPHIE sample, we could derive the Ti abundance from both Ti I and Ti II lines.

To derive $A(\text{Ti})$ from Ti II lines, we used from 14 to 26 features. For the sample we obtained $\langle [\text{Ti}/\text{Fe}] \rangle = 0.38 \pm 0.11$ when Fe abundance is from Fe II lines. The line-to-line scatter in the $A(\text{Ti})$ determination is $\langle \sigma \rangle = 0.13 \pm 0.04$. The NLTE corrections for $A(\text{Ti})$ when derived from Ti II lines are small (never exceeding 0.03 dex in absolute value). We can then safely use the LTE investigation.

Titanium abundance from Ti I is very sensitive to NLTE effects (see Mashonkina, Sitnova & Pakhomov 2016b), we then decided to rely on the Ti II results for $A(\text{Ti})$.

4.2.8 Scandium

One Sc I line at 568.6 nm was used to derive Sc abundance for 10 stars in the SOPHIE sample, obtaining for the sample $\langle [\text{Sc}/\text{Fe}] \rangle = 0.12 \pm 0.08$. Nine stars of the 10 have an oversolar $[\text{Sc}/\text{Fe}]$ ratio.

For all the stars in the sample $A(\text{Sc})$ was derived from a set of Sc II lines (from one to seven) and we obtained $\langle [\text{Sc}/\text{Fe}] \rangle = 0.30 \pm 0.11$, with Fe abundance from Fe II lines in this case. The $[\text{Sc}/\text{Fe}]$ ratio is rather large, and this oversolar value is not justified by a large line-to-line scatter, that for Sc II is $\langle \sigma \rangle = 0.14 \pm 0.05$.

Sc I lines yield the lower $[\text{Sc}/\text{Fe}]$ ratios compared with those from the Sc II lines and this is due to the use of the LTE assumption. As shown by Zhang, Gehren & Zhao (2008), Sc I is subject to overionization in the solar atmosphere resulting in weakened lines and positive NLTE abundance corrections. For the Sc I at 568.6 nm, Zhang et al. (2008) computed $\Delta_{\text{NLTE}} = 0.14$ dex. As a rule, the departures from LTE grow towards lower surface gravity and lower metallicity. Therefore, Δ_{NLTE} for the 568.6 nm Sc I in our sample stars is expected to be positive and greater than 0.1 dex. Sc II is a majority species in the atmospheres of our sample stars, and the departures from LTE for Sc II lines are expected to be smaller. Using

the model atom of Sc II from Mashonkina & Romanovskaya (2022), we computed the NLTE abundance corrections for the Sc II lines investigated for all the stars and we verified that the NLTE corrections are small, with an average $|\Delta_{\text{NLTE}}| < 0.07$ dex for all stars.

4.2.9 Vanadium

From a sample of V I lines (from one to 19), we derived V abundances for all the SOPHIE stars in the sample. The $[\text{V}/\text{Fe}]$ ratio is close to solar for all ($\langle [\text{V}/\text{Fe}] \rangle = 0.04 \pm 0.16$) but one star (TYC 1172–486–1, $[\text{V}/\text{Fe}] = +0.60$ from one line). When removing this star for the sample, we derive: $\langle [\text{V}/\text{Fe}] \rangle = 0.01 \pm 0.09$ and the number of V I lines used is from four to 19.

4.2.10 Chromium

We investigated a sample of Cr I (from 8 to 19) and of Cr II (from 3 to 7) lines to derive the Cr abundances for all the SOPHIE stars. The average $[\text{Cr}/\text{Fe}]$ ratios are close to zero for both ionization ($\langle [\text{Cr}/\text{Fe}] \rangle$ of -0.08 ± 0.07 for neutral and 0.04 ± 0.09 for ionized Cr).

4.2.11 Manganese

A sample from two to 20 lines allowed us to derive Mn abundance for all the stars in the SOPHIE sample. The $[\text{Mn}/\text{Fe}]$ ratio is negative for all the stars ($\langle [\text{Mn}/\text{Fe}] \rangle = -0.28 \pm 0.07$). We could derive Mn abundance for 12 stars in the Neo-Narval sample using from one to eight Mn lines, with results in perfect agreement with the SOPHIE sample ($\langle [\text{Mn}/\text{Fe}] \rangle = -0.29 \pm 0.14$).

These undersolar ratios are compatible with the literature values and are due to strong NLTE effects (see Bergemann & Gehren 2008). Matas Pinto et al. (2022) investigated two stars of similar parameters and searched for the NLTE corrections computed by Bergemann & Gehren (2008), deriving an NLTE effect larger than $+0.3$ dex. With such a correction, the $[\text{Mn}/\text{Fe}]$ ratio of our stars would become around zero.

Looking at the results by Bergemann & Gehren (2008) for some of the lines we used, we have in fact an average NLTE correction of 0.40 dex, with the smallest values unsurprisingly for TYC 2299–342–1, which is the more metal-rich star in the sample, and the highest of about 0.5 dex for the most metal-poor stars (TYC 1125–548–1, TYC 1172–486–1, and TYC 1205–397–1).

4.2.12 Cobalt

For 19 stars of the SOPHIE sample, we could derive $A(\text{Co})$ by using a sample from three to 17 Co I lines. For the sample we derived $\langle [\text{Co}/\text{Fe}] \rangle = 0.11 \pm 0.06$, slightly oversolar, but, taking into account the uncertainties ($\langle \sigma \rangle = 0.13 \pm 0.04$), compatible with zero. An NLTE correction for these stars derived by Bergemann, Pickering & Gehren (2010) would be in the range $+0.3$ to $+0.4$ dex, bringing the $[\text{Co}/\text{Fe}]$ ratios oversolar. According to Bergemann et al. (2010), taking into account the lines we used with available NLTE corrections, for our stars the corrections are in the range $+0.16$ to $+0.64$ with $+0.38$ as the average value.

4.2.13 Nickel

All the SOPHIE stellar spectra have a good sample of Ni I lines (from 17 to 57) that allowed us to derive $A(\text{Ni})$. For all the stars in the sample the $[\text{Ni}/\text{Fe}]$ ratio is close to zero ($\langle [\text{Ni}/\text{Fe}] \rangle = -0.02 \pm 0.05$).

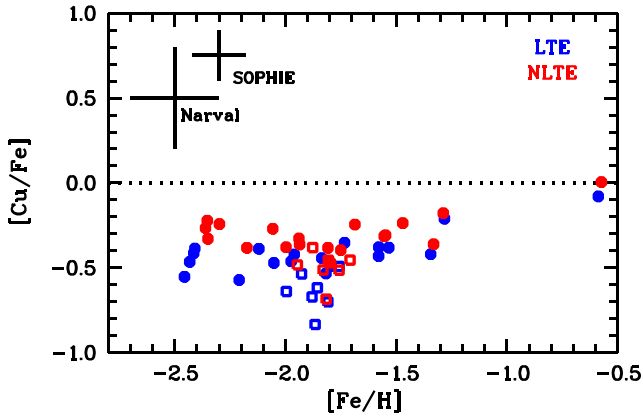


Figure 9. $[\text{Cu}/\text{Fe}]$ versus $[\text{Fe}/\text{H}]$, filled circles the SOPHIE sample and open squares the Neo-Narval. The uncertainties represent the average line-to-line scatter, except for Cu in the Neo-Narval stars, where it is derived from the Cayrel formula added in quadrature with the line-to-line scatter in Fe.

In the Neo-Narval sample, we derived Ni abundance for 14 stars, with $\langle [\text{Ni}/\text{Fe}] \rangle = -0.03 \pm 0.08$, perfectly consistent with the SOPHIE sample.

4.2.14 Copper

The Cu investigation is based on four Cu I lines at 510.5, 521.8, 570.0, and 578.2 nm. For all the stars except one in the SOPHIE sample, we could derive the Cu abundance using from one to four lines. For the sample, we derived: $\langle [\text{Cu}/\text{Fe}] \rangle = -0.41 \pm 0.11$, a very small star-to-star scatter, which reduces even more, to 0.08, if we remove the most metal-rich star (TYC 2299–342–1, with $[\text{Cu}/\text{Fe}] = -0.08$). If we remove also the next most Cu-rich star (TYC 2270–1021–1, with $[\text{Cu}/\text{Fe}] = -0.21$), we obtain a star-to-star scatter of 0.06. Only in seven stars in the Neo-Narval sample could we derive the Cu abundance using the 578.2 nm line and, for two stars, also the line at 570.0 nm, providing $\langle [\text{Cu}/\text{Fe}] \rangle = -0.62 \pm 0.11$. In Fig. 9, the results are shown.

The underabundance of Cu with respect to Fe of all the stars investigated is surely related to NLTE effects on Cu. In fact, Cu I is subject to overionisation in the range of stellar parameters of the stars here investigated. For the stars whose $A(\text{Cu})$ is based on more than one line, the line-to-line scatter is small (in the range 0.03 to 0.12 dex). The 510.5, 570.0, and 578.2 nm lines belong to the same multiplet, so we expect not too different NLTE corrections for these three lines. The 521.8 nm line arises from the higher excitation level ($E_{\text{exc}} = 3.82$ eV) compared with that of the first three lines ($E_{\text{exc}} = 1.39$ – 1.64 eV). For dwarf stars with $[\text{Fe}/\text{H}] \simeq -1.5$, Yan et al. (2016) obtain slightly smaller NLTE corrections for 521.8 nm compared with that for 510.5 nm. Thus, we do not expect an increase in the line-to-line scatter in NLTE.

Shi et al. (2018) investigated the NLTE effects on the 510.5 nm Cu I line for two metal-poor set of parameters ($T_{\text{eff}}/\log g/[\text{Fe}/\text{H}]$ of 4600/1.60/–2.50 and 4600/1.32/–2.63, respectively) and derived NLTE–LTE of +0.30 and +0.40 dex, respectively. Our stars bracket in parameters the cases investigated by Shi et al. (2018), we can then expect NLTE corrections of this order of magnitude.

From the same 510.5 nm Cu I line, Andrievsky et al. (2018) derived an NLTE correction of about +0.3 dex for HD 9051 (4925/1.95/–1.78) and about +0.7 dex for HD 122563 (4600/1.10/–2.82). The larger NLTE correction by Andrievsky et al. (2018) with respect to Shi et al. (2018) could be due to a smaller $\log g$ and/or

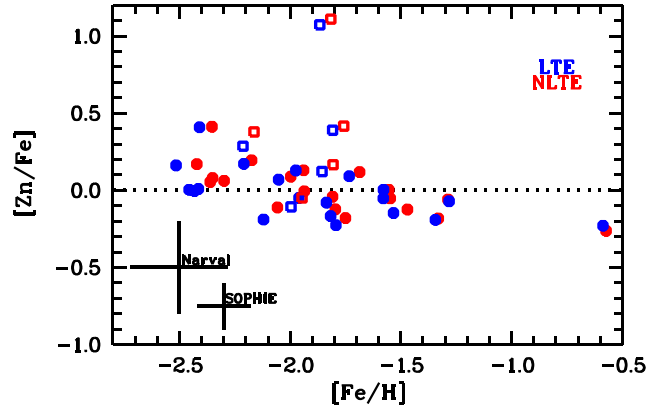


Figure 10. $[\text{Zn}/\text{Fe}]$ versus $[\text{Fe}/\text{H}]$, filled circles the SOPHIE stars and open squares the Neo-Narval ones. The uncertainties are derived as for Cu.

smaller $[\text{Fe}/\text{H}]$ of the stars by Andrievsky et al. (2018), or some differences in the Cu model atom.

To make our own mind on the NLTE effects on the Cu I lines, we produced a new model atom of Cu I–Cu II (Sitnova, in preparation) to take into account the NLTE corrections. The model includes 59 levels of Cu I, 20 levels of Cu II, and the ground state of Cu III. The list of energy levels and transitions is taken from R. Kurucz webpage.¹ For the majority of levels, the fine structure is taken into account. The high-excitation levels of Cu I are combined in four super-levels according to their parity. For Cu I, we use photoionization cross-sections from Liu et al. (2014) calculated with the R-matrix method. For Cu II, we calculate hydrogen-like cross-sections. We employ data for inelastic collisions with hydrogen atoms from Belyaev, Yakovleva & Kraemer (2021). Electron-impact excitation rates are calculated with the van Regemorter (1962) and Woolley & Allen (1948) formulae, for radiatively allowed and forbidden transitions, respectively. Electron impact ionization is calculated with the Seaton (1962) formula. Using new data for Cu + H collisions leads to smaller non-LTE corrections.

As it can be appreciated from the figure, the NLTE corrections result in a smaller star-to-star scatter at any metallicity. The general trend at low metallicities is still flat, like in LTE, but the mean value is slightly higher by about 0.1 dex.

4.2.15 Zinc

For all stars in the SOPHIE sample we could derive $A(\text{Zn})$ by using from one to two Zn I lines (472.215 and 481.052 nm). For the sample we derive: $\langle [\text{Zn}/\text{Fe}] \rangle = -0.02 \pm 0.16$. For six of the Neo-Narval stars, we could derive $A(\text{Zn})$, with $\langle [\text{Zn}/\text{Fe}] \rangle = 0.19 \pm 0.47$.

The NLTE correction is not negligible and ranges from –0.02 to +0.18. In Fig. 10, the effects of NLTE are shown by comparing the LTE and NLTE results.

One of the stars observed with Neo-Narval, TYC 891–750–1, displays a very high $[\text{Zn}/\text{Fe}] \sim 1.1$. This value is even higher than the two Zn-rich stars highlighted by Lombardo et al. (2022): HE 2252–4335 and CS 30312–100. Unfortunately, we do not have an Ni measurement for this star. Lombardo et al. (2022) highlighted the existence of two branches in the $[\text{Ni}/\text{Fe}]$ – $[\text{Zn}/\text{Fe}]$ plane (see fig. 8 of Lombardo et al. 2022). One branch with high $[\text{Zn}/\text{Fe}]$ that Lombardo et al. (2022) suggested as formed from gas polluted by hypernovae

¹<http://kurucz.harvard.edu/atoms.html>

(see e.g. Nomoto, Kobayashi & Tominaga 2013) and a branch with lower $[Zn/Fe]$ that they suggested as formed from gas polluted by normal supernovae.

4.2.16 Yttrium

The Y abundances have been derived from 7 to 12 Y II lines in all the stars in the SOPHIE sample. For the stellar sample, we derived $\langle [Y/Fe] \rangle = -0.14 \pm 0.12$.

4.2.17 Zirconium

For 12 stars in the SOPHIE sample, we could derive $A(Zr)$ from one Zr I line at 473.948 nm. For the 12 stars we derived: $\langle [Zr/Fe] \rangle = -0.03 \pm 0.21$. The NLTE correction is positive and large, ranging from +0.39 to +0.77.

One to two Zr II lines (at 461.394 and 511.227 nm) allowed us to derive $A(Zr)$ for 16 stars in the Neo-Narval sample, that provides $\langle [Zr/Fe] \rangle = 0.62 \pm 0.24$. Taking into account the NLTE corrections, this provides $\langle Zr/Fe \rangle = 0.55 \pm 0.21$.

5 DISCUSSION

For all the investigated elements, except marginally Sc II, the abundances derived for these stars are compatible with the literature samples of stars with comparable parameters that we looked at (Fulbright 2000; Gratton et al. 2000; Ishigaki, Chiba & Aoki 2012; Ishigaki, Aoki & Chiba 2013) (see Appendix C).

The stars are classical metal-poor stars, enhanced in α elements. One star, TYC 1172–486–1, stands out for the high $[V/Fe] = 0.60 \pm 0.19$ ratio. The star TYC 1205–397–1 has the largest $[Zn/Fe]$ and $[Zr/Fe]$ ratios in the sample ($[Zn/Fe] = +0.41 \pm 0.11$ and $[Zr/Fe] = +0.50 \pm 0.15$). In the Neo-Narval sample, two stars (TYC 333–942–1 and *Gaia* DR3 1180300688463921792) seem low in Ca, but both stars have poor-quality spectra. One star in the Neo-Narval sample, TYC 891–750–1, shows a high $[Zn/Fe]$ ratio ($[Zn/Fe] = 1.05 \pm 0.25$), while TYC 914–128–1 shows the lowest $[Zn/Fe]$ ratio ($[Zn/Fe] = -0.31 \pm 0.26$).

We selected the 19 SOPHIE stars more metal-poor than $[Fe/H] < -1.0$ and we investigated the star-to-star scatter of the element-to-iron ratios. We found that they are generally well below 0.10 dex (0.07 dex for Ca and Cr II, 0.08 dex for Mg, 0.10 dex for Ti II, 0.04 dex for Ni, 0.06 dex for Co and Cr I). For Zn instead the star-to-star scatter is 0.16 dex. Even removing the ‘high Zn’ star TYC 1205–397–1 the star to star scatter remains larger than for the other elements (0.12 dex). The mean error on Zn is 0.07 dex, thus this extra scatter cannot be due to larger errors on the Zn abundances. To further investigate the scatter in Zn we divided the sample into two subsamples: $-2 \leq [Fe/H] < -1$ (11 stars) and $[Fe/H] < -2$ (8 stars). In this case, the star-to-star scatter is 0.11 and 0.17 dex, respectively. If we exclude from the most metal-poor sample TYC 1205–397–1 (7 stars), the stars-to-star scatter is 0.12 dex. An increase in the scatter of Zn, with respect to other elements, could be explained if a fraction of our stars were low-mass long-lived stars formed in an environment predominantly enriched by a PISN (>50 per cent of the total amounts of metals), but also by subsequent generation of ‘normal’ Pop II SNe (Salvadori et al. 2019). In fig. 7 of Salvadori et al. (2019, right-hand panel), when normal SNI contribute to pollute the ISM at a 50 per cent level, there is a double peak in the zinc-to-iron value, the highest being at $[Zn/Fe] \approx -0.3$. In Fig. 11, we have assembled some literature values for $[Zn/Fe]$, the extremely

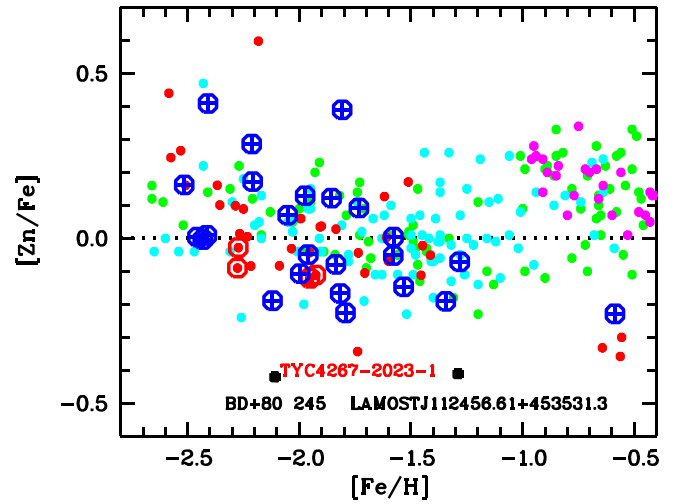


Figure 11. $[Zn/Fe]$ versus $[Fe/H]$: from this analysis (blue crossed circles); the MINCE project (Cescutti et al. 2022, red filled circles and the two stars with two independent spectra are surrounded by an open red circle); from Mishenina et al. (2002, green circles); from Mishenina et al. (2011, pink circles); from Ishigaki et al. (2013, light blue circles); the Zn-poor stars BD+80 245 by Ivans et al. (2003) and LAMOSTJ112456.61+453531.3 by Xing et al. (2019) (black squares).

low $[Zn/Fe]$ of BD+80 245, LAMOSTJ112456.61+453531.3 and TYC 4267–2023–1 clearly stand out. It is interesting to concentrate on the stars in our sample around $[Zn/Fe] = -0.3$: as discussed above, they are consistent with being formed from ≤ 50 per cent of PISN and the rest of SNI polluted gas.

The fact that there is a continuity in the $[Zn/Fe]$ ratio, from solar to about -0.4 , could be related to the fraction of the PISN contribution to the gas from where the star formed. This is not obviously the case for Cu whose star-to-star scatter (0.08 dex) is similar to the values derived for the other elements. But the relatively high star-to-star scatter for Zn could be simply related to the fact that there is a known correlation $[Zn/Fe]$ versus $[Fe/H]$ (99 per cent confidence for the SOPHIE sample) and this dependence increases the star-to-star scatter. This was pointed out in other samples of metal-poor stars (see e.g. Lombardo et al. 2022).

The likely PISN descendent BD+80 245 (see Fig. 11), analysed by Ivans et al. (2003, $T_{\text{eff}}/\log g$ of 5225/3.0) and Roederer et al. (2014, 5360/3.15), has been already discussed by Salvadori et al. (2019). We investigated in our sample if we could find other stars likely descendent from PISN, by comparing the observed stellar chemical pattern with those theoretically derived by Salvadori et al. (2019) for a gaseous environment predominantly enriched by PISNe (>50 per cent of metals in the gas). The χ^2 methodology is described in section 5.2 from Salvadori et al. (2019) and it will be further detailed in Aguado et al. (in preparation). In brief: we built a grid of theoretical predictions from Salvadori et al. (2019) including mass of Pop III, percentage of Pop III, and f_*/f_{dil} (with f_* the star formation efficiency and f_{dil} the effectively fraction of metals injected into the interstellar medium and of the gas used to dilute them (see Salvadori et al. 2019, for details) as free parameters. Then we use the FERRE code to interpolate between the nodes of the grid, calculate the best set of PISN parameters, and provide the best model (a set of elemental abundances from C to Zn) according to these parameters.

In our sample, three candidates (the Halo TYC 1118–595–1, the two GSE TYC 1194–507–1, and TYC 2207–992–1) seem to be

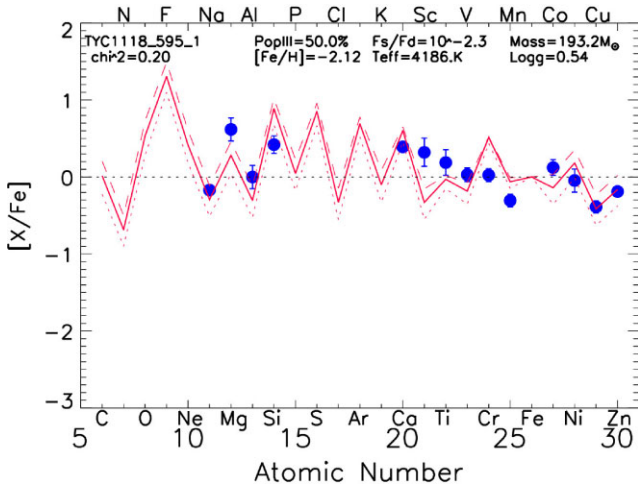


Figure 12. Comparison of the chemical abundances derived for TYC 1118–595–1 (blue dots) compared to the PISN model best fit (red line) with the following parameters $f_{\text{PISN}} = 50$ per cent; $f_* / f_{\text{dil}} = 10^{-2.3}$; and $m_{\text{PISN}} = 193.2 M_{\odot}$. For reference, we also show a model with same parameters but higher PISN contribution $f_{\text{PISN}} = 65$ per cent (red dotted line) and with different PISN mass $m_{\text{PISN}} = 208 M_{\odot}$. Main stellar parameters are also shown.

interesting. When compared to the theoretical models the stars are compatible as being formed from:

- (i) TYC 1118–595–1 a gas enriched 50 per cent by a PISN of initial mass of almost $200 M_{\odot}$, with a high probability ($\chi^2_{\text{PISN}} = 0.20$, see Fig. 12);
- (ii) TYC 2207–992–1 a gas mostly (83 per cent) enriched by an almost $170 M_{\odot}$, with a quite high probability ($\chi^2_{\text{PISN}} = 0.38$);
- (iii) TYC 1194–507–1 also a gas mostly (90 per cent) enriched by an almost $170 M_{\odot}$, but with a lower probability ($\chi^2_{\text{PISN}} = 0.50$) than the previous star.

Here, $\chi^2_{\text{PISN}} = \chi^2 / (N - M)$ where N is the number of fitted abundances and M is the number of free parameters in the model. Unfortunately, we could not get any information on nitrogen abundance because in the range of the CN band (at about 388 nm) the S/N was really low. Anyway, all these stars are mixed, and part of carbon has been converted into nitrogen. We stress that we do not claim that these chemical patterns can only be formed if the original gas is partially polluted by PISNs. There may be other, probably more contrived ways, to explain them. What is important is that we have employed the full chemical pattern of these stars and did not rely uniquely on few elements (Aguado et al., in preparation). This sample is certainly very small, but it is remarkable that we have found three stars that could have been formed by PISN polluted material. Once a much larger sample of Zn abundances in metal-poor stars shall be available, for example from the 4MOST Milky Way Halo High-Resolution Survey (Christlieb et al. 2019), the fraction of these possible PISN descendants will strongly constrain the number of PISNs that polluted the early Galaxy.

In Fig. 12, we show the observed and best-fitting abundance pattern for TYC 1118–595–1. For the lighter elements, we clearly see an odd-even effect, as expected from the PISN nucleosynthesis as well as for the Ni-Cu-Zn sequence. We attribute deviations from a strict odd-even effect to the fact that we are not seeing ‘pure’ PISN ejecta, but material that has also been mixed with SNIi polluted material, thus weakening the odd-even effect. An odd-even effect at this level is also predicted by some core-collapse SNe models (e.g. Tominaga,

Umeda & Nomoto 2007), thus the detected odd-even effect, by itself, cannot discriminate between diluted PISN ejecta and core-collapse SNe ejecta.

A complete and systematic investigation on the probability and characteristic on the stellar formation from a gas enriched by a PISN is presented by Aguado et al. (in preparation).

6 CONCLUSIONS

The Pristine photometry, coupled with *Gaia* parallaxes and photometry, proved to be extremely effective in selecting stars of metallicity around -2.0 (77 per cent success for the SOPHIE sample and 100 per cent success for the Neo-Narval sample).

This outstanding efficiency in selecting metal-poor stars allowed us to investigate a sample of 36 bright giant stars for which we derived detailed chemical abundances using small-size telescopes. The main goal of this investigation was to increase the statistics of Cu and Zn measurements in this poorly examined metallicity regime to look for possible PISN descendants. The frequency of stars like BD+80245 (Salvadori et al. 2019), will provide us information on the high-mass end of the primordial initial mass function ($140 M_{\odot} < M_{\text{PopIII}} < 260 M_{\odot}$), which is populated by the stellar progenitors of energetic PISNe. Three stars in the sample (TYC 1118–595–1, TYC 2207–992–1, and TYC 1194–507–1) are possible PISN descendants. Clearly the number of stars investigated in the present paper is too small to derive conclusions. The WEAVE (Dalton et al. 2020) survey at high resolution could provide a large sample of Cu and Zn measurements in metal-poor stars. If the green grating, covering the wavelength range 473 nm to 545 nm, is used, we will be able to measure the Zn I 481.0 nm and the Cu I 510.5 nm lines for all the metal-poor Pristine targets, which shall be available to WEAVE.

The kinematics of our sample confirms the existence of metal-poor star on disc orbits (17 per cent of the sample), and even on thin disc orbits (8 per cent of the sample). Four stars belong to the GSE structure, one more (TYC 11159–895–1, $[\text{Fe}/\text{H}] = -1.97$) is on the border. Given the variety of ways in which the GSE structure has been defined in different kinematical spaces, in the literature we may consider also this star a likely member of GSE. So in a chemically selected sample, spanning the metallicity range $-2.6 \leq [\text{Fe}/\text{H}] \leq -1.3$ we have from 11 to 14 per cent of stars belonging to GSE and 17 per cent belonging to the disc (thin and thick). This leaves us with about 70 per cent of the stars that are something else, likely: stars formed in the disc and scattered into halo orbits; stars that were formed in other galaxies or stellar clusters and accreted by the Milky Way; and, possibly, stars formed ‘*in situ*’ in the Milky Way Halo. To determine if any fraction of the Halo was indeed formed ‘*in situ*’, it is very important to understand the formation of the Milky Way. To form stars ‘*in situ*’, the Halo must have had a gas component, with overdensities large enough to start the star formation process at least in some places. At present we cannot confirm, nor refute the existence of this ‘*in situ*’ component. Again, the WEAVE–Pristine sample shall provide a large sample of stars to study correlations between kinematical and chemical properties, from which the present results on the fractions of metal-poor stars belonging to the different Galactic components shall be more robustly confirmed, or refuted.

ACKNOWLEDGEMENTS

We are grateful to Arturo Lopez Ariste and Philippe Mathias of the Observatoire Midi Pyrénées for their help in dealing with the Neo-Narval data and for the great improvements in the Neo-Narval DRS

and for reprocessing all the spectra with the improved version. We are grateful to the CNRS Institut National des Sciences de l'Univers - Programme National de Cosmologie et Galaxies for allocating to our project time on the 1.93-m telescope at Observatoire de Haute Provence and on the 2-m T el escope Bernard Lyot at the Observatoire du Pic du Midi. We gratefully acknowledge support from the French National Research Agency (ANR) funded project 'Pristine' (ANR-18-CE31-0017). SS and AD acknowledge funding from the European Research Council (ERC) under the European Union's Horizon 2020 research and innovation programme (grant agreement no. 804240). JIGH acknowledges financial support from the Spanish Ministry of Science and Innovation (MICINN) project PID2020-117493GB-I00. TS acknowledges support from the MK project, grant 5127.2022.1.2. EFA acknowledge support from the Agencia Estatal de Investigaci n del Ministerio de Ciencia e Innovaci n (AEI-MCINN) under grant 'At the forefront of Galactic Archaeology: evolution of the luminous and dark matter components of the Milky Way and Local Group dwarf galaxies in the *Gaia* era' with reference PID2020-118778GB-I00/10.13039/501100011033. EFA also acknowledges support from the 'Mar a Zambrano' fellowship from the Universidad de La Laguna. This work presents results from the European Space Agency (ESA) space mission *Gaia*. *Gaia* data are being processed by the *Gaia* Data Processing and Analysis Consortium (DPAC). Funding for the DPAC is provided by national institutions, in particular the institutions participating in the *Gaia* MultiLateral Agreement (MLA). The *Gaia* mission website is <https://www.cosmos.esa.int/gaia>. The *Gaia* archive website is <https://archives.esac.esa.int/gaia>.

This is based on observation obtained at Observatoire de Haute-Provence in programme 21B.PNGC.MATA and at Observatoire du Pic de Midi under programme L212N07.

DATA AVAILABILITY

The abundances derived in the present analysis are provided in machine readable format at the Centre de Donn es astronomiques de Strasbourg. The SOPHIE spectra are available from the SOPHIE archive <http://atlas.obs-hp.fr/sophie/>. The Neo-Narval archive is not yet operational, until then, the DRS reduced spectra are available on request directly from P. Bonifacio (Piercarlo.Bonifacio@observatoiredeparis.psl.eu).

REFERENCES

Aguado D. S. et al., 2019, *MNRAS*, 490, 2241
 Alam S. et al., 2015, *ApJS*, 219, 12
 Alexeeva S., Pakhomov Y., Mashonkina L., 2014, *Astron. Lett.*, 40, 406
 Andrievsky S., Bonifacio P., Caffau E., Korotin S., Spite M., Spite F., Sbordone L., Zhukova A. V., 2018, *MNRAS*, 473, 3377
 Belokurov V., Erkal D., Evans N. W., Koposov S. E., Deason A. J., 2018, *MNRAS*, 478, 611
 Belyaev A. K., Yakovleva S. A., Kraemer W. P., 2021, *MNRAS*, 501, 4968
 Bennett M., Bovy J., 2019, *MNRAS*, 482, 1417
 Bergemann M., Gehren T., 2008, *A&A*, 492, 823
 Bergemann M., Pickering J. C., Gehren T., 2010, *MNRAS*, 401, 1334
 Bihain G., Israelian G., Rebolo R., Bonifacio P., Molaro P., 2004, *A&A*, 423, 777
 Binney J., 2012, *MNRAS*, 426, 1328
 Bisterzo S., Gallino R., Pignatari M., Pompeia L., Cunha K., Smith V., 2004, *Mem. Soc. Astron. Ital.*, 75, 741
 Bisterzo S., Pompeia L., Gallino R., Pignatari M., Cunha K., Heger A., Smith V., 2005, *Nucl. Phys. A*, 758, 284
 Bonifacio P., Monai S., Beers T. C., 2000, *AJ*, 120, 2065

Bonifacio P. et al., 2019, *MNRAS*, 487, 3797
 Bonifacio P. et al., 2021, *A&A*, 651, A79
 Bouchy F., Sophie Team, 2006, in Arnold L., Bouchy F., Moutou C., eds, Tenth Anniversary of 51 Peg-b: Status of and Prospects for Hot Jupiter Studies. Published by Frontier Group, Paris, p. 319
 Bovy J., 2015, *ApJS*, 216, 29
 Bressan A., Marigo P., Girardi L., Salasnich B., Dal Cero C., Rubele S., Nanni A., 2012, *MNRAS*, 427, 127
 Butler K., 1984, PhD thesis, University of London
 Caffau E., Ludwig H. G., Steffen M., Freytag B., Bonifacio P., 2011, *Sol. Phys.*, 268, 255
 Carney B. W., Latham D. W., Stefanik R. P., Laird J. B., Morse J. A., 2003, *AJ*, 125, 293
 Cescutti G. et al., 2022, preprint ([arXiv:2211.06086](https://arxiv.org/abs/2211.06086))
 Christlieb N. et al., 2019, *The Messenger*, 175, 26
 Dalton G. et al., 2020, in Evans C. J., Bryant J. J., Motohara K., eds, Proc. SPIE Conf. Ser. Vol. 11447, Ground-Based and Airborne Instrumentation for Astronomy VIII. SPIE, Bellingham, p. 1144714
 de Bressan A., Salvadori S., Schneider R., Valiante R., Omukai K., 2017, *MNRAS*, 465, 926
 Delgado Mena E., Tsantaki M., Adibekyan V. Z., Sousa S. G., Santos N. C., Gonz lez Hern andez J. I., Israelian G., 2017, *A&A*, 606, A94
 Duffau S. et al., 2017, *A&A*, 604, A128
 Feuillet D. K., Feltzing S., Sahlholdt C. L., Casagrande L., 2020, *MNRAS*, 497, 109
 Fulbright J. P., 2000, *AJ*, 120, 1841
 Gaia Collaboration, 2021, *A&A*, 649, A1
 Giddings J., 1981, PhD thesis, University of London
 Gonz lez Hern andez J. I., Bonifacio P., 2009, *A&A*, 497, 497
 Gratton R. G., Sneden C., Carretta E., Bragaglia A., 2000, *A&A*, 354, 169
 Gravity Collaboration, 2020, *A&A*, 636, L5
 Haywood M., Di Matteo P., Lehnert M. D., Snaith O., Khoperskov S., G mez A., 2018, *ApJ*, 863, 113
 Helmi A., Babusiaux C., Koppelman H. H., Massari D., Veljanoski J., Brown A. G. A., 2018, *Nature*, 563, 85
 Henden A. A., Levine S. E., Terrell D., Smith T. C., Welch D., 2012, *J. Am. Assoc. Var. Star Obs.*, 40, 430
 Hirai Y., Saitoh T. R., Ishimaru Y., Wanajo S., 2018, *ApJ*, 855, 63
 Ishigaki M. N., Chiba M., Aoki W., 2012, *ApJ*, 753, 64
 Ishigaki M. N., Aoki W., Chiba M., 2013, *ApJ*, 771, 67
 Ivans I. I., Sneden C., James C. R., Preston G. W., Fulbright J. P., H fflich P. A., Carney B. W., Wheeler J. C., 2003, *ApJ*, 592, 906
 Kordopatis G. et al., 2022, preprint ([arXiv:2206.07937](https://arxiv.org/abs/2206.07937))
 Kratz K. L., Farouqi K., Mashonkina L. I., Pfeiffer B., 2008, *New Astron. Rev.*, 52, 390
 Lindegren L. et al., 2021, *A&A*, 649, A4
 Liu Y. P., Gao C., Zeng J. L., Yuan J. M., Shi J. R., 2014, *ApJS*, 211, 30
 Lodders K., 2019, preprint ([arXiv:1912.00844](https://arxiv.org/abs/1912.00844))
 Lodders K., Palme H., Gail H. P., 2009, *Landolt B rnstein*, 4B, 712
 Lombardo L. et al., 2021, *A&A*, 656, A155
 Lombardo L. et al., 2022, *A&A*, 665, A10
 McMillan P. J., 2017, *MNRAS*, 465, 76
 Marigo P. et al., 2017, *ApJ*, 835, 77
 Mashonkina L., 2013, *A&A*, 550, A28
 Mashonkina L., 2020, *MNRAS*, 493, 6095
 Mashonkina L., Romanovskaya A., 2022, *Astron. Lett.*, 48, 577
 Mashonkina L., Gehren T., Shi J.-R., Korn A. J., Grupp F., 2011, *A&A*, 528, A87
 Mashonkina L., Belyaev A. K., Shi J.-R., 2016a, *Astron. Lett.*, 42, 366
 Mashonkina L. I., Sitnova T. N., Pakhomov Y. V., 2016b, *Astron. Lett.*, 42, 606
 Mashonkina L., Jablonka P., Pakhomov Y., Sitnova T., North P., 2017a, *A&A*, 604, A129
 Mashonkina L., Sitnova T., Belyaev A. K., 2017b, *A&A*, 605, A53
 Matas Pinto A. d. M. et al., 2022, *Astron. Nachr.*, 343, e210032
 Mishenina T. V., Kovtyukh V. V., Soubiran C., Travaglio C., Busso M., 2002, *A&A*, 396, 189

- Mishenina T. V., Gorbaneva T. I., Basak N. Y., Soubiran C., Kovtyukh V. V., 2011, *Astron. Rep.*, 55, 689
- Mishenina T., Kovtyukh V., Soubiran C., Adibekyan V. Z., 2016, *MNRAS*, 462, 1563
- Mucciarelli A., Bellazzini M., Massari D., 2021, *A&A*, 653, A90
- Naidu R. P., Conroy C., Bonaca A., Johnson B. D., Ting Y.-S., Caldwell N., Zaritsky D., Cargile P. A., 2020, *ApJ*, 901, 48
- Nomoto K., Kobayashi C., Tominaga N., 2013, *ARA&A*, 51, 457
- Pignatari M., Gallino R., Heil M., Wiescher M., Käppeler F., Herwig F., Bisterzo S., 2010, *ApJ*, 710, 1557
- Reid M. J., Brunthaler A., 2020, *ApJ*, 892, 39
- Roederer I. U., Barklem P. S., 2018, *ApJ*, 857, 2
- Roederer I. U., Preston G. W., Thompson I. B., Shectman S. A., Sneden C., Burley G. S., Kelson D. D., 2014, *AJ*, 147, 136
- Romano D., Matteucci F., 2007, *MNRAS*, 378, L59
- Romano D., Karakas A. I., Tosi M., Matteucci F., 2010, *A&A*, 522, A32
- Rossi M., Salvadori S., Skúladóttir Á., 2021, *MNRAS*, 503, 6026
- Sakhibullin N. A., 1983, *Tr. Kazanskaia Gorodkoj Astron. Obs.*, 48, 9
- Salvadori S., Bonifacio P., Caffau E., Korotin S., Andreevsky S., Spite M., Skúladóttir Á., 2019, *MNRAS*, 487, 4261
- Sanders J. L., Binney J., 2016, *MNRAS*, 457, 2107
- Sbordone L., Caffau E., Bonifacio P., Duffau S., 2014, *A&A*, 564, A109
- Schlegel D. J., Finkbeiner D. P., Davis M., 1998, *ApJ*, 500, 525
- Seaton M. J., 1962, in Bates D. R., ed., *Atomic and Molecular Processes*. Academic Press, New York, p. 375
- Shi J. R., Yan H. L., Zhou Z. M., Zhao G., 2018, *ApJ*, 862, 71
- Sitnova T. M., Mashonkina L. I., Ryabchikova T. A., 2016, *MNRAS*, 461, 1000
- Sitnova T. M., Yakovleva S. A., Belyaev A. K., Mashonkina L. I., 2022, *MNRAS*, 515, 1510
- Skrutskie M. F. et al., 2006, *AJ*, 131, 1163
- Starkenburger E. et al., 2017, *MNRAS*, 471, 2587
- Tominaga N., Umeda H., Nomoto K., 2007, *ApJ*, 660, 516
- van Regemorter H., 1962, *ApJ*, 136, 906
- Velichko A. B., Mashonkina L. I., Nilsson H., 2010, *Astron. Lett.*, 36, 664
- Woolley R. D. V. R., Allen C. W., 1948, *MNRAS*, 108, 292
- Woosley S. E., Heger A., Weaver T. A., 2002, *Rev. Mod. Phys.*, 74, 1015
- Xing Q.-F., Zhao G., Aoki W., Honda S., Li H.-N., Ishigaki M. N., Matsuno T., 2019, *Nat. Astron.*, 3, 631
- Yan H. L., Shi J. R., Zhao G., 2015, *ApJ*, 802, 36
- Yan H. L., Shi J. R., Nissen P. E., Zhao G., 2016, *A&A*, 585, A102
- York D. G. et al., 2000, *AJ*, 120, 1579

- Zhang H. W., Gehren T., Zhao G., 2008, *A&A*, 481, 489
- Zhang B., Liu C., Deng L.-C., 2020, *ApJS*, 246, 9

APPENDIX A: ABUNDANCES

Two online tables provide the stellar parameters and the detailed chemical abundances. For each set of data a table is provided because the delivered abundances are not the same for the two sets of data.

For both samples we provide: the name of the star, the stellar parameters (T_{eff} , $\log g$, ξ), and for each element X: the abundance $A(X)$, the line-to-line scatter, and the number of lines. In the case, the abundance is based on one single line, the σ provided is the highest among the other elements.

For the SOPHIE sample, the abundances provided are for: Fe (from Fe I lines), Na, Mg, Al, Si, Ca, Sc (from Sc I and Sc II lines), Ti (from Ti I and Ti II lines), V, Cr (from Cr I and Cr II lines), Mn, Fe (from Fe I and Fe II lines), Co, Ni, Cu, Zn, Sr, Y, Zr (from Zr I and Zr II lines), Ba, in this order. The abundance from Fe I lines is repeated to be close to the stellar parameters and then next to the values relative to the Fe II lines. For the Neo-Narval sample, the abundances provided are for: Fe, Na, Si, Ca, Mn, Ni, Cu, and Zn, in this order. No detection for the element X provide an empty space in the table in the column $A(X)$, 0.000 in the line-to-line scatter and 0 for number of lines.

APPENDIX B: LINES USED FOR THE CHEMICAL INVESTIGATION

The online table available at the CDS contains, for the lines used, for each element, for each star, the oscillator strength and the lower energy (in cm^{-1}).

APPENDIX C: PLOT WITH THE ABUNDANCES

We here provide the plots (see Figs C1 and C2) of the abundances derived, compared to the literature results. In Table C1, the Pristine names for all stars analysed are provided.

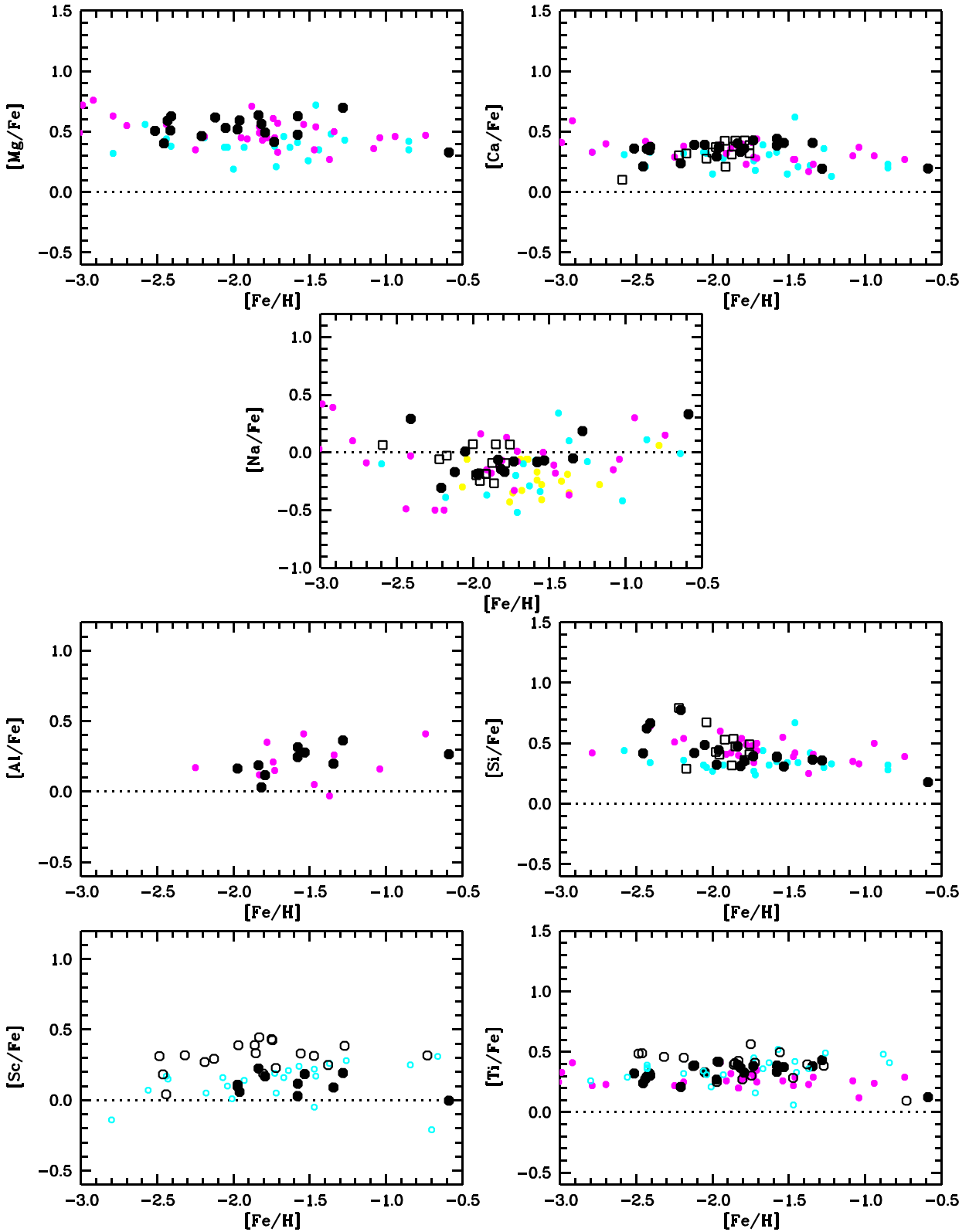


Figure C1. Abundances. Reference samples: yellow: Gratton et al. (2000); violet: Fulbright (2000); light blue: Ishigaki et al. (2012, 2013). Open symbols for the Sc and Ti panels refer to abundances from ionized Sc, Ti and Fe.

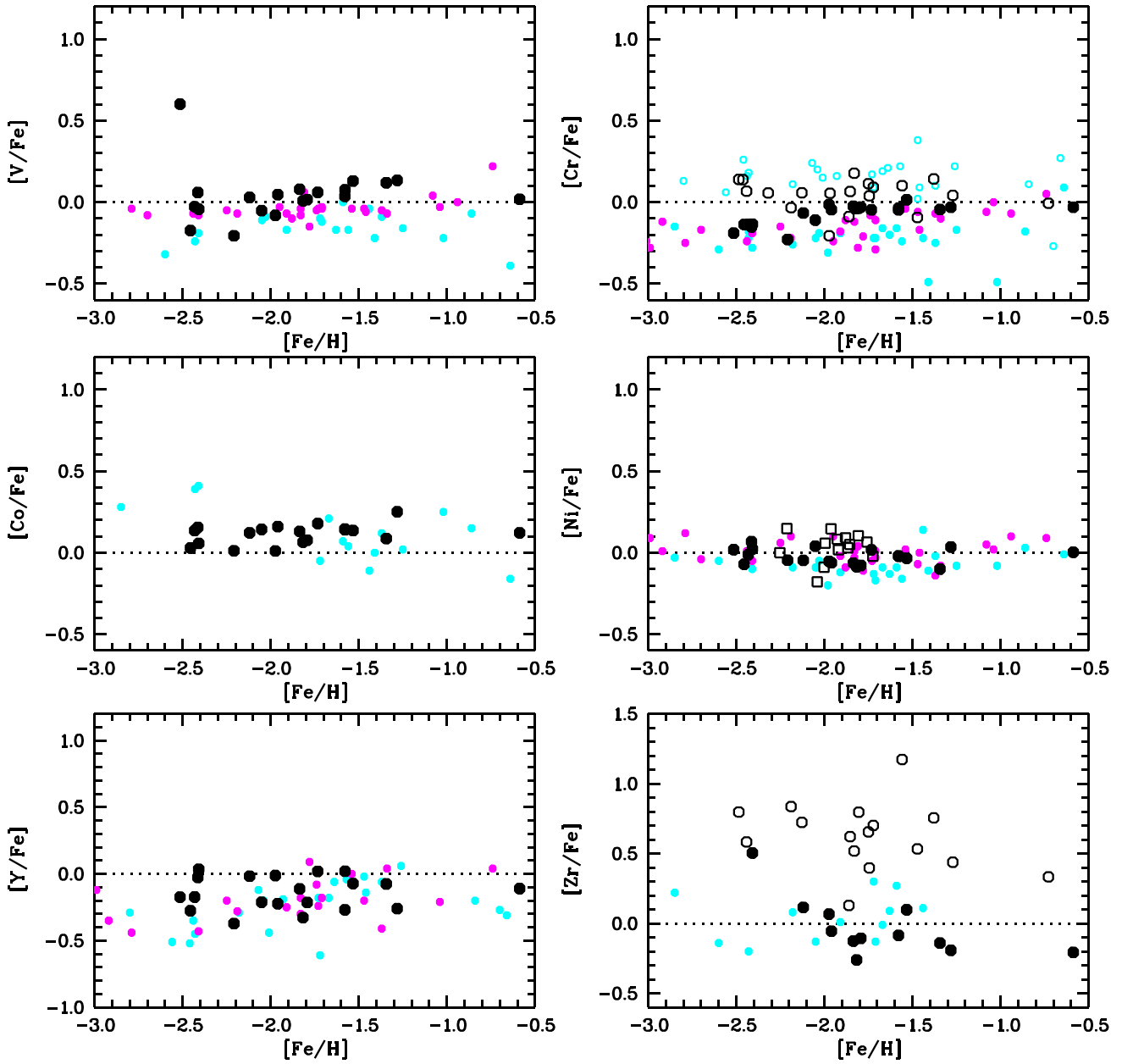


Figure C2. Abundances. Reference samples: yellow: Gratton et al. (2000); violet: Fulbright (2000); light blue: Ishigaki et al. (2012, 2013). Open symbols for the Cr and Zr panels refer to abundances from ionized Cr, Zr, and Fe.

Table C1. Identification and Pristine identification for our targets.

Main identification	Pristine identification
TYC 2270–1021–1	Pristine_008.06789207+34.37548830
TYC 1194–507–1	Pristine_011.36015797+20.18855860
TYC 1742–324–1	Pristine_012.17517471+25.86319920
TYC 1753–1167–1	Pristine_018.76822472+28.41813090
TYC 2299–342–1	Pristine_019.39557838+35.10896300
TYC 1205–397–1	Pristine_025.60008812+16.20835300
TYC 1760–612–1	Pristine_029.75453758+26.64141460
TYC 2457–2294–1	Pristine_112.57359314+32.94884110
TYC 1406–971–1	Pristine_143.23533630+18.38591960
TYC 3006–1127–1	Pristine_153.06271362+44.16487500
TYC 286–299–1	Pristine_180.77297974+06.38266660
TYC 284–358–1	Pristine_182.67672729+03.05452230
TYC 877–422–1	Pristine_186.53616333+10.25012490
TYC 3458–611–1	Pristine_187.89250183+48.82968900
TYC 3458–980–1	Pristine_189.59397888+49.61645130
TYC 891–750–1	Pristine_200.01441956+07.70733360
TYC 31–2–1416–1	Pristine_207.62947083+03.95404720
TYC 905–551–1	Pristine_212.37841797+12.06830790
TYC 914–128–1	Pristine_221.91290283+12.39337250
<i>Gaia</i> DR3 1180300688463921792	Pristine_223.83322144+10.66756150
TYC 333–942–1	Pristine_223.86860657+06.74538900
TYC 4182–1043–1	Pristine_235.15843201+61.95952610
TYC 3060–408–1	Pristine_238.06059265+44.21089550
TYC 3084–1083–1	Pristine_255.56152344+43.47154620
TYC 2086–422–1	Pristine_260.16348267+28.17633630
TYC 1118–595–1	Pristine_320.67050171+13.26118370
<i>Gaia</i> DR3 1745739764412146816	Pristine_321.88916016+11.24667260
TYC 1123–1454–1	Pristine_321.98461914+11.11573890
TYC 1125–548–1	Pristine_325.93469238+10.88442230
TYC 2207–992–1	Pristine_330.64309692+25.23588940
TYC 1688–640–1	Pristine_330.87582397+19.44488910
TYC 1709–674–1	Pristine_340.01919556+21.36958120
TYC 1159–895–1	Pristine_343.41021729+13.80131910
TYC 1172–486–1	Pristine_352.71221924+10.22986980
TYC 2772–378–1	Pristine_359.24597168+32.26105120
HU Peg	Pristine_359.84237671+13.78651710

This paper has been typeset from a $\text{\TeX}/\text{\LaTeX}$ file prepared by the author.



Pristine XXI: exploring the metal-poor boundary with ESPaDoNS

Journal:	<i>Monthly Notices of the Royal Astronomical Society</i>
Manuscript ID	MN-22-4640-MJ
Manuscript type:	Main Journal
Date Submitted by the Author:	21-Nov-2022
Complete List of Authors:	Lombardo, L.; CNRS, Bonifacio, Piercarlo; Observatoire de Paris, GEPI Caffau, Elisabetta; Observatoire de Paris, GEPI Francois, Patrick; Paris Observatory, GEPI Jablonka, Pascale; EPFL Kordopatis, Georges; Observatoire de la Côte d'Azur, Lagrange Martin, Nicolas; Observatoire astronomique de Strasbourg Starkenburger, Else; Rijksuniversiteit Groningen Yuan, Z.; Observatoire Astronomique de Strasbourg Sbordone, Luca; European Southern Observatory Sestito, Federico; University of Victoria Hill, Vanessa; Observatoire de la Cote d'Azur, Lagrange Venn, Kim; University of Victoria, Physics & Astronomy
Keywords:	Stars, stars: abundances < Stars, stars: Population II < Stars

SCHOLARONE™
Manuscripts

Pristine XXI: exploring the metal-poor boundary with ESPaDoNS

Linda Lombardo,^{1*} Piercarlo Bonifacio,¹ Elisabetta Caffau,¹ Patrick François,^{2,3} Pascale Jablonka,^{1,4} Georges Kordopatis,⁵ Nicolas Martin,⁶ Else Starkenburg,⁷ Zhen Yuan,⁶ Luca Sbordone,⁸ Federico Sestito,⁹ Vanessa Hill,¹⁰ Kim Venn⁹

¹GEPI, Observatoire de Paris, Université PSL, CNRS, 5 place Jules Janssen, 92195 Meudon, France

²GEPI, Observatoire de Paris, Université PSL, CNRS, 77 Av. Denfert-Rochereau, 75014 Paris, France

³UPJV, Université de Picardie Jules Verne, 33 rue St Leu, 80080, Amiens, France

⁴Laboratoire d'Astrophysique, Ecole Polytechnique Fédérale de Lausanne (EPFL), Observatoire de Sauvigny, CH-1290 Versoix, Switzerland

⁵Université Côte d'Azur, Observatoire de la Côte d'Azur, CNRS, Laboratoire Lagrange, France

⁶Université de Strasbourg, CNRS, Observatoire astronomique de Strasbourg, UMR 7550, F-67000, France

⁷Kapteyn Astronomical Institute, University of Groningen, Landleven 12, NL-9747 AD Groningen, the Netherlands

⁸European Southern Observatory, Alonso de Cordova 3109, Vitacura, Santiago, Chile

⁹Department of Physics and Astronomy, University of Victoria, PO Box 3055, STN CSC, Victoria BC V8W 3P6, Canada

¹⁰Université Côte d'Azur, Observatoire de la Côte d'Azur, CNRS, Laboratoire Lagrange, Bd de l'Observatoire, CS 34229, 06304 Nice cedex 4, France

Accepted XXX. Received YYY; in original form ZZZ

ABSTRACT

In this paper we study high resolution spectra of 19 stars that have metallicity estimates below -3.5 using at least two metallicity sensitive photometric indices based on Pristine photometry. The purpose is to understand what kind of stars populate this parameter space, together with extremely metal-poor stars. This because we plan to extensively use the Pristine photometry to provide extremely metal-poor targets to the WEAVE spectroscopic survey and wish to understand the nature of possible contaminants. We find that this extreme sample of stars is heavily contaminated by variable stars, in particular short period eclipsing binaries. We thus found, serendipitously, eight double-lined spectroscopic eclipsing binaries that could be further followed spectroscopically to provide reliable masses and distances for these systems. We also found two stars that have metallicity below -3.0 , one of which may belong to the Gaia-Sausage-Enceladus structure. The lesson to be learned from this investigation is that to select truly metal-poor stars one should be able to remove all photometrically variable stars, which requires complementary information beyond the Pristine photometry. We show how the Gaia photometry can be used to remove about 85% of the photometrically variable stars. Our investigation also shows that there is a clear potential for Pristine photometry to find double-lined spectroscopic binaries among short period eclipsing binaries.

Key words: stars: abundances – stars: Population II

1 INTRODUCTION

The Pristine survey (Starkenburg et al. 2017) is observing the northern hemisphere using the MegaCam wide field imager (Boulade et al. 2003) on the Canada France Hawaii Telescope at Mauna Kea, with a narrow band filter centered on the Ca II H&K lines in the near UV. This narrow band filter, combined with Sloan Digital Sky Survey (SDSS) *gri* filters (Doi et al. 2010) has been proven to provide reliable metallicity estimates and to be an excellent tool to find metal-poor stars. After the excellent results obtained in the previous papers of this series (e.g. Starkenburg et al. 2018; Bonifacio et al. 2019; Aguado et al. 2019; Venn et al. 2020; Caffau et al. 2020; Kielty et al. 2021; Lardo et al. 2021; Lucchesi et al. 2022), we de-

ecided to boldly target a sample of stars with estimated metallicity less than -3.5 , disregarding any complementary information. The purpose was to see what kind of stars we would find and to explore the limitations of a selection based on Pristine and SDSS photometry alone. The purpose of this is to help us to use Pristine photometry to select metal-poor stars for the spectroscopic survey to be conducted in the next five years with the multi-object facility WEAVE (Jin et al., MNRAS, submitted) on the William Herschel 4.2 m telescope.

We did expect several kinds of contaminants, that is stars that are not as metal poor as predicted by the Pristine photometry. Among these we expected young, chromospherically active stars, with emission in the cores of the Ca II H&K lines. All kinds of variable stars (RR Lyrae are typically found in the colour range investigated by us) are also expected to be contaminants, since the SDSS broad band photometry was taken at a different time with respect to the Pris-

* E-mail: Linda.Lombardo@observatoiredeparis.psl.eu

2 *L. Lombardo et al.*

tine photometry and this leads to combining photometric bands that are observed at different phases in the light curve. What we did not expect was to find a majority of short-period eclipsing binaries, as discussed in Sect. 4, and especially double-lined spectroscopic binary (SB2) stars. With hindsight, a percentage of such contaminants should have been expected. One of the characteristics of short period binaries is the tidal locking, that leads to a synchronisation of orbital and rotational velocities. In turn this results in larger rotational velocities than found in non-double stars of the same spectral type. These high rotational velocities imply that the Ca II H&K lines are shallow and their narrow band photometry mimics a low metallicity. This effect comes on top of the above-mentioned photometric variability.

2 TARGET SELECTION

The 19 stars in the sample were selected from the Pristine catalogue with the request that both metallicity based on *CaHK* narrow-band and both $g - i$ and $g - r$ broad-band colours were below -3.5 . Complementary requests were also the observability in α in the CFHT period 20B and $g < 15.5$. In Fig. 1 we show the positions of our targets in the usual colour-colour plot used by the Pristine collaboration, coloured with their metallicity estimate derived from the Pristine *CaHK* and $g - i$, compared with theoretical colours for two different surface gravities and metallicities. The most commonly used version of this plot is shown in figure 3 of [Starkenburger et al. \(2017\)](#), in that plot the solid lines represent exponential fits to theoretical colours of different gravities; for $g - i > 1.0$ the gravities of the Red Giant Branch predicted by 12 Gyr old isochrones is followed. In our plot we explicit the gravity dependence of the index $(CaHK - g)_0 - 1.5(g - i)_0$. These theoretical colours are slightly different from those of [Starkenburger et al. \(2017\)](#), that were computed using a grid of MARCS models ([Gustafsson et al. 2008](#)), while these have been computed by us using the [Castelli & Kurucz \(2003\)](#) ATLAS 9 models. The figure shows how all the stars of our sample are beyond the -4.0 theoretical curves. The Pristine metallicities are computed through a calibration process and not merely through comparison with theoretical curves, hence it is not surprising that the Pristine metallicities of all the targets are slightly below -4.0 .

3 OBSERVATIONS

The spectra were observed with ESPaDOnS ([Donati et al. 2006](#)) in the Queued Service Observation mode of CFHT between November 29th 2020 and December 8th 2020. Each star was observed twice, one exposure after the other, with exposure times that range from 1300 s to 2400 s. A complete log of the observations is provide in Table 1.

The reduced data were provided to us by CFHT, the spectra are processed with the Upena¹ pipeline using routines of the LibreESPRIT software ([Donati et al. 1997](#)). We used the “Star+Sky” mode that covers the spectral range 370 nm to 1051 nm with resolving power of 65 000. We perform the order merging using an ESO-MIDAS² script developed by us for this purpose. The script performs the order merging using the ESO-MIDAS task `merge/spec`, which computes a weighted average in the overlapping region of adjacent orders. Out of the overlaps, the spectra of

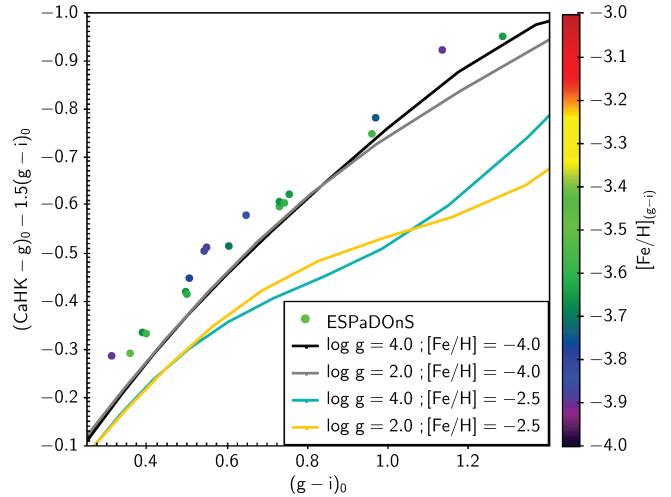


Figure 1. Colour-colour for our selected targets. The solid lines are theoretical curves for two values of metallicity and surface gravity. The points are coloured according to their photometric metallicity estimate.

adjacent orders are copied to the output spectrum. Within the overlaps, for computing the weights, our procedure uses the formula $spec_{out} = spec_1 \cdot (1 - c) + spec_2 \cdot c$, where $spec_{out}$ is the output spectrum, $spec_1$ and $spec_2$ are the spectra of adjacent orders, and c is a ramp varying from 0 to 1 in the overlap. In this way we recover all the information from each order. This is different from what was done in [Lucchesi et al. \(2022\)](#), where the overlapping regions were simply cut out and the spectra joined. In that paper the normalised spectrum was merged. We prefer instead to use the non-normalised spectrum, since MyGIsFOS ([Sbordone et al. 2014](#)) is capable of providing an excellent pseudo-continuum and works better on non-normalized spectra, see Sect. 4.4 for further details. Upena corrects the spectra for the heliocentric radial velocity, so the pairs of spectra were co-added and ready for analysis.

4 ANALYSIS

4.1 Radial velocities

Before analysing the stars, we visually inspected the spectra, and this quick-look led us to suspect that some of these stars were in binary systems. We then checked for spectroscopic binaries through cross-correlation, and found that 8 out of 19 stars are SB2 binaries. To measure the radial velocities of each component, we used the technique of cross-correlation ([Tonry & Davis 1979](#)). To compute the cross-correlation functions we use our own code that computes the cross-correlation in Fourier space using the routine `correl` ([Press et al. 1992](#)). As template we use a synthetic spectrum computed with SYNTH4 from an ATLAS 9 model ([Kurucz 2005](#)). The stellar parameters are estimated as described in Sect. 4.3. Although the method is not applicable to binary stars, the practice showed that the derived parameters are adequate to compute a template to be used for cross-correlation. Finally the velocity of each component is estimated by fitting two gaussians to the cross-correlation peaks, using the `iraf`³ task `splot` with the `deblending` option. The radial velocities can be found in Table 2, the uncertainties are estimated as

¹ <http://www.cfht.hawaii.edu/Instruments/Upena/>

² <https://www.eso.org/sci/software/esomidas/>

³ <https://iraf-community.github.io>

Table 1. Log of the observations. Radial velocities for SB2 stars are given in Table 2

star	date YYY MM DD	UT hms	HJD days	Texp s	g_0 mag	V_R km s ⁻¹	$\sigma(V_R)$ km s ⁻¹
Pristine_326.5701+19.2445	2020 11 29	04:40:55	2459182.69458	2400.0	15.323	-77.553	0.091
Pristine_326.5701+19.2445	2020 11 29	05:21:31	2459182.72277	2400.0		-77.434	0.088
Pristine_355.2747+26.4757	2020 11 29	06:09:54	2459182.75884	2400.0	13.803	-14.271	0.026
Pristine_355.2747+26.4757	2020 11 29	06:50:30	2459182.78705	2400.0		-14.343	0.024
Pristine_024.5944+25.4689	2020 11 29	09:04:03	2459182.88178	2400.0	15.247		
Pristine_024.5944+25.4689	2020 11 29	09:44:39	2459182.90997	2400.0			
Pristine_029.3591+21.3783	2020 12 03	07:14:54	2459186.80599	2400.0	14.711		
Pristine_029.3591+21.3783	2020 12 03	07:55:31	2459186.83420	2400.0			
Pristine_034.7189+25.9539	2020 12 04	10:41:09	2459187.94933	1770.3	14.116		
Pristine_034.7189+25.9539	2020 12 04	11:11:29	2459187.97040	1798.5			
Pristine_148.3782+53.0957	2020 12 04	13:11:14	2459188.05071	2222.0	14.599	23.606	0.049
Pristine_148.3782+53.0957	2020 12 04	13:48:55	2459188.07689	2227.7		23.503	0.050
Pristine_159.5695+57.1688	2020 12 04	14:47:41	2459188.11710	2393.0	14.993	-135.220	0.054
Pristine_159.5695+57.1688	2020 12 04	15:27:53	2459188.14502	2359.8		-135.259	0.056
Pristine_109.8329+41.3782	2020 12 05	11:06:51	2459188.96665	2400.0	15.149	18.360	0.015
Pristine_109.8329+41.3782	2020 12 05	11:47:28	2459188.99485	2400.0		18.566	0.015
Pristine_163.9735+13.4823	2020 12 05	14:46:24	2459189.11558	1371.3	15.195	22.88	4.17
Pristine_163.9735+13.4823	2020 12 05	15:09:48	2459189.13183	1363.7		30.90	6.61
Pristine_327.5170+19.8622	2020 12 06	04:35:28	2459189.69016	2400.0	14.930	-122.611	0.030
Pristine_327.5170+19.8622	2020 12 06	05:16:04	2459189.71836	2400.0		-121.771	0.030
Pristine_328.6116+20.3914	2020 12 06	05:58:37	2459189.74801	2400.0	15.187	-282.961	0.092
Pristine_328.6116+20.3914	2020 12 06	06:39:14	2459189.77621	2400.0		-284.115	0.131
Pristine_002.0937+22.6545	2020 12 06	07:22:25	2459189.80903	2400.0	15.268		
Pristine_002.0937+22.6545	2020 12 06	08:03:01	2459189.83721	2400.0			
Pristine_008.1724+21.8215	2020 12 06	08:45:21	2459189.86709	2400.0	15.447	-120.437	0.126
Pristine_008.1724+21.8215	2020 12 06	09:25:57	2459189.89529	2400.0		-120.986	0.158
Pristine_331.5576+27.2164	2020 12 07	04:31:50	2459190.68800	1944.8	15.041		
Pristine_331.5576+27.2164	2020 12 07	05:06:44	2459190.71224	2171.9			
Pristine_333.2010+09.6132	2020 12 07	05:48:03	2459190.74079	2400.0	15.230		
Pristine_333.2010+09.6132	2020 12 07	06:28:38	2459190.76898	2400.0			
Pristine_348.1325+11.2206	2020 12 07	07:15:53	2459190.80314	1572.5	14.444		
Pristine_348.1325+11.2206	2020 12 07	07:42:51	2459190.82187	1591.9			
Pristine_333.2117+20.1267	2020 12 08	04:27:58	2459191.68523	1544.0	14.712		
Pristine_333.2117+20.1267	2020 12 08	04:54:47	2459191.70385	1599.8			
Pristine_335.8411+09.0218	2020 12 08	05:20:47	2459191.72198	1307.7	15.471	62.307	0.059
Pristine_335.8411+09.0218	2020 12 08	05:43:09	2459191.73751	1304.2		63.898	0.056
Pristine_009.1439+15.7850	2020 12 08	06:07:40	2459191.75749	1252.4	15.483	-63.249	0.238
Pristine_009.1439+15.7850	2020 12 08	06:29:07	2459191.77239	1252.2		-64.053	0.193

described in [Tonry & Davis \(1979\)](#). For each star, we call “A” component the one with the highest peak in the cross-correlation function. For stars that did not show sign of a secondary spectrum we measured the radial velocity with our own template matching code, and the velocities can be found in Table 1. Template matching is a technique in which a template spectrum is matched to an observed spectrum by minimizing a χ^2 function in which the radial velocity is one of the fitting parameters, it is described for example in [Koposov et al. \(2011\)](#). We use our own code to perform template matching, in which the radial velocity is the only free parameter. We normalise the observed spectrum by fitting a spline through interactively chosen continuum points using an updated version of the NORMA code ([Bonifacio 1989](#)). As template, we use a synthetic spectrum computed with the parameters derived as described in Sec. 4.3. [Koposov et al. \(2011\)](#) showed that template matching performs better than cross-correlation, provided that the template is close to the observed spectrum and this is confirmed by our own tests.

We do not provide parameters nor perform chemical analysis for any of the SB2 binaries, since to disentangle the spectra we need information on the luminosities of the two star (see e.g. [Venn et al.](#)

[2003; González Hernández et al. 2008](#)). This information may come from the orbital solution, combined with theoretical isochrones. We thus defer such an analysis to when an orbital solution, and therefore a mass function, of the system shall be available. We also do not analyse four more stars, because they were rotating rapidly and the signal-to-noise ratio (S/N) was too low ($S/N \sim 5$ at 550 nm) to allow for a proper analysis. Further details on the 12 non-analyzed stars are provided in Sect. 5.2, and in the last but one column of Table 3 the stars are marked as “N”. The uncertainties in radial velocity are the formal uncertainties derived from the χ^2 in case of the template matching and from the [Tonry & Davis \(1979\)](#) formalism for cross-correlation. To these uncertainties, that are of statistical nature, one should add a systematic of 0.02 km s^{-1} , for the stability of ES-PaDONs⁴. In several cases the difference in radial velocity between the two consecutive exposures is larger than the combined statistical and systematic uncertainties. We believe that these variations are

⁴ http://www.ast.obs-mip.fr/projets/espados/espados_new/stability.html

4 *L. Lombardo et al.***Table 2.** Radial velocities for SB2 binaries. Stars marked with \star are the three stars (four spectra) classified as fast rotators in [Lucchesi et al. \(2022\)](#).

ID	HJD days	$V_R(A)$ km s $^{-1}$	$\sigma[V_R(A)]$ km s $^{-1}$	$V_R(B)$ km s $^{-1}$	$\sigma[V_R(B)]$ km s $^{-1}$	CCF template $T_{\text{eff}}/\log g/\text{metallicity}$
Pristine_002.0937+22.6545	2459189.80903	-61.27	0.83	11.31	0.87	5400/4.0/-1.0
Pristine_002.0937+22.6545	2459189.83721	-54.68	2.33			
Pristine_024.5944+25.4689	2459182.88178	-138.30	6.00	166.60	5.60	5000/4.0/-1.0
Pristine_024.5944+25.4689	2459182.90997	-138.30	5.60	145.10	5.40	
Pristine_029.3591+21.3783	2459186.80599	71.70	6.80	-212.70	3.20	5600/4.0/-1.0
Pristine_029.3591+21.3783	2459186.83420	83.80	6.80	-243.70	3.60	
Pristine_034.7189+25.9539	2459187.94933	-12.00	2.90	269.10	1.60	5800/4.0/-1.0
Pristine_034.7189+25.9539	2459187.97040	-20.50	4.40	282.30	2.30	
Pristine_331.5576+27.2164	2459190.68800	66.09	5.90	-253.58	3.60	5600/4.0/-1.0
Pristine_331.5576+27.2164	2459190.71224	65.88	6.60	-194.60	4.60	
Pristine_333.2010+09.6132	2459190.74079	-25.63	0.28	71.83	0.40	5400/4.0/-1.0
Pristine_333.2010+09.6132	2459190.76898	-31.07	0.33	77.05	0.94	
Pristine_333.2117+20.1267	2459191.68523	43.50	6.01	-256.85	3.30	5800/4.0/-1.0
Pristine_333.2117+20.1267	2459191.70385	67.58	7.10	-262.50	3.50	
Pristine_348.1325+11.2206	2459190.80314	-13.68	0.25	12.43	0.23	5800/4.0/-1.0
Pristine_348.1325+11.2206	2459190.82187	-15.08	0.23	13.41	0.23	
Pristine_181.3698+117645 \star^a	2457447.10106	78.87	0.17	-42.19	0.18	5400/3.00/-1.5
Pristine_213.2814+14.8983 \star^b	2457819.15463	-8.94	0.29	-20.16	0.43	6000/3.50/-2.0
Pristine_254.3844+12.9652 \star^c	2457887.02381	-379.71	0.26	-391.79	0.21	5200/3.00/-2.5
Pristine_254.3844+12.9652 \star^c	2457887.05204	-378.10	0.23	-390.84	0.22	

\star^a This stars is named Pristine_181.3708+11.7636 in [Lucchesi et al. \(2022\)](#) and is also present in [Venn et al. \(2020\)](#) with the SDSS coordinates RA=181.3699 DEC=+11.7636

\star^b this star is also present in [Venn et al. \(2020\)](#), in this case Pristine and SDSS are identical, to four decimal places.

\star^c In [Lucchesi et al. \(2022\)](#) this star is named Pristine_254.3844+12.9653

Table 3. Stars observed with ESPaDoNS in period 20B. Label A indicates the stars that have been analysed, while label N indicates the stars that have not. The abbreviation ECL stands for eclipsing binary, SB2 for double-lined spectroscopic binary, RS CVn for RS Canum Venaticorum stars, and RR Lyr for RR Lyrae.

Star	RA(CaHK) deg	DEC(CaHK) deg	DR3 Name	G mag	$G_{BP} - G_{RP}$ mag	A/N	Comment
Pristine_002.0937+22.6545	2.09372497	+22.65452766	Gaia DR3 2847119325004632960	14.590	1.024	N	ECL, SB2
Pristine_008.1724+21.8215	8.1724329	+21.82150269	Gaia DR3 2799728346622900480	15.252	0.700	A	
Pristine_009.1439+15.7850	9.1439209	+15.78506374	Gaia DR3 2780656630244179712	15.371	0.692	A	
Pristine_024.5944+25.4689	24.59447861	+25.46895218	Gaia DR3 292459170887172352	14.471	1.253	N	ECL, SB2
Pristine_029.3591+21.3783	29.35915756	+21.3783741	Gaia DR3 97471675738184576	14.474	0.910	N	ECL, SB2
Pristine_034.7189+25.9539	34.71894073	+25.95391083	Gaia DR3 106031957876177024	13.881	0.848	N	ECL, SB2
Pristine_109.8329+41.3782	109.83296967	+41.37827682	Gaia DR3 948549265398560512	14.844	0.940	N	ECL
Pristine_148.3782+53.0957	148.37820435	+53.09577179	Gaia DR3 828505655325207680	13.562	1.207	N	RS CVn
Pristine_159.5695+57.1688	159.56959534	+57.16887665	Gaia DR3 853989036322676224	14.334	1.129	A	
Pristine_163.9735+13.4823	163.973526	+13.48232746	Gaia DR3 3872789126248434560	14.668	0.772	N	ECL
Pristine_326.5701+19.2445	326.57019043	+19.24455833	Gaia DR3 1780400940765306624	14.509	1.500	N	RS CVn
Pristine_327.5170+19.8622	327.51705933	+19.8622036	Gaia DR3 1780495017728775680	15.014	0.913	A	ECL, RS CVn(?)
Pristine_328.6116+20.3914	328.61169434	+20.39147758	Gaia DR3 1780903486298463872	14.953	1.009	A	
Pristine_331.5576+27.2164	331.55767822	+27.21646309	Gaia DR3 1892821297421984128	14.628	0.988	N	ECL, SB2
Pristine_333.2010+09.6132	333.2010498	+9.61327744	Gaia DR3 2723881217040192640	14.545	1.041	N	ECL, SB2
Pristine_333.2117+20.1267	333.21176147	+20.126791	Gaia DR3 1778301217153109760	14.294	0.849	N	ECL, SB2, RR-Lyr(?)
Pristine_335.8411+09.0218	335.84118652	+9.02187824	Gaia DR3 2723074347304080384	15.223	0.727	A	RR-Lyr
Pristine_348.1325+11.2206	348.13250732	+11.22061634	Gaia DR3 2810661890249732480	13.813	0.816	N	ECL, SB2
Pristine_355.2747+26.4757	355.27474976	+26.47573662	Gaia DR3 2864940415627238784	13.645	0.942	A	

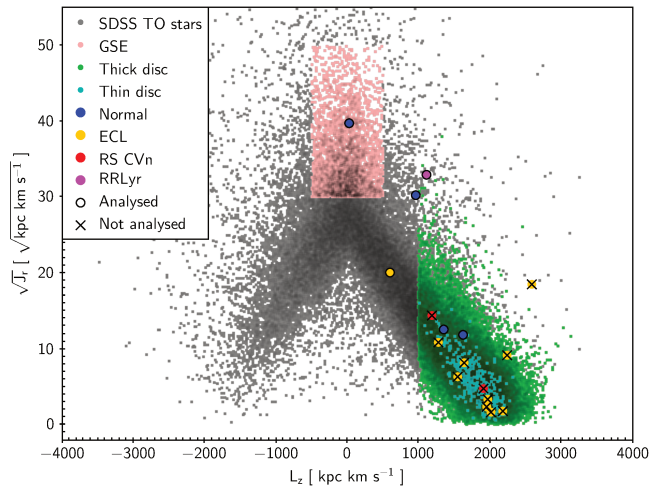


Figure 2. The $L_z - \sqrt{J_r}$ plane for our sample of stars. The properties of our stars are specified in the legend. The grey dots that we use as reference stars are the Turn Off stars from Bonifacio et al. (2021). Further details can be found in the text.

real, as is surely the case for the two RR Lyrae stars observed, that show clear radial velocity variations.

Lucchesi et al. (2022) homogeneously analysed a sample of Pristine metal-poor candidates observed with ESPaDOnS. The majority of the Lucchesi et al. (2022) observations are described in Venn et al. (2020), that also provides an independent homogeneous analysis. Three stars in Lucchesi et al. (2022) sample were excluded from the analysis and labelled as “fast rotators”, two of which had already been analysed by Venn et al. (2020). Since the targets in Venn et al. (2020) and Lucchesi et al. (2022) were selected in a similar way to ours, we looked at the spectra of these three stars to see if they could be variables or SB2 binaries. In deriving the radial velocities by cross-correlation, we found that these stars show a double peak in the cross-correlation function, thus suggesting that they are SB2 binaries. The last 4 rows of Table 2 provide the radial velocities we measured for these three stars in Lucchesi et al. (2022) from the two peaks of the cross-correlation function. For star Pristine_181.3708+11.7636, the two peaks are well distinct, while for the other stars the two peaks are only visible in the red part of the spectra, in the 600-655 nm range. In our opinion, the absence of the second peak in the blue part of the spectra could mean that the companion is cooler and, therefore, less observable in the blue. However, the absence of the second peak in the blue could be also due to the fact that the S/N ratio is too low and the lines of the secondary are not detectable. Star Pristine_213.2814+14.8983 has also been identified as a RR Lyrae with a period of 0.63 days by several studies (Drake et al. 2013; Sesar et al. 2013; Abbas et al. 2014; Greer et al. 2017; Sesar et al. 2017; Heinze et al. 2018).

4.2 Kinematics

With our radial velocities and the Gaia DR3 parallaxes and proper motions we compute the actions for our sample of stars, as done in Kordopatis et al. (2022). The parallaxes were corrected for the zero point according to the prescriptions of Lindegren et al. (2021). For the SB2 stars we took as radial velocity the mean of the velocities of the two peaks in the cross correlation function, that is the velocity of the centre of mass of the system. For the stars that are recognised

as binaries by Gaia, proper motions and parallaxes take into account the orbital motion (Halbwachs et al. 2022). For the RR Lyrae star we use the mean observed radial velocity since we do not have a radial velocity curve available.

In Fig. 2 we plot the angular momentum (L_z) versus $\sqrt{J_r}$ for our sample of stars and use as background reference the sample of Bonifacio et al. (2021). Stars that fall in the Gaia-Sausage-Enceladus accretion event (Belokurov et al. 2018; Haywood et al. 2018; Helmi et al. 2018, GSE hereafter) according to the kinematic selection criterion of Feuillet et al. (2020)⁵ are coloured in pink. Thick disc stars are coloured in green⁶. Thin disc stars⁷ are coloured in light blue. Stars in our sample that have not been analyzed are covered by a black \times sign, eclipsing binaries (ECL) are shown as yellow dots, RS Canum Venaticorum stars (RS CVns) as red dots, and the RR Lyrae (RR Lyr) is shown as magenta circle. Most of the eclipsing binaries and both of the RS CVns are found in the thin disc. Only one eclipsing binary is found in the thick disc.

The two most metal-poor stars and the RR Lyrae star are unsurprisingly found to have low L_z and high J_r , what a few years ago one would have described as “halo” orbits. However it is remarkable that one of the two most metal-poor stars found in our sample, Pristine_159.5695+57.1688 ([Fe/H] \sim -3.1), is clearly in the region occupied by the GSE structure. There is a debate on the metallicity distribution function (MDF) of the GSE, with Feuillet et al. (2020) and Naidu et al. (2020) favouring an MDF peaking at metallicity -1.0 and a quick drop providing essentially no stars below -3.0 , while (Bonifacio et al. 2021) show an MDF peaking at -1.8 . Since our sample is clearly biased in favour of low metallicity stars we should compare with the MDF of (Bonifacio et al. 2021) not corrected for the bias. That MDF has in fact a sizeable fraction of stars below -3 , while no stars this metal-poor should be observed if the MDF were as proposed by Feuillet et al. (2020) or Naidu et al. (2020). Two things should be borne in mind: *i*) a purely kinematical selection of GSE, like shown in Fig. 2, will have about 20% contamination (Bonifacio et al. 2021), thus the fact that Pristine_159.5695+57.1688 is in that region of action space does not guarantee that it is a member of GSE; *ii*) it is possible that the differences among the GSE MDFs found in the literature are rooted in the different selection functions of the samples used to derive the MDFs.

4.3 Stellar parameters

To derive the stellar parameters for our sample of stars, we use the Gaia Data Release 3 (DR3) photometry (G , $G_{BP} - G_{RP}$) and parallaxes (Gaia Collaboration et al. 2016, 2022) adopting the same procedure described in Lombardo et al. (2021). The grid of ATLAS9 model atmosphere we use to derive stellar parameters has effective temperatures (T_{eff}), and surface gravities ($\log g$) in the range $3500 \leq T_{\text{eff}} \leq 6750$ K, $0.5 \leq \log g \leq 5.0$ dex, with a step of 250 K in T_{eff} , and 0.5 dex in $\log g$, for metallicities $[M/H] = -4, -2.5, -2.0, -1.5, -1.0, -0.5, +0.0, +0.2, +0.5$. The α -elements are enhanced by $+0.4$ for models with $[M/H] \leq -1$ and solar-scaled for the others. The micro-turbulent velocity is 2 km s^{-1} for all models. The Gaia parallaxes are corrected for the zero point according to Lindegren et al. (2021). We adopted the reddening values provided by Schlafly & Finkbeiner (2011) maps. Micro-turbulent velocities are derived

⁵ $-500 < L_z < 500 \text{ kpc km s}^{-1}$ and $30 < \sqrt{J_r} < 50 \text{ (kpc km s}^{-1})^{1/2}$

⁶ $L_z < 1000 \text{ kpc km s}^{-1}$ and $z_{\text{max}} < 3.0 \text{ kpc}$

⁷ $L_z < 1000 \text{ kpc km s}^{-1}$ and $z_{\text{max}} < 0.3 \text{ kpc}$

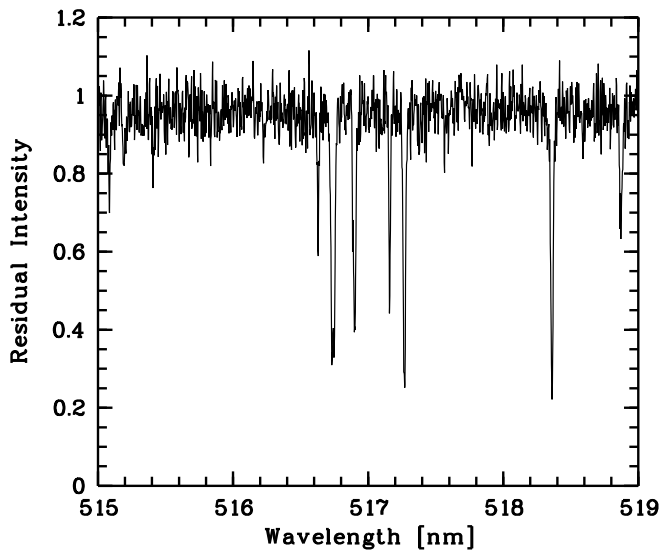


Figure 3. The region of Mg I b triplet in star Pristine_159.5695+57.1688.

using the empirical calibration in Mashonkina et al. (2017). The derived stellar parameters for our sample stars are listed in Table 4.

4.4 Chemical abundances

We were able to derive the chemical abundances for 7 out of 19 stars in our sample. A portion of one of our higher S/N ratio spectra (S/N = 28 at 550 nm), that of Pristine_159.5695+57.1688, is shown in Fig. 3. This star is also one of the two most metal-poor in the sample. The abundances are derived using MyGIsFOS (Sbordone et al. 2014). Our adopted solar abundances are from Caffau et al. (2011) and from Lodders et al. (2009) for all the elements not included in Caffau et al. (2011). MyGIsFOS performs a line-by-line χ^2 fitting on selected spectral features, interpolating in a pre-computed grid of synthetic spectra. We use synthetic grids computed from a grid of ATLAS 12 model atmospheres, using the SYNTH code (Kurucz 2005). This method has already been used and described in several of the Pristine papers (Caffau et al. 2017; Starkenburg et al. 2018; Bonifacio et al. 2019; Caffau et al. 2020). The atomic data for the spectrum synthesis are taken from Heiter et al. (2021). The molecular data are taken from the site of R.L. Kurucz⁸, including the CH lines by Masseron et al. (2014)⁹. We stress that, by fitting synthetic spectra, MyGIsFOS takes into account all the blending features, in this respect it is different from codes that use equivalent widths to derive abundances. The analysed stars are present in several catalogues, but no chemical analysis is available in the literature. In this study, the chemical abundances of these stars are provided for the first time. The derived abundances are listed in Table 5. In Fig. 4, 5, 6, and 7, we show [Mg/Fe], [Ca/Fe], [Sc/Fe], and [Ba/Fe] abundance ratios as a function of [Fe/H]. As reference, we have taken the stars of the ESO Large Programme “First Stars” (Cayrel et al. 2004; François et al. 2007), of Ishigaki et al. (2012, 2013), of papers Pristine V (Bonifacio et al. 2019) and Pristine XV (Lucchesi et al. 2022), and of Lombardo et al. (2022).

⁸ <http://kurucz.harvard.edu/linelists/linesmol/>

⁹ <http://kurucz.harvard.edu/molecules/ch/>

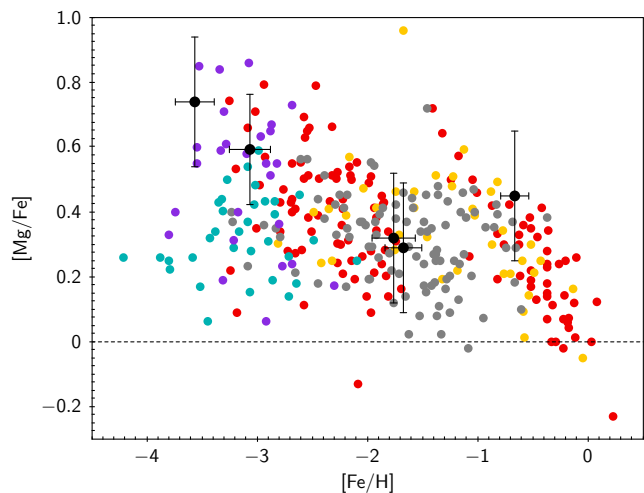


Figure 4. [Mg/Fe] as a function of [Fe/H] for our sample stars (black dots). Red dots are the stars from the Pristine XV paper (Lucchesi et al. 2022), yellow dots are from the Pristine V paper (Bonifacio et al. 2019), magenta dots are from the Pristine II paper (Caffau et al. 2017), purple dots are from the Pristine XII paper (Kielty et al. 2021), cyan dots are from Cayrel et al. (2004), and grey dots are from Ishigaki et al. (2012).

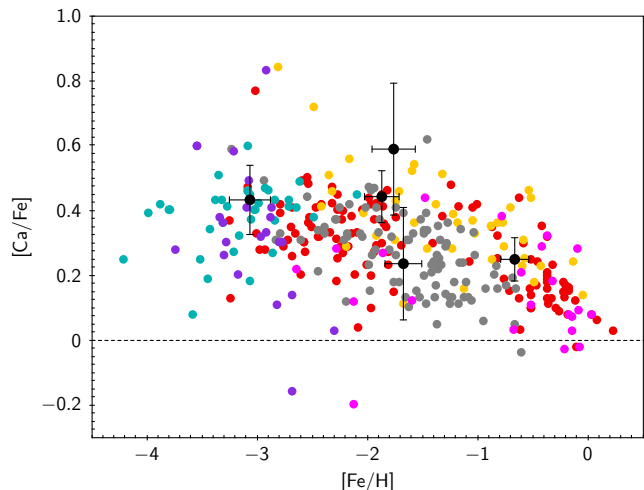


Figure 5. [Ca/Fe] as a function of [Fe/H] for our sample stars (black dots). The other symbols are like in Fig. 4.

Ca has been measured in five out of seven stars. In our sample, star Pristine_327.5170+19.8622 has [Ca/Fe]= +0.6, which is slightly higher than the reference samples values (Fig. 5). However, this star has [Mg/Fe]=+0.3 (Fig. 4), and, taking into account the uncertainties, this appears to be consistent with an average $[\alpha/\text{Fe}] \sim +0.4$.

We could measure the Sc abundance for five out of seven stars. One remarkable star is the most metal-rich star of the sample, Pristine_355.2747+26.4757, that has [Sc II/Fe II]=+0.49. Since the measure is based on seven Sc II lines with a line-to-line scatter of 0.1 dex, we consider the measure precise. Although the Sc abundance in Pristine_355.2747+26.4757 is higher than that in the other stars in the sample, it is still compatible with the values found in the literature for stars of similar metallicity, as shown in Fig. 6. Another remarkable star is Pristine_335.8411+09.0218, which shows

Table 4. Derived stellar parameters for stars analysed chemically. In column 5th and 6th, in parenthesis the number of lines is reported.

ID	T_{eff} K	$\log g$ dex	v_t km s ⁻¹	[FeI/H] dex	[FeII/H] dex	[Fe/H] _{gi} dex	[Fe/H] _{gr} dex	S/N @550 nm
Pristine_008.1724+21.8215	6051	2.39	2.07	-1.87 ± 0.16 (20)	-1.91 ± 0.08 (2)	-3.52	-3.56	12
Pristine_009.1439+15.7850	6278	4.29	1.29		-2.58 ± 0.20 (1)	-3.90	-3.81	10
Pristine_159.5695+57.1688	4798	1.42	2.06	-3.07 ± 0.19 (43)	-3.23 ± 0.14 (5)	-3.74	-3.52	28
Pristine_327.5170+19.8622	5817	2.53	1.91	-1.76 ± 0.20 (46)	-1.57 ± 0.20 (3)	-3.67	-3.51	18
Pristine_328.6116+20.3914	5245	2.87	1.62	-3.56 ± 0.17 (5)		-3.85	-3.63	13
Pristine_335.8411+09.0218	6091	2.88	1.88	-1.68 ± 0.17 (28)	-1.12 ± 0.17 (5)	-3.58	-3.55	12
Pristine_355.2747+26.4757	5586	4.10	0.98	-0.66 ± 0.13 (147)	-0.47 ± 0.16 (19)	-3.88	-3.72	30

Table 5. Derived chemical abundances for analysed stars.

Star	A(Na) $\pm\sigma$ (Na) (N)	A(Mg) $\pm\sigma$ (Mg) (N)	A(Al) $\pm\sigma$ (Al) (N)	A(SiI) $\pm\sigma$ (SiI) (N)	A(SiII) $\pm\sigma$ (SiII) (N)	A(Ca) $\pm\sigma$ (Ca) (N)
Pristine_008.1724+21.8215						4.91 ± 0.08 (5)
Pristine_009.1439+15.7850						
Pristine_159.5695+57.1688	3.22 ± 0.20 (1)	5.07 ± 0.17 (2)				3.70 ± 0.11 (5)
Pristine_327.5170+19.8622		6.10 ± 0.20 (1)				5.16 ± 0.21 (9)
Pristine_328.6116+20.3914		4.71 ± 0.20 (1)				
Pristine_335.8411+09.0218		6.15 ± 0.20 (1)				4.89 ± 0.17 (5)
Pristine_355.2747+26.4757	5.79 ± 0.03 (3)	7.33 ± 0.20 (1)	6.03 ± 0.20 (1)	7.14 ± 0.03 (8)	7.52 ± 0.20 (1)	5.92 ± 0.07 (8)
	A(ScII) $\pm\sigma$ (ScII) (N)	A(TiI) $\pm\sigma$ (TiI) (N)	A(TiII) $\pm\sigma$ (TiII) (N)	A(V) $\pm\sigma$ (V) (N)	A(CrI) $\pm\sigma$ (CrI) (N)	A(CrII) $\pm\sigma$ (CrII) (N)
Pristine_008.1724+21.8215	1.34 ± 0.20 (1)		3.40 ± 0.20 (1)			
Pristine_009.1439+15.7850						
Pristine_159.5695+57.1688	0.14 ± 0.18 (3)	1.94 ± 0.19 (2)	2.11 ± 0.07 (5)			
Pristine_327.5170+19.8622	1.70 ± 0.17 (5)		3.73 ± 0.18 (5)		3.69 ± 0.20 (1)	
Pristine_328.6116+20.3914						
Pristine_335.8411+09.0218	1.83 ± 0.20 (1)	3.84 ± 0.20 (1)	3.71 ± 0.23 (2)			
Pristine_355.2747+26.4757	3.13 ± 0.10 (7)	4.51 ± 0.07 (16)	4.79 ± 0.17 (17)	3.36 ± 0.07 (4)	4.95 ± 0.11 (8)	5.37 ± 0.20 (5)
	A(Mn) $\pm\sigma$ (Mn) (N)	A(Co) $\pm\sigma$ (Co) (N)	A(Cu) $\pm\sigma$ (Cu) (N)	A(Zn) $\pm\sigma$ (Zn) (N)	A(YII) $\pm\sigma$ (YII) (N)	A(BaII) $\pm\sigma$ (BaII) (N)
Pristine_008.1724+21.8215						0.36 ± 0.07 (2)
Pristine_009.1439+15.7850						
Pristine_159.5695+57.1688						-1.76 ± 0.21 (2)
Pristine_327.5170+19.8622					0.65 ± 0.02 (2)	1.17 ± 0.22 (1)
Pristine_328.6116+20.3914						-1.00 ± 0.20 (1)
Pristine_335.8411+09.0218						0.85 ± 0.08 (2)
Pristine_355.2747+26.4757	4.59 ± 0.15 (10)	4.45 ± 0.25 (2)	3.51 ± 0.11 (2)	4.30 ± 0.15 (2)	1.35 ± 0.20 (1)	1.64 ± 0.31 (2)

[Sc II/Fe II]=−0.15. However, we note that, for this star, the Sc abundance is A(Sc II)=1.83, while [Fe II/H]=−1.12, which is 0.55 dex higher than [Fe I/H]. This value is similar to the Sc abundance derived for Pristine_327.5170+19.8622, A(Sc II)=1.70, which has [Fe I/H]=−1.76.

We are able to measure Ba for six out of seven stars, for four of which two Ba II lines could be measured. As shown in Fig. 7, when compared with other stars in the literature, five out of six of our [Ba/Fe] measurements seem compatible with those of other stars at similar metallicity. The possibly odd star is Pristine_327.5170+19.8622, that appears to display a higher [Ba/Fe] than stars of similar metallicity. It would be interesting to measure abundances of other *n*-capture elements in this star. As discussed below this star is a binary of RS CVn type.

5 REMARKS ON INDIVIDUAL STARS

5.1 Stars with chemical analysis

We first discuss the information in the literature we found for stars for which we performed a chemical analysis.

5.1.1 Pristine_009.1439+15.7850

The star was classified from its spectrum as a subdwarf A star (sdA)¹⁰ with $T_{\text{eff}}=6926$ K and $\log g=5.48$ dex by Kepler et al. (2016). This effective temperature and gravity are inconsistent with Gaia photometry and parallaxes, and from our high resolution spectrum. We classify it as metal-poor G dwarf.

5.1.2 Pristine_327.5170+19.8622

Watson et al. (2006) classify this star as a RS CVn variable, and provide a period of 0.9147628 days and an amplitude of 0.116 mag. Also Chen et al. (2020) classify it as a RS CVn variable, with the same period and a 0.128 mag amplitude. This star was identified as a variable with a period of 1.829439 days by Heinze et al. (2018). According to Jayasinghe et al. (2018), this star is an eclipsing W Ursae Majoris-type binary¹¹, with an amplitude of 0.18 mag and a

¹⁰ According to Kepler et al. (2016), sdA stars show hydrogen-dominated spectra with $5.5 \leq \log g \leq 6.5$ dex and $T_{\text{eff}} \leq 20000$ K.

¹¹ According the General Catalogue of Variable Stars Samus' et al. (2017) this type of eclipsing binaries, of which W UMa is the prototype, are short

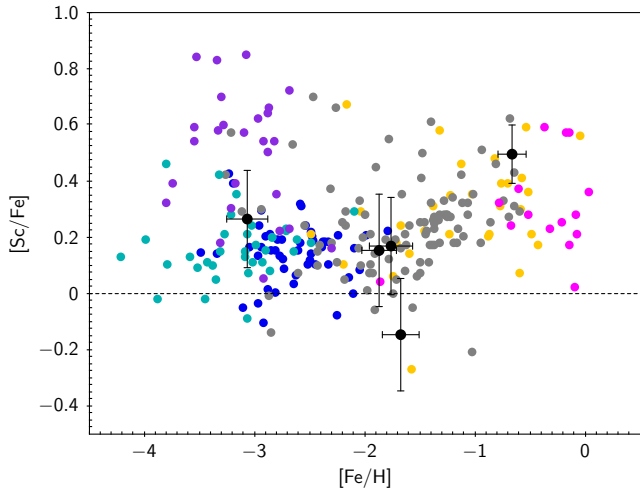


Figure 6. $[\text{Sc}/\text{Fe}]$ as a function of $[\text{Fe}/\text{H}]$ for our sample stars (black dots). Blue dots are the stars from (Lombardo et al. 2022), yellow dots are from the Pristine V paper (Bonifacio et al. 2019), magenta dots are from the Pristine II paper (Caffau et al. 2017), purple dots are from the Pristine XII paper (Kielty et al. 2021), cyan dots are from Cayrel et al. (2004), and grey dots are from Ishigaki et al. (2013).

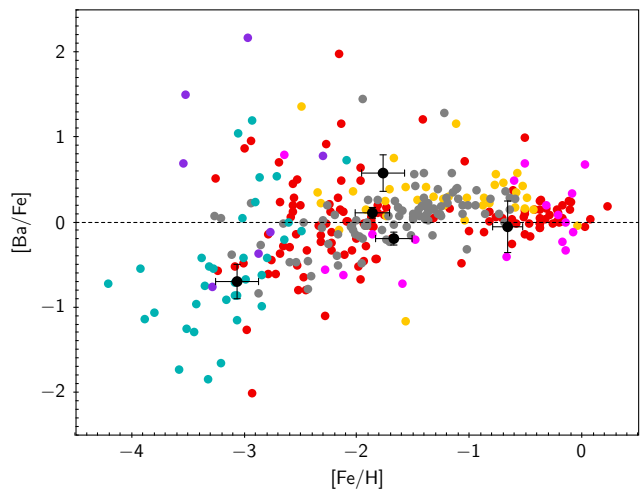


Figure 7. $[\text{Ba}/\text{Fe}]$ as a function of $[\text{Fe}/\text{H}]$. Red dots are the stars from the Pristine XV paper (Lucchesi et al. 2022), yellow dots are from the Pristine V paper (Bonifacio et al. 2019), magenta dots are from the Pristine II paper (Caffau et al. 2017), purple dots are from the Pristine XII paper (Kielty et al. 2021), cyan dots are from François et al. (2007), and grey dots are from Ishigaki et al. (2013).

period of 1.8294812 days. The star is also present in the Gaia DR3 catalogue as an eclipsing binary, with a period of 1.829375 days and an amplitude of variation in the G band of 0.122 mag. The period provided by Heinze et al. (2018), Jayasinghe et al. (2018) and Gaia DR3 is probably an alias of the shorter period provided by other catalogues. Our two 40 minutes exposures display a difference in radial velocity that is of almost 1 km s^{-1} supporting the notion of a rather

period (< 1 day), in contact, so that the components have an ellipsoidal shape. The light curve is such that it is impossible to determine the exact time of the eclipses.

short period. Assuming the shorter period one can guess a velocity amplitude of 16 km s^{-1} . RS CVn binaries are systems in which the primary is a giant or sub-giant of type F to K and the secondary is a dwarf of type G to M (see e.g. Martínez et al. 2022, and references therein). The spectral parameters we derived for this star are consistent with a giant of G-type, however its low metallicity make it more likely a Horizontal Branch star. RS CVn stars are generally very active chromospherically and strong X-ray emitters. Our spectrum is of too low S/N ratio around Ca II H&K lines to detect any core emission ($S/N < 2$), and we do not find emission in $H\alpha$ or other signs of chromospheric activity. We searched the Second ROSAT all-sky survey (2RXS) source catalogue (Boller et al. 2016), but we could not find any X-ray source within 2 arcminutes from this star. We believe that this star is not an RS CVn star, at least in the classical sense. Other known RS CVn are at most moderately metal-poor (see e.g. Randich et al. 1994) and this star, to our knowledge, would be the most metal-poor known RS CVn.

5.1.3 Pristine_335.8411+09.0218

Several studies have identified this star as a fundamental-mode RR Lyrae variable (RRab) (Drake et al. 2014; Sesar et al. 2017; Heinze et al. 2018; Chen et al. 2020) with a period of ~ 0.67 days. Drake et al. (2014) find a period of 0.672505 days with a V magnitude amplitude of 0.23 mag. The star is listed in the Gaia DR2 RR Lyrae catalogue as a RRab with a period of 0.67251854 days and a peak-to-peak G magnitude variability of 0.241601 mag. In the Gaia DR3 RR Lyrae catalogue, the star is listed as a RRab with a period of 0.672527 days and a peak-to-peak G magnitude variability of 0.24454159 mag. Our two spectra taken at about 22 minutes distance show a variation in the radial velocity of about 1.5 km s^{-1} . We checked the light curve of the star and interpolated the colour using the observation date, that implies a phase of 0.18. The effective temperature thus derived was just 40 K hotter than that derived using the mean Gaia colour. We also tried to determine the effective temperature from the excitation equilibrium, but we have too few iron lines and the iteration does not converge. Our spectroscopic metallicity is in stark disagreement with that provided by Gaia DR3 from the Fourier decomposition of the G light curve (see Clementini et al. 2022, and references therein). Gaia DR3 provides $[\text{M}/\text{H}] = -0.15 \pm 0.34$ to be compared with our $[\text{Fe}/\text{H}] = -1.68 \pm 0.17$. Although our iron abundance is based on only 28 lines, we consider it robust and uncertainties in the adopted effective temperature, as discussed above, cannot bridge the about 1 dex difference with the Gaia DR3 metallicity. Also star Pristine_213.2814+14.8983 in the Venn et al. (2020) and Lucchesi et al. (2022) sample is an RR Lyr. It is in the Gaia DR3 catalogue, with an estimated metallicity from the Fourier decomposition of the G light curve of $[\text{M}/\text{H}] = -0.81 \pm 0.39$, while Lucchesi et al. (2022) derived a spectroscopic metallicity of $[\text{Fe}/\text{H}] = -1.95$ and Venn et al. (2020) derived $[\text{Fe}/\text{H}] = -2.64$. Although the two spectroscopic metallicities disagree, essentially because of the difference in effective temperature (6002 K in Lucchesi et al. 2022 and 5289 K in Venn et al. 2020), they are both at odds with the metallicity from the light curve.

The reason for these discrepancies is not entirely clear to us. The method used in Clementini et al. (2022) employs the empirical calibration found by Nemeč et al. (2013), that links the pulsation period and ϕ_{31} parameter of the G light curve Fourier decomposition to the metallicity of RR Lyrae. Looking at Figure 11 in Nemeč et al. (2013),

we note that the outliers are predominantly Blazhko¹² stars. Therefore, it is possible that these stars may be unrecognised Blazhko RR Lyrae. Another possibility could be that, although the RR Lyrae sample used by Nemeč et al. (2013) for the calibration is of very good quality, the number of calibrators (41) is not sufficient to provide a precise relation.

5.2 Stars not chemically analysed.

In this section we detail the properties of the non-analysed stars.

5.2.1 *Pristine_002.0937+22.6545*

According to Jayasinghe et al. (2018), this star is a detached eclipsing binary of Algol¹³ type with a period of 1.3535699 days and an amplitude of 0.35 mag. Watson et al. (2006) provide a period of 1.35357 days, maximum V magnitude of 14.74, and minimum V magnitude of 15.020. Heinze et al. (2018) classify as “dubious” and provide a period of 0.676723 days. The Gaia DR3 catalogue classifies this star as an eclipsing binary with a G amplitude of 0.279763 mag and a period of 0.6720462 days. Our Pristine photometry combined with Gaia photometry and parallax provides 5288./4.35/−1.87. Our spectra are compatible with that of a rapidly rotating K dwarf with a rotational velocity of the order of 70 km s^{−1}. The first spectrum shows a secondary peak, blended with the primary peak, shifted by 72.6 km s^{−1} to the red. The next exposure, taken 40 minutes after the first one, shows a single peak, albeit slightly asymmetric.

5.2.2 *Pristine_024.5944+25.4689*

This star is an eclipsing binary of W UMa type according to Jayasinghe et al. (2018) with a period of 0.3159093 days and an amplitude of 0.48 mag. A similar period (0.3159084000 days) is provided by Watson et al. (2006). Also Chen et al. (2018) classify it as an W UMa type eclipsing binary with a period of 0.31591 days and an amplitude of 0.49 mag. Also Tian et al. (2020), Heinze et al. (2018) and Marsh et al. (2017) provide an eclipsing binary classification and similar period and amplitude. This star is classified as an eclipsing binary with a period of 0.3159104 days and an amplitude in the G band of 0.519114 mag in the Gaia DR3 catalogue.

Our spectra show very wide lines implying a rotation in excess of 100 km s^{−1}. No H α absorption is visible, a weak emission is clearly visible. H β is also hardly detectable. The star is an SB2 binary, since the cross correlation functions show clearly two very wide peaks. The fact that the peaks are so wide make the radial velocity measurement uncertain. The large rotational velocity of both components can be explained by the short orbital period and synchronization of rotational and orbital periods.

¹² The Blazhko effect is a quasi-periodic modulation of the light curve of an RR Lyr star, first observed by Blažko (1907). Kovacs (2016) suggests that 40% to 50% of the fundamental mode pulsators in the Galaxy display the Blazhko effect. The percentage in the lower metallicity Magellanic Clouds is lower, at most 22%. This effect still lacks an explanation.

¹³ The star Algol (β Persei) is the prototype of this class of eclipsing binaries, the luminosity is almost constant except at eclipses, when it sharply drops, with a characteristic almost triangular shape.

5.2.3 *Pristine_029.3591+21.3783*

This star is a variable star (Drake et al. 2014; Heinze et al. 2018) and, in fact, an eclipsing binary of W UMa type with a period of 0.35 days (Marsh et al. 2017; Sun et al. 2020). It is classified in the Gaia DR3 catalogue as an eclipsing binary with a period of 0.3500455 days and an amplitude in the G band of 0.599029 mag. According to Sun et al. (2020), the two components have effective temperatures of 5614 K and 5637 K, and the masses are 1.35 M $_{\odot}$ and 0.34 M $_{\odot}$. The primary evolved in order to attain almost equal effective temperatures. The luminosities are 2.21 and 0.68 L $_{\odot}$. Our spectra show wide lines, compatible with this kind of stars. The cross correlation functions with a synthetic template show two very wide peaks, implying the star is an SB2 binary. The two 40 minute exposures, taken one after the other, show displacement of the peaks about 12 km s^{−1} for the primary and 31 km s^{−1} for the secondary. Also in this case, the rapid rotation of both stars can be explained by synchronisation of rotational and orbital periods.

5.2.4 *Pristine_034.7189+25.9539*

This star is a known eclipsing binary (Drake et al. 2014). According to Marsh et al. (2017), it is a contact binary system with a period of 0.3136680 days and amplitude of 0.307 mag, the depth of the eclipse is about 0.02 mag, and the effective temperature from the $g-r$ colour is 5792 K. The star is classified as an eclipsing binary in the Gaia DR3 catalogue with an amplitude in the G band of 0.41668 mag and a period of 0.3136690 days.

The spectrum is typical of a G-type dwarf that is rapidly rotating (about 180 km s^{−1}) and shows signs of emission in the Ca II H&K lines. Its metallicity is likely solar. We estimated $T_{\text{eff}} = 5908$ K and $\log g = 4.16$ dex from the $G_{BP}-G_{RP}$ colour and the Gaia parallax and G magnitude. Such a rapidly rotating G dwarf must be very young, which is consistent with a solar metallicity. The reason why this star has a CaHK photometry that implies a low metallicity is thus clear. The high rotational velocity is probably due to the synchronisation of rotational and orbital velocity. The cross correlation functions show two wide peaks, and the two exposures of about half an hour, taken one after the other, show a change of 7.5 km s^{−1} in the position of the primary peak, and 13.2 km s^{−1} for the secondary. The measurements are however uncertain due to the large width of the cross-correlation peaks.

5.2.5 *Pristine_109.8329+41.3782*

This star has no Gaia parallax, not even a geometrical distance. According to Heinze et al. (2018) the star is a distant eclipsing binary with a period of 1.053790 days and a 0.26 mag min-max variation. According to Jayasinghe et al. (2018) it has a period of 1.0538387 days and an amplitude of 0.21 mag and they classify it as a detached Algol-type system. The two spectra at our disposal show a slight shift in radial velocity over half an hour of the order of 200 m s^{−1}.

5.2.6 *Pristine_148.3782+53.0957*

This star is a known variable (Yao et al. 2015), with amplitude of variation of 0.19 mag and a period of 9.14013200 days. However Heinze et al. (2018) find a period of 27.580872 days, a factor of three larger, probably an alias of the shorter period, and a much smaller amplitude of variation, 0.09 mag. Tsantaki et al. (2022) compilation of radial velocities flags this star as a binary. Tian et al. (2020) report this star in their catalogue of LAMOST radial velocity variables

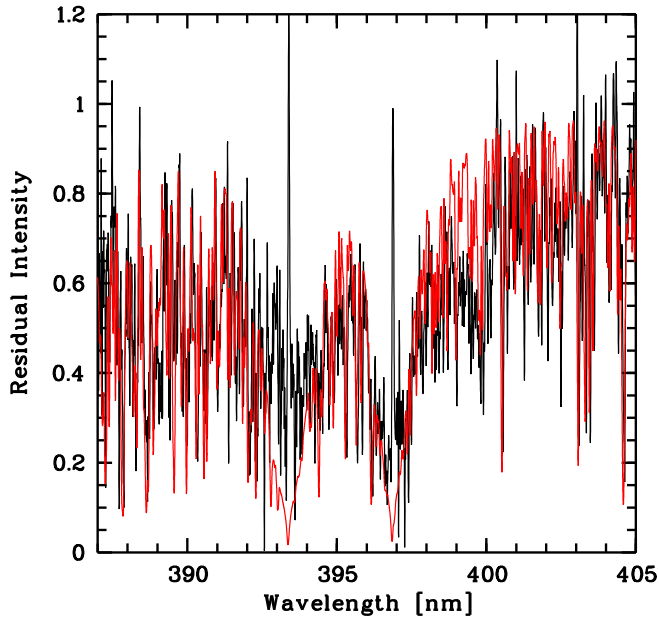


Figure 8. The Ca II H&K lines of Pristine_148.3782+53.0957, showing a strong emission. For display purposes the spectrum, sum of the two observed spectra, has been smoothed with a Gaussian with FWHM of 15 km s^{-1} . To guide the eye, the red line is a synthetic spectrum with $T_{\text{eff}}/\log g/[M/H]$ 4527/3.16/−1.5 and a rotational velocity of 26.5 km s^{-1} .

with one spectrum, providing a radial velocity of 9.9 km s^{-1} and another of 45.6 km s^{-1} . The LAMOST effective temperatures, surface gravities and metallicities are 5082,5902 ; 3.01, 4.36; −0.21, −0.35. Gaia DR2 has no variability flag for this star, and Gaia EDR3 provides an uncertainty in G of 1.8 mmag over 477 observations, of 6.6 mmag in G_{BP} over 53 observations and 5.1 mmag in G_{RP} over 54 observations. Gaia DR3 has finally identified the star as a variable. Our derived parameters from the Gaia photometry and parallaxes are $T_{\text{eff}}= 4527$ and $\log g= 3.16$. According to Gaia DR3 catalogue, this star is a RS CVn rotational variable with an amplitude of variation of 0.14391868 mag in the G band. No period is provided. Our spectra do not show any radial velocity variability. The spectrum is characterized by wide lines, that, if interpreted as rotation, imply a $v \sin i$ of 26.5 km s^{-1} . The star is probably slightly metal-poor, in Fig. 8 we show the Ca II H&K lines, characterised by a strong core emission, sign of vigorous chromospheric activity. For display purposes we plot in Fig. 8 a synthetic spectrum of metallicity −1.5, that is likely a lower limit to the metallicity of this star. The chromospheric activity, testified also by a strong $H\alpha$ emission, confirms the RS CVn classification for this star.

5.2.7 Pristine_163.9735+13.4823

According to Sun et al. (2020), this star is an eclipsing binary of W UMa type with a period of 0.32593 days. The two components have 5825 and 6123 K and the masses are 1.24 and $0.3 M_{\odot}$. The star is also classified as an eclipsing binary in the Gaia DR3 catalogue, with an amplitude of variation in the G band of 0.346752 mag and a period of 0.3259241 days. Although our spectra have a $S/N < 5$ at 550 nm, one can see very wide lines. If the luminosities provided by Sun et al. (2020) are correct ($1.56, 0.26 L_{\odot}$) it seems unlikely that we are seeing the secondary spectrum. In fact the cross-correlation function

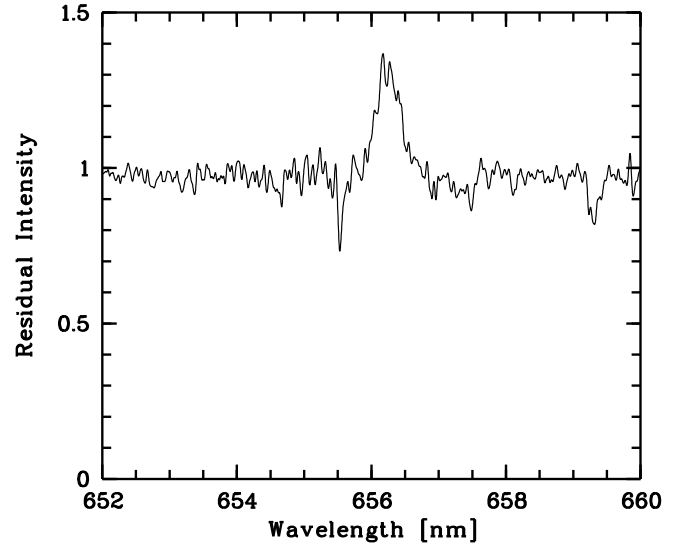


Figure 9. The $H\alpha$ emission in one of the two spectra of Pristine_326.5701+19.2445. For display purposes the spectrum has been smoothed with a Gaussian of 15 km s^{-1} FWHM.

shows a single very wide peak. The radial velocities measured from both our spectra are consistent within uncertainties.

5.2.8 Pristine_326.5701+19.2445

According to Jayasinghe et al. (2018) this star is a spotted star with variability induced by rotation, with a period of 4.5143809 days and an amplitude of 0.2 mag. The period provided by Watson et al. (2006) is 4.5241693000 days and the amplitude 0.191 mag. Chen et al. (2018) classify as a RS CVn star with a period of 4.5241693 days and an amplitude in g of 0.214 mag and 0.191 mag in r . Heinze et al. (2018) classify it as a Long Period variable and provide a period of 9.011580 days, that looks suspiciously like an alias of the 4.5 days period provided by the other catalogs. The star is also identified as a RS CVn star in the Gaia DR3 catalogue, with an amplitude of variation in the G band of 0.236 mag. No period is available. Our spectra show wide lines, implying a rotational velocity around 50 km/s. There is no evidence of radial velocity variation. There is no measurable flux on Ca II H&K, however, both spectra show an $H\alpha$ emission, shown in Fig. 9, that supports the classification as RS CVn.

5.2.9 Pristine_331.5576+27.2164

According to Jayasinghe et al. (2018), this star is an eclipsing binary of type W UMa type with a period of 0.3182321 days and an amplitude of 0.57 mag. Gaia DR3 catalogue classifies this star as an eclipsing binary with a G amplitude of 0.624458 mag and a period of 0.3182328 days. Our spectra show very wide lines, expected for this kind of star. The star is an SB2 spectroscopic binary. The cross-correlation functions in Fig. 10 show two wide peaks (due to the high rotational velocity), and it is clear that the two peaks move between the two poses. A very sharp peak appears at -24.78 km s^{-1} . This is the Sun, as this spectrum was taken in twilight, while the next one was already in the astronomical night. Such peaks in the cross-correlation functions of spectra taken at twilight are regularly seen in our spectra. This is due to the fact that the data reduction software does not subtract the solar spectrum, visible in the sky fibre, but just

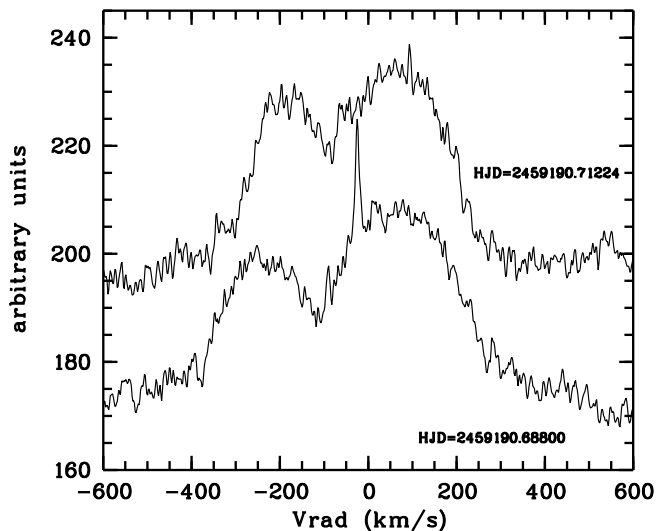


Figure 10. Cross correlation functions for Pristine_331.5576+27.2164. The sharp peak at -24.78 km s^{-1} is due to the solar spectrum, since the observations were taken in twilight.

the mean flux. For stars with such wide cross-correlation peaks this is not a problem for the radial velocity measurement.

5.2.10 Pristine_333.2010+09.6132

According to Jayasinghe et al. (2018) this star is detached Algol-like eclipsing binary with a period of 9.61327744 days and a magnitude amplitude of 0.32 mag. Heinze et al. (2018) classify it as “dubious” and provide a period of 3.199939. No variability flag is provided in the Gaia DR3 catalogue. Our spectra allow us to clearly identify Pristine_333.2010+09.6132 as an SB2 system. The cross-correlation function with a synthetic template is clearly double peaked, and there is sizeable difference in the radial velocities between the two exposures, especially for the secondary. There is hardly any signal around the Ca II H&K lines.

5.2.11 Pristine_333.2117+20.1267

Numerous sources agree that this star is a variable with a period of around 0.35 days (see e.g. Watson et al. 2006; Drake et al. 2014; Sesar et al. 2017; Chen et al. 2018; Heinze et al. 2018). Watson et al. (2006) and Chen et al. (2018) classify it as an eclipsing binary of W UMa type, while Sesar et al. (2017) classify it as an RR-Lyr variable. The star is classified as an eclipsing binary also in the Gaia DR3 catalogue, with a period of 0.3549904 days and a G amplitude of 0.593793 mag. The lines in the spectrum are very wide, implying a high rotational velocity, which can be compatible with a W UMa type eclipsing variable, but not with an RR Lyr. The cross-correlation peaks are very wide and there is a considerable radial velocity difference between the two exposures. As for other similar stars, the high rotational velocity of both stars is likely due to synchronisation of rotational and orbital periods.

5.2.12 Pristine_348.1325+11.2206

The star has been identified as an eclipsing binary candidate with a period of 1.75 days by Ferreira Lopes et al. (2015). Both Gaia DR2

and DR3 have no variability flag for this star. The LAMOST DR7 catalogue (Luo et al. 2022) provides $T_{\text{eff}} = 5327 \text{ K}$, $\log g = 3.175$, $[\text{Fe}/\text{H}] = -0.744$, and a radial velocity of 27.58 km s^{-1} . Our spectra show a clear double peak, although the stars are separated by little more than 1 km s^{-1} . The double system of lines can be also appreciated by visual inspection of the spectra. Our radial velocities are very different from that of LAMOST.

6 DISCUSSION AND CONCLUSIONS

It is certainly dismaying that out of the 19 observed stars only 7 could be subject to our standard analysis, and only two of these were found to be extremely metal-poor. It is however instructive to note how all these stars are indeed extreme, in the sense that there are reasons that make their Ca II H&K photometry “weak”. For the stars not analysed the main reason is the photometric variability. In the second place, SB2 binaries contribute a large fraction of these “weak” Ca II H&K stars (8 out of 19). Fast rotators and active stars also have “weak” Ca II H&K. These reasons explain all the stars not analysed.

Looking at the stars that have been analysed two are photometric variables, Pristine_328.6116+20.3914 and Pristine_335.8411+09.0218, and so it is not surprising that, although metal-poor, they are not as metal-poor as expected from the Pristine photometry. We consider Pristine_009.1439+15.7850, Pristine_159.5695+57.1688 and Pristine_328.6116+20.3914 metal-poor, although the first two stars are not quite as metal-poor as expected. Pristine_008.1724+21.8215 and Pristine_355.2747+26.4757 are significantly more metal-rich than expected, but we have no obvious reason why the metallicity estimate based on Pristine and SDSS photometry failed.

It is interesting to consider if some of the variable stars could have been discarded using the information in the Gaia DR3 catalogue. Of the 14 photometrically variable stars in our sample 11 are correctly flagged as VARIABLE in the Gaia DR3 catalogue, however three are not. Fernández-Alvar et al. (2021) suggested using the parameter

$$\sigma_{\text{flux}} = \frac{\sqrt{\text{phot_g_n_obs}}}{\text{phot_g_mean_flux_over_error}} \quad (1)$$

to clean a sample from photometrically variable stars. Since the flux error provided in the Gaia catalogue is the error in the mean, i.e. the standard deviation of the flux measurements divided by the square root of the number of measurements, this amounts to using the relative flux error, where the error is simply the standard deviation. If we select only the stars with $\sigma_{\text{flux}} < 0.015$ we still select two eclipsing variables: Pristine_333.2010+09.6132 and Pristine_348.1325+11.2206. At the same time, Pristine_328.6116+20.3914 and Pristine_335.8411+09.0218 that are variables, but could not be analysed, are removed from the sample. Thus, a cut of this kind can be expected to remove about 85% of the photometric variables from the sample.

With respect to the expected contaminants we did not find any young, chromospherically active stars. The only two stars with clear chromospheric activity are Pristine_148.3782+53.0957 and Pristine_326.5701+19.2445 that are RS CVn binaries. In this case the chromospheric activity is enhanced by the binary interaction and is not a sign of young age. In fact the primary is a giant or sub-giant, thus they cannot be very young, because it is necessary for the primary to have evolved. We have no clear explanation for the lack of young stars in our sample. One possibility is that only the most active stars have strong enough emission to affect the Pristine photometry, and these stars are relatively rare. This hypothesis needs to be tested

with a larger sample of stars with Pristine photometric metallicity below -3.5 .

The results of this investigation are interesting in the prospect of extensively using Pristine photometry in large spectroscopic surveys, like WEAVE (Jin et al., MNRAS, submitted), to select metal-poor stars. The final lesson to be taken for this sample is that, in order to construct samples with reliable metallicity estimates, one should always remove variable stars, possibly by cross-matching with catalogs that contain variability information. In any case, when extracting the candidates at the extremely low metallicity, one should always expect a few catastrophic mistakes.

ACKNOWLEDGEMENTS

We are grateful to Nadine Manset of CFHT for her help in the interpretation of ESPaDOnS data. We gratefully acknowledge support from the French National Research Agency (ANR) funded project “Pristine” (ANR-18-CE31-0017). PJ acknowledges financial support from the Swiss National Foundation. Z.Y. acknowledge funding from the Agence Nationale de la Recherche (ANR project ANR-18-CE31-0017). Based on observations obtained with MegaPrime/MegaCam, a joint project of CFHT and CEA/DAPNIA, at the Canada-France-Hawaii Telescope (CFHT) which is operated by the National Research Council (NRC) of Canada, the Institut National des Science de l’Univers of the Centre National de la Recherche Scientifique (CNRS) of France, and the University of Hawaii. The observations at the Canada-France-Hawaii Telescope were performed with care and respect from the summit of Maunakea which is a significant cultural and historic site. This work has made use of data from the European Space Agency (ESA) mission *Gaia* (<https://www.cosmos.esa.int/gaia>), processed by the *Gaia* Data Processing and Analysis Consortium (DPAC, <https://www.cosmos.esa.int/web/gaia/dpac/consortium>). Funding for the DPAC has been provided by national institutions, in particular the institutions participating in the *Gaia* Multilateral Agreement.

DATA AVAILABILITY

The abundance data derived in this paper shall be provided through the Centre de Données astronomiques de Strasbourg. The ESPaDOnS spectra are available through the Canadian Astronomy Data Centre.

REFERENCES

Abbas M. A., Grebel E. K., Martin N. F., Burgett W. S., Flewelling H., Wainscoat R. J., 2014, *MNRAS*, **441**, 1230
 Aguado D. S., et al., 2019, *MNRAS*, **490**, 2241
 Belokurov V., Erkal D., Evans N. W., Koposov S. E., Deason A. J., 2018, *MNRAS*, **478**, 611
 Blažko S., 1907, *Astronomische Nachrichten*, **175**, 325
 Boller T., Freyberg M. J., Trümper J., Haberl F., Voges W., Nandra K., 2016, *A&A*, **588**, A103
 Bonifacio P., 1989, Technical report, NORMA-A Program for the Normalisation of Spectra. Dipartimento di Astronomia dell’ Università degli Studi di Trieste
 Bonifacio P., et al., 2019, *MNRAS*, **487**, 3797
 Bonifacio P., et al., 2021, *A&A*, **651**, A79

Boulade O., et al., 2003, in Iye M., Moorwood A. F. M., eds, Society of Photo-Optical Instrumentation Engineers (SPIE) Conference Series Vol. 4841, Instrument Design and Performance for Optical/Infrared Ground-based Telescopes. pp 72–81, doi:10.1117/12.459890
 Caffau E., Ludwig H. G., Steffen M., Freytag B., Bonifacio P., 2011, *Sol. Phys.*, **268**, 255
 Caffau E., et al., 2017, *Astronomische Nachrichten*, **338**, 686
 Caffau E., et al., 2020, *MNRAS*, **493**, 4677
 Castelli F., Kurucz R. L., 2003, in Piskunov N., Weiss W. W., Gray D. F., eds, Symposium of the International Astronomical Union Vol. 210, Modelling of Stellar Atmospheres. p. A20 (arXiv:astro-ph/0405087)
 Cayrel R., et al., 2004, *A&A*, **416**, 1117
 Chen X., Deng L., de Grijs R., Wang S., Feng Y., 2018, *ApJ*, **859**, 140
 Chen X., Wang S., Deng L., de Grijs R., Yang M., Tian H., 2020, *ApJS*, **249**, 18
 Clementini G., et al., 2022, arXiv e-prints, p. arXiv:2206.06278
 Doi M., et al., 2010, *AJ*, **139**, 1628
 Donati J. F., Semel M., Carter B. D., Rees D. E., Collier Cameron A., 1997, *MNRAS*, **291**, 658
 Donati J. F., Catala C., Landstreet J. D., Petit P., 2006, in Casini R., Lites B. W., eds, Astronomical Society of the Pacific Conference Series Vol. 358, Solar Polarization 4. p. 362
 Drake A. J., et al., 2013, *ApJ*, **763**, 32
 Drake A. J., et al., 2014, *ApJS*, **213**, 9
 Fernández-Alvar E., et al., 2021, *MNRAS*, **508**, 1509
 Ferreira Lopes C. E., Dékány I., Catelan M., Cross N. J. G., Angeloni R., Leão I. C., De Medeiros J. R., 2015, *A&A*, **573**, A100
 Feuillet D. K., Feltzing S., Sahlholdt C. L., Casagrande L., 2020, *MNRAS*, **497**, 109
 François P., et al., 2007, *A&A*, **476**, 935
 Gaia Collaboration et al., 2016, *A&A*, **595**, A1
 Gaia Collaboration et al., 2022, arXiv e-prints, p. arXiv:2208.00211
 González Hernández J. I., et al., 2008, *A&A*, **480**, 233
 Greer P. A., Payne S. G., Norton A. J., Maxted P. F. L., Smalley B., West R. G., Wheatley P. J., Kolb U. C., 2017, *A&A*, **607**, A11
 Gustafsson B., Edvardsson B., Eriksson K., Jørgensen U. G., Nordlund Å., Plez B., 2008, *A&A*, **486**, 951
 Halbwachs J.-L., et al., 2022, arXiv e-prints, p. arXiv:2206.05726
 Haywood M., Di Matteo P., Lehnert M. D., Snaith O., Khoperskov S., Gómez A., 2018, *ApJ*, **863**, 113
 Heinze A. N., et al., 2018, *AJ*, **156**, 241
 Heiter U., et al., 2021, *A&A*, **645**, A106
 Helmi A., Babusiaux C., Koppelman H. H., Massari D., Veljanoski J., Brown A. G. A., 2018, *Nature*, **563**, 85
 Ishigaki M. N., Chiba M., Aoki W., 2012, *ApJ*, **753**, 64
 Ishigaki M. N., Aoki W., Chiba M., 2013, *ApJ*, **771**, 67
 Jayasinghe T., et al., 2018, *MNRAS*, **477**, 3145
 Kepler S. O., et al., 2016, *MNRAS*, **455**, 3413
 KIELTY C. L., et al., 2021, *MNRAS*, **506**, 1438
 Koposov S. E., et al., 2011, *ApJ*, **736**, 146
 Kordopatis G., et al., 2022, arXiv e-prints, p. arXiv:2206.07937
 Kovacs G., 2016, Communications of the Konkoly Observatory Hungary, **105**, 61
 Kurucz R. L., 2005, Memorie della Societa Astronomica Italiana Supplementi, **8**, 14
 Lardo C., et al., 2021, *MNRAS*, **508**, 3068
 Lindegren L., et al., 2021, *A&A*, **649**, A4
 Lodders K., Palme H., Gail H. P., 2009, *Landolt BÖrstein*, **4B**, 712
 Lombardo L., et al., 2021, *A&A*, **656**, A155
 Lombardo L., et al., 2022, *A&A*, **665**, A10
 Lucchesi R., et al., 2022, *MNRAS*, **511**, 1004
 Luo A. L., Zhao Y. H., Zhao G., et al. 2022, VizieR Online Data Catalog, p. V/156
 Marsh F. M., Prince T. A., Mahabal A. A., Bellm E. C., Drake A. J., Djorgovski S. G., 2017, *MNRAS*, **465**, 4678
 Martínez C. I., Mauas P. J. D., Buccino A. P., 2022, *MNRAS*, **512**, 4835
 Mashonkina L., Jablonka P., Pakhomov Y., Sitnova T., North P., 2017, *A&A*, **604**, A129

- 1
2 Masseron T., et al., 2014, [A&A](#), 571, A47
3 Naidu R. P., Conroy C., Bonaca A., Johnson B. D., Ting Y.-S., Caldwell N.,
4 Zaritsky D., Cargile P. A., 2020, [ApJ](#), 901, 48
5 Nemeec J. M., Cohen J. G., Ripepi V., Derekas A., Moskalik P., Sesar B.,
6 Chadid M., Bruntt H., 2013, [ApJ](#), 773, 181
7 Press W. H., Teukolsky S. A., Vetterling W. T., Flannery B. P., 1992, Numerical
8 recipes in FORTRAN. The art of scientific computing
9 Randich S., Giampapa M. S., Pallavicini R., 1994, [A&A](#), 283, 893
10 Samus' N. N., Kazarovets E. V., Durlevich O. V., Kireeva N. N., Pastukhova
11 E. N., 2017, [Astronomy Reports](#), 61, 80
12 Sbordone L., Caffau E., Bonifacio P., Duffau S., 2014, [A&A](#), 564, A109
13 Schlafly E. F., Finkbeiner D. P., 2011, [ApJ](#), 737, 103
14 Sesar B., et al., 2013, [AJ](#), 146, 21
15 Sesar B., et al., 2017, [AJ](#), 153, 204
16 Starkenburg E., et al., 2017, [MNRAS](#), 471, 2587
17 Starkenburg E., et al., 2018, [MNRAS](#), 481, 3838
18 Sun W., Chen X., Deng L., de Grijs R., 2020, [ApJS](#), 247, 50
19 Tian Z., et al., 2020, [ApJS](#), 249, 22
20 Tonry J., Davis M., 1979, [AJ](#), 84, 1511
21 Tsantaki M., et al., 2022, [A&A](#), 659, A95
22 Venn K. A., Tolstoy E., Kaufer A., Skillman E. D., Clarkson S. M., Smartt
23 S. J., Lennon D. J., Kudritzki R. P., 2003, [AJ](#), 126, 1326
24 Venn K. A., et al., 2020, [MNRAS](#), 492, 3241
25 Watson C. L., Henden A. A., Price A., 2006, Society for Astronomical Sciences
26 Annual Symposium, 25, 47
27 Yao X., et al., 2015, [AJ](#), 150, 107

28
29
30
31
32
33
34
35
36
37
38
39
40
41
42
43
44
45
46
47
48
49
50
51
52
53
54
55
56
57
58
59
60
This paper has been typeset from a $\text{\TeX}/\text{\LaTeX}$ file prepared by the author.

RÉSUMÉ

Ce travail de thèse présente plusieurs études qui utilisent la spectroscopie à haute résolution pour déterminer les propriétés chimiques des différentes populations stellaires de la Voie Lactée.

Le document est structuré comme suit :

Le premier chapitre de la thèse, divisée en 3 sections, est une introduction générale à la structure de la Voie lactée et à ses populations stellaires, suivie d'une partie décrivant les différentes méthodes utilisées pour mesurer les abondances chimiques des étoiles. La première section décrit les différents scénarios concernant la structure et la formation de la Voie Lactée, en présentant en particulier les découvertes les plus récentes. La deuxième section introduit les concepts physiques de base nécessaires et les objectifs des études présentes dans ce travail de thèse. La troisième section décrit les méthodes utilisées dans l'analyse des données spectroscopiques.

Le deuxième chapitre présente les travaux effectués dans le cadre du projet MINCE. La première étude concerne l'analyse de la composition chimique d'un échantillon d'étoiles géantes jeunes qui ont été découvertes par hasard au cours des premières missions d'observations du projet MINCE. J'ai déterminé les paramètres stellaires, analysé les spectres, mesuré les vitesses de rotation de ces étoiles et comparé les résultats aux modèles théoriques, en reportant tous ces résultats dans un article. La deuxième étude présente les résultats obtenus par l'analyse du premier échantillon d'étoiles propres au projet MINCE. J'ai contribué à l'analyse d'une partie des spectres stellaires de ce tout premier jeu de spectres MINCE.

Le troisième chapitre porte sur les résultats d'une analyse faite dans le contexte du projet CERES. La première partie de ce travail présente une détermination détaillée de la composition chimique de l'étoile RAVE J110842.1-715300, dont le but est de savoir si cette étoile provient de l'amas globulaire Omega Centauri. Ma contribution porte sur la détermination des paramètres stellaires de cette étoile. La deuxième étude menée dans le contexte de ce projet CERES est constituée de l'analyse d'un échantillon d'étoiles. J'ai déterminé les paramètres stellaires, calculé les modèles d'atmosphère et les abondances chimiques, et écrit l'article.

Le quatrième chapitre porte sur un travail fait dans le contexte du projet "High-speed stars" s'intéressant aux étoiles à grande vitesse transversales héliocentriques (≥ 500 km/s). La première étude porte sur le suivi spectroscopique à haute résolution de deux étoiles jeunes et pauvres en métaux de l'échantillon de Caffau et al. (2020), afin de déterminer si ces étoiles sont des "blue stragglers". J'ai obtenu et analysé les spectres UVES de ces deux étoiles. Les résultats ne sont pas encore publiés. La deuxième étude concerne une analyse détaillée de deux étoiles à grande vitesse observées avec le spectrographe HDS au télescope Subaru. Pour cette étude, j'ai déterminé l'abondance du Carbone.

Le cinquième chapitre présente les résultats obtenus à partir de l'analyse d'un échantillon d'étoiles sélectionnées au moyen de la photométrie de PRISTINE. La première étude porte sur la détermination de la composition chimique d'un échantillon d'étoiles qui ont pu être enrichies par les éjecta de l'explosion de supernovae à instabilité de paires. Mon travail a consisté à sélectionner les candidats les plus intéressants, puis d'effectuer une mission d'observation avec le spectrographe SOPHIE à l'Observatoire de la Haute Provence (OHP). La deuxième étude présente les résultats préliminaires de la détermination de la composition chimique d'un échantillon d'étoiles Pristine sélectionnées comme extrêmement pauvres en métaux. Mon travail a porté sur la détermination des paramètres stellaires et le calcul des abondances chimiques. Un article est en préparation.

Le sixième chapitre présente les conclusions de ce travail de thèse et apporte quelques réflexions sur les projets à venir.

MOTS CLÉS

étoiles de faible métallicité, structure et évolution de la Galaxie, populations stellaires, nucleosynthèse, spectroscopie stellaire, abondances chimiques

ABSTRACT

This thesis project presents several studies that are focused on the investigation of the chemical properties of different stellar populations in the Milky Way by means of high-resolution spectroscopy.

The thesis is structured as follows:

The first chapter is an introduction to the thesis project, and is divided into three sections. The first section describes the structure and formation scenarios of the Milky Way, in particular by referring to the most recent discoveries. The second section introduces the basic concepts and objectives of the studies presented in this thesis work. The third section describes the methods used to analyse the spectroscopic data.

The second chapter presents the studies carried out in the context of the MINCE project. The first study is devoted to the chemical analysis of a sample of young giant stars that was serendipitously discovered during the first MINCE observations. My contribution in this work was to derive the stellar parameters, analyse the spectroscopic data, measure the rotational velocities, compare the results with theoretical models and write the paper. The second study presents the results obtained from the analysis of the first sample of MINCE stars. In this work, I contributed to the analysis of some of the stars in the sample.

The third chapter presents the results obtained in the context of the CERES project. The first study presents a detailed chemical analysis of the star RAVE J110842.1-715300, with the aim of understanding whether or not it originated in the Omega Centauri globular cluster. My contribution in this study was to derive the stellar parameters of the star. The second study presents the results obtained for the CERES star sample. My contribution was to derive the parameters, compute model atmospheres, measure the chemical abundances, and write the paper.

The fourth chapter presents the results obtained in the context of the High-speed stars project. The first study reports the results obtained from the high-resolution follow-up of two young and metal-poor stars in the sample of Caffau et al. (2020), to check whether they are blue stragglers or not. My contribution in this study was to obtain the high-resolution observations with UVES and to analyse the data. These results have not been published yet. The second study presents a detailed analysis of two high-speed stars observed with Subaru. In this study I was involved in the C abundance determination.

The fifth chapter presents the results obtained from the chemical analysis of samples of stars selected using the Pristine photometry. The first study presents the chemical analysis of a sample of metal-poor stars that may have been enriched by the explosion of pair instability supernovae. My contribution was to select promising candidates and observe them with the SOPHIE spectrograph at Observatoire de la Haute Provence (OHP) in visitor mode. The second study presents the preliminary results obtained from the chemical analysis of a sample of Pristine extremely metal-poor candidates. My contribution in this study was to derive the stellar parameters and the chemical abundances. The paper is in preparation.

The sixth chapter concludes the thesis and gathers final reflections and future projects.

KEYWORDS

stars of low metallicity, structure and evolution of the Galaxy, stellar populations, nucleosynthesis, stellar spectroscopy, chemical abundances